

# Brno University of Technology

Vysoké učení technické v Brně

Faculty of Mechanical Engineering

Energy Institute

Fakulta strojního inženýrství

Energetický ústav

## Flow and deposition of aerosols in models of human airways

Habilitation Thesis

Habilitační práce

**Author: Ing. František Lízal, Ph.D.**

Autor práce

Brno 2019



## ABSTRACT

The improved knowledge of flow and deposition of aerosols in human lungs is necessary for both more efficient inhaled therapy and reduction of toxicological effects of harmful particles. Due to the recent fast development in the field of modelling of human airways, it is possible to predict overall and regional lung deposition fractions with reasonably good precision. Computational simulations can be performed on realistic geometries of the tracheobronchial tree. There are experimental data available for validation of calculated velocity fields within human lungs and deposition of inhaled particles.

The habilitation thesis documents author's contribution to the current knowledge in the following areas: 1) physical airway model preparation and production, 2) experimental techniques applicable to human lungs and their replicas, 3) research of inhaled fibres in a lung replica, and 4) computational simulations of fluid and particle flow. All the topics are closely related, and they are driven by an effort to gradually increase reliability of computational simulations on the basis of conscientiously performed experiments.

The work evidences that progress in the experimental and computational modelling of inhaled particles depends on interdisciplinary collaboration with a significant and irreplaceable contribution of mechanical engineers. An appealing feature of this research is the fact that it is directly related to human health, and hence it is rewarded by a public recognition of its social benefit.

## ABSTRAKT

Kvalitnější poznání mechanismů proudění a usazování aerosolů v lidských plicích je nezbytné jak pro účinnější inhalační léčbu, tak pro snížení účinků vdechování škodlivých částic. Díky současnému rychlému vývoji v oblasti modelování lidských dýchacích cest je možné s velmi dobrou přesností předpovídat celkovou i regionální depoziční frakci. Počítačové simulace lze dnes provádět na realistických geometriích tracheobronchiálního stromu. Jsou k dispozici i experimentální výsledky vhodné pro validaci vypočítaných rychlostních polí v plicích a množství usazených vdechnutých částic.

Habilitační práce prokazuje autorův přínos k současnému poznání v následujících oblastech: 1) příprava a výroba modelu dýchacích cest, 2) experimentální techniky použitelné v lidských plicích a jejich modelech, 3) výzkum inhalovaných vláken v modelech plic, a 4) počítačové simulace proudění tekutiny a částic. Všechna témata spolu úzce souvisejí a jsou motivována snahou postupně zlepšit spolehlivost počítačových simulací pomocí pečlivě prováděných experimentů.

Předložená práce dokazuje, že vývoj v oblasti experimentálního a počítačového modelování inhalovaných částic závisí na mezioborové spolupráci s výrazným a nezastupitelným příspěvkem strojního inženýrství. Nesmírně přitažlivou vlastností tohoto výzkumu je fakt, že přímo souvisí s lidským zdravím, což je logicky odměněno všeobecným uznáním společenské prospěšnosti

**Acknowledgement:**

I would like to express my thanks to my current or former colleagues Jan Jedelsky, Miroslav Jicha, Jakub Elcner, Árpád Farkas, and Miloslav Belka who were an invaluable asset to this work. I would also like to express my gratitude to my wife Elena for her support and intelligible explanations of medical topics related to the respiratory system; and my kids Eliska, Matous, Dominik and Anna for inspiring me with their perpetual enthusiasm, and patience during my work on this thesis.

# CONTENTS

Abstract .....	3
Abstrakt.....	3
Contents .....	5
1. Introduction.....	7
2. Aerosols .....	8
2.1. Terminology related to inhalable particles.....	8
2.2. Particle and aerosol properties .....	10
2.3. Particle deposition mechanisms .....	14
2.4. Aerosol – health interactions .....	15
3. Respiratory system.....	17
3.1. Airway anatomy .....	18
3.2. Lung clearance mechanisms .....	18
4. Modelling and measurement of the aerosol-airway interactions.....	19
4.1. Experimental techniques and their application.....	19
4.2. Description of the modelling approaches.....	20
4.3. Deposition of fibers in human lungs.....	26
5. Conclusions and future work .....	26
Nomenclature .....	28
References to the commentary.....	30
The core of the habilitation thesis – the scientific papers.....	33



# 1. INTRODUCTION

People have been aware of the effect of inhaled particles on human health since time immemorial. The reason is obvious—the respiratory system is a straight route to the bloodstream. Accordingly, it represents a great opportunity for medical treatment using inhaled aerosols, as the onset of the effect of inhaled pharmaceuticals is virtually immediate (Patton and Byron, 2007). At the same time, the airways represent a dangerous gate for harmful and toxic particles (Pope and Dockery, 2006). Hence, regardless of their purposes, both pharmacists and toxicologists need to know the fate of inhaled particles in the human respiratory system.

Understanding the mechanics and consequent health effects of inhaled particles is a complex task that requires collaboration of physicians, engineers, pharmacists, mathematicians, chemists, and programmers. It is evident that communication between experts from various disciplines challenges all its participants. Despite the decades of research in the field, there remains a gap between these communities and the transformation of knowledge between disciplines flounders due to the differences in terminology and the way of thinking.

The contribution of mechanical engineering to the research of aerosol transport is substantial, and the development of the field will undoubtedly gain from the engineering approach in the future as well. This habilitation thesis covers specifically these four topics: 1) physical airway model preparation and production, 2) experimental techniques applicable to human lungs and their replicas, 3) measurements of inhaled fibres in a lung replica, and 4) numerical calculations of fluid and particle flow. All the topics are closely related, and they are driven by the effort to gradually increase reliability of computational fluid dynamics (CFD) on the basis of conscientiously performed experiments and simulations.

It is generally accepted that CFD will bring detailed insight and improved predictions of the fate of inhaled particles, provided the method is indubitably verified and validated. The area of expertise of the author lies particularly in the experimental methods which form the basis for the CFD either as boundary conditions or as a validation tool. Hence, this habilitation thesis presents the current state-of-the-art in the area of experimental methods applicable in the field. It should help the readers coming not only from engineering but also from medical and pharmaceutical communities understand the principles and form realistic expectations regarding the achievable results and their precision.

The core of this thesis is composed of eleven scientific papers, published in impacted journals by the author and his co-workers, divided into the four above mentioned thematic groups. As it was presupposed that the readers of the papers were familiar with several topics, which might not be known to the readers of this text, an introductory commentary is included to expound the topics of aerosols, the respiratory system, and basic approaches to the modelling of human airways in the extent that is necessary to understand the specific problems described in the papers.

## 2. AEROSOLS

The term *aerosol* can be in the simplest way described as a suspension of liquid or solid particles in a gas. Hinds (1999) adds that: “Aerosols are usually stable for at least a few seconds and in some cases may last a year or more. The term *aerosol* includes both the particles and the suspending gas, which is usually air. Particle size ranges from about 0.002 to more than 100  $\mu\text{m}$ .” This definition is in contrast to the popularly used meaning of the word aerosol only as a product of pressurized spray-cans. The broader definition proposed by Hinds, and accepted within this thesis, encompasses phenomena such as smoke, fog, smog, dust, mist, or fume. Several examples of aerosol particles together with a representation of their sizes can be seen at Fig. 1.

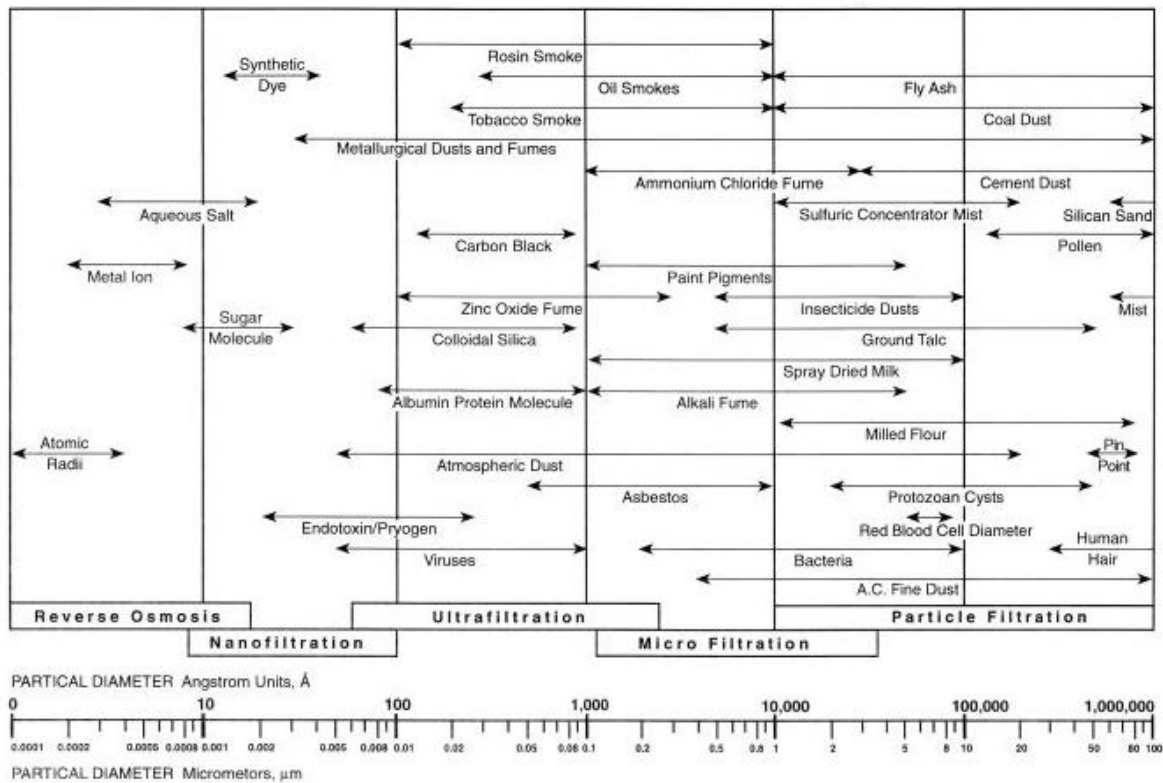


Fig. 1 Particle size ranges. Source: (APEC, 2018)

### 1.1. Terminology related to inhalable particles

As this thesis focuses on the interaction of aerosols with the human respiratory system, it is worth introducing the terminology developed by communities dealing with inhalable particles. Definitions of inhalation-related fractions were introduced in the field of occupational hygiene, in particular, within the European Union (EU), by the European Committee for Standardization (CEN) (CEN, 1993):

- Inhalable fraction – the mass fraction of total airborne particles which is inhaled through the nose and mouth.
- Extrathoracic fraction – the mass fraction of inhaled particles failing to penetrate beyond the larynx.
- Thoracic fraction – the mass fraction of inhaled particles penetrating beyond the larynx.

- Respirable fraction – the mass fraction of inhaled particles penetrating to the unciliated airways.

Apparently, particle dimensions were not mentioned in the definitions. The reason is that the ability of the particle to penetrate into the respiratory system is not an exclusive function of the particle size but also a function of the wind velocity and direction. Detailed discussion on these indicators was published by (Brown et al., 2013).

Other important definitions come from atmospheric/ambient air quality measurement community. In the EU, the Air Quality Framework Directive (AQFD) and its daughter directives have established air quality limit values for (besides others) particulate matter (PM). The Directive 2008/50/EC (CEC, 2008) defines two classes:

“ ‘PM-10’ shall mean particulate matter which passes through a size selective inlet as defined in the reference method for the sampling and measurement of PM-10, EN 12341, with a 50 % efficiency cutoff at 10  $\mu\text{m}$  aerodynamic diameter;”

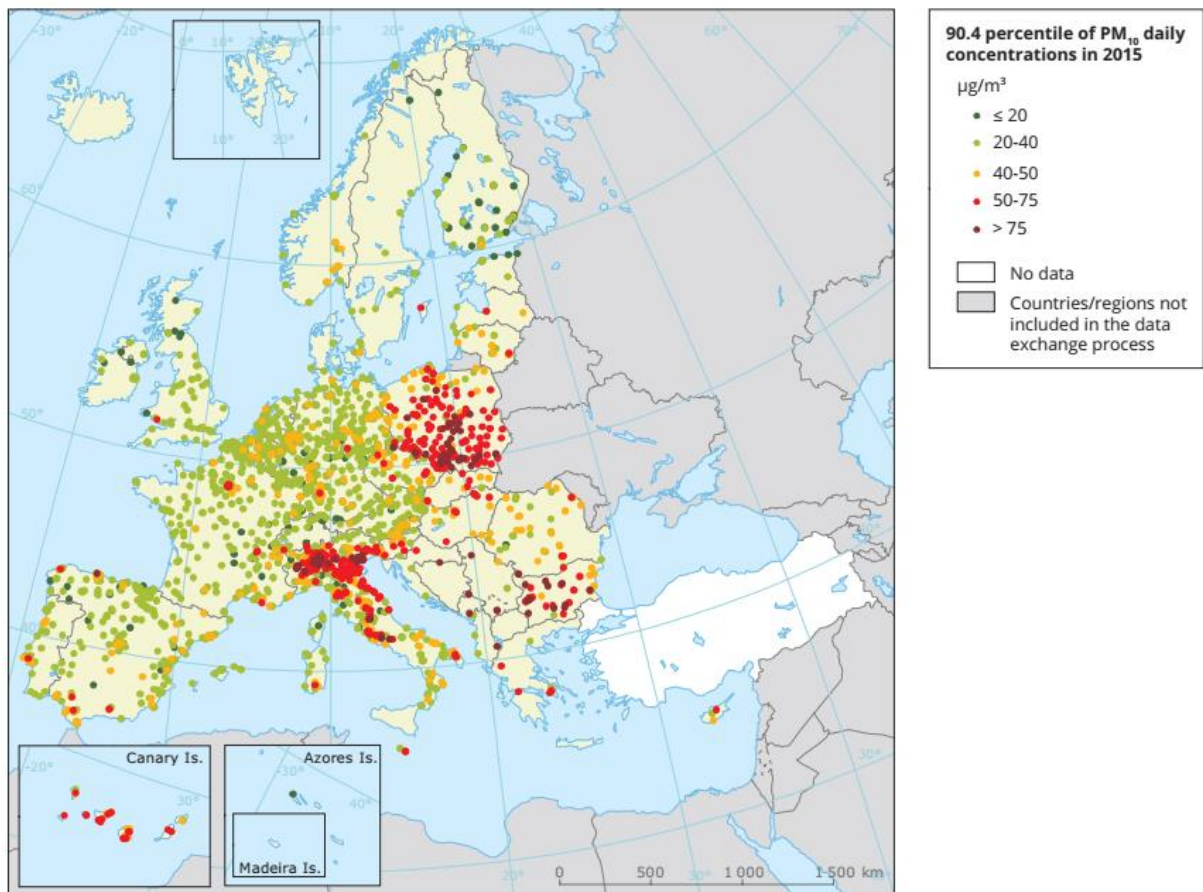


Fig. 2 „Observed concentrations of PM-10 in 2015. The map shows the 90.4 percentile of the PM-10 daily mean concentrations, representing the 36th highest value in a complete series. It is related to the PM-10 daily limit value, allowing 35 exceedances of the 50  $\mu\text{g}/\text{m}^3$  threshold over 1 year. The red and dark red dots indicate stations with concentrations above this daily limit value.“ Source: (EEA, 2017)

“ ‘PM-2.5’ shall mean particulate matter which passes through a size selective inlet as defined in the reference method for the sampling and measurement of PM-2.5, EN 14907, with a 50 % efficiency cutoff at 2.5  $\mu\text{m}$  aerodynamic diameter; “

Said more simply, the PM-10 (see Fig. 2) are ambient particles smaller than 10  $\mu\text{m}$ , and PM-2.5 are particles smaller than 2.5  $\mu\text{m}$ . These boundaries were selected with regard to the hypothetical health effects. The PM-10 fraction is supposed to enter the respiratory system, while PM-2.5 can reach lower respiratory airways. Particles smaller than 10  $\mu\text{m}$  are sometimes called thoracic particles, particles in the class of PM-2.5 are called fine particles. The particles in sizes within 2.5 and 10  $\mu\text{m}$  are then referred to as coarse particles (Kulkarni et al., 2011). By analogy, PM-1 and even PM-0.1 fractions were defined; however, these are used less frequently.

It must be emphasized, that premature judging on the health effects of ambient pollution just on the basis of PM-10 and PM-2.5 values would be simplifying. First, the true deposition site of an inhaled particle is also a function of the breathing pattern, size and shape of the airways, and several other factors. It means that the real exposure is highly individual. Second, the classes defined by the limits of 10 and 2.5  $\mu\text{m}$  are too coarse. The behaviour of 2.6 and 10  $\mu\text{m}$  particles is different, and it is even more distinct from, e.g. 100nm particles, which are, however, included in both the classes (the smaller class is always included in the upper class, such as PM-2.5 is included in PM-10). Third, real health effects naturally depend on the chemical composition of aerosol. The discussion on the drawbacks of PM and its definition could continue, especially concerning nanoparticles (Schmid and Stoeger, 2016). However, as PM values are well-established measure within the emission monitoring and regulation system, and correlations between the PM and increased morbidity and mortality in adults and children have been proved by many studies, e.g. (Hime et al., 2018, Salvi, 2007, Soh et al., 2018), we should use it to our benefit, though we are aware of their limits.

## 1.2. Particle and aerosol properties

Particle size is the most important characteristics of aerosols, as the behaviour of a particle depends mostly on this parameter. Determination of the size is straightforward for liquid particles, which almost exclusively have an ideal spherical shape. Then the size is related to its diameter  $d_p$ . For non-spherical particles, the size is expressed by means of an *equivalent diameter*, which is the diameter of a sphere that has the same value of a particular physical property as that of an irregular particle.

Another important property is the *particle density*  $\rho$ . It relates the mass per unit volume of the particle itself (not of the bulk aerosol). Non-porous particles have the density of their parent material. Porous particles have an apparent density significantly lower than that calculated from their chemical composition due to the large volume of void space in their structure (Hinds, 1999). The density of particles is sometimes related to the so-called *standard density*  $\rho_0$ , equal to the density of water, 1000  $\text{kg}/\text{m}^3$ .

The parameter related to an ensemble of aerosol particles is the *mass concentration*, defined as the mass of particulate matter per unit volume of aerosol, commonly expressed in units of  $\text{g}/\text{m}^3$ ,  $\text{mg}/\text{m}^3$ , or  $\mu\text{g}/\text{m}^3$ . In some cases, e.g. when dealing with fibres, the *number concentration* defined as the number of particles per unit volume of aerosol, expressed in  $\text{number}/\text{cm}^3$ , or  $\text{number}/\text{m}^3$ , is more useful.

The description of an aerosol using the particle diameter would be easy if all the particles in an ensemble had the same diameter. Such a system would be called *monodisperse aerosol*. Regrettably, this situation never occurs. There are always

particles of diverse diameters within the aerosol. Therefore, a statistical description of the distribution of particles among various sizes must be used. The particles can be divided into size intervals, where the upper limit of the lower size bin coincides with the lower limit of the upper bin. A number of particles in each such size bin can be counted and plotted as a histogram. If the size intervals are fine enough, this distribution is called a differential size distribution (Kulkarni et al., 2011) and, more specifically, as the dependent variable is the number of particles, it is referred to as a *number distribution*. The number of particles  $dN$  in the size interval from  $d_p$  to  $d_p + dd_p$  can be expressed as:

$$dN = n(d_p)dd_p, \quad (1)$$

where  $n(d_p)$  is the number distribution function. The subscript  $p$  stands for a particle. It is more practical to use  $d \ln d_p$  for the size interval, as the particle diameter usually ranges over several orders of magnitude. The number distribution then becomes:

$$dN = n(\ln d_p)d \ln d_p. \quad (2)$$

Similar equations can be given for the surface, volume or mass distribution simply by replacing  $N, n$  by  $S, s$ ;  $V, v$ ; and  $M, m$ , respectively (Kulkarni et al., 2011).

To facilitate the description of the distribution only by few parameters, the data is usually fitted by a suitable function. The most frequent is the log-normal function, which is obtained from the normal function by using logarithmic variables:

$$n(\ln d_p) = \frac{N_T}{\sqrt{2\pi} \ln \sigma_G} \exp\left(\frac{-(\ln d_p - \ln \text{CMD})^2}{2(\ln \sigma_G)^2}\right), \quad (3)$$

where  $N_T$  is the total number of particles, CMD is the count (i.e. number) median diameter, which, for a lognormal distribution, is equal to the geometric mean diameter  $d_G$ , defined as:

$$\ln d_G = \frac{1}{N_T} \int_0^\infty (\ln d_p) dn, \quad (4)$$

and  $\sigma_G$  is the geometric standard deviation (often referred to by its abbreviation GSD), defined as:

$$\ln \sigma_G = \sqrt{\frac{\int_0^\infty (\ln d_p - \ln d_G)^2 dn}{N_T - 1}}. \quad (5)$$

Sometimes also mass median diameter (MMD), surface median diameter (SMD) or length median diameter (LMD) is needed. All these median diameters divide the sample into halves, meaning that 50 % of the count, mass, surface, or length is contained in particles that are smaller than the appropriate median diameter. For lognormal size distribution it is easy to relate these diameters by the ‘‘Hatch-Choate’’ relations:

$$\text{MMD} = \text{CMD} \exp(3 \ln^2 \sigma_G), \quad (6)$$

$$\text{SMD} = \text{CMD} \exp(2 \ln^2 \sigma_G), \quad (7)$$

$$\text{LMD} = \text{CMD} \exp(1 \ln^2 \sigma_G). \quad (8)$$

If the (count) mode diameter (representing the particle size most frequently found in the sample) or mass mean diameter (a diameter of a spherical particle with a mass equal to the mean mass of all the particles in a population) is to be calculated, following formulas can be used:

$$\text{Count mode diameter} = \text{CMD} \exp(-1 \ln^2 \sigma_G), \quad (9)$$

$$\text{Mass mean diameter} = \text{CMD} \exp(3.5 \ln^2 \sigma_G). \quad (10)$$

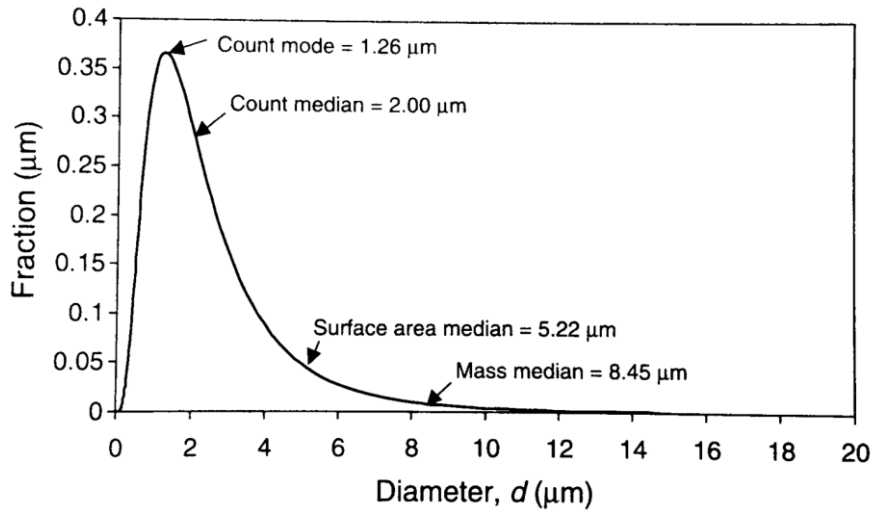


Fig. 3 An example of lognormal number distribution with CMD of 2  $\mu\text{m}$  and  $\sigma_G = 2$ . Source: (Kulkarni et al., 2011).

The number (or frequency) distribution curve with marked count mode diameter, CMD, SMD, and MMD is depicted in Fig. 3.

It is very common in aerosol science to plot the cumulative distribution function,  $F(a)$ , defined as:

$$F(a) = \int_0^a n(d_p) dd_p, \quad (1)$$

where  $F(a)$  gives the fraction of the particles having diameters less than  $a$ . An example of such a curve is in Fig. 4. The advantage of this representation is that e.g. the CMD can be easily found directly from the plot by locating the fraction of 0.5 on the vertical axis and associating it with the point on the curve, which is exactly above that particular size (Hinds, 1999). The horizontal axis is often in a logarithmic scale because the size of particles frequently ranges over several orders of magnitude.

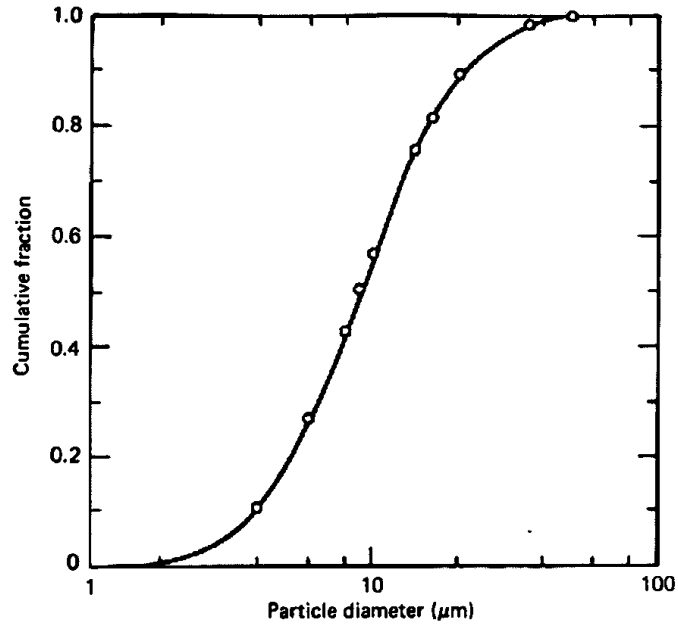


Fig. 4 Cumulative distribution curve (logarithmic size scale). Source: (Hinds, 1999).

All the equations mentioned above assume that we know the diameter of the measured particle. However, as there are numerous measuring methods based on distinct physical principles, there are also various results delivered by different instruments even in the case they all measured the same particle. From this perspective, the concept of the equivalent diameter mentioned earlier in this chapter becomes yet more important and useful, namely in the case that you want to compare diameters measured by instruments based on different physical features of the particle.

As this work is focused on inhaled particles, it is essential to understand the *aerodynamic diameter*,  $d_a$ . It is defined as the diameter of a standard density ( $\rho_0 = 1000 \text{ kg/m}^3$ ) sphere that has the same gravitational settling velocity as the examined particle. For a spherical particle, the  $d_a$  is given by:

$$d_a = d_p \left( \frac{\rho_p}{\rho_0} \right)^{1/2}. \quad (2)$$

It means that if a particle has, e.g.  $d_a = 1 \text{ } \mu\text{m}$ , it is aerodynamically indistinguishable from other particles with  $d_a = 1 \text{ } \mu\text{m}$  although they might have a different shape, density or size. The calculation of  $d_a$  for irregular particles can be performed using the dynamic shape factor  $\chi$  defined as the ratio of the actual resistance force of the nonspherical particle to the resistance force of a sphere having the same volume and velocity as the nonspherical particle. For details see (Hinds, 1999). The diameter of the actual irregular particle is then represented in the equations by the *equivalent volume diameter*  $d_e$ , which is the diameter of a sphere having the same volume as that of the irregular particle.

Optical counters measure the *optical equivalent diameter*, which is the diameter of a particle that scatters as much light in a specific instrument as the particle being measured. A vast number of instruments is based on the measurement of electrical characteristics of particles. Therefore, the *electrical mobility equivalent diameter* was defined as the diameter of a unit-density spherical particle moving at the same velocity

in an electric field as the particle in question. The *diffusion equivalent diameter* is the diameter of a unit-density sphere with the same rate of diffusion as the particle in question (Kulkarni et al., 2011). The list of equivalent diameters could continue, however, the essential fact remains that converting one equivalent diameter to another is difficult or often impossible without detailed knowledge of the aerosol and the instruments used for its characterization.

### 1.3. Particle deposition mechanisms

Every sophisticated prediction of the deposited fraction of the inhaled aerosol in human airways must consider the five basic particle deposition mechanisms: *inertial impaction*, *gravitational settling*, *Brownian and turbulent dispersion*, *interception* and *electrostatic precipitation*.

**Inertial impaction** – is the dominant mechanism for particles of larger sizes ( $\sim 5 \mu\text{m}$  and larger), whose inertia is so high that the particle is unable to follow the streamline on the curved path, and hits the airway wall. The probability of a particle to deposit by inertial impaction is proportionate to the Stokes number, given as:

$$\text{Stk} = \frac{\rho d_p^2 U}{18\mu D}, \quad (11)$$

where  $U$  and  $\mu$  are velocity and dynamic viscosity of the carrier gas (air) and  $D$  is a characteristic length, usually diameter of the airway.

**Gravitational settling** – is important mostly in smaller airways where the particles have smaller distances to travel before touching the wall and where they have enough time to settle. The settling velocity,  $U_s$ , is defined as:

$$U_s = \frac{\rho d_p^2 g}{18\mu}, \quad (12)$$

where  $g$  is the gravitational acceleration.

**Brownian dispersion** – originates from the random collisions of aerosol particles with air molecules. The influence of this mechanism increases with decreasing size of particles. It is proportional to the Brownian diffusion coefficient  $D_B$  defined as:

$$D_B = \frac{C_c k T}{3\pi\mu d_p}, \quad (13)$$

where  $C_c$  is a slip correction factor accounting for the increased velocity of the particles as a result of “slipping” through the space between the molecules before colliding with another molecule or object in path (for details see, e.g. (Musante et al., 2002)),  $k$  is the Boltzmann’s constant and  $T$  is the absolute temperature. **Turbulent dispersion** – is caused by the turbulent fluctuations of the flow; it is significant mostly in the upper and larger airways, where the turbulent flow appears (Darquenne, 2012).

**Interception** – means that the particle follows the fluid streamline, but comes into contact with the wall due to its size or shape. This mechanism is considered important mainly for fibres in lower airways, while for spherical particles remains negligible.

**Electrostatic precipitation** – appears in the case of charged particles, which come close to the wall and induce image charge on the surface. Then they are electrically attracted to the airway wall and deposit.

#### **1.4. Aerosol – health interactions**

A penetration of aerosols through the upper airways is sometimes seen as negative (in the case of harmful particles in the environment), otherwise as positive (in the case of therapeutic aerosols). Consequently, both groups focus on different tasks and have developed different tools for handling the description of aerosols.

##### **Workplace, indoor and ambient aerosol exposure measurement**

People are exposed to aerosols in all environments. However, the nature of aerosols and their potential toxicity differ, and hence, if the health relevant measurement has to be prepared, different strategies must be followed. In general, aerosols can enter the organism through the eyes, skin, or digestive system, however, the respiratory system is usually the most vulnerable. For workplace exposure, the measurements are focused on the estimation of the dose delivered to the body and its potential adverse effect. Unfortunately, the actual intake is highly individual (Chan and Lippmann, 1980). The measurements are performed either by personal samplers (filters and pumps) or by direct-reading measurements (Lehocky and Williams, 1996).

The indoor aerosol exposure represents many types of environments, but generally can be described as a nonoccupational environment outside the workplace, namely residences and vehicle cabins (Maroni et al., 1995). There is a variety of available aerosol monitors, and it is expected that there will be a notable increase in interest in indoor aerosol exposure among the general public with the onset of low-cost sensors.

The ambient aerosol monitoring delivers mostly the PM<sub>10</sub> and PM<sub>2.5</sub> values and usually relies on stationary sampling systems of various types. The selection of the appropriate instrument (and hence the quality and type of delivered results) depends on the specific needs of the contracting authority (McMurry, 2000).

##### **Pharmaceutical aerosols**

The aerosols for a medical application can be divided into two groups. Aerosols intended for therapy of diseased airways, and aerosols for systemic delivery via inhalation. The great potential of the latter group grounds in the fact, that the inhaled particles which manage to penetrate down to the alveoli are rapidly absorbed into the blood circulation. The onset of the therapeutic effect of such drug is virtually immediate, comparable to administration by injection. Moreover, avoiding the enteral route and injections is appreciated by some patients.

Pharmaceutical aerosols can be delivered by metered dose inhalers (MDIs), nebulizers and dry powder inhalers (DPIs). MDIs are the most popular devices. With this method,

the drug is mixed in a canister with a propellant gas, and precisely the prescribed amount of aerosol is released upon the actuation of the patient (Hickey, 2007). Some patients may have problems with coordination of inhalation and actuation of the MDI. (Breath-actuated MDIs were introduced to avoid this problem. However, they are available only for some drugs.)

Nebulizers are larger devices, which are used in emergency care units and for home therapy. Jet nebulizers generate the aerosol by a high-velocity airstream directed against a thin layer of liquid solution. Ultrasonic and vibrating mesh nebulizers use vibrating elements which aerosolize the solution. The main drawbacks of nebulizers compared to MDIs and DPIs is their lack of portability, high demands on maintenance and higher cost as a result of requirements of higher doses to achieve the therapeutic effect. The therapeutic session also takes longer (usually 5 to 10 minutes) compared to MDIs. Nonetheless, some psychological benefits in patients treated for acute asthma by inhalers were observed (Hickey, 2007).

Dry powder inhalers use patient's own breath for actuation and dispersion of the drug in the form of powder. Therefore, there is no difficulty with coordination of inhalation and actuation of the device. On the other hand, the user must be able to generate sufficiently strong flow, which limits its applicability to less severe diseases.

Particles generated or dispersed by the above-mentioned devices are mostly polydisperse, usually in sizes from 1 to 8  $\mu\text{m}$ . The application of nanoparticles for pharmaceutical purposes is limited by difficult deagglomeration of particle clusters which necessarily form in the canisters, capsules or blisters. There is a potential of application of porous particles, which have a low aerodynamic diameter, and hence can penetrate deep into the lungs, resist the cleaning mechanism by macrophages and produce a long-term therapeutic effect (Edwards et al., 1997).

Nevertheless, in order to fully utilize the possibilities of inhaled drug therapy, it is necessary to master the precise prediction of the patient-specific deposition of inhaled particles. It is the main purpose of this work to contribute to these efforts and bring a better understanding of the mechanisms influencing the transport and deposition of inhaled particles.

### 3. RESPIRATORY SYSTEM

The respiratory system provides continuous absorption of oxygen and excretion of carbon dioxide. This exchange of gases between the atmosphere and the blood circulation is called external respiration. Apart from that, the upper airways serve as a protection against harmful aerosol particles (Kacmarek et al., 2013) and they also humidify and warm up the air.

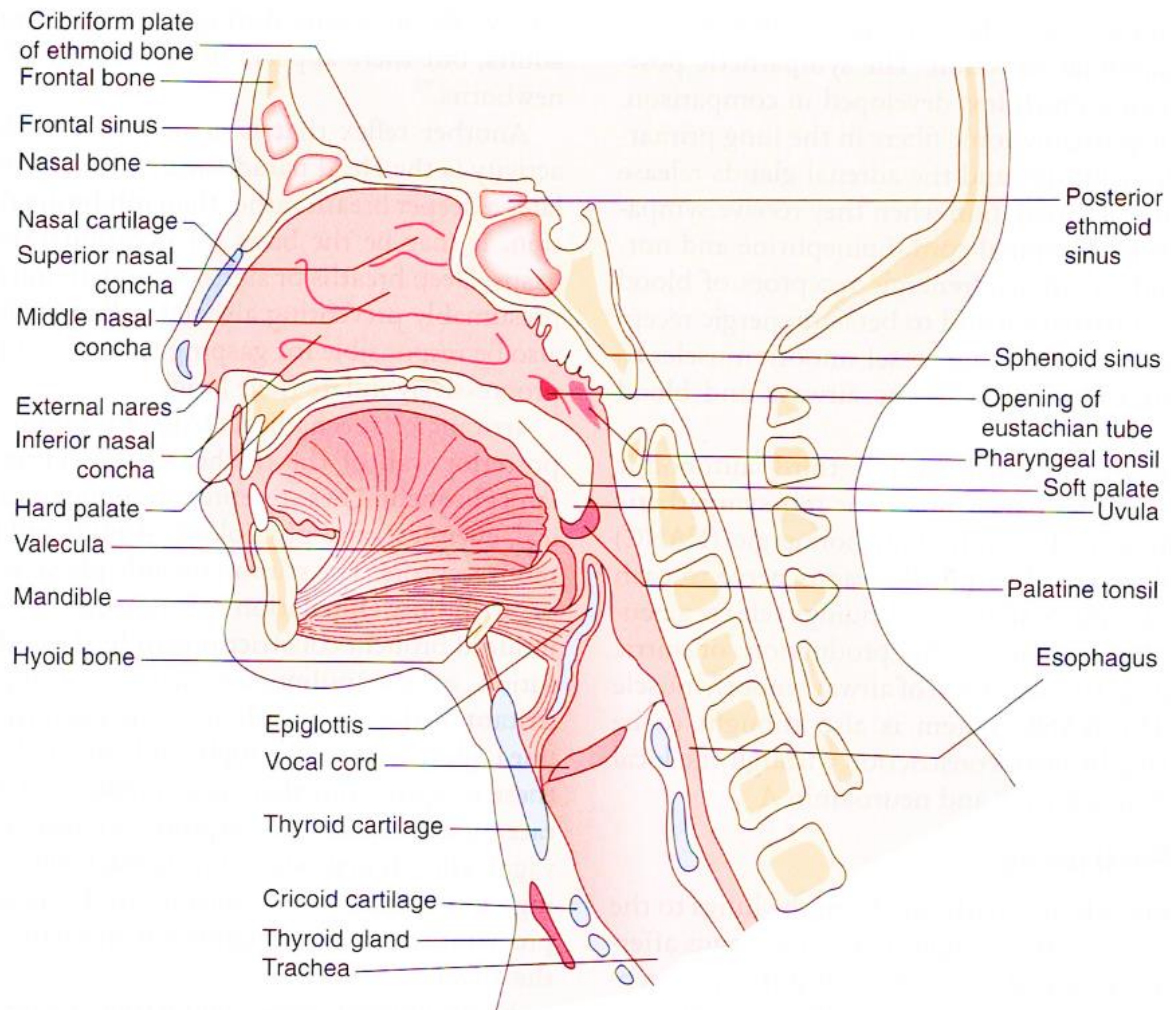


*Fig. 5 Human upper airways (Kacmarek et al., 2013)*

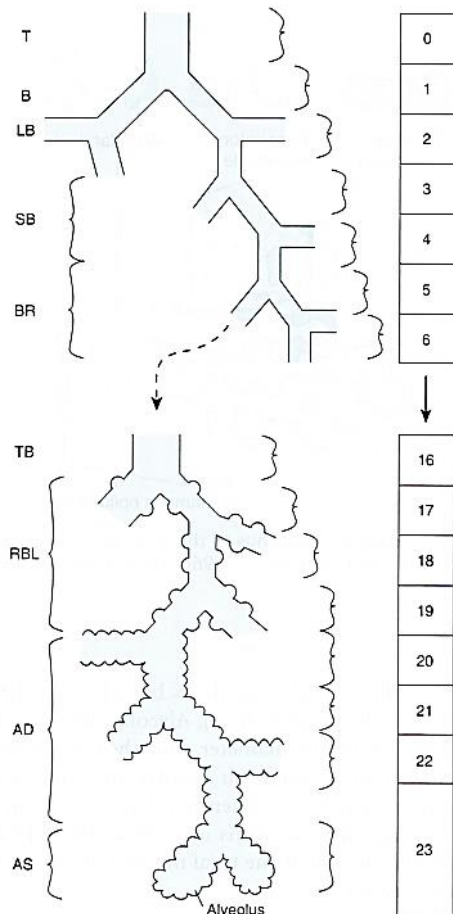


Fig. 6 Conducting (generation 0 through 16) and respiratory zone (generation 17 through 23): T, trachea; B, bronchi; LB, lobar bronchi; SB, segmental bronchi; BR, bronchioles; TB, terminal bronchioles; RBL, respiratory bronchioles; AD, alveolar ducts; AS, alveolar sacs (Kacmarek et al., 2013).

## 1.5. Airway anatomy

The first detailed description of the morphometry of human lungs was published by Ewald Weibel (Weibel, 1963). He statistically evaluated diameters, lengths, angles of branching and other characteristics of conducting and respiratory airways. He found that people have on average 23 generations of dichotomous branching, and extracted a symmetrical and asymmetrical model, which became very popular as a basis for mathematical and numerical modelling of lung deposition. His model was later followed by a more advanced asymmetrical model of Horsfield (Horsfield and Cumming, 1967, Horsfield and Cumming, 1968, Horsfield et al., 1971).

A basic description of airways is depicted in Fig. 5 and Fig. 6. The inner surface of the airways in the conducting zone (generation 0–16) is ciliated. The walls of the trachea and following bronchi are supported by cartilaginous rings, which prevent the airways from collapsing during the expiration. The rings keep the relatively stable diameter of the airway tubes during the breathing cycle, and hence the airways can be modelled by rigid tubes (nonmoving walls). The cartilages eventually disappear in generation 12 – 15 (Tu et al., 2013); therefore the downstream branches expand during the breathing cycle significantly. The process of development of digital models and fabrication of replicas of human airways has been published by the author

in the paper (HAB-1)<sup>1</sup>, which is an integral part of this thesis.

## 1.6. Lung clearance mechanisms

Although the primary task of this work is to enlighten the transport of particles to the airway walls, it is important to know what happens after the particles deposit to the airway wall. As normal air contains  $10^3$  to  $10^4$  particles in every  $\text{cm}^3$ , the lungs must have an efficient self-cleaning system. The knowledge of lung clearance mechanisms is crucial for both toxicologist and pharmacist, as the length of time in which particles are

<sup>1</sup> Lizal, F., Elcner, J., Hopke, P. K., Jedelsky, J. and Jicha, M. (2012) 'Development of a realistic human airway model', *Proceedings of the Institution of Mechanical Engineers Part H- Journal of Engineering in Medicine*, 226(H3), pp. 197-207. IF(2012) = 1,419.

in contact with the lung cells determine the negative or positive effects of inhaled particles.

The clearance rate depends on the deposition site. Particles deposited in the entrance region (one-third) of the nose are efficiently cleared by blowing the nose. The rest of the particles entrapped in the nasal cavity are moved by the mucociliary clearance to the throat from where they can be coughed out or swallowed (Beachey, 2013). Particles which deposit in the conducting airways are mostly cleared within 24 hours due to the synchronized upward motion of the cilia and transported to the digestive system (Finlay, 2001). The most important mechanism of clearance in the respiratory zone is phagocytosis by alveolar macrophages and subsequent migration to the mucociliary escalator (Kulkarni et al., 2011). Solubility plays an important role, especially in the pulmonary region. It is very important as a defence against, e.g. mineral fibres, whose dissolution by lung fluids leads to breakage of long fibres into short ones that can be phagocytosed. It is known, that asbestos fibres are more persistent compared to glass or rock wool. Fibres longer than the macrophages are poorly cleared, and the repeatedly failed attempts to engulf the fibre trigger the release of reactive products, which, eventually, leads to chronic inflammation and cancer (Kulkarni et al., 2011). Ultrafine particles are also cleared by the tracheobronchial lymphatic system. It has been shown that they migrate to lymph nodes faster than fine particles of the same composition (Sager et al., 2008).

## 4. MODELLING AND MEASUREMENT OF THE AEROSOL-AIRWAY INTERACTIONS

The fate of inhaled particles, namely prediction of the distribution of deposited particles, is studied either *in vivo* (on living subjects using experimental techniques), in replicas of human airways<sup>2</sup>, or *in silico* (using computational simulations). All these approaches lead eventually to the creation of models which can be used for better understanding of particle-lung interactions.

### 1.7. Experimental techniques and their application

Before we approach the models itself, we must describe the basic experimental techniques available for measurements performed *in vivo*, *in vitro*, *in silico* or in replicas of human airways. There has been great progress in the experimental methods in the last years. A thorough description of the available traditional and emerging techniques was given in the review paper (HAB-2)<sup>3</sup> by the author of this thesis, which constitutes an integral part of the thesis. The experimental methods are not used

---

<sup>2</sup> Sometimes the term *in vitro* is used within the aerosol community for this approach, however, in biological sciences *in vitro* means “performed with cells, or biological molecules outside their normal biological context” (Lizal et al., 2018).

<sup>3</sup> Lizal, F., Jedelsky, J., Morgan, K., Bauer, K., Llop, J., Cossio, U., Kassinos, S., Verbanck, S., Ruiz-Cabello, J., Santos, A., Koch, E. and Schnabel, C. (2018) 'Experimental methods for flow and aerosol measurements in human airways and their replicas', *European Journal of Pharmaceutical Sciences*, 113, pp. 95-131. IF(2017) = 3,466

independently nowadays, but more and more frequently as a validation tool for numerical simulations. The best results are acquired by a combination of experiments (which also provide boundary conditions and validation for CFD) and numerical simulations.

Some particular topics regarding the experimental techniques were also studied by the author and his co-workers. Specifically, the application of positron emission tomography for measurement of deposition of particles in a realistic replica of lungs was reported in (HAB-3)<sup>4</sup>; the turbulent behaviour of flow within the airways was studied by phase Doppler anemometry in (HAB-4)<sup>5</sup>, and deposition of multicomponent particles was investigated in (HAB-5)<sup>6</sup>

## 1.8. Description of the modelling approaches

One of the key motivations for the development of human airway models is the requirement to precisely predict the dose of delivered particles into specific regions of airways after inhalation of adverse or therapeutic aerosols. There are three main modelling approaches: 1) Traditional (mechanistic) models – based on simplified airway geometries where the deposition rates are calculated from equations derived for the relevant particle deposition mechanisms; 2) Empirical and semi-empirical models which are based on experimental data fitted with equations; and 3) CFD models which can predict local deposition in anatomically realistic geometries. The work of the author documented in this thesis mostly extends into the latter two groups. The calculated delivered dose can then be used in another type of models called physiologically based pharmacokinetic (PBPK) models. They focus on internal processes within the human body after inhalation and predict kinetics of absorption, distribution, metabolism, excretion and storage of inhaled aerosols (Phalen and Raabe, 2016). PBPK modelling is not the subject of this thesis.

### Traditional mechanistic models

The first model utilizing simplified division of airways into several compartments and applying the mechanisms of sedimentation, impaction, diffusion, and interception was published by Findeisen<sup>7</sup> (1935). He was the first one to assume that once the particle

---

<sup>4</sup> Lizal, F., Belka, M., Adam, J., Jedelsky, J. and Jicha, M. (2015) 'A method for in vitro regional aerosol deposition measurement in a model of the human tracheobronchial tree by the positron emission tomography', *Proceedings of the Institution of Mechanical Engineers Part H- Journal of Engineering in Medicine*, 229(10), pp. 750-757. IF(2015) = 0,996.

<sup>5</sup> Jedelsky, J., Lizal, F. and Jicha, M. (2012) 'Characteristics of turbulent particle transport in human airways under steady and cyclic flows', *International Journal of Heat and Fluid Flow*, 35, pp. 84-92. IF(2012) = 1,581.

<sup>6</sup> Nordlund, M., Belka, M., Kuczaj, A. K., Lizal, F., Jedelsky, J., Elcner, J., Jicha, M., Sauser, Y., Le Bouhellec, S., Cosandey, S., Majeed, S., Vuillaume, G., Peitsch, M. C. and Hoeng, J. (2017) 'Multicomponent aerosol particle deposition in a realistic cast of the human upper respiratory tract', *Inhalation Toxicology*, 29(3), pp. 113-125. IF(2017) = 1,819.

<sup>7</sup> There is a strong link of T. R. W. Findeisen to Prague. After he finished his work on aerosols, he focused on basic research in meteorology. He died untimely in the age of 36 during the Prague uprising on May 9, 1945 during the massacre of 763 local German residents. Before his death he was director of the Research Center of Prague Reich office for weather service (Phalen and Raabe, 2016).

touches the airway wall, it is irreversibly deposited. He also deduced the U-shaped curve of the dependence of deposition efficiency on particle diameter, where the minimum was predicted for particles between 0.2 to 0.6  $\mu\text{m}$  in diameter (Phalen and Raabe, 2016). In this perspective, it is surprising, that some communities still believe that nanometer-sized particles are easily exhaled, although there had been an indication that this supposition was wrong already in the 1930s.

This type of models was later improved by Landahl (1950) and Beeckmans (1965) to include the upper airways, the effects of interpulmonary gas mixing and re-entrainment of nondepositing particles, and, eventually, to incorporate the lowest airways (Stuart, 1984).

Slightly different type of models was proposed by Yu (1978), later improved by Robinson and Yu (2001) to include cigarette smoke-related features. Their approach is called the trumpet model. It simplifies the many lung generations into a single trumpet-like path. The cross-sectional area increases with increasing lung generation. It calculates the one-dimensional transport equation for aerosol concentration loss (Rostami, 2009).

### **Empirical and semi-empirical models**

This group includes models (or in general experimental data-fits, tables and figures) measured either in vivo (on living humans) or in vitro (on replicas of human lungs). These models have usually limited applicability for cases matching the experimental conditions. However, many of these measurements became eventually parts of more sophisticated complex models which utilized data from numerous studies and gathered them to create generally valid predictions. Following papers co-authored by the author of this thesis fall into this category: (HAB-5; HAB-6<sup>8</sup>), as they include experimental data fits for multicomponent and fibre particles, respectively, which enhances our abilities to predict the deposition of these special types of particles.

The most typical example of the complex “summarizing” models was published by International Commission on Radiological protection (Bailey, 1994, ICRP, 1994) and National Council on Radiation Protection and Measurements (NCRP, 1997). Both models were implemented in commercial software. However, there is also a freeware alternative in so-called Multiple path Dosimetry (MPPD) model (available from <https://www.ara.com/products/multiple-path-particle-dosimetry-model-mppd-v-304>; Accessed 15/02/2019).

---

<sup>8</sup> Belka, M., Lizal, F., Jedelsky, J., Elcner, J., Hopke, P. K. and Jicha, M. (2018) 'Deposition of glass fibers in a physically realistic replica of the human respiratory tract', *Journal of Aerosol Science*, 117, pp. 149-163. IF(2017) = 1,926.

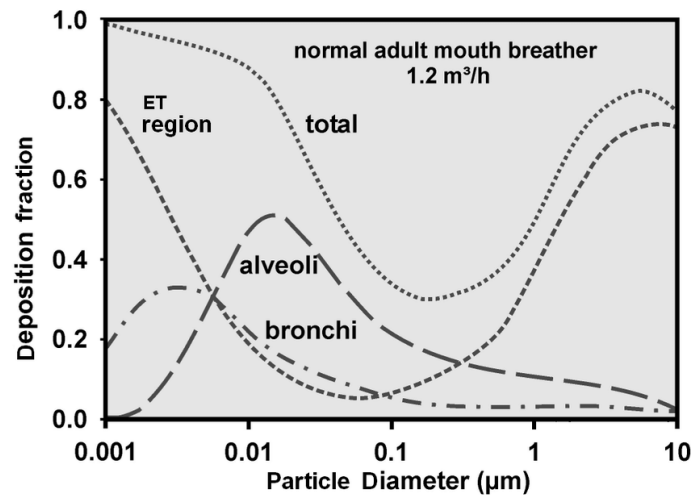


Fig. 7 Average predicted total and regional lung deposition fraction based on ICRP (1994) model for light exercise breathing conditions (Hussain et al., 2011).

An example of a result which can be acquired from the ICRP model is depicted in Fig. 7. It shows regional and total deposition fraction as a function of particle diameter. It is an illustration of the previously mentioned U-shaped curve of deposition. Apparently, nanoparticles deposit even more efficiently than micrometre-sized particles.

The empirical and semi-empirical models are useful for prediction of total and regional aerosol deposition. They frequently serve as an input for PBPK models. Naturally, they cannot simulate interpersonal variability, local deposition on a millimetre scale or the patient-specific influence of diseases; however, they provide sufficient data for the “average” person aerosol dosimetry.

The author and his team have recently developed more sophisticated approach, where specific features of a particular disease can be accounted for. The research has been published in (HAB-11)<sup>9</sup>. The paper focused on the prediction of aerosol deposition to the lungs of patients with chronic obstructive pulmonary disease (COPD). At first, realistic inhalation profiles were recorded. These profiles were used as an input to the stochastic lung model, a special type of empirical model developed by Koblinger and Hofmann (1990). The results showed that the aerosol dose delivered to the lungs of COPD patients was significantly lower compared to healthy subjects although exactly the opposite is needed.

### CFD models

The fast development of computational capabilities allowed more detailed calculations of aerosol deposition in realistic geometries in the last decades. This approach is frequently referred to also as CFPD (Computational Fluid and Particle Dynamics). It consists of several steps: 1) acquisition of a suitable airway geometry (either the simplified Weibel or Horsfield models, or, more frequently, a realistic geometry acquired by medical imaging methods, such as computed tomography or magnetic

<sup>9</sup> Farkas, Á., Lizal, F., Jedelsky, J., Elcner, J., Horváth, A. and Jicha, M. (2019) 'Simulation of Airway Deposition of an Aerosol Drug in COPD Patients', *Pharmaceutics*, 11(4). IF(2017) = 3,746.

resonance imaging performed *in vivo*, or on airways excised at an autopsy); 2) creation of a computational mesh which is necessary for discretization of the problem and allows solution of complex equations of fluid and particle motion; 3) solving the Navier–Stokes equation for fluid flow and applying Lagrangian, or Eulerian approach for particles and 4) post-processing, i.e. analysis of the results and calculation of deposition rates in all regions of lungs.

The main advantage of this type of modelling is that it allows calculations of patient-specific lungs. Various pathologies can be easily simulated and compared to healthy lungs. On the other hand, there cannot be a complete whole-lung model, because, first, there is no complete digital geometry of lungs available (due to the limitations on the side of imaging methods, see (HAB-2) for details), and second, calculations on such complex geometry in realistic conditions would be impossible even for current top-class computer clusters.

There is a vast number of publications on the CFD modelling of human airways. The development in the field has been reviewed by (Rostami, 2009, Hofmann, 2011, Longest et al., 2019). Only a very brief selection of essential aspects of CFD modelling is presented here.

The first step is always the selection of a suitable geometry. In order to take advantage of the best features of CFD (ability to focus on detail), it is advisable to use realistic, patient-specific geometries. Preferably those, for which enough experimental data is available for boundary conditions setting and for validation purposes. However, such cases are sporadic. Therefore, it has been a major objective of the author of this thesis to prepare a digital geometry that would serve for both fabrication of physical models and numerical modelling. The whole procedure has been reported in the paper (HAB-1) which is a part of this thesis. This effort has been appreciated by the community of scientists gathered within the COST Action 1404 SimInhale (<http://www.siminhale-cost.eu/>), who selected the model developed by the author's team as a benchmark case for comparison of CFD calculations among six international teams (for details see (HAB-8)<sup>10</sup>).

The second step, creation of the computational mesh, is crucial because if the calculations are performed on a poor mesh, the results are worthless. The requirements on the density and type of the mesh differ depending on the proposed numerical method. Usually, a mesh convergence study is performed at the beginning of calculations. In brief, the search is for the compromise between the speed of the calculation (coarse mesh) and the accuracy of the results (dense mesh). This means that several variants of the mesh are created, from a coarse mesh with the fewest reasonable number of cells to denser and denser meshes. Then calculations are performed on all meshes, and the results (e.g. velocity on a line crossing some complicated area) are compared. The

---

<sup>10</sup> Koullapis, P., Kassinos, S. C., Muela, J., Perez-Segarra, C., Rigola, J., Lehmkuhl, O., Cui, Y., Sommerfeld, M., Elcner, J., Jicha, M., Saveljic, I., Filipovic, N., Lizal, F. and Nicolaou, L. (2018) 'Regional aerosol deposition in the human airways: The SimInhale benchmark case and a critical assessment of in silico methods', *European Journal of Pharmaceutical Sciences*, 113, pp. 77-94. IF(2017) = 3,466.

results converge to the best value delivered by the densest mesh. The coarsest mesh, whose results are consistent with the best calculation is then selected.

Within the third step, the Navier–Stokes equation is being solved. It describes the fluid flow and is used for calculation of velocity field providing the correct boundary conditions were set. The movement of fluid can be studied by either Eulerian or Lagrangian approach. In the Lagrangian approach, the observer is connected with the observed parcel of the fluid, and the path of the parcel can be completely described as a function of its original coordinates and time. On the contrary, when using the Eulerian approach, the observer focuses on a specific location through which the fluid flows. Then, the flow velocity in the specific location is given as a function of the location coordinates and time.

The Navier–Stokes equation (14) in CFD calculations of airway flow is usually solved by the Eulerian approach.

$$\rho \left( \frac{\partial \mathbf{U}}{\partial t} + \mathbf{U} \cdot \nabla \mathbf{U} \right) = -\nabla p + \mu \nabla^2 \mathbf{U}, \quad (14)$$

where  $p$  is pressure.

The solution of the Navier–Stokes equation is performed on the discretized mesh by a suitable numerical method. The actual direct solving of the equation requires calculation of a wide range of time and length scales. It can be achieved by direct numerical simulation (DNS); however, it is extremely computationally expensive, which limits the applicability of this method only to the low-Reynolds number cases and the limited extent of airways. As an alternative, large eddy simulation (LES) can be used. It actually solves only the large scale fluctuations, while the small-scale fluctuations are modelled. The least computationally expensive approach is solving the Reynolds-averaged Navier–Stokes (RANS) equations, which provides the time-averaged approximate solution to the Navier–Stokes equation. It uses the so-called Reynolds decomposition, i.e. division of the actual quantities to the time-averaged and fluctuating components. Application of this decomposition to Navier–Stokes equation leads to the introduction of the Reynolds stress term. It is a nonlinear term, which requires additional turbulence models. Although it seems to be complicating the solution procedure, it is actually faster than LES. Nonetheless, it is on the expense of receiving only the mean flow values. The author’s team contribution in the field of RANS simulations was documented in (HAB-8; HAB-9<sup>11</sup>).

In short, the velocity field can be calculated by either DNS, LES, or RANS approach; however, in any case, results of simulations should always be validated by experimental data to exclude the possibility of inaccuracy and consequent misinterpretation. The author with his colleagues applied phase-Doppler anemometry for investigation of the

---

<sup>11</sup> Elcner, J., Lizal, F., Jedelsky, J., Jicha, M. and Chovancova, M. (2016) 'Numerical investigation of inspiratory airflow in a realistic model of the human tracheobronchial airways and a comparison with experimental results', *Biomechanics and Modeling in Mechanobiology*, 15(2), pp. 447-469. IF(2016) = 3,323.

turbulence characteristics (HAB-4) and reported results, which serve for the CFD validation.

After the successful validation of the velocity field, the flow of particles can be calculated. It can be performed by both Lagrangian and Eulerian approaches, while Lagrangian tracking is more common for dilute, and Eulerian approach for dense aerosols. The solution can be performed in two ways—either the particles just interact with the flow, but the flow is not influenced by the presence of particles (one-way coupling), or the particles and fluid interact mutually (two-way coupling). Again, the second option is demanded only for dense aerosols (e.g. cigarette smoke). The author's team dealt with both Lagrangian (HAB-9) and Eulerian approach (HAB-10)<sup>12</sup>.

In the Lagrangian approach, the equation of motion of a particle is usually expressed as (Rostami, 2009):

$$m_p \frac{dU_p}{dt} = F_D + m_p g + F_{add}, \quad (15)$$

where  $m$  means mass,  $F_D$  denotes the drag force,  $g$  is gravitational acceleration and  $F_{add}$  are additional forces, such as Brownian, thermophoretic, electrostatic or others.

In the Eulerian approach, where the focus is on the elemental control volume through which the particles flow, the transport equation is solved for aerosol concentration (Rostami, 2009):

$$\frac{\partial \rho C}{\partial t} + \nabla \cdot (\rho U C) = \nabla \cdot (\Gamma \nabla C) + S_C, \quad (16)$$

where  $C$  is the particle (mass or number) concentration,  $\Gamma$  is the effective particle diffusivity (due to the Brownian motion and turbulent eddy diffusivity), and  $S_C$  is the particle source or sink term.

The above-mentioned equation can be used for monodisperse aerosols; however, as was shown in the previous chapters, real aerosol (including pharmaceutical) is polydisperse. For such cases a modification called 3D general dynamic equation (GDE) is used (Rostami, 2009):

$$\frac{\partial n_k}{\partial t} + \nabla \cdot (U n_k) = \nabla \cdot (\Gamma \nabla n_k) + \left( \frac{\partial n_k}{\partial t} \right)_{growth} + \left( \frac{\partial n_k}{\partial t} \right)_{coag}, \quad (17)$$

where  $n_k$  is the discrete size distribution function (concentration of particles in the size range  $k$ ), and the source term  $S_C$  was replaced by the term accounting for hygroscopic growth, condensation and evaporation from the particle; and coagulation of particles respectively. Other modifications, accounting for additional forces, chemical

---

<sup>12</sup> Frederix, E. M. A., Kuczaj, A. K., Nordlund, M., Belka, M., Lizal, F., Jedelsky, J., Elcner, J., Jicha, M. and Geurts, B. J. (2018) 'Simulation of size-dependent aerosol deposition in a realistic model of the upper human airways', *Journal of Aerosol Science*, 115, pp. 29-45. IF(2017) = 2,281.

composition of particles, etc. can be made. For details see the paper (HAB-10), which is a part of this thesis.

### **1.9. Deposition of fibres in human lungs**

A scientific gap has appeared in the area of modelling of inhaled fibres. The reason why this topic remained temporarily aside of the main research interest grounded in two facts: first, there has been a seeming lack of motivation for the further study of fibre flow after the successful hunt for asbestos fibres and global ban of their production. Public opinion was that this problem had been solved and it is not necessary to invest in new research in this area. Second, calculation of fibre motion in human airways is significantly more complicated compared to spherical particles. Such simulations require more complex equations and multiple iterations in a single time step to account for the changes in orientation and rotation of a fibre. Moreover, there has not been enough experimental data available for validation of the simulations.

It should be clearly stated, that asbestos is not the only harmful fibre that can get into human lungs. Glass and mineral fibres are being used as asbestos substitutes in thermal insulations; carbon nanotubes are produced in amounts exceeding several thousand tons per year for various purposes (De Volder et al., 2013). Therefore, the ability to predict the fate of inhaled fibres in authentic airways becomes important nowadays.

The author of this thesis and his team focused initially on experiments and performed a series of measurements in the realistic replica of human lungs with glass fibres. The work has been reported in two papers: (HAB-7)<sup>13</sup> focused on the method for detection of fibres on samples created after the exposition of the airway replica to the fibres. In (HAB-6), the author's team has published empirical equations for prediction of deposition efficiency as a function of Stokes number. The work in this area is ongoing and more papers will be published soon on numerical modelling of the fibre flow.

## **5. CONCLUSIONS AND FUTURE WORK**

The recent fast development in the field of modelling of human airways documented in the commentary and the papers constituting the core of this thesis brings interesting opportunities for more efficient treatment of patients suffering with (not only) the lung diseases. It also allows a better description of the fate of inhaled harmful particles.

It is possible to predict overall and regional deposition fractions for an average population with reasonably good precision. Numerical simulations can be performed on realistic airway geometries with up to 16 generations of branching. There are experimental data available for validation of velocity fields within human lungs and deposition of spherical and, partly, fibrous particles.

---

<sup>13</sup> Belka, M., Lizal, F., Jedelsky, J., Starha, P., Druckmullerova, H., Hopke, P. K. and Jicha, M. (2016) 'Application of image analysis method to detection and counting of glass fibers from filter samples', *Aerosol Science and Technology*, 50(4), pp. 353-362. IF(2016) = 1,926.

Current limits are set by the absence of the complete model or just digital geometry of real human lungs spanning from the nasal and oral cavity to alveoli. Also, the computational power is not sufficient for solving the flow field precisely by DNS. Various numerical approaches deliver different results. Hence, the experimental validation remains an indispensable part of the process. Acquisition of correct boundary conditions represents significant challenge during not only *in vivo* but also *in vitro* measurements.

Nonetheless, future goals appear clearly on the horizon. The medical community hopes for a bright future of a patient-tailored medicine. In brief, the idea is the following: a patient suffering from a particular problem visits the physician, who scans their lungs by CT or MRI. The images are processed, airway geometry is segmented and prepared for numerical simulations. The calculations are performed overnight, resulting in the prescription of the most suitable drug administered by the most efficient inhalation device. It reduces the cost of the treatment (smaller doses are necessary due to the precise targeting), and it minimizes the side effects (as the drug is delivered solely to the predetermined region, the organism does not need to process the pharmaceuticals from other locations). Similarly, the protection against harmful particles can be more efficient if the toxicological limits are set to the appropriate values, and efficient lung protection tools are produced.

In order for these dreams to become reality, it is necessary to focus the research into following areas: improved prediction of the local deposition (hot-spots on millimeter or even micrometer scale); better simulations of non-ideal particles (fibers, porous particles); and incorporation of physiologically realistic features of airways (wall motion in lower airways, mucociliary mechanisms, hygroscopic growth, surface roughness, and electrostatic effects).

An important topic for further research is also the influence of lung diseases on the flow and deposition of particles. The inhaled medication is, apparently, administered to sick, not healthy patients. However, the development process of inhalation systems in the pharmaceutical industry is often based on healthy volunteers' data, cascade impactors or extremely simplified airway geometries. Likewise, more realistic predictions are needed on the side of PBPK modelling and the fate of deposited particles in general (Forbes et al., 2015). A scientific gap remains in the area of aerosol–lung interactions during the development of lungs from the fetal stage to adulthood, and there is a lack of data on gender differences.

The future progress in the field of inhaled particles modelling obviously depends on the interdisciplinary collaboration, which inevitably pushes experts from all disciplines to their limits. This thesis documents that the contribution of mechanical engineers is significant, and that there will be enough opportunities for application of the engineering approach also in the future. The appealing feature of this research is the fact that it is directly related to human health, and hence it is rewarded by the public recognition of the societal benefit.

## NOMENCLATURE

$C$	concentration (count/m <sup>3</sup> )
$C_c$	slip correction factor (–)
$d, D$	diameter (μm), characteristic length (m), or diffusion coefficient (m <sup>2</sup> /s)
$dN$	number of particles in a size interval (–)
$F$	fraction (–)
$g$	gravitational acceleration (m/s <sup>2</sup> )
$k$	Boltzmann’s constant (–)
$M, m$	mass (kg)
$n(d_p)$	number distribution function (–)
$N, n$	number (count) (–)
$p$	pressure (Pa)
$S, s$	surface (m <sup>2</sup> )
$Sc$	particle source or sink term (a.u.)
$t, T$	time (s), temperature (K)
$U$	velocity (m/s)
$V, v$	volume (m <sup>3</sup> )

### Greek symbols:

$\Gamma$	effective particle diffusivity (m <sup>2</sup> /s)
$\mu$	dynamic viscosity (Pa s)
$\rho$	particle density (kg/m <sup>3</sup> )
$\sigma_G$	geometric standard deviation

### Subscripts:

$0$	standard value, or reference value
$a$	aerodynamic
$add$	additional
$B$	Brownian
$D$	drag

<i>e</i>	equivalent
<i>G</i>	geometric
<i>k</i>	size range
<i>p</i>	particle, or pressure
<i>s</i>	settling
<i>T</i>	total

## REFERENCES TO THE COMMENTARY

- APEC (2018) *APEC Water*. Available at: <https://www.freedrinkingwater.com/images-new/particle-size-removal.jpg> (Accessed: 19.09. 2018).
- Bailey, M. R. (1994) 'THE NEW ICRP MODEL FOR THE RESPIRATORY-TRACT', *Radiation Protection Dosimetry*, 53(1-4), pp. 107-114.
- Beachey, W. (2013) *Respiratory care anatomy and physiology : foundations for clinical practice*. 3rd edn. St. Louis, Mo.: Elsevier.
- Beeckmans, J. M. (1965) 'The deposition of aerosols in the respiratory tract. I. Mathematical analysis and comparison with experimental data', *Can J Physiol Pharmacol*, 43, pp. 157-72.
- Belka, M., Lizal, F., Jedelsky, J., Elcner, J., Hopke, P. K. and Jicha, M. (2018) 'Deposition of glass fibers in a physically realistic replica of the human respiratory tract', *Journal of Aerosol Science*, 117, pp. 149-163.
- Belka, M., Lizal, F., Jedelsky, J., Starha, P., Druckmullerova, H., Hopke, P. K. and Jicha, M. (2016) 'Application of image analysis method to detection and counting of glass fibers from filter samples', *Aerosol Science and Technology*, 50(4), pp. 353-362.
- Brown, J. S., Gordon, T., Price, O. and Asgharian, B. (2013) 'Thoracic and respirable particle definitions for human health risk assessment', *Particle and Fibre Toxicology*, 10.
- CEC (2008) *Directive 2008/50/EC of the European Parliament and of the Council of 21 May 2008 on ambient air quality and cleaner air for Europe* L152). Available at: <https://eur-lex.europa.eu/legal-content/EN/TXT/PDF/?uri=CELEX:02008L0050-20150918&from=EN>.
- CEN (1993) *Workplace atmospheres-size fraction definitions for measurement of airborne particles*, London, England: European Committee for Standardization (CEN), British Standards Institute (BS EN 481:1993. Available at: <http://legacy.library.ucsf.edu:8080/i/e/m/iem52d00/Siem52d00.pdf>.
- Darquenne, C. (2012) 'Aerosol deposition in health and disease', *J Aerosol Med Pulm Drug Deliv*, 25(3), pp. 140-7.
- De Volder, M. F. L., Tawfick, S. H., Baughman, R. H. and Hart, A. J. (2013) 'Carbon Nanotubes: Present and Future Commercial Applications', *Science*, 339(6119), pp. 535-539.
- Edwards, D. A., Hanes, J., Caponetti, G., Hrkach, J., BenJebria, A., Eskew, M. L., Mintzes, J., Deaver, D., Lotan, N. and Langer, R. (1997) 'Large porous particles for pulmonary drug delivery', *Science*, 276(5320), pp. 1868-1871.
- EEA (2017) *Air quality in Europe — 2017 report*, Luxembourg: European Environment Agency. Available at: <https://www.eea.europa.eu/publications/air-quality-in-europe-2017>.
- Elcner, J., Lizal, F., Jedelsky, J., Jicha, M. and Chovancova, M. (2016) 'Numerical investigation of inspiratory airflow in a realistic model of the human tracheobronchial airways and a comparison with experimental results', *Biomechanics and Modeling in Mechanobiology*, 15(2), pp. 447-469.
- Findeisen, W. (1935) 'Über das Absetzen kleiner, in der Luft suspendierter Teilchen in der menschlichen Lunge bei der Atmung', *Pflügers Archiv European Journal of Physiology*, 236(1), pp. 367-379.
- Finlay, W. H. (2001) *The mechanics of inhaled pharmaceutical aerosols : an introduction*. San Diego, Calif. ; London: Academic Press.

- Forbes, B., Backman, P., Christopher, D., Dolovich, M., Li, B. V. and Morgan, B. (2015) 'In Vitro Testing for Orally Inhaled Products: Developments in Science-Based Regulatory Approaches', *Aaps Journal*, 17(4), pp. 837-852.
- Frederix, E. M. A., Kuczaj, A. K., Nordlund, M., Belka, M., Lizal, F., Jedelsky, J., Elcner, J., Jicha, M. and Geurts, B. J. (2018) 'Simulation of size-dependent aerosol deposition in a realistic model of the upper human airways', *Journal of Aerosol Science*, 115, pp. 29-45.
- Hickey, A. J. (2007) *Inhalation aerosols : physical and biological basis for therapy. Lung biology in health and disease* 2nd edn. New York: Informa Healthcare.
- Hime, N. J., Marks, G. B. and Cowie, C. T. (2018) 'A Comparison of the Health Effects of Ambient Particulate Matter Air Pollution from Five Emission Sources', *International Journal of Environmental Research and Public Health*, 15(6).
- Hinds, W. C. (1999) *Aerosol technology : properties, behavior, and measurement of airborne particles*. 2nd edn. New York: Wiley.
- Hofmann, W. (2011) 'Modelling inhaled particle deposition in the human lung-A review', *Journal of Aerosol Science*, 42(10), pp. 693-724.
- Horsfield, K. and Cumming, G. (1967) 'Angles of branching and diameters of branches in the human bronchial tree', *Bulletin of Mathematical Biology*, 29(2), pp. 245-259.
- Horsfield, K. and Cumming, G. (1968) 'Morphology of the bronchial tree in man', *Journal of applied physiology*, 24(3), pp. 373-383.
- Horsfield, K., Dart, G., Olson, D. E., Filley, G. F. and Cumming, G. (1971) 'Models of the human bronchial tree', *J Appl Physiol*, 31(2), pp. 207-17.
- Hussain, M., Renate, W.-H. and Werner, H. (2011) 'Effect of intersubject variability of extrathoracic morphometry, lung airways dimensions and respiratory parameters on particle deposition', *Journal of Thoracic Disease*, 3(3), pp. 156-170.
- Chan, T. L. and Lippmann, M. (1980) 'Experimental Measurements and Empirical Modeling of the Regional Deposition of Inhaled Particles in Humans', *American Industrial Hygiene Association Journal*, 41(6), pp. 399-408.
- ICRP (1994) 'Human respiratory tract model for radiological protection. A report of a Task Group of the International Commission on Radiological Protection', *Ann ICRP*, 24(1-3), pp. 1-482.
- Jedelsky, J., Lizal, F. and Jicha, M. (2012) 'Characteristics of turbulent particle transport in human airways under steady and cyclic flows', *International Journal of Heat and Fluid Flow*, 35, pp. 84-92.
- Kacmarek, R. M., Stoller, J. K., Heuer, A. J. and Egan, D. F. (2013) *Egan's fundamentals of respiratory care*. 10th edn. St. Louis, Mo.: Elsevier/Mosby.
- Koblinger, L. and Hofmann, W. (1990) 'Monte-Carlo Modeling of Aerosol Deposition in Human Lungs .1. Simulation of Particle-Transport in a Stochastic Lung Structure', *Journal of Aerosol Science*, 21(5), pp. 661-674.
- Koullapis, P., Kassinos, S. C., Muela, J., Perez-Segarra, C., Rigola, J., Lehmkuhl, O., Cui, Y., Sommerfeld, M., Elcner, J., Jicha, M., Saveljic, I., Filipovic, N., Lizal, F. and Nicolaou, L. (2018) 'Regional aerosol deposition in the human airways: The SimInhale benchmark case and a critical assessment of in silico methods', *European Journal of Pharmaceutical Sciences*, 113, pp. 77-94.
- Kulkarni, P., Baron, P. A. and Willeke, K. (2011) *Aerosol measurement : principles, techniques, and applications*. 3rd edn. Hoboken, N.J.: Wiley.
- Landahl, H. (1950) 'On the removal of air-borne droplets by the human respiratory tract: I. The lung', *Bulletin of Mathematical Biology*, 12(1), pp. 43-56.

- Lehocky, A. H. and Williams, P. L. (1996) 'Comparison of respirable samplers to direct-reading real time aerosol monitors for measuring coal dust', *American Industrial Hygiene Association Journal*, 57(11), pp. 1013-1018.
- Lizal, F., Belka, M., Adam, J., Jedelsky, J. and Jicha, M. (2015) 'A method for in vitro regional aerosol deposition measurement in a model of the human tracheobronchial tree by the positron emission tomography', *Proceedings of the Institution of Mechanical Engineers Part H-Journal of Engineering in Medicine*, 229(10), pp. 750-757.
- Lizal, F., Elcner, J., Hopke, P. K., Jedelsky, J. and Jicha, M. (2012) 'Development of a realistic human airway model', *Proceedings of the Institution of Mechanical Engineers Part H-Journal of Engineering in Medicine*, 226(H3), pp. 197-207.
- Lizal, F., Jedelsky, J., Morgan, K., Bauer, K., Llop, J., Cossio, U., Kassinos, S., Verbanck, S., Ruiz-Cabello, J., Santos, A., Koch, E. and Schnabel, C. (2018) 'Experimental methods for flow and aerosol measurements in human airways and their replicas', *European Journal of Pharmaceutical Sciences*, 113, pp. 95-131.
- Longest, P. W., Bass, K., Dutta, R., Rani, V., Thomas, M. L., El-Achwah, A. and Hindle, M. (2019) 'Use of computational fluid dynamics deposition modeling in respiratory drug delivery', *Expert Opinion on Drug Delivery*, 16(1), pp. 7-26.
- Maroni, M., Seifert, B. and Lindvall, T. (1995) *Indoor air quality : a comprehensive reference book. Air quality monographs* Amsterdam ; New York: Elsevier Science.
- McMurry, P. H. (2000) 'A review of atmospheric aerosol measurements', *Atmospheric Environment*, 34(12-14), pp. 1959-1999.
- Musante, C. J., Schroeter, J. D., Rosati, J. A., Crowder, T. M., Hickey, A. J. and Martonen, T. B. (2002) 'Factors affecting the deposition of inhaled porous drug particles', *Journal of Pharmaceutical Sciences*, 91(7), pp. 1590-1600.
- NCRP (1997) *Deposition, retention, and dosimetry of inhaled radioactive substances : recommendations of the National Council on Radiation Protection and Measurements. NCRP report* Bethesda, MD: National Council on Radiation Protection and Measurements.
- Nordlund, M., Belka, M., Kuczaj, A. K., Lizal, F., Jedelsky, J., Elcner, J., Jicha, M., Sauser, Y., Le Bouhellec, S., Cosandey, S., Majeed, S., Vuillaume, G., Peitsch, M. C. and Hoeng, J. (2017) 'Multicomponent aerosol particle deposition in a realistic cast of the human upper respiratory tract', *Inhalation Toxicology*, 29(3), pp. 113-125.
- Patton, J. S. and Byron, P. R. (2007) 'Inhaling medicines: delivering drugs to the body through the lungs', *Nature Reviews Drug Discovery*, 6(1), pp. 67-74.
- Phalen, R. F. and Raabe, O. G. (2016) 'The evolution of inhaled particle dose modeling: A review', *Journal of Aerosol Science*, 99, pp. 7-13.
- Pope, C. A. and Dockery, D. W. (2006) 'Health effects of fine particulate air pollution: Lines that connect', *Journal of the Air & Waste Management Association*, 56(6), pp. 709-742.
- Robinson, R. J. and Yu, C. P. (2001) 'Deposition of cigarette smoke particles in the human respiratory tract', *Aerosol Science and Technology*, 34(2), pp. 202-215.
- Rostami, A. A. (2009) 'Computational Modeling of Aerosol Deposition in Respiratory Tract: A Review', *Inhalation Toxicology*, 21(4), pp. 262-290.
- Sager, T. M., Kommineni, C. and Castranova, V. (2008) 'Pulmonary response to intratracheal instillation of ultrafine versus fine titanium dioxide: role of particle surface area', *Particle and Fibre Toxicology*, 5.
- Salvi, S. (2007) 'Health effects of ambient air pollution in children', *Paediatric Respiratory Reviews*, 8(4), pp. 275-280.

- Schmid, O. and Stoeger, T. (2016) 'Surface area is the biologically most effective dose metric for acute nanoparticle toxicity in the lung', *Journal of Aerosol Science*, 99, pp. 133-143.
- Soh, S. E., Goh, A., Teoh, O. H., Godfrey, K. M., Gluckman, P. D., Shek, L. P. C. and Chong, Y. S. (2018) 'Pregnancy Trimester-Specific Exposure to Ambient Air Pollution and Child Respiratory Health Outcomes in the First 2 Years of Life: Effect Modification by Maternal Pre-Pregnancy BMI', *International Journal of Environmental Research and Public Health*, 15(5).
- Stuart, B. O. (1984) 'Deposition and Clearance of Inhaled Particles', *Environmental Health Perspectives*, 55(Apr), pp. 369-390.
- Tu, J., Inthavong, K. and Ahmadi, G. (2013) *Computational fluid and particle dynamics in the human respiratory system. Biological and medical physics, Biomedical engineering*, Dordrecht ; New York: Springer,. Available at: SpringerLink <http://dx.doi.org/10.1007/978-94-007-4488-2> MIT Access Only.
- Weibel, E. (1963) *Morphometry of the Human Lung*. Berlin, New York: Springer Verlag and Academic Press, p. 151.
- Yu, C. P. (1978) 'Exact Analysis of Aerosol Deposition during Steady Breathing', *Powder Technology*, 21(1), pp. 55-62.

## THE CORE OF THE HABILITATION THESIS – THE SCIENTIFIC PAPERS

### **Topic 1: The physical airway model preparation and production**

- HAB-1 Lizal, F., Elcner, J., Hopke, P. K., Jedelsky, J. and Jicha, M. (2012) 'Development of a realistic human airway model', Proceedings of the Institution of Mechanical Engineers Part H-Journal of Engineering in Medicine, 226(H3), pp. 197-207. IF(2012) = 1,419.

### **Topic-2: Experimental techniques applicable to human lungs and their replicas**

- HAB-2 Lizal, F., Jedelsky, J., Morgan, K., Bauer, K., Llop, J., Cossio, U., Kassinos, S., Verbanck, S., Ruiz-Cabello, J., Santos, A., Koch, E. and Schnabel, C. (2018) 'Experimental methods for flow and aerosol measurements in human airways and their replicas', *European Journal of Pharmaceutical Sciences*, 113, pp. 95-131. IF(2017) = 3,466.
- HAB-3 Lizal, F., Belka, M., Adam, J., Jedelsky, J. and Jicha, M. (2015) 'A method for in vitro regional aerosol deposition measurement in a model of the human tracheobronchial tree by the positron emission tomography', Proceedings of the Institution of Mechanical Engineers Part H-Journal of Engineering in Medicine, 229(10), pp. 750-757. IF(2015) = 0,996.
- HAB-4 Jedelsky, J., Lizal, F. and Jicha, M. (2012) 'Characteristics of turbulent particle transport in human airways under steady and cyclic flows', *International Journal of Heat and Fluid Flow*, 35, pp. 84-92. IF(2012) = 1,581.

HAB-5 Nordlund, M., Belka, M., Kuczaj, A. K., Lizal, F., Jedelsky, J., Elcner, J., Jicha, M., Sauser, Y., Le Bouhellec, S., Cosandey, S., Majeed, S., Vuillaume, G., Peitsch, M. C. and Hoeng, J. (2017) 'Multicomponent aerosol particle deposition in a realistic cast of the human upper respiratory tract', *Inhalation Toxicology*, 29(3), pp. 113-125. IF(2017) = 1,819.

### **Topic 3: Measurements of inhaled fibres in a lung replica**

HAB-6 Belka, M., Lizal, F., Jedelsky, J., Elcner, J., Hopke, P. K. and Jicha, M. (2018) 'Deposition of glass fibers in a physically realistic replica of the human respiratory tract', *Journal of Aerosol Science*, 117, pp. 149-163. IF(2017) = 2,281.

HAB-7 Belka, M., Lizal, F., Jedelsky, J., Starha, P., Druckmullerova, H., Hopke, P. K. and Jicha, M. (2016) 'Application of image analysis method to detection and counting of glass fibers from filter samples', *Aerosol Science and Technology*, 50(4), pp. 353-362. IF(2016) = 1,926.

### **Topic 4: Numerical calculations of fluid and particle flow**

HAB-8 Koullapis, P., Kassinos, S. C., Muela, J., Perez-Segarra, C., Rigola, J., Lehmkuhl, O., Cui, Y., Sommerfeld, M., Elcner, J., Jicha, M., Saveljic, I., Filipovic, N., Lizal, F. and Nicolaou, L. (2018) 'Regional aerosol deposition in the human airways: The SimInhale benchmark case and a critical assessment of in silico methods', *European Journal of Pharmaceutical Sciences*, 113, pp. 77-94. IF(2017) = 3,466.

HAB-9 Elcner, J., Lizal, F., Jedelsky, J., Jicha, M. and Chovancova, M. (2016) 'Numerical investigation of inspiratory airflow in a realistic model of the human tracheobronchial airways and a comparison with experimental results', *Biomechanics and Modeling in Mechanobiology*, 15(2), pp. 447-469. IF(2016) = 3,323.

HAB-10 Frederix, E. M. A., Kuczaj, A. K., Nordlund, M., Belka, M., Lizal, F., Jedelsky, J., Elcner, J., Jicha, M. and Geurts, B. J. (2018) 'Simulation of size-dependent aerosol deposition in a realistic model of the upper human airways', *Journal of Aerosol Science*, 115, pp. 29-45. IF(2017) = 2,281.

HAB-11 Farkas, Á., Lizal, F., Jedelsky, J., Elcner, J., Horváth, A. and Jicha, M. (2019) 'Simulation of Airway Deposition of an Aerosol Drug in COPD Patients', *Pharmaceutics*, 11(4). IF(2017) = 3,746.

# Development of a realistic human airway model

Proc IMechE Part H:  
*J Engineering in Medicine*  
226(3) 197–207  
© IMechE 2011  
Reprints and permissions:  
sagepub.co.uk/journalsPermissions.nav  
DOI: 10.1177/0954411911430188  
pjh.sagepub.com  


Frantisek Lizal<sup>1</sup>, Jakub Elcner<sup>1</sup>, Philip K Hopke<sup>2</sup>,  
Jan Jedelsky<sup>1</sup> and Miroslav Jicha<sup>1</sup>

## Abstract

Numerous models of human lungs with various levels of idealization have been reported in the literature; consequently, results acquired using these models are difficult to compare to in vivo measurements. We have developed a set of model components based on realistic geometries, which permits the analysis of the effects of subsequent model simplification. A realistic digital upper airway geometry except for the lack of an oral cavity has been created which proved suitable both for computational fluid dynamics (CFD) simulations and for the fabrication of physical models. Subsequently, an oral cavity was added to the tracheobronchial geometry. The airway geometry including the oral cavity was adjusted to enable fabrication of a semi-realistic model. Five physical models were created based on these three digital geometries. Two optically transparent models, one with and one without the oral cavity, were constructed for flow velocity measurements, two realistic segmented models, one with and one without the oral cavity, were constructed for particle deposition measurements, and a semi-realistic model with glass cylindrical airways was developed for optical measurements of flow velocity and in situ particle size measurements. One-dimensional phase doppler anemometry measurements were made and compared to the CFD calculations for this model and good agreement was obtained.

## Keywords

Human airway model, tracheo-bronchial tree, particle transport, particle deposition, oral cavity

Date received: 27 June 2011; accepted: 20 October 2011

## Introduction

The study of particle transport in the respiratory tract has been ongoing for more than 50 years. An appropriate description of the lung morphology is critical to these studies. In 1963, Weibel<sup>1</sup> described an idealized representation of human lung morphology from the trachea to alveoli. The symmetric Weibel 'A' model represents the lung in terms of regular features whereas the 'B' model includes asymmetric tracheo-bronchial branches. Weibel numbered the generations from the top of the model starting with the trachea, which was denoted as the zeroth generation. Horsfield and Cumming<sup>2</sup> and Horsfield<sup>3</sup> focused on lung asymmetry and proposed a more realistic model. Horsfield et al.<sup>4</sup> were the first to number the generations from the terminal bronchioles allowing a better description of the asymmetric branches. Lung morphology was thoroughly described by Raabe et al.<sup>5</sup>

All of these models are idealized representations of real lungs since they do not consider the protuberances and surface roughness that occur in nature. Therefore, to study realistic geometries, models were created by

casting of cadaver lungs. Such models were used by Zhou and Cheng<sup>6</sup> and Corcoran and Chigier.<sup>7</sup> With computerized tomography (CT) and magnetic resonance imaging (MRI), it became possible to obtain the airway geometries of live volunteers. Imaging is the most common way to acquire geometric data. However, it is very difficult to achieve sufficient image quality at or beyond the third branching generation because of chest movement caused by the heart beating during the image acquisition. Therefore, a combination of methods is used in which a lung cast is scanned by CT, and the digital model can be reproduced or used in numerical modelling studies. Models down to the 17th generation can be produced by this method.<sup>8,9</sup> CT and

<sup>1</sup>Faculty of Mechanical Engineering, Brno University of Technology, Czech Republic

<sup>2</sup>Center for Air Resources Engineering and Science, Clarkson University, USA

## Corresponding author:

Frantisek Lizal, Department of Thermodynamics and Environmental Engineering, Technicka 2, Brno 61669, Czech Republic.  
Email: lizal@fme.vutbr.cz



The segments of scanned data were processed with a marching cubes tracing method. Smoothing of the acquired geometric model resulted in a vector model with a polygonal triangular net. This model was saved as an STL file and imported into a Rhinoceros 4.0

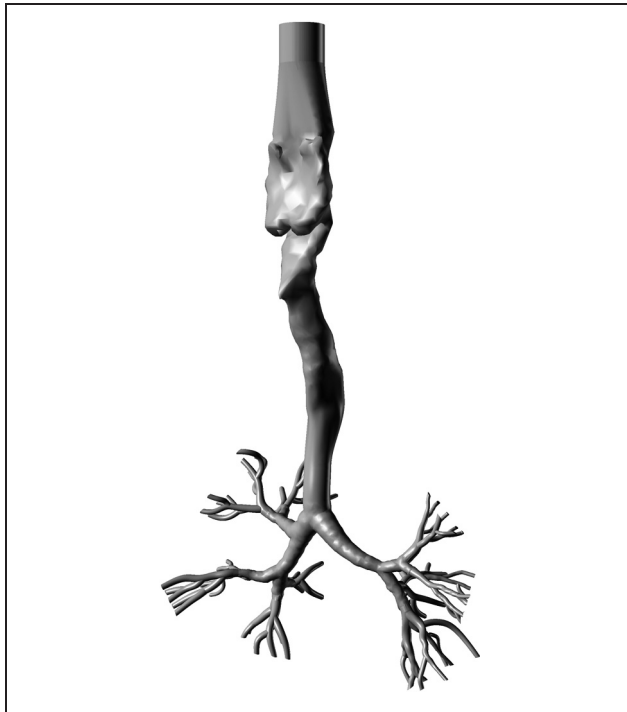


**Figure 2.** Geometry of the model without an oral cavity.

CAD system (McNeel, Seattle, WA) for final manual geometric correction (Figure 2).

### *Geometry of human airway with an oral cavity*

The next step was to develop a model with an oral cavity. This model allows the verification of the numerical simulations of Lin et al.<sup>16</sup> by comparing velocities at specific points in the model with and without the oral cavity. An upper part of the Lovelace Respiratory Research Institute 'A model'<sup>6</sup> was used to construct the new model. The wax model was scanned by an Atos (GOM, Braunschweig, Germany) device, converted to STL format, and concatenated with our original model at the trachea (Figure 3). The dimensions of this realistic model are listed in Table 1.

### *Geometry of semi-realistic model of human airways*

Phase Doppler anemometry (PDA) measurements were difficult to perform in the realistic model due to the complex shape of the airways. Measurements could only be performed at a few locations. To extend the range of possible measurement locations, the geometry was simplified using thin-walled glass tubes as the airways. The geometric simplification was designed to preserve the volume of each branch (see Table 2). Bifurcations were designed so they allowed connection of glass tubes with diameters corresponding to actual branches while preserving the branch angle. The oral

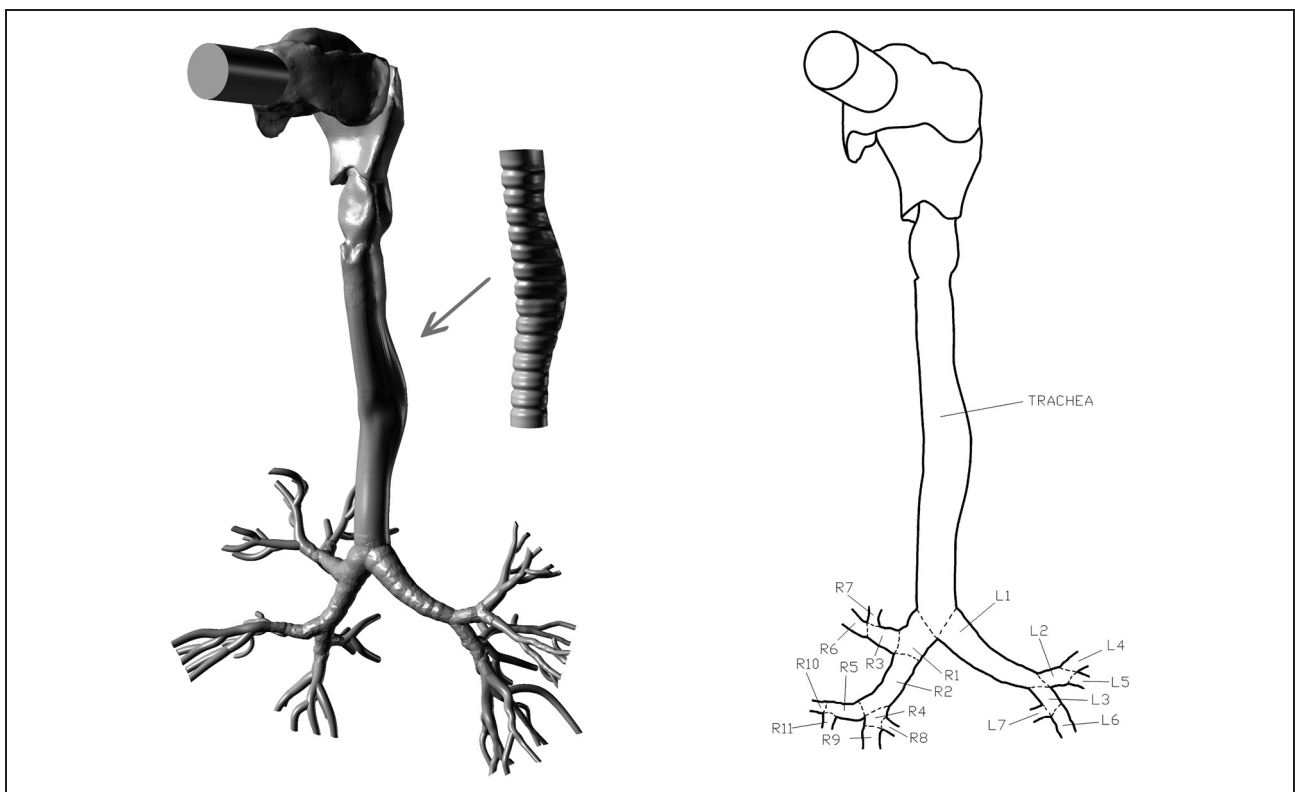


**Figure 3.** Realistic model geometry with the oral cavity.

cavity remained unchanged and generated the same flow field at the entrance of the trachea as in the original model (Figure 4). All of these models can be used for numerical simulations since their geometry can be transformed into STL format providing suitable input to the mesh generator.

### Physical experimental models

The digital geometries were used to fabricate five physical models. Additional models were fabricated to allow the use of optical methods for particle velocity and size measurement. Optically transparent thin walls were required. For the measurement of particle deposition, durable, segmented models were needed.

**Table 1.** Dimensions of the realistic models (notation corresponds to Figure 3).

Left			Right		
Branch	Length (mm)	Diameter (mm)	Branch	Length (mm)	Diameter (mm)
L1	42	10	R1	13	13
L2	16	6	R2	24	9
L3	7	6	R3	21	8
L4	3	6	R4	6	8
L5	6	5	R5	14	6
L6	10	6	R6	6	8
L7	9	5	R7	9	6
			R8	7	5
			R9	4	7
			R10	4	5
			R11	8	4

### Realistic models for optical measurements

For optical measuring methods such as laser doppler velocimetry it is necessary to avoid optical distortions created by complex airway shapes since differences in the refractive indices between air and the model material cause problems. If only the velocity field is to be measured, the media can be changed to a liquid mixture with the same refractive index as the model material.<sup>19</sup> However, measurement of aerosol transport is impossible in this manner. For velocity and particle size measurements using PDA under realistic conditions, refraction of light can be avoided by using a thin-walled model. The refraction of a beam passing through the model wall is proportional to the wall thickness. Therefore, the wall is made as thin as possible.

Initially the model geometry without the oral cavity was created. Since the model was intended for PDA measurements, it was not necessary to use transparent sections down to the seventh bifurcation since the PDA measurement volume is about 0.1 mm<sup>3</sup>. Thus, the airway diameter cannot be less than 4 mm. Also airway curvature limits the use of PDA. The transparent part of the model was restricted to the first four bifurcations on the right and to three bifurcations on the left. The model could be extended up to the seventh bifurcation level using non-transparent segments to produce realistic pressure and flow conditions.

The fabrication by Hopkins et al.<sup>8</sup> used transparent silicone poured around a water-soluble core encased in a box. After the silicone hardened, the core was dissolved leading to a transparent physical model. Our aim was to create a thin-walled model, so the methodology was modified. The silicone was brushed as a thin coat on the core. It was not possible to produce the whole core en bloc, so the geometry was divided in

**Table 2.** Dimensions of the semi-realistic model geometry.

Part	Realistic model		Semi-realistic model		
	Branch volume (mm <sup>3</sup> )	Branch length (mm)	Corresponding diameter of ideal cylinder (mm)	Inner diameter of tube (mm)	Corresponding length of tube (mm)
g1	24510	117	16.33	15.2	135.1
g2	3089	38	10.17	10.7	34.4
g3	201	6.0	6.53	6.0	7.1
g4	107	3.3	6.43	6.0	3.8
g5	28	1.0	5.97	6.0	1.0
g6	79	4.1	4.95	4.8	4.4
g7	117	5.6	5.16	4.8	6.5
g8	209	7.5	5.96	6.0	7.4
g9	992	8.0	12.57	10.7	11.0
g10	749	15.2	7.92	7.5	17.0
g11	96	3.7	5.75	6.0	3.4
g12	126	6.5	4.97	4.8	7.0
g13	1022	17.1	8.72	8.7	17.2
g14	78	2.3	6.57	6.0	2.8
g15	237	8.2	6.07	6.0	8.4
g16	57	3.9	4.31	4.0	4.5
g17	36	2.0	4.79	4.8	2.0
g18	87	4.3	5.08	4.8	4.8

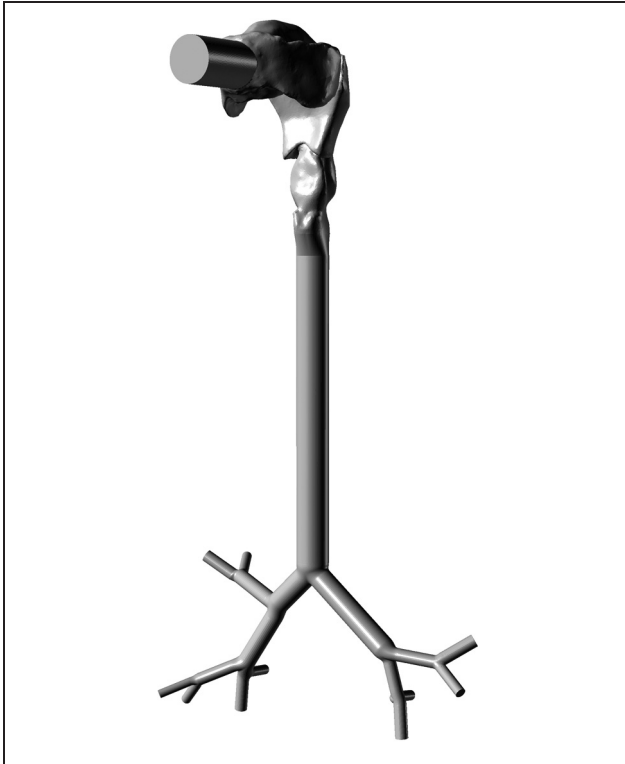


**Figure 4.** Semi-realistic model geometry.

the trachea and the two segments were arranged with slip-over connections. The geometry of the model is presented in Figure 5. Another model was prepared with an oral cavity using the same methodology.

Initially we used the same methodology as Hopkins et al. for the fabrication of the cores, but later we tested a different method because the water-soluble core material was no longer available. We used fused deposition modelling and the soluble core was produced on a Fortus 400 MC (Fortus, Eden Prairie, MN) from the polymer SR-30 that is commonly used as the soluble support for acrylonitrile butadiene styrene models. The core was dissolved in standard soluble support removal tank after application of silicone. Based on the need for transparency and good mechanical properties, Sylgard 184 (Dow Corning, Midland, MI) was found to be suitable for the brush coating and produced good transparent physical models. The refractive index of Sylgard 184 is 1.43.<sup>8</sup>

Layers of Sylgard 184 were applied successively. Each layer was cured for 10 min at 150 °C. The core was regularly rotated to ensure a uniform silicone layer. The thickness of silicone was approximately 2 mm at the entrance and 1 mm at the outlet. The resulting model was not fully transparent because the inner surface retained imprints of the core surface. A layer of silicone was applied to the inner surface to smooth the surface and render it fully transparent. The shape of the model was maintained with a wire frame connected to the model at the inlet and outlet by metal cylinders. Changes in the model geometry because of silicone wall elasticity were negligible for all of the tested breathing patterns

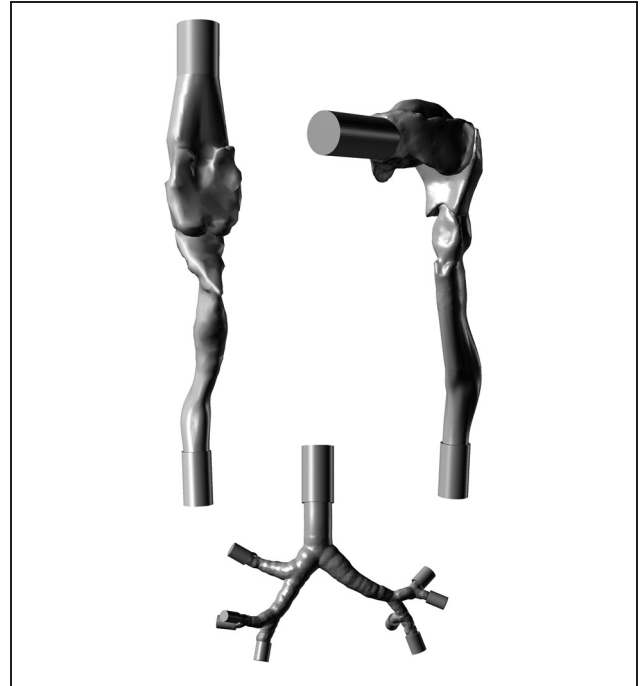


**Figure 5.** Cores for fabrication of realistic models.

(tidal volume  $V_t = 0.51$  l/min and period  $T = 4$  s,  $V_t = 1.1$  l/min and  $T = 4$  s,  $V_t = 1.51$  l/min and period  $T = 3$  s) since the outputs are tightly connected with the cylinders and the upper part is sufficiently thick 2 mm wall to maintain its shape. The flow control through different branches is described in the next section.

Fulfillment of the required optical and mechanical demands on the model for optical measurement was confirmed using following setup: airborne particles were generated from di-2-ethylhexyl sebacate using condensation monodisperse aerosol generator (TSI 3475, TSI Inc., Shoreview, MN) in size range 1–8  $\mu\text{m}$ . A sinusoidal breathing pattern was simulated by a computer-controlled pneumatic mechanism. Measurements were performed at 16 different cross-sections using one-dimensional PDA<sup>20</sup> (Dantec Dynamics, Skovlunde, Denmark).

The PDA results were used to validate the CFD simulation performed on an identical geometry (Figure 6). Recent developments in computational hardware capacity allow using large eddy simulation (LES) methods for airflow modelling in human lungs. However, the Reynolds averaged Navier–Stokes method using the  $k-\omega$  turbulence model is simpler, numerically more efficient, and in good agreement with in vitro data provided that near-wall turbulent fluctuations are correctly simulated.<sup>21,22</sup> Therefore, Wilcox's  $k-\omega$  model was implemented in commercial software (StarCCM + CD-ADAPCO) with  $y+$  wall treatment. The near-wall area was treated as a prism layer. The computational mesh consisted of polyhedral cells and contained approximately 400,000 cells resulting in at least 20 cells in the smallest bronchial cross-sections. Simulations were performed for a tidal volume of 0.51 and a period of 4 s. The inlet velocity condition was

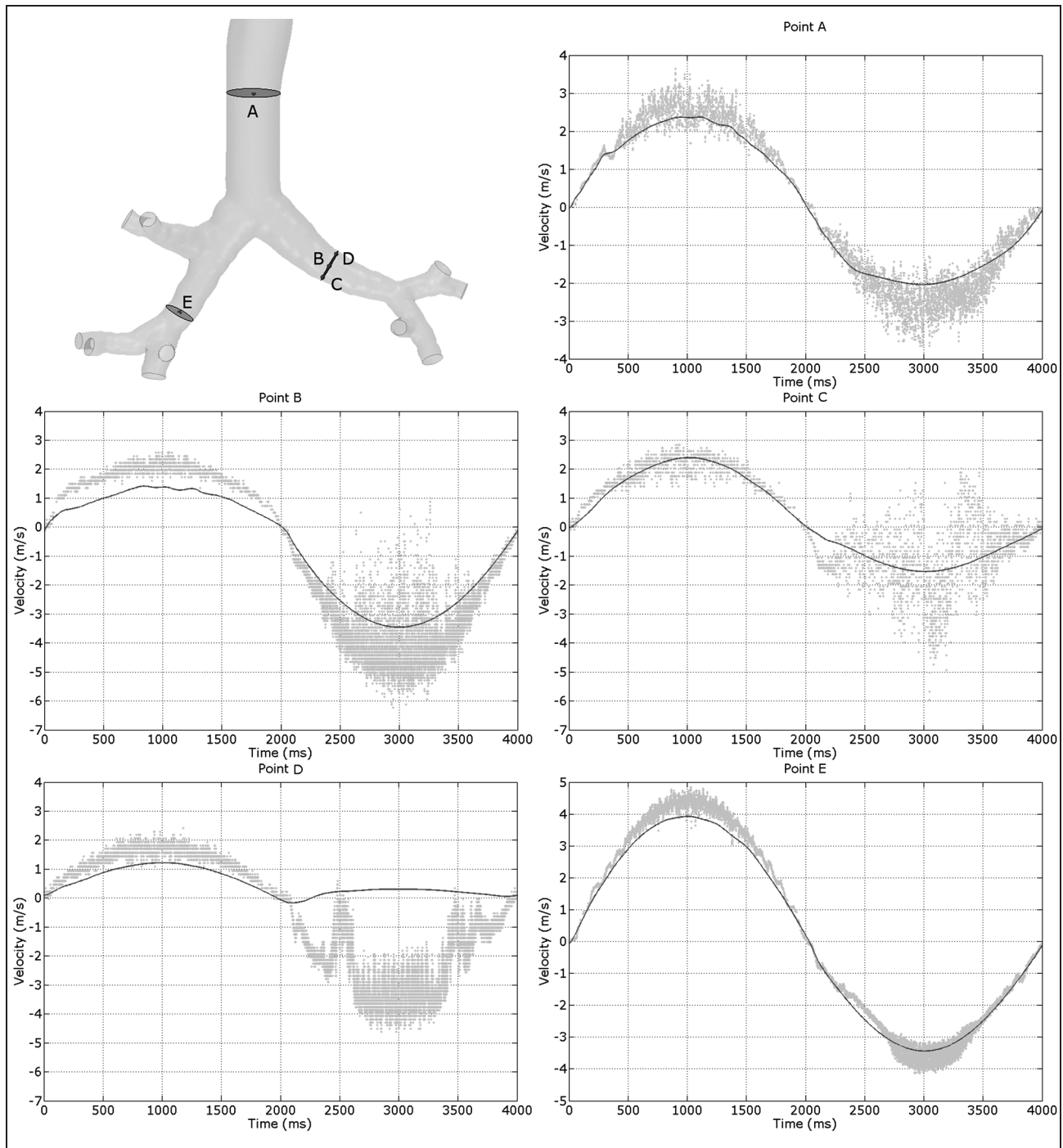


**Figure 6.** Comparison of measured (points) and simulated (line) axial velocity. Positive values stand for inhalation.

prescribed as input to the model, outlet pressure conditions were set at the end of branches. Comparisons of the axial velocities estimated by the CFD modelling (lines) with the experimental results (points) are presented in Figure 6. Each plot represents 10 consecutive breathing cycles. Each point signifies the velocity of one particle at a specific time as measured by PDA. Broader dispersion of velocities within a specific cycle is a consequence of higher turbulence intensity, while visible oscillations distinct from sinusoidal induced flow denotes repeated processes inherent to the flow at the measured location. The lines denoting the mean

axial velocity provided by the CFD model agree well with the measurement for all of the values with the exception of the exhalation phase at location D. This difference is most likely caused by limitations in the numerical method and associated boundary conditions. Using the LES method would probably result in a more accurate simulation of velocities at this location.

#### *Realistic model for deposition studies*

The next objective was to design and manufacture a physical model suitable for regional particle deposition

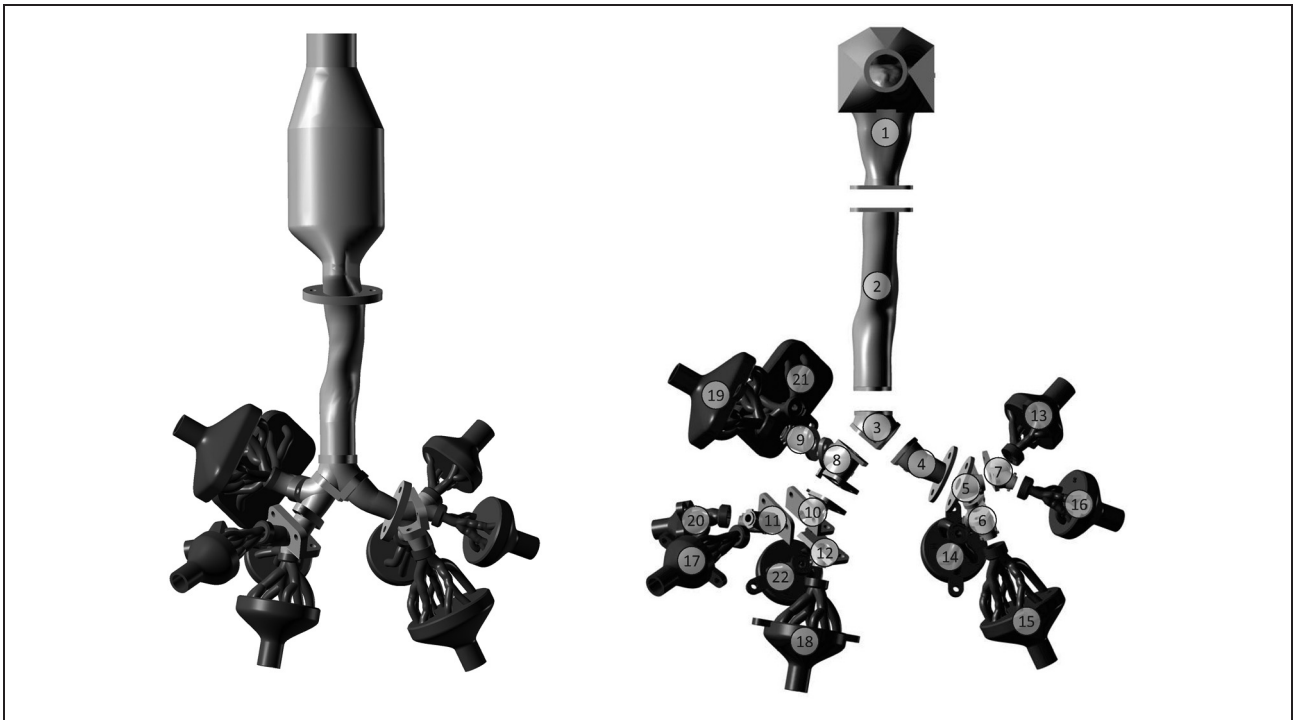


**Figure 7.** Realistic segmented models for measurement of deposition; without the oral cavity (left) and with the oral cavity (right).

measurements. For measurement of regional deposition by gravimetry or fluorometry, it is necessary to divide the model into separable segments connected to ensure an airtight model. The model spans branches whose diameter is above 3 mm and contains airways down to the seventh bifurcation. There was no need for optical transparency so the model could be directly produced by rapid prototyping. A 3 mm thick envelope was formed around the airway and flanges were added to each segment.

The terminal bronchi segments were connected to 10 outlets. Segments involving branches from the fourth to the seventh bifurcation (dark segments in Figure 7) were connected by joints sealed with silicone. The outlets were also sealed with silicone. In addition, a model based on the geometry with an oral cavity was built. To simplify the assembly, bayonet mounts were used to connect segments involving branches from the fourth to the seventh bifurcation. Ultimately, screw connections were used for the outlet.

Cartilaginous rings in trachea influence the deposition. For instance, Zhang and Finlay<sup>23</sup> used an idealized oral cavity and Weibel's symmetric geometry for three bronchial generations with and without cartilaginous rings in trachea. They found higher regional deposition in trachea with the rings, but no significant difference in following branches. Katz et al.<sup>24</sup> assumed, based on a numerical simulation that the effect of cartilaginous rings influenced several generations into the lung. Two versions of tracheal segment, with and without cartilaginous rings (Figure 3), were fabricated to study their effect on particle deposition in the bronchial region using the dimensions outlined in Putz and Pabst.<sup>25</sup>

The model was fabricated by stereolithography (Viper, 3D Systems, Rock Hill, SC) using WaterShed XC 11122. The built layer capability was 20  $\mu\text{m}$ , vertical resolution was 25  $\mu\text{m}$  and position repeatability was 7.6  $\mu\text{m}$ . Dark segments were also fabricated by PolyJet technology on an Eden 250 (Objet Geometries, Rehovot, Israel) from FullCure 720. The quality of the surface of these segments was poor with some material constantly crumbling from the inner surface after the fabrication, even after several cycles of ultrasonic cleaning. Therefore, stereolithography is preferable. Flow through the branches is controlled by valves in rotameters connected to each outlet. Measurements of sinusoidal or realistic breathing patterns is usually performed with the same boundary condition for each output<sup>26-28</sup> or a separate piston with a specific diameter for a given branch can be attached to each output in order to achieve more realistic conditions.

### Semi-realistic transparent model

Because of the complicated shape of the optically transparent model, data could only be acquired at a limited number of locations. To simplify the measurements, provide accurate positioning of the measurement volume in the model, and obtain additional information on the flow and motion of particles, a semi-realistic model was developed with cylindrical airways made of thin-walled glass. The glass tubes were connected with bifurcation segments made by rapid prototyping.

Initially, cross-sectional contours were obtained for a few cross-sections of each branch of interest using the software package Rhinoceros. The centres of the

contours were interpolated using splines. The length of a spline defined the length of an idealized straight branch. Diameters of glass tubes were calculated from the known volumes of realistic branches and their lengths. Bifurcations were created by following procedure:

*Step 1:* the bifurcation angles were preserved.

*Step 2:* the axis of parent/progeny branches were aligned with spline curves derived in the previous step.

*Step 3:* circles around each bifurcation were created perpendicular to appropriate branch axis. These circles formed bifurcation inlets and outlets. The bifurcations were manually simplified from the realistic bifurcations.

*Step 4:* the bifurcation tubes were connected by sockets in the bifurcation with O-ring grooves. The bifurcations were equipped with lugs to allow attachment to a frame.

The bifurcations were manufactured from a biocompatible thermoplastic material (ABS-M30i) with the Fortus 400 MC. The layer thickness was 0.127 mm and the accuracy was either 0.127 mm or 0.0381 mm per mm, whichever was greater. The surface was smoothed by a Fortus Finishing Station. The final parts were rigid, durable and opaque.

## Discussion

Our set of three geometries all based on Schmidt's geometry is compared to previously published models in Table 3. All physical models are presented in Figure 8. An advantage of our models is that they are based on realistic morphologies with asymmetric, three-dimensional bifurcations. Nagels and Cater<sup>29</sup> and Van Ertbruggen et al.<sup>30</sup> have predicted that the asymmetry of the bifurcations affects flow profiles and deposition. In comparison with previously published models, our models permit flow and deposition measurements and numerical modelling using the same geometry. Using data from different individuals was an appropriate solution when the complete geometry including oral cavity and tracheobronchial airways up to the seventh bifurcation were not available for any specific person. All of the constituent geometries are sufficiently realistic so that the resulting geometry is a representation of

human airways although it does not represent any specific individual. In vitro experiments performed on a specific individual over a period of time will represent slightly different airway geometries. Prior studies by Grgic et al.<sup>31</sup> of models based on multiple individuals has suggested that the small changes in the human airways due to natural or pathological changes do not have a large impact on results from such models. That work supports the combining of realistic geometries to form a realistic non-specific individual geometry. Thus, it is important to replicate the geometry created from realistic data so that it reasonably represents human physiology. In our case, it is only limited by the repeatability of the rapid prototyping systems, for a Fortus machine, the accuracy is either 0.127 mm or 0.0381 mm per mm, whichever is greater, and for Viper machine the vertical resolution is 0.025 mm and the position repeatability is 0.0076 mm.

The most important dimensionless numbers for transport and deposition of aerosol were calculated

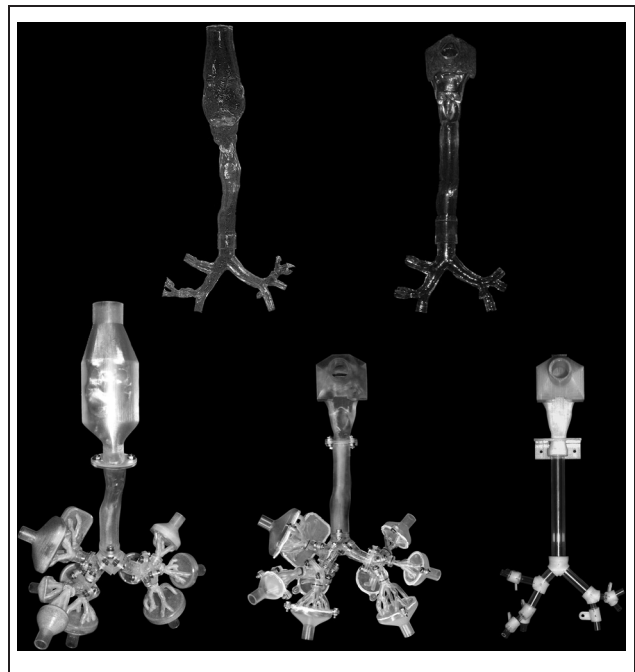


**Figure 8.** Current physical realistic models for in vitro measurements.

**Table 3.** Comparison of model geometries.

Generation no.	Weibel <sup>1</sup>		Present models		Kim and Fisher <sup>33</sup>		Tanaka et al. <sup>34</sup>		Adler and Brücker <sup>19</sup>		Zhou and Cheng <sup>6</sup>	
	Diameter (mm)		Diameter (mm)		Diameter (mm)		Diameter (mm)		Diameter (mm)		Diameter (mm)	
	Left	Right	Left	Right	Left	Right	Left	Right	Left	Right	Left	Right
Trachea 0	18.0		16.3				16.0		18.0		15.8	
Trachea 1	12.2		10.2	12.6			12.0	11.1	12.2		7.1	12.3
Trachea 2	8.3		6.5	8.3			7.8	8.1	8.3		6.0	7.8
Trachea 3	5.6		5.6	5.9		6.0	6.0	5.8	5.6		5.9	6.5
Trachea 4	4.5		3.8	4.4		5.0		5.2	4.4			5.6
Trachea 5	3.5		2.8	3.9		3.5			3.5			

**Table 4.** Minimum and maximum values of dimensionless numbers during experiments.

	Segment number																					
	1	2	3	4	5	6	7	8	9	10	11	12	13	14	15	16	17	18	19	20	21	22
Equivalent diameter (mm)	20.0	16.3	14.7	10.2	7.0	5.5	6.0	12.1	7.8	8.5	6.5	7.0	3.0	3.3	3.3	2.5	3.6	4.1	3.6	2.6	3.4	3.4
Minimum values																						
Reynolds number <sup>a</sup>	1053	1411	1433	735	903	715	398	1219	612	1173	735	742	564	412	1657	766	778	1150	1128	1312	587	629
Womersley number <sup>b</sup>	3.2	2.6	2.4	1.6	1.1	0.9	1.0	2.0	1.3	1.4	1.0	1.1	0.5	0.5	0.5	0.4	0.6	0.7	0.6	0.4	0.5	0.5
Stokes number <sup>c</sup> ( $\times 10^{-04}$ )	1	2	3	3	9	10	5	4	5	8	8	7	20	20	40	50	30	20	30	70	30	20
Dean number <sup>d</sup>	412	127	1005	230	363	176	192	390	259	532	295	331										
Reynolds number	4213	5170	5732	2465	3591	2885	1545	4886	2449	4709	2874	3050	1285	1404	3385	2227	2766	3155	2960	3414	2487	2436
Womersley number	3.7	3.0	2.7	1.9	1.3	1.0	1.1	2.3	1.5	1.6	1.2	1.3	0.5	0.6	0.6	0.5	0.7	0.8	0.7	0.5	0.6	0.6
Stokes number ( $\times 10^{-02}$ )	2	3	4	4	10	10	7	5	6	10	10	10	20	20	50	60	30	30	40	80	30	30
Dean number	1648	467	4019	772	1443	709	745	1563	1037	2135	1156	1361										

<sup>a</sup>Re =  $D_e U/\nu$ , <sup>b</sup>  $\alpha = (D_e/2) \sqrt{\omega/\nu}$ , <sup>c</sup> St =  $\rho_p d_p^2 C_c U / 18 \mu D_e$ , <sup>d</sup> De =  $Re \sqrt{D_e/2R_c}$ .

and are presented in Table 4. These calculations were based on an equivalent diameter of a conceptual cylinder having the same volume and surface as the airway. The volume and inner surface of all segments were determined from the digitized model geometry. The input diameter was used as an equivalent diameter for segments containing a single bifurcation. Different calculations of equivalent diameter were used for segments containing additional bifurcations. Equivalent diameters of conceptual cylinders were calculated for each branch of the same generation in a segment. The resulting conceptual cylinders were then averaged over all branches within a generation and over all generations of a segment to obtain the final equivalent diameter. Values of dimensionless numbers were calculated for all combinations of three breathing patterns (resting conditions with tidal volume  $V_t = 0.5$  l/min and period  $T = 4$  s, deep breathing  $V_t = 1$  l/min and  $T = 4$  s, light activity  $V_t = 1.5$  l/min and period  $T = 3$  s) and three sizes of aerosol particles (1, 3 and 6  $\mu\text{m}$ ).

The Womersley number is the ratio of pulsatile flow frequency to viscous forces. When its value is below one, it means that pulsations are slow and the parabolic velocity profile has enough time to develop during each cycle. When the Womersley number is higher than 10, the pulsations are so fast that the velocity profile is flat and the flow lags the pressure gradient by  $\pi/2$ . The Stokes number is the ratio of the particle stopping distance to a characteristic dimension of the obstacle. When its value is much less than one, the particle follows the fluid streamlines. When its value is much higher than one, particles continue in a straight line and impact on the obstacle. The Dean number represents the effects of flow curvature compared to viscosity and hence the strength of secondary flow. Correlations between the Dean number and aerosol deposition were presented by Longest and Vinchurkar.<sup>32</sup> Determination of the Dean number in a realistic model is complicated, as the daughter branches deflect in different angles and therefore, form two radii of curvature. We calculated two Dean numbers for each bifurcation and their average values are presented in Table 4. The radius of curvature was measured using the axes of the parent and daughter branches that were tangent to a circle whose radius is equal to radius of curvature. The circle was constructed using Rhinoceros software on the digitized geometry.

## Conclusions

For detailed experimental studies of the flow field and particle transport and deposition in human airways, we need multiple especially designed models to provide the measurement capabilities needed for these studies. Based on a realistic human airway geometry, three model geometries have been developed permitting the manufacture of five different physical models. The same digitized geometries were also used for

numerical airflow simulations. One of the physical models was a realistic transparent model without an oral cavity and a corresponding model for deposition studies. A second transparent model with an oral cavity and its corresponding deposition model were developed. Finally, a semi-realistic model with glass tubes was created, which is suitable for both optical measurements and deposition studies. Our complete set of models permits comparison of results acquired with numerical simulations and particle transport experiments.

## Funding

This work was supported by the Czech Science Foundation under grant GA P105/11/1339, by COST Action 0806 projects OC10049 and OC10052 and by project ME 09030 of the program KONTAKT supported by the Czech Ministry of Education, Youth and Sports.

## Acknowledgements

The authors gratefully acknowledge Andres Kriete (Drexel University) for providing the bronchial geometry, Young-Sung Cheng (LRRRI Albuquerque) for providing the wax cast of the 'A model', St. Anna University Hospital for a realization of CT of airways, Premysl Krsek from the Faculty of Information Technology of the Brno University of Technology for data processing, Zuocheng Wang for his valuable advice and Douglas Leonard (both from Clarkson University) for manufacturing of segmented models.

## Conflict of interest

The authors declare that there is no conflict of interest related to the work in this paper.

## References

1. Weibel ER. *Morphometry of the human lung*. New York: Academic Press, 1963.
2. Horsfield K and Cumming G. Angles of branching and diameters of branches in human bronchial tree. *Bull Math Biophys* 1967; 29(2): 245–259.
3. Horsfield K. Morphometry of small pulmonary-arteries in man. *Circulation Res* 1978; 42(5): 593–597.
4. Horsfield K, Dart G, Olson DE, et al. Models of human bronchial tree. *J Appl Physiol* 1971; 31(2): 207–217.
5. Raabe OG, Yeh HC, Schum GM and Phalen RF. Tracheobronchial geometry: human, dog, rat, hamster. Lovelace Foundation Report, LF-53, Albuquerque, NM, 1976, <http://mae.ucdavis.edu/wexler/lungs/LF53-Raabe/> (accessed on 9 November 2011).
6. Zhou Y and Cheng YS. Particle deposition in a cast of human tracheobronchial airways. *Aerosol Sci Technol* 2005; 39(6): 492–500.
7. Corcoran TE and Chigier N. Inertial deposition effects: a study of aerosol mechanics in the trachea using laser doppler velocimetry and fluorescent dye. *Trans ASME, J Biomech Engng* 2002; 124(6): 629–637.

8. Hopkins LM, Kelly JT, Wexler AS and Prasad AK. Particle image velocimetry measurements in complex geometries. *Exp Fluids* 2000; 29(1): 91–95.
9. Clinkenbeard RE, Johnson DL, Parthasarathy R, et al. Replication of human tracheobronchial hollow airway models using a selective laser sintering rapid prototyping technique. *AIHAJ* 2002; 63(2): 141–150.
10. National Library of Medicine/National Institutes of Health. Visible human project, [http://www.nlm.nih.gov/research/visible/visible\\_human.html](http://www.nlm.nih.gov/research/visible/visible_human.html) (2009) (accessed February 2010).
11. Schmidt A, Zidowitz S, Kriete A, et al. A digital reference model of the human bronchial tree. *Comput Med Imaging Graphics* 2004; 28(4): 203–211.
12. Chen JS and Kim J. Micro particle transport and deposition in human upper airways. In: *ASME International mechanical engineering congress and exposition 2007* November 11–15, 2007, Seattle, Washington, USA, Proceedings of the ASME International Mechanical Engineering Congress And Exposition 2007, Vol 2: Biomedical and Biotechnology Engineering, AMER Soc Mechanical Engineers, New York, 2008, pp. 271–280.
13. Isaacs KK, Schlesinger RB and Martonen TB. Three-dimensional computational fluid dynamics simulations of particle deposition in the tracheobronchial tree. *J Aerosol Med-Deposition Clearance Effects Lung* 2006; 19(3): 344–352.
14. Martonen TB, Zhang ZQ, Yu GQ and Musante CJ. Three-dimensional computer modeling of the human upper respiratory tract. *Cell Biochem Biophys* 2001; 35(3): 255–261.
15. Nowak N, Kakade PP and Annapragada AV. Computational fluid dynamics simulation of airflow and aerosol deposition in human lungs. *Ann Biomed Engng* 2003; 31(4): 374–390.
16. Lin CL, Tawhai MH, McLennan G and Hoffman EA. Characteristics of the turbulent laryngeal jet and its effect on airflow in the human intra-thoracic airways. *Respiratory Physiol Neurobiol* 2007; 157(2-3): 295–309.
17. Choi J, Tawhai MH, Hoffman EA and Lin CL. On intra- and intersubject variabilities of airflow in the human lungs. *Phys Fluids* 2009; 21(10): article number 101901.
18. Roupec M. Comparison of the real and idealized human airways model. Report, Department of Thermodynamics and Environmental Engineering, Brno University of Technology, Brno, 2009, p. 25.
19. Adler K and Brücker C. Dynamic flow in a realistic model of the upper human lung airways. *Exp Fluids* 2007; 43(2-3): 411–423.
20. Jedelsky J, Lizal F and Jicha M. Realistic transparent human airway model: flow distribution and aerosol transport under steady and unsteady flows. In: *20th International symposium on transport phenomena*, Victoria BC, 7–10 July 2009, University of Victoria, published in Victoria, BC, Canada. 2009, pp. 1–7.
21. Longest PW and Holbrook LT. In silico models of aerosol delivery to the respiratory tract — development and applications. *Adv Drug Delivery Rev*, in press, 2011.
22. Kleinstreuer C, Zhang Z and Li Z. Modeling airflow and particle transport/deposition in pulmonary airways. *Respiratory Physiol Neurobiol* 2008; 163(1-3): 128–138.
23. Zhang Y and Finlay WH. Measurement of the effect of cartilaginous rings on particle deposition in a proximal lung bifurcation model. *Aerosol Sci Technol* 2005; 39(5): 394–399.
24. Katz IM, Davis BM and Martonen TB. A numerical study of particle motion within the human larynx and trachea. *J Aerosol Sci* 1999; 30(2): 173–183.
25. Putz R and Pabst R. *Atlas of human anatomy*. Prague, Czech Republic: Grada Publishing, 2007.
26. De Rochefort L, Vial L, Fodil R, et al. In vitro validation of computational fluid dynamic simulation in human proximal airways with hyperpolarized He-3 magnetic resonance phase-contrast velocimetry. *J Appl Physiol* 2007; 102: 2012–2023.
27. Grosse S, Schroder W, Klaas M, et al. Time resolved analysis of steady and oscillating flow in the upper human airways. *Exp Fluids* 2007; 42: 955–970.
28. Lieber B and Zhao Y. Oscillatory flow in a symmetric bifurcation airway model. *Ann Biomed Engng* 1998; 26: 821–830.
29. Nagels MA and Cater JE. Large eddy simulation of high frequency oscillating flow in an asymmetric branching airway model. *Med Engng Phys* 2009; 31(9): 1148–1153.
30. Van Ertbruggen C, Hirsch C and Paiva M. Anatomically based three-dimensional model of airways to simulate flow and particle transport using computational fluid dynamics. *J Appl Physiol* 2005; 98(3): 970–980.
31. Grgic B, Finlay WH, Burnell PKP and Heenan AF. In vitro intersubject and intrasubject deposition measurements in realistic mouth-throat geometries. *J Aerosol Sci* 2004; 35(8): 1025–1040.
32. Longest PW and Vinchurkar S. Inertial deposition of aerosols in bifurcating models during steady expiratory flow. *J Aerosol Sci* 2009; 40(4): 370–378.
33. Kim CS and Fisher DM. Deposition characteristics of aerosol particles in sequentially bifurcating airway models. *Aerosol Sci Technol* 1999; 31(2-3): 198–220.
34. Tanaka G, Ogata T, Oka K and Tanishita K. Spatial and temporal variation of secondary flow during oscillatory flow in model human central airways. *Trans ASME, J Biomech Engng* 1999; 121(6): 565–573.

## Appendix I

### Notation

$C_c$	Cunningham correction factor
$d_p$	particle diameter (m)
$D_e$	equivalent diameter (m)
$R_c$	radius of curvature (m)
$T$	period (s)
$U$	mean flow velocity (m/s)
$V_t$	tidal volume (m <sup>3</sup> )
$\mu$	absolute viscosity (kg/m/s)
$\nu$	kinematic viscosity (m <sup>2</sup> /s)
$\rho_p$	particle density (kg/m <sup>3</sup> )
$\omega$	angular frequency of oscillations (s <sup>-1</sup> )



## Experimental methods for flow and aerosol measurements in human airways and their replicas



Frantisek Lizal<sup>a</sup>, Jan Jedelsky<sup>a,\*</sup>, Kaye Morgan<sup>b,c,d</sup>, Katrin Bauer<sup>e</sup>, Jordi Llop<sup>f</sup>, Unai Cossio<sup>f</sup>, Stavros Kassinos<sup>g</sup>, Sylvia Verbanck<sup>h</sup>, Jesús Ruiz-Cabello<sup>i,j</sup>, Arnaldo Santos<sup>i</sup>, Edmund Koch<sup>k</sup>, Christian Schnabel<sup>k</sup>

<sup>a</sup> Faculty of Mechanical Engineering, Brno University of Technology, Technická 2896/2, Brno 61669, Czech Republic

<sup>b</sup> School of Physics and Astronomy, Monash University, Clayton, Victoria 3800, Australia

<sup>c</sup> Institute for Advanced Studies, Technical University of Munich, Lichtenbergstrasse 2 a, 85748 Garching, Germany

<sup>d</sup> Chair of Biomedical Physics, Department of Physics, Technical University of Munich, James-Frank-Str. 1, 85748 Garching, Germany

<sup>e</sup> Institute of Mechanics and Fluid Dynamics, TU Bergakademie Freiberg, Lampadiusstr. 4, 09599 Freiberg, Germany

<sup>f</sup> Radiochemistry and Nuclear Imaging Group, CIC biomaGUNE, Paseo Miramon 182, 20014 San Sebastian, Gipuzkoa, Spain

<sup>g</sup> Computational Science Laboratory, Department of Mechanical and Manufacturing Engineering, University of Cyprus, Kallipoleos Ave. 75, Nicosia 1678, Cyprus

<sup>h</sup> Respiratory Division, University Hospital UZ Brussel, Vrije Universiteit Brussel, Belgium

<sup>i</sup> Universidad Complutense de Madrid (UCM), Av. Séneca, 2, 28040 Madrid, Spain

<sup>j</sup> Ciber de Enfermedades Respiratorias (CIBERES), Av. Monforte de Lemos, 3-5. Pabellón 11. Planta 0, 28029 Madrid, Spain

<sup>k</sup> TU Dresden, Faculty of Medicine Carl Gustav Carus, Anesthesiology and Intensive Care Medicine, Clinical Sensing and Monitoring, Fetscherstrasse 74, 01307 Dresden, Germany

### ARTICLE INFO

#### Keywords:

Computational fluid particle dynamics  
Human airways  
Lungs  
Experimental methods  
Medical imaging  
Aerosol deposition  
Velocimetry techniques  
Flow measurement techniques  
Gas–liquid two-phase flow  
CFD validation

### ABSTRACT

Recent developments in the prediction of local aerosol deposition in human lungs are driven by the fast development of computational simulations. Although such simulations provide results in unbeatable resolution, significant differences among distinct methods of calculation emphasize the need for highly precise experimental data in order to specify boundary conditions and for validation purposes. This paper reviews and critically evaluates available methods for the measurement of single and disperse two-phase flows for the study of respiratory airflow and deposition of inhaled particles, performed both *in vivo* and in replicas of airways. Limitations and possibilities associated with the experimental methods are discussed and aspects of the computational calculations that can be validated are indicated. The review classifies the methods into following categories: 1) point-wise and planar methods for velocimetry in the airways, 2) classic methods for the measurement of the regional distribution of inhaled particles, 3) standard medical imaging methods applicable to the measurement of the regional aerosol distribution and 4) emerging and nonconventional methods. All methods are described, applications in human airways studies are illustrated, and recommendations for the most useful applications of each method are given.

### 1. Introduction

Several methods for predicting the results of pulmonary drug delivery have established themselves in recent years. One such method, used for drugs with very high bioavailability, predicts the total expected lung dose for healthy lungs and uses that to estimate the concentration of drug in blood plasma against time (expressed by the area under the plasma drug concentration–time curve, AUC) (Olsson et al., 2013). In order to improve these predictions, two distinct trends are emerging that require accurate predictions of local (as opposed to global/total) deposition. First, there is a push toward the development of drugs that

are customised for a particular class of patients, e.g. for asthma or chronic obstructive pulmonary disease (COPD) patients. Even though they are not likely to be achieved in the very near future, inhalational products that are tailored to individual patients or classes of patients are envisioned and their development also relies on accurate estimates of local deposition (Bettoncelli et al., 2014; Forbes et al., 2016). On the other hand, there is an increasing momentum for the use of large-scale population studies to be used as the basis for the development of statistical correlations linking airway structural, functional and phenotype parameters to the observed trends of regional deposition for various patient classes. Such statistical trends can then form the basis for the

\* Corresponding author.

E-mail address: [jedelsky@fme.vutbr.cz](mailto:jedelsky@fme.vutbr.cz) (J. Jedelsky).

**Nomenclature and units**

<i>A</i>	radioactivity, (Ci, Bq)
<i>c</i>	number concentration, (1/m <sup>3</sup> )
CPS	counts per second, (1/s)
CV	coefficient of variation, (–)
<i>D</i>	diameter, (m, μm)
<i>d</i>	the Gaussian beam diameter, (m)
<i>D<sub>qr</sub></i>	mean droplet diameter with indices <i>q</i> and <i>r</i> used for determination of the diameter type, (μm)
<i>E</i>	energy, (MeV, keV)
<i>f</i>	frequency, (Hz)
FD	fibre density, (1/mm <sup>2</sup> )
<i>f<sub>w</sub></i>	weighting factor, (–)
<i>N</i>	number of particles, number of radioactive atoms, (–)
<i>n</i>	refractive index, (–)
<i>n̄</i>	mean sampling rate, (Hz)
<i>p</i>	<i>P</i> value, or calculated probability, (–)
PSD	power spectral density, (m <sup>2</sup> /s)
<i>R2*</i>	transverse relaxivity, (s)
<i>S</i>	area, (m <sup>2</sup> )
<i>s</i>	fringe spacing (fringe separation distance), (m)
SR	spatial resolution, (1/m)
<i>T</i>	time period, (s)
<i>t</i>	time, (h)
<i>T1</i>	longitudinal relaxation time, (s)
<i>T<sub>1/2</sub></i>	half-life of a radioisotope, (h, min, s)
<i>T2</i>	spin–spin relaxation time, (s)
<i>T2*</i>	decay of transverse magnetization, (s)
TDF	total deposited fraction, (–)
TI	turbulence intensity, (–)
TV	tidal volume, (l)
<i>u</i>	velocity, (m/s, cm/s, mm/s, μm/s)
<i>V</i>	volume, (ml)
<i>V̇</i>	flow rate, (l/s, l/min, ml/s)
<i>x, y, z</i>	Cartesian coordinates, (m)
%ID/g	percentage of injected dose per gram of tissue, (1/g)

**Greek characters**

$\beta$	attenuation of the x-ray, (–)
$\Delta t$	time lag of two signals (LDA, PDA), delay between laser pulses (PIV), (s)
$\Delta\varphi$	phase difference, (rad)
$\delta$	change of the phase of the x-ray, (–)
$\nu$	kinematic viscosity, (m <sup>2</sup> /s)
$\Theta$	Intersection angle of two beams, (deg)
$\Lambda$	wavelength of the laser light, (nm)
$\lambda$	decay constant, (–)
$\tau_i$	integral time-scale, (s)
$\Phi$	parameter of the PDA system, (–)

**Subscripts**

0	initial number
B	frequency shift
b	breathing
D	Doppler
i	index number
in	inhaled
max	maximum
n	normal velocity component
out	exhaled
p	particle
T	transit

**Dimensionless numbers**

Re	Reynolds number
Stk	Stokes number
$\alpha$	Womersley number

**Abbreviations**

[ <sup>18</sup> F]FDG	2-deoxy-2-( <sup>18</sup> F)fluoro-D-glucose
2C, 3C	two-component, three-component
2D, 3D, 4D	two-dimensional, three-dimensional, four-dimensional
AM	additive manufacturing
aOCT	anatomical OCT
AUC	area under the curve
CCA	constant current anemometer
CCD	charge-coupled device
CFD	computational fluid dynamics
CFPD	computational fluid particle dynamics
CMOS	complementary metal–oxide–semiconductor
COPD	chronic obstructive pulmonary disease
CS	compressed sensing
CT	computed tomography
CTA	constant temperature anemometer
DTPA	diethylene triamine penta acetic acid
DOTA	1,4,7,10-tetraazacyclododecane-1,4,7,10-tetraacetic acid
EIT	electrical impedance tomography
FBP	filtered-back-projection
FD-OCT	Fourier domain OCT, also frequency domain OCT
FDA	Food and Drug Administration
FDML	Fourier domain mode locked
FOV	field of view
fps	frames per second
FWHM	full width at half maximum
GC–MS	gas chromatography – mass spectrometry
HFOV	high frequency oscillatory ventilation
HUA	human upper airways
HWA	hot-wire anemometry
ICRP	International Commission on Radiological Protection
ID	injected dose
LD	laser Doppler
LDA	laser Doppler anemometry
LDV	laser Doppler velocimetry
LES	large eddy simulation
MEMS	microelectromechanical systems
MPI	magnetic particle imaging
MRI	magnetic resonance imaging
MRV	magnetic resonance velocimetry
NIR	near infrared wavelength range
NP	nanoparticle
OCT	optical coherence tomography
OFDI	optical frequency domain imaging
OSEM	ordered subset expectation maximization
PBPK	physiologically based pharmacokinetic
PCM	phase contrast microscopy
PCXI	phase contrast x-ray imaging
PD	phase Doppler
PDA	phase Doppler anemometry, particle dynamics analysis
PDI	phase Doppler interferometer
PDMS	polydimethylsiloxane
PDPA, P/DPA	phase Doppler particle analyser
PET	positron emission tomography
PIV	particle image velocimetry
ppm	parts per million
ppp	particles per pixel
PTV	particle tracking velocimetry

px	pixel	SMI	Soft Mist™ Inhaler
RANS	Reynolds-averaged Navier–Stokes	SNR	signal to noise ratio
RMS	root-mean-square	SPECT	single photon emission computed tomography
ROI	region of interest	SUV	standard uptake value
RP	rapid prototyping	TD-OCT	time domain OCT
SCPN	single-chain polymer nanoparticle	TEM	transmission electron microscopy
SD-OCT	spectral domain OCT	UTE	ultra-short echo
SEM	scanning electron microscopy	VOI	volume of interest
SLA	stereolithography		

development of improved physiologically-based pharmacokinetic (PBPK) models for use in the drug development, approval and regulation cycle (Backman et al., 2017). In both of these emerging trends, the synergistic use of experimental and *in silico* methods is playing a central role.

Impressive work has been carried out in the area of *in silico* modelling of aerosol flow and deposition in last decades. This approach is based largely on Computational Fluid Particle Dynamics (CFPD), developed as a branch of fluid mechanics and involving numerical analysis of fluid and particle flows in digital representations of real or idealised geometries. CFPD is capable of calculating fluid, particle and structure interactions provided the correct boundary conditions were set. The general overview was given e.g. by Tu et al. (2013).

Overall lung deposition can be predicted both experimentally and by CFPD with sufficient precision nowadays. It is also possible to calculate “regional” deposition at the macroscale, usually per lung lobe or per generation. These equations are available e.g. from the International Commission for Radiological Protection (ICRP) (Bailey, 1994). However, assessing the local deposition at the microscale (e.g. in units of mm<sup>2</sup>), either experimentally or *in silico*, remains a challenging task. Experimental methods, particularly in imaging, face problems with difficult and obstructed access to the deposition sites in the human lungs, limited resolution, and/or associated health hazards depending on the particular method. In this regard, *in silico* methods can fill the gaps left by *in vivo* methods that use the current state of the art in pulmonary imaging. *In silico* methods can provide detailed information regarding the deposition of aerosol particles in individual airway branches. The typical workflow for such studies begins with the acquisition of chest Computed Tomography (CT) scans of the patient, followed by the use of specialised software to segment the airways and generate CFPD meshes on which the discretized form of the governing transport equations can be solved. The resolution limitations of current imaging equipment set the limit of such detailed airway reconstruction between roughly the 7<sup>th</sup> and 10<sup>th</sup> bronchial generation, depending on the specific airway configuration for each patient. *In silico* estimates of aerosol deposition in the upper part of the bronchial tree using one of the CFPD methods called Large Eddy Simulation (LES) have become fairly routine, especially under conditions of steady inhalation rate. However, for drug development one needs to consider the entire lung and the full respiratory cycle, allowing for variations in possible inhalation manoeuvres. To do this requires coupling the LES simulation in the upper airways with reduced models for the central bronchial tree and models of the acinus. This represents an area of intense research and development with different groups adopting varying approaches for such coupled simulations (Kolanjiyil and Kleinstreuer, 2013; Koullapis et al., 2017a; Longest et al., 2012). The impact of such integrated simulations on drug development and patient care could potentially be quite strong, yet a number of conditions need to be satisfied before these approaches can deliver on their promise.

In modelling airflow and deposition in the various regions of the lung, a number of choices can be made in terms of both the computational tools used and the physical effects that are modelled. As a result of work carried out over the last decade by several groups, many of the factors that contribute to the fidelity of *in silico* studies are now

understood much better. However, this understanding should be documented and clearly spelt out in the specific context of deposition studies in human airways.

The community consensus is that the airflow in the mouth, extra-thoracic and upper tracheobronchial tree can be resolved with satisfactory accuracy using LES (Choi et al., 2009; Jayaraju et al., 2008; Koullapis et al., 2017b; Longest and Holbrook, 2012). But even within LES there are a multitude of choices to be made regarding the use of inlet and boundary conditions, the use of sub-grid scale models, the discretization schemes and the mesh design. Furthermore, these issues are often interconnected, for example, the accuracy of a particular discretization scheme often depends on the particular mesh design adopted. While a large volume of information is available in the literature regarding the factors that affect the performance of LES, these are often examined in the context of canonical flows. When LES is used in the context of aerosol deposition studies, additional questions arise related to the particle tracking algorithms and the modelling of physical effects acting on the dispersed phase. For example, it is often argued, on the ground of dimensional considerations, that certain forces such as the Saffman lift force should be negligible in airway deposition simulations (Finlay et al., 1996). However, this assumption has not been subjected to a systematic validation. Therefore, there is currently a need for systematic evaluation and validation of LES that will specifically target best practice recommendations for *in silico* deposition studies. Such evaluation and validation must rely at least in part on independent flow and deposition data originating from studies on human airway replicas or directly *in vivo*. The problem one is faced with is that *in silico* methods are recruited to fill the gap created by the limited resolution of current imaging technologies, yet the validation and verification of *in silico* methods must, at least to some extent, rely on such limited data. This apparent paradox makes necessary the careful selection of data validation metrics that are both meaningful and reliable at the same time.

Clear guidelines on best practice in the design of *in silico* deposition studies must be the result of a systematic effort that will result in the necessary community consensus. The value of such a consensus from the purely technical point of view is clear. The significance, however, extends beyond technical considerations. One has to appreciate that such a community consensus is a necessary ingredient for enabling the routine use of *in silico* population studies in the drug development and regulatory approval cycle. Without clearly spelt out design rules and validation metrics, both the pharmaceutical industry and the regulatory agencies are likely to resist admitting *in silico* methods in their workflow. Without acceptance from these key stakeholders, the potential of *in silico* methods is destined to be kept locked in the realm of academic and research institutions. These considerations should make clear that the establishment of best practice guidelines for simulation methods used in airway deposition studies is of paramount importance to the future of *in silico* population studies for inhaled drug development.

The main aim of this paper is to provide an overview of experimental techniques that can be used to validate *in silico* methods. We have prepared a summary of principles, features, precisions, strengths, weaknesses, and practical applications of available experimental methods applied on flow and aerosol measurements in human airways

and their replicas. Our work can be used as a guide for the selection of a suitable lung geometry and the correct validation approach. It should help the readers to understand the physical limitations of various experimental methods and hence to shape realistic expectations. Experimentalists may find this paper useful when deciding the appropriate experimental method for their research in terms of experimental acquisition and interpretation, and in the context of any existing findings with the described techniques.

This paper also aims to diminish the remaining gap between pharmaceutical/medical and engineering communities, which limits the practical use of *in silico* modelling in medical applications. A frequent source of dispute is how much an *in silico* model simplifies the reality. Some experts insist on using solely *in vivo* measurements for validation of *in silico* models. However, as will become obvious in the next section, performing simulations on the identical *in vivo* geometry with completely controlled and correct boundary conditions is virtually impossible. Therefore, measurements are performed on replicas of human airways for validation purposes. In that case, extreme attention should be paid to include all the relevant forces (inertial, gravity, thermophoretic and electrostatic force, etc.) and features of materials (surface roughness, electrical conductivity...). However, controlling all these conditions is significantly easier than performing measurements *in vivo*. Nonetheless, it is important to understand limitations of this approach. The replica-based validated results represent an indispensable source of data, however, they have to be contextualised using the *in vivo* data, to make sure that all the relevant phenomena were covered. In respect to this issue, we decided to include experimental methods applicable to replicas, *in vitro*, and *in vivo* set-ups in order to cover the complete range of possible needs of researchers. Nevertheless, measurements performed on animals are not included in this review (except for the emerging methods where animal studies are the only source of data), although they surely provide an important source of information. Animal-based experiments represent a very broad spectrum of data, and cannot be covered here with the thoroughness they deserve.

We need to clarify several terms that are frequently used in the related literature, however, sometimes with slightly different meaning. In this paper, the term *in vivo* denotes experiments performed on a whole, living human subject; the term *ex vivo* refers to measurements performed on tissue detached from an organism and placed in an external environment with minimal alteration of natural conditions; the term *in vitro* is used to indicate studies performed with cells, or biological molecules outside their normal biological context. This is contrary to the CFPD papers where this term sometimes also includes experiments on physical replicas of parts of the human body (normally without any cells or intentionally introduced living cultures). As we wanted to detach this special group, we designate these experiments as being performed “in replica” (not italicised, as it is used verbatim and not constructed from Latin). The term *in silico* denotes computer simulations, and lastly, *in situ* means performed “on site” or “in place”.

### 1.1. Validation of CFPD predictions

The reliability of CFPD predictions is directly related to the method and data used for validation. Longest and Holbrook (2012) emphasize the need for improved experimental data sets to better validate computational predictions in local lung regions. It was recognised, e.g. by Fleming et al. (2015), that the local deposition will remain questionable unless proper validation is performed. A troublesome fact is that even the meaning of the term “validation” is not fully accepted among researchers in different fields (Oldham, 2006). The exhaustive discussion of all aspects of Computational Fluid Dynamics (CFD) validation was performed elsewhere (Holbrook and Longest, 2013; Oldham, 2006). Following the recommendations that are given in their studies we need to: 1) clarify our understanding of the term validation, and 2) describe what can be done to improve the accuracy of numerical predictions using both the currently available and emerging experimental methods.

For this paper, we have decided to adopt the definition of validation given by Versar Inc. (1988) “The process of defining the range of problems or situations for which model predictions are satisfactory”. The problem is that even if the model agrees well with experiments for a specific set of boundary conditions, it does not mean it will agree if the boundary conditions were to change. Moreover, there can always be some suspicion that the agreement is only fortuitous.

Another issue that cannot be disregarded is connected with measurement errors and uncertainties. Therefore, we include a paragraph on associated uncertainties in the description of individual measurement methods.

## 2. Airway model geometry and airway replicas

An acquisition of the airway geometry is the first step for both CFD calculations and experiments in replicas. The fidelity of the geometry is a crucial issue, which may result in the failure of an attempt to validate the CFD predictions. It has been proven, e.g. by Kelly et al. (2004a, 2004b), that the quality of the inner surface of the airway replica has a significant effect on the measured deposition. Kelly et al. manufactured two models of the same nasal cavity using different stereo-lithographical methods and compared their results with data acquired on other three replicas manufactured by micro-milling or hand carving from the same Magnetic Resonance Imaging (MRI) scans. They found that the deposition efficiency varied significantly among the replicas for particles from 1 to 10  $\mu\text{m}$  in size, whereas the differences for particles in the size range 0.005 to 0.15  $\mu\text{m}$  were negligible. Interestingly, the deposition efficiency did not form a trend with increasing surface roughness even for the inertial regime particles. Instead, the authors speculated that the discontinuities in replicas, that are assembled from several thin elements, can have a major effect on the increased deposition. It is obvious that even a slight change of geometry can significantly alter the results and hence it makes no sense to validate results of CFPD at the microscale (the local deposition sites) by experiments performed on a different geometry.

The real human lungs represent a very complex three-dimensional (3D), multiscale, flexible geometry with moving boundaries, which has to be simplified for both CFD and experimental use. The first approximate airway geometries became available since the 1970s, when the idealised symmetric Weibel A model (Weibel, 1963) and the asymmetric model by Horsfield et al. (1971) were published, followed by the model by Raabe et al. (1976). These geometries were based on morphometric measurements of human lungs and statistical evaluation of the lower airways. These models are still frequently used, often geometrically truncated to a different extent. Some investigators applied even simpler models, such as the trivial Y-shape, to study lung flow in a single symmetrical bifurcation (Corieri and Riethmuller, 1989; Lieber and Zhao, 1998; Peattie and Schwarz, 1998). A more complex model comprising five generations of airways, made of straight hollow glass tubes, was used recently by Kerekes et al. (2016). A common feature of all these idealised models is a significant simplification of the actual lung geometry, by neglecting surface irregularities, physiological traits, protuberances and surface roughness.

With the onset of 3D imaging methods (CT and MRI), realistic models have become available via scans of a living human or *ex vivo* preparations of the human lungs. Examples of such models are those CT models published by Hopkins et al. (2000), Clinkenbeard et al. (2002) or Schmidt et al. (2004), and the MRI model used by Guilmette et al. (1989). Such models were adapted for Hot-Wire Anemometry (HWA), Particle Image Velocimetry (PIV) or Phase Doppler Anemometry (PDA) measurements (Elcner et al., 2016; Jedelsky et al., 2012). The process of development of such a model was described e.g. by Lizal et al. (2012) and Verbanck et al. (2016).

It has to be noted that certain details of the geometry are always altered or lost during the process of imaging and, in the case of an experimental approach, also during fabrication of the physical replica.

Generally, the geometry can be acquired to the 10<sup>th</sup> generation from *in vivo* measurements at most and to approximately the 17<sup>th</sup> generation from high-resolution CT of a rubber cast originating from *in vitro* preparation (Schmidt et al., 2004). Firstly, not all the details of the airway surface can be detected by the imaging method. Secondly, some of the resolved physiological protuberances are then lost during the segmentation of the data and digital processing. Generally, it is difficult to get below a resolution of 0.6 mm in the final images even when using high-resolution CT and MRI (Mirsadraee and van Beek, 2015). It means that structures below 1 mm in size tend to be smoothed out in the geometries acquired using standard medical imaging methods.

Let us now focus on the methods that are available for the manufacture of a physical replica of airways. The first replicas were made by casting (Phalen et al., 1973). One such replica, which has been used for many experimental studies (e.g. (Su and Cheng, 2015; Su and Cheng, 2006; Zhou and Cheng, 2000)), was manufactured at Lovelace Respiratory Research Institute (Cheng et al., 1999). The oral part of the replica comes from a dental impression of the oral cavity from a volunteer and the rest of the airways come from a cadaver. These two parts, sourced from different individuals, were moulded in wax and coupled together by hand sculpture (Cheng et al., 1997). Then a production mould from silicone rubber was made to cast the secondary wax casts. Each final replica was made from one secondary wax cast by applying a conductive silicone rubber compound and melting the wax core in boiling water. The precision of the manufacturing process and the repeatability of the geometry were not specified by the authors, but it likely did not exceed  $\pm 1$  mm.

Micro-milling was used to produce the model of Guilmette and Gagliano (1994), and reported to have an accuracy of 0.02 mm. The same team later produced a second replica using the same tools (Zwartz and Guilmette, 2001), however, they claimed that the second replica is a better representation of the original MRI scan with 3 mm scan intervals, as a more accurate trace of the MRI was used. Moreover, hand filing was performed to smooth out the discontinuities between adjacent plates of the replica. This led to a 9% difference in olfactory volume between the replicas although they came from the same original images (Kelly et al., 2004a).

A different approach was used by Kerekes et al. (2016), who connected smooth glass tubes using standard glass manufacturing methods to obtain a simplified model of the human airways. In their case the repeatability of the geometry reproduction was not reported, however, if they used high precision glass tubes (e.g. Schott Medica GmbH, 2017) we can assume the tolerance of the tube diameters to fall between  $\pm 0.003$  and  $\pm 0.01$  mm. The precision of connecting angles of the joined tubes is difficult to assess.

The majority of replicas used in recent years are, however, produced by rapid prototyping (RP, sometimes also referred to as additive manufacturing, AM, methods), namely 3D printing. There have been several reviews published on applications of 3D printing in medicine recently (Lee Ventola, 2014; Liaw and Guvendiren, 2017; Yap et al., 2017). All these studies predict an illustrious future for 3D printing in many medical applications, such as dentistry, tissue and organ implantation, anatomical models, and drug formulation. There are four main groups of 3D printing techniques (Liaw and Guvendiren, 2017): 1) **Vat polymerization-based printing**, which includes stereolithography (SLA) and direct light processing and their derivatives. These techniques use laser light which is directed to cure a liquid resin in a vat, layer by layer. 2) **Powder-based printing** (e.g. selective laser sintering, electron beam melting), which is characterised by local heating and fusing of a powdered material. 3) **Droplet-based printing** (e.g. multijet modelling, binder jetting), which resembles classical ink printing, but upgraded to a third dimension. 4) **Extrusion-based printing**, namely fused deposition modelling, which extrudes suitable composite through a hot nozzle.

The precision of printing differs in lateral and vertical directions, as the printed objects are always built layer by layer. The minimal

thickness of the layer, therefore, limits the resolution in the vertical dimension. The powder- and extrusion-based methods are generally less precise (Islam et al., 2017), although they represent an attractive choice due to their low price. Islam et al. (2017) measured the accuracy of objects printed by SLA and powder-based methods, and found that SLA was generally far more precise, although it was possible to get better dimensional accuracy in the lateral directions using the powder printer. However, the SLA was more consistent, which meant that, for example, the hole in the object had a slightly smaller diameter, but the diameter did not significantly change through the hole, whereas for the powder printer the diameter oscillated, resulting in more jagged surface. The maximal dimensional errors were in the order of hundreds of  $\mu\text{m}$  for both methods, when the printed object size was 126 mm. Another comparison of the accuracy in a medical application of 3D printing methods was published by Salmi et al. (2013). In their case, the droplet-based method proved to be the best with a mean difference in dimensions of  $0.18 \pm 0.13\%$ .

It should be noted that the accuracy of the dimensions of the particular replica of airways depends on the respective technique, precision of the machine and competence of the operator. Additional problems can be caused by any artificial features or textures that are introduced as an artefact of the fabrication process. On the other hand, when the same digital geometry is produced using an identical 3D printer, the repeatability is undoubtedly higher than any attempt to measure within the same geometry *in vivo*.

Several other problems arise in the physical airway replicas. First of all, they usually have rigid walls. This does not cause significant error in the upper airways and the airways supported by cartilaginous rings, however, in the lower airways this may lead to misinterpretation of results. Another source of possible error is the electrical conductivity of the replica. If charged particles arrive in a non-conductive replica, they create mirror charges on the wall and are deposited, and this mechanism is largely impossible to detect during the evaluation of the data, as the electrostatic mechanism of deposition is difficult to include into the deposition equations. Last, but not least, the inner surface of real lungs is covered by a mucous layer, which should be simulated in replica. However, it is usually impossible to mimic all features of the lining, e.g. density, viscosity, conductivity, movement driven by cilia etc. Similar problems have to be solved during CFD geometry preparation, however, it seems clear that simulating these conditions in the *in silico* airways is significantly easier than in a physical lung replica.

It is obvious that issues with inducing and controlling the flow are indivisible from experiments performed in replicas of human airways. However, the simulation of physiologically realistic flow is not a trivial issue. The main problem is grounded in the fact that the replicas do not contain complete lungs and hence the missing parts must be simulated. The situation is somewhat easier for flow measurement studies. The easiest solution is to simulate only stationary inhalation (or exhalation). Then only the flow distribution has to be solved e.g. using linear resistors. If an oscillatory flow is to be simulated, the flow distribution can be provided by several cylinders with pistons, whose movement is controlled using a computer (Ramuzat and Riethmuller, 2002). It should be noted that the realistic course of flow rate is not easy to mimic and hence the sinusoidal course of breath is most frequently used. For aerosol deposition studies, the circumstances are even more complex. Researchers need to distinguish between 1) the particles deposited in the replica during inhalation, 2) the particles that would pass the simulated regions and would deposit in deeper regions during inhalation, 3) the particles deposited in deep regions or 4) the replica during exhalation and 5) particles exhaled after the complete cycle. Therefore, the inhalation component and the exhalation component are simulated separately, where all the particles passing through are usually collected on filters without any other information on their possible fate in real lungs. Moreover, the majority of such experiments are performed for steady inhalation or exhalation only. Simulations of aerosol deposition during cyclic inhalation are very rare (Kim and

Fisher, 1999).

Some of the above-mentioned problems are naturally solved during *in vivo* measurements. However, repeatability and reproducibility remain an issue there. It is necessary to instruct the volunteers to breathe steadily and monitor the breath with a pneumotachograph or another suitable instrument, ideally using feedback to help the volunteer establish a repeatable breath pattern. It cannot be expected that the breathing pattern of a live human will follow any machine-like rhythm.

### 3. Flow and particle velocimetry in the airways

The main source of data for validation of calculated velocity fields and other flow characteristics are experiments performed in replicas of lungs. The reason is obvious – the obstructed view and complicated access to the human airways. We will focus on methods routinely applied in fluid mechanics, which can be divided into two groups based on their influence on the fluid. The non-intrusive methods usually require a direct optical path to the replica, however, some of them can provide planar or even volumetric data. In this section, we have paid special attention to laser Doppler based methods and their application in human airway flows, as these have not yet been the subject of a comprehensive review, despite being able to provide important data on turbulent characteristics of the flow, provided proper data processing is performed. The second group, the intrusive methods, is represented by hot-wire anemometry (HWA).

#### 3.1. Hot-wire anemometry in lungs

The first in-depth studies of flow profiles in replicas of human lungs were performed in the 1960s, after Weibel (1963) and Horsfield and Cumming (1967) published their morphometries of human lungs. First flow visualisations were performed using smoke and photography. Velocities were measured by HWA often supplemented with Pitot tubes to sense the flow direction.

The HWA was developed at the beginning of the 20<sup>th</sup> century and quickly became a fundamental tool for turbulence measurements. The method is based on the measurement of the cooling effect of surrounding flow on a heated element, usually a wire or a thin metal film (Bruun, 1995). The heat transfer from the element depends on the temperature, geometrical configuration and physical properties of both the element and fluid. Two modalities that differ in the way of heating the element are available currently: a) Constant Current Anemometer (CCA) and b) Constant Temperature Anemometer (CTA), noting the latter is more popular as it is easier to use and is therefore implemented in the majority of commercially available instruments. However, both modalities are equivalent in regards to the electronic noise and measurement frequencies (Bestion et al., 1983).

##### 3.1.1. Constant temperature anemometer (CTA) principle

The CTA modality utilises a Wheatstone bridge to compensate the cooling effect of the flowing fluid on the probe while maintaining a constant wire temperature (see Fig. 1). The current flowing through the wire creates heat, which is equal to the (mainly convective) heat losses to the fluid, once in the state of equilibrium. After the change of velocity, a servo amplifier immediately changes the current to the wire to keep the bridge in balance, and hence the wire has constant resistance, and consequently constant temperature.

The voltage drop across the sensor is proportional to the velocity of the fluid flow. As the heated elements are usually wires of several  $\mu\text{m}$  in diameter, they have very low thermal inertia and therefore allow the measurement of extremely fast fluctuations, up to several hundred kHz in the best configuration (Jensen, 2004). Because the voltage output is not directly proportional to the velocity, the voltage output has to be calibrated prior to the measurement (Bruun et al., 1988). It has to be noted that the heat transfer from the sensor is a function of many properties, namely heat conductivity, viscosity, density, concentration

and of course the velocity of the fluid.

The main advantages of HWA are:

- fast frequency response: measurements up to several hundred kHz possible,
- analogue output signal — both time domain and frequency domain analysis can be carried out,
- no seeding is required,
- high signal to noise ratio (SNR) — resolution of 1 part in 10,000 is accomplished,
- velocity measurement: measures velocity magnitude and fluctuations, also turbulent characteristics like Reynolds stresses or vorticity possible (Lemonis, 1997),
- wide velocity range (few cm/s to supersonic speed),
- allows measurement of other fluid quantities (temperature, concentration),
- relatively cheap.

The main drawbacks of HWA are:

- intrusive technique — disturbs the velocity field,
- rectification error — insensitive to a reversal of flow direction (which appears also in a flow with high turbulence intensity (TI)),
- contamination: deposition of impurities in flow on the sensor alters the calibration characteristics and reduces the frequency response,
- fragility — probe breakage and burn out,
- single-point measuring method,
- inaccurate at low velocities due to natural convection,
- calibration is required,
- accuracy of HWA is really a function of calibration, contamination, temperature changes and other factors, which generally limit the accuracy to a few percent.

3.1.1.1. Applications of HWA in lung flow studies. Probably the first study to use HWA in a simple model of human airways was Schroter and Sudlow (1969). They manufactured Y-shaped single and double bifurcation models and measured inspiratory and expiratory velocity profiles using a single-wire probe. They clearly demonstrated that developed laminar parabolic flow cannot be assumed in lungs, as each bifurcation disturbs the flow and the disturbances do not dissipate before the next bifurcation. The influence of the local geometry at a junction was also investigated. Change of radius of curvature of the outer wall at the junction in a ratio of 1:4 caused the appearance of flow separation, which was expected to influence the local mass transport.

Another attempt to measure the flow in human lungs was undertaken by Olson et al. (1973), who used Pitot tubes and HWA to measure velocity direction and flow instabilities, respectively. Their geometry covered the airways from the mouth to the second bifurcation and was

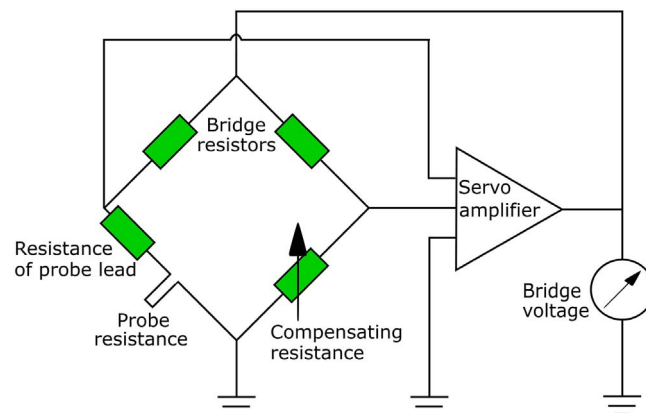


Fig. 1. The principle of CTA.

made of clear rubber. Velocity contours in nine cross sections of the airways were presented demonstrating basic features of the flow. The authors observed a velocity peak on the posterior portion of the trachea as a result of the vocal cords shape. Also, flow instabilities were discussed based on fluctuating velocity measured by HWA. The authors noticed that random fluctuations exist even in sub-lobar bronchi where the Reynolds numbers,  $Re$ , fall below 100. They explained that turbulence is generated by the separation just below the larynx, where the disturbances are so large that they are transported several bifurcations downstream. Despite the inspiring discussion, their data can hardly be used for validation of CFD results as many important details of the geometry and experimental setup are missing.

The most exhaustive measurement using HWA in a model of human lungs was published in a series of papers by a team from McGill University, Canada (Chang and Elmasry, 1982; Isabey and Chang, 1982; Menon et al., 1984). All measurements were performed in a 3:1 scale model of the human central airways based on the Horsfield geometry (Horsfield et al., 1971). The model comprised the trachea and the first 2 or 3 generations of branching. In the first study (Chang and Elmasry, 1982), they extended the work of (Schroter and Sudlow, 1969) and published steady inspiratory and expiratory velocity profiles for two flow rates (0.4 and 1.7 l/s in the trachea). They found that the velocity profiles depend on the airway geometry rather than on the  $Re$ . The flow separation was observed in the right main bronchus only. By simulating different inlet velocity profiles, they wanted to investigate the effect of factors like vagal stimulation or upper airway geometry. The results showed that only small differences were found in the main bronchi for the various inlet conditions. Their results also proved that curvature of the left main bronchus influences the evolution of the velocity profile.

The second study (Isabey and Chang, 1982) represents truly admirable work measuring secondary velocities during steady inspiratory and expiratory flow. Measurement of secondary velocities using HWA in a confined space is extremely demanding and even despite maximal effort is burdened with significant measurement error. Isabey and Chang used single slanted hot-wire probes that were inserted axially and rotated around their own axis to determine the secondary velocities. The measurement error ranged between 10 and 30%. The secondary velocities never exceeded 21.5% of the mean axial velocity, while the maximal secondary velocities were always observed near the wall. Several regularly appearing eddies at their typical sites were identified. The authors emphasized the influence of geometry, although they were unable to directly link the geometrical features to their effect on the flow.

The last paper of the series (Menon et al., 1984) focused on oscillatory velocity profiles. The velocity profiles resembled the steady regimes for low  $Re$  flows. For higher flow rates the velocity profiles tend to flatter, except in the right main bronchus, where the skewed profile persists even during the highest breathing frequencies.

Nasal airflow patterns were measured using HWA by Hahn et al. (1993). They manufactured a 20:1 scale replica of the nasal cavity based on axial CT. A single velocity component was measured in six planes using 77 probe-inserting holes in total. Hahn et al. managed to create detailed velocity maps that were presented as isospeed contour plots and normalised velocity profiles. The recorded velocity was used for calculation of turbulence intensity (TI) and total shear stress, which enabled the calculation of longitudinal pressure drop across the nasal cavity.

Johnstone et al. (2004) combined several measurement and visualisation methods and presented interesting results acquired on an idealised replica of upper airways. The measurements were performed for seven different inspiratory flow rates in a range between 10 and 120 l/min. Single and X-shape hot-wire probes were used, and therefore mean and Root-Mean-Square (RMS) velocities of two components of velocity can be measured. This study confirmed that the velocity profiles depended primarily on the geometry of airways and were almost independent of the  $Re$ .

In summary, HWA provides useful data for the validation of CFD, with the most valuable contribution the temporal resolution available for velocity measurement. However, the usability of the published data for validation purposes is limited, because detailed information on the model geometry and position of the measuring points is often missing. The method is intrusive, which means that insertion of the sensing probe can potentially alter the flow. Also, the measuring uncertainty is relatively high for low velocities (e.g. Hahn et al., 1993 presented uncertainty of  $\pm 46\%$  for 0.045 m/s which drops to 14% for 0.09 m/s; for higher velocities, it further decreases to  $\pm 5\%$  (Johnstone et al., 2004)). Nevertheless, if the method is available within a given institute, the lung geometry for CFD is available for the manufacture of the physical model, and local development of velocity is of interest, HWA can be recommended as a relatively simple, reliable and yet sufficiently precise tool.

### 3.2. Laser Doppler based methods

Laser Doppler (LD) based methods and Particle Image Velocimetry (PIV) form a specific group called optical flow measuring techniques. They have several common features, namely the optical access requirement and the need for tracing particles to be introduced into the flowing media. The following two subsections are thus valid for both instrumentations.

#### 3.2.1. Requirements on the physical replicas of airways for optical methods

Optical flow measuring techniques require visual access to the flow field within the object and a limited distortion of the optical path. This disqualifies these methods from *in vivo* application and requires the creation of transparent physical models for these studies. On the other hand, the experiments in replicas, in contrast to the studies on living humans, are not subject to ethical rules and do not suffer from the “intra-subject” variability and repeatability problems. The experiments in replicas need an appropriate geometrical model of the respiratory tract and its physical realisation. The replicas can be fabricated by different types of RP and casting, or by machine cutting.

The simplest models use cylindrical glass, Perspex, silicon or plastic tubes as the airway representation.<sup>1</sup> A critical issue of the laser beam pair passing through the curved model wall is the beam deflection/refraction and deformation of the measurement volume which increases the measurement uncertainties. The beam deflection is proportional to the wall thickness and the tube curvature and can be calculated according to Durst et al. (1981). This deflection negatively influences the measurement of secondary velocities and the axial velocity and shifts the probe volume from its intended location.<sup>2</sup> The irregular shapes of the realistic models limit the applicability of the optical methods even more.

The optical distortions can be eliminated if the ventilated fluid is replaced with a liquid mixture with the refractive index precisely matched with the model material, which is commonly done with PIV (Adler and Brucker, 2007; Fresconi and Prasad, 2007; Theunissen and Riethmuller, 2008). Up to date, no transparent liquid with the refractive index of air ( $n_{air} = 1.00$ ) is known. Typical model materials are **silicone** (for PIV e.g. (Adler and Brucker, 2007; Grosse et al., 2007), for PDA e.g. Lizal et al. (2012)) with an optical refractive index of about 1.41, **glass** (Corcoran and Chigier, 2000; Corieri and Riethmuller, 1989) or **acrylic plastic** (Frag et al., 2000; Tanaka et al., 1999). Especially for 3D evaluation methods, the refractive index must be matched to a precision of 0.01 to guarantee adequate reconstruction of 3D PIV images from the planar images. A mixture of water and glycerin

<sup>1</sup> For LD measurements of flow in transparent models, circular pipes and behind windows see (Zhang, 2010).

<sup>2</sup> Corcoran and Chigier (2002) however reported the probe shift in the order of 0.3 mm negligible to the scale of their measurement.

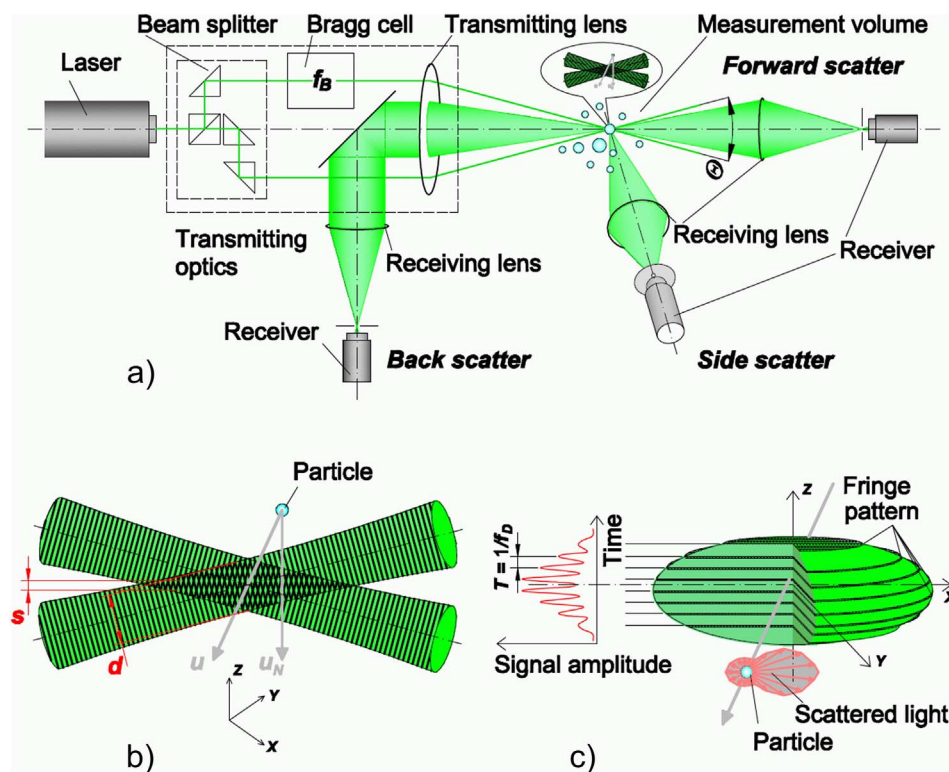


Fig. 2. The LDA principle: a) the optical configuration in the forward, side and backscatter mode, b) fringe pattern with the fringe separation distance  $s$  and the Gaussian beam diameter  $d$ , c) the “Doppler burst” signal received by the photodetector and the measurement volume with a conceptual cross-sectional cut.

with a mass ratio of 0.42:0.58 (water:glycerin) is typically used as working fluid here (PIV: (Adler and Brucker, 2007; Grosse et al., 2007; Janke et al., 2017), LD: (Corieri and Riethmuller, 1989; Zhao and Lieber, 1994b), and others).

The approach with a liquid is possible if only the velocity field is of interest. However, tracking of aerosol particles is impossible in this manner. For optical studies of particle dynamics inside a realistic geometry, the light refraction in gas as a carrier medium can be minimised by using thin-walled models (Lizal et al., 2012). Elcner et al. (2016) used such a model for PDA measurement and pointed out that manual positioning and beam-crossing adjustment at each measurement point was compulsory, with carefully selected sections for measurement, nevertheless, it was not possible to measure near-walls.

The flow studies using a liquid instead of the air must satisfy the flow similarity condition. The characteristic flow parameters for the case of respiration with an oscillatory flow are the  $Re$  and the Womersley number,  $\alpha$ , with  $Re = 4TV \cdot f_b / (\nu \cdot D)$ , where  $TV$  denotes the tidal volume,  $f_b$  the breathing frequency,  $\nu$  the kinematic viscosity and  $D$  the characteristic diameter of the flow tube. The  $\alpha$  represents a relation of transient inertial to viscous forces and is defined by  $\alpha = D \cdot \sqrt{2\pi \cdot f_b / \nu}$ . With a viscosity ratio of  $\nu_{air} / \nu_{w+g} = (15.9 \times 10^{-6} \text{ m}^2/\text{s}) / (8.4 \times 10^{-6} \text{ m}^2/\text{s}) = 1.9$ ,  $Re$  can be reduced by the same factor, and  $\alpha$  by  $\sqrt{1.9}$ . These dimensionless groups must be matched also when scaled models used. This can apply for scaled-up optical measurements in small airways<sup>3</sup> or using mechanical probes (Heraty et al., 2008). In contrast to the flow field studies, the measurements in dispersed two-phase flows involve no scaling since several additional similarity criteria must be matched.

### 3.2.2. Particle size/shape and dynamics, tracer particles, particle issues

Optical diagnostic methods rely on scattering particles dispersed in the flow to provide the velocity information for the continuous medium

<sup>3</sup> For example, Lizal et al. (2012) reported their PDA measurement volume about 0.1 mm<sup>3</sup> which limited the minimum diameter of airway for a reliable measurement to 4 mm.

(liquid or gas). Durst et al. (1981) specified several requirements for these tracer (seeding) particles; they should be: able to follow the flow, good light scatterers, conveniently generated, cheap, non-toxic, non-corrosive, non-abrasive, non-volatile, or slow to evaporate, chemically inactive and clean. Additionally, the particles must be sufficient in number to provide the required temporal resolution of the flow velocity (Albrecht, 2003) but their mass loading must be small enough to not dump the flow turbulence (Hetsroni, 1989) or alter the flow momentum. The size of the seeding particles must be set *via* compromise; the scattered light improves with increasing particle size, but the opposite results in terms of fidelity in following the flow and its fluctuations. Particles of around 0.5–1  $\mu\text{m}$  are required for most seeding materials to follow the instantaneous motion of the gas phase to ensure acceptable flow tracking (Melling, 1997). In applications that involve liquids, significantly larger particles in the order of 5–20  $\mu\text{m}$  can be used (Tropea et al., 2007). Tracing accuracy errors are below 1% for the Stokes number of particles in the flow  $St_k < 0.1$  according to Tropea et al. Methods generating particles (for an overview see (Albrecht, 2003; Melling, 1997) with a uniform seeding size are favoured to prevent excessive intensity of light reflected from larger particles producing a background noise and resulting in the low visibility of small particles.

### 3.2.3. Principles of laser Doppler (LD)/phase Doppler (PD) systems

LD instrumentation provides accurate non-intrusive measurements of complex flows with separation regions and flow reversals. Before its introduction, HWA was the only means to measure single-point turbulence quantities. Laser Doppler anemometry (LDA), or Laser Doppler velocimetry (LDV), came into widespread use in the 1970s and the PD technique<sup>4</sup> arrived 20 years later. LDA/PDA instruments became standard and

<sup>4</sup> Commercially available PD systems are generally referred to according to their manufacturer. The first systems came from Aerometrics, in the USA, and Dantec Dynamics, in Denmark. They were known as Phase Doppler Particle Analyser (PDPA) and Particle Dynamics Analyser (PDA) respectively. The latter became better known as the Phase Doppler Anemometer. TSI, in the USA, later acquired Aerometrics and kept the name PDPA. A third alternative is now available from Artium Technologies, USA, and is offered as a Phase Doppler Interferometer, PDI.

commercially available. These instruments have found important applications for lung flow and aerosol characterisations in airway replicas. LD/PD techniques are point-wise optical methods that capture a Eulerian description of the flow field using embedded fluid markers. They are attractive for CFD (Albrecht, 2003) and provide statistical moments of the flow velocity and, in the case of PDA, also of particle size.

The LDA principle is illustrated in Fig. 2a. A continuous-wave monochromatic laser beam is split into two coherent beams that intersect symmetrically, at a small angle  $\theta$ , via a transmitting lens. The beams interfere in their intersection volume (the measurement volume) generating a series of parallel planes of light and darkness, referred to as fringes (Fig. 2b). Any small inhomogeneities (particles or bubbles) that are present in the flow will scatter the light as they pass through the fringes. In order to eliminate the ambiguity around which direction a given particle is travelling, the frequency of one of the beams is shifted by  $f_B$ , using a Bragg cell, so that the fringe pattern “rolls” with a known velocity. A receiving lens<sup>5</sup> projects the fringe patterns scattered by the particle onto a photodetector (receiver) which produces a “Doppler burst” signal (Fig. 2c) with a Doppler frequency  $f_D$ . This is proportional to the velocity component ( $u_n$ ) of particle motion normal to the fringes, divided by the fringe spacing  $s$ :

$$f_D = f_B + \frac{u_n}{s} = f_B + \frac{2 \sin(\theta/2)}{\Lambda} u_n \quad (1)$$

where  $\Lambda$  is the laser light wavelength. The light signal is then processed to yield the velocity and arrival time of each particle.

The beam intersection provides an optical demarcation of the probe volume as a prolate ellipsoid (Fig. 2c). This measurement volume is usually considerably  $< 0.1 \text{ mm}^3$  with corresponding spatial resolution  $SR = 1 / (\text{characteristic size}) \approx 10^4 \text{ m}^{-1}$ . For further details on LDA, we refer to (Durst et al., 1981; Zhang, 2010).

A PDA extends the LDA technique to provide the particle size and velocity simultaneously. This system uses the same transmitting optics as the LDA and a separate receiving optics. The scattered Doppler signals are sensed by at least two detectors. One of them is located in the observation plane, and the other is elevated, at an angle with respect to that plane. The signals collected at different angles show a phase difference  $\Delta\phi$  with respect to each other. This phase shift depends on the particle diameter,  $D_p$ , and is a function of the scattering direction and the difference in elevation angles between the detectors. It may also depend on the particle/fluid refractive index,  $n_p$ , and fluctuations may be seen in the size diagram, caused by partial wave resonances. Using the “fringe model” gives a simple relationship between the diameter and the measured phase shift:

$$\Delta\phi = \frac{2\pi D_p n_p}{\Lambda} \phi \quad (2)$$

The parameter  $\phi$  depends on the scattering mode and the PDA configuration (detailed by Albrecht (2003)). The measured bursts are sent to a signal processor which extracts the velocity, transit and arrival time, and size data.

The main advantages of the LDA/PDA systems are:

- high spatial and temporal resolution of the fluid/particle flow measurements, with on-line evaluation of single to three velocity components simultaneously,
- the sampled data enables estimation of instantaneous and time-averaged local fluid velocity and TI, and other quantities such as Reynolds stresses or particle path lines can be derived,
- non-contact measurement at a distance of centimetres to metres at an affordable price,
- highly accurate flow measurements with directional sensitivity, suitable for complex unsteady reversal flows with turbulent,

- transitory and laminar characteristics, as seen in the airways,
- the PDA adds the particle sizing capability with a spatial and temporal resolution that is not available with any other sizing technique,
- the measurement is absolute, linear with velocity and size (see Eqs. (1) and (2)) and does not require a system pre-calibration.

The main drawbacks of the LDA/PDA are:

- the LDA and in particular the PDA cover numerous complex physical processes and require a wide interdisciplinary insight to be operated successfully,
- the optical access required to the measurement space limits these methods for experiments in airway replicas, and introduces issues related to refractive index variations in the complex optical systems,
- it is a slow scanning technique, traversing a point matrix to provide planar or volumetric information (see Fig. 3c), and as a point-wise method, it lacks spatial coherency of the signal so only time-averaged, ensemble-averaged or phase-locked flow fields can be resolved,
- it is an indirect measurement technique, since it measures the velocity of inhomogeneities in the flow, typically tracer particles, that must be carefully chosen to provide sufficient tracking capability (see Section 3.2.2).

### 3.2.4. Processing of LD/PD data

LD/PD anemometers provide comparatively high spatial and temporal resolution of velocity and size data (where appropriate) in particle–air flows, making these single-particle counting instruments suitable for estimation of the moments and spectra of turbulent velocity fluctuations and analysis of the particle/fluid dynamics. For illustrative results of time-resolved flow velocity and frequency spectra in a single-point and for flow fields see Fig. 3.

**3.2.4.1. Estimation of velocity moments.** Fluid tracer-based methods face two inherent problems when providing statistical analysis of the measured data; velocity bias and the random arrival of tracing particles to the measurement volume. The velocity bias is a problem when calculating simple statistics, such as mean and RMS values, while the random sampling complicates the estimation of quantities that depend on the event timing, such as spectrum and correlation functions.

If one considers a statistically uniform particle distribution in space with mean concentration  $c$ , and convective velocity  $u$ , the mean sampling rate is  $\dot{n} \propto cSu$ , where  $S$  is the area of the measurement volume projected in the flow direction. The sampling rate is proportional to the particle velocity (see Fig. 3b) and therefore the sampling process is not independent of the event being sampled (McLaughlin and Tiederman, 1973). An application of the arithmetic average to the velocity samples will bias the results in favour of the higher velocities. Several methods were proposed to treat this so-called velocity bias. The signal processors can use a “dead time” feature, when they process only the first Doppler burst that appears during a time window which is set equal to  $2\tau_t$ , where  $\tau_t$  is the integral time-scale of the flow. This filtering of the data results in a low data rate, so it is often favoured to instead use a method that utilises a weighting factor  $f_w$ , to estimate arithmetical means of the respective flow parameters, e.g. the mean velocity, the second moment and the joint moment (Albrecht, 2003):

$$\bar{u} = \frac{\sum_{i=1}^N f_{w,i} u_i}{\sum_{i=1}^N f_{w,i}} \quad (3)$$

$$\sigma_u^2 = \frac{\sum_{i=1}^N f_{w,i} (u_i - \bar{u})^2}{\sum_{i=1}^N f_{w,i}} \quad (4)$$

$$\overline{u'v'} = \frac{\sum_{i=1}^N f_{w,i} (u_i - \bar{u})(v_i - \bar{v})}{\sum_{i=1}^N f_{w,i}} \quad (5)$$

<sup>5</sup> which can be positioned in the forward, side or backscatter direction

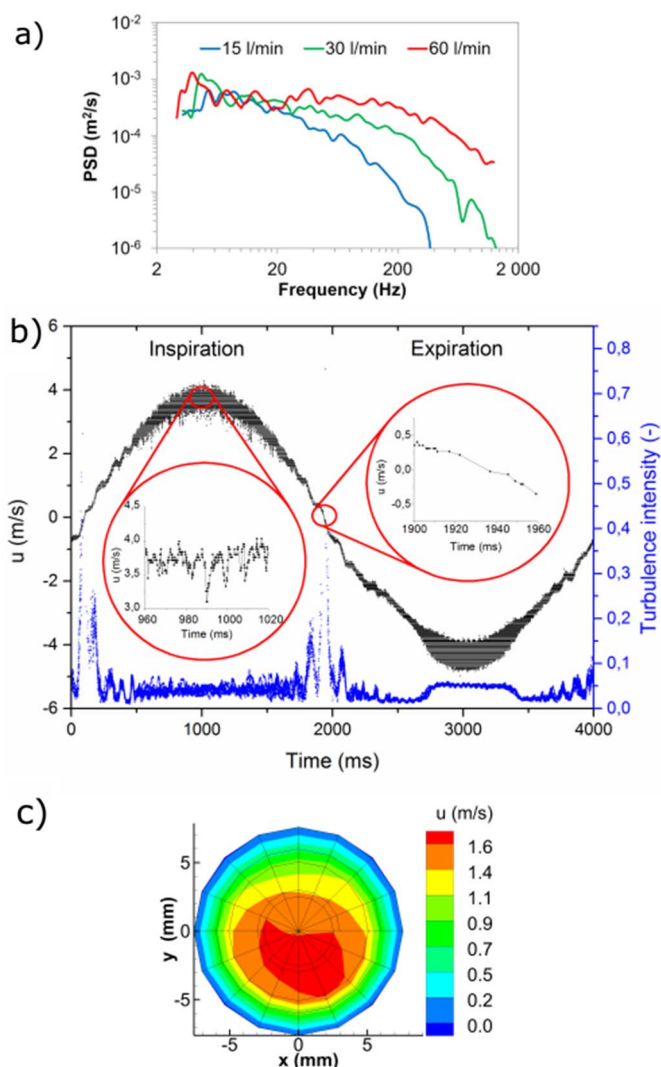


Fig. 3. a) An example of PSD of the velocity fluctuations of airflow in the centre line of the trachea, with different inspiratory flow rates, tracing 4  $\mu$ m particles. b) A PDA record of airflow velocity during sinusoidal controlled breathing ( $TV = 0.5$  l, breathing period 4 s) with ten overlapped (phase-averaged) cycles. Time intervals with the laminar and turbulent character of the flow are visible. Zoomed windows document irregularly sampled data and the velocity bias effect. c) Mean axial velocity in a cross section in the trachea for steady inspiration, 30 l/min.

McLaughlin and Tiederman (1973) suggested the use of inverted magnitude of velocity vectors as the weighting factor. An equivalent, and more readily available, weighting factor is the transit time  $f_{w,i} = t_{Ti}$  of each particle while passing through the LDA measurement volume.

**3.2.4.2. Estimation of power spectral density (PSD) of velocity fluctuations.** Particles dispersed in a fluid appear randomly in space, and hence tracer-based methods are associated with irregular particle arrival times. Presuming a statistically uniform particle distribution in space with a constant convective velocity and mean data rate of the measurement  $\dot{n}$ , the intervals between the particles,  $\Delta t_p$ , are distributed exponentially:  $p(\Delta t_p) = \dot{n} \cdot \exp(-\dot{n} \Delta t_p)$ . The probability of inter-particle arrival time increases with a reduction in  $\Delta t_p$ , so that data can contain information about very high-frequency fluctuations. Nevertheless, the maximum reliable frequency is  $f_{\max} \cong \dot{n}/2\pi$  according to Adrian and Yao (1987). The non-equidistant sampling intervals due to naturally seeded particles in the flow inhibit a direct application of the fast Fourier transform for the estimation of the PSD of the velocity fluctuations, and other methods must be applied. The most reliable spectral estimation techniques developed to address this problem are

explained in detail by Benedict et al. (2000). For an example of conversion of the PDA velocity data from temporal to the frequency domain see Fig. 3a and the results in Jedelsky et al. (2012).

The velocity time series allows the calculation of two-time statistics such as correlation and covariance. Integral time-scales can be estimated by use of the auto covariance function.

**3.2.4.3. Particle sizing.** The droplet size dataset provided by the PDA instrument determines a particle number distribution as the primary distribution function.<sup>6</sup> Weight or volumetric distributions are derived quantities. It is convenient to work, not with the entire size distribution, but with mean diameters whose general definition is:

$$D_{qr} = q^{-r} \frac{\sum_{i=1}^N D_i^q}{\sum_{i=1}^N D_i^r} \quad (6)$$

Then, for example,  $D_{10}$  stands for arithmetic or number mean diameter,  $D_{32}$  for volume/surface mean (also called the Sauter mean) diameter. The PDA-based size data must be interpreted with care as the particle size is optically measured while the aerodynamic diameter is mostly used in aerosol flow studies.

**3.2.4.4. Other single-point statistics.** The joint particle velocity, diameter and transit time data provided by PDA offer a potential for separation and filtering according to the size or velocity classes. Their mutual correlations and calculation of other derived quantities further characterise two-phase flow systems. Several methods were published (Aisa et al., 2002; Bachalo et al., 1988) to calculate the local particle number concentration and mass/volume flux data. Their estimations, however, face several difficulties and a system calibration, together with sophisticated corrections, is required to obtain bias-free results (Calvo et al., 2009; Dullenkopf et al., 1998; Roisman and Tropea, 2001; Widmann et al., 2001).

Important turbulence characteristics (TI, Reynolds normal and shear stresses, turbulent kinetic energy) can be calculated with multi-component velocity measurements as indicated in Eqs. (3) to (5). Various methods were developed for analysis of point-wise data of the dispersed two-phase flows. Of interest, for lung flow dynamics, can be the ideal spray theory of Edwards and Marx (Edwards and Marx, 1995; Marx et al., 1994) which is based on the particle arrival statistics and allows for particle clustering and flow steadiness analysis. The particle collision phenomena can be studied according to the classic kinetic theory of gases (Santolaya et al., 2013).

### 3.2.5. The cost and availability of LD instrumentation

The instrumentation costs depend on the system specification, robustness, measurement capabilities, extensibility and variability of the configuration. The cost ranges from approximately 40,000 €/channel for a basic system to > 80,000 €/channel for a state-of-the-art, well-equipped system. One channel allows for a measurement of one single velocity component, and a PDA system requires an additional channel for particle sizing. Mitchell et al. (2011) report that PD systems are generally > 60,000 US\$/unit and their cost depends on the number of detector units, as well as the sophistication of the data processing equipment. The LD methods are utilised widely for fluid mechanic experiments and such instruments are routinely used in high-tech laboratories today.

### 3.2.6. Measurement precision and uncertainties

LD-based techniques face some experimental uncertainties associated with the instrument's optics, lasers, and electronics that require attention. The main factors affecting the measurement accuracy are: (1) the geometrical alignment and quality of the optical parts including the

<sup>6</sup> It is in contrast with other sizing instruments, e.g. with laser diffraction technique, which measures the size distribution by volume (Fdida et al., 2010; Robart et al., 2001).

crucial effect of the crossing laser beams and the optical properties of the airway model (discussed in Section 3.2.1), (2) the flow scales with respect to the measurement volume dimensions (see Note 3 in Section 3.2.1), (3) the optical and electronic noise of the photodetectors and other parts of the signal chain and the time response of the system, (4) the flow tracking capability and light scattering properties of the tracer particles<sup>7</sup> (discussed in Section 3.2.2) and (5) the system capabilities for the Doppler burst signal processing for particles randomly dispersed in the flow.

The measured size and velocity data are converted into discrete intervals with a finite resolution. This *discretisation error* was quantified as 0.25% for velocity measurements by PDA (Roth, 1995). Urbán et al. (2017) reported the typical discretisation error for velocity and size measured with the newer Doppler burst spectral analysis technique as 0.002% and 0.08% respectively.

Negus and Drain (1982) documented that the LDA can measure the particle velocity in the range from 1 to 200 m/s in two-dimensional (2D) or 3D with a typical accuracy of 1%. Bovendeerd et al. (1987) estimated an error for axial (secondary) velocities in a 90° bend of the circular cross section of 1% (5%) for these velocities with 95% probability intervals.

The PDA applies a linear relation between particle size and the phase difference on bursts that are measured by the photodetectors (see Eq. (2)). The linearity assumption, based on the geometric optical theory, is precise for particles greater than a few wavelengths, but does not adequately describe the optical effects on small particles where Mie scattering theory has to be considered. Sankar et al. (1991) reported a sizing uncertainty of  $\pm 0.4 \mu\text{m}$  for particles below  $5 \mu\text{m}$  and scattering angle 60°. Similar results were published by Taylor et al. (1994). The detection and processing limit of the PDA is  $\sim 0.5 \mu\text{m}$  and the quoted accuracy is 4% according to Prokop et al. (1995). Liu (2000) and Tropea et al. (2007) refer the sizing capability of PDA to the 0.5–3000  $\mu\text{m}$  and 1–1000  $\mu\text{m}$  range respectively. We refer the reader to Albrecht (2003) for a comprehensive accuracy analysis and guidelines for the design of LDA/PDA systems.

PDA cannot correctly size non-spherical or heterogeneous particles. It is not an issue for liquid aerosols of inhalable size but it is a problem for irregularly shaped *i.e.* porous, fibrous or crystalline solid particles where other sizing methods must be used.

Further uncertainty might come from the inaccuracy of the model positioning relative to the LDA measurement volume. Elcner et al. (2016) estimated the uncertainty of the measurement probe positioning to be  $\pm 0.3 \text{ mm}$ . Corieri and Riethmüller (1989) reported a positioning accuracy in three directions of 0.1 mm.

### 3.2.7. Citations of relevant works

Girardin et al. (1983) used LDV to determine the pointwise velocity of water droplets suspended in air flowing through a nasal model made from a cadaver cast for a flow rate of 166 ml/s. They studied different cross sections of the nasal fossa and showed the influence of shapes and dimensions as well as flow direction on velocity fields. The flow was generally turbulent; the turbinates provided a streamlining effect on the velocity while the liminal valve had a directional effect.

Bovendeerd et al. (1987) measured steady axial and secondary flow velocities in a 90° bend of circular cross section with LDV. They explained in detail the development of the complete flow field.

One of the first LD measurements, targeted to lung flow, was provided by Corieri and Riethmüller (1989) with glycerine and highly idealised glass bifurcation model. They built the Y shape model to a scale of 40, respecting the ratio of diameters and the angles corresponding to generation 12 to 17 and shown the availability and

accuracy of LDV to measure the flow in the bifurcating model.

Zhao and Lieber (1994a, 1994b) conducted multiple experiments, using a two velocity component LDA in a symmetric single bifurcation airway model of analytically known geometry with aqueous glycerine mixture to simulate flow in the upper human central airways. They measured axial and secondary velocity profiles over the range  $Re = 518\text{--}2089$  both for steady inspiratory and expiratory flow. The results showed that in the junction plane, velocity profiles in the daughter branches are skewed toward the inner walls. The inspiratory flow formed “m” shaped velocity profiles in the transverse plane. The biconcave velocity profile also appeared during the inspiratory flow in the parent tube, just downstream of the flow divider, but this rapidly transformed into a velocity peak. These authors (Lieber and Zhao, 1998) later found for oscillatory flow conditions, with a peak of  $Re$  700, 1278, and 2077, that a quasi-steady flow assumption is valid for oscillatory flow for only about 50% of the period. So, quasi-steady equivalents cannot be used to analyse the complexity of flows during the transition between the respiratory phases.

Also, Peattie and Schwarz (1998) used a symmetrically bifurcating tube model. They investigated oscillatory flow using hydrogen bubbles visualisation and quantitative pointwise LDV velocity measurements. They measured the secondary velocities (the velocities perpendicular to the axial velocity) under both low and high-frequency ventilation conditions. They pointed out significant differences that developed in the flow properties. At low frequency, the axial velocity field was found to approximate that of a steady flow through a bifurcation. However, even at  $\alpha = 3$  only, secondary velocity fields were confined to within a few diameters of the bifurcation.

Ramuzat et al. (Ramuzat et al., 1998; Ramuzat and Riethmüller, 1997) investigated steady and oscillating flows by means of the laser measurement techniques in a 2D lung bifurcation model and realised later (Ramuzat and Riethmüller, 2002) that the 2D configuration does not represent the complex 3D flow structures, which exist in bifurcating airways.

Tanaka et al. (1999) studied the spatial and temporal variation of secondary flow during a high-frequency sinusoidal oscillating flow with  $3.8 < \alpha < 7.5$ . They measured using the two-colour LDV technique on an idealised three-generational asymmetrical Horsefield airway geometry materialised from acrylic plastic. They found the secondary velocity magnitudes and the deflection of axial velocity dependent on the branching angle and curvature ratio of each bifurcation and also on the shape of the path formed by the branch cascade.

Farag et al. (2000) investigated axial and secondary velocity profiles in a large-scale Perspex model using LDV. The experiments were conducted with steady inspiratory air flow seeded with salt particles at  $Re = 1500$  and the simple bifurcating 70° symmetrical bifurcation model with 1/7 curvature ratio which mimicked the morphometry of small human airways. They observed a rapid development of strong secondary flows consisting of two main vortices, with two smaller secondary vortex motions toward the inner wall of curvature. The calculated vorticity transport showed the interaction between the viscous force at the boundary layer along the carinal surface and centrifugal force of curvature with further consequences.

Corcoran and Chigier (2000), in one of the ever most cited papers on PDA experiments in lungs, studied the axial velocity and TI contours in the tracheal section of a cadaver-based larynx–trachea model. Measurements were conducted on a model formed by a polyurethane casting of a human larynx and a round glass tube with an inside diameter chosen to match the cadaver tracheal diameter. They assessed the effects of the laryngeal jet on inhalation airflow patterns for steady state flow at three  $Re$  numbers (1250, 1700, and 2800) and noted significant reverse flows with high levels of axial TI in the anterior trachea downstream of the larynx for all three flow cases, indicating the potential for turbulent deposition at positions further downstream. Consequently, Corcoran and Chigier (2002) in a similar way studied the axial velocity and axial TI patterns at two different steady inhalation

<sup>7</sup> Some principal difficulties appear with the PDA measurement of large particles — particles with diameter exceeding about one third of the diameter of the measurement volume. As inhalable particles do not reach that size, these problems are not discussed here.

flow rates (18.1 and 41.1 l/min) and qualitatively, using fluorescent dye assessed aerosol deposition in the model. They compared regions with high TI and deposition regions and noted no correspondence between these regions. Gemci et al. (2002) followed with a study of an inhalation aerosol–air flow numerically using the CFD and experimentally with PDA in a simplified throat model (a triangular orifice with a shape similar to that of the glottal lumen contained within a glass cylinder). The authors showed several significant spray deposition mechanisms that were notable in both the experimental and the numerical results.

DeHaan (2002), in his thesis, focused on the enhancement of aerosol deposition in the mouth–throat region by non-ballistic pharmaceutical aerosol devices. He performed tests in a replica of airways and CFD in an idealised mouth and throat geometry in a healthy adult male using monodisperse aerosols entering through various inlets. He used LDV for velocity measurements at the entrance and inside the oral cavity and PDA for particle sizing in front of the model.

Lizal et al. (2012) developed a realistic model of the human upper airways (HUA), which consisted of the throat, trachea and tracheo-bronchial tree up to the fourth generation. They fabricated the physical model from a transparent silicone and used a sinusoidal breathing pattern with a tidal volume of 0.5 l and a period of 4 s for 1-component PDA measurements of the air–particle flow during full inspiration/expiration breathing cycle in comparison with CFD calculations. Good agreement was found between the experimental and computational velocity courses. Jedelsky et al. (2012) continued with the PDA measurements in the same model, aiming to compare differences in the PSD of velocity fluctuations among (1) steady-flow regimes and equivalent cyclic regimes, (2) inspiration and expiration breathing phase and (3) particle sizes in the size range 1–8  $\mu\text{m}$ . Systematically higher velocity fluctuations in the upper part of the frequency range (30–500 Hz) were found for cyclic flows in comparison with the steady flows. Both the steady and cyclic expiratory flows produced more high-frequency fluctuations than the inspiratory flow. Later Elcner et al. (2016) presented new CFD simulations on the same model in comparison with the previous PDA experiments in eight cross sections in the trachea and the left and right bronchi. They used a full inspiration/expiration breathing cycle with tidal volumes 0.5 and 1 l and the cycle duration of 4 s (sedentary regime and a deep breath). The Reynolds-averaged Navier–Stokes (RANS) simulation agreed with the experiments in almost all the sections and showed unstable local flow structures. The RANS was proven to be a quantitatively acceptable solution for the time-averaged flow field.

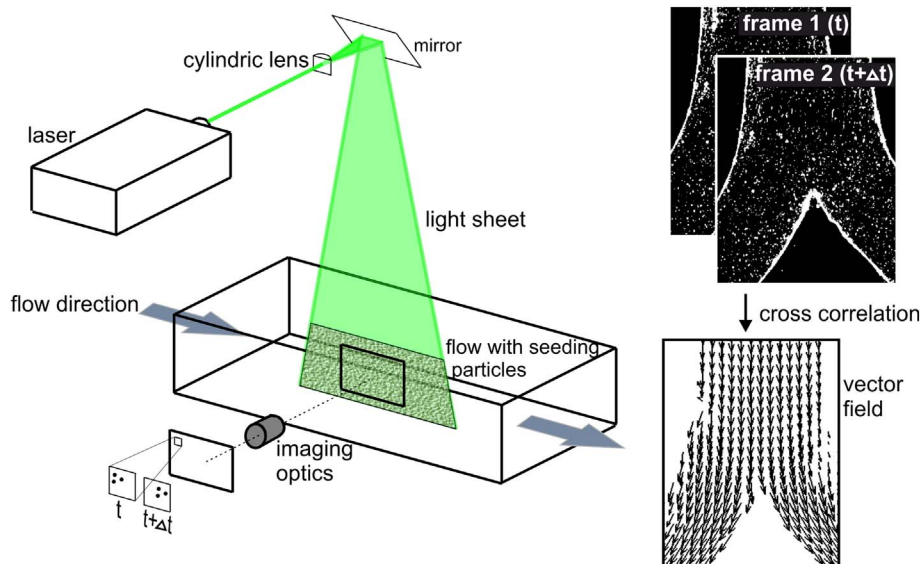


Fig. 4. Typical PIV set-up for planar PIV.

Liu et al. (2016) adopted the LDA to measure the airflow velocity profiles in the HUA model for testifying the reliability of LES approach. The study was done under continuous inspiration and expiration with varied respiratory intensities in a realistic HUA based on the medical CT-scan images of a Chinese male patient, the 3D anatomically accurate HUA model including an obstruction resulting from pharyngeal collapse. The LDA velocity profiles and values were almost the same as calculated in the entire measurable region, which identified the LES method as suitable to study airflow dynamics in the obstructed HUA model.

Kerekes et al. (2016) built an idealised 3D human airway model consisting of the trachea and the first five bronchi generations. They used a custom built LDA to obtain velocity profiles in the central airway region for validation of a CFD model they developed. The airway geometry was reproduced from transparent glass tubes, and the LDA measured the axial velocity of monodisperse polystyrene latex particles under an airflow rate of 30 l/min. A high correlation was found between the velocity profiles obtained with the two methods. The results showed the flow to be laminar in the trachea but affected by the airway geometry in subsequent airways.

The PDA is also often applied as a rapid and space-resolved research-based instrument for size/velocity measurements of nebuliser sprays (Kippax et al., 2004; Roth et al., 2003; Stapleton et al., 2000).

### 3.3. Planar and volumetric flow visualisation techniques

While LDA provides only pointwise flow information, PIV and Particle Tracking Velocimetry (PTV) enable us to measure the 3D flow field. Depending on the specific technique, very high spatial and temporal resolution can be achieved.

#### 3.3.1. Planar PIV

For planar PIV, the seeding particles that represent the flow (compare Section 3.2.2) are typically illuminated by laser light where the laser beam is now widened to a light sheet. In general, two short light pulses with a distinctive time delay are emitted and two images of the illuminated flow are captured by a camera. A typical PIV set-up is shown in Fig. 4.

Within this delay  $\Delta t$  between the two images, particles will have moved by a certain distance. In order to evaluate the corresponding particle shift, images are subdivided into small interrogation windows that contain a certain number of particles forming a distinctive pattern. The size of the interrogation windows depends on the particle density in

the flow. The higher the density, the smaller the size of the interrogation window can be, since each window needs to contain at least 6 particles in order to determine particle displacement with sufficient statistical accuracy. In contrast, the window size needs to be small enough since each vector represents an averaged velocity within the corresponding interrogation window. Thus, regions with large velocity gradients, e.g. near wall regions, need to be subdivided into small interrogation windows in order to resolve the boundary layer adequately. Typical interrogation windows sizes are  $16 \times 16$  or  $32 \times 32$  pixels with particle densities of about 0.1 particles per pixel (ppp) (Scarano, 2013).

The acquired particle image patterns from two subsequent images are compared by cross correlation. Thereby, a shift in each of the x- and y-directions is calculated forming a displacement vector. By applying the time delay between the images, a velocity vector can be determined for each interrogation window, thus forming a 2D-2C (two-dimensional, two-component) velocity field. An example for planar PIV measurements in the upper bronchial tree is presented in Fig. 5. Here, arrows denote the velocity vector and the velocity magnitude is shown with a colour code.

The particle shift between two subsequent images should be in the range of about  $\frac{1}{4}$  of the interrogation window size. Assuming a  $32 \times 32$  pixel window, the shift should be about 8 pixels. If the particle shift is too large, i.e. the time delay between two subsequent images too large, the particle images cannot be adequately correlated by cross correlation leading to spurious vectors. In addition, unsteady flow features may be neglected by this kind of averaging. Furthermore, especially applicable to the human lung, in highly 3D flows particles might leave the light sheet plane in the time between two subsequent images and are thus missing in the cross correlation. If instead, the time delay between the images is too short, the distance travelled by particles may be under-sampled, not representative of the flow and/or zero velocity may be determined.

By analogy with LDA special care needs to be taken to match the refractive index of the lung model and the flow. Thus, PIV in realistic human lung models by using air as a medium is not possible. As mentioned in Section 3.2.1 a mixture of water/glycerine is used instead and typical flow parameters are adapted in order to maintain flow similarity.

### 3.3.2. Stereoscopic PIV

The method of stereo PIV allows measurement of all three velocity components, all within one measurement plane. Hence, this method is known as 2D-3C technique. Typically, two cameras focus from different viewing angles on the same plane in order to measure the out of plane component more accurately. A parallel camera arrangement (called “translation” (Adrian and Westerweel, 2011)) is also employed. The advantage of the translational configuration is the uniform magnification of the images, which is not the case for angular positioning. Here, remapping of the distorted image data on a Cartesian grid is necessary. The translation set-up provides constant magnification, avoiding image correction issues, but the viewing angle is limited. As a result, the angular configuration is most frequently used. In the case of measurements in liquids, the change of the refractive index when light passes through different media must be corrected. This is either realised with liquid-filled prisms fixed at outer walls or alternatively, surrounding walls are positioned in an octagonal configuration (see Fig. 6) in order to receive the optical axis of the camera normal to the viewing window. Scheimpflug adapters need to be implemented in order to correct the focal plane.

Special care needs to be taken during the measurements to receive high levels of accuracy since otherwise, errors in reconstruction of the 3D displacement vector will occur. This is even more critical for measurements in turbulent flows where velocity fluctuations can be small (Adrian and Westerweel, 2011).

### 3.3.3. Volumetric PIV

In order to capture a 3D-3C velocity field at least three cameras have to capture an image of the flow from different viewing angles while the domain is illuminated volumetrically. Consequently, volumetric PIV is substantially more complex than planar PIV, since the 3D particle distribution of the viewing domain needs to be reconstructed from the planar images of each camera. A greater number of cameras reduce the reconstruction uncertainty. The 3D-3C PIV method is also known as Tomo-PIV since tomographic image reconstruction methods are employed.

Accurate calibration of the field of view captured by the cameras is most important. Reconstruction deviations in the sub-pixel range of  $< 0.2$  pixels are required for adequate cross correlation evaluation. Wieneke (2008) introduced the volume self-calibration that needs to be applied at every measurement in order to reduce the calibration errors.

Accuracy problems additionally occur due to spuriously reconstructed particles, so called ghost particles at high particle densities. Thus, the particle density for volumetric PIV cannot be as high as for planar PIV, typically values of 0.05 ppp need to be applied (Elsinga et al., 2006), but this value also depends on the number of cameras being used.

The problem of ghost particles can be circumvented by an advanced PTV technique where the motion of single particles is tracked, so that particle path lines that include local velocities can be reconstructed. Thereby, the history of the particle traces is employed to estimate the exact particle position in the subsequent time step. To determine particle positions in a new time step, an educated prediction of the new position is made and refined by an image matching scheme (Schanz et al., 2013). Hence, higher particle densities (up to 0.125 ppp) can be used than for 3D PIV. Additionally, computational time is strongly decreased since only single particle tracks need to be considered and not the whole voxel volume of a Tomo-PIV algorithm (Schanz et al., 2014).

#### Advantages of PIV/PTV

- 2D and 3D information of the whole flow field can be obtained simultaneously.
- nonintrusive measurement method — no flow disturbances
- high spatial and temporal resolution possible, depending on camera and light source

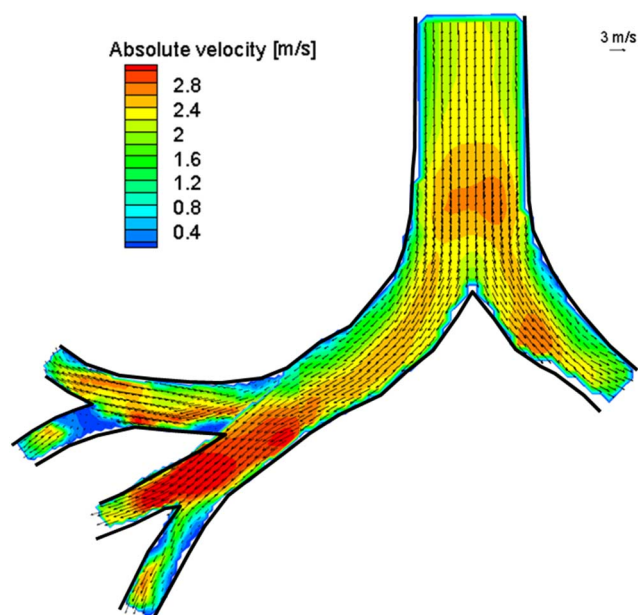


Fig. 5. Velocity vectors and magnitude received from PIV in the upper bronchial tree during inspiration.

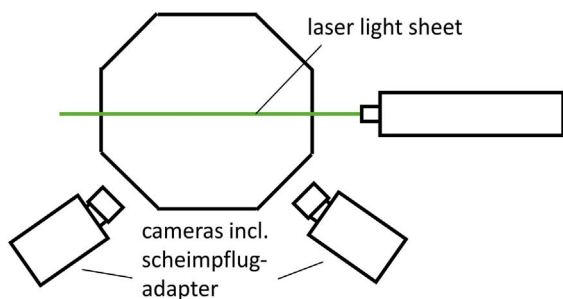


Fig. 6. Camera set-up with octagonal tank walls for stereo PIV, more cameras can be added here for volumetric PIV.

#### Disadvantages of PIV/PTV

- Refractive index matching is required.
- Use of small particles often requires use of high-intensity light sources (class 4 lasers).
- expensive measurement method
- reduced quality of results in high shear flows
- Tracer particles must follow the flow without slip and should have the same density as the fluid, hence only very small/light particles can be used in air.

**3.3.3.1. Applications of planar, 2D PIV measurements.** Due to their experimental simplicity, 2D PIV measurements have frequently been applied in the upper and lower airways. Earliest measurements have been carried out by Brückner (1998) at a planar double bifurcation based on Weibel's (Weibel, 1963) statistical dichotomic lung model, but with rectangular cross section, thus avoiding image deformations due to deviations of the refractive index. Brückner's work covers steady inspiratory flow for a Re range from 900 to 2700 which represents flow conditions in large airways from the trachea down to the 5<sup>th</sup> generation (Brückner, 1998). The authors observe cyclic oscillations of flow patterns and a strong influence from upstream generation flows in the downstream generations, which might not occur in more realistic geometries with a round cross section of airway branches.

More recently, Ramuzat and Riethmüller (2002) applied planar PIV measurements in a double bifurcation model with round cross branch sections. They investigated the variation of velocity profiles for oscillatory flow during one breathing cycle. Breathing parameters include normal and High Frequency Oscillatory Ventilation (HFOV) while varying Re from 400 to 1000. Moreover, during post processing, they analysed the spatial displacement of various selected points near the

outer walls and the carina after one cycle. The net motion thus denotes steady streaming indicating a bidirectional streaming direction between near wall and central locations. In contrast, points very close to the carina hardly show any net displacement. Hence, they associated these zones with higher deposition rates.

A rather exceptional PIV method was applied by Heenan et al. (2003) to measure mean and turbulence RMS velocities. They applied endoscopic PIV in an oropharynx model that allowed flow measurements in air since the camera view was not obstructed by any sidewalls that might alter the refractive index. Their method only required optical access for the laser light source from outside the model. Nevertheless, their field of view was limited by the size and position of the endoscope. The endoscope furthermore had a wide-angle view leading to image distortions that needed correction. Additionally, the surface of focus was not planar, leading to out of focus areas in the image. Hence, the uncertainty for the PIV analysis was increased. Despite the challenges and difficulties of the endoscopic imaging technique, these measurements were well suited as a validation technique for CFD modelling.

PIV measurements at more complex representations of the human airways have been carried out in the following years by Adler and Brucker (2007) and Grosse et al. (2007). Both groups used a 3D lung model made from transparent silicone. Their geometry started with the trachea and bifurcated down to the 6<sup>th</sup> daughter generation. While Grosse et al. (2007) used a geometry based on a CT scan, Adler and Brucker (2007) developed a generic geometry based on statistical data from Horsfield and Cumming (1968) and Weibel (1963). Both groups used oscillatory flow according to typical breathing scenarios, and time-resolved PIV measurements were applied to investigate the flow patterns in selected planes of the model geometry. Grosse et al. (2007) additionally applied steady flow conditions under varying Re from 1250 to 1700 and stated that the influence of the Re was relatively low. On the other hand, they emphasized the strong influence of  $\alpha$ , i.e. oscillatory flow conditions which strongly altered the flow structures during the breathing cycle. Adler and Brucker (2007) additionally investigated the influence of varying  $\alpha$  for breathing under rest conditions as well as HFOV. In contrast to Grosse et al. (2007), their results reveal the low influence that varying  $\alpha$  has on flow patterns, especially at peak flow conditions. Fig. 7 depicts PIV results for varying breathing parameters representing breathing under rest conditions. Colour coded is here the vorticity distribution indicating local shear rates.

Following this, Fresconi and Prasad (2007) carried out a systematic study on secondary velocity profiles in a symmetric planar bifurcation model incorporating three bifurcating generations. They applied steady inspiratory and expiratory as well as oscillatory flow conditions and varied the Re in a low range from 6 to 200. Based on the measurements

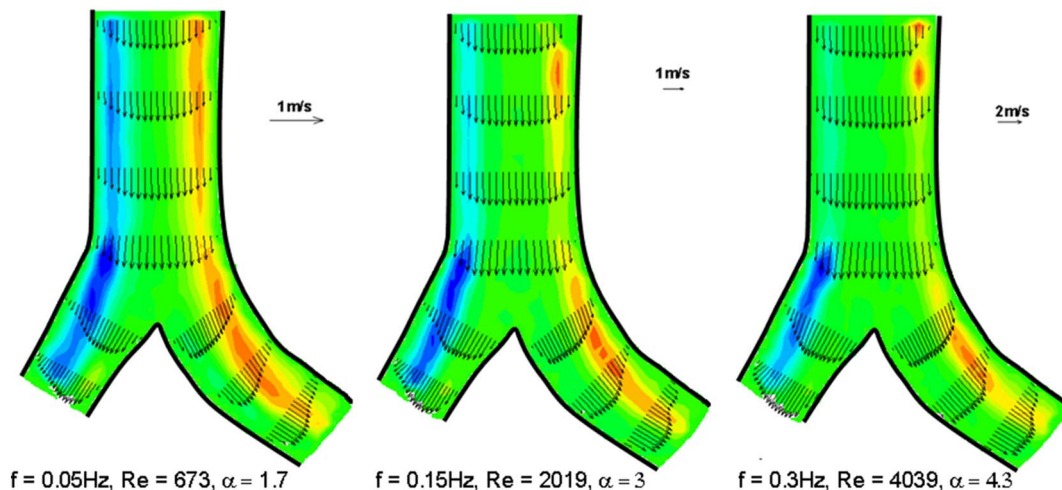


Fig. 7. Velocity vectors and normalised vorticity during peak inspiration for different breathing parameters (with permission reprinted from (Adler and Brucker, 2007)).

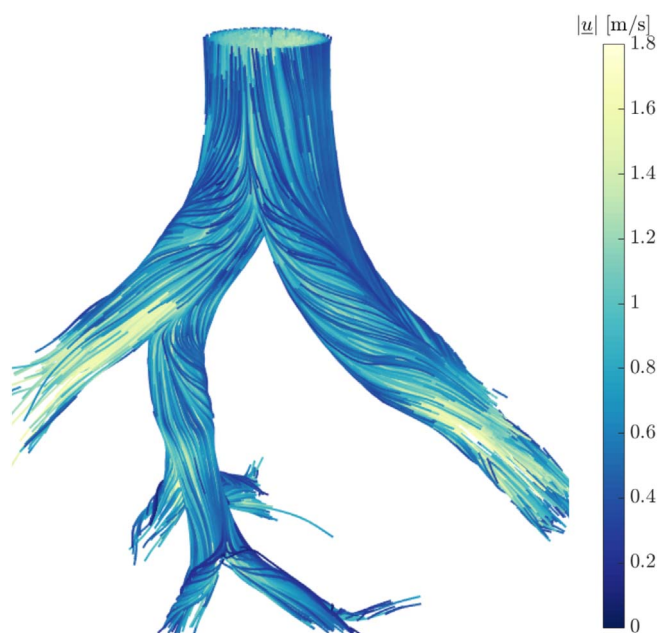


Fig. 8. Particle trajectories received from 3D-PTV during the peak inspiration phase. Trajectories are colour coded by the velocity magnitude (Janke and Bauer, 2016).

they could identify the critical Re and Dean numbers at which secondary flows start to develop in the human airways.

**3.3.3.2. Application of stereo-scanning PIV in the airways.** Soodt et al. (2013) applied stereo-scanning PIV measurements at the lung model already described in Grosse et al. (2007). The technique allows fully 3C-3D measurements. In addition to the stereoscopic set-up, the authors applied a moving (scanning) light sheet which was generated by a rotating mirror drum driven by a stepper motor. The principle was first described by Brückner (1996). Thereby, the whole measurement domain is scanned by a moving light sheet so that one whole scan can illuminate several adjacent planes simultaneously, *i.e.* the time span between the first and the last plane is small enough to prevent large particle motion. A new full scan can be regarded as the second set of images, necessary for cross correlation. Limiting factors are the rotation speed of the stepper motor for the mirror drum and the camera frame rate for image acquisition. Modern high-speed cameras work at typical frame rates of 6000 frames per second (fps) or even up to 20,000 fps at a full resolution of about 1 Megapixel. With a frame rate of 6000 fps, only those flows with velocities below 1 m/s can be investigated. Hence, realistic flows in the upper airways cannot be investigated by using scanning PIV. The maximum Re that Soodt et al. (2013) employed in their stereo scanning study was 150 at oscillatory conditions, a value which is more than a factor of 10 below realistic Re numbers in the upper airways.

A further restriction of scanning PIV measurements is the requirement for lenses with a large focal depth, so that they can provide constant magnification at a range of lens-to-object distances in order to avoid correlation uncertainties. Thus, so called telecentric lenses need to be employed.

**3.3.3.3. Applications of volumetric measurements.** As a result of improvements in evaluation techniques and equipment, volumetric measurement techniques have been employed only recently in the human lungs. Banko et al. (2015) carried out magnetic resonance<sup>8</sup> velocimetry (MRV) measurements in a CT based replica of an airway geometry from the mouth down to the 8<sup>th</sup> bifurcating generation

fabricated by stereolithography. Flow patterns were visualised by a 3 Tesla General Electric whole-body scanner (Banko et al., 2015). The technique thus does not require optical access and refractive index matching to the measurement domain. The authors used water as a working fluid in a translucent model, generated by 3D printing techniques. The MRV did not allow time-resolved measurements due to large scanning times of 45 min. Results show a fully 3D Eulerian velocity field with a resolution of 0.7 mm in each direction, yielding a similar resolution as PIV measurements in geometries of the same size. In an ongoing study, Banko et al. (2016) investigated oscillatory flow by applying phase-locked measurements. Nemes et al. (2016) used MRV in an idealised planar and symmetric lung model for the systematic study of how the Re influences the development of secondary flows, especially in the transitional regime. They found that after the onset of turbulence, secondary flow intensity started to decrease after reaching a maximum in the still laminar regime.

3D particle path lines have been visualised by Janke and Bauer (2016), see Fig. 8. The measurement technique is based on 3D particle tracking velocimetry (3D-PTV) yielding direct visualisation of 3D patterns in the human airways. Janke et al. (2017) used high-power light emitting diodes instead of a laser as the light source and three high-speed cameras for image acquisition. Particle tracking was applied by employing a Shake-the-Box algorithm according to Schanz et al. (2013). The method helped to reduce particle reconstruction ambiguities.

**3.3.3.4. Micro PIV measurements.** So far, we have only considered flow measurements in the large, conductive airways. Flow in the bronchioles and alveolar region can be captured by micro PIV measurements. Flow channels are usually made from PDMS (Polydimethylsiloxane) and have typical dimensions in the range of 500  $\mu\text{m}$ . Due to the small FOV microscopic imaging needs to be employed. A very simple representation was presented by Lee et al. (2006). They investigated Pendelluft flow during HFOV conditions at a single bifurcation model by implementing compliant boundary conditions.

Fishler et al. (2013) developed more complex models in order to mimic pulmonary acinar flows. Their PDMS models are still planar but contain bronchial branches spanning five generations with alveolar sacs. Via a syringe pump, they applied oscillatory flow within the domain. As a working fluid Fishler et al. (2013) also used a mixture of water and glycerin. Yielded flow velocities were in the range of a few  $\mu\text{m/s}$  to mm/s. Their model was capable of featuring typical alveolar flow patterns including recirculations. In a further study, Fishler et al. (2015) used airflow added by particles in order to investigate particle transport and deposition under realistic flow conditions. Their model geometry was improved with walls that could move in a similar way to alveoli. Recently, Fishler et al. (2017) investigated particle dispersion mechanisms in the alveolar ducts by single particle tracking. They observed an irreversible net motion of particles, which they attributed to streamline crossing.

#### 4. Classical methods for the measurement of total and regional aerosol deposition

The following section represents a conservative choice of common methods that are used to measure total or regional aerosol deposition. Some of these methods offer measurements of local deposition when applied in airway replicas. Although they normally provide lower resolution than some of the emerging methods, they are still popular as a result of their availability, and in many cases, low price.

##### 4.1. Measurements of inhalation and exhalation concentrations using particle counters, spectrometers or photometers

One of the simplest methods for measuring aerosol deposition works by capturing the concentration of aerosol entering the airways during inhalation and the concentration exiting the airways during exhalation,

<sup>8</sup> Please refer to Section 5.2 for description of principles of magnetic resonance.

and calculating the difference. The method can be applied both *in vivo* and in replicas (in a simplified manner). Using the basic setup, either overall lung deposition or nasal airway (Kesavanathan and Swift, 1998) deposition can be measured *in vivo*. The usual experimental setup includes a source of (preferably monodisperse) particles, an in-line aerosol concentration measuring instrument (e.g. laser aerosol photometer (Kim and Kang, 1997)), to be positioned as close as possible to the mouth piece, a flow rate measurement device, and a set of valves allowing the intake to switch between clean air and aerosol during inhalation, and between inhaled and exhaled air-aerosol mixtures, with as little cross sectional changes as possible between these components. The experiment can be performed in the following way: the volunteer inhales a well-characterised monodisperse aerosol out of an aerosol generator or holding chamber through a mouthpiece, and then exhales. The concentration of particles and the actual flow rate are measured in-line during the whole in- and exhalation. The total deposited fraction can then be calculated as  $TDF = (\text{average } C_{in} \times \text{inhaled volume} - \text{average } C_{out} \times \text{exhaled volume}) / (\text{average } C_{in} \times \text{inhaled volume})$ . This can be done in a single or a multiple breath manoeuvre.

An interesting variation of this method is the so-called aerosol bolus method. It can be applied *in vivo* and in replicas and the main idea of this approach is that the aerosol is not delivered throughout the entire inhalation, but in smaller volumes (typically 20–300 ml) inserted at various time points in the inhalation. By delivering the aerosol bolus followed by a progressively larger volume of inhaled air, the aerosol bolus can be pushed deeper into the lungs. Upon recovery of the aerosol bolus during exhalation, one can determine local aerosol deposition at various lung depths (Kim et al., 1996). While sometimes referred to as regional lung delivery, this specifically refers to the aerosol being delivered to more proximal or more peripheral lung regions. On its way through the lungs, the bolus will inevitably split between an increasing number of parallel pathways that may affect aerosol transport in a different way. This is the key to the aerosol bolus being used as a diagnostic tool, whereby the dispersion of the aerosol bolus is considered a measure of convective gas mixing, which can be greatly altered in lung disease (Blanchard, 1996). While aerosol bolus deposition measurement requires a mono-dispersed aerosol, aerosol bolus dispersion data can even be obtained with a saline aerosol (Verbanck et al., 2001a; Verbanck et al., 2001b). The (monodisperse) aerosol bolus deposition has also been used as a diagnostic tool, for instance, to estimate the size of widened air spaces in the deep lung in patients with emphysema (Kohlhauff et al., 1998); in that case the aerosol derived airway diameter is an average measure of airway size for a given lung depth.

Either total or nasal deposition can be calculated from the non-bolus method, whereas deposition and dispersion at various lung depths can be derived from the bolus method. The main benefits of both the bolus and non-bolus methods are: relevance of the data — since these measures can be obtained *in vivo*, no radioactive substance needs to be inhaled, and the latex particles or oil droplets that will guarantee monodisperse aerosols can be inhaled in very low concentrations and still be reliably detected (for deposition measurement). With this, however, come several issues, the main one being repeatability of the experiments: repeatability is limited by the ability of subjects to reproduce the same breathing pattern, and in the case of bolus experiments, the accuracy of the setup in injecting the small aerosol volumes at a specific time point in the inhalation; as a result, repeated experiments are needed on the same subject to obtain reliable data. The other issue that is particularly relevant for comparison with CFD-derived 3D flow fields and aerosol trajectories is that aerosol concentration measurements with a photometer typically cover the middle 75% of the tube cross section, and intrinsically produce just an average concentration value for a given tube cross section.

Advantages:

- no radioactivity involved,
- no simplification of the reality,
- can provide diagnostic indices.

Disadvantages:

- complicated control of boundary conditions (to be temporarily stable and inter and intra-subject invariable),
- difficulty with obtaining the geometry and boundary conditions for CFD.

#### 4.1.1. Examples of application — *in vivo* and in replica

As measuring the concentration of inhaled and exhaled particles is a relatively straightforward procedure, it was used as one of the first methods to assess the total deposited fraction. The pioneering works in this area have been reviewed by Lippmann et al. (1980). The first measurements were done by Landahl in the 1950s (Landahl et al., 1951), who collected the exhaled triphenyl phosphate particles using an impactor, washed the samples out using alcohol and estimated the quantity colourimetrically. Many studies followed, however sometimes performed under poorly controlled conditions, rendering the comparison of results difficult. In fact, Lippmann suggested that the data collected by Heyder et al. (1978) could serve as the lower limit of aerosol deposition, since their experiments were well controlled and indeed reported the lowest deposition, compared to other total deposition studies.

The aerosol bolus method was applied by several teams *in vivo* (Altshuler, 1969; Darquenne et al., 1998; Kim et al., 1996; Scheuch, 1994) and also in a canine lung cast (Scheuch et al., 1993). Because of the substantial differences among existing aerosol bolus results in the literature, experimental sources of error in the bolus method were examined by Verbanck et al. (1999). These authors showed how differences in the bolus deposition of up to 25% can arise in the same normal subject as a result of the aerosol delivery and measurement system. Depending on the tubing system and how developed the velocity profile of the aerosol bolus is upon entering the lungs, the photometer measurement will produce an aerosol concentration curve that is not representative of the average concentration over the entire tube cross section. Since the inspiratory quantity of aerosol ( $\text{average } C_{in} \times \text{inhaled volume}$ ) serves as a reference for the TDF computation, an inaccurate estimate of the inhaled concentration profile will lead to TDF errors; in the case of proximal boluses, undergoing very little deposition, this artefact can lead to the paradoxical result that TDF becomes negative.

#### 4.2. Microscopy

Optical microscopy has been used mainly to count and analyse fibres. As we are not discussing invasive techniques, only those experiments performed in replicas of human lungs will be described. The method is very simple in principle. The fibres are dispersed, usually using a fluidized bed generator, treated to equalize the electric charge and mixed with inspiratory air. Then the fibres enter the model of lungs with coated walls, where a certain fraction deposits. The rest of the fibres are then collected on output filters. The fibres deposited in the model are consequently either counted directly *in situ* using the microscope (Myojo, 1987, 1990), or washed out, filtrated, and counted on the filter (Belka et al., 2016).

Several variants of microscopy are available currently. The first established method was the Phase Contrast Microscopy (PCM). This method was developed for detection of samples that are optically transparent and therefore are invisible to an observer with a basic optical microscope, because the human eye is sensitive only to changes in intensity of the light, which is not attenuated by passing through the transparent sample. Since the phase of the passing light is shifted, these phase changes can be converted to an observable intensity change using e.g. Zernike's method (Zernike, 1942).

The PCM method was utilised and standardized for counting of asbestos and other fibres as part of NIOSH 7400 (NIOSH, 1994), WHO (WHO, 1997) or ISO 8672 methodology for occupational protection and toxicology. Other variants of microscopy, such as the Transmission Electron Microscopy (TEM) or Scanning Electron Microscopy (SEM) (Baron, 2001), can be used in principle for the analysis of deposited fibres, however, these methods are mainly being used in toxicological studies and have not obtained popularity comparable with PCM for non-invasive particle deposition studies.

Analysis performed by microscopy provides data in the form of a number of particles (usually fibres) deposited in either whole replica, or separate segments commonly containing one bifurcation.

#### 4.2.1. Examples of application

PCM has been applied by several teams in replicas of human airways. Deposition of carbon fibres in nasal replica was measured by Su and Cheng (2005). They found that deposition of fibres is generally lower compared to equivalent spherical particles. A year later they performed a follow-up study focused on the deposition of particles in oral airways and part of the tracheobronchial tree (Su and Cheng, 2006). They proved that low inertia fibres can easily penetrate through the first four generations of bronchial branching and deposit in the lowest regions of lungs. As a next step, comparison of fibre deposition in two realistic replicas was performed by Zhou et al. (2007). Although they observed a large variability among bifurcations from the same generation when comparing the two replicas, they stated that general trends could be drawn from their study: fibre deposition in the tracheobronchial tree is lower than that of the equivalent spherical particles. The authors also emphasized the need to use a realistic airway model, including larynx, for plausible simulation of flow patterns in the airways. Lastly, the same team added TiO<sub>2</sub> and glass fibres to get very low momentum fibres (Su et al., 2008). Their results confirmed an overall continuity between fibre materials. The equations used to estimate a fibre's regional deposition efficiency in the human respiratory airways were devised based on this experimental data. The numbers of fibres in samples from all the above-mentioned studies were counted manually using adapted NIOSH 7400 methodology. A similar approach was used also by Wang et al. (2008) for the analysis of nasal deposition of fibres. Because the manual counting of fibres is demanding and subjective, due to the human factor involved in the analysis, attempts were made to develop an automated counting methodology based on image analysis techniques. Such a technique was presented e.g. by Belka et al. (2016). Their method was tested against the standard manual method and proved to be consistent with the results obtained by a trained human operator, while avoiding those factors that contribute to subjectivity such as mood, fatigue or the health state of the PCM operator. However, only high-quality filters free of impurities can be evaluated using the automated algorithm (Fig. 9).

#### 4.2.2. Uncertainties

Both manual and automated counting provide data with relatively

high uncertainties. The precision of the manual counting using PCM for the determination of airborne fibre number concentrations was discussed by WHO (1997). The coefficient of variation (CV) in the number of counted fibres depends on the density of fibres on the filter. Microscopists generally tend to under-count dense samples and over-count sparse samples. The recommended density range for optimal accuracy is between 100 and 1000 fibre/mm<sup>2</sup>. The intra-laboratory CV is in the range of 21 to 49% depending on the number of counted fibres. However, inter-laboratory CV can be twice as great as intra-laboratory CV. These values are acceptable in occupational protection measurements as the counts of particles are evaluated in orders of magnitude, nonetheless, the usability of this method for validation of CFD results is limited. Automated counting can decrease the CV, however, values below 20% can hardly be expected. Therefore, only confirmation of general trends can be provided, while comparing the exact counts in specific segments of lungs is questionable.

Advantages:

- simple and relatively cheap method,
- no radioactivity needed,
- can provide diagnostic indices.

Disadvantages:

- relatively high uncertainty,
- time-consuming,
- applicable only on replicas.

#### 4.3. Gravimetry and fluorometry

The term gravimetry refers to a method based on weighing filters or collecting plates that contain deposited aerosol particles. This method is commonly used with cascade impactors, but can be generally used for the analysis of samples washed out from lung replicas. The term fluorometry refers to those methods that are based on fluorescence measurements on the samples collected by washing out the segments of airways. Both methods are routinely used in many laboratories as standard methods in many disciplines. Their application in deposition studies usually employs replicas of lungs. The most common setup consists of the particle generator or disperser, a charge equilibrater, an aerosol-air mixer, a replica of lungs with connected output filters and a vacuum pump. Then, for gravimetry, either the whole replica or its parts are washed out, the resulting dispersion is filtrated and the filters analysed. This requires filters that are insensitive to temperature and humidity changes, and are not easily electrically charged. The samples for fluorometric analysis are created directly by washing out the model. The particles must be dissolved using a suitable solvent. A second set of samples is created from the output filters, while the material of the filters is commonly dissolved to provide a pure sample. Procedures similar to fluorometry can also serve for other common chemical methods, such as Gas Chromatography – Mass Spectrometry (GC–MS).

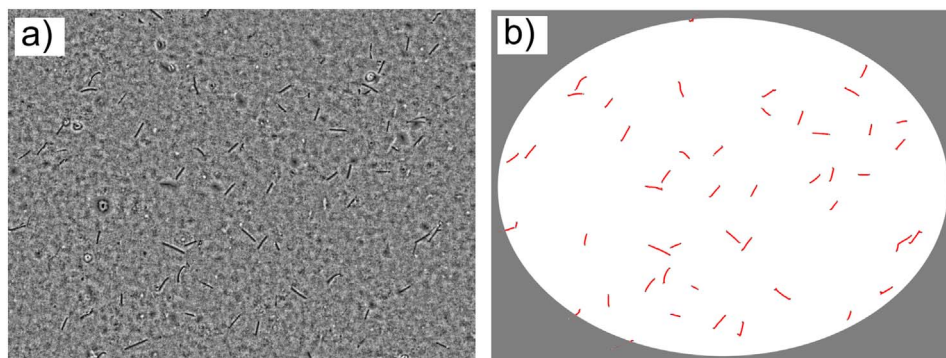


Fig. 9. Example of an automated fibre detection method applied on glass fibres deposited on a nitrocellulose filter: a) a processed image with fibres enhanced by a special algorithm, b) automatically detected fibres in the identical image.

GC–MS is suitable for analysis of multicomponent particles (Nordlund et al., 2017).

#### 4.3.1. Examples of application

The gravimetric analysis was applied e.g. by Grgic et al. (2004) or Zhang and Finlay (2005), who measured deposition in three idealised proximal lung bifurcation models with an idealised mouth–throat. They revealed the important role of the laryngeal jet on tracheal deposition, and that its effect in the following bifurcations was negligible. Fluorometry was applied e.g. by Kim and Iglesias (1989) and more recently Cheng et al. (2015), who used sodium-fluorescein-tagged oleic acid particles. Solid polystyrene latex fluorescent particles in the size range of 0.93 to 30  $\mu\text{m}$  were used by Cheng et al. (1999). As a proof that fluorescence based methods can be used *in vivo*, we present the study of Bowes and Swift (1989), who (apart from using  $^{99\text{m}}\text{Tc}$  tagged particles) let their volunteers inhale fluorescence tagged di-ethylhexyl sebacate particles. After the inhalation, the subjects gargled to remove the deposited fluorescent tracer from the oral airway and the solution was analysed. The study focused on the sensitivity of the filtration efficiency of the oral airway to different levels of physical activity. Somewhat surprisingly the deposition efficiency was lower during heavy exercise than during moderate exercise, although the inhalation flow rates increased. The explanation was that because the mouth was opened more widely, the cross-sectional area of the oral airway probably resulted in decreased particle velocities and hence lower inertia of particles.

#### 4.3.2. Uncertainty

For gravimetry, an analytical balance with a resolution about 0.1 mg is needed. It is necessary to select suitable filters that do not absorb humidity and keep them in well-controlled conditions. The uncertainty of results is usually expressed only as the standard deviation of measured values, which is typically around 5%. The advantage of fluorometry can be seen in higher sensitivity, providing the suitable tracer is used.

Advantages:

- simple and relatively cheap methods,
- both routinely used in many laboratories.

Disadvantages:

- low spatial resolution (especially for gravimetry).

## 5. Standard medical imaging methods

A relatively wide database of experimental results describing

aerosol deposition has come from standard medical imaging modalities. The main advantage of this group of methods is that the instrumentation is broadly available in hospitals and specialised centres and the methods are routinely used in clinical practice. The results are acquired mainly *in vivo*, although several applications in lung replicas have been reported as well. The crucial issue for a successful nuclear measurement is proper labelling of the aerosol particles. The tracer can be either directly chemically incorporated into the molecule of the particle material, attached to the surface of the particle or physically embedded into the volume of the particle. In any case, proper labelling is necessary to ensure that the signal received from the tracer truly represents the distribution of particles.

### 5.1. Nuclear imaging methods

Nuclear imaging techniques, which comprise Positron Emission Tomography (PET), Single Photon Emission Computed Tomography (SPECT) and planar gamma-camera imaging or 2D–scintigraphy, are *in vivo* and minimally invasive imaging modalities which allow the determination of the spatiotemporal distribution of a radiolabelled tracer (radiotracer) after administration into a living organism. Gamma ray-emitters or positron emitters (which ultimately result in the emission of gamma rays, see below) are suitable radioisotopes for this purpose, as high-energy gamma rays can travel through biological tissues without suffering significant scatter or attenuation. Such gamma rays can be detected and quantified using specific instrumentation and tomographic reconstruction algorithms.

It should be noted that although the nuclear imaging was developed for *in vivo* measurements, successful attempts have also been made in replicas as documented e.g. by Lizal et al. (2015) or Verbanck et al. (2016).

#### 5.1.1. The basis of nuclear imaging: radioactivity, radioactive isotopes and radiotracers

When the nucleus of an atom has an excess of energy, it undergoes a spontaneous and stochastic process called radioactive decay. In this process, the nucleus reaches a lower-energy state while emitting radiation in the form of alpha particles, beta particles (electrons or positrons), gamma rays or conversion electrons. The emission type, the level of transition energy and the lifetime of the radionuclide before decaying are characteristic for each radionuclide.

Radioactive decay is a stochastic process in which the probability of an atom to undergo radioactive decay is constant over time. The radioactive decay formula is expressed as:

$$N(t) = N_0 e^{-\lambda t} \quad (7)$$

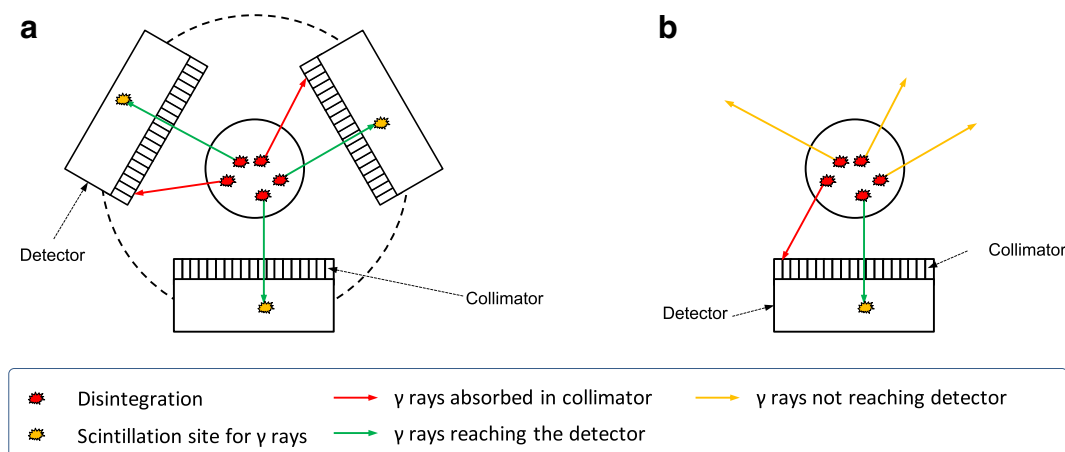


Fig. 10. Schematic representation of the detection of photons using SPECT (a) or planar gamma-camera imaging (b). Only a fraction of the emitted gamma rays reaches the detectors, while others are absorbed in the collimator or never reach the detectors.

where  $N_0$  is the initial number of radioactive atoms,  $N(t)$  is the number of radioactive atoms at time  $t$ ,  $\lambda$  is the decay constant ( $\ln 2/T_{1/2}$ ).  $T_{1/2}$  is the half-life of the radioisotope, and corresponds to the period of time required to decrease the number of radioactive atoms to one half of the starting value. In the International System of Units (SI) the activity is expressed in Becquerel (Bq), 1 Bq corresponding to one disintegration per second. Curies (Ci) are also commonly employed, with  $1 \text{ Ci} = 37 \text{ GBq}$ .

Radioactive isotopes are usually administered after attachment or incorporation into a molecule (radiotracer). During recent decades, many radiochemical strategies have been developed that enable the radiolabelling of a wide range of molecular formats including small molecules, peptides, proteins, antibodies, affibodies and nanoparticles (NPs) using a wide range of positron and gamma emitters. For some reviews, refer to (Gillings, 2013; Li and Conti, 2010; Miller et al., 2008; Morais et al., 2012; Pratt et al., 2016; Price and Orvig, 2014; Stockhofe et al., 2014).

### 5.1.2. SPECT

SPECT relies on the detection of gamma rays originated during radioactive decay of single photon-emitting radionuclides. Single-photon emitters commonly used in nuclear imaging have half-lives ranging from a few hours to a few days and photon energies in the range 100–300 keV. Among single photon emitters, metastable technetium-99 ( $^{99m}\text{Tc}$ ) is the most commonly used, with nearly 80% of nuclear medicine imaging procedures currently performed with this radionuclide: It has a favourable gamma-energy (141 keV), a suitable half-life of 6.02 h, and well-known coordination chemistry. Additionally, it can easily be obtained as  $^{99m}\text{TcO}_4$  in an aqueous buffer from commercially available  $^{99}\text{Mo}/^{99m}\text{Tc}$  generators. Other widely used gamma emitters include  $^{123}\text{I}$  ( $T_{1/2} = 13.22 \text{ h}$ ,  $E = 159 \text{ keV}$ ),  $^{111}\text{In}$  ( $T_{1/2} = 2.8 \text{ d}$ ,  $E = 171$  and  $245 \text{ keV}$ ) and  $^{67}\text{Ga}$  ( $T_{1/2} = 3.26 \text{ d}$ ,  $E = 93, 185, 300, \text{ and } 394 \text{ keV}$ ).

SPECT scanners consist of at least one gamma-ray detection module and one collimator. The core of the detection module is normally a scintillation crystal which absorbs the energy of incident gamma rays and re-emits a flash of light, which is subsequently detected by a photo-electronic system. Both the location in the crystal and the intensity of the flash of light, which is proportional to the energy of the incidental gamma-ray, are recorded. The collimator most commonly consists of a lead plate containing a large number of holes, which stop all the rays that do not reach the detector in a given direction. Hence, the collimator forms a projected image of the radioisotope distribution on the surface of the scintillation crystal. SPECT systems are typically composed of one or more detection heads which are mounted on a gantry that rotates around the imaged subject. If only one set of static detectors is used, the imaging modality is referred to as planar gamma-camera

**Table 1**  
Typical positron emitters (with half-life and positron range).

Isotope	Half-life	$\beta^+$ Energy
$^{18}\text{F}$	109.8 min	0.63 MeV
$^{11}\text{C}$	20.4 min	0.96 MeV
$^{13}\text{N}$	9.97 min	1.20 MeV
$^{15}\text{O}$	122 s	1.73 MeV
$^{68}\text{Ga}$	67.6 min	1.89 MeV

imaging or 2D-scintigraphy (Fig. 10).

### 5.1.3. PET

The positron is the antiparticle of the electron, with equivalent mass but positive electrical charge. When a positron is emitted, it interacts with other charged particles and loses kinetic energy while transiting a random path. When most of this energy has been lost, the positron annihilates with an electron of a surrounding atom, resulting in the emission of a pair of gamma rays travelling in directions  $180^\circ$  apart and each with an energy of 511 keV. The distance between the locations where disintegration and annihilation take place is called positron range, and depends on the energy of the emitted positron and the media. Typical positron emitters have positron ranges of a few mm in water. The unique feature of gamma rays generated by positron–electron annihilation is exploited by coincidence detectors, which are placed around the subject under investigation. Two photons detected almost simultaneously by two detectors are assumed to arise from one single annihilation. The position of annihilation is determined by tracing a line between the two detectors, and hence PET imaging relies on back-to-back detection heads (coincidence detection). As a result of this, PET scanners do not need collimators: The detection of “pairs of photons” is known as “electronic” collimation. A schematic representation of a PET scanner is shown in Fig. 11.

Positron emitters typically used in the medical or biomedical fields have shorter half-lives than single photon emitters. The most commonly used radionuclides are presented in Table 1.

Both in PET and in SPECT a set of projections at different angular positions around the subject under investigation is acquired. The images are then reconstructed using different algorithms (e.g. Filtered-Back-Projection or FBP, Ordered Subset Expectation Maximization or OSEM) and the resulting images can be analysed to gain quantitative information about the spatiotemporal distribution of the radiotracer.

### 5.1.4. Nuclear imaging: important remarks

As mentioned above, nuclear imaging techniques offer information on the spatiotemporal distribution of the radionuclide within the organism under investigation. Importantly, the radiotracer is usually

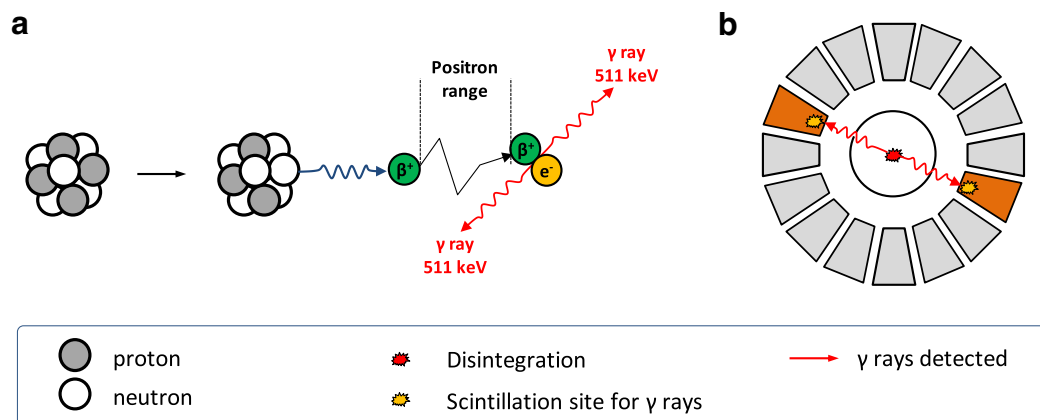


**Fig. 11.** a) Schematic representation of the annihilation process of one positron and one electron, with subsequent emission of two gamma rays. b) Representation of a PET camera. The two photons emitted after the annihilation process are detected simultaneously by two detectors of the ring, placed around the subject under investigation.

injected in a sub-pharmacological amount (trace amount) and hence no pharmacological, adverse or toxicological effects are expected. However, these techniques have certain limitations that are worth mentioning and which need to be taken into consideration.

**5.1.4.1. Lack of anatomical information.** Nuclear imaging techniques do not provide any anatomical information of the subject under investigation. Because of this, nuclear imaging techniques are often combined with other imaging modalities which can provide accurate anatomical information, essential to unequivocally determine the location of the radioactivity. CT (3D x-ray imaging) is the most commonly used, and most of PET and SPECT scanners currently available exist only as hybrid systems (PET–CT or SPECT–CT). Besides providing anatomical information, the CT image is also used to create the attenuation map for appropriate correction during image reconstruction (for more details, refer to [Ay and Sarkar \(2007\)](#)). In the recent years, hybrid PET–MRI systems have been developed. MRI provides excellent spatial resolution and high contrast in soft tissue. However, determination of the attenuation map is still a challenge and hence this hybrid technology is still not fully established ([Paulus and Quick, 2016](#)).

**5.1.4.2. Limited spatial resolution.** Contrary to other imaging modalities such as CT or MRI, one of the major limitations of nuclear imaging techniques is the spatial resolution. Preclinical SPECT devices provide high spatial resolution that can reach well below a millimetre, whereas it is very difficult for PET scanners to attain sub-millimetre spatial resolutions, due to the effect of the positron range. On the other hand, PET systems are typically much more sensitive than SPECT cameras as no collimator is required for imaging. In general terms, PET cameras can achieve resolutions in the range of 1 mm in the preclinical setting and around 5 mm in the case of clinical scanners.

**5.1.4.3. Motion effects.** One of the major challenges in nuclear imaging is to correct for motion effects. This is especially relevant when imaging the thorax or the abdomen, as the subject's breathing causes artefacts. Many different approaches for artefact avoidance or correction have been developed, most of them based on gated acquisition and synchronization between the respiratory signal and image acquisition. Although routinely performed in routine clinical practice, this approach fails to adequately correct for respiratory motion because each gate can mix several tissue positions. Other correction techniques integrate motion information before, during, or after the reconstruction process. For a recent review, refer to [Pépin et al. \(2014\)](#).

**5.1.4.4. Quantification of the images.** Quantification is the process of deriving meaningful quantitative data from the images. The physical property that is directly measured in nuclear imaging cameras is the concentration or radioactivity. However, the cameras can only detect a small fraction of the gamma rays emitted. Consequently, it is necessary to calibrate these devices by scanning objects with a known activity concentration and derive a multiplicative calibration factor that will be applied subsequently. Of note, activity concentration values depend on a number of confounding factors which require correction during the quantification process. The most obvious factor is the injected amount of activity (injected dose, ID): the larger the ID, the higher the signal. A common way to correct for this is to express activity concentration values as a percentage of the total injected dose per gram of tissue (% ID/g). The value of %ID/g can be misleading when comparing subjects of different weights, because the total body volume in which the radiotracer distributes also affects the concentration value. To overcome this drawback, the Standard Uptake Values (SUV), calculated as activity concentration/(ID/subject weight), are usually determined. As the activity concentration is normalised by body weight, the resulting SUV of a radiotracer with an even distribution in the whole body would be 1. It is important to take into account that

the limited spatial resolution of nuclear imaging techniques poses some limitations in the quantification of the images. When the object or structure that is imaged is smaller than 2–3 times the spatial resolution of the scanner, as measured by its Full Width at Half Maximum (FWHM), activity concentration values obtained after quantification are underestimated (partial volume effect). Reciprocally, the concentration of radioactivity in small regions with low activity surrounded by regions with high concentration of radioactivity can be over-estimated (spill over effect). In this scenario, accurate estimation of the activity concentration requires knowledge about the size of the object and the reconstructed image spatial resolution. There are several possible approaches to correct or minimise the partial volume effect. A detailed description is beyond the scope of this review ([Bettinardi et al., 2014](#)).

**5.1.4.5. Stability of the radiotracer.** Nuclear imaging cameras detect the position of the radionuclide. Hence, if detachment of the radioisotope or metabolism occurs during imaging studies, the distribution of the *in situ* generated labelled species may significantly differ from that of the parent compound, leading to misinterpretation of the results or a decrease in the signal-to-noise ratio. Hence, a crucial aspect to guarantee reliable data is the stability of the radiotracer once it has been administered to the subject under investigation.

**5.1.5. Use of nuclear imaging in the assessment of aerosol distribution in the lungs**

Lung administration of drugs has recently gained attention because pulmonary administration offers numerous advantages ([Loira-Pastoriza et al., 2014](#)). However, one of the major challenges of lung administration is determining the dose actually deposited in the lungs and the regional distribution of the drug, and these parameters will have an impact on the clinical effect. When the drug is administered in the form of an aerosol, the regional distribution can be determined using nuclear imaging techniques, by just labelling the aerosol (or the drug itself) with a positron or gamma emitter that enables subsequent imaging studies using PET or SPECT/2D-scintigraphy, respectively.

**5.1.5.1. Determination of regional distribution using SPECT/2D-scintigraphy.** As mentioned above,  $^{99m}\text{Tc}$  can be obtained from commercially available generators, it is reasonably inexpensive, it has a relatively long half-life, close to 6 h, and has appropriate emission properties. Not surprisingly, it has been one of the most commonly used radionuclides to tackle the determination of regional lung distribution of aerosols in the lung. The most straightforward route to incorporate  $^{99m}\text{Tc}$  in the aerosol consists of adding the radionuclide to the nebuliser solution, to achieve a physical association of the label and the drug. However, the chemical form plays an important role. When  $^{99m}\text{Tc}$  is added as pertechnetate (as obtained from the generator) its residence time in the lungs is very short (close to 15 min, ([Walker et al., 2001](#))) and hence long term investigations are not possible. However, information about the regional distribution of the aerosol immediately after administration can be obtained. Other forms of technetium can be used to enable longer-term investigations, such as the complex  $^{99m}\text{Tc}$ -DTPA ( $^{99m}\text{Tc}$ -diethylene triamine penta acetic acid) ([Eberl et al., 2001](#)) or a colloidal suspension of albumin (human serum albumin freeze-dried micro colloid) ([Fleming et al., 2011](#)). It is important to take into account that images reflect the distribution and clearance of the labelled entity. Hence, differences in the behaviour of the labelled entity with the drug itself may lead to misinterpretation of the results. Additionally, it is important to demonstrate that the radiolabelling process has no effect on the properties of the aerosol in order to get reliable data.

After the acquisition of images, qualitative information can be obtained by visual inspection. To obtain quantitative data, regions of interest (ROIs) or volumes of interest (VOIs) can be delineated on the 2D-scintigraphy or SPECT images, respectively, and the concentration of

radioactivity in the region/volume of interest can be determined. However, such delineation is often challenging because the radioactivity does not necessarily distribute in the whole lung. Nowadays, with multimodal (hybrid) systems available in most clinical centres, x-ray or CT scans can be carried out sequentially to the nuclear image acquisition, enabling accurate delineation of the lungs on the x-ray or CT images. The ROIs or VOIs are then translated to the 2D-scintigraphy or SPECT images, respectively, for quantification. In the past, when no hybrid imaging systems were available, delineation of the lungs was carried out with transmission scans using external radioactive sources or from ventilation scans using radiolabelled gases (e.g.  $^{81m}\text{Kr}$ ) (Newman and Fleming, 2011).

Examples of  $^{99m}\text{Tc}$ -labelling to assess deposition of drugs in the lungs can be found both in the context of SPECT and 2D-scintigraphy. For example, Brand et al. used 2D-scintigraphy to compare the deposition pattern of  $^{99m}\text{Tc}$ -labelled Berodual® (fenoterol hydrobromide 50 µg/ipratropium bromide 20 µg per actuation) in COPD patients using two different inhalers (Respimat® Soft Mist™ Inhaler (SMI) and a pressurized metered-dose inhaler) before and after training the patients on the use of the inhaler (Brand et al., 2008). One of the inhalers (Respimat® SMI) showed superiority in terms of global deposition in the lungs. Additionally, training improved the inhalation profiles (Fig. 12). In another study, Behr et al. investigated lung deposition of a liposomal cyclosporine A solution consisting of uni-lamellar 50 nm liposomes in single and double lung transplanted patients using a customised nebuliser and planar scintigraphy (Behr et al., 2009). The authors could quantify total and peripheral lung deposition as a function of the administered dose.

The main limitation of 2D-scintigraphy relies on the fact that 3D

information is condensed in a 2D-image (projection). To overcome this drawback, SPECT imaging can be used. In this modality, volumetric information can be obtained and the images can be displayed as slices in three different views (transverse, coronal and sagittal planes). However, even in this case quantification of the images to get volumetric information about the regional distribution of the aerosol is not trivial. Firstly, most of the gamma emitters used in nuclear medicine have relatively low gamma energy emission (e.g. 141 keV for  $^{99m}\text{Tc}$ ) and hence attenuation effects have to be taken into account. As mentioned above, this can be easily solved nowadays because CT scans can be obtained using hybrid systems to determine the attenuation map for correction of the SPECT images. Secondly, the relation between the number of gamma rays detected by the detectors and the number of disintegrations taking place depends on many different factors, such as the injected activity, the geometry of the collimator, the energy of the gamma rays, and the geometry and material of the detectors, among others. Hence, appropriate calibration is paramount to achieve absolute quantitative data.

Just to mention one example of the use of SPECT in the determination of aerosol deposition in the lungs, Dugernier et al. have compared the total and regional pulmonary deposition of aerosol particles generated by two different nebulisers (a vibrating-mesh nebuliser and a jet nebuliser) in six healthy male subjects (Dugernier et al., 2017). With that aim, nebulisers were filled with  $^{99m}\text{Tc}$ -DTPA and pulmonary deposition was measured using SPECT-CT. As demonstrated by the authors, aerosol deposition was six times increased with the vibrating-mesh nebuliser as compared to the jet nebuliser ( $34.1 \pm 6.0\%$  versus  $5.2 \pm 1.1\%$ ,  $p < 0.001$ ) (Fig. 13). However, aerosol penetration (calculated as the normalised ratio of the outer and the inner regions of

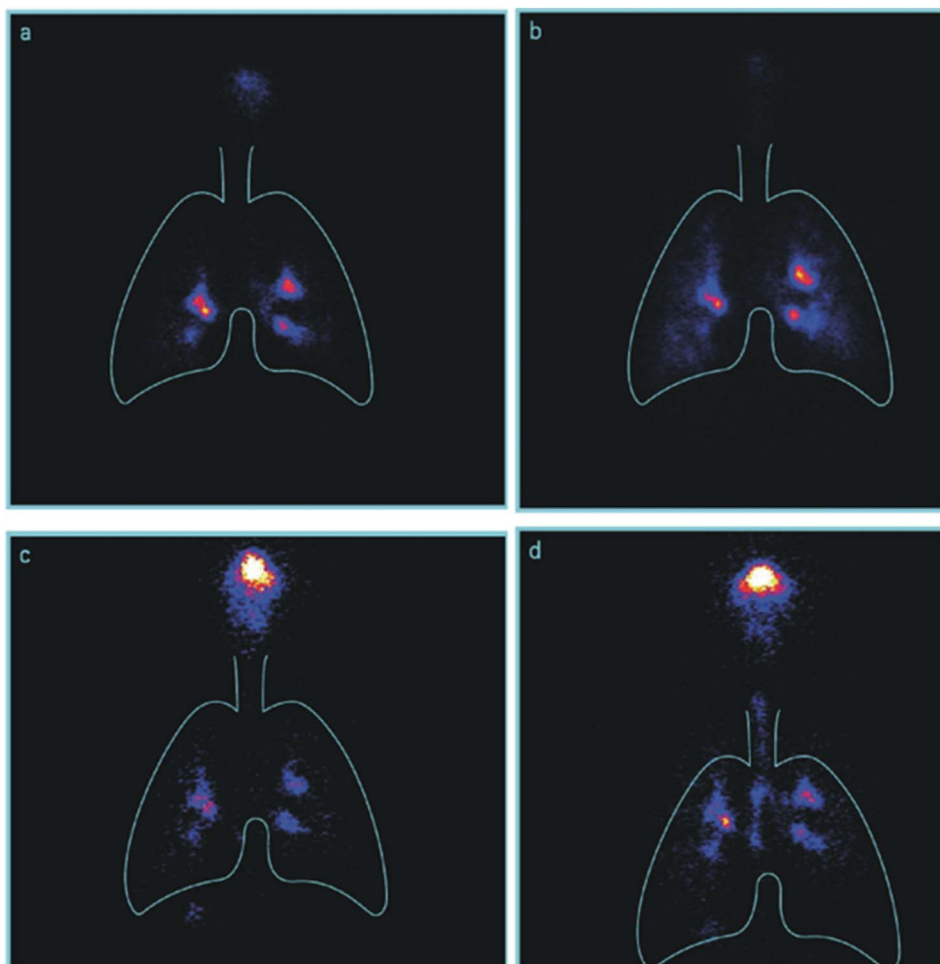
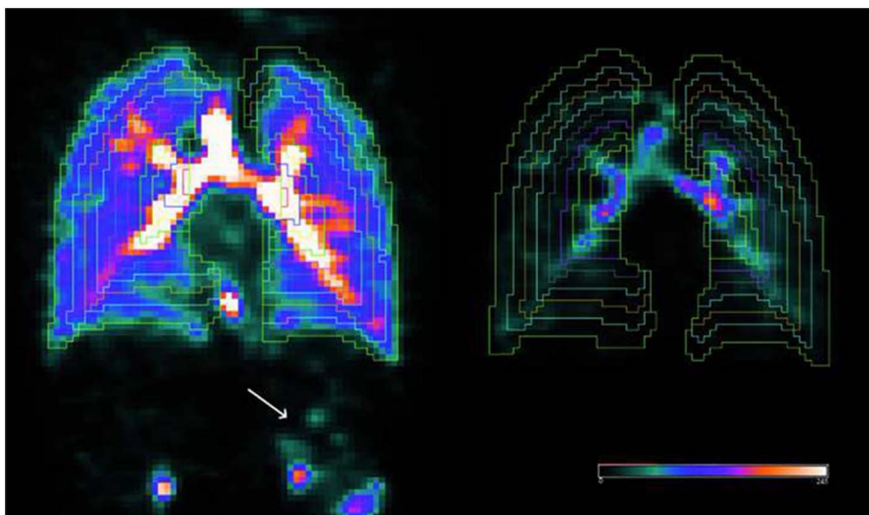


Fig. 12. Samples of scintigraphic images from a patient showing deposition pattern from Respimat® SMI before training (a) and after training (b), and from pressurized metered-dose inhaler before training (c) and after training (d). Reprinted with permission of (Brand et al., 2008).



**Fig. 13.** Shell decomposition of SPECT-CT coronal slices at the level of the right hilum for both nebulisers on the same subject, with the same level of brightness. Both lungs were divided in ten shells (coloured lines through both lungs) distributed from the hilum to the lung periphery. The deposition of the radiolabelled particles of aerosol, depicted in colour, is highly increased with the vibrating-mesh nebuliser with its specific valve-holding chamber in comparison to the constant-output jet nebuliser with a corrugated tube. Activity is seen in the stomach with the vibrating-mesh nebuliser (white arrow). Reprinted from (Dugernier et al., 2017), with permission of Springer.

the lungs) was similar between the two nebulisers.

Examples of the use of SPECT-CT to assess regional lung deposition of aerosols are also found in the pre-clinical setting. For example, Gracia et al. recently reported the synthesis of water-dispersible dextran-based single-chain polymer nanoparticles (SCPNS), which might be used as drug carriers for inhalation. Radiolabelling of these biocompatible NPs with the gamma emitter  $^{67}\text{Ga}$  followed by SPECT-CT imaging allowed the longitudinal investigation of lung deposition of the NPs in rats after intratracheal nebulisation using the Penn-Century MicroSprayer® (Gracia et al., 2017) (see Fig. 14a). Acquisition of CT images enabled appropriate delineation of the VOIs in the whole lungs (Fig. 14b). In this case, the species of interest (the NPs) and not the aerosol was labelled, and hence the SPECT images reflect the deposition and clearance of the NPs (and not the aerosol). This example is a proof that nuclear imaging can be effectively employed in the determination of drug deposition in the lungs after aerosol administration. Of note, pre-clinical studies in small animals face the main drawback of limited spatial resolution (1 mm in preclinical scanners), which, together with motion effects due to breathing and heart rate, will limit the accurate quantitative determination of regional distribution.

**5.1.5.2. Determination of regional distribution using PET.** PET has higher sensitivity and higher spatiotemporal resolution than SPECT, and absolute quantification of the images is less challenging. Hence, PET is a valuable option to assess lung deposition of aerosols. However, most of the commonly used short-lived positron emitters are cyclotron-produced, and hence their use is restricted to centres with a cyclotron in house.

Due to this limitation, PET studies performed to date to assess lung deposition have been conducted with the well-known indirect proliferation marker 2-deoxy-2- $(^{18}\text{F})$  fluoro-D-glucose ( $[^{18}\text{F}]\text{FDG}$ ), which is widely used in the clinical field, with a production/distribution network well established in most developed countries. A nice collection of examples on the use of this radiotracer to evaluate changes in the deposition of inhaled aerosols within the lung, related to the presence of disease or resulting from inhalation challenge interventions or inhaled therapies, has been recently reported (Dolovich, 2009), and one representative example of the work reported there is shown in Fig. 15. In this particular study, 13 patients with asthma and 10 healthy volunteers were challenged with methacholine aerosol and PET images were obtained after inhalation of  $1.5\ \mu\text{m}$  aerosol containing  $[^{18}\text{F}]\text{FDG}$ . As it can

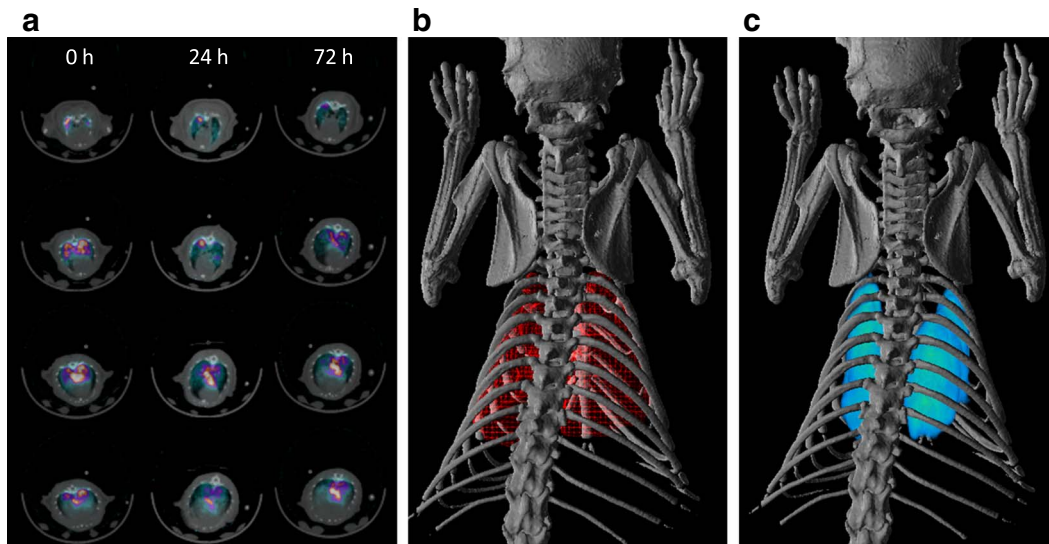


**Fig. 14.** a) Representative axial slices of SPECT-CT images obtained at  $t = 0, 24$  and  $72\ \text{h}$  after administration of  $^{67}\text{Ga}$ -labelled particles by intra-tracheal nebulisation; SPECT images are co-registered with CT images for easy localisation of the radioactivity; b) 3D CT images of the skeleton (grey) co-registered with surface-rendered 3D CT images of the lungs; c) 3D CT images of the skeleton (grey) co-registered with volume-rendered SPECT images of the lungs (green tones). (For interpretation of the references to colour in this figure legend, the reader is referred to the web version of this article.)

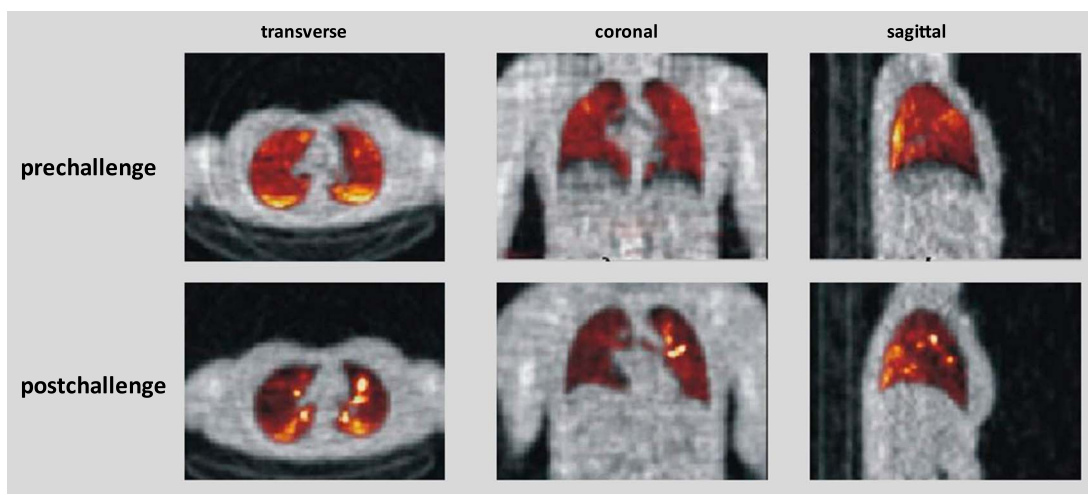


Fig. 15. Images from a PET scan obtained following inhalation of [<sup>18</sup>F]FDG aerosol in one subject with asthma and immediately after a methacholine challenge. The baseline scan is reasonably uniform with ventilation posterior and basal as seen in the one slice in the transaxial plane. On the repeat scan, hot spots are evident throughout the lung as seen on these single slices from the transaxial, coronal, and sagittal planes. Adapted from (Dolovich, 2009).

be seen, quite a uniform distribution was found pre-challenge, although hot spots could be observed in the anterior third of the lung (transaxial view). The images acquired post-challenge show a patchier ventilation scan, with localised areas of tracer deposition throughout the lung.

Advantages

- high sensitivity (especially PET),
- images can be acquired at the whole organ or body level,
- quantitative information can be obtained (especially PET).

Disadvantages

- low spatial resolution, in the order of a few millimetres in the clinical setting,
- low temporal resolution,
- use of ionising radiation,
- expensive (especially PET), sophisticated equipment and specialised personnel are required.

5.2. Proton MRI for aerosol deposition studies

Conventional MRI is based on the principle that atomic nuclei can absorb and emit electromagnetic energy when manipulated using an external magnetic field. First, a strong magnetic field is applied to align the ‘spin’ of protons in hydrogen atoms, which are found in water molecules within the body. A radio frequency signal is then used to resonate the atoms, and the relaxation signal is measured by conductive coils placed around the patient. Parameters of the magnetic field pulse sequence can be varied and hence different contrasts can be acquired between various tissues due to the relaxation properties of the hydrogen atoms in different tissues.

Using proton MRI for lung studies is especially challenging due to the low water content of lung parenchyma (about 15%) and the large difference between tissue and air susceptibilities (around 10 magnetic field homogeneity units in parts per million, ppm), which normally results in a low MRI signal that can be a source of a new contrast possibility using susceptibility mapping approaches. The study of aerosol deposition using proton MRI is based in 1) the use of oxygen as

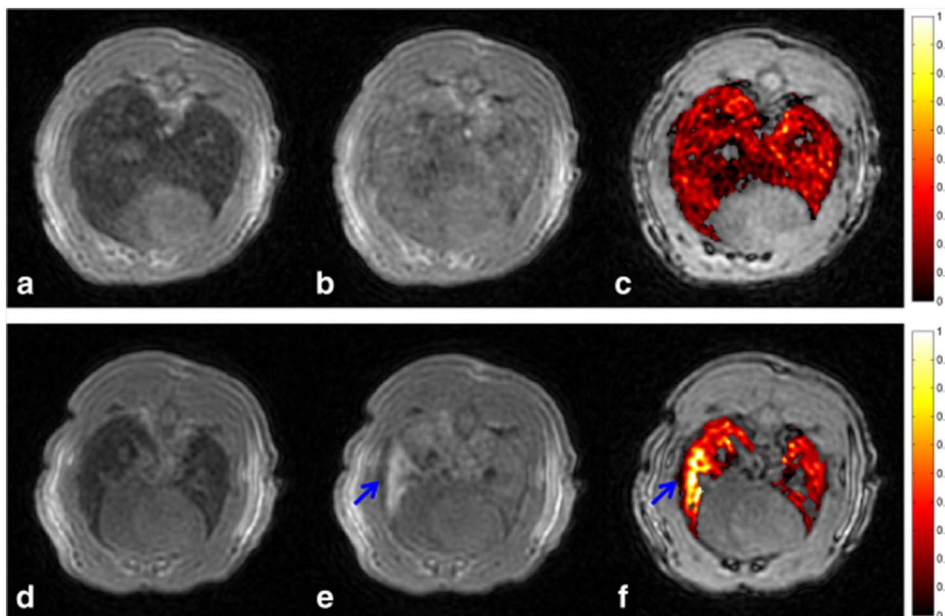


Fig. 16. Aerosol deposition in the lungs of spontaneously breathing rats using Gd-DOTA-based contrast agents and ultra-short echo time MRI at 1.5 Tesla. Reprinted from (Wang et al., 2016) with permission of John Wiley and Sons.

paramagnetic contrast agent, 2) the use of chelated Gadolinium (diethylene triamine penta acetic acid, Gd-DTPA, or 1,4,7,10-tetraazacyclododecane-1,4,7,10-tetraacetic acid, Gd-DOTA) as an inhaled paramagnetic contrast inhaled agent, and 3) the use of ultra-short echo (UTE) time sequences more adapted to lung parenchyma imaging and new applications especially in the paediatric field to reduce respiratory artefacts and deal with the short lung  $T2^*$  (decay of transverse magnetization caused by combination of spin–spin relaxation time, T2, and magnetic field inhomogeneity). The first two options have the advantage of studying aerosol inhalation based on longitudinal relaxation time (T1, hot spot or positive contrast). In general, paramagnetic agents reduce both the T1 and T2 relaxation times of the water in the lung parenchyma, and thus can be used to quantify the regional delivery of this tracer based on the significant increase in signal intensity with the ventilation of these agents (Sood et al., 2010; Sood et al., 2008). The vast majority of studies have utilised the reduction of T1 times with increasing contrast concentration to detect the agents (Thompson and Finlay, 2012), which area surrogate marker of aerosol deposition of other therapeutic components. The combination of this technology with UTE-MRI data acquisition has proven to provide more accurate concentration measurements (Wang et al., 2016).

### 5.2.1. Application of MRI in aerosol deposition studies

The results using Gd-DOTA aerosol nebulisation with spontaneously breathing rats (see Fig. 16) yielded a homogenous signal enhancement in the lung despite a reduced and less controlled dose (Wang et al., 2016). Still, the protocol was applied with smaller doses of contrast agent to previous results and it is the first quantitative map of aerosol deposition *in vivo* using MRI. For reproducibility, regional distribution in the lungs was analysed using an automatic procedure to divide the lung into equal volume regions. A comparison of regional aerosol distribution images showed significant differences for left *versus* right, head *versus* feet and central *versus* peripheral dependencies (Wang et al., 2016).

Compared to other T1-weighted MRI applications, this UTE imaging has also the advantage of opening the field to the use of superparamagnetic iron oxide NPs with or without drug loaded in the final preparation to study direct aerosol deposition. Due to the enhanced pulmonary signal intensity, this imaging modality facilitates the real quantification of the tracer using, for instance, parametric transverse relaxivity ( $R_2^*$ ) mapping with two or more echo time datasets, utilising the linear relationship between this parameter and particle concentration (Oakes et al., 2013). In this study, superparamagnetic iron oxide particles were employed to study *ex vivo* regional aerosol deposition on rat lungs nebulised during conventional mechanical ventilation. As expected from previous experiments using radiolabelled particles, deposition was higher in the lung periphery than in the central airways, and no differences were found in the gravitational dependent and independent regions of the lung, such as is known from previous multiple-breath washout experiments in ventilated rats (Verbanck et al., 1991).

As observed in the above-mentioned studies, although the advantages of proton MRI for human application have been described for many applications, proton MRI is still far from clinical applicability (except for paediatric patients with restricted and controlled radiation exposure). Also, besides the described lung MRI problems, studies on aerosol deposition are mainly based on the ability of MRI to trace the surrogate marker and not any other component of the aerosol. If specific compounds are to be traced, the MRI contrast should be incorporated into that compound. The use of aerosolised iron oxide particles compared to oxygen or Gd-based contrast has then the potential to be applied in humans more than any other alternative, especially at low magnetic fields, and facilitates the possibility of integrating these extra compounds in the final formulation. Finally, current approaches require contrast agent doses that are too high to be considered competitive with traditional radionuclide aerosol deposition measurement methods in humans (Thompson and Finlay, 2012).

Advantages:

- No radioactivity (suitable for paediatric patients),
- Both flow velocity and aerosol distribution can be measured.

Disadvantages:

- Trace marker needed,
- long imaging time (low temporal resolution),
- low differences in contrast between lung parenchyma and air,
- High doses of contrast agents needed.

## 6. Emerging methods in aerosol flow and deposition measurements

The rapid development of experimental methods in recent years promises to provide results of a quality and resolution that was inconceivable in the past. Three of the methods (Hyperpolarised gas MRI, Optical Coherence Tomography (OCT) and Phase Contrast X-ray Imaging (PCXI)) are described in detail in this paper. However, several other methods that are not discussed here are also expected to expand our knowledge of the inhaled aerosol flow in the near future. Because of the lack of human imaging with these techniques to date, we break the convention of this review and include animal experiments in this section.

There is a large group of methods that can be grouped under the title “intravital microscopy”. These techniques are based on fluorescence light microscopy and their growth is driven by the progress in the non-linear microscopy. Intravital microscopy can be used for dynamic imaging of cellular and even subcellular structures, which will be especially useful for drug delivery studies. The reader who is interested in this group of methods is referred to the well-written review by Amornphimoltham et al. (2011). One method that is suitable for the acquisition of airway geometries is multi-planar 3D ultrasound imaging (Or et al., 2013). Its main advantages include a high level of safety for patients and a relatively low price.

As the flow distribution within human airways is of great importance, especially for CFD boundary conditions, it can be expected that Electrical Impedance Tomography (EIT) will gain popularity, serving as a source of such data (Moerer et al., 2011; Riera et al., 2013). EIT is based on measurement of potential differences between electrodes positioned around patient's thorax after the injection of high frequency and low amplitude electrical currents.

Distribution of magnetic nanoparticles with unique spatial and temporal resolution can be measured by Magnetic Particle Imaging (MPI). The method achieved rapid growth after Gleich and Weizenecker (2005) published the principles of the technique. MPI utilises superparamagnetic iron oxide nanoparticles as tracers and a key advantage is the absence of any radiation delivered to the patient. Recent developments in this area were reported recently in (Knopp et al., 2017).

### 6.1. Hyperpolarised gas MRI

The introduction of hyperpolarised gas has improved the development of functional lung MRI by allowing measurements that are impossible with conventional proton-based MRI and maybe beyond the limits of any other technique (van Beek et al., 2004). In all possible applications, hyperpolarised gas MRI appears as a solution for one of the most important problems regarding the MRI of the lung, e.g. the weak signal intensity coming from the low density of air-filled lung parenchyma that results in low proton density (Mosbah et al., 2008).

Noble gases are hyperpolarised through the transfer of angular momentum from circularly polarised light to the nucleus, known as optical pumping. This process allows the hyperpolarised gas to exhibit polarizations exceeding the thermal equilibrium level (Moller et al., 2002). Such processes have been demonstrated on  $^3\text{He}$  and  $^{129}\text{Xe}$ , both

with potential clinical applications, starting from 1994 when the first publication appeared (Albert et al., 1994) from the Princeton group and Magnetic Imaging Technologies Inc. was created. Despite all the problems including a  $^3\text{He}$  shortage in 2008, the field has demonstrated a continuous improvement in polarization performance, but is still facing regulatory and technical hindrances. In order to facilitate universal access to the technology, this field is demanding a coordinating effort to bring a comprehensive package solution with the input and collaboration of many types of expertise and businesses. For a real final clinical application, any new user needs to take into account that this will need: 1) an MRI system with a broadband amplifier (for not proton based applications), 2) a gas polariser (probably different for  $^{129}\text{Xe}$  and  $^3\text{He}$ ), 3) a polarimetry and calibration method, 4) a dose delivery system with an automatic or semi-automatic gas delivery applicator, 5) a dedicated chest coil (dual  $^1\text{H}$ - $^{129}\text{Xe}$  or  $^1\text{H}$ - $^3\text{He}$ , or triple nuclei coil ( $^{129}\text{Xe}$ - $^3\text{He}$ - $^1\text{H}$  and applications have been demonstrated by some investigators and coil manufacturers), 6) hyperpolarised-proofed MRI pulse sequences, 7) gas phantoms for quality control, 8) more affordable access to  $^3\text{He}$  (almost impossible in Europe, except in the Sheffield group) or  $^{129}\text{Xe}$  supplies, 9) special software for data analysis, and 10) lastly any application needs to go through the corresponding Investigational New Drug Application and obtain the Institutional Review Board approval to start these studies. For Food and Drug Administration (FDA) clearance, phase II clinical trials have finished in Summer 2016 and the Phase III trial is about to begin in 2017.

Despite all these issues, hyperpolarised gases still appear to be a promising technique and probably the only one that can evaluate and quantify airflow and aerosol deposition into the airways ( $^{19}\text{F}$  MRI is probably far from this due to sensitivity restraints). Although some different data acquisition encoding methods are possible, De Rochefort et al. proposed a novel application; combining dynamic radial MRI with phase contrast and hyperpolarised  $^3\text{He}$  to map velocities *in vivo* and in replicas of the human airways (de Rochefort et al., 2006). Phase contrast is a well-known and established technique in proton MRI to map blood velocities and relies on the quantification of the signal phase.

Phase contrast makes it possible to quantify motion and is not constrained by signal-amplitude variations. Radial encoding (Song et al., 2001) was used to improve the temporal and spatial resolution of the final application. This combination overcomes previous approaches for measuring gas flow in lung replicas using thermally polarised  $^1\text{H}$  (Koptug et al., 2000) or hyperpolarised  $^{129}\text{Xe}$  (Brunner et al., 1999). In previous approaches, acquisition times were not appropriate for *in vivo* measurements due to the time scale of a breathing cycle.

In the next section, we summarize the different steps of the first demonstration of human gas flow measurements in the trachea using  $^3\text{He}$  performed by de Rochefort et al. to illustrate the potential and the difficulties that MRI-based methods exhibit, noting these are similar to other imaging techniques included in this article. Immediately after the gas is produced, a mixture, in this case with nitrogen, is prepared at atmospheric pressure, for rapid transferral to the imaging system. In this first application, authors did not include any automatic or semi-automatic gas delivery device, so the gas was directly inhaled by a volunteer from a Tedlar bag containing the gas mixture, and the gas was extracted through a valve with a mass flowmeter to monitor the input gas flow. The volunteer was previously trained to breathe slowly by the mouth to establish a steady flow in the trachea, placed in a prone position with a dedicated MRI coil to increase SNR. Proton MRI was initially performed for scout and localisation imaging. A hyperpolarised gas mixture ( $52\% \pm 10\% ^3\text{He}$ ,  $48\% \pm 10\% \text{N}_2$  in this case) was inhaled via a deep inhalation from the volunteer's lung residual volume. The bolus volume of the tracer gas (around 800 ml) was first inhaled and then supplemented with air to make the total inhaled gas volume (the total volume was not specified by the authors). For a reproducible location, cross-sectional MRI slices were positioned in the trachea, 4 cm downstream from the vocal cords. ROIs were manually selected for each reconstructed image. Due to the radial acquisition, data reconstruction was performed by complex FBP (this is not standard in all MRI vendors, so it will probably require offline reconstruction). For a set of projections, the raw data was first filtered by a ramp, and then Fourier-transformed and back-projected. The velocity component of each voxel

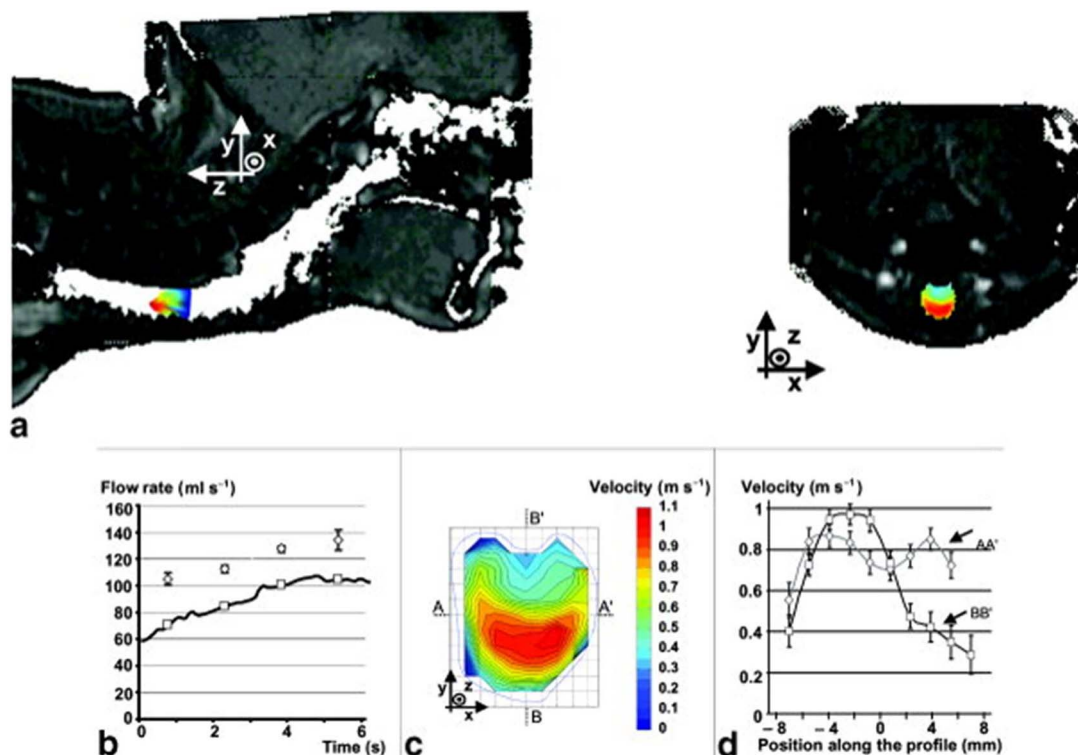


Fig. 17. Phase-contrast velocimetry with hyperpolarised  $^3\text{He}$  for *in vitro* and *in vivo* characterisation of airflow. Reprinted from (de Rochefort et al., 2006) with permission of John Wiley and Sons.

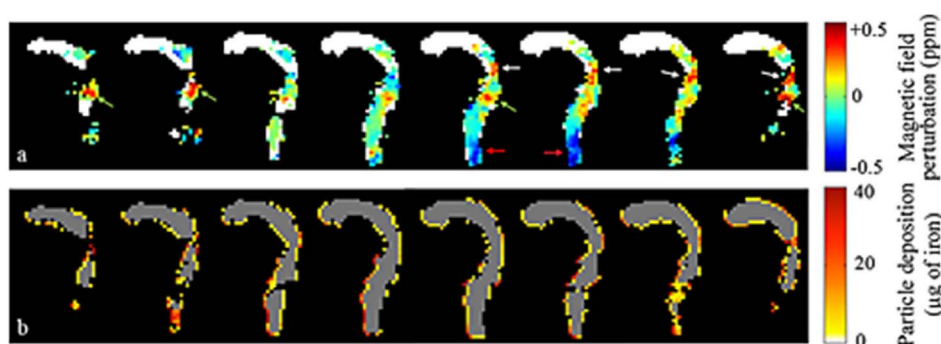


Fig. 18. Phase-contrast helium-3 MRI of aerosol deposition in human airways. Reprinted from (Sarracanie et al., 2015) with permission of John Wiley and Sons.

was determined by the phase difference between the corresponding encoded image and the reference image scaled with a phase-conversion factor. The integration of through-plane velocity over the chosen section provided a measurement of the flow rate.

The results of the measurements of this experiment are shown in Fig. 17 (Fig. 7 from reference (de Rochefort et al., 2006)). Human trachea velocity maps found by de Rochefort et al. agreed with findings from airway replicas and CFD (Heenan et al., 2003). The profiles of the through-plane velocities presented an M-shape along the left-right axis, and an asymmetrical shape along the anteroposterior axis, with higher velocity magnitude in the anterior part.

In another example, Collier and Wild (2015) conveniently implemented the Compressed Sensing technique (Lustig et al., 2007) to reduce the ever shorter acquisition times of hyperpolarised gases in human lung MRI in order to measure flow velocity maps in free breathing lungs. Compressed sensing works by acquiring a small number of random linear combinations of the signal values, much smaller than the number of signal samples nominally defining it. The signal is still reconstructed with good accuracy from these measurements by a nonlinear procedure. For MRI, the sampled linear combinations are simply the individual Fourier coefficients ( $k$ -space samples). In that setting, compressed sensing is expected to be able to make accurate reconstructions from a small subset of  $k$ -space rather than an entire  $k$ -space matrix. Application of compressed sensing to lung MRI with hyperpolarised gases is based on the intrinsic sparsity of the images, as the gas is confined to the airways only. Collier and Wild extended the sparsity of the complex difference image (Kwak et al., 2013) to a four point velocity encoded scheme and developed a compressed sensing reconstruction algorithm for hyperpolarised gas flow in three directions with a time resolution of 1.2 s. This temporal resolution still needs to be improved for rapid flow fluctuations during a normal breathing cycle at rest. The feasibility of these methods was demonstrated with both  $^3\text{He}$  and  $^{129}\text{He}$  mixed with nitrogen in the trachea and main bronchi (see Fig. 3 from reference (Collier and Wild, 2015)).

Due to the high sensitivity and possibilities of hyperpolarised gases, these techniques present also a potentially unique opportunity for the study of aerosol deposition into the human airways. In a study using mouth–throat replicas Sarracanie et al. (2015) measured extra-thoracic aerosol deposition using phase-contrast  $^3\text{He}$  MRI and compared the results with gold-standard SPECT. For this application, a double-labelled aerosol with superparamagnetic iron oxide (for MRI labelling) and radioisotope  $^{99\text{m}}\text{Tc}$  (for SPECT) was prepared to ensure the same deposition pattern for both measurements. Iron-based markers placed in the magnetic field of an MRI unit generate dipolar fields that locally modify the magnetic field, which typically leads to regions of low signal amplitude (Branca et al., 2010). The magnetic field perturbations induced by the presence of iron are embedded in the phase of the magnetic resonance signal and can be processed to obtain absolute quantification of the iron mass distribution (de Rochefort et al., 2008; Mills et al., 2008). By measuring the relaxation times of the total magnetic

moment or by mapping the static magnetic field perturbations in the presence of superparamagnetic iron oxide markers, the spatial distribution of the absolute aerosol particle quantification can be determined (Martin et al., 2008). Hyperpolarised  $^3\text{He}$  was used to overcome the low-SNR and long-acquisition time limitations of lung imaging. The results of both the magnetic perturbation and quantified aerosol particle deposition are seen in Fig. 18 (Fig. 6 from reference (Sarracanie et al., 2015)). Results from this work show that particle deposition can be assessed with  $^3\text{He}$  MRI and iron oxide labelling through measurement of the inferred static magnetic field perturbations.

The introduction of hyperpolarised gases has allowed MRI to enter into the field of airflow quantification using velocity-encoding MRI. This measurement and applications will evolve in a clinical setting in parallel to the resolution of all technical difficulties and regulatory approval related to the use of these gases. Still, the field of hyperpolarised gas applications requires complex infrastructure for gas production and the confluent effort of different technology providers. As far as we perceive the field of quantification of aerosol deposition by MRI, this field can only benefit and expand, aligned with the expansion of MRI systems equipped with broadband amplifiers (required for all non-proton based MRI applications), the growth of the hybrid imaging systems markets and the corresponding development of dual makers. In this line,  $^{19}\text{F}$  solutions, mainly using perfluorinated compounds and doped iron oxides can benefit. As we have seen in this article, Gd preparations have been also introduced, but safety investigations related to Gd deposits in different regions are currently under evaluation and will suppose a barrier difficult to overcome for future applications. The use of dual systems, such as those based on metastable  $^{99\text{m}}\text{Tc}$  (SPECT) and  $^{68}\text{Ga}$  (PET)- $^1\text{H}$  protons, combined with the use of hyperpolarised SNR can then have enormous potential and future.

Advantages:

- Both flow field and particle deposition can be measured,
- Can be combined with SPECT and PET (for simultaneous measurements).

Disadvantages:

- Complex infrastructure and highly skilled personnel needed,
- Low resolution for flow measurement compared to PIV.

## 6.2. Optical coherence tomography (OCT)

OCT was introduced in 1991 (Huang et al., 1991) as a method to image biological samples at high resolution. OCT is based on white light interferometry using near infrared wavelength (NIR) due to the relatively high penetration of NIR. A probe shines light onto the sample and the scattered light is collected in reflection, hence OCT needs access to the sample only from one side. The resolution in beam direction (axial),

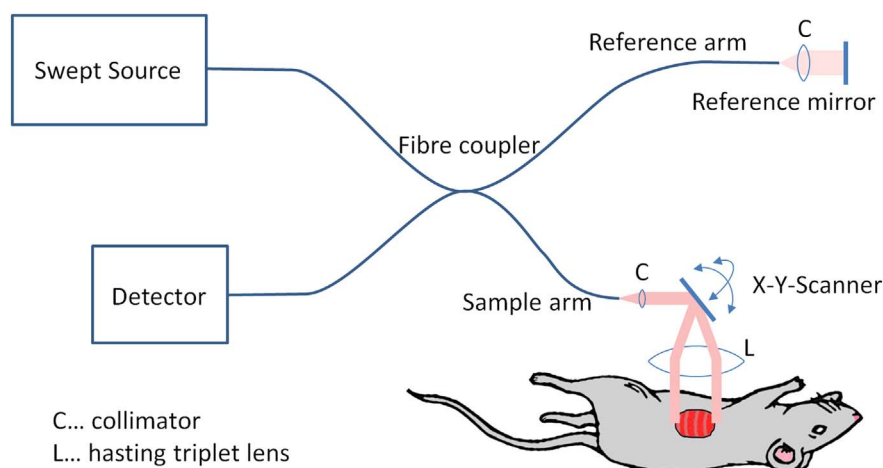


**Fig. 19.** Principle of SS OCT. The light from a tunable laser source is guided by optical fibres to a fibre coupler. While one part is reflected at the reference mirror the other part is scattered and partially reflected at the sample, placed underneath a two dimensional scanner, steering the light over the sample. The interfering light is recorded with a detector in the fourth arm of the fibre coupler as a function of wavelength. From the spectrum, the depth information is retrieved.

as well as perpendicular (transversal), is of the order of 1 to 15  $\mu\text{m}$  (Drexler et al., 1999). The imaging range is limited by absorption and scattering, reaching no deeper than 1 mm in most tissues. Moreover, the Rayleigh length of the Gaussian beam that is typically used will limit the sensitive range to  $< 1$  mm. For a single depth scan, called A-scan, the length of the reference arm has to be varied over the measurement range. Due to this mechanical depth scanning, the speed of OCT was rather limited until a breakthrough in speed was achieved by introducing the concept of Fourier Domain OCT (FD-OCT), also known as Frequency Domain OCT. In FD-OCT, the mechanical depth scanning is replaced by spectral analysis of the interfering light. Interfering light causes, as a function of wavenumber (reciprocal of wavelength), periodic oscillations with a frequency proportional to the optical length difference between sample and reference arm. It can be shown that FD-OCT is not only much faster, but achieves a better SNR compared to the previous method, called Time Domain OCT (TD-OCT) (de Boer et al., 2003; Choma et al., 2003; Leitgeb et al., 2003). The interference spectrum can alternatively be acquired by analysing the light with a spectrometer, resulting in a technique called Spectral Domain OCT (SD-OCT), or by sweeping the wavelength of the incident light, known as optical frequency domain imaging (OFDI) (Vakoc et al., 2009) or Swept-Source OCT (SS OCT) (see Fig. 19). The first is limited in speed by the spectral read out of the CCD<sup>9</sup> or CMOS<sup>10</sup> cameras while the second achieves even higher speeds after the introduction of Fourier domain mode locked (FDML) lasers. Fast SD-OCT systems achieve today  $> 200,000$  A-scans/s, while FDML systems regularly accomplish up to 1.5 million A-scans/s. 20 million A-scans/s have been demonstrated, which means video rate volume scans (Wieser et al., 2010). The acquisition of 2D and 3D images is achieved by deflecting the beam using galvanometers (Duma et al., 2011), resonant scanners or micro-electromechanical systems (MEMS) (Jung et al., 2006; Lu et al., 2014). A 2D image, with intensity colour coded as a function of depth and one coordinate, is called, in analogy to ultrasound, a B-scan. For other promising clinical applications, rotating fibre optic catheters were developed enabling the imaging of hollow organs and cavities like the esophagus (Tearney et al., 1997; Vakoc et al., 2007) and human vessels (Bezerra et al., 2009; Brezinski, 2006; Tearney et al., 1997) by OCT. Optics with smaller numerical apertures and therefore longer Rayleigh lengths can collect over a larger distance of 10–30 mm only a fraction of the scattered light, which reduces the signal intensity and transversal resolution (100–200  $\mu\text{m}$ ). This is still sufficient for the anatomical structure, which explains the name of the method “anatomical OCT” (aOCT) (Armstrong et al., 2006; Bu et al., 2017; Wijesundara et al., 2014).

### 6.2.1. Imaging airway and alveolar structures

In order to image the airway and alveolar structures by OCT, three different attempts have been made. External scanning can be applied to isolated lungs by visualising the alveolar structure close to the pleura (Meissner et al., 2009a; Meissner et al., 2009b). With some effort, this method can also be applied to anaesthetised animals by opening the chest or by preparing a thoracic window *in vivo* (Meissner et al., 2010a). This method has been applied to mouse and rabbit models to study alveolar sizes and the change during ventilation in healthy and injured lungs (see Fig. 20). While in the early systems gated imaging was used to study the dynamic shape during the ventilation cycle (Meissner et al., 2010b), modern high-speed systems capture complete alveoli with some tens of fps, sufficient for breathing rates of the order of one per second (Kirsten et al., 2013). In larger animals, the movement of the lung prevents single alveoli to be followed through the complete ventilation cycle. Therefore, lightweight MEMS-based probes were developed to resting on the lung and follow the alveolar structures (Namati et al., 2013). These measurements confirmed that most of the compliance of the lung is caused by the cyclic dilatation of the alveoli.

To access internal regions of the lung, endoscopic OCT probes have been used. Typically, such probes use radial scanning by rotating the entire probe or by using micro-mechanical motors placed in the probe (Yang et al., 2004). While the rotation provides circumferential 2D images, the fibre may be retracted while accumulating subsequent radial images to provide 3D information (Armstrong et al., 2006; Bu et al., 2017; Wijesundara et al., 2014) (See Fig. 21).

A third strategy uses miniaturised OCT needle probes. The needle probe can be inserted through the tissue into the region of interest that may be located several centimetres below the surface. Scanning is again performed by rotating the needle or the focusing optics inside the needle. Although the size of needle probes has been reduced to a diameter of about 310  $\mu\text{m}$ , the insertion of the needle will cause some trauma (Lorenser et al., 2011). As the needle can hardly be translated forth and back, the same tissue cannot be imaged during different states of the ventilation cycle. For repetitive scans, probes consisting of an inner part that translates rapidly back and forth multiple times per second was developed to allow 2D image acquisition (McLaughlin et al., 2012).

The imaging of alveolar structures is hampered by the repeated refractive index change from air to liquid, limiting the useful depth to only one or two layers of alveoli. Therefore, several attempts have been made to fill the lung with an index matching fluid. For *ex vivo* imaging, the lung can be filled completely with saline water (Lorenser et al., 2011) or ethanol (Meissner et al., 2009a) increasing the useful imaging depth to 5 or more alveoli in depth. While these approaches are not suited for *in vivo* imaging, a small amount of fluid around the probe can enhance imaging without causing trauma to the animal (Quirk et al.,

<sup>9</sup> Charge-coupled device

<sup>10</sup> Complementary metal–oxide–semiconductor

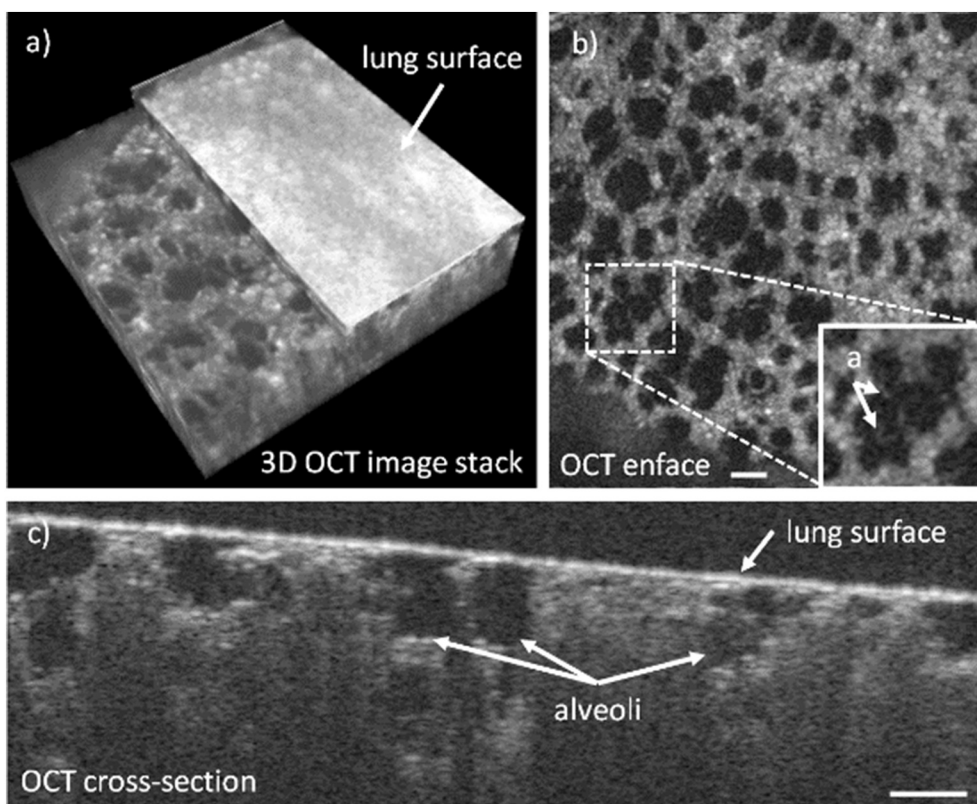


Fig. 20. Imaging of alveolar structures with OCT in ventilated rats. OCT allows the imaging of morphological features of lung tissue. Even the inner alveolar walls can be visualised. Scale bar 100 μm. While a) shows the 3D image with part of the lung surface (pleura) removed from the data set, b) shows a plane approximately 50 μm beneath the lung surface, c) shows a cross section perpendicular to the pleura. Imaging of deeper alveoli is hampered by the refractive index step between tissue and air.

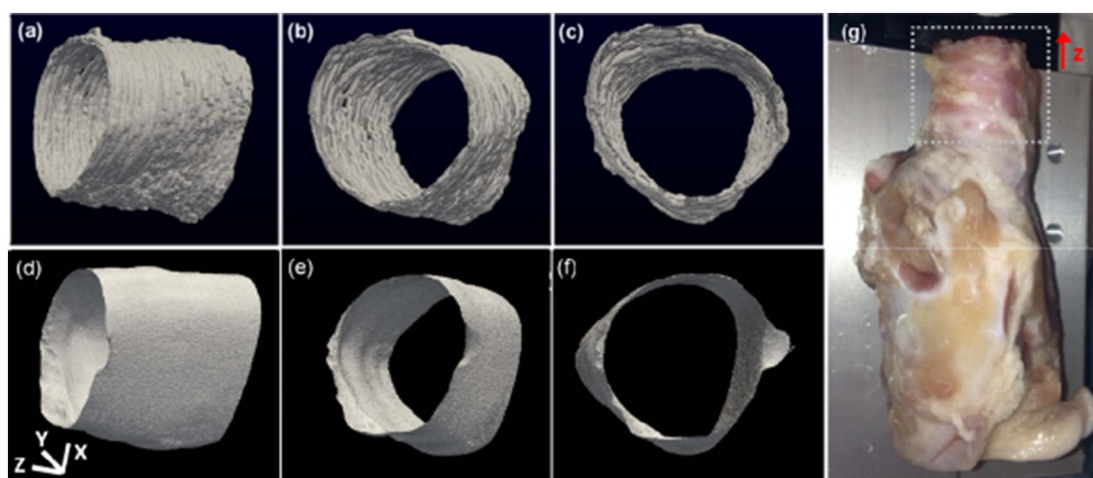


Fig. 21. Anatomical OCT images of a swine trachea displayed in three different viewing angles. (d)–(f): corresponding CT images. (g): photograph of the swine airway; the region that was imaged is indicated by the dotted square. The x, y, and z scale bars each represent 3 mm. With permission reprinted from (Wijesundara et al., 2014).

2014). Moreover, the lungs could be ventilated with a liquid with perfluorocarbons that have a high transport capacity for oxygen and carbon dioxide, in order to enable enhanced OCT imaging *in vivo* (Schnabel et al., 2013).

### 6.2.2. Potential for flow and aerosol measurements

In Doppler OCT, mostly used to visualise the velocity of scattering particles in flowing fluids, the phase of the signal between A-scans at the same or nearly the same position is analysed (Leitgeb et al., 2003). The phase difference is proportional to the velocity component in the direction of the optical beam. The transversal velocity component can be estimated by phase noise (Walther and Koch, 2009) or by using multiple beam OCT (Haindl et al., 2016; Chen et al., 2017), the latter

resulting in a 3D velocity field. Besides Doppler OCT, PTV<sup>11</sup> (Jonas et al., 2011), PIV (Buchsbaum et al., 2015) and correlation-based approaches (Huang et al., 2015) are used to quantify the flow field.

While Doppler methods are mostly applied to the measurement of blood flow, where the erythrocytes form the scattering particles, oil droplets from Intralipid (Kirsten et al., 2015), polystyrene microspheres (Jonas et al., 2011; Kirsten et al., 2015) and other particles down to sub-micrometre size (Cimalla et al., 2015; Grombe et al., 2016) can be used as tracers.

Flow measurements in the airway will be hampered by the OCT

<sup>11</sup> For the PTV and PIV see Section 3.3.

probe, especially in the deeper and therefore slimmer parts of the airway. Visualisation of flow in the alveoli needs particles to reach the alveoli after flowing through multiple airways and bifurcations, which may be difficult to achieve. Moreover, due to the low flow expected in the alveoli, the movement of particles may be dominated by Brownian motion.

The deposition of particles in the airways can likely be detected using suitable OCT probes. OCT can be tailored to detect labelled particles with high sensitivity. Labelling can be performed magnetically and by plasmonic resonance, leading to selective absorption and scattering (Oldenburg et al., 2016). Moreover, contrast can be generated by optical anisotropy and diffusion (Kalkman et al., 2010).

While OCT has so far not been used extensively to measure flow and aerosols in airways, OCT has significant potential to contribute considerably to this field. Measurements on replicas do not suffer from regulatory requirements, but the results may be of limited value because of differences in the dynamic behaviour and surface properties, as discussed earlier. Animal experiments may be challenging due to experimental and regulatory demands but the results would be more comparable to humans. While many of the measurements mentioned above cannot be justified with humans, because of the negative side effects, any possible experiments with humans should only be performed if the individual can benefit from the measurement.

Advantages:

- fast 3D information without ionizing radiation,
- resolution in the  $\mu\text{m}$  range,
- Doppler information without additional hardware,
- only one optical port needed.

Disadvantages:

- difficult marking of particles,
- optical access needed,
- depth range limited to some mm, maximal few cm at lower resolution.

### 6.3. Phase contrast x-ray imaging (PCXI)

In the last two decades, new methods of x-ray imaging have been developed that are sensitive to soft tissue structures like the respiratory system, via the use of “phase contrast” (Wilkins et al., 2014). Research groups in the field are focusing on realising this technique in a clinical imaging system (Bravin et al., 2013) and are increasingly applying this kind of imaging in biomedical research with animal models.

A conventional x-ray image captures the attenuating properties of structures, in effect creating a shadow image. A phase contrast x-ray image is also sensitive to the refractive properties, and in some cases scattering properties, of any structures. In Fig. 22, we see that attenuation by the sample (described by  $\beta$  for a given material) causes a reduction in the amplitude of the incident x-ray waves (shown the by red arrows), resulting in reduced intensity at the image detector. While this produces strong contrast in the case of bones, soft tissues attenuate weakly and hence are not clearly seen in a conventional image. If an x-ray wavefield passes through materials with different refractive properties (described by  $\delta$ ), a difference in the phase of the x-ray wavefield is introduced (shown by the blue lines of constant phase), in effect

changing the direction the wavefield is propagating (see the black arrows). Phase contrast imaging is sensitive to these phase shifts, resulting in much better visualisation of soft tissue structures. The lungs and airways are particularly well-suited to PCXI because the difference in  $\delta$  between air and tissue is large compared to that between other tissues, resulting in strong x-ray phase variations from air-filled tissue structures. This means that the respiratory system can be visualised with high sensitivity and resolution down to the  $\mu\text{m}$  scale.

Because the x-ray phase variations introduced by the lungs cannot be directly recorded in the same way as x-ray intensity variations, a special optical set-up must be used to extract x-ray phase shifts or variations. There are several different PCXI set-ups that have been developed, including propagation-based (Cloetens et al., 1996; Snigirev et al., 1998), crystal and grating interferometry (Bonse, 1965; David et al., 2002; Pfeiffer et al., 2006), analyser-crystal (Förster et al., 1980; Ingal and Beliaevskaya, 1995), edge-illumination (Olivo and Speller, 2007) and speckle-tracking (Bérubon et al., 2012; Morgan et al., 2012)/single exposure single-grid set-ups (Morgan et al., 2011; Takeda et al., 1982; Wen et al., 2010). Each set-up provides a different set of advantages in terms of speed, resolution, sensitivity and the requirements on the x-ray source (Wilkins et al., 2014).

Because many of these set-ups require relatively uniform x-ray phase (e.g. see the incoming waves in Fig. 22), much of the development has taken place using highly coherent synchrotron x-rays. A synchrotron facility accelerates electrons around a circular path that is hundreds to thousands of metres in circumference. These electrons travel at near-relativistic speeds, guided by magnets to produce bright, low-divergence x-rays that can be made monochromatic and used in a range of investigative techniques. Imaging applications typically take place tens to hundreds of metres from the x-ray source point, resulting in a highly coherent beam. The translation of PCXI techniques from the synchrotron to more accessible, lower-cost x-ray sources is an active area of research (Olivo and Castelli, 2014), and in particular has investigated liquid-metal-jet sources (Larsson et al., 2011) and compact sources driven by inverse Compton scattering (Bech et al., 2009). Nevertheless, a synchrotron is an invaluable biomedical research tool, in particular because the associated high x-ray flux enables fast imaging (e.g. 200 Hz in Morgan et al. (2016)), such that the movement and detail of the lungs can be captured in exquisite detail.

#### 6.3.1. Literature to date

Several studies to date have used PCXI to better understand the respiratory system and assist in treatment development, with some examples shown in Fig. 23. High-resolution structural characterisation of the airways is possible by combining PCXI with CT (Parsons et al., 2008), capable of revealing individual alveoli (Sera et al., 2013), even within an *in vivo* volumetric time series (Lovrić, 2015).

By capturing a time sequence of images, it is possible to image the lung dynamics, or any changes to the respiratory system in response to a treatment. One of the very first dynamic PCXI experiments performed at a synchrotron monitored the respiratory action of a beetle (Westneat et al., 2003), capturing the dilation and contraction of tracheal airways. More recent *in vivo* work has utilised animal models of human lung conditions, primarily in mice, rabbits and rats (Donnelley et al., 2010), with some recent work performed in pigs (Donnelley et al., 2017) and sheep. The highest resolution work (see Fig. 23a) has monitored *in vivo*  $\mu\text{m}$ -sized changes in the tracheal airway surface liquid depth in mice in

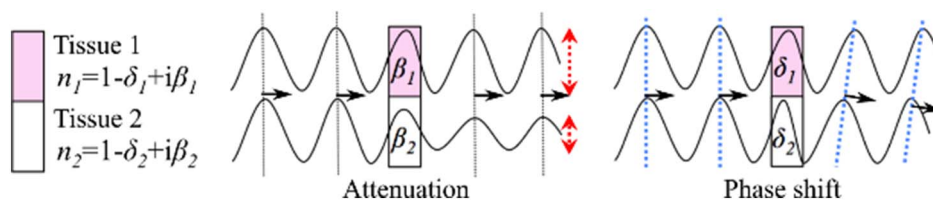
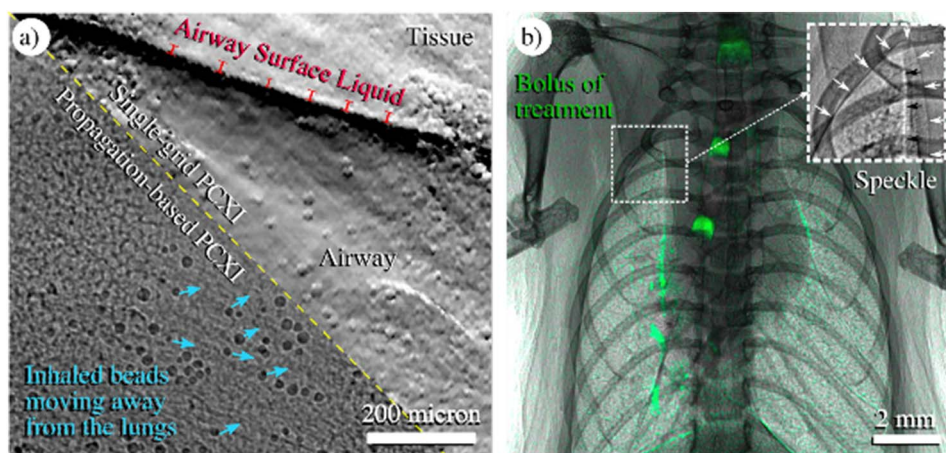


Fig. 22. The x-ray properties of different tissues at a given x-ray energy can be described using a complex refractive index  $n$ , where  $\beta$  describes how much the tissue will attenuate the x-ray wavefield and  $\delta$  describes how the tissue will change the phase of the x-ray wavefield. PCXI extracts quantitative measures of how the phase has been altered by soft tissue structures.



**Fig. 23.** Examples of respiratory images at various scales obtained using synchrotron-based PCXI. a) One side of the trachea (running horizontally) in a mouse, allowing measurements of the airway surface liquid, shown in red (Morgan et al., 2014) and the clearance velocity of inhaled 10–25  $\mu\text{m}$  debris, shown in blue (Donnelley et al., 2014a). Note the upper right is captured with single-grid PCXI, which displays the rate of change of tissue thickness/composition and the lower left with propagation-based PCXI, where edges are enhanced. b) The delivery of a liquid bolus of treatment into the lungs of a mouse, with digital subtraction highlighting treatment location in green (Donnelley et al., 2013). This image also shows the extra detail obtained in propagation-based phase contrast (inset), with dark lines highlighting the edges of major airways and the periphery of the lungs (posterior surface shown with white arrows, anterior with black arrows), and a speckle pattern seen from the lungs. (For interpretation of the references to colour in

this figure legend, the reader is referred to the web version of this article.)

response to the nebulised delivery of surface-rehydrating treatments (Morgan et al., 2014). This is in the context of treating cystic fibrosis airway disease, which develops as a result of a reduced airway surface liquid depth that impairs the clearance of inhaled debris (Tarran et al., 2001). Also in this context, airway surface liquid changes have been monitored in response to the deposition of bacteria in excised pig tracheas (Luan et al., 2014). Studies have directly investigated the *in vivo* clearance of inhaled debris via mucociliary clearance (Fig. 23a), monitoring individual glass particles, several tens of micrometres in diameter, studying changes in clearance rate in response to treatment (Donnelley et al., 2014a) and over a period of 25 h (Donnelley et al., 2014b), in mouse and pig models. The clearance of larger particles in the form of 350  $\mu\text{m}$  diameter tantalum disks has also been imaged in new-born pigs via multi-detector-row CT (Hoegger et al., 2014). The ability of x-ray imaging to monitor such behaviours *in vivo* presents obvious advantages over studies that use excised tissue or a tissue culture.

At the scale of the entire lungs, several different PCXI modalities have been applied in biomedical research. Propagation-based phase contrast, which enhances the air/tissue interfaces (Kitchen et al., 2004) (Fig. 23b), has been used to monitor the regional distribution of air as newborn rabbit pups take their first breaths (Hooper et al., 2007), enabling optimisation of the ventilation strategy for pre-term infants (te Pas et al., 2009). The many overlapping alveoli act like lenses in propagation-based PCXI, creating a speckle pattern, as seen in Fig. 23b), that can be analysed to infer information about the alveolar size and density (Carnibella et al., 2014; Kitchen et al., 2015). This speckle pattern can also be tracked through the breath cycle using PIV techniques (see Section 3.3) to map the movement of the lungs (Dubsy et al., 2012). When combined with CT and appropriate boundary conditions, CT-PIV can be performed to extract local airflows (Dubsy et al., 2012). This is useful clinically in locating areas of disease (Fouras et al., 2012; Stahr et al., 2016), and the detailed airflow measurements can inform treatment deposition simulations (Dubsy and Fouras, 2015).

Grating interferometry PCXI has also been used to image the lungs, in particular using the scattering/dark field signal. A reduced dark field signal will be seen where there are fewer alveoli to scatter the x-rays, either due to breakdown from emphysema (Hellbach et al., 2015) or wall thickening from fibrosis (Yaroshenko et al., 2015) (note these cases could be differentiated using the attenuation signal as complementary information).

Finally, the inhalation of a xenon contrast agent has been captured at synchrotron sources in the lungs of mice (Bayat et al., 2001), and combined with CT. This unique set-up at the European Synchrotron uses two beams in parallel, one with energy just below and the other

just above the K-edge for xenon, so that the difference in attenuation between the two images is large for xenon, but no other part of the image. Digital subtraction can then isolate xenon in the image, tracing the flow of the gas into the lungs. In a similar way, iodine, a highly attenuating liquid, has been used as a substitute for liquid bolus treatments, with high-speed imaging determining the regional distribution in the nasal airways for a given volume (Donnelley et al., 2013). Bolus treatments were also tracked in the lungs, but only down to the third generation, due to an overlapping signal from the lungs and a reduced volume of iodine resulting in weak contrast.

### 6.3.2. Potential for flow and aerosol measurements

While most of the PCXI respiratory applications so far have focused on assessing the effects of a treatment or a disease, PCXI also presents opportunities for flow and treatment deposition measurements, most easily in animal models. Human imaging at synchrotron x-ray sources requires several years of planning in order to ensure radiation dose is well-controlled and within safety limits (e.g. see dosimetry requirements for radiation therapy in humans at the ESRF<sup>12</sup> (Prezado et al., 2011) or mammography at Elettra<sup>13</sup> (Longo, 2016)). There is also some development required to achieve the field of view necessary to image the whole human lung, for example manufacturing large gratings for grating interferometry (Schröter et al., 2017). Commercial scanners to date that use phase contrast have focused on mammography (e.g. Konica Minolta's PCM system), however lung scanners are a topic of ongoing research by several medical imaging companies.

X-ray CT-PIV already captures useful functional information for *in vivo* local airflow measurements in animal models (Fouras and Dubsy, 2015), and there are clinical trials underway for 2D x-ray PIV (4Dx Limited, 2017). With sufficiently sensitive detectors to ensure a clinically-compatible radiation dose, CT-PIV could become available for human imaging. Imaging the inhalation of Xenon is also a possibility in imaging flow, although the time resolution is limited when capturing 3D information from a single inhalation. At synchrotron x-ray sources, the patient must be rotated to perform CT, and a high rotation speed, necessary for high time resolution, could influence the flow of gas and any deposition of treatment.

Aerosol measurements via PCXI are more difficult than airflow measurements. Unlike nuclear methods, treatment cannot be easily separated in an image from the attenuating and phase-shifting effects of the surrounding organs. Bolus deliveries allow the concentrated localisation of a contrast agent, increasing the contrast of the treatment relative to surrounding anatomy (Donnelley et al., 2013) (Fig. 23b).

<sup>12</sup> The European Synchrotron Radiation Facility

<sup>13</sup> The third-generation Italian synchrotron radiation facility

Aerosolised treatment does not offer this benefit, and hence sensitivity is much lower, particularly given the lungs are constantly moving and do not present a static background, and even when images are triggered to a single point in the breath cycle, cardiovascular movement remains. One alternative would be to focus on just a small region of the airway system so that any deposited treatment is easier to resolve. If an aerosolised treatment were to be detected by PCXI in the whole lung, it must either be strongly attenuating or effectively change the diameter of the airspaces sufficiently that the speckle pattern changes in propagation-based PCXI or the dark-field signal changes in grating interferometry PCXI. The sensitivity of these techniques to these changes is currently under investigation. An alternative solution would be to introduce to the aerosolised treatment some highly attenuating or refractive particles or a contrast agent that would not be absorbed by the body, and then capture the deposit sites *via* a high-resolution PCXI–CT (either post-mortem in an animal model, or triggered by ventilation to the same point in the breath cycle). Note that the PCXI techniques discussed here could also be used with models of human airways, however there is not a strong advantage to using x-rays compared to visible light in an optically-transparent model, besides the possibility to increase the spatial resolution, which is not a real issue in any case.

While the suite of PCXI techniques is not currently used in flow or aerosol deposition measurements, these new modalities provide significantly increased soft-tissue sensitivity and present opportunities in terms of *in vivo* spatial and temporal resolution.

#### Advantages

- high spatial resolution (down to 1  $\mu\text{m}$ ),
- high temporal resolution (up to 1000 Hz),
- 3D visualisation possible,
- possible *in vivo*.

#### Disadvantages

- radiation dose,
- signal from treatment not easily separated from the background in the way seen with nuclear imaging methods.

## 7. Conclusions

The ongoing development of technology for the administration of therapeutic aerosols leads to a pressing need to predict and assess the precise deposition sites of inhaled particles on a microscale level. This task calls for a sophisticated combination of methods ranging from fluid mechanics, mathematics, engineering, pharmacology to medicine. Modern computational methods allow researchers to solve the equations that govern flow and particle motion within human lungs at sufficient resolution. However, these calculations are extremely sensitive to boundary conditions, the method used to solve them, and the practical numerical implementation of the method in the software. Quality experimental data describing deposition is immensely important both for setting boundary conditions in simulation and validating CFPD results.

The description of available experimental methods given here has shown that there is no method that can be used as a universal tool to cover all aspects and demands of CFPD calculations. Keeping in mind that the prediction of local deposition sites at the microscopic level in individualised human airways seems to be the next goal, we should find methods capable of acquiring the deposition data at sub-millimetre resolution. The review presented here showed that the common *in vivo* methods are unable to provide results in such resolution. The CFPD predictions provide results with a resolution that surpasses conventional experimental methods. However, if no *in vivo* experimental data is available for validation, measurements must be performed either *in vitro* or in replicas of human lungs. In the case of airway replicas, all of the methods described here can be useful at a certain stage of the

simulation (acquiring the lung geometry, defining the boundary conditions, validating the local flow velocities and particle deposition) and inevitably must be combined. Note that their physical limits, expressed as measurement uncertainties, need to be carefully considered. To summarize the main features, strengths and limits of the presented methods, we prepared Table 2, which lists all the methods in a way to enable fast comparisons. We needed to make some simplifications to fit all the methods to the limited space of Table 2, so the reader is kindly asked to refer to the respective section of this paper to obtain deeper insight on the selected method.

In conclusion, some recommendations can be given regarding the suitable application of the methods: HWA is a standard flow measurement method applicable in lung flows, but is limited almost exclusively to replicas of lungs. This technique provides high temporal resolution and thus can be used to assess turbulence, for example at the inlet of the replica, and hence helps in determining boundary condition settings. However, HWA is point-wise and intrusive and therefore the optical methods are becoming more popular. LD-based methods are also point-wise, but do not alter the flow and (as well as HWA) can be applied with air as a flowing media. This is their main advantage compared to planar and volumetric methods, which require exact refractive index matching fluid. On the other hand, planar/volumetric methods offer unique details of flow structures usable for CFD validation.

Regarding the data available from aerosol deposition measurements, there is a basis of results acquired using conventional non-imaging methods. However, since these measurements were predominantly performed some time ago, the details of the geometry and measurement procedure have not always been presented in publications. The availability of the methods and their low price facilitate performing new, case-tailored experiments on the appropriate well-described airway replica if necessary. Standard medical imaging methods (PET, SPECT) approach the required resolution, however, they are already reaching their physical limits and therefore cannot be expected to attain the sub-millimetre resolution range. The emerging methods that are anticipated to progress lung flow measurements can image airflow *in vivo* (Hyperpolarised gas MRI), measure detailed structures in alveoli (FD-OCT) or even track individual particles (x-ray Phase Contrast Imaging). However, these techniques have limited accessibility and are not easily or inexpensively implemented more widely. Nevertheless, they promise to bring extremely interesting data that, together with CFPD, can provide great advancement in patient-tailored inhaled medicine.

This review described the broad portfolio of available experimental methods and showed that the selection of suitable methods is not straightforward. The crucial step for the selection of a suitable combination of experimental data or instrumentation seems to be at the beginning of the whole process — acquiring and reproducing the lung geometry. Especially when comparing distinct methods of CFPD calculations, it is necessary to use the identical lung geometry, preferably with sufficient experimental data to evaluate success. After the validation in a standard lung geometry model, the simulation could be extended and compared to *in vivo* data to verify agreement with real physiological processes in general terms. This already points to intensive interdisciplinary and international collaboration since individual teams do not usually have sufficient human and technological resources to provide both highly sophisticated CFPD calculations and specialised experiments.

## Acknowledgements

This article is based upon work from COST Action MP1404 SimInhale ‘Simulation and pharmaceutical technologies for advanced patient-tailored inhaled medicines’, supported by COST (European Cooperation in Science and Technology) (MPNS COST Action MP1404).

Jan Jedelsky and Frantisek Lizal would like to acknowledge the financial support from the project GA16-23675S funded by the Czech

**Table 2**  
Main features of the experimental methods.

Technique	Spatial/time resolution	In vivo/in vitro/replicas	Quantities acquired/uncertainties	Fluid(s) <sup>a</sup>	Particles <sup>b</sup>	Cost <sup>c</sup> /availability	Requirements	Special features	Calibration/adjustment <sup>d</sup>
HWA	1 mm/<100 kHz	R	$u$ (min. $\pm 0.03$ m/s; 5%)/1C–3C	Gas	N	4 k€ for a single channel device/common in fluid mechanics	Inserting holes	Equidistant sampling, intrusive measurement	Daily/daily
LDA/PDA	0.1 mm/<100 kHz	R	$u$ ( $\pm 1\%$ ); $D$ ( $\pm 0.5 \mu\text{m}$ ); $c$ ( $\pm 20\%$ )	Both	Y	40–80 k€ per channel/common in fluid dynamics	Optical access, seeding	Random time sampling, on-line	No/daily
PIV/PTV	$\geq 1 \mu\text{m}$ (for $\mu\text{-PIV}$ )/<10 kHz	R	$u$ , 2C–3C/0.2 px	Both	Y	80–200 k€ depending on PIV-type	Optical access, refractive index matching, seeding	Stereo PIV, Tomo-PIV, $\mu\text{-PIV}$ , scanning-PIV, endoscopic PIV	For each measurement
Concentration meas.	Airway generation/single breath	V/R	$c$ ( $\pm 10\%$ )	Gas	Y	About 20 k€	Trained volunteers/lung replica	Simple, easily available	Annually/per experiment
Microscopy	1 mm to generation/per breath	R	$c$ ( $\pm 30\%$ )	Gas	Y	3.5 k€ per equipped microscope/common in environmental sciences	Separable replica of airways, filter preparation equipment	Simple, time-consuming, established methodology	Monthly; regular intra and inter-laboratory checks
Gravimetry/Fluorometry	Bifurcation, several $\text{cm}^2$	R/V	$c$ ( $\pm 10\%$ )	Gas	Y	3 k€ (laboratory balance), units of k€ for fluorometer	Separable replica or volunteer (for fluorometry)	Simple, low resolution or reduced extent	Annually/per experiment
PET	1–5 min	V	CPS	Gas	Y	Expensive, human scanners > 1 M€, radiochemistry facilities required.	Species to be tracked labelled with a positron emitter	In vivo, 4D (time + space), minimally invasive	Periodically (e.g. monthly)
SPECT/CT	Typically 5–10 min in clinical scanners	V	CPS	Gas	Y	Cheaper than PET, most hospitals have SPECT, radiochemistry facilities required.	Species to be tracked labelled with a gamma emitter	In vivo, 3D, minimally invasive	Periodically (e.g. monthly)
<sup>3</sup> He MRI		T/V	$u$ , 3C, $\pm 6.4\%$ ; $\pm 25$ mm/s	Air	N	Low availability	MRI with broadband amplifier; gas polarizer; dedicated chest coil; <sup>3</sup> He or <sup>129</sup> Xe supplies	3D flow dynamics	Yes
PCXI	1 $\mu\text{m}$ /100 Hz	V	X-ray image sequence $\rightarrow u$	Both	Y	Access to set-ups available via peer-reviewed application, without cost	X-ray absorbing or phase-shifting features	PIV of lung motion, 2D, 3D (time/space), 4D (time + space), individual particle motion	No
OCT	1–10 $\mu\text{m}$ /single depth line $\sim 1$ –10 $\mu\text{s}$ , plane $\sim 1$ ms, volume 0.1 s	V/T/R	$u$ , $c$	Both	Y	50–200k€	Optical access, seeding	In vivo, 3D	No/rare

Particles Flow Flow and particles

V/T/R – in vivo/in vitro/in replicas;  $u$  – flow velocity;  $D$  – particle diameter;  $c$  – particle concentration; CPS – counts per second, which can be converted to radioactivity per unit volume and to % of injected dose per unit volume, a calibrated standard within the FOV is required for absolute quantitation; Y/N – yes/no; <sup>a</sup>it indicates the possibility to measure in air (or other gas) directly, or in a substitute liquid; <sup>b</sup>capability of the method to measure inhaled particles; <sup>c</sup>the cost is referred as a purchase price of the instrument; <sup>d</sup>the term adjustment express the frequency of adjustments of the system by operator; <sup>e</sup>depends on the size of the FOV in mm and the pixel number of the camera chip, can be determined by the formula: FOV/number of pixels of the chip, example: FOV is  $100 \times 100 \text{ mm}^2$ , camera has  $1024 \times 1024 \text{ px}^2$ , resolution is  $100 \mu\text{m}/\text{px}$ .

Science Foundation.

Arnoldo Santos is a M + Visión COFUND Advanced Fellow and has received funding from Consejería de Educación, Juventud y Deporte of the Comunidad de Madrid and the People Programme (Marie Curie Actions) of the European Union Seventh Framework Programme (FP7/2007–2013) under Research Executive Agency grant agreement no 291820.

Kaye Morgan was supported by a Veski VPRF and completed this work with the support of the Technische Universität München Institute for Advanced Study, funded by the German Excellence Initiative (291763) and the European Union Seventh Framework Programme under grant agreement no 291763 and co-funded by the European Union.

Jordi Llop and Unai Cossio would like to thank the PneumoNP project (FP7-NMP/604434) for financial support.

## Disclaimer

The content of this article is the authors' responsibility and neither COST nor any person acting on its behalf is responsible for the use, which might be made of the information contained in it.

## References

- 4Dx Limited, 2017. 4Dx, Melbourne, Australia. <http://4dx.com>.
- Adler, K., Brucker, C., 2007. Dynamic flow in a realistic model of the upper human lung airways. *Exp. Fluids* 43, 411–423.
- Adrian, R.J., Westerweel, J., 2011. Particle Image Velocimetry. Cambridge Univ. Press.
- Adrian, R.J., Yao, C.S., 1987. Power spectra of fluid velocities measured by laser doppler velocimetry. *Exp. Fluids* 5, 17–28.
- Aisa, L., Garcia, J.A., Cerecedo, L.M., Palacin, I.G., Calvo, E., 2002. Particle concentration and local mass flux measurements in two-phase flows with PDA. Application to a study on the dispersion of spherical particles in a turbulent air jet. *Int. J. Multiphase Flow* 28, 301–324.
- Albert, M.S., Cates, G.D., Driehuys, B., Happer, W., Saam, B., Springer Jr., C.S., Wishnia, A., 1994. Biological magnetic resonance imaging using laser-polarized  $^{129}\text{Xe}$ . *Nature* 370, 199–201.
- Albrecht, H.-E., 2003. Laser Doppler and Phase Doppler Measurement Techniques. Springer, Berlin, New York.
- Altshuler, B., 1969. Behaviour of Airborne Particles in the Respiratory Tract, Ciba Foundation Symposium - Circulatory and Respiratory Mass Transport. John Wiley & Sons, Ltd., pp. 215–235.
- Amornphimoltham, P., Masedunskas, A., Weigert, R., 2011. Intravital microscopy as a tool to study drug delivery in preclinical studies. *Adv. Drug Deliv. Rev.* 63, 119–128.
- Armstrong, J.J., Leigh, M.S., Sampson, D.D., Walsh, J.H., Hillman, D.R., Eastwood, P.R., 2006. Quantitative upper airway imaging with anatomic optical coherence tomography. *Am. J. Respir. Crit. Care Med.* 173, 226–233.
- Ay, M.R., Sarkar, S., 2007. Computed tomography based attenuation correction in PET/CT: Principles, instrumentation, protocols, artifacts and future trends. *Iran. J. Nucl. Med.* 15, 1–29.
- Bachalo, W., Rudoff, R., Brena De La Rosa, A., 1988. In: Mass flux measurements of a high number density spray system using the phase Doppler particle analyzer. 26th Aerospace Sciences Meeting. American Institute of Aeronautics and Astronautics.
- Backman, P., Tehler, U., Olsson, B., 2017. Predicting exposure after oral inhalation of the selective glucocorticoid receptor modulator, AZD5423, based on dose, deposition pattern, and mechanistic modeling of pulmonary disposition. *J. Aerosol Med. Pulm. Drug Deliv.* 30, 108–117.
- Bailey, M.R., 1994. The new ICRP model for the respiratory-tract. *Radiat. Prot. Dosim.* 53, 107–114.
- Banko, A.J., Coletti, F., Schiavazzi, D., Elkins, C.J., Eaton, J.K., 2015. Three-dimensional inspiratory flow in the upper and central human airways. *Exp. Fluids* 56, 1–12.
- Banko, A.J., Coletti, F., Elkins, C.J., Eaton, J.K., 2016. Oscillatory flow in the human airways from the mouth through several bronchial generations. *Int. J. Heat Fluid Flow* 61, 45–57.
- Baron, P.A., 2001. Measurement of airborne fibers: a review. *Ind. Health* 39, 39–50.
- Bayat, S., Le Duc, G., Porra, L., Berruyer, G., Nemoz, C., Monfrais, S., Fiedler, S., Thomlinson, W., Suortti, P., Standertskjöld-Nordenstam, C.G., Sovijärvi, A.R.A., 2001. Quantitative functional lung imaging with synchrotron radiation using inhaled xenon as contrast agent. *Phys. Med. Biol.* 46, 3287–3299.
- Bech, M., Bunk, O., David, C., Ruth, R., Rifkin, J., Loewen, R., Feidenhansl, R., Pfeiffer, F., IUCr, 2009. Hard X-ray phase-contrast imaging with the compact light source based on inverse Compton X-rays. *J. Synchrotron Radiat.* 16, 43–47.
- Behr, J., Zimmermann, G., Baumgartner, R., Leuchte, H., Neurohr, C., Brand, P., Herpich, C., Sommerer, K., Seitz, J., Menges, G., Tillmanns, S., Keller, M., 2009. Lung deposition of a liposomal cyclosporine inhalation solution in patients after lung transplantation. *J. Aerosol Med. Pulm. Drug Deliv.* 22, 121–129.
- Belka, M., Lizal, F., Jedelský, J., Starha, P., Druckmullerova, H., Hopke, P.K., Jicha, M., 2016. Application of image analysis method to detection and counting of glass fibers from filter samples. *Aerosol Sci. Technol.* 50, 353–362.
- Benedict, L.H., Nobach, H., Tropea, C., 2000. Estimation of turbulent velocity spectra from laser Doppler data. *Meas. Sci. Technol.* 11, 1089–1104.
- Bérújon, S., Ziegler, E., Cerbino, R., Peverini, L., 2012. Two-Dimensional X-Ray Beam Phase Sensing. *Phys. Rev. Lett.* 108, 158102.
- Bestion, D., Gaviglio, J., Bonnet, J.P., 1983. Comparison between constant-current and constant-temperature hot-wire anemometers in high-speed flows. *Rev. Sci. Instrum.* 54, 1513–1524.
- Bettinardi, V., Castiglioni, I., De Bernardi, E., Gilardi, M.C., 2014. PET quantification: Strategies for partial volume correction. *Clin. Trans. Imag.* 2, 199–218.
- Bettoncelli, G., Blasi, F., Brusasco, V., Centanni, S., Corrado, A., De Benedetto, F., De Michele, F., Di Maria, G.U., Donner, C.F., Falcone, F., Mereu, C., Nardini, S., Pasqua, F., Polverino, M., Rossi, A., Sanguinetti, M., 2014. The clinical and integrated management of COPD an official document of Aimar (interdisciplinary association for research in lung disease), Aipo (Italian association of hospital pulmonologists), Simer (Italian society of respiratory medicine), Simg (Italian society of general medicine). *Sarcoidosis Vasc. Dif.* 31, 3–21.
- Bezerra, H.G., Costa, M.A., Guagliumi, G., Rollins, A.M., Simon, D.I., 2009. Intracoronary optical coherence tomography: a comprehensive review: clinical and research applications. *J. Am. Coll. Cardiol. Interv.* 2, 1035–1046.
- Blanchard, J.D., 1996. Aerosol bolus dispersion and aerosol-derived airway morphology: assessment of lung pathology and response to therapy, part 2. *J. Aerosol Med.* 9, 453–476.
- Bonse, U., 1965. An X-ray interferometer. *Appl. Phys. Lett.* 6, 155.
- Bovendeerd, P.H.M., Vansteenhoven, A.A., Vandevosse, F.N., Vossers, G., 1987. Steady entry flow in a curved pipe. *J. Fluid Mech.* 177, 233–246.
- Bowes, S.M., Swift, D.L., 1989. Deposition of inhaled particles in the oral airway during oronasal breathing. *Aerosol Sci. Technol.* 11, 157–167.
- Branca, R.T., Cleveland, Z.I., Fubara, B., Kumar, C.S., Maronpot, R.R., Leuschner, C., Warren, W.S., Driehuys, B., 2010. Molecular MRI for sensitive and specific detection of lung metastases. *Proc. Natl. Acad. Sci. U. S. A.* 107, 3693–3697.
- Brand, P., Hederer, B., Austen, G., Dewberry, H., Meyer, T., 2008. Higher lung deposition with Respimat® Soft Mist™ inhaler than HFA-MDI in COPD patients with poor technique. *Int. J. COPD* 3, 763–770.
- Bravin, A., Coan, P., Suortti, P., 2013. X-ray phase-contrast imaging: from pre-clinical applications towards clinics. *Phys. Med. Biol.* 58, R1–R35.
- Brezinski, M.E., 2006. Optical coherence tomography for identifying unstable coronary plaque. *Int. J. Cardiol.* 107, 154–165.
- Brücker, C., 1996. 3-D scanning particle image velocimetry: technique and application to a spherical cap wake flow. *Appl. Sci. Res.* 56, 157–179.
- Brücker, C., 1998. In: A time-recording Dpiv-study of the swirl switching effect in a 90° bend flow. Proc. 8th International Symposium on Flow Visualization, Sorrento(NA), Italy. Vol. 171. pp. 171–171.176.
- Brunner, E., Haake, M., Kaiser, L., Pines, A., Reimer, J.A., 1999. Gas flow MRI using circulating laser-polarized  $^{129}\text{Xe}$ . *J. Magn. Reson.* 138, 155–159.
- Bruun, H.H., 1995. Hot-wire anemometry: principles and signal analysis. Oxford University Press, Oxford, New York.
- Bruun, H.H., Khan, M.A., Alkayiem, H.H., Fardad, A.A., 1988. Velocity calibration relationships for hot-wire anemometry. *J. Phys. E Sci. Instrum.* 21, 225–232.
- Bu, R., Balakrishnan, S., Iftimia, N., Price, H., Zdanski, C., Oldenburg, A.L., 2017. Airway compliance measured by anatomic optical coherence tomography. *Biomed. Opt. Express* 8, 2195–2209.
- Buchsbaum, A., Egger, M., Burzic, I., Koepplmayr, T., Aigner, M., Miethlinger, J., Leitner, M., 2015. Optical coherence tomography based particle image velocimetry (OCT-PIV) of polymer flows. *Opt. Lasers Eng.* 69, 40–48.
- Calvo, E., García, J.A., García, I., Aisa, L.A., 2009. Errors analysis in the evaluation of particle concentration by PDA on a turbulent two-phase jet: application for cross section and transit time methods. *Exp. Fluids* 47, 489–508.
- Carnibella, R.P., Kitchen, M.J., Fouras, A., 2014. Single-shot X-ray measurement of alveolar size distributions. In: SPIE Medical Imaging 9038, 90380V-90380V-90387.
- Chang, H.K., Elmasry, O.A., 1982. A model study of flow dynamics in human central airways. 1. Axial velocity profiles. *Respir. Physiol.* 49, 75–95.
- Chen, C., Cheng, K.H.Y., Jakubovic, R., Jivraj, J., Ramjist, J., Deorajh, R., Gao, W., Barnes, E., Chin, L., Yang, V.X.D., 2017. High speed, wide velocity dynamic range Doppler optical coherence tomography (part V): optimal utilization of multi-beam scanning for Doppler and speckle variance microvascular imaging. *Opt. Express* 25, 7761–7777.
- Cheng, K.H., Cheng, Y.S., Yeh, H.C., Swift, D.L., 1997. Measurements of airway dimensions and calculation of mass transfer characteristics of the human oral passage. *J. Biomech. Eng. Transac. ASME* 119, 476–482.
- Cheng, Y.S., Zhou, Y., Chen, B.T., 1999. Particle deposition in a cast of human oral airways. *Aerosol Sci. Technol.* 31, 286–300.
- Cheng, Y.S., Zhou, Y., Su, W.C., 2015. Deposition of particles in human mouth-throat replicas and a USP induction port. *J. Aerosol Med. Pulm. Drug Deliv.* 28, 147–155.
- Choi, J., Tawhai, M.H., Hoffman, E.A., Lin, C.L., 2009. On intra- and intersubject variabilities of airflow in the human lungs. *Phys. Fluids* 21, 17.
- Choma, M., Sarunic, M., Yang, C., Izatt, J., 2003. Sensitivity advantage of swept source and Fourier domain optical coherence tomography. *Opt. Express* 11, 2183–2189.
- Cimalla, P., Werner, T., Winkler, K., Mueller, C., Wicht, S., Gaertner, M., Mehner, M., Walther, J., Rellinghaus, B., Wittig, D., 2015. Imaging of nanoparticle-labeled stem cells using magnetomotive optical coherence tomography, laser speckle reflectometry, and light microscopy. *BIOMEDO* 20, 036018.
- Clinkenbeard, R.E., Johnson, D.L., Parthasarathy, R., Altan, M.C., Tan, K.H., Park, S.M., Crawford, R.H., 2002. Replication of human tracheobronchial hollow airway models using a selective laser sintering rapid prototyping technique. *Aihaj* 63, 141–150.
- Cloetens, P., Barrett, R., Baruchel, J., Guigay, J.-P., Schlenker, M., 1996. Phase objects in

- synchrotron radiation hard x-ray imaging. *J. Phys. D. Appl. Phys.* 29, 133–146.
- Collier, G.J., Wild, J.M., 2015. *In vivo* measurement of gas flow in human airways with hyperpolarized gas MRI and compressed sensing. *Magn. Reson. Med.* 73, 2255–2261.
- Corcoran, T.E., Chigier, N., 2000. Characterization of the laryngeal jet using phase Doppler interferometry. *J. Aerosol Med.* 13, 125–137.
- Corcoran, T.E., Chigier, N., 2002. Inertial deposition effects: a study of aerosol mechanics in the trachea using laser Doppler velocimetry and fluorescent dye. *J. Biomech. Eng. Transac. ASME* 124, 629–637.
- Corieri, P., Riethmuller, M.L., 1989. In: Laser Doppler velocimetry and computer automation to measure low velocities in a pulmonary model. *Iciasf 89 Record: International Congress on Instrumentation in Aerospace Simulation Facilities*. pp. 226–236.
- Darquenne, C., West, J.B., Prisk, G.K., 1998. Deposition and dispersion of 1- $\mu$ m aerosol boluses in the human lung: effect of micro- and hypergravity. *J. Appl. Physiol.* 85, 1252–1259.
- David, C., Nöhhammer, B., Solak, H.H., Ziegler, E., 2002. Differential x-ray phase contrast imaging using a shearing interferometer. *Appl. Phys. Lett.* 81, 3287–3289.
- de Boer, J.F., Cense, B., Park, B.H., Pierce, M.C., Tearney, G.J., Bouma, B.E., 2003. Improved signal-to-noise ratio in spectral-domain compared with time-domain optical coherence tomography. *Opt. Lett.* 28, 2067–2069.
- de Rochefort, L., Maitre, X., Fodil, R., Vial, L., Louis, B., Isabey, D., Croce, C., Darrasse, L., Apiou, G., Caillibotte, G., Bittoun, J., Durand, E., 2006. Phase-contrast velocimetry with hyperpolarized  $^3\text{He}$  for *in vitro* and *in vivo* characterization of airflow. *Magn. Reson. Med.* 55, 1318–1325.
- de Rochefort, L., Nguyen, T., Brown, R., Spincemaille, P., Choi, G., Weinsaft, J., Prince, M.R., Wang, Y., 2008. *In vivo* quantification of contrast agent concentration using the induced magnetic field for time-resolved arterial input function measurement with MRI. *Med. Phys.* 35, 5328–5339.
- DeHaan, W.H., 2002. Mouth-throat deposition with non-ballistic pharmaceutical aerosol inhalation devices (PhD diss.). University of Alberta, Edmonton, Alberta, Canada.
- Dolovich, M.B., 2009. 18F-fluorodeoxyglucose positron emission tomographic imaging of pulmonary functions, pathology, and drug delivery. *Proc. Am. Thorac. Soc.* 6, 477–485.
- Donnelley, M., Parsons, D., Morgan, K.S., Siu, K., 2010. In: *Animals in synchrotrons: overcoming challenges for high-resolution, live, small-animal imaging*. AIP Conference Proceedings.
- Donnelley, M., Morgan, K.S., Siu, K.K.W., Parsons, D.W., 2013. Variability of *in vivo* fluid dose distribution in mouse airways is visualized by high-speed synchrotron x-ray imaging. *J. Aerosol Med. Pulm. Drug Deliv.* 26, 307–316.
- Donnelley, M., Morgan, K.S., Siu, K.K.W., Farrow, N.R., Stahr, C.S., Boucher, R.C., Fouras, A., Parsons, D.W., 2014a. Non-invasive airway health assessment: Synchrotron imaging reveals effects of rehydrating treatments on mucociliary transit *in-vivo*. *Sci Rep* 4, 146.
- Donnelley, M., Morgan, K.S., Siu, K.K.W., Fouras, A., Farrow, N.R., Carnibella, R.P., Parsons, D.W., IUCr, 2014b. Tracking extended mucociliary transport activity of individual deposited particles: longitudinal synchrotron X-ray imaging in live mice. *J. Synchrotron Radiat.* 21, 768–773.
- Donnelley, M., Morgan, K.S., Awadalla, M., Farrow, N.R., Hall, C., Parsons, D.W., 2017. High-resolution mucociliary transport measurement in live excised large animal trachea using synchrotron X-ray imaging. *Respir. Res.* 18 (1), 95.
- Drexler, W., Morgner, U., Kärtner, F.X., Pitris, C., Boppart, S.A., Li, X.D., Ippen, E.P., Fujimoto, J.G., 1999. *In vivo* ultrahigh-resolution optical coherence tomography. *Opt. Lett.* 24, 1221–1223.
- Dubsky, S., Fouras, A., 2015. Imaging regional lung function: a critical tool for developing inhaled antimicrobial therapies. *Adv. Drug Deliv. Rev.* 85, 100–109.
- Dubsky, S., Hooper, S.B., Siu, K.K.W., Fouras, A., 2012. Synchrotron-based dynamic computed tomography of tissue motion for regional lung function measurement. *J. R. Soc. Interface* 9, 2213–2224.
- Dugernier, J., Hesse, M., Vanbever, R., Depoortere, V., Roeseler, J., Michotte, J.B., Laterre, P.F., Jamar, F., Reyckler, G., 2017. SPECT-CT comparison of lung deposition using a system combining a vibrating-mesh nebulizer with a valved holding chamber and a conventional jet nebulizer: a randomized cross-over study. *Pharm. Res.* 34, 290–300.
- Dullenkopf, K., Willmann, M., Wittig, S., Schone, F., Stieglmeier, M., Tropea, C., Mundo, C., 1998. Comparative mass flux measurements in sprays using a patternator and the phase-Doppler technique. *Part. Part. Syst. Charact.* 15, 81–89.
- Duma, V.F., Lee, K.S., Meemon, P., Rolland, J.P., 2011. Experimental investigations of the scanning functions of galvanometer-based scanners with applications in OCT. *Appl. Opt.* 50, 5735–5749.
- Durst, F., Melling, A., Whitelaw, J.H., 1981. *Principles and Practice of Laser-Doppler Anemometry*, 2nd Ed. Academic Press, London; New York.
- Eberl, S., Chan, H.K., Daviskas, E., Constable, C., Young, I., 2001. Aerosol deposition and clearance measurement: a novel technique using dynamic SPET. *Eur. J. Nucl. Med.* 28, 1365–1372.
- Edwards, C.F., Marx, K.D., 1995. Multipoint Statistical Structure of the Ideal Spray Part II: Evaluating Steadiness Using the Interparticle Time Distribution. Vol. 5. pp. 457–505.
- Elcner, J., Lizal, F., Jedelsky, J., Jicha, M., Chovanova, M., 2016. Numerical investigation of inspiratory airflow in a realistic model of the human tracheobronchial airways and a comparison with experimental results. *Biomech. Model. Mechanobiol.* 15, 447–469.
- Elsing, G.E., Van Oudheusden, B.W., Scarano, F., 2006. In: *Experimental assessment of Tomographic-PIV accuracy*. 13th Int Symp on Applications of Laser Techniques to Fluid Mechanics Lisbon, Portugal, 26–29 June, 2006.
- Farag, A., Hammersley, J., Olson, D., Ng, T., 2000. Mechanics of the flow in the small and middle human airways. *J. Fluids Eng. Transac. ASME* 122, 576–584.
- Fda, N., Blaisot, J.B., Floch, A., Dechaume, D., 2010. Drop-size measurement techniques applied to gasoline sprays. *Atomization Sprays* 20 (2), 141–162.
- Finlay, W.H., Stapleton, K.W., Yokota, J., 1996. On the use of computational fluid dynamics for simulating flow and particle deposition in the human respiratory tract. *J. Aerosol Med.* 9, 329–341.
- Fishler, R., Mulligan, M.K., Sznitman, J., 2013. Acinus-on-a-chip: a microfluidic platform for pulmonary acinar flows. *J. Biomech.* 46, 2817–2823.
- Fishler, R., Hofemeier, P., Etzion, Y., Dubowski, Y., Sznitman, J., 2015. Particle dynamics and deposition in true-scale pulmonary acinar models. *Sci Rep* 5, 14071.
- Fishler, R., Ostrovski, Y., Lu, C.-Y., Sznitman, J., 2017. Streamline crossing: an essential mechanism for aerosol dispersion in the pulmonary acinus. *J. Biomech.* 50, 222–227.
- Fleming, J.S., Conway, J., Majoral, C., Tossici-Bolt, L., Katz, I., Caillibotte, G., Perchet, D., Pichelin, M., Muellinger, B., Martonen, T., Kroneberg, P., Apiou-Sbirlea, G., 2011. The use of combined single photon emission computed tomography and X-ray computed tomography to assess the fate of inhaled aerosol. *J. Aerosol Med. Pulm. Drug Deliv.* 24, 49–60.
- Fleming, J., Conway, J., Majoral, C., Katz, I., Caillibotte, G., Pichelin, M., Montesantos, S., Bennett, M., 2015. Controlled, parametric, individualized, 2-D and 3-D imaging measurements of aerosol deposition in the respiratory tract of asthmatic human subjects for model validation. *J. Aerosol Med. Pulm. Drug Deliv.* 28, 432–451.
- Forbes, B., Danani, A., Borchard, G., Kassinos, S., 2016. Introducing European COST Action—Siminhale. *Inhalation*.
- Förster, E., Goetz, K., Zaumseil, P., 1980. Double crystal diffractometry for the characterization of targets for laser fusion experiments. *Cryst. Res. Technol.* 15, 937–945.
- Fouras, A., Dubsky, S., 2015. The Role of Functional Lung Imaging in the Improvement of Pulmonary Drug Delivery. John Wiley & Sons, Ltd., Chichester, UK.
- Fouras, A., Allison, B.J., Kitchen, M.J., Dubsky, S., Nguyen, J., Hourigan, K., Siu, K.K.W., Lewis, R.A., Wallace, M.J., Hooper, S.B., 2012. Altered lung motion is a sensitive indicator of regional lung disease. *Ann. Biomed. Eng.* 40, 1160–1169.
- Fresconi, F.E., Prasad, A.K., 2007. Secondary velocity fields in the conducting airways of the human lung. *J. Biomech. Eng. Transac. ASME* 129, 722–732.
- Gemci, T., Corcoran, T.E., Chigier, N., 2002. A numerical and experimental study of spray dynamics in a simple throat model. *Aerosol Sci. Technol.* 36, 18–38.
- Gillings, N., 2013. Radiotracers for positron emission tomography imaging. *MAGMA* 26, 149–158.
- Girardin, M., Bilgen, E., Arbour, P., 1983. Experimental study of velocity-fields in a human nasal fossa by laser anemometry. *Ann. Otol. Rhinol. Laryngol.* 92, 231–236.
- Gleich, B., Weizenbecker, R., 2005. Tomographic imaging using the nonlinear response of magnetic particles. *Nature* 435, 1214–1217.
- Gracia, R., Marradi, M., Cossio, U., Benito, A., Pérez-San Vicente, A., Gómez-Vallejo, V., Grande, H.J., Llop, J., Loiaz, I., 2017. Synthesis and functionalization of dextran-based single-chain nanoparticles in aqueous media. *J. Mater. Chem. B* 5, 1143–1147.
- Grčić, B., Finlay, W.H., Heenan, A.F., 2004. Regional aerosol deposition and flow measurements in an idealized mouth and throat. *J. Aerosol Sci.* 35, 21–32.
- Grombe, R., Kirsten, L., Mehner, M., Linsinger, T.P., Koch, E., 2016. Improved non-invasive optical coherence tomography detection of different engineered nanoparticles in food-mimicking matrices. *Food Chem.* 212, 571–575.
- Grosse, S., Schroder, W., Klaas, M., Klockner, A., Roggenkamp, J., 2007. Time resolved analysis of steady and oscillating flow in the upper human airways. *Exp. Fluids* 42, 955–970.
- Guilmette, R.A., Gagliano, T.J., 1994. Construction of a model of human nasal airways using *in vivo* morphometric data. *Inhaled Part. VII*, 69–75.
- Guilmette, L.A., Wicks, J.D., Wolff, R.K., 1989. Morphometry of human nasal airways *in vivo* using magnetic resonance imaging. *J. Aerosol Med. Pulm. Drug Deliv.* (1941–2711) 2, 365–377.
- Hahn, I., Scherer, P.W., Mozell, M.M., 1993. Velocity profiles measured for air-flow through a large-scale model of the human nasal cavity. *J. Appl. Physiol.* 75, 2273–2287.
- Haindl, R., Trasischker, W., Wartak, A., Baumann, B., Pircher, M., Hitznberger, C.K., 2016. Total retinal blood flow measurement by three beam Doppler optical coherence tomography. *Biomed. Opt. Express* 7, 287–301.
- Heenan, A.F., Matida, E., Pollard, A., Finlay, W.H., 2003. Experimental measurements and computational modeling of the flow field in an idealized human oropharynx. *Exp. Fluids* 35, 70–84.
- Hellbach, K., Yaroshenko, A., Meinel, F.G., Yildirim, A.Ö., Conlon, T.M., Bech, M., Mueller, M., Velroyen, A., Notohamiprodjo, M., Bamberg, F., Auweter, S., Reiser, M., Eickelberg, O., Pfeiffer, F., 2015. *In vivo* dark-field radiography for early diagnosis and staging of pulmonary emphysema. *Investig. Radiol.* 50, 430–435.
- Heraty, K.B., Laffey, J.G., Quinlan, N.J., 2008. Fluid dynamics of gas exchange in high-frequency oscillatory ventilation: *in vitro* investigations in idealized and anatomically realistic airway bifurcation models. *Ann. Biomed. Eng.* 36, 1856–1869.
- Hetsroni, G., 1989. Particles turbulence interaction. *Int. J. Multiphase Flow* 15, 735–746.
- Heyder, J., Gebhart, J., Roth, C., Stahlhofen, W., Stuck, B., Tarroni, G., DeZaiacono, T., Formignani, M., Melandri, C., Prodi, V., 1978. Intercomparison of lung deposition data for aerosol particles. *J. Aerosol Sci.* 9, 147–155.
- Hoegger, M.J., Awadalla, M., Namati, E., Itani, O.A., Fischer, A.J., Tucker, A.J., Adam, R.J., McLennan, G., Hoffman, E.A., Stoltz, D.A., Welsh, M.J., 2014. Assessing mucociliary transport of single particles *in vivo* shows variable speed and preference for the ventral trachea in newborn pigs. *Proc. Natl. Acad. Sci.* 111, 2355–2360.
- Holbrook, L.T., Longest, P.W., 2013. Validating CFD predictions of highly localized aerosol deposition in airway models: *in vitro* data and effects of surface properties. *J. Aerosol Sci.* 59, 6–21.
- Hooper, S.B., Kitchen, M.J., Wallace, M.J., Yagi, N., Uesugi, K., Morgan, M.J., Hall, C., Siu, K.K.W., Williams, I.M., Siew, M., Irvine, S.C., Pavlov, K., Lewis, R.A., 2007. Imaging lung aeration and lung liquid clearance at birth. *FASEB J.* 21, 3329–3337.
- Hopkins, L.M., Kelly, J.T., Wexler, A.S., Prasad, A.K., 2000. Particle image velocimetry measurements in complex geometries. *Exp. Fluids* 29, 91–95.

- Horsfield, K., Cumming, G., 1967. Angles of branching and diameters of branches in the human bronchial tree. *Bull. Math. Biol.* 29, 245–259.
- Horsfield, K., Cumming, G., 1968. Morphology of the bronchial tree in man. *J. Appl. Physiol.* 24, 373–383.
- Horsfield, K., Dart, G., Olson, D.E., Filley, G.F., Cumming, G., 1971. Models of the human bronchial tree. *J. Appl. Physiol. Respir. Environ. Exerc. Physiol.* 31, 207–217.
- Huang, D., Swanson, E.A., Lin, C.P., Schuman, J.S., Stinson, W.G., Chang, W., Hee, M.R., Flotte, T., Gregory, K., Puliafito, C.A., Fujimoto, J.G., 1991. Optical coherence tomography. *Science* 254, 1178–1181.
- Huang, B.K., Gamm, U.A., Bhandari, V., Khokha, M.K., Choma, M.A., 2015. Three-dimensional, three-vector-component velocimetry of cilia-driven fluid flow using correlation-based approaches in optical coherence tomography. *Biomed. Opt. Express* 6, 3515–3538.
- Ingal, V.N., Beliaevskaya, E.A., 1995. X-ray plane-wave topography observation of the phase contrast from a non-crystalline object. *J. Phys. D. Appl. Phys.* 28, 2314–2317.
- Isabey, D., Chang, H.K., 1982. A model study of flow dynamics in human central airways. 2. Secondary flow velocities. *Respir. Physiol.* 49, 97–113.
- Islam, M.N., Gomer, H., Sacks, S., 2017. Comparison of dimensional accuracies of stereolithography and powder binder printing. *Int. J. Adv. Manuf. Technol.* 88, 3077–3087.
- Janke, T., Bauer, K., 2016. In: Development of a 3D-PTV algorithm for the investigation of turbulent flow structures in the upper human bronchial tree. 18th International Symposium on Applications of Laser Techniques to Fluid Mechanics.
- Janke, T., Schwarze, R., Bauer, K., 2017. Measuring three-dimensional flow structures in the conductive airways using 3D-PTV. *Exp. Fluids* 58 (10).
- Jayaraju, S.T., Brouns, M., Lacor, C., Belkassam, B., Verbanck, S., 2008. Large eddy and detached eddy simulations of fluid flow and particle deposition in a human mouth-throat. *J. Aerosol Sci.* 39, 862–875.
- Jedelsky, J., Lizal, F., Jicha, M., 2012. Characteristics of turbulent particle transport in human airways under steady and cyclic flows. *Int. J. Heat Fluid Flow* 35, 84–92.
- Jensen, K.D., 2004. Flow measurement. *J. Braz. Soc. Mech. Sci. Eng.* 26, 400–419.
- Johnstone, A., Uddin, M., Pollard, A., Heenan, A., Finlay, W.H., 2004. The flow inside an idealised form of the human extra-thoracic airway. *Exp. Fluids* 37, 673–689.
- Jonas, S., Bhattacharya, D., Khokha, M.K., Choma, M.A., 2011. Microfluidic characterization of cilia-driven fluid flow using optical coherence tomography-based particle tracking velocimetry. *Biomed. Opt. Express* 2, 2022–2034.
- Jung, W., McCormick, D.T., Zhang, J., Wang, L., Tien, N.C., Chen, Z., 2006. Three-dimensional endoscopic optical coherence tomography by use of a two-axis microelectromechanical scanning mirror. *Appl. Phys. Lett.* 88, 163901.
- Kalkman, J., Sprik, R., van Leeuwen, T.G., 2010. Path-length-resolved diffusive particle dynamics in spectral-domain optical coherence tomography. *Phys. Rev. Lett.* 105, 198302.
- Kelly, J.T., Asgharian, B., Kimbell, J.S., Wong, B.A., 2004a. Particle deposition in human nasal airway replicas manufactured by different methods. Part I: inertial regime particles. *Aerosol Sci. Technol.* 38, 1063–1071.
- Kelly, J.T., Asgharian, B., Kimbell, J.S., Wong, B.A., 2004b. Particle deposition in human nasal airway replicas manufactured by different methods. Part II: ultrafine particles. *Aerosol Sci. Technol.* 38, 1072–1079.
- Kerekes, A., Nagy, A., Veres, M., Rigo, I., Farkas, A., Czitrovsky, A., 2016. In vitro and in silico (IVIS) flow characterization in an idealized human airway geometry using laser Doppler anemometry and computational fluid dynamics techniques. *Measurement* 90, 144–150.
- Kesavanathan, J., Swift, D.L., 1998. Human nasal passage particle deposition: the effect of particle size, flow rate, and anatomical factors. *Aerosol Sci. Technol.* 28, 457–463.
- Kim, C.S., Fisher, D.M., 1999. Deposition of aerosol particles in successively bifurcating airways models. *Aerosol Sci. Technol.* 31, 198–220.
- Kim, C.S., Iglesias, A.J., 1989. Deposition of inhaled particles in bifurcating airway models: I. Inspiratory deposition. *J. Aerosol Med.* 2, 14.
- Kim, C.S., Kang, T.C., 1997. Comparative measurement of lung deposition of inhaled fine particles in normal subjects and patients with obstructive airway disease. *Am. J. Respir. Crit. Care Med.* 155, 899–905.
- Kim, C.S., Hu, S.C., DeWitt, P., Gerrity, T.R., 1996. Assessment of regional deposition of inhaled particles in human lungs by serial bolus delivery method. *J. Appl. Physiol.* 81, 2203–2213.
- Kippax, P., Krarup, H., Suman, J., 2004. Applications for droplet sizing: manual versus automated actuation of nasal sprays. *Pharm. Technol.* 30–39.
- Kirsten, L., Gaertner, M., Schnabel, C., Meissner, S., Koch, E., 2013. Four-dimensional imaging of murine subpleural alveoli using high-speed optical coherence tomography. *J. Biophotonics* 6, 148–152.
- Kirsten, L., Domaschke, T., Schneider, C., Walther, J., Meissner, S., Hampel, R., Koch, E., 2015. Visualization of dynamic boiling processes using high-speed optical coherence tomography. *Exp. Fluids* 56.
- Kitchen, M., Paganin, D., Lewis, R., Yagi, N., Uesugi, K., Mudie, S., 2004. On the origin of speckle in X-ray phase contrast images of lung tissue. *Phys. Med. Biol.* 49 (18), 4335.
- Kitchen, M.J., Buckley, G.A., Leong, A.F., Carnibella, R.P., Fouras, A., Wallace, M.J., Hooper, S.B., 2015. X-ray specks: low dose *in vivo* imaging of lung structure and function. *Phys. Med. Biol.* 60, 7259–7276.
- Knopp, T., Conolly, S.M., Buzug, T.M., 2017. Recent progress in magnetic particle imaging: from hardware to preclinical applications. *Phys. Med. Biol.* 62, E4–E7.
- Kohlhauf, M., Brand, P., Selzer, T., Scheuch, G., Meyer, T., Weber, N., Schulz, H., Haussinger, K., Heyder, J., 1998. Diagnosis of emphysema in patients with chronic bronchitis: a new approach. *Eur. Respir. J.* 12, 793–798.
- Kolanijyil, A.V., Kleinstreuer, C., 2013. Nanoparticle mass transfer from lung airways to systemic regions-part I: whole-lung aerosol dynamics. *J. Biomech. Eng. Transac. ASME* 135.
- Koptyug, I.I., Altobelli, S.A., Fukushima, E., Matveev, A.V., Sagdeev, R.Z., 2000. Thermally polarized (1)H NMR microimaging studies of liquid and gas flow in monolithic catalysts. *J. Magn. Reson.* 147, 36–42.
- Koullapis, P.G., Hofemeier, P., Sznitman, J., Kassinos, S.C., 2017a. An efficient computational fluid-particle dynamics method to predict deposition in a simplified approximation of the deep lung. *Eur. J. Pharm. Sci.*
- Koullapis, P.G., Kassinos, S.C., Muela, J., Segarra, C., Rigola, J., Lehmkuhl, O., Cui, Y., Sommerfeld, M., Elcner, J., Jicha, M., Saveljic, I., Filipovic, N., Lizal, F., Nicolaou, L., 2017b. Regional aerosol deposition in the human airways: The SimInhale benchmark case and a critical assessment of in silico methods. <http://dx.doi.org/10.1016/j.ejps.2017.09.003>.
- Kwak, Y., Nam, S., Akcakaya, M., Basha, T.A., Goddu, B., Manning, W.J., Tarokh, V., Nezafat, R., 2013. Accelerated aortic flow assessment with compressed sensing with and without use of the sparsity of the complex difference image. *Magn. Reson. Med.* 70, 851–858.
- Landahl, H.D., Tracewell, T.N., Lassen, W.H., 1951. On the retention of air-borne particulates in the human lung 2. A.M.A. Arch. Ind. Hyg. Occup. Med. 3, 359–366.
- Larsson, D.H., Takman, P.A.C., Lundström, U., Burvall, A., Hertz, H.M., 2011. A 24 keV liquid-metal-jet x-ray source for biomedical applications. *Rev. Sci. Instrum.* 82, 123701.
- Lee Ventola, C., 2014. Medical applications for 3D printing: current and projected uses. *P and T* 39, 704–711.
- Lee, W.J., Kawahashi, M., Hirahara, H., 2006. Experimental analysis of pendelluft flow generated by HFOV in a human airway model. *Physiol. Meas.* 27, 661–674.
- Leitgeb, R., Hitzinger, C., Fercher, A., 2003. Performance of Fourier domain vs. time domain optical coherence tomography. *Opt. Express* 11, 889–894.
- Lemonis, G., 1997. Three-dimensional measurement of velocity, velocity gradients and related properties in turbulent flows. *Aerosol Sci. Technol.* 1, 453–461.
- Li, Z., Conti, P.S., 2010. Radiopharmaceutical chemistry for positron emission tomography. *Adv. Drug Deliv. Rev.* 62, 1031–1051.
- Liaw, C.Y., Guvendiren, M., 2017. Current and emerging applications of 3D printing in medicine. *Biofabrication* 9.
- Lieber, B., Zhao, Y., 1998. Oscillatory flow in a symmetric bifurcation airway model. *Ann. Biomed. Eng.* 26, 821–830.
- Lippmann, M., Yeates, D.B., Albert, R.E., 1980. Deposition, retention, and clearance of inhaled particles. *Br. J. Ind. Med.* 37, 337–362.
- Liu, H., 2000. Science and Engineering of Droplets: Fundamentals and Applications. Noyes Publications, William Andrew Pub., Park Ridge, N.J. Norwich, N.Y.
- Liu, X., Yan, W., Liu, Y., Choy, Y.S., Wei, Y., 2016. Numerical investigation of flow characteristics in the obstructed realistic human upper airway. *Comput. Math. Methods Med.* 2016, 10.
- Lizal, F., Elcner, J., Hopke, P.K., Jedelsky, J., Jicha, M., 2012. Development of a realistic human airway model. *Proc. Inst. Mech. Eng. H J. Eng. Med.* 226, 197–207.
- Lizal, F., Belka, M., Adam, J., Jedelsky, J., Jicha, M., 2015. A method for in vitro regional aerosol deposition measurement in a model of the human tracheobronchial tree by the positron emission tomography. *Proc. Inst. Mech. Eng. H J. Eng. Med.* 229, 750–757.
- Loira-Pastoriza, C., Todoroff, J., Vanbever, R., 2014. Delivery strategies for sustained drug release in the lungs. *Adv. Drug Deliv. Rev.* 75, 81–91.
- Longest, P.W., Holbrook, L.T., 2012. In silico models of aerosol delivery to the respiratory tract - development and applications. *Adv. Drug Deliv. Rev.* 64, 296–311.
- Longest, P.W., Tian, G., Delvadia, R., Hindle, M., 2012. Development of a stochastic individual path (SIP) model for predicting the deposition of pharmaceutical aerosols: effects of turbulence, polydisperse aerosol size, and evaluation of multiple lung lobes. *Aerosol Sci. Technol.* 46, 1271–1285.
- Longo, R., 2016. Current studies and future perspectives of synchrotron radiation imaging trials in human patients. *Nucl. Instrum. Methods Phys. Res., Sect. A* 809, 13–22.
- Lorenser, D., Yang, X., Kirk, R.W., Quirk, B.C., McLaughlin, R.A., Sampson, D.D., 2011. Ultrathin side-viewing needle probe for optical coherence tomography. *Opt. Lett.* 36, 3894–3896.
- Lovrić, G., 2015. *In Vivo* Study of Lung Physiology with Dynamic Synchrotron-Based Tomographic Microscopy (PhD thesis). ETH, Zurich.
- Lu, C.D., Kraus, M.F., Potsaid, B., Liu, J.J., Choi, W., Jayaraman, V., Cable, A.E., Hornegger, J., Duker, J.S., Fujimoto, J.G., 2014. Handheld ultrahigh speed swept source optical coherence tomography instrument using a MEMS scanning mirror. *Biomed. Opt. Express* 5, 293–311.
- Luan, X., Campanucci, V.A., Nair, M., Yilmaz, O., Belev, G., Machen, T.E., Chapman, D., Ianowski, J.P., 2014. *Pseudomonas aeruginosa* triggers CFTR-mediated airway surface liquid secretion in swine trachea. *Proc. Natl. Acad. Sci.* 111, 12930–12935.
- Lustig, M., Donoho, D., Pauly, J.M., 2007. Sparse MRI: the application of compressed sensing for rapid MR imaging. *Magn. Reson. Med.* 58, 1182–1195.
- Martin, A.R., Thompson, R.B., Finlay, W.H., 2008. MRI measurement of regional lung deposition in mice exposed nose-only to nebulized superparamagnetic iron oxide nanoparticles. *J. Aerosol Med. Pulm. Drug Deliv.* 21, 335–342.
- Marx, K.D., Edwards, C.F., Chin, W.K., 1994. Limitations of the ideal phase-Doppler system - extension to spatially and temporally inhomogeneous particle flows. *Atom. Spray* 4, 1–40.
- McLaughlin, D., Tiederman, W., 1973. Biasing correction for individual realization of laser anemometer measurements in turbulent flows. *Phys. Fluids* 16, 2082–2088.
- McLaughlin, R.A., Yang, X.J., Quirk, B.C., Lorenser, D., Kirk, R.W., Noble, P.B., Sampson, D.D., 2012. Static and dynamic imaging of alveoli using optical coherence tomography needle probes. *J. Appl. Physiol. Respir. Environ. Exerc. Physiol.* 113, 967–974.
- Meissner, S., Knels, L., Koch, E., 2009a. Improved three-dimensional Fourier domain optical coherence tomography by index matching in alveolar structures. *BIOMEDO* 14, 064037.
- Meissner, S., Muller, G., Walther, J., Morawietz, H., Koch, E., 2009b. *In-vivo* Fourier

- domain optical coherence tomography as a new tool for investigation of vasodynamics in the mouse model. *BIOMEDO* 14, 034027.
- Meissner, S., Knels, L., Schnabel, C., Koch, T., Koch, E., 2010a. Three-dimensional Fourier domain optical coherence tomography *in vivo* imaging of alveolar tissue in the intact thorax using the parietal pleura as a window. *BIOMEDO* 15, 016030.
- Meissner, S., Tabuchi, A., Mertens, M., Kuebler, W.M., Koch, E., 2010b. Virtual four-dimensional imaging of lung parenchyma by optical coherence tomography in mice. *BIOMEDO* 15, 036016.
- Melling, A., 1997. Tracer particles and seeding for particle image velocimetry. *Meas. Sci. Technol.* 8, 1406–1416.
- Menon, A.S., Weber, M.E., Chang, H.K., 1984. Model study of flow dynamics in human central airways. 3. Oscillatory velocity profiles. *Respir. Physiol.* 55, 255–275.
- Miller, P.W., Long, N.J., Vilar, R., Gee, A.D., 2008. Synthesis of <sup>11</sup>C, <sup>18</sup>F, <sup>15</sup>O, and <sup>13</sup>N radiolabels for positron emission tomography. *Angew. Chem. Int. Ed.* 47, 8998–9033.
- Mills, P.H., Wu, Y.J., Ho, C., Ahrens, E.T., 2008. Sensitive and automated detection of iron-oxide-labeled cells using phase image cross-correlation analysis. *Magn. Reson. Imaging* 26, 618–628.
- Mirsadraee, S., van Beek, E.J.R., 2015. Functional imaging computed tomography and MRI. *Clin. Chest Med.* 36, 349–363.
- Mitchell, J., Bauer, R., Lyapustina, S., Tougas, T., Glaab, V., 2011. Non-impactor-based methods for sizing of aerosols emitted from orally inhaled and nasal drug products (OINDPs). *AAPS PharmSciTech* 12, 965.
- Moerer, O., Hahn, G., Quintel, M., 2011. Lung impedance measurements to monitor alveolar ventilation. *Curr. Opin. Crit. Care* 17, 260–267.
- Moller, H.E., Chen, X.J., Saam, B., Hagspiel, K.D., Johnson, G.A., Altes, T.A., de Lange, E.E., Kauczor, H.U., 2002. MRI of the lungs using hyperpolarized noble gases. *Magn. Reson. Med.* 47, 1029–1051.
- Morais, G.R., Paulo, A., Santos, I., 2012. Organometallic complexes for SPECT imaging and/or radionuclide therapy. *Organometallics* 31, 5693–5714.
- Morgan, K.S., Paganin, D.M., Siu, K.K.W., 2011. Quantitative single-exposure x-ray phase contrast imaging using a single attenuation grid. *Opt. Express* 19, 19781–19789.
- Morgan, K.S., Paganin, D.M., Siu, K.K.W., 2012. X-ray phase imaging with a paper analyzer. *Appl. Phys. Lett.* 100, 124102.
- Morgan, K.S., Donnelley, M., Farrow, N.R., Fouras, A., Yagi, N., Suzuki, Y., Takeuchi, A., Uesugi, K., Boucher, R.C., Siu, K.K.W., Parsons, D.W., 2014. *In Vivo* X-ray imaging reveals improved airway surface hydration after a therapy designed for cystic fibrosis. *Am. J. Respir. Crit. Care Med.* 190, 469–472.
- Morgan, K.S., Petersen, T.C., Donnelley, M., Farrow, N.R., Parsons, D.W., Paganin, D.M., 2016. Capturing and visualizing transient X-ray wavefront topological features by single-grid phase imaging. *Opt. Express* 24, 24435–24450.
- Mosbah, K., Ruiz-Cabello, J., Berthezene, Y., Cremillieux, Y., 2008. Aerosols and gaseous contrast agents for magnetic resonance imaging of the lung. *Contrast Media Mol. Imaging* 3, 173–190.
- Myojo, T., 1987. Deposition of fibrous aerosol in model bifurcating tubes. *J. Aerosol Sci.* 18, 337–347.
- Myojo, T., 1990. The effect of length and diameter on the deposition of fibrous aerosol in a model lung bifurcation. *J. Aerosol Sci.* 21, 651–659.
- Namat, E., Warger, W.C., Unglert, C.I., Eckert, J.E., Hostens, J., Bouma, B.E., Tearney, G.J., 2013. Four-dimensional visualization of subpleural alveolar dynamics *in vivo* during uninterrupted mechanical ventilation of living swine. *Biomed. Opt. Express* 4, 2492–2506.
- Negus, C.R., Drain, L.E., 1982. Mie calculations of the scattered-light from a spherical-particle traversing a fringe pattern produced by 2 intersecting laser-beams. *J. Phys. D. Appl. Phys.* 15, 375–402.
- Nemes, A., Jalal, S., Moortele, T.V.d., Coletti, F., 2016. In: Oscillatory flow in a human airway model: MRV and PIV. 18th International Symposium on the Application of Laser and Imaging Techniques to Fluid Mechanics, LISBON | PORTUGAL, JULY 4–7, 2016. pp. 345–354.
- Newman, S., Fleming, J., 2011. Challenges in assessing regional distribution of inhaled drug in the human lungs. *Expert Opin. Drug Deliv.* 8, 841–855.
- NIOSH, 1994. *Fibers, Method 7400 issue #2 (8/15/94)*, in NIOSH manual of analytical methods. In: N.I.F.O.S.a. (Ed.), Health. NIOSH, Cincinnati, USA.
- Nordlund, M., Belka, M., Kuczaj, A., Lizal, F., Jedelsky, J., Elcner, J., Jicha, M., Sausner, Y., Le Bouhellec, S., Cosandey, S., Majeed, S., Vuillaume, G., Peitsch, M., Hoeng, J., 2017. Multicomponent aerosol particle deposition in a realistic cast of the human upper respiratory tract. *Inhal. Toxicol.* 29 (3), 113–125.
- Oakes, J.M., Scadeng, M., Breen, E.C., Prisk, G.K., Darquenne, C., 2013. Regional distribution of aerosol deposition in rat lungs using magnetic resonance imaging. *Ann. Biomed. Eng.* 41, 967–978.
- Oldenburg, A.L., Blackmon, R.L., Sierchio, J.M., 2016. Magnetic and Plasmonic contrast agents in optical coherence tomography. *IEEE J. Sel. Top. Quantum Electron.* 22, 133–145.
- Oldham, M.J., 2006. Challenges in validating CFD-derived inhaled aerosol deposition predictions. *Inhal. Toxicol.* 18, 781–786.
- Olivo, A., Castelli, E., 2014. X-ray Phase Contrast Imaging: From Synchrotrons to Conventional Sources. *Rivista Del Nuovo Cimento*.
- Olivo, A., Speller, R., 2007. A coded-aperture technique allowing x-ray phase contrast imaging with conventional sources. *Appl. Phys. Lett.* 91, 074106.
- Olson, D.E., Sudlow, M.F., Horsfield, K., Filley, G.F., 1973. Convective patterns of flow during inspiration. *Arch. Intern. Med.* 131, 51–57.
- Olsson, B., Borgstrom, L., Lundback, H., Svensson, M., 2013. Validation of a general *in vitro* approach for prediction of total lung deposition in healthy adults for pharmaceutical inhalation products. *J. Aerosol Med. Pulm. Drug Deliv.* 26, 355–369.
- Or, D.Y.L., Karmakar, M.K., Lam, G.C.S., Hui, J.W.Y., Li, J.W., Chen, P.P., 2013. Multiplanar 3D ultrasound imaging to assess the anatomy of the upper airway and measure the subglottic and tracheal diameters in adults. *Brit. J. Radiol.* 86.
- Parsons, D.W., Morgan, K.S., Donnelley, M., Fouras, A., Crosbie, J., Williams, I., Boucher, R.C., Uesugi, K., Yagi, N., Siu, K.K.W., 2008. High-resolution visualization of airspace structures in intact mice *via* synchrotron phase-contrast X-ray imaging (PCXI). *J. Anat.* 213, 217–227.
- Paulus, D.H., Quick, H.H., 2016. Hybrid positron emission tomography/magnetic resonance imaging: challenges, methods, and state of the art of hardware component attenuation correction. *Investig. Radiol.* 51, 624–634.
- Peattie, R.A., Schwarz, W., 1998. Experimental investigation of oscillatory flow through a symmetrically bifurcating tube. *J. Biomech. Eng. Transac. ASME* 120, 584–593.
- Pépin, A., Daouk, J., Bailly, P., Hapdey, S., Meyer, M.E., 2014. Management of respiratory motion in PET/computed tomography: the state of the art. *Nucl. Med. Commun.* 35, 113–122.
- Pfeiffer, F., Weitkamp, T., Bunk, O., David, C., 2006. Phase retrieval and differential phase-contrast imaging with low-brilliance X-ray sources. *Nat. Phys.* 2, 258–261.
- Phalen, R.F., Yeh, H.-C., Raabe, O.G., Velasquez, D.J., 1973. Casting the lungs *in-situ*. *Anat. Rec.* 177, 255–263.
- Pratt, E.C., Shaffer, T.M., Grimm, J., 2016. Nanoparticles and radiotracers: advances toward radionanomedicine. *Wiley Interdiscip. Rev. Nanomed. Nanobiotechnol.* 8, 872–890.
- Prezado, Y., Vautrin, M., Martínez Rovira, I., Bravin, A., Estève, F., Elleaume, H., Berkvens, P., Adam, J.F., 2011. Dosimetry protocol for the forthcoming clinical trials in synchrotron stereotactic radiation therapy (SSRT). *Med. Phys.* 38, 1709–1717.
- Price, E.W., Orvig, C., 2014. Matching chelators to radiometals for radiopharmaceuticals. *Chem. Soc. Rev.* 43, 260–290.
- Prokop, R.M., Finlay, W.H., Stapleton, K.W., 1995. An *in-vitro* technique for calculating the regional dosages of drugs delivered by an ultrasonic nebulizer. *J. Aerosol Sci.* 26, 847–860.
- Quirk, B.C., McLaughlin, R.A., Pagnozzi, A.M., Kennedy, B.F., Noble, P.B., Sampson, D.D., 2014. Optofluidic needle probe integrating targeted delivery of fluid with optical coherence tomography imaging. *Opt. Lett.* 39, 2888–2891.
- Raabe, O.G., Yeh, H.C., Schum, G.M., Phalen, R.F., 1976. *Tracheobronchial Geometry: Human, dog, rat, Hamster*. Lovelace Foundation Report, Albuquerque, NM. <http://mae.ucdavis.edu/wexler/lungs/LF53-Raabe/>, Accessed date: 1 January 2010.
- Ramuzat, A., Riethmuller, M.L., 1997. In: Application of 2D Laser Doppler Velocimetry to biomedical flows experimental investigations of flows within lung bifurcations. 7th International Conference Laser Anemometry Advances and Applications, Karlsruhe, Germany.
- Ramuzat, A., Riethmuller, M.L., 2002. In: PIV investigations of oscillating flows with a 3D lung multiple bifurcation model. 11th Int. Symp. on Appl. of Laser Techniques to Fluid Flows. pp. 8–11.
- Ramuzat, A., Day, S., Riethmuller, M.L., 1998. In: Steady and unsteady LDV and PIV investigations of flow within 2D lung bifurcations model. 9th International Symposium on Applications of Laser Techniques to Fluid Mechanics, Lisbon, Portugal.
- Riera, J., Perez, P., Cortes, J., Roca, O., Masclans, J.R., Rello, J., 2013. Effect of high-flow nasal cannula and body position on end-expiratory lung volume: a cohort study using electrical impedance tomography. *Respir. Care* 58, 589–596.
- Robart, D., Breuer, S., Reckers, W., Kneer, R., 2001. Assessment of pulsed gasoline fuel sprays by means of qualitative and quantitative laser-based diagnostic methods. *Part. Part. Syst. Charact.* 18, 179–189.
- Roisman, I.V., Tropea, C., 2001. Flux measurements in sprays using phase Doppler techniques. *Atom. Spray* 11, 667–699.
- Roth, K.W., 1995. Deposition and Dispersion of Inertial Aerosols in Secondary and Turbulent Flow Structures. Mechanical Engineering. Massachusetts Institute of Technology.
- Roth, A.P., Lange, C.F., Finlay, W.H., 2003. The effect of breathing pattern on nebulizer drug delivery. *J. Aerosol Med.* 16, 325–339.
- Salmi, M., Paloheimo, K.S., Tuomi, J., Wolff, J., Makitie, A., 2013. Accuracy of medical models made by additive manufacturing (rapid manufacturing). *J. Cranio-Maxillofac. Surg.* 41, 603–609.
- Sankar, S.V., Weber, B.J., Kamemoto, D.Y., Bachalo, W.D., 1991. Sizing fine particles with the phase Doppler interferometric-technique. *Appl. Opt.* 30, 4914–4920.
- Santolaya, J.L., Garcia, J.A., Calvo, E., Cerecedo, L.M., 2013. Effects of droplet collision phenomena on the development of pressure swirl sprays. *Int. J. Multiphase Flow* 56, 160–171.
- Sarracanie, M., Grebenkov, D., Sandeau, J., Coulibaly, S., Martin, A.R., Hill, K., Perez Sanchez, J.M., Fodil, R., Martin, L., Durand, E., Caillibotte, G., Isabey, D., Darrasse, L., Bittoun, J., Maitre, X., 2015. Phase-contrast helium-3 MRI of aerosol deposition in human airways. *NMR Biomed.* 28, 180–187.
- Scarano, F., 2013. Tomographic PIV: principles and practice. *Meas. Sci. Technol.* 24, 012001.
- Schanz, D., Schröder, A., Gesemann, S., Michaelis, D., Wieneke, B., 2013. In: ‘Shake The Box’: a highly efficient and accurate Tomographic Particle Tracking Velocimetry (TOMO-PTV) method using prediction of particle positions. 10th International Symposium on Particle Image Velocimetry - PIV13. Delft, The Netherlands, July 1–3. pp. 1–13.
- Schanz, D., Schröder, A., Gesemann, S., 2014. In: ‘Shake The Box’ – a 4D PTV algorithm: accurate and ghostless reconstruction of Lagrangian tracks in densely seeded flows. 17th International Symposium on Applications of Laser Techniques to Fluid Mechanics. pp. 7–10.
- Scheuch, G., 1994. Particle recovery from human conducting airways after shallow aerosol bolus inhalation. *J. Aerosol Sci.* 25, 957–973.
- Scheuch, G., Stahlfhofen, W., Fang, C.P., Lippmann, M., 1993. 320 O2 Aerosol recovery after bolus inhalations into an airway cast. *J. Aerosol Sci.* 24 (Supplement 1), S355–S356.
- Schmidt, A., Zidowitz, S., Kriete, A., Denhard, T., Krass, S., Peitgen, H.O., 2004. A digital

- reference model of the human bronchial tree. *Comput. Med. Imaging Graph.* 28, 203–211.
- Schnabel, C., Gaertner, M., Kirsten, L., Meissner, S., Koch, E., 2013. Total liquid ventilation: a new approach to improve 3D OCT image quality of alveolar structures in lung tissue. *Opt. Express* 21, 31782–31788.
- Schott Medica GmbH, 2017. Precision glassware made by SCHOTT. [http://www.schott.com/d/uk/d5759008-05ec-4556-a60a-4b06e341fa54/1.0/precision\\_glass\\_rd326.pdf](http://www.schott.com/d/uk/d5759008-05ec-4556-a60a-4b06e341fa54/1.0/precision_glass_rd326.pdf).
- Schroter, R.C., Sudlow, M.F., 1969. Flow patterns in models of human bronchial airways. *Respir. Physiol.* 7, 341–355.
- Schröter, T.J., Koch, F.J., Meyer, P., Kunka, D., Meiser, J., Willer, K., Gromann, L., De Marco, F., Herzen, J., Noel, P., Yaroshenko, A., Hofmann, A., Pfeiffer, F., Mohr, J., 2017. Large field-of-view tiled grating structures for X-ray phase-contrast imaging. *Rev. Sci. Instrum.* 88, 015104.
- Sera, T., Yokota, H., Tanaka, G., Uesugi, K., Yagi, N., Schroter, R.C., 2013. Murine pulmonary acinar mechanics during quasi-static inflation using synchrotron refraction-enhanced computed tomography. *J. Appl. Physiol.* 115, 219–228.
- Snigirev, A., Snigireva, I., Kohn, V., Kuznetsov, S., Schelokov, I., 1998. On the possibilities of x-ray phase contrast microimaging by coherent high-energy synchrotron radiation. *Rev. Sci. Instrum.* 66, 5486–5492.
- Song, H.K., Dougherty, L., Schnell, M.D., 2001. Simultaneous acquisition of multiple resolution images for dynamic contrast enhanced imaging of the breast. *Magn. Reson. Med.* 46, 503–509.
- Sood, B.G., Shen, Y., Latif, Z., Chen, X., Sharp, J., Neelavalli, J., Joshi, A., Slovis, T.L., Haacke, E.M., 2008. Aerosol delivery in ventilated newborn pigs: an MRI evaluation. *Pediatr. Res.* 64, 159–164.
- Sood, B.G., Shen, Y., Latif, Z., Galli, B., Dawe, E.J., Haacke, E.M., 2010. Effective aerosol delivery during high-frequency ventilation in neonatal pigs. *Respirology* 15, 551–555.
- Sood, T., Pott, D., Klaas, M., Schröder, W., 2013. Analysis of basic flow regimes in a human airway model by stereo-scanning PIV. *Exp. Fluids* 54.
- Stahr, C.S., Samarage, C.R., Donnelley, M., Farrow, N.R., Morgan, K.S., Zosky, G., Boucher, R.C., Siu, K.K.W., Mall, M.A., Parsons, D.W., Dubsy, S., Fouras, A., 2016. Quantification of heterogeneity in lung disease with image-based pulmonary function testing. *Sci Rep* 6, 15.
- Stapleton, K.W., Guentsch, E., Hoskinson, M.K., Finlay, W.H., 2000. On the suitability of k-ε turbulence modeling for aerosol deposition in the mouth and throat: a comparison with experiment. *J. Aerosol Sci.* 31, 739–749.
- Stockhofe, K., Postema, J.M., Schieferstein, H., Ross, T.L., 2014. Radiolabeling of nanoparticles and polymers for PET imaging. *Pharmaceuticals* 7, 392–418.
- Su, W.C., Cheng, Y.S., 2005. Deposition of fiber in the human nasal airway. *Aerosol Sci. Technol.* 39, 888–901.
- Su, W.C., Cheng, Y.S., 2006. Deposition of fiber in a human airway replica. *J. Aerosol Sci.* 37, 1429–1441.
- Su, W.-C., Cheng, Y.S., 2015. Estimation of carbon nanotubes deposition in a human respiratory tract replica. *J. Aerosol Sci.* 79, 72–85.
- Su, W.C., Wu, J., Marjnisson, C.M., Cheng, Y.S., 2008. Deposition of man-made fibers in a human nasal airway. *Aerosol Sci. Technol.* 42, 173–181.
- Takeda, M., Ina, H., Kobayashi, S., 1982. Fourier-transform method of fringe-pattern analysis for computer-based topography and interferometry. *J. Opt. Soc. Am.* 72, 156–160.
- Tanaka, G., Ogata, T., Oka, K., Tanishita, K., 1999. Spatial and temporal variation of secondary flow during oscillatory flow in model human central airways. *J. Biomech. Eng. Transac. ASME* 121, 565–573.
- Tarran, R., Grubb, B.R., Parsons, D., Picher, M., Hirsh, A.J., Davis, C.W., Boucher, R.C., 2001. The CF salt controversy. *Mol. Cell* 8, 149–158.
- Taylor, P., Dudek, R., Flaherty, D., Kaempfe, T., 1994. Evaluation of two instruments for the measurement of aerosols. *J. Aerosol Sci.* 25, 419–423.
- te Pas, A.B., Siew, M.L.L., Wallace, M.J., Kitchen, M.J., Fouras, A., Lewis, R.A., Yagi, N., Uesugi, K., Donath, S., Davis, P.G., Morley, C.J., Hooper, S.B., 2009. Establishing functional residual capacity at birth: the effect of sustained inflation and positive end-expiratory pressure in a preterm rabbit model. *Pediatr. Res.* 65, 537–541.
- Tearney, G.J., Brezinski, M.E., Bouma, B.E., Boppart, S.A., Pitris, C., Southern, J.F., Fujimoto, J.G., 1997. *In vivo* endoscopic optical biopsy with optical coherence tomography. *Science* 276, 2037–2039.
- Theunissen, R., Riethmuller, M.L., 2008. Particle image velocimetry in lung bifurcation models. In: *Particle Image Velocimetry: New Developments and Recent Applications*. Vol. 112. pp. 73–101.
- Thompson, R.B., Finlay, W.H., 2012. Using MRI to measure aerosol deposition. *J. Aerosol Med. Pulm. Drug Deliv.* 25, 55–62.
- Tropea, C., Yarin, A.L., Foss, J.F., 2007. *Springer Handbook of Experimental Fluid Mechanics*. Springer, Berlin.
- Tu, J., Inthavong, K., Ahmadi, G., 2013. Computational fluid and particle dynamics in the human respiratory system, Biological and medical physics. In: *Biomedical Engineering*. Springer, Dordrecht; New York, pp. 1 (Online resource).
- Urbán, A., Zaremba, M., Malý, M., Józsa, V., Jedelský, J., 2017. Droplet dynamics and size characterization of high-velocity airstream atomization. *Int. J. Multiphase Flow* 95, 1–11.
- Vakoc, B.J., Shishko, M., Yun, S.H., Oh, W.Y., Suter, M.J., Desjardins, A.E., Evans, J.A., Nishioka, N.S., Tearney, G.J., Bouma, B.E., 2007. Comprehensive esophageal microscopy by using optical frequency-domain imaging (with video). *Gastrointest. Endosc.* 65, 898–905.
- Vakoc, B.J., Lanning, R.M., Tyrrell, J.A., Padera, T.P., Bartlett, L.A., Stylianopoulos, T., Munn, L.L., Tearney, G.J., Fukumura, D., Jain, R.K., Bouma, B.E., 2009. Three-dimensional microscopy of the tumor microenvironment *in vivo* using optical frequency domain imaging. *Nat. Med.* 15, 1219–1223.
- van Beek, E.J., Wild, J.M., Kauczor, H.U., Schreiber, W., Mugler 3rd, J.P., de Lange, E.E., 2004. Functional MRI of the lung using hyperpolarized 3-helium gas. *J. Magn. Reson. Imaging* 20, 540–554.
- Verbanck, S., Gonzalez Mangado, N., Peces-Barba, G., Paiva, M., 1991. Multiple-breath washout experiments in rat lungs. *J. Appl. Physiol.* 71, 847–854 (1985).
- Verbanck, S., Darquenne, C., Prisk, G.K., Vincken, W., Paiva, M., 1999. A source of experimental underestimation of aerosol bolus deposition. *J. Appl. Physiol.* 86, 1067–1074.
- Verbanck, S., Schuermans, D.L., Paiva, M., Vincken, W., 2001a. Saline aerosol bolus dispersion. II. The effect of conductive airway alteration. *J. Appl. Physiol.* 90, 1763–1769.
- Verbanck, S., Schuermans, D.L., Vincken, W., Paiva, M., 2001b. Saline aerosol bolus dispersion. I. The effect of acinar airway alteration. *J. Appl. Physiol.* 90, 1754–1762.
- Verbanck, S., Ghorbaniasl, G., Biddiscombe, M.F., Dragojlovic, D., Ricks, N., Lator, C., Ilsen, B., de Mey, J., Schuermans, D., Underwood, S.R., Barnes, P.J., Vincken, W., Usmani, O.S., 2016. Inhaled aerosol distribution in human airways: a scintigraphy-guided study in a 3D printed model. *J. Aerosol Med. Pulm. Drug Deliv.* 29, 525–533.
- Versar Inc., 1988. *Current and Suggested Practices in the Validation of Exposure Assessment Models*. Office of Health and Environmental Assessment. United States Environmental Protection Agency, Washington DC, USA.
- Walker, P.S., Conway, J.H., Fleming, J.S., Bondesson, E., Borgström, L., 2001. Pulmonary clearance rate of two chemically different forms of inhaled pertechnetate. *J. Aerosol Med.* 14, 209–215.
- Walther, J., Koch, E., 2009. Transverse motion as a source of noise and reduced correlation of the Doppler phase shift in spectral domain OCT. *Opt. Express* 17, 19698–19713.
- Wang, Z., Hopke, P.K., Ahmadi, G., Cheng, Y.S., Baron, P.A., 2008. Fibrous particle deposition in human nasal passage: the influence of particle length, flow rate, and geometry of nasal airway. *J. Aerosol Sci.* 39, 1040–1054.
- Wang, H., Sebric, C., Ruaud, J.P., Guillot, G., Bouazzizi-Verdier, K., Willoquet, G., Maitre, X., Darrasse, L., de Rochefort, L., 2016. Aerosol deposition in the lungs of spontaneously breathing rats using Gd-DOTA-based contrast agents and ultra-short echo time MRI at 1.5 tesla. *Magn. Reson. Med.* 75, 594–605.
- Weibel, E.R., 1963. *Morphometry of the Human Lung*. Springer-Verlag.
- Wen, H.H., Bennett, E.E., Kopace, R., Stein, A.F., Pai, V., 2010. Single-shot x-ray differential phase-contrast and diffraction imaging using two-dimensional transmission gratings. *Opt. Lett.* 35, 1932–1934.
- Westnate, M.W., Betz, O., Blob, R.W., Fezzaa, K., Cooper, W.J., Lee, W.-K., 2003. Tracheal respiration in insects visualized with synchrotron X-ray imaging. *Science* 299, 558–560.
- WHO, 1997. *Determination of Airborne Fibre Number Concentrations. A Recommended Method by Phase-Contrast Optical Microscopy (Membrane Filter Method)*. WHO, Geneva, pp. 53.
- Widmann, J.F., Presser, C., Leigh, S.D., 2001. Improving phase Doppler volume flow measurements in low data rate applications. *Meas. Sci. Technol.* 12, 1180–1190.
- Wieneke, B., 2008. Volume self-calibration for 3D particle image velocimetry. *Exp. Fluids* 45, 549–556.
- Wieser, W., Biedermann, B.R., Klein, T., Eigenwillig, C.M., Huber, R., 2010. Multi-megahertz OCT: high quality 3D imaging at 20 million A-scans and 4.5 GVoxels per second. *Opt. Express* 18, 14685–14704.
- Wijesundara, K., Zdanski, C., Kimbell, J., Price, H., Iftimia, N., Oldenburg, A.L., 2014. Quantitative upper airway endoscopy with swept-source anatomical optical coherence tomography. *Biomed. Opt. Express* 5, 788–799.
- Wilkins, S.W., Nesterov, Y.I., Gureyev, T.E., Mayo, S.C., Pogany, A., Stevenson, A.W., 2014. On the evolution and relative merits of hard X-ray phase-contrast imaging methods. *Philos. Trans. R. Soc. A Math. Phys. Eng. Sci.* 372, 20130021.
- Yang, Y., Whiteman, S., van Pittius, D.G., He, Y.H., Wang, R.K.K., Spiteri, M.A., 2004. Use of optical coherence tomography in delineating airways microstructure: comparison of OCT images to histopathological sections. *Phys. Med. Biol.* 49, 1247–1255.
- Yap, Y.L., Tan, Y.S.E., Tan, H.K.J., Peh, Z.K., Low, X.Y., Yeong, W.Y., Tan, C.S.H., Laude, A., 2017. 3D printed bio-models for medical applications. *Rapid Prototyp. J.* 23, 227–235.
- Yaroshenko, A., Hellbach, K., Yildirim, A.Ö., Conlon, T.M., Fernandez, I.E., Bech, M., Velroyen, A., Meinel, F.G., Auweter, S., Reiser, M., Eickelberg, O., Pfeiffer, F., 2015. Improved *in vivo* assessment of pulmonary fibrosis in mice using X-ray dark-field radiography. *Sci Rep* 5, 17492.
- Zernike, F., 1942. Phase contrast, a new method for the microscopic observation of transparent objects. *Physica* 9, 686–698.
- Zhang, Z., 2010. *LDA Application Methods Laser Doppler Anemometry for Fluid Dynamics*, Experimental Fluid Mechanics. Springer, Berlin; London.
- Zhang, Y., Finlay, W.H., 2005. Experimental measurements of particle deposition in three proximal lung bifurcation models with an idealized mouth-throat. *J. Aerosol Med.* 18, 460–473.
- Zhao, Y., Lieber, B.B., 1994a. Steady expiratory flow in a model symmetric bifurcation. *J. Biomech. Eng.* 116, 318–323.
- Zhao, Y., Lieber, B.B., 1994b. Steady inspiratory flow in a model symmetric bifurcation. *J. Biomech. Eng.* 116, 488–496.
- Zhou, Y., Cheng, Y.S., 2000. Particle deposition in first three generations of a human lung cast. *J. Aerosol Sci.* 31 (Supplement 1), 140–141.
- Zhou, Y., Su, W.C., Cheng, Y.S., 2007. Fiber deposition in the tracheobronchial region: experimental measurements. *Inhal. Toxicol.* 19, 1071–1078.
- Zwartz, G.J., Guilmette, R.A., 2001. Effect of flow rate on particle deposition in a replica of a human nasal airway. *Inhal. Toxicol.* 13, 109–127.

# A method for in vitro regional aerosol deposition measurement in a model of the human tracheobronchial tree by the positron emission tomography

Proc IMechE Part H:  
*J Engineering in Medicine*  
2015, Vol. 229(10) 750–757  
© IMechE 2015  
Reprints and permissions:  
sagepub.co.uk/journalsPermissions.nav  
DOI: 10.1177/0954411915600005  
pih.sagepub.com  


Frantisek Lizal<sup>1</sup>, Miloslav Belka<sup>1</sup>, Jan Adam<sup>2,3</sup>, Jan Jedelsky<sup>1</sup> and Miroslav Jicha<sup>1</sup>

## Abstract

Researchers have been studying aerosol transport in human lungs for some decades. The overall lung deposition can be predicted with sufficient precision nowadays. However, the prediction of local deposition remains an unsolved problem. Numerical modeling of aerosol transport can provide detailed data with such precision and spatial resolution which were unavailable in the past. Yet, the necessary validation of numerical results represents a difficult task, as the experimental data in a sufficient spatial resolution are hardly available. This article introduces a method based on positron emission tomography, which allows acquisition of detailed experimental data on local aerosol deposition in a realistic model of human lungs. The method utilizes the Condensation Monodisperse Aerosol Generator modified for a safe production of radioactive aerosol particles and a special measuring rig. The scanning of the model is performed on a positron emission tomography–computed tomography scanner. The evaluation of aerosol deposition is based on a volume radioactivity analysis in a specialized, yet publicly available software. The reliability of the method was tested and its first results are discussed in the article. The measurements performed using the presented method can serve for validation of numerical simulations, since the presented lung model digital geometry is available.

## Keywords

Aerosol, aerosol deposition, positron emission tomography, targeted drug delivery

Date received: 15 April 2015; accepted: 20 July 2015

## Introduction

The study of deposition of inhaled particles in human lungs has been going on for some decades. Despite this effort, the potential of inhalation therapy is not fully utilized. Especially, a targeted delivery to specific regions of the lungs remains a challenge for scientists.<sup>1</sup> At the same time, the harmful effects of localized deposition of pollutants and its effect on cancer development are not fully understood.<sup>2</sup> It is partially caused by the fact that until now, detailed regional and local deposition data for precisely defined lung geometry and the corresponding boundary conditions are not easily available. However, comprehension of local deposition can lead to significantly improved health, for it is expected that local inhomogeneities and formation of deposition “hot spots” contribute to the selective occurrence of bronchial carcinoma.<sup>3</sup> The development of the computational fluid dynamics (CFD) promises to bring deeper understanding to the flow mechanics as well as

aerosol deposition in human lungs.<sup>2</sup> Yet, the validation of numerically acquired results remains a difficult challenge, considering that the experimental data of sufficient resolution and quality are rarely available for the identical lung geometry. Recently, studies from Zhang and Finlay<sup>4</sup> or Borojeni et al.<sup>5</sup> have been published, where in vitro methods were used to measure particle deposition in realistic models of conducting airways of children and adults. However, as Longest and

<sup>1</sup>Department of Thermodynamics and Environmental Engineering, Faculty of Mechanical Engineering, Brno University of Technology, Brno, Czech Republic

<sup>2</sup>Division of Radiopharmaceuticals, UJV Rez a.s., Husinec, Czech Republic

<sup>3</sup>Masaryk Memorial Cancer Institute, Brno, Czech Republic

### Corresponding author:

Frantisek Lizal, Department of Thermodynamics and Environmental Engineering, Faculty of Mechanical Engineering, Brno University of Technology, Technicka 2, Brno 61669, Czech Republic.  
Email: lizal@fme.vutbr.cz

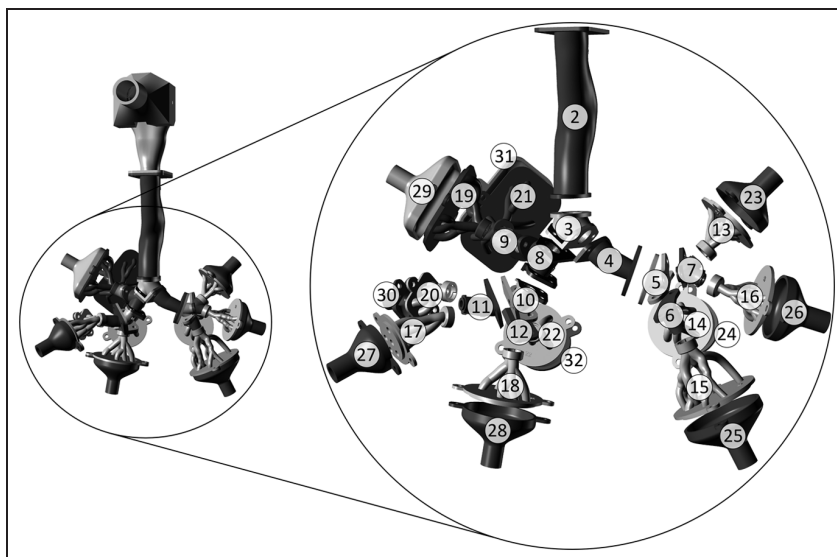


**Figure 1.** Realistic lung model (external model geometry).

Holbrook<sup>6</sup> emphasized, improved experimental data sets are needed to better validate computational predictions in local regions of the lungs.

Validation can be performed either *in vivo* or *in vitro* using radiological imaging methods. Although it is clear that *in vivo* measurements have irreplaceable role as they describe the real state, *in vitro* methods have certain advantages. They can be performed on the geometry identical to the numerical simulation and they also provide better spatial resolution of data due to higher applicable doses of radioactivity.

Two-dimensional gamma scintigraphy was the first method applied to aerosol deposition measurements. This method is, however, limited in its potential to image specific regions: only information regarding deposition in the tracheobronchial (TB) and alveolar regions can be obtained even in the best configuration.<sup>7</sup> More precise and detailed results can be obtained using single photon emission computed tomography (SPECT) and positron emission tomography (PET) methods, which are capable of three-dimensional imaging.<sup>8</sup> The PET method provides the best spatial resolution. In addition to local deposition in the various sections, the deposition hot spots can also be evaluated. However, in comparison to the PET methodology, which is routinely applied to clinical examination, using this method in the *in vitro* design requires major modifications both in the aerosol preparation and, in particular, in the experiment evaluation approach. The method, based on PET and fulfilling the above-mentioned criteria, is presented in this article.

## Experimental setup

### *Respiratory tract model and the aerosol deposition measurement procedure*

First of all, a suitable realistic model of the respiratory tract had to be set up. A realistic model of human lungs

whose manufacture and properties have been described in Lizal et al.<sup>9</sup> was developed and used for measurements. The model includes the oral cavity and the following seven generations of TB tree branching (the TB is nonsymmetrical and the left and right sides of the tree are different). The model has 10 terminal endings, see Figure 1.

The oral portion of the model was acquired from Lovelace Respiratory Research Institute (Albuquerque, NM, USA) and its dimensions were published by Cheng et al.<sup>10</sup> The anterior oral cavity was molded from *in vivo* dental impression of a living Caucasian male in approximately 50% of the full opening. The TB airways geometry comes from a high-resolution CT of the lungs of an adult male free of pathological alterations, excised at autopsy and fixed in nearly end-inspiratory volume as published by Schmidt et al.<sup>11</sup>

The original (inner) geometry was transformed into the stereolithographic (STL) format and imported into Rhinoceros 4.0 computer-aided design (CAD) system (McNeel, Seattle, WA, USA), where a 3-mm-thick envelope around the airways was created. The model was also divided into sections to facilitate the measurement of aerosol deposition by traditional methods, such as optical microscopy or gravimetry. The terminal bronchi of the model (seventh generation of branching with diameter less than 3 mm) were connected to 10 outlets (see Figure 1). The model was fabricated by stereolithography (Viper; 3D Systems Rock Hill, SC, USA) using Somos® WaterShed XC 11122 material (DSM, Heerlen, the Netherlands). The built layer capability is 20  $\mu\text{m}$ , the vertical resolution is 25  $\mu\text{m}$  and the position repeatability is 7.6  $\mu\text{m}$ .

It is a common practice to coat the inner surface of the model, especially when using solid particles. Since we used liquid di-2-ethyl hexyl sebacate (DEHS) particles, we did not need to coat the inner surface of the model to prevent the bounce of the particles hitting the surface. Another reason for the coating usage can be in

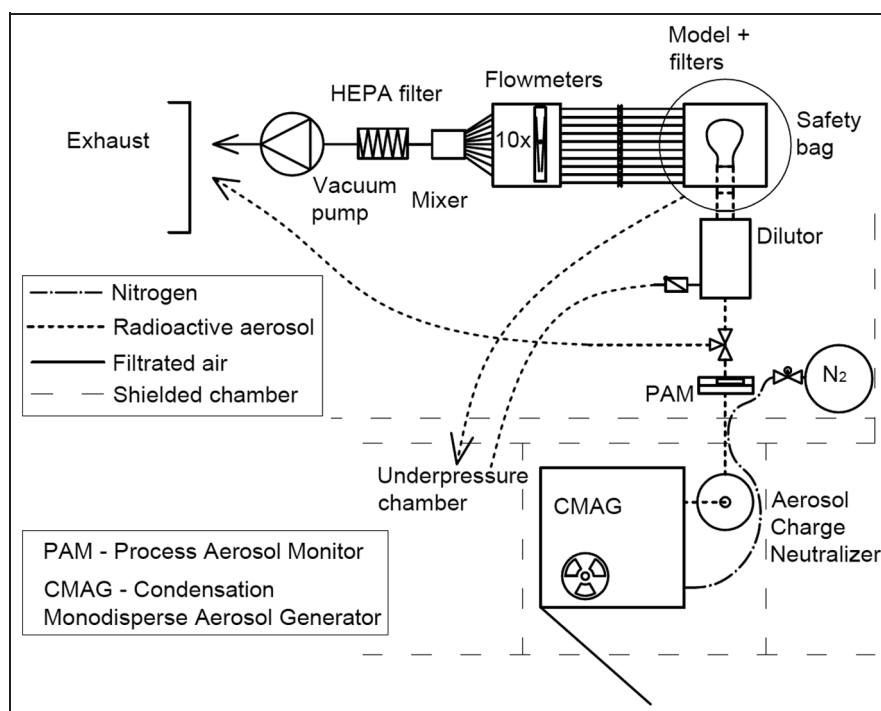


**Figure 2.** Layout of the experimental setup.

an effort to prevent surface wetting. In our case, the exposure time was short (5–15 min) and only small amounts of DEHS deposited on the walls; therefore, the possible flooding of the surface was not an issue.

Aerosol particles were generated by a TSI 3475 Condensation Monodisperse Aerosol Generator (CMAG) from TSI, Inc., Shoreview, MN, USA which works on the controlled heterogeneous condensation principle. Vapors of a suitable material, specifically DEHS, condense by a controlled method on small sodium chloride particles serving as the condensation nuclei. The advantage of DEHS is that it is not hydrophilic and does not evaporate resulting in a constant size of generated particles. In a standard operating mode, the generator can produce particles with aerodynamic diameters within the 0.1–8  $\mu\text{m}$  range. The density of DEHS used for the experiments was 0.914 g/cm<sup>3</sup> at 25 °C.

Radioactive aerosol particles were needed for the PET measurement of deposition. Therefore, the solution in the atomizer of the generator had to be tagged by a suitable radioactive substance. Fluorine 18 was the logical choice of the positron emitter, being easily available at the cooperating PET center and possessing a suitable half-life (109 min).

A solution of fluorine 18 in the form of fluoride ions was prepared by irradiation of H<sub>2</sub><sup>18</sup>O enriched water on an IBA Cyclone 18/9 (IBA, Louvain-La-Neuve, Belgium) cyclotron (irradiation time 25 min, integrated irradiation current 11  $\mu\text{A h}$ ) at the UJV Rez's PET Centre in Brno. The irradiated water was transferred by a capillary transport system to a shielded dispensing box, where the fluorine 18 ions were captured on an ion-exchange resin (AG1-X8; BioRad, Hercules, CA, USA) column and subsequently eluted with 300 mL

of 10% sodium chloride solution, followed by 1 mL of water for injection. The resulting solution was repeatedly diluted with water for injection until the desired initial radioactivity was achieved.

The CMAG was modified for the deposition measurement by using PET so that the atomizer vessel was accommodated in a protective lead container to shield off ionizing radiation. The atomizer was filled with a sodium chloride solution containing <sup>18</sup>F at an initial activity of 2.5 GBq. The concentration of sodium chloride solution was 20 mg/L. The experimental rig is shown in Figure 2.

The generated aerosol was fed through a <sup>85</sup>Kr-based NEKR-10 charge equilibrater (Eckert & Ziegler Cesio, Praha, Czech Republic) to a PAM aerosol monitor (TSI 3375, TSI, Inc., Shoreview, MN, USA) for continuous particle size and concentration measurement. The operation and precision of the aerosol monitor were validated using aerodynamic particle sizer (APS) TSI 3321. The validation was performed prior to the experiment using the identical setup, apart from adding the radioactive substance into the atomizer. The size of the particles generated by CMAG was adjusted according to APS and the size displayed by the aerosol monitor was recorded. Subsequently, during the experiment, only the radioactive substance was added to the atomizer and the particles of the same size were produced. Usually, only a small correction of saturator flow was needed at the beginning of the experiments. Only one size of the particles was measured during 1 day; therefore, no further adjustments of the generator were needed. The aerosol monitor served as an on-line indication that the process of aerosol generation is stable. It was easily accomplished, as the exposure of the model to the aerosol took only 5–15 min.



**Figure 3.** A photograph of the model in a box before the connection of hoses to flow meters.

Filters Millipore AP40 (Merck Millipore, Darmstadt, Germany) consisting of glass fibers were attached to the output branches of the respiratory tract model. The entire system (Figure 3) was enclosed in a plastic bag which was kept in a vacuum to prevent the active aerosol from leaking into the laboratory. All the 10 terminal branches with flow meters for flow rate control were combined into one branch with a protective high efficiency particulate air (HEPA) filter. The vacuum was generated with a Busch R 5 PA 0008 C (Busch, Maulburg, Germany) rotary oil vacuum pump. The flow distribution in each section of the model is provided in Table 1.

The whole exposure of the model to the aerosol was performed in a shielded laboratory with an underpressure ventilating system, which would prevent the aerosol from escaping the room in case of a primary safety system failure. The laboratory personnel were not present in the laboratory during the exposure, with the exception of the regular instrument supervision. Whenever they had to enter the laboratory, they wore half mask respirators.

The experiments were performed in a steady-state inhalation mode with the flow rates of 15, 30 and 60 L/min. Liquid monodisperse particles with mass median aerodynamic diameter of 2.5 and 4.3  $\mu\text{m}$  were used. The standard geometric deviation of size was less than 1.24 for all measured regimes. The models were exposed for 10–15 min depending on radioactivity decrease by radionuclide decay. The peak activity in the models was

**Table 1.** Flow rates through individual sections of the model.

Identification of section	Flow rate (L/min)		
1	15.0	30.0	60.0
2	15.0	30.0	60.0
3	15.0	30.0	60.0
4	4.5	8.9	17.8
5	4.5	8.9	17.8
6	2.8	5.6	11.2
7	1.7	3.3	6.6
8	10.6	21.1	42.2
9	3.4	6.9	13.7
10	7.1	14.3	28.5
11	3.3	6.7	13.3
12	3.8	7.6	15.2
13	0.7	1.4	2.8
14	0.8	1.6	3.2
15	2.0	4.0	8.0
16	1.0	1.9	3.8
17	1.8	3.6	7.1
18	2.3	4.7	9.3
19	1.9	3.8	7.6
20	1.6	3.1	6.2
21	1.5	3.1	6.1
22	1.5	3.0	5.9
Total flow rate	15	30	60

4–60 Bq/cm<sup>2</sup> (depending on the particle size and concentration, measuring mode and model used), as measured with an RP-2000 portable contamination meter (VF, a.s., Cerna Hora, Czech Republic).

#### *Deposited activity evaluation method*

The model was transported to a Siemens Biograph 64 Truepoint (Siemens Medical Solutions, Malvern, PA, USA) PET-CT scanner immediately after the radioactive exposure. The transportation took approximately 3 min. The PET-CT scanner acquired first CT images, which were promptly followed by PET images. Both the CT and PET images could be attributed unambiguously to the given geometry, due to the assigned geometrical coordinates. The CT images are important for a precise localization of the edges of the sections, whereas the PET images contain the essential information about aerosol deposition.

The CT and PET images were imported into Carimas 2.4, ver. 2.2.44.7002 SW<sup>12</sup> (Turku PET Centre, Turku, Finland) with the CT images as the main images and the PET images as background images. The software Carimas is a medical image processing tool, which was developed primarily for analysis of PET images at Turku PET Centre in Finland and is available as a free-ware for non-commercial use from: <http://www.turkupetcentre.fi/carimas/download/>. Carimas was developed in an “interactive data language” (IDL) and it runs on IDL Virtual Machine™ (Exelis Visual Information Solutions, Inc., Boulder, CO, USA), a cross-platform utility for running IDL code. It supports multiple input formats (DICOM, ECAT, Analyse, Interfile, Nifti, Interfile, MicroPET) and general bitmap formats (JPG,

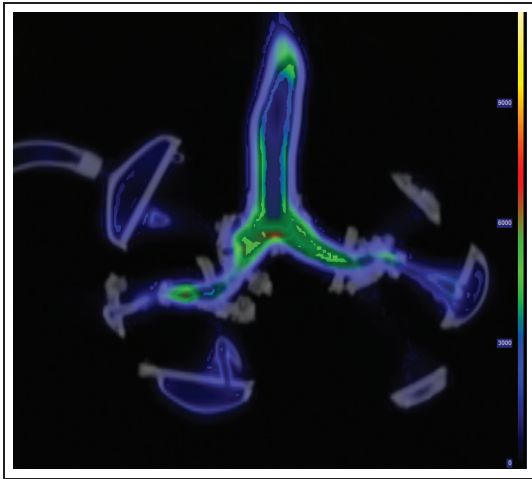


Figure 4. CT and PET image presentation in Carimas software.

TIFF, PNG and BMP). Researchers can perform visualization, segmentation, statistical analysis or modeling of PET data. It is possible to perform the image fusion, that is, to coregistrate PET and CT or magnetic resonance (MR) images. Users can define a volume of interest (VOI) and, using the static image analysis, they can calculate the mean activity in the VOI (in units of the PET image), standard deviation, minimal and maximal values, the number of voxels analyzed and the volume of the region. The software was tested and compared to commercial tools with an excellent agreement as documented by Nesterov et al.<sup>13</sup> and Harms et al.<sup>14</sup> To facilitate the identification of the hot spots in the Carimas software, the BGRY color system was used to display the PET images and the system range was reduced so that the hot spots were clearly seen in the model sections (Figure 4).

The sections of the model were marked as VOIs, and the mean volume activity (in Bq/mL) was evaluated using the Carimas software. Each section was enveloped in an independent VOI. A cylinder or a sphere was selected as the starting shape of the VOI, depending on the shape of the sections. First, the starting shape of the VOI was positioned and shaped as a whole to attain a suitable orientation and an adequate size. In the next step, each VOI was shaped in the vertex mode for a local mesh adjustment, so that the VOI surrounded the section with an overreach, while preventing an overlap of different VOIs. If the latter was not avoided, the observed activity would be attributed to both VOIs, resulting in biased results. The degree of mesh density can be modified by reducing the number of nodes or by enlarging or shrinking the mesh.

With regard to the PET precision, a VOI should optimally overreach the section by roughly 5 mm on all sides to cover all the radiation emitted from the section. However, due to the complex lung geometry, it was impossible to form all the VOIs with such a large overreach, and so the uncounted radioactivity was accounted for in a correction VOI. Two additional

VOIs had to be created to determine the magnitude of the correction: a VOI for the top part of the box, accommodating the model with the hoses, and a correction VOI for the bottom part of the box, accommodating the filters downstream of the terminal branches. They encompass the large top space with the model and the bottom space between the two horizontal partitions, respectively, in Figure 3. Two separate corrections were needed for the model and filters, because the difference in volume radioactivity is in few orders of magnitude, and therefore, it is necessary to assign the uncounted radioactivity to its real source. It is essential to preserve the true ratio of the radiation deposited in model sections and on filters.

The correction factor for the sections was calculated as the ratio of the total activity obtained from the VOI encompassing the whole model to the activity obtained by summing up the section VOIs. Similarly, the correction factor for the filters was calculated as the ratio of the total activity of the large VOI encompassing all the filters to the sum of the activities of the filter VOIs.

The corrections for the model sections ( $Corr_m$ ) and the filters ( $Corr_f$ ) were calculated as follows

$$Corr_m = \frac{A_{cm}}{\sum_1^n A_i} \quad (1)$$

$$Corr_f = \frac{A_{cf}}{\sum_1^p A_j} \quad (2)$$

where  $A_i$  and  $A_j$  are the activities measured in the model sections and on the filters, respectively, and  $A_{cm}$  and  $A_{cf}$  are the activities measured in the correction VOI for the model and filters, respectively.

We assume that the distribution of uncounted radioactivity is proportional to the measured activity in the sections of the model. The higher the activity measured in the filter, the higher the activity spread around the section. Therefore, the uncounted activity is to be accounted for by the sections proportionally to their measured activity. The correction formula then is simply

$$A_i^* = Corr_m \cdot A_i \quad (3)$$

$$A_j^* = Corr_f \cdot A_j \quad (4)$$

The asterisk (\*) indicates that the data have been corrected.

The magnitude of the correction factor can also be regarded as a model tightness indicator. If the model was not tight enough and some aerosol leaked beyond the model, the amount of aerosol in the correction VOI would be appreciably higher than in the sections; also, the calculated correction factor would be higher. The correction factors for the model sections and the filters lie largely within the ranges of 1.0–1.2 and 1.0–1.1, respectively. Aerosol leaks should be suspected if these ranges were exceeded.

The VOIs created can be saved in VRML (Virtual Reality Modeling Language) format in the Carimas software and imported to another model. Therefore, the same set of VOIs was used for the analysis of all models.

The corrected activities served to calculate the deposition fractions (DFs) for two aerosol particle sizes. (DF is defined as the ratio of inhaled particles deposited in the lungs section  $A_i^*$  to the total number of particles entering the lungs.) The total amount of aerosol was calculated as the sum of activities in the model, in the output sections, in the connection hoses and on the filters. The observed activity is assumed to be directly proportional to the number of deposited particles. This is based on the fact that the radioactive atoms are dispersed uniformly in the constantly stirred atomizer, and that each particle generated contains a nucleus of the same size, on which DEHS has condensed

$$DF_i = \frac{A_i^*}{\sum_i^n A_i^*} \quad (5)$$

where  $n$  is the total number of all sections including the hoses and filters.

### Sources of error in PET imaging

The quality of the images obtained with PET is affected by the following parameters: the spatial resolution, sensitivity, noise, scattered radiation and contrast. The parameters are interrelated, thus any efforts to reduce the effect of one parameter often result in an increased effect of another parameter.<sup>15</sup> The accuracy of determining of the deposition point for a specific particle is related to the attainable spatial resolution of the PET scanner. The resolution is affected by the detector size, positron range, noncolinearity, reconstruction method and localization of the detectors:

The actual spatial resolution of a particular PET scanner is measured by the standardized method recommended by the National Electrical Manufacturers Association (NEMA).<sup>16</sup> The full width at half maximum (FWHM) is the quantity serving as the measure of resolution. This quantity can be understood as the magnitude of point source “blurring” in the photograph or as the shortest distance at which two point sources

can be discerned as such. The spatial resolutions (based on NEMA<sup>16</sup>) for the PET Siemens Biograph 64 system are listed in Table 2.

The remaining parameters of our PET scanner were as follows: the sensitivity 4.2 cps/kBq, noise equivalent count rate 96 kcps at 35 kBq/cm<sup>3</sup> and scatter fraction < 38%.

*Inter-person variability.* To assess the error connected to the analysis of images, in particular to the definition of VOIs, the whole process, beginning with forming the VOIs, was performed by two technicians independently and their results were compared. The average of the differences between corresponding sections was 3% of the average value of the calculated radioactivity. More experiments should be performed to calculate the actual uncertainty of the whole method, but the above-mentioned test confirmed that even if the VOIs were formed independently by two different individuals, their results were in close agreement.

*Validation of the method.* The experimental setup and deposition measuring technique were validated by optical microscopy. Nickel-coated particles (M-18-Ni; Cospheric, Santa Barbara, CA, USA) with Mass mean aerodynamic diameter (MMAD) 14.1  $\mu\text{m}$  were dispersed by the Small Scale Powder Disperser TSI 3433 (TSI, Inc., Shoreview, MN, USA) and deposited in the model. The model was disassembled and the particles were rinsed out of each section using ultrasonic bath. The particles were then filtered out and counted using optical microscopy. The results were consistent with the results acquired by PET. However, the presented PET method is capable of achieving a significantly higher spatial resolution. Therefore, more detailed data on local deposition can be obtained, as the size of VOIs can be smaller than the size of the sections of the model and is limited only by the spatial resolution of the PET scanner, in our case 5 mm. The agreement between the results acquired through the presented PET method and the previously published data will be documented in the next chapter.

## Results

The proposed method was used to evaluate the deposition of particles of 2.5 and 4.3  $\mu\text{m}$  in size by applying a steady-state inhalation mode with flow rates of 15, 30 and 60 L/min. The measurement for 60 L/min was made in duplicate. The DF difference between the two measurements was calculated for each section, and the observed difference within the repeated measurements was drawn in the plot in the form of error lines as the estimate of measurement variability.

The plot in Figure 5 demonstrates that the majority of particles were deposited in the oral cavity and in the trachea in all the applied variants. A comparison of the regimes shows that the amount of deposited particles increases with their increasing momentum, which confirms that inertial impaction was the dominant

**Table 2.** Spatial resolution of the PET scanner used for experiments.<sup>17</sup>

	Average resolution (mm)
Transaxial resolution	
FWHM at 1 cm	4.2
FWHM at 10 cm	4.8
Axial resolution	
FWHM at 1 cm	4.7
FWHM at 10 cm	5.7

FWHM: full width at half maximum.

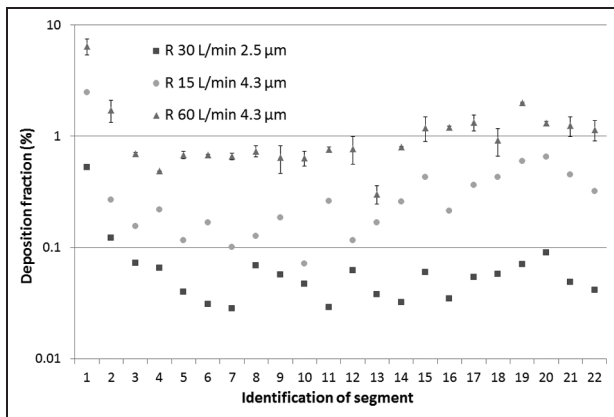


**Figure 5.** Results obtained by measurements on a realistic model applying three breathing regimes and using three different sizes of particles (section identification numbers are presented in Figure 1). Error bars indicate the difference between two measurements performed on two separate, but geometrically identical models. Measurements for 15 and 30 L/min were performed just once.

deposition mechanism in our case. The results demonstrate that the in vitro deposition measurement method based on the PET technique enables the DF to be evaluated with adequate precision for distinguishing the effects of the particle size and the breathing regime.

In the following step, a comparison with previously published data was performed. Few studies presenting in vitro measured local aerosol deposition in TB airways have been published in the past years. The most suitable for comparison with our data were the results acquired by Zhou and Cheng<sup>18</sup> and Chan and Lippmann,<sup>19</sup> as they both used realistic lung casts. However, their models had less generations of branching (four and six, respectively) compared to our model. The comparison of deposition efficiency (DE) defined as the ratio of the number of particles deposited in the section to the number of particles entering the section showed close agreement with both the studies mentioned above (see Figure 6). The practical calculation of DE was performed as a ratio of corrected activity in the examined section to the sum of activities in all downstream sections including filters and hoses, and the activity in the examined section

$$DE_i = \frac{A_i^*}{\sum A_j^* + A_i^*} \quad (6)$$

where  $A_j^*$  is the corrected activity in the section downstream of the  $i$ th section.

DE was plotted as a function of Stokes number defined as

$$Stk = \frac{\rho d_p^2 U}{18\mu D} \quad (7)$$

where  $d_p$  ( $\mu\text{m}$ ) is the aerodynamic diameter of a particle,  $U$  (m/s) is the velocity,  $\mu$  (Pa s) is the viscosity of air and  $D$  (m) is the characteristic diameter (of the

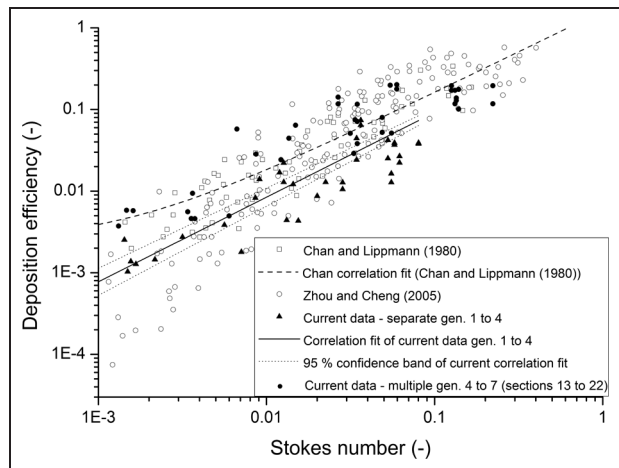


**Figure 6.** Comparison of the current results with previously published experimental data (symbols) and correlation fits (lines). The filled triangles represent the current data for single bifurcations in the first to fourth generation. The filled circles represent the current data for the model sections no. 13–22 (Figure 1), which contain multiple bifurcations.

airway), which was measured on the digital geometry in Rhinoceros 4.0 software (McNeel, Seattle, WA, USA). The diameter of the entrance airway was used as the characteristic diameter, in accordance with Zhou and Cheng.<sup>18</sup>

Chan and Lippmann<sup>19</sup> introduced the following correlation fit based on their experimental data for the first six generations

$$DE = 1.606Stk + 0.0023 \quad (8)$$

Similar correlation fit was calculated based on the current data for first to fourth generation

$$DE = 1.038Stk + 0.0012 \quad (9)$$

Both the empirical equations are plotted to the graph in Figure 6. The airways in the fourth to seventh generation, which create separate parts of the model (identification numbers 13–22), were evaluated as a whole section and plotted in Figure 6 as well. The DF can be calculated in a higher resolution (creating smaller sections) down to the resolution of the PET scanner (5 mm). This resolution is significantly better than the resolution of other commonly used methods (e.g. gravimetry or fluorometry), but the evaluation of deposition in single airways with diameters smaller than PET scanner resolution is not possible.

## Conclusion

This article presents a method that has been developed and applied in an “in vitro” measurement of aerosol deposition in a human respiratory tract model. The method is suitable for validation of numerically calculated aerosol deposition. Although the method uses a routinely clinically used PET, distinct procedures had to be developed, allowing unbiased spatially resolved

determination of the DF and DE. The method involves the following basic steps:

- Preparation of the lung model and system for aerosol delivery, including safety measures to prevent the radioactive aerosol from leaking into the laboratory.
- Precise adjustment and measurement of the boundary conditions (air flow rate, particle size, conditions in the surrounding environment, lung model type) during the experiment.
- Optimum definition of the VOIs avoiding their overlap (which would cause the recorded activity to be attributed to more than one VOI, thus biasing the results).
- Proposal for a division of the whole model (the model of the TB tree itself plus inlet tubing) enabling activity corrections to be performed.
- Determination of the corrections.
- Calculation of the deposition parameters.

The advantages of this method are high spatial resolution in comparison with other methods for measurement of aerosol deposition (e.g. gravimetry or fluorometry), the possibility of performing experiments repeatedly on an absolutely identical geometry and accurate control of the boundary conditions. With these advantages come a certain degree of simplification of the reality, lung geometry and physiology in particular, hence in vivo experiments will always be irreplaceable in this regard. The method is limited by the special resolution of the PET scanner (5 mm) and the steady inhalation regime. Nevertheless, the presented in vitro method proved to have an added value in providing data on local aerosol deposition and therefore helps to bring deeper insight into small-scale aerosol transport.

#### Declaration of conflicting interests

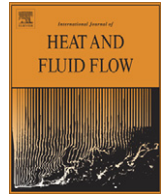
The author(s) declared no potential conflicts of interest with respect to the research, authorship and/or publication of this article.

#### Funding

This work was supported by the Czech Science Foundation under the grant P105/11/1339. F.L. was supported by the project CZ.1.07/2.3.00/30.0039 of Brno University of Technology and J.A. was supported by the project MEYS-NPS I-LO1413.

#### References

1. Cheng YS. Mechanisms of pharmaceutical aerosol deposition in the respiratory tract. *AAPS PharmSciTech* 2014; 15: 630–640.
2. Hofmann W. Modelling inhaled particle deposition in the human lung—a review. *J Aerosol Sci* 2011; 42: 693–724.
3. Churg A and Vedal S. Carinal and tubular airway particle concentrations in the large airways of non-smokers in the general population: evidence for high particle concentration at airway carinas. *Occup Environ Med* 1996; 53: 553–558.
4. Zhang Y and Finlay WH. Experimental measurements of particle deposition in three proximal lung bifurcation models with an idealized mouth-throat. *J Aerosol Med* 2005; 18: 460–473.
5. Borojeni AAT, Noga ML, Vehring R, et al. Measurements of total aerosol deposition in intrathoracic conducting airway replicas of children. *J Aerosol Sci* 2014; 73: 39–47.
6. Longest PW and Holbrook LT. In silico models of aerosol delivery to the respiratory tract - Development and applications. *Adv Drug Deliv Rev* 2012; 64: 296–311.
7. Dolovich MB. Measuring total and regional lung deposition using inhaled radiotracers. *J Aerosol Med* 2001; 14: S35–S44.
8. Conway J. Lung imaging—two dimensional gamma scintigraphy, SPECT, CT and PET. *Adv Drug Deliv Rev* 2012; 64: 357–368.
9. Lizal F, Elcner J, Hopke PK, et al. Development of a realistic human airway model. *Proc IMechE, Part H: J Engineering in Medicine* 2012; 226: 197–207.
10. Cheng KH, Cheng YS, Yeh HC, et al. Measurements of airway dimensions and calculation of mass transfer characteristics of the human oral passage. *J Biomech Eng* 1997; 119: 476–482.
11. Schmidt A, Zidowitz S, Kriete A, et al. A digital reference model of the human bronchial tree. *Comput Med Imaging Graph* 2004; 28: 203–211.
12. Turku PET Centre. *Carimas 2.4., version 2.2.44.7002 SW*. Turku: Turku PET Centre, 2012, <http://www.turkupet-centre.fi/carimas/download/>
13. Nesterov SV, Han CL, Maki M, et al. Myocardial perfusion quantitation with (15)O-labelled water PET: high reproducibility of the new cardiac analysis software (Carimas (TM)). *Eur J Nucl Med Mol I* 2009; 36: 1594–1602.
14. Harms HJ, Nesterov SV, Han C, et al. Comparison of clinical non-commercial tools for automated quantification of myocardial blood flow using oxygen-15-labelled water PET/CT. *Eur Heart J* 2014; 15: 431–441.
15. Saha GB. *Basics of PET imaging physics, chemistry, and regulations*. 2nd ed. New York; London: Springer, 2010.
16. National Electrical Manufacturers Association (NEMA). *NEMA standards publication NU 2-2001 performance measurements of positron emission tomographs*. Arlington, VA: NEMA, 2001.
17. Siemens. *Biograph™ TruePoint PET CT: system specifications*. Siemens, 2014, [http://www.activexray.com/pdf/Siemens\\_Biograph.pdf](http://www.activexray.com/pdf/Siemens_Biograph.pdf)
18. Zhou Y and Cheng YS. Particle deposition in a cast of human tracheobronchial airways. *Aerosol Sci Tech* 2005; 39: 492–500.
19. Chan TL and Lippmann M. Experimental measurements and empirical modeling of the regional deposition of inhaled particles in humans. *Am Ind Hyg Assoc J* 1980; 41: 399–408.



# Characteristics of turbulent particle transport in human airways under steady and cyclic flows

Jan Jedelsky\*, Frantisek Lizal, Miroslav Jicha

Faculty of Mechanical Engineering, Brno University of Technology, Technicka 2896/2, 61669 Brno, Czech Republic

## ARTICLE INFO

### Article history:

Available online 10 February 2012

### Keywords:

Aerosol  
Human airway model  
Power spectral density  
Velocity fluctuations  
Stokes number  
Steady flows  
Cyclic flows  
Laser Doppler Anemometry

## ABSTRACT

Motion of monodispersed aerosol particles suspended in air flow has been studied on realistic transparent model of human airways using Phase Doppler Particle Analyser (P/DPA). Time-resolved velocity data for particles in size range 1–8  $\mu\text{m}$  were processed using Fuzzy Slotting Technique to estimate the power spectral density (PSD) of velocity fluctuations. The optimum processing setup for our data was found and recommendations for future experiments to improve PSD quality were suggested. Typical PSD plots at mainstream positions of the trachea and the upper bronchi are documented and differences among (1) steady-flow regimes and equivalent cyclic breathing regimes, (2) inspiration and expiration breathing phase and (3) behaviour of particles of different sizes are described in several positions of the airway model. Systematically higher level of velocity fluctuations in the upper part of the frequency range (30–500 Hz) was found for cyclic flows in comparison with corresponding steady flows. Expiratory flows in both the steady and cyclic cases produce more high-frequency fluctuations compared to inspiratory flows. Negligible differences were found for flow of particles in the inspected size range 1–8  $\mu\text{m}$  at frequencies below 500 Hz. This finding was explained by Stokes number analysis. Implied match of the air and particle flows thereby indicates turbulent diffusion as important deposition mechanism and confirms the capability to use the P/DPA data as the air flow velocity estimate.

© 2012 Elsevier Inc. All rights reserved.

## 1. Introduction

Transport and deposition of aerosol in human airways has been of research interest for several decades. Main present motivation for elucidation of related phenomena is the increasing tendency of therapeutical drug application in the form of the inhaled aerosol (Azarmi et al., 2008). Aerosol deposition in the human airways is also extensively studied in many industrial hygiene related researches (Kleinstreuer et al., 2008; Sosnowski et al., 2007; Su and Cheng, 2009 and others).

Published works show that the air flow in the multiple-bifurcating airway system is a very complex phenomena showing turbulent, transitional and laminar behaviour depending on breathing conditions, morphology and position in the airways (Cohen et al., 1993; Guan and Martonen, 2000; Ramuzat and Riethmuller, 2002; Martonen et al., 2002; Kleinstreuer and Zhang, 2003; Fresconi et al., 2003; Li et al., 2007). Transitional and turbulent flows often occur in the mouth–throat and upper conducting airways while laminar flow controls transport beyond approximately the 9th generation of the bronchi. Within this wide range of conditions,

fate of the inhaled particles depends on their size in conjunction with the local flow dynamics. Aerosol deposition may occur due to impaction, sedimentation, diffusion, and turbulent dispersion.

The occurrence of upstream turbulent flows may influence both the inlet velocity and particle profiles entering the bifurcation and may enhance deposition within the model (Longest and Holbrook, in press). The turbulence induced by the laryngeal jet significantly affects airway flow patterns as well as tracheal wall shear stress (Lin et al., 2007) and is responsible for increased local particle deposition (Gemci et al., 2002; Chan et al., 1980). Kleinstreuer and Zhang (2003) demonstrated the importance of transitional and turbulent flows on particle deposition throughout an oral-trachea airway model. They reported enhanced particle deposition in the trachea near the larynx due to turbulence and throughout the airway mainly for small particles ( $Stk < 0.06$ ) due to turbulent dispersion. Sosnowski et al., 2007 used CFD modelling to study behaviour of aerosol particles with size 0.3–10  $\mu\text{m}$  in the oro-pharynx under unsteady air flow and found higher deposition efficiency for smaller particles due to strong effects of turbulent diffusion. Kleinstreuer et al., 2008 modelled deposition of micron-size particles in pulmonary airway replicas and located particles mainly around the carinal ridges deposited due to inertial impaction but some particles also landed outside the vicinities of the cranial ridges due to secondary flows and turbulent dispersion. Cheng

\* Corresponding author.

E-mail addresses: [jedelsky@fme.vutbr.cz](mailto:jedelsky@fme.vutbr.cz) (J. Jedelsky), [lizal@fme.vutbr.cz](mailto:lizal@fme.vutbr.cz) (F. Lizal), [jicha@fme.vutbr.cz](mailto:jicha@fme.vutbr.cz) (M. Jicha).

et al. (1997) used oral airway replicas and found that turbulent diffusional deposition is the dominant deposition mechanism of ultrafine particles ( $<0.1 \mu\text{m}$ ).

Turbulence in the respiratory tract is generated by several mechanisms. Primary source of turbulence is often the inhaler, which delivers particles into the mouth producing high momentum turbulent spray jet. A high-speed laryngeal jet is formed as the flow passes through the glottis; this jet induces turbulent flow in the trachea. Lin et al. (2007) found out that regions of maximum local turbulence in the trachea are associated with Taylor-Görtler-like coherent vortical structures in the supraglottis and the subglottis. Hiemenz flow (characterised by transition to turbulence at low Reynolds numbers (250) (Obrist et al., 2011)) at the carinal ridges can be related to the increased turbulence in daughter branches during inspiration. Overall fluid motion in curved airway tubes has helical character (Guan and Martonen, 2000); the vortices formed contribute to turbulence. It was confirmed in the left curved bronchus by Große et al. (2007). Mixing of streams from daughter branches is a source of turbulence for expiratory flows. Complex flow structures containing different types of vortices, flow detachment, wakes, simultaneous bidirectional flow, recirculation zones and velocity oscillations observed particularly for cyclic breathing as described in a number of papers (brief review in Jedelsky et al., 2010a) contribute to the turbulence as well. The turbulence in airways is generally strongly anisotropic with major part of turbulent kinetic energy (TKE) contained preferably in axial direction of the flow (Longest and Holbrook, in press).

Turbulent flow contains unsteady vortices which appear on many different length scales and interact with each other. Most of the kinetic energy of the turbulent motion is contained in the large-scale structures generated by the flow. These energetic structures transform to smaller-scale vortices by an inertial and basically inviscid mechanism. Smaller and smaller structures are produced until they are small enough for molecular diffusion to become important and viscous dissipation of energy finally takes place. This process known as the energy “cascade” leads to essentially continuous frequency spectrum of TKE. The largest eddies appear at low frequencies and are followed by energy containing eddies that are characterised by maximum amplitude at the spectrum. Inertial subrange, at higher frequencies, shows decreasing TKE tendency with frequency and successive dissipation subrange at the highest frequencies shows even faster TKE decay with frequency. The TKE spectrum can be estimated using time-resolved measurement of velocity of particle laden turbulent flows by laser-Doppler techniques such as P/DPA. Fate of airborne particles in turbulent flows depends on their  $Stk$ . Very small particles ( $Stk \ll 1$ ) follow the fluid motion, while larger particles ( $Stk \sim 1$ ) tend to be centrifuged toward the peripheries of the vortical structures. For  $Stk \gg 1$  the particles move essentially independent of the fluid (Crowe et al., 1998). Small  $Stk$  particles, transported by turbulent eddies, can deposit if forced by these eddies towards the airway wall. Particles with  $Stk \sim 1$ , concentrated at the peripheries of turbulent structures (Zhang and Kleinstreuer, 2002), can deposit as well. Turbulent dispersion is therefore responsible for increased deposition efficiency.

Continuous movement from simple airway models and steady flows to realistic models and lifelike cyclic flow regimes is seen on present CFD simulations and experimental studies. Realistic, CT based, lung models were proved to be a must for valid results of flow and particle transport. Several works report significant quantitative and qualitative differences between aerosol transport/deposition characteristics under steady flows, most frequently studied in the past, and lifelike oscillatory flows (Lieber and Zhao, 1998; Zhang and Kleinstreuer, 2004; Zhang et al., 2001).

Several methods have been applied for flow studies in airway models. Intrusive Hot Wire Anemometry (HWA) was used for

in vitro air flow measurements in the past while optical methods prevail today. The most common is Particle Image Velocimetry (PIV). Laser Doppler Anemometry (LDA) (Corieri and Riethmuller, 1989; Lieber and Zhao, 1998; Tanaka et al., 1999; Corcoran and Chigier, 2000) and P/DPA (Gemci et al., 2002) are less frequent. Complex design of realistic models hampers application of optical methods for aerosol transport studies. PIV, in realistic models, requires application of a liquid with refraction index equal to the one of the model walls instead of air, as the real breathed fluid, or usage of simple models with cylindrical walls if air used. LDA (or P/DPA), as point-wise technique is more suitable for measurements in the composite optical system of transparent model with flowing air. This method moreover allows direct particle flow measurement with high spatial resolution and high data rate. Aside basic flow characteristics as mean and rms velocities also spectral flow properties could be estimated therefore. Estimation of PSD from Laser-Doppler based data faces a problem of irregular time sampling. A number of different techniques was developed to treat this problem; it was formerly solved using analogue filters of the velocity signals or by equidistant time re-sampling. Scott (1974) derived an expectation of the spectrum on the basis of a Slot Correlation technique (SC) which remains even today one of the most viable means for PSD estimations. Large group of estimators is based on the concept of signal reconstruction and re-sampling at equal time intervals. The most common reconstruction is zeroth-order interpolation or sample and hold (S+H) method. Other spectral estimator for LDA data, introduced by Nobach et al. (1996), was based on one-point reconstruction techniques employing a refinement which accounts, in a statistical manner, for the velocity change between a particle arrival and the sample instant. The most reliable spectral estimation techniques are explained in detail by Benedict et al. (2000).

In this work, we have focused on description of the turbulence in frequency domain for the case of the complex flow in the multiple bifurcating airways, which is not sufficiently studied topic so far. We have processed exemplary P/DPA data acquired during our earlier study<sup>1</sup> with the aim to document spectral properties of turbulent particle transport in human airways. Brief description of our experiment and measured data is made first. Kern software program (Nobach, 2002) is used for estimation of PSD of particle velocity fluctuations. Setup of the program has been optimised for our data and several P/DPA data sets are processed. Arbitrary PSD plots are shown to describe nature of the particle-air flow. Differences between steady and cyclic flows at several positions of the airway model and the influence of the flow regime and particle size on the PSD are discussed. Several recommendations for future to improve the PSD estimations are given.

## 2. Experimental apparatus

Our experimental device (Fig. 1) uses a computer controlled motor (6) which drives piston through pneumatic cylinder (5) as a source of oscillating air flow. Steady air flows were maintained using a downstream suction source – vacuum air pump. Three steady breathing regimes (15, 30 and 60 l/min) and three corresponding cyclic sinusoidal breathing regimes were used (tidal volume 0.5 l and breathing period 4 s, 1 litre & 4 s and 1.5 litre & 3 s). Monodispersed aerosol particles of di-2-ethyl hexyl sebacate (DEHS) ranging from 1 to 8  $\mu\text{m}$  are generated by condensation generator (4). One-half of the particles is mixed with the air in a chamber (3) using static mixer and flows into the airway model (Fig. 1).

<sup>1</sup> This study of transport of monodispersed micron-sized liquid particles dispersed in air was made in realistic transparent human airway model for a range of steady and cyclic flows and particles of various sizes. P/DPA was used to acquire time-resolved data of particle velocity (Jedelsky et al., 2010a).

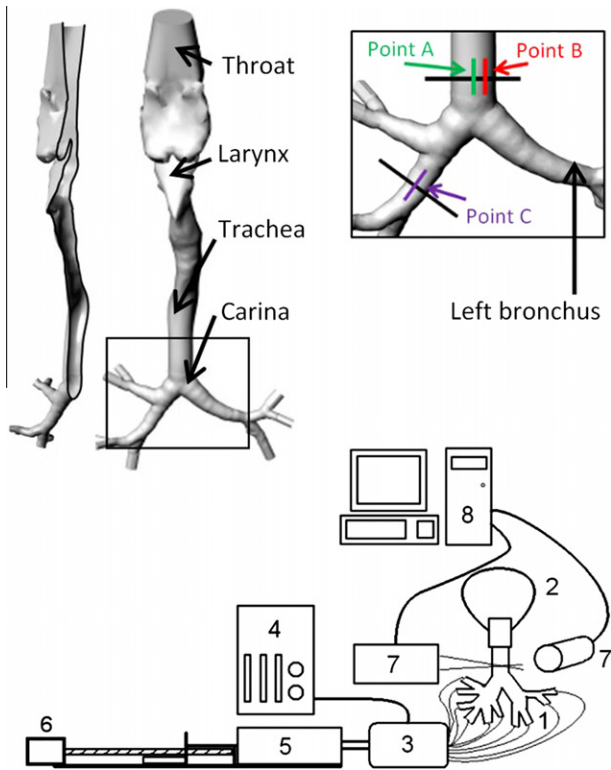


**Fig. 1.** The airway model with measurement positions in expanded window (top). A schematic diagram of the test rig (bottom). (1) The airway model, (2) a collecting sac, (3) mixing chamber, (4) condensation monodisperse aerosol generator, (5) pneumatic cylinder with piston, (6) computer controlled step motor with motion screw, (7) P/DPA, and (8) PC.

The second half flows into a sac (2), that collects the particle–air mixture for the second breathing cycle phase. The particle-laden air flow is incompressible, subsonic, isothermal, and viscous, with high particle/air density ratio of 760 and the DEHS aerosol is non-evaporating/non-condensing. 1D P/DPA by Dantec Dynamics (7) was used for measurement of the particle size and mainly for time-resolved measurement of the axial velocity component of the particle motion during breathing cycle in several cross-sections of the model.<sup>2</sup>

A transparent thin-walled human airway model with realistic geometry was used for the investigation. The airway geometry was captured using high resolution CT scan of an adult Caucasian male. The model, made of transparent silicon Sylgard 184 (Dow Corning), covers airways from mid-pharynx to 3rd–4th generation of bronchi, it preserves realistic shapes of the airways with complex structures of glottis and epiglottis and 3-D asymmetric branching as seen in Fig. 1, top. Mean tube diameters in each generation are documented in Table 1. Geometry and fabrication of the model is described in detail by Lizal et al. (2011), flow rate distribution into particular branches of the tracheobronchial tree for different steady and cyclic breathing regimes is documented in Jedelsky et al. (2009). The model was placed in upstanding human position and it was fixed in a frame mounted to a traversing mechanism for positioning during experiments.

Thin model walls are required for optical access into the model without strong optical distortions when the air flow or particle transport with air as a carrier medium to be studied. This approach

<sup>2</sup> P/DPA was chosen instead of simpler LDA to verify particle size and also to reduce unwanted sources of noise in PSD estimation such as reflections and multiple-particle scattering. For more information on the P/DPA setup and data processing see Jedelsky et al. (2010a).

**Table 1**  
Dimensionless numbers in individual branching levels.

Gen.	$\bar{Q}$ (l/min)	$\bar{D}$ (mm)	$\bar{v}$ (m/s)	$d_p$ ( $\mu$ m)	$Stk$	$Re$	
L	15	15.4	1.34	1	3.32E–04	1368	5.0
	30		2.68	4	9.75E–03	2736	5.0
	60		5.37	8	7.69E–02	5472	5.7
0	15	17.4	1.05	1	2.30E–04	1211	5.6
	30		2.10	4	6.76E–03	2421	5.6
	60		4.21	8	5.33E–02	4843	6.5
1	15	11.6	1.18	1	3.90E–04	908	3.7
	30		2.37	4	1.14E–02	1816	3.7
	60		4.73	8	8.89E–02	3632	4.3
2	15	8.3	1.16	1	5.40E–04	635	2.7
	30		2.31	4	1.56E–02	1269	2.7
	60		4.62	8	1.21E–01	2538	3.1
3	15	7.3	0.75	1	4.00E–04	361	2.4
	30		1.49	4	1.14E–02	721	2.4
	60		2.99	8	8.89E–02	1443	2.7
4	15	5.5	0.66	1	4.60E–04	239	1.8
	30		1.32	4	1.33E–02	479	1.8
	60		2.63	8	1.05E–01	958	2.0

differs from other fluid dynamics experiments in complex airway models, where liquids with the refraction index matched to the one of the model material are used (Ramuzat and Riethmuller, 2002; Fresconi and Prasad, 2007; Große et al., 2007; Adler and Brücker, 2007; Theunissen and Riethmuller, 2008). The realistic transparent airway model is asymmetric, it has non-circular cross-sections, walls of varying thickness and varying curvature. Optical measurement in this model requires very precise setup and approach different to the one used for measurement with simple optical path. It is necessary to adjust the laser beam crossing every time the measurement position changes. An accurate choice of the measurement position is needed to avoid strong distortion of the laser beam even when thin-wall model used. Measurement in near-wall regions of the model faces stronger optical distortion and therefore main-stream positions are preferred to guarantee good results.

### 3. Results and discussion

Table 1 documents basic flow characteristics in the human model and shows variation of Reynolds ( $Re$ ), Stokes ( $Stk$ ) and Womersley ( $\alpha$ ) numbers<sup>3</sup> with flow rate  $\bar{Q}$  and position in the airways. The  $\bar{Q}$  values used for steady flows correspond to rms flow rate values during cyclic flows. The tracheobronchial tree is numbered according to Weibel (0 = trachea, L = larynx). Average tube diameter,  $\bar{D}$ , in particular generation is taken from Schmidt et al. (2004) and represents the average value over all branch diameters within the generation. The larynx diameter was defined as a hydraulic diameter in the location of the smallest cross-sectional area between mid-pharynx and trachea.  $Re$  is proportional to the mean flow velocity  $\bar{v}$  and it decreases as tube diameter,  $\bar{D}$ , drops down. Only several combinations for  $Stk$  were calculated: the smallest particle size & minimal flow rate, medium particle size & medium flow rate and the largest particles & maximal flow rate. Maximum  $Stk$  about 0.1 was found in the second generation for 8  $\mu$ m particles and flow rate 60 l/min; for all other cases usually  $Stk \ll 1$ .

Exemplary results of the two-phase air–particle flow under cyclic breathing are illustrated in Fig. 2. The measurement was performed at point C (Bronchus Intermedius, centreline, see Fig. 1) for flow regime 1 l & 4 s; 4  $\mu$ m particles were used. The time-

<sup>3</sup> All the dimensionless numbers are calculated for the average diameter,  $\bar{D}$ , as characteristic length scale of given tube.

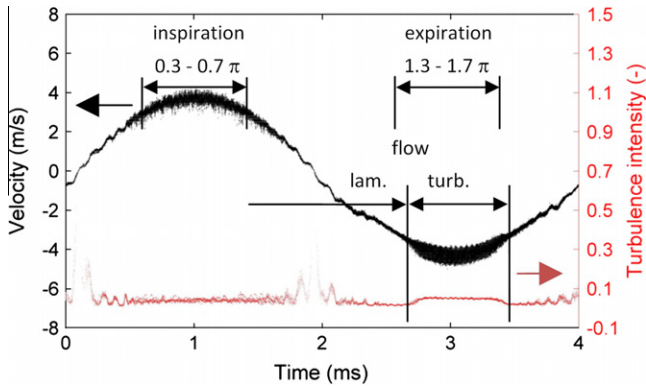


Fig. 2. Ten overlapped (phase-averaged) cycles. Inspiratory and expiratory time windows used for PSD estimations are marked. Sections with laminar and turbulent character of flow during the expiratory phase are distinguished.

resolved axial velocity of individual aerosol particles passing through the measurement volume of P/DPA as well as the axial turbulence intensity are displayed in the plot. We assume that particles follow the air flow with no significant slip due to their low  $Stk$  and discuss this assumption in chapter Stokes number in detail. Particle velocity data are thus used for air velocity and turbulence intensity estimation. It is seen that the particle velocity during the cyclic flow approximately corresponds to the sinusoidal shape of the cyclic breathing. The positive velocity values stand for inspiration, negative stand for expiration.

Extensive documentation of further results of the particle transport supported with explanation of the effect of various factors (particle size, steady/cyclic flows, spatial and temporal nature of the flow) was already made in (Jedelsky et al., 2010b). The average axial turbulence intensities at point A (placed in trachea centreline, 20 mm above carina, see Fig. 1) at steady and cyclic inspiration flows are compared in Table 2 to illustrate typical results of these basic flow characteristics. Small differences between both the cases and also among different flow rates and particle sizes were found. Turbulence intensity covers range 0.07–0.11 for all the cases and no significant correlation between the flow regime and the turbulence intensity is seen. It is interesting as  $Re$  varies significantly: from 1200 to 4800 (see Table 1). The relatively high and regime independent turbulence intensity can be attributed to the complexity of the upstream geometrical structures of larynx.

The probability density function (PDF) of the particle velocity was evaluated for steady flow conditions 30 l/min at point A. The particle velocity samples were classified into bins with size of 0.15 m/s. Velocity counts in each bin were then divided by the total sample number to give the relative counts displayed in Fig. 3. The velocity distribution corresponds to log-normal distribution with moderate inclination of the maximum to higher velocities. This bias is caused by specific P/DPA sampling rate; where for spatially uniform particle concentration the data rate is proportional to

Table 2  
Axial turbulence intensity at point A.

Size ( $\mu\text{m}$ )	Steady inspiration (l/min)			Cyclic inspiration <sup>a</sup>		
	15	30	60	0.5&4 <sup>b</sup>	1.0&4	1.5&3
1	0.104	0.085	0.071	NaN	0.092	NaN
4	0.107	0.110	0.091	0.095	0.097	0.084
8	0.109	0.092	0.074	NaN	0.095	NaN

<sup>a</sup> The turbulence intensity in cyclic inspiration flow is calculated as an average value during a phase window  $0.3\text{--}0.7\pi$  (see Fig. 2) averaged for ten consequent cycles.

<sup>b</sup> Tidal volume (l) and period of cycle (s).

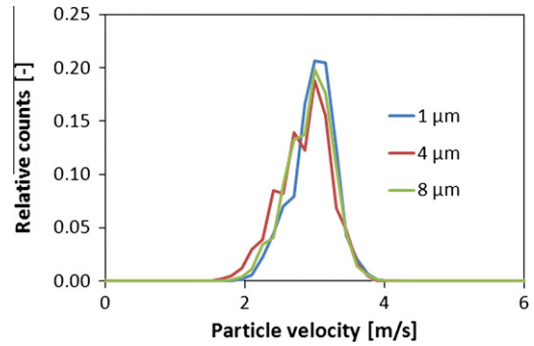


Fig. 3. PDF of particle velocity.

actual flow velocity (see Eq. (2)). Different particle sizes give similar PDF shapes with no significant systematic differences. As seen above, neither the mean value of turbulence intensity (Table 2) nor the PDF of the particle velocity can resolve differences in flow for different flow regimes and particles of different sizes.

### 3.1. Estimation of PSD of velocity fluctuations

Laser-Doppler based techniques provide flow velocity data with comparatively high temporal resolution so they can serve for estimation of the moments and spectra of the turbulent velocity fluctuations. P/DPA is a tracer-based method with irregular particle arrival times. Presuming an equal particle distribution in space with constant concentration and mean data rate of the measurement  $\dot{n}$ , the intervals  $t$  between the particles are distributed exponentially:  $p(\Delta t) = \dot{n} \cdot e^{-\dot{n}\Delta t}$ , as seen in Fig. 11. The most probable interparticle arrival time is zero so information about very high frequency fluctuations is contained in the data. Nevertheless maximum reliable frequency is  $f_{\text{max}} \cong \dot{n}/2\pi$  according to Adrian and Yao (1987). The irregularity of the sampling time caused by naturally seeded particles in flow brings difficulties to the estimation of the PSD of the velocity fluctuations.

We employed SC technique for the estimation of the PSD as described by Benedict et al. (2000) and calculated the PSD using Kern software (Nobach, 2002). The software has a number of options and variables to set with no guideline for optimum setup. However resulting PSD is very sensitive to the input parameter values. A large data set was tested to find out the best setup. Published HWA and LDA data of identical flow (Nobach, 2006) were compared first. After successful agreement between these HWA and LDA results we focused on our P/DPA data. A set of three consequent data records was chosen to describe the PSD estimation process. The data were acquired at point A for steady flow regime

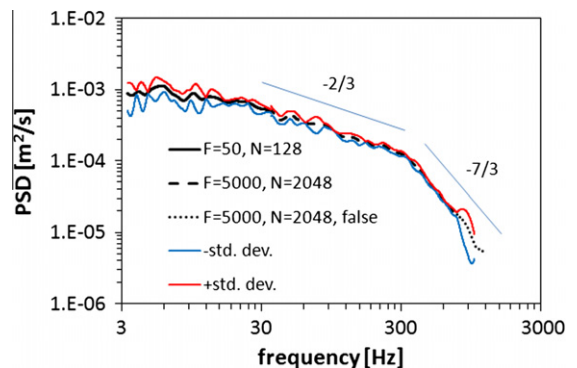


Fig. 4. Average PSD with marked standard deviation limits.

30 l/min and 1  $\mu\text{m}$  particles. Each file had 16,384 samples and measurement period  $\sim 5.8$  s (average sampling frequency 2825 Hz).

Fig. 4 shows PSD of the velocity fluctuations versus frequency,  $f$ , using a log–log plot. The average PSD curve based on the three records together with standard deviation was calculated. We have ascertained that any unique software setup does not produce the PSD over the whole frequency range provided by the measured data. So the spectra is composed of two curves; the lower frequency part (3.3–35 Hz) was calculated using: SC,  $F = 70$ ,  $K = 128$ ,  $N_F = 1000$  and standard options (+fil – self + mbv + vw + ln + fst + fbat + lte + cft)<sup>4</sup>, the upper frequency part was calculated as: SC,  $F = 5000$ ,  $K = 2048$ ,  $N_F = 1000$  and standard options. Individual PSD plots (not shown here) are very consistent in the frequency range 15–750 Hz as indicated by the standard deviation curves. Small fluctuations in the amplitude inside this frequency range that were observed in each PSD plot change record to record and therefore are not an inherent property of the flow. Low frequency fluctuations in the PSD amplitude (up to  $\sim 15$  Hz) are a product of natural variations of flow that cannot be fully resolved by the relatively short data record. They lead to differences in particular records and are reflected by increased deviation in Fig. 4. The results differ significantly also for frequencies higher than about 1 kHz due to lack of useful data from P/DPA measurement. The differences can be partially caused by the processing algorithm as well. This part of the plot is not realistic and cannot be used for analysis.

Variable windowing (vw) (Tummers and Passchier, 1996) used in this calculation leads to smoothing and averaging of fluctuations in individual spectral lines. Larger fluctuations are preserved. The amplitude of velocity fluctuations at the inspected point shows only very mild decreasing tendency with frequency up to about 30 Hz, then slightly higher and relatively constant-slope decrease according  $f^{-2/3}$  in range 30–300 Hz and more distinct decrease with constant slope  $f^{-7/3}$  for frequencies higher than 300 Hz. No distinct peak in the PSD is obvious. Very similar shape of the PSD was found also at other measurement points, for other particle sizes and other flow regimes in the trachea. The first part of the spectra up to 30 Hz can be attributed to the energy-containing range, followed by inertial subrange. The exponent  $-2/3$  at the first part of inertial subrange suddenly changes to  $-7/3$ . This shape of inertial subrange differs from the usual Kolmogorov-like constant value slope  $-5/3$  due to several reasons. Generated turbulence is anisotropic in large scales due to character of the flow. Energy containing eddies are continually generated during flow in the complex airway geometry. The cumulative TKE was calculated for given data. The amplitude of oscillations at frequencies higher than 800 Hz was approximated using the  $f^{-7/3}$  rule. Low frequency oscillations up to 140 Hz participate on 50% of the total TKE and 90% is covered in range up to 620 Hz.

The calculation made with the same setup as with the previous results but without vw produced PSD plots containing strong scatter in the amplitude. No significant coherence of this “noise” in spectra among individual records was found. Averaging of the PSD from the three records (Fig. 5) reduces this scatter so processing of multiple data files or long measurements is convenient for statistically correct results. Variable windowing is even stronger instrument for the data smoothing mainly at high frequencies as indicated in the plot.

### 3.2. Steady flows

Several P/DPA data sets were used to find out the influence of the flow regime and particle size on the PSD of velocity fluctuations

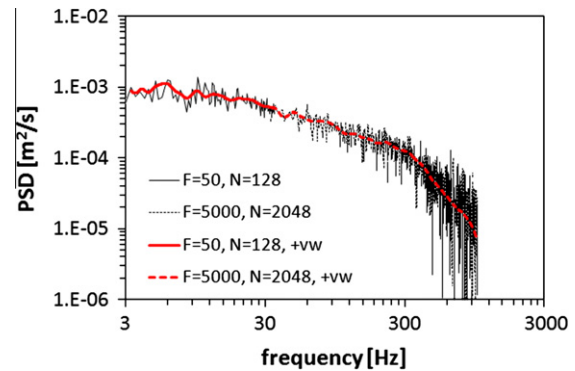


Fig. 5. PSD with/without vw, average of three records.

and to describe differences between inspiration and expiration flows and spatial variations of the PSD. The data in main-stream positions showing relatively simple flows without wakes and recirculation zones were used.

#### 3.2.1. Flow Regimes

PSD plots for three inspiratory flow rates (15, 30 and 60 l/min, particles with diameter 4  $\mu\text{m}$ ) at point B (placed in trachea 4 mm off the centreline, 20 mm above carina, see Fig. 1) are compared in Fig. 6a. All three cases give similar PSD values for low frequencies (up to  $\sim 30$  Hz) but higher flow rates produce significantly higher PSD levels in the upper part of the spectra. The PSD is almost constant up to 200 Hz for 60 l/min but drops down for 15 l/min and 30 l/min reaching only 20–30 Hz. The difference among the different regimes is especially distinct for frequencies higher than 200 Hz. Velocity fluctuations in range 30–300 Hz are therefore responsible for rising TKE with the increase in flow rates. The same behaviour was also found at other measurement positions for both the inspiratory and the expiratory flows. Fig. 6b with

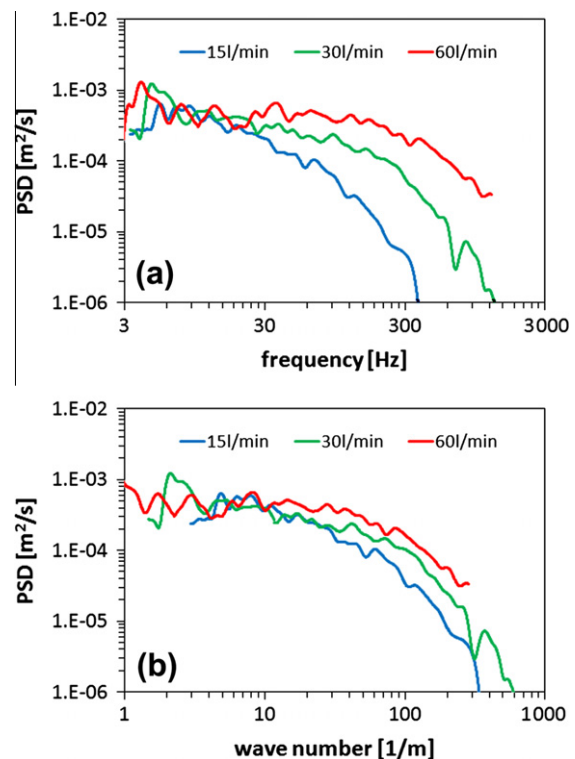


Fig. 6. Comparison of different flow regimes.

<sup>4</sup>  $F$  is the frequency used to define the time lag between samples in the autocorrelation function (ACF),  $K$  is the number of samples in the ACF,  $N_F$  is the number of samples in the spectrum, for better description see Nobach, 2002.

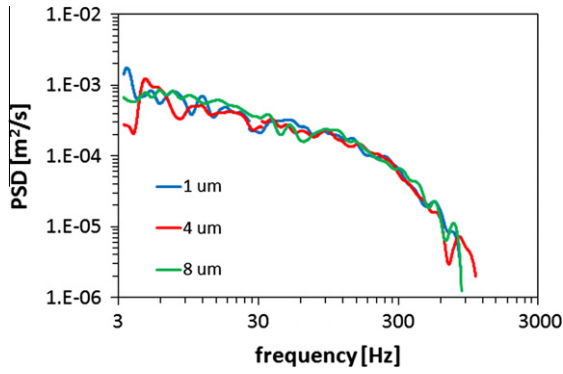


Fig. 7. PSD for different particle sizes.

horizontal axis rescaled using wave number  $k = f/\bar{v}$  also shows increased PSD levels at high frequencies for high flow rate which denotes effect of flow rate on energy of small vortices.

### 3.2.2. Particle size

Steady inspiration flow of particles with 1, 4 and 8  $\mu\text{m}$  in diameter was measured at point B at 30 l/min. No distinct differences in PSDs up to about 500 Hz (the maximum available correct frequency) are seen in Fig. 7, except the differences at low frequency part of the spectra due to short record as already mentioned. This result (found also at other measurement positions and for expiration flow) is important and confirms that particles up to 8  $\mu\text{m}$  in diameter respond the same way to the vortices at the most energetic frequencies.

### 3.2.3. Stokes number

Behaviour of airborne particles of different sizes at various breathing conditions can be explained and discussed by means of Stokes number ( $Stk$ ).  $Stk$  is a ratio between the particle response time and a characteristic time of the flow field (Crowe et al., 1998). The mean  $Stk$  (spatially and temporally averaged) in the case of flow in air through a tube of diameter  $D$  for a particle having aerodynamic diameter  $d_p$  and density  $\rho_p$  is

$$Stk = \frac{\rho_p C_c d_p^2 \bar{v}}{18\mu D} = \frac{4}{18\pi} \cdot \frac{\rho_p}{\mu} \cdot \frac{C_c d_p^2 \bar{Q}}{m D^3} \quad (1)$$

where  $\mu$  is air dynamic viscosity,  $m$  is number of the branches in given branching generation of the model,  $\bar{Q}$  is the total mean flow rate,  $\bar{v}$  is mean (spatially and temporally) flow velocity and  $C_c$  is Cunningham correction factor (Theodore, 2005). Mean particle velocity is supposed to be equal to mean flow velocity  $\bar{v}$ .  $Stk$  of the particles in our model falls within the range  $0.0002 < Stk < 0.12$ , particular  $Stk$  value depends on the branching level, particle size and flow rate (Table 1).

Turbulent flow contains vortices on many different length scales. Let consider a vortical structure with characteristic dimension  $D_v$ . It will produce fluctuations of the particle velocity measured by P/DPA probe at frequency  $f = \bar{v}/D_v$  with corresponding  $Stk_v = \rho_p C_c d_p^2 f / 18\mu$  (we assume that the air velocity corresponds to the particle velocity if  $Stk \ll 1$ ). Such defined  $Stk_v$ , contrary to the one given by Eq. (1), does not directly depend on flow regime and position within the lung model. The size of vortices is 2.1, 4.2 and 8.4  $\text{mm}^3$  for flow-rates of 15, 30 and 60 l/min respectively

<sup>5</sup> Characteristic size of, for example, Dean vortices in bent tubes (Guan and Martonen, 2000) and vortices produced by mixing of streams from daughter branches (Fresconi and Prasad, 2007) is  $\sim 1/2$  of the tube diameter. These vortices are in mm scale in trachea and main stem bronchi. Taylor-Görtler-like coherent vortical structures in the supraglottis and the subglottis (Lin et al., 2007) or large horseshoe/hairpin-type vortices (Fresconi et al., 2003) are also mm sized.

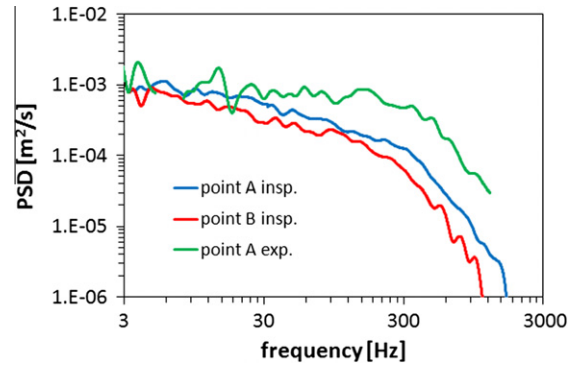


Fig. 8. PSD for steady inspiratory and expiratory flows at point A and for steady inspiratory flow at point B.

at  $f = 500$  Hz (calculation based on data in Table 1) and corresponding  $Stk_v$  is 0.002 for  $d_p = 1 \mu\text{m}$ , 0.028 for 4  $\mu\text{m}$ , and 0.1 for 8  $\mu\text{m}$  respectively. Such reasonably small  $Stk$  suggests that the particles should follow the air flow smoothly at frequencies up to hundreds Hz as confirmed by our observations (Fig. 7) and other studies (Choi et al., 2010). For such particles, turbulent diffusion could therefore significantly contribute to their deposition.

### 3.2.4. Other factors

There is not enough space to describe spatially resolved results in this paper so only an illustrative plot with PSD acquired at two points of the same cross-section (A and B) for inspiration flow at 30 l/min is shown in Fig. 8. Point B gives higher intensities of velocity fluctuations in the whole range and mainly at frequencies higher than 200 Hz, but shape of the PSD plot is consistent with the other point. The increased TKE at off-axis position B could be caused by shear forces (interaction of the fast axial jet with slower near wall air or by asymmetric character of the jet (see Lin et al., 2007).

Comparison of inspiratory and expiratory flows at point A for 30 l/min (Fig. 8) shows much higher amount of TKE contained at high frequencies for the expiration flow. This difference can be explained by different way of the turbulence generation which is due to the laryngeal jet flowing into the trachea during inspiration and due to mixing of streams from daughter branches for expiration flow.

### 3.3. Cyclic flows

Flow during breathing cycle changes from positive (inspiratory phase) to negative (expiratory phase) and, in the major section of the upper part of the tracheobronchial tree, transition from laminar to turbulent flow occurs with increasing  $Re$  (Fig. 2). High-velocity parts of the cycle near inspiration/expiration peaks are the most important for particle deposition. The PSD of cyclic velocity fluctuations was evaluated by applying Kern in a similar way as for the steady flows above on fragments of the breathing cycle considering the flow here as quasi-steady. The PSD estimates acquired such way give only overall information on the average content of TKE in the spectra in the inspected fragment of time. The length of the time window is a compromise to fulfil the quasi-steady flow character and to acquire enough data for a reasonable PSD estimate.<sup>6</sup>

<sup>6</sup> A sort of short-time Fourier transform or Hilbert transform working with non-equidistant sampling would be useful to estimate PSD of velocity fluctuations for individual breathing phases but these are not at disposal yet.

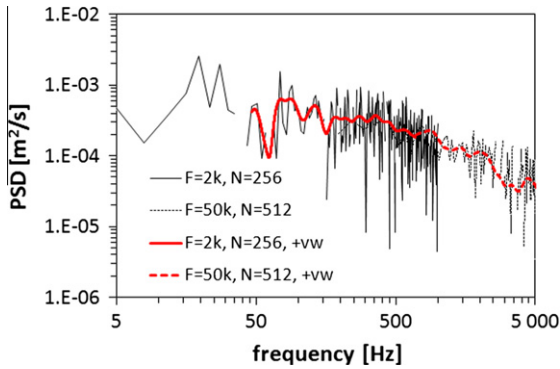


Fig. 9. Average PSD for inspiratory cyclic flow at point C.

Fig. 9 shows such PSD averaged from four records. The data measured at point C (see Fig. 1) for particle velocity in time window  $0.3\text{--}0.7\pi$  (peak inspiration, see Fig. 2) were processed. These data, with mean data rate about 6.7 kHz, enabled reliable spectra evaluation up to 1 kHz. The short time window  $\sim 0.6$  s leads to only 4096 samples in each record and problematic evaluation for frequencies lower than 30 Hz. Large scatter in the PSD spectra and large record-to-record differences were found. The spectrum shows relatively constant values up to 300 Hz. Slow decrease with frequency above 300 Hz compared to the steady data is seen. Relatively high amplitudes of low frequency fluctuations (below 30 Hz) with local minimum at about 40 Hz are observed here and at other measurement points/regimes. These fluctuations are supposed to be related to large-scale vortices that propagate through the tubes and their influence is recognisable also in time plots of the droplet velocity (Fig. 2), where these vortices lead to deformations of the mean velocity from the original sinusoidal course (more in Jedelsky et al., 2010a). Such character of flow differs from results found for steady breathing – these vortices are typical for cyclic flows.

Exhalation phase of the cyclic flow produces more high-frequency fluctuations than the inspiration flow (Fig. 10) from the same reason as in the steady flow case (Fig. 8).

Corresponding steady and cyclic flows 15 l/min and 0.5 l and 4 s respectively with  $4\text{ }\mu\text{m}$  particles were compared at point A (Fig. 10). Cyclic flows contain more high-frequency velocity fluctuations than the steady flows for both flow directions. PSDs differ from frequencies about 50 Hz and about half-order difference appears at 100 Hz already.

### 3.4. Data rate of LDA measurements

The PSD of velocity fluctuations contains interesting information on flow turbulence, which spans over several

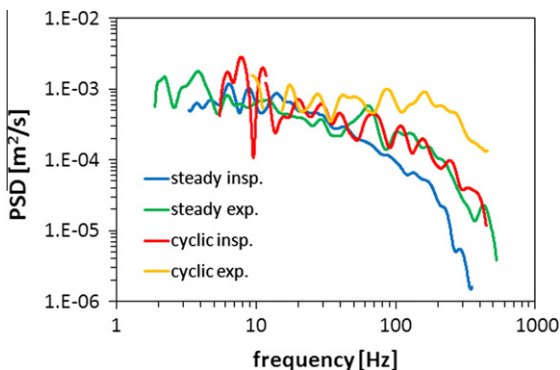


Fig. 10. Steady and cyclic insp. and exp. flows.

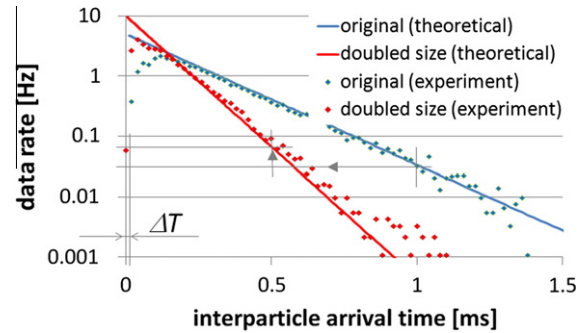


Fig. 11. Frequency plot of arrival time between two particles for  $1\text{ }\mu\text{m}$  particles and flow rate 30 l/min at point A.

frequency orders, however quality of the results and upper limit of the frequency range  $f_{\text{max}} \cong \dot{n}/2\pi$  depends on LDA data rate.

Our CMAG generator produces aerosol with mean concentration  $\bar{c}$  in range  $10^4\text{--}10^6$  particles/cm<sup>3</sup>. After diluting of the aerosol in the mixing system a homogeneous air-particle mixture is delivered into the airway model with  $\bar{c} \cong 10^3\text{--}10^5$  particles/cm<sup>3</sup>. This dilute aerosol (mean free path in order of hundreds particle diameters) gives a typical data rate of P/DPA measurement in order of kHz. Mean data rate

$$\dot{n} = \bar{v} \cdot \bar{c} \cdot S \cdot K \quad (2)$$

where  $S$  is area of the measurement volume (mv) projected in the flow direction,  $\bar{v}$  is mean particle velocity and yield  $K$  depends on visibility of droplets by P/DPA and its validation rate. Laser-Doppler based techniques are capable to measure only one particle at given time; if the system detects a particle, then other particles appearing in the mv at the same time or flowing in before the first one exits the mv will be rejected from evaluation. The theoretical maximum measurement frequency would be (assuming equidistant sampling for simplification):

$$\dot{n}_{\text{max}} \cong 1/\Delta T = v/a = v \cdot \cos \theta / D_1 \quad (3)$$

where size  $a$  of the mv along the flow direction depends on the angle between incident laser beams  $\theta$  and on their diameter,  $D_1$ .  $\Delta T$  is particle residence time in the mv. Eq. (3) is valid for particle diameter  $d_p \ll D_1$ . The mv is defined by the intersection of two Gaussian laser beams. This volume in the shape of an ellipsoid is seen by receiving optics through a slit of width  $s$  which reduces its length. Resulting mv has roughly the shape of an oblique cylinder with lengths of main half-axes  $a/2$  and  $D_1/(2\cos\theta)$  and height  $s$ . The increase in slit size enlarges the projection area of mv into the flow direction, which is approximately  $S = s \cdot d / \cos \varphi$  where  $\varphi$  is scattering angle and thereby increases data rate according to Eq. (2). It however also reduces spatial resolution of the measurement. Variation in the laser beam diameter  $D_1$  influences  $S$  and therefore changes number of detected particles with interparticle arrival time gaps that are larger than  $\Delta T$ . Change in size  $a$  would reduce  $\dot{n}_{\text{max}}$  (Eq. (3)). For instance doubling  $D_1$  will also double up detected particle number  $p(\Delta t)$  and simultaneously will twice reduce corresponding interparticle arrival time  $\Delta t$  as seen at Fig. 11. A simulation made for our setup ( $D_{10} = 0.27$  mm,  $s = 0.3$  mm,  $k = 0.9$ ,  $\theta = 11.4^\circ$ ,  $\varphi = 50^\circ$ ,  $c = 10^4$  cm<sup>-3</sup>,  $\bar{v} = 3$  m/s, which leads to  $\dot{v} = 3.4$  kHz according Eq. (2)) has shown optimum  $D_1 = 1.3 D_{10}$  with increase in data rate by about 10%.

Particle concentration is limited by the particle source used and by desired character of the flow. Higher concentration is generally better, but the two-phase mixture would change from dilute to dense with increase in the concentration which could affect the particle flow. The yield  $K$  is given by the measurement system

setup and its technical condition. Also monodispersity of the seeding particles could have an effect. The detector sensitivity of a system measuring polydisperse aerosol must be set to a value at which large particles will not saturate the detector yet and, in such case, small particles might not meet detection limit.

#### 4. Conclusions

Extensive data on particle flow in time domain are contained in P/DPA results acquired in steady and cyclic flows in realistic airway model. The possibility of estimation of the velocity fluctuation PSD from these data was presented. Kern software was used to calculate the PSDs and optimised for our data. Similar fundamental character of TKE spectra was found for all processed data with systematic quantitative differences for (1) inspiration and expiration flows, (2) different positions in the airway tubes and (3) different flow regimes.

The amplitude of velocity fluctuations in PSD representation is relatively constant up to certain frequency ( $\sim 30$ – $50$  Hz depending on the flow regime), followed by moderately decreasing trend (up to  $\sim 300$  Hz for steady and  $\sim 500$  Hz for cyclic flows) and more rapid drop afterwards. The PSD curves are generally smooth with no distinct peaks identified in any analysed main-stream data file.

The PSD in the inspected frequency range ( $\sim 2$ – $700$  Hz) is practically independent of the particle size within  $1$ – $8$   $\mu\text{m}$  in whole range of flow regimes under consideration. This important finding, explained by low *Stk* values for observed cases, implies that micron sized aerosol particles closely follow the air flow. Particle P/DPA data can therefore be used for estimation of time-resolved local air velocity and for description of air flow structures in the airways. Further conclusion is that for these low *Stk* particles turbulent diffusion could significantly contribute to their deposition on the airway walls.

Successfulness of PSD estimation depends on available data. Present P/DPA results with mean data rate  $0.5$ – $10$  kHz (depending on position, particle size and flow conditions) allow for maximum usable frequency  $0.5$ – $1.6$  kHz. The most energetic fluctuations (energy-containing range + inertial subrange of the spectra) are included within such spectra but information on high-frequency fluctuations (dissipation range) can be hardly resolved. High concentration aerosol, larger measurement volume and optimum and precise LDA setup are crucial for an increase of the frequency range of PSD estimations. Improved results for velocity fluctuations could be used for validation of LES and DNS predictions where more effective turbulence models are to be developed (Longest and Holbrook, in press).

#### Acknowledgements

This work was supported by Projects ME 09030 of the Program KONTAKT and OC10052, COST Action Particles No. MP0806 funded by the Ministry of Education, Youth and Sports of the Czech Republic, by Project GA 105/11/1339 funded by the Czech Science Foundation and by the Project FSI-S-11-6 of the Brno University of Technology.

#### References

Adler, K., Brücker, C., 2007. Dynamic flow in a realistic model of the upper human lung airways. *Experiments in Fluids* 43 (2–3), 411–423.

Adrian, R.J., Yao, C.S., 1987. Power spectra of fluid velocities measured by laser Doppler velocimetry. *Experiments in Fluids* 5, 17–28.

Azarmi, S., Roa, W.H., Löbenberg, R., 2008. Targeted delivery of nanoparticles for the treatment of lung diseases. *Advanced Drug Delivery Reviews* 60, 863–875.

Benedict, L.H., Nobach, H., Tropea, C., 2000. Estimation of turbulent velocity spectra from laser Doppler data. *Measurement Science & Technology* 11, 1089.

Chan, T.L., Schreck, R.M., Lippmann, M., 1980. Effect of the laryngeal jet on particle deposition in the human trachea and upper bronchial airways. *Journal of Aerosol Science* 11 (5–6), 447–459.

Cheng, K.H., Cheng, Y.S., Yeh, H.C., Swift, D.L., 1997. An experimental method for measuring aerosol deposition efficiency in the human oral airway. *American Industrial Hygiene Association Journal* 58, 207–213.

Choi, Y., Park, Y., Lee, Ch., 2010. Helicity and geometric nature of particle trajectories in homogeneous isotropic turbulence. *International Journal of Heat and Fluid Flow* 31 (3), 482–487.

Cohen, B.S., Sussman, R.G., Lippmann, M., 1993. Factors affecting distribution of airflow in a human tracheobronchial cast. *Respiration Physiology* 93 (3), 261–278.

Corcoran, T.E., Chigier, N., 2000. Characterization of the laryngeal jet using Phase Doppler Interferometry. *Journal of Aerosol Medicine* 13 (2), 125–137.

Corieri, P., Riethmuller, M.L., 1989. Laser Doppler Velocimetry and Computer Automation to Measure Low Velocities in a Pulmonary Model, ICIAFS Record, Int. Congress on Instrumentation in Aerospace Simulation Facilities, pp. 226–236.

Crowe, C.T., Sommerfeld, M., Tsuji, Y., 1998. *Multiphase Flows with Droplets and Particles*. CRC Press, New York.

Fresconi, F.E., Prasad, A.K., 2007. Secondary velocity fields in the conducting airways of the human lung. *Journal of Biomechanical Engineering* 129 (5), 722–732.

Fresconi, F.E., Wexler, A.S., Prasad, A.K., 2003. Expiration flow in a symmetric bifurcation. *Experiments in Fluids* 35 (5), 493–501.

Gemci, T., Corcoran, T.E., Chigier, N., 2002. A numerical and experimental study of spray dynamics in a simple throat model. *Aerosol Science and Technology* 36 (1), 18–38.

Große, S., Schröder, W., Klaas, M., Klöckner, A., Roggenkamp, J., 2007. Time resolved analysis of steady and oscillating flow in the upper human airways. *Experiments in Fluids* 42 (6), 955–970.

Guan, X., Martonen, T.B., 2000. Flow transition in bends and applications to airways. *Journal of Aerosol Science* 31 (7), 833–847.

Jedelsky, J., Lizal, F., Jicha, M., 2009. Realistic transparent human airway model: flow distribution and aerosol transport under steady and unsteady flows. In: *Proceedings of the 20th International Symposium on Transport Phenomena*, Victoria, Canada, 7p.

Jedelsky, J., Lizal, F., Jicha, M., 2010a. Some aspects of particle motion under cyclic flow in realistic human airway model. In: *Proceedings of the 21st ISTP*, Kaohsiung, Taiwan, pp. 1–8, ISBN 978-986-6184-25-3.

Jedelsky, J., Lizal, F., Jicha, M., 2010b. Particle motion in a realistic human airway model under steady and cyclic flows. In: *Proceedings XXIV. Symposium on Anemometry*, Prague, ASCR, pp. 1–9.

Kleinstreuer, C., Zhang, Z., 2003. Laminar-to-turbulent fluid-particle flows in a human airway model. *International Journal of Multiphase Flow* 29, 271–289.

Kleinstreuer, C., Zhang, Z., Li, Z., 2008. Modeling airflow and particle transport/deposition in pulmonary airways. *Respiratory Physiology and Neurobiology* 163, 128–138.

Li, Z., Kleinstreuer, C., Zhang, Z., 2007. Simulation of airflow fields and microparticle deposition in realistic human lung airway models. Part I: Airflow patterns. *European Journal of Mechanics B/Fluids* 26, 632–649.

Lieber, B.B., Zhao, Y., 1998. Oscillatory flow in a symmetric bifurcation airway model. *Annals of Biomedical Engineering* 26 (5), 821–830.

Lin, C., Tawhai, M.H., McLennan, G., Hoffman, E.A., 2007. Characteristics of the turbulent laryngeal jet and its effect on airflow in the human intra-thoracic airways. *Respiratory Physiology and Neurobiology* 157 (2–3), 295–309.

Lizal, F., Elcner, J., Hopke, P.K., Jedelsky, J., Jicha, M., 2011. Development of a realistic human airway model. *Proceedings of the Institution of Mechanical Engineers, Part H: Journal of Engineering in Medicine* 0954411911430188, First Published on December 16, 2011. doi: 10.1177/0954411911430188.

Longest, P.W., Holbrook, L.T., in press. In silico models of aerosol delivery to the respiratory tract—development and applications. *Advanced Drug Delivery Reviews*. Available online 27 May 2011, doi:10.1016/j.addr.2011.05.009.

Martonen, T., Quan, L., Zhang, Z., Musante, C., 2002. Flow simulation in the human upper respiratory tract. *Cell Biochemistry and Biophysics* 37, 27–36.

Nobach, H., 2002. Local time estimation for the slotted correlation function of randomly sampled LDA data. *Experiments in Fluids* 32, 337–345.

Nobach, H., 2006. Data for Comparison of Spectra Measured by CTA and LDA Techniques. <<http://ldvproc.nambis.de/data/dtdata.html>> (accessed 2011).

Nobach, H., Müller, E., Tropea, C., 1996. Refined reconstruction techniques for LDA data analysis. In: *Proceedings of the 8th International Symposium on Applications of Laser Techniques to Fluid Mechanics*, Lisbon, Portugal.

Obrist, D., Henniger, R., Kleiser, L., 2011. Subcritical spatial transition of swept Hiemenz flow. In: *TSFP7 – 7th International Symposium on Turbulence and Shear Flow Phenomena*, Ottawa, Canada, 2011.

Ramuzat, A., Riethmuller, M.L., 2002. PIV investigations of oscillating flows within a 3D lung Multiple Bifurcation model. In: *11th International Symposium on Appl. of Laser Techniques to Fluid Flows*, Lisbon, Portugal, paper 19-1.

Schmidt, A., Zidowitz, S., Kriete, A., Denhard, T., Krass, S., Peitgen, H.O., 2004. A digital reference model of the human bronchial tree. *Journal of Computerized Medical Imaging and Graphics* 28, 203–211.

Scott, P.F., 1974. *Random Sampling Theory and Its Application to Laser Velocimeter Turbulent Spectral Measurements*, Report 74CRD216, General Electric Co., Corporate Research and Development.

- Sosnowski, T.R., Moskal, A., Gradon, L., 2007. Mechanism of aerosol particle deposition in the oro-pharynx under non-steady airflow. *Annals of Occupational Hygiene* 51 (1), 19–25.
- Su, W.C., Cheng, Y.S., 2009. Deposition of man-made fibers in human respiratory airway casts. *Journal of Aerosol Science* 40 (3), 270–284.
- Tanaka, G., Ogata, T., Oka, K., Tanishita, K., 1999. Spatial and temporal variation of secondary flow during oscillatory flow in model human central airways. *Journal of Biomechanical Engineering* 121 (6), 565–573.
- Theodore, L., 2005. *Nanotechnology: Basic Calculations for Engineers and Scientists*. Wiley-Interscience, ISBN: 0471739510.
- Theunissen, R., Riethmuller, M.L., 2008. Particle image velocimetry in lung bifurcation model. *Topics in Applied Physics* 112, 73–101.
- Tummers, M.J., Passchier, D.M., 1996. Spectral estimation using a variable window and the slotting technique with local normalization. *Measurement Science & Technology* 7, 1541.
- Zhang, Z., Kleinstreuer, C., 2002. Transient airflow structures and particle transport in a sequentially branching lung airway model. *Physics of Fluids* 14 (2).
- Zhang, Z., Kleinstreuer, C., 2004. Airflow structures and nano-particle deposition in a human upper airway model. *Journal of Computational Physics* 198 (1), 178–210.
- Zhang, Z., Kleinstreuer, C., Kim, C.S., 2001. Flow structure and particle transport in a triple bifurcation airway model. *Journal of Fluids Engineering Transactions of the ASME* 123, 320–330.

RESEARCH ARTICLE



## Multicomponent aerosol particle deposition in a realistic cast of the human upper respiratory tract

Markus Nordlund<sup>a</sup>, Miloslav Belka<sup>b</sup>, Arkadiusz K. Kuczaj<sup>a,c</sup>, Frantisek Lizal<sup>b</sup>, Jan Jedelsky<sup>b</sup>, Jakub Elcner<sup>b</sup>, Miroslav Jicha<sup>b</sup>, Youri Sauser<sup>a</sup>, Soazig Le Bouhellec<sup>a</sup>, Stephane Cosandey<sup>a</sup>, Shoaib Majeed<sup>a</sup>, Grégory Vuillaume<sup>a</sup>, Manuel C. Peitsch<sup>a</sup> and Julia Hoeng<sup>a</sup>

<sup>a</sup>Philip Morris International Research & Development, Philip Morris Products S.A., Neuchâtel, Switzerland; <sup>b</sup>Energy Institute, Faculty of Mechanical Engineering, Brno University of Technology, Brno, Czech Republic; <sup>c</sup>Department of Applied Mathematics, University of Twente, Enschede, The Netherlands

### ABSTRACT

Inhalation of aerosols generated by electronic cigarettes leads to deposition of multiple chemical compounds in the human airways. In this work, an experimental method to determine regional deposition of multicomponent aerosols in an *in vitro* segmented, realistic human lung geometry was developed and applied to two aerosols, i.e. a *monodisperse glycerol aerosol* and a *multicomponent aerosol*. The method comprised the following steps: (1) *lung cast model preparation*, (2) *aerosol generation and exposure*, (3) *extraction of deposited mass*, (4) *chemical quantification* and (5) *data processing*. The method showed good agreement with literature data for the deposition efficiency when using a *monodisperse glycerol aerosol*, with a mass median aerodynamic diameter (MMAD) of 2.3  $\mu\text{m}$  and a constant flow rate of 15 L/min. The highest deposition surface density rate was observed in the bifurcation segments, indicating inertial impaction deposition. The experimental method was also applied to the deposition of a nebulized *multicomponent aerosol* with a MMAD of 0.50  $\mu\text{m}$  and a constant flow rate of 15 L/min. The deposited amounts of glycerol, propylene glycol and nicotine were quantified. The three analyzed compounds showed similar deposition patterns and fractions as for the *monodisperse glycerol aerosol*, indicating that the compounds most likely deposited as parts of the same droplets. The developed method can be used to determine regional deposition for multicomponent aerosols, provided that the compounds are of low volatility. The generated data can be used to validate aerosol deposition simulations and to gain insight in deposition of electronic cigarette aerosols in human airways.

### ARTICLE HISTORY

Received 27 September 2016  
Revised 28 March 2017  
Accepted 29 March 2017

### KEYWORDS

Aerosol particle deposition; regional deposition; lung cast; respiratory tract; monodisperse glycerol aerosol; multicomponent aerosol; gas chromatography-mass spectrometry

## Introduction

*In vivo* inhalation studies are commonly used to assess the toxicity of deposited aerosol constituents and their influence on biological systems. However, when using standard inhalation toxicology approaches both the costs associated with testing and the time required to conduct the assays, generate, and analyze the data make it challenging to extensively test a large number of aerosols. Furthermore, in many parts of the world, there are mounting legal, regulatory, economic and social pressures that demand a reduction in animal testing and development of suitable alternatives such as *in vitro* and/or *in silico* testing (European Parliament, 2010; Schiffelers et al., 2012). As a result, new approaches are needed to obtain the knowledge of aerosol exposure and deposition mechanisms to determine the potential hazards for human health exposure.

Humans are continuously exposed to aerosols, solid or liquid particles suspended in a gas, during inhalation, which serves as a major pathway into the human body (Kreyling et al., 2010). During inhalation, an aerosol travels through different regions of the respiratory tract, which have

different geometric shapes and dimensions. Starting from the mouth and nasal cavity, the aerosol flows through the pharynx (throat) and larynx (upper respiratory tract) down to the trachea and bronchial tubes before it finally reaches the alveoli. During this journey, the aerosol experiences a variety of conditions and undergoes dynamic evolution. Aerosol particles may deposit on airway walls and gaseous compounds may be absorbed by the surrounding biological tissues. Aerosol particle deposition is strongly dependent on the flow pattern. Depending on the sizes of the particles in the aerosol, deposition locations inside the respiratory tract may vary greatly and regions of locally increased deposition, called “hot spots”, may be formed (Longest & Holbrook, 2012; Srirama et al., 2012). This locally increased exposure, may lead to inflammation and the onset of certain exposure-related diseases (Balásházy et al., 2003).

To evaluate the impact of deposited compounds from aerosols on biological tissues, experimental dosimetry *in vitro* is increasingly used to study the effect of direct deposition on living cell-cultures in exposure systems, such as air-liquid interface (ALI) systems (Comouth et al., 2013;

Paur et al., 2011; Tippe et al., 2002). For example, the Vitrocell<sup>®</sup> 24/48 ALI exposure system has been extensively used to evaluate the toxicity of cigarette smoke (Iskandar et al., 2013; Mathis et al., 2013; Schlage et al., 2014) as well as electronic cigarette aerosols (Neilson et al., 2015).

*In vitro* exposure systems using organotypic cell cultures are important to complement *in vivo* assessments for modern toxicology and have the potential to serve as a replacement. The systems should be robust, and the aerosol exposure equivalent or at least translatable to that of *in vivo*. It is therefore important to fully understand the aerosol dynamics in both *in vitro* exposure systems and the human respiratory tract. To determine the exposure and local deposition in the complex human airways at realistic flow conditions, aerosol particle deposition has been studied experimentally using physical *in vitro* replicas of the human respiratory tract (Chan & Lippmann, 1980; Cheng et al., 1999; Sosnowski et al., 2006), which are often generated from computed tomography or magnetic resonance imaging images. Many studies have been performed on extrathoracic deposition in mouth and throat replica (Cheng, 2012; Golshahi et al., 2013; Grgic et al., 2004a,b; Zhang et al., 2004). In most of these studies, gamma scintigraphy and gravimetry were used to determine deposition of controlled single component aerosol particles. These two methods are less suitable for determining deposition of multicomponent aerosols, such as those generated by electronic cigarettes.

Deposition experiments are challenging to perform for volatile, evolving aerosols and limited to the number of branches of the physical airway model. Aerosol particle deposition patterns in the respiratory tract can also be predicted using physical and chemical characteristics of the aerosol with realistic inhalation conditions and geometries in computational fluid dynamic (CFD) simulations with integrated physical models of aerosol transport, evolution, and deposition mechanisms (Longest & Holbrook, 2012). The generic CFD approach offers detailed, noninvasive information about the physics of the formation, evolution, transport and deposition of the aerosol, provided that the computational approach can be validated with high quality experimental deposition data. CFD simulations are used to identify local deposition patterns in human lungs, which indicate the level of dosing that biological cells in these regions are exposed to.

Regardless of whether the focus is on estimating the deposition in the respiratory tract to link the local tissue exposure to the onset of exposure-related diseases, to relate the aerosol exposure in *in vitro* exposure systems or validating aerosol deposition CFD models, experimental data on aerosol deposition under controlled conditions are highly valuable. Experimental deposition data in the human airways have mostly been generated for solid aerosol particles or for single compound liquid aerosols (Chan & Lippmann, 1980; Lizal et al., 2015; Zhou & Cheng, 2005), implying that there is a lack of experimental data and methods to determine and quantify deposition of multicomponent liquid aerosol particles, such as those generated from nebulizers or electronic cigarettes.

In this work, we focus on the experimental determination and quantification of the regional deposition of liquid-based

single-compound and multicomponent aerosol particles in a human respiratory tract cast model. The *in vitro* cast model of the human respiratory tract developed by Lizal et al. (2012), which includes the oral cavity and tracheobronchial region down to generation 7, was used experimentally to quantify deposition of a *monodisperse glycerol* aerosol and a nebulized *multicomponent aerosol* generated under carefully controlled conditions. To allow for measurements of multicomponent deposited matter in different locations of the realistic respiratory tract geometry, the cast model was divided into sections and a sensitive chemical quantification method was adopted.

## Materials and methods

The aerosol deposition experiments carried out in this work are based on the works by Belka et al. (2014) and Lizal et al. (2015) with a modified quantification technique for multicomponent aerosols. The experimental procedure comprises the following main steps: (1) *Lung cast model preparation*, (2) *Aerosol generation and exposure*, (3) *Extraction of deposited mass*, (4) *Chemical quantification*, and (5) *Data processing*.

### Lung cast model preparation

A segmented airway model based on the geometry of a real human lung was used for the experiments. This model was developed by Lizal et al. (2012) and used for the aerosol deposition study of monodisperse di-2-ethyl hexyl sebacate particles of different sizes by Lizal et al. (2015). The cast consisted of an oral cavity and subsequent airways down to the 7th generation of branching.

The internal geometry of the model was created by combining a digital reference model of the human tracheobronchial tree developed by Schmidt et al. (2004) and the oral cavity of *model A* from the Lovelace Respiratory Research Institute (Cheng et al., 1999), which was scanned and digitized at the Brno University of Technology. The resulting *in silico* representation of the human tracheobronchial tree is shown in Figure 1 (left). A physical model with 32 segments, shown in Figure 1 (right), was built from the digital geometry in the computer-aided design software Rhinoceros (McNeel, Barcelona, Spain) and produced by a Polyjet rapid prototyping method on an Objet machine (Stratasys, Eden Prairie, MN) with an accuracy of 0.1 mm and a layer thickness of 0.016 mm. The material used to construct the model was Veroclear from Stratasys. The segments of the cast model are constructed to separate the geometrical features of the airways. The model segments were numbered from top to bottom starting with the oral cavity as number one followed by the trachea as the second part as shown in Figure 1. Going down the airway, bifurcations as well as connecting sections in the upper parts of the airways, where the physical dimensions are relatively large, were isolated into separate segments. Further down the lung cast, where the physical dimensions are smaller, several bifurcations and channels were

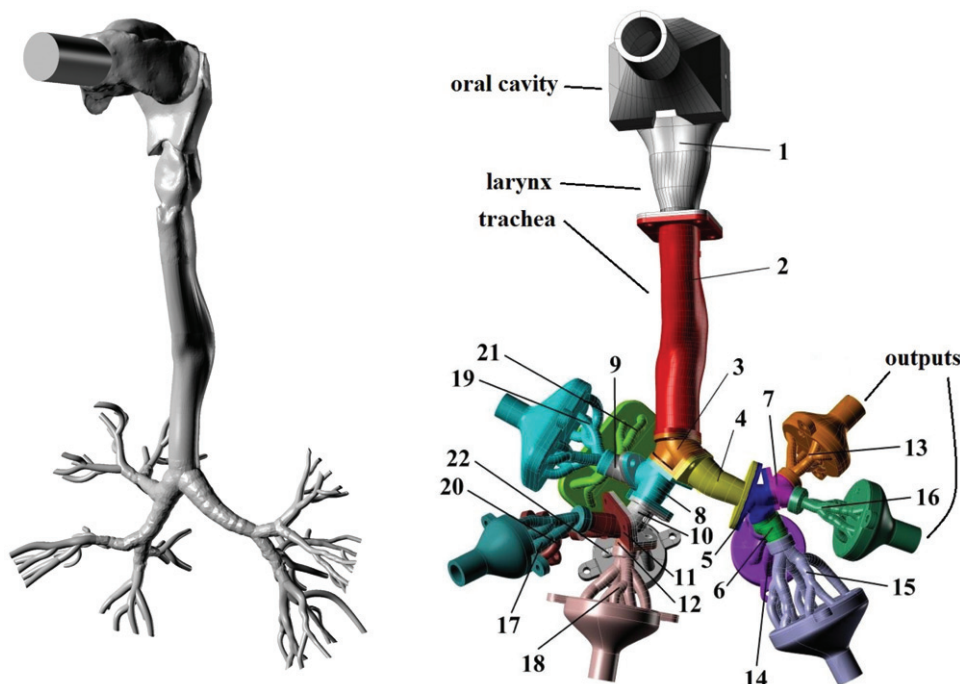


**Figure 1.** Visualization of the digital geometry (left) and the complete segmented cast model of human airways (right). Reproduced from Belka et al. (2014) with kind permission of The European Physical Journal (EPJ).

combined into complex segments numbered from 13 to 22 in Figure 1. To connect each of these complex shaped segments to an outlet tube, outlet connection segments numbered from 23 to 32 were also part of the entire model, as shown in Figure 1. The above-mentioned segmentation of the model resulted in parts of widely different internal surface areas ( $A_i$ ) and equivalent diameters ( $D_{e,i}$ ) for the airway segments, as shown in Table 1. Following the strategy by Lizal et al. (2012), the input diameter was used as the equivalent diameter for segments containing a single bifurcation. For segments containing more bifurcations, the average equivalent output diameters were first calculated for all the output cross sections in the segment. Thereafter, the average of all input and output equivalent diameters of the segment was used to represent the final  $D_{e,i}$  of the segment (Lizal et al., 2012).

Prior to each exposure experiment, all model parts were washed with a 2-propanol Chromasolv<sup>®</sup>, 99.9% solution from Sigma-Aldrich (St. Louis, MO) to ensure that no residual deposited mass was carried over from previous exposures. After the initial washing, the model parts were left to dry prior to being assembled by screwing together the 32 segments to form the final lung cast model. To avoid leakage during the aerosol exposures, a thin layer of silicone gel was applied to seal the joints between the segments. No explicit discharging of the assembled cast model was performed prior to the exposure experiments.

### Aerosol generation and exposure

The *monodisperse glycerol aerosol* and the *multicomponent aerosol* were in this work generated using different aerosol generation technologies, which are described separately in the following subsections.

**Table 1.** Internal surface area  $A_i$  and equivalent diameter  $D_{e,i}$  of the airway segments of the lung cast.

Segment	$A_i$ (cm <sup>2</sup> )	$D_{e,i}$ (mm)	Segment	$A_i$ (cm <sup>2</sup> )	$D_{e,i}$ (mm)
1 (—)	174.20	20.0	12 (G4)	4.13	7.0
2 (G0)	60.23	16.3	13 (G4 – G6)	10.11	3.0
3 (G1)	9.68	14.7	14 (G4 – G6)	16.13	3.3
4 (G1)	9.22	10.2	15 (G4 – G7)	25.23	3.3
5 (G2)	3.64	7.0	16 (G4 – G6)	10.72	2.5
6 (G3)	5.70	5.5	17 (G5 – G6)	14.41	3.6
7 (G3)	4.01	6.0	18 (G5 – G7)	17.71	4.1
8 (G2)	8.58	12.1	19 (G4 – G6)	21.94	3.6
9 (G3)	5.99	7.8	20 (G4 – G6)	5.92	2.6
10 (G3)	4.89	8.5	21 (G4 – G6)	20.97	3.4
11 (G4)	6.06	6.5	22 (G5 – G6)	10.60	3.4

The airway generations represented in each segment are shown in parentheses in the segments column.

### Generation of the monodisperse glycerol aerosol

Aerosol particles were generated by a TSI 3475 Condensation Monodisperse Aerosol Generator (CMAG) from TSI, Inc. (Shoreview, MN). A sodium chloride solution was used to form nuclei onto which glycerol vapors were condensed in the condensation chimney of the CMAG. The temperature of the CMAG saturator was set to 140 °C and the output flow rate was adjusted to 4 L/min. The generated glycerol aerosol was fed through a Krypton-85 (Kr-85) neutralizer. The neutralizer imparts a Boltzmann equilibrium charge distribution on the aerosol droplets. The glycerol aerosol exiting the neutralizer was measured using a TSI 3321 Aerodynamic Particle Sizer<sup>®</sup> (APS) spectrometer to be close to monodisperse with a count median aerodynamic diameter (CMAD) of 2.1  $\mu$ m and a geometric standard deviation (GSD) of 1.19, as shown in Figure 2(a). The mass median aerodynamic diameter (MMAD) was calculated using the Hatch-Choate equation (Hinds, 1999) to be 2.3  $\mu$ m. The conversion from CMAD to MMAD was done

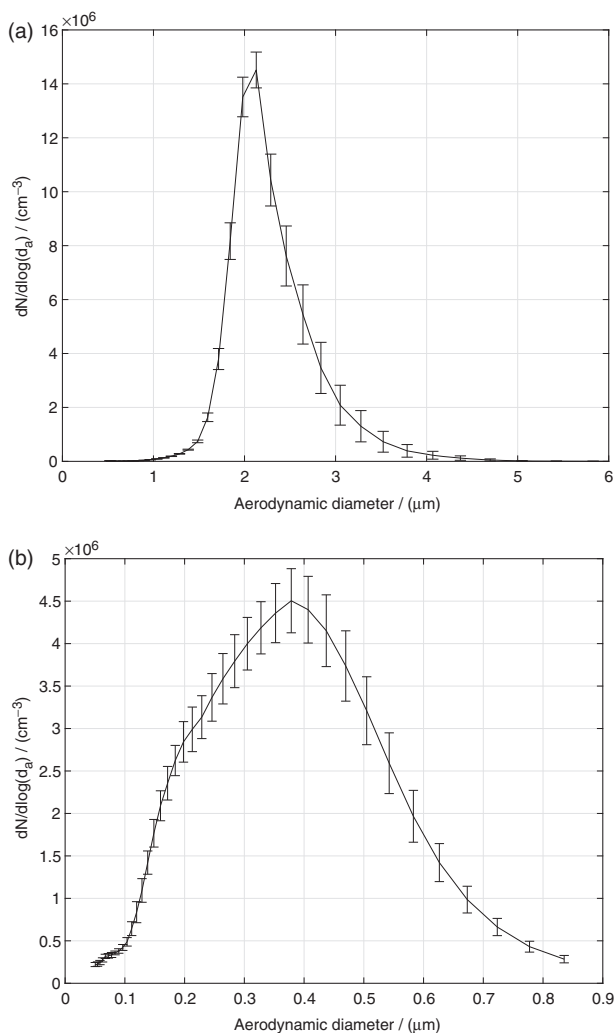


**Figure 2.** (a) Monodisperse glycerol and (b) multicomponent aerosol droplet size distributions, where  $d_a$  is the aerodynamic diameter and the error bars represent the SD (i.e. variability over the duration of a representative experiment).

using the Hatch-Cloate equation instead of using the APS software output directly, to avoid that potential APS signal artifacts in large size bins would influence the calculated MMAD. The particle size of  $2.3\ \mu\text{m}$  was chosen, as it was the largest glycerol particle size that could be generated with the CMAG without sacrificing the monodispersity of the aerosol particle size distribution. The transient behavior of the glycerol aerosol generation using the CMAG was characterized by the APS spectrometer to determine the time required for the aerosol generation to stabilize. The aerosol droplet number density,  $N$ , as well as the aerosol droplet size distribution were found to be stable after around 2000 s from the start of the aerosol generation. The experiments in this work were carried out after the CMAG reached a stable operating mode. The SD (i.e. variability over time for a representative experiment) represented by the error bars in [Figure 2](#) indicates the stability of the droplet size distribution during the course of the exposures. The SD was calculated from aerosol size distributions recorded every 5 min during the duration of an exposure. The mass concentration of the *monodisperse glycerol aerosol* exiting the CMAG was

determined to be  $7.3\ \mu\text{g}/\text{cm}^3$ . It was determined by first collecting the aerosol on Cambridge filters (Cambridge Filter Corporation, East Syracuse, NY) after 5, 10, 15, and 20 min of exposure, and thereafter extracting the captured aerosol mass from the filters and quantifying it by chemical analysis according to the procedure described in a later subsection.

#### Generation of the multicomponent aerosol

Aerosol particles were generated via nebulization of a multicomponent liquid solution typically used in cartridges of electronic cigarettes. The multicomponent solution consisted of propylene glycol, glycerol, nicotine and water with their mass fractions being 52.6%, 28.1%, 1.9%, and 17.4%, respectively. Nebulization was chosen as aerosol generation technique, as it is challenging to generate a stable multicomponent aerosol based on propylene glycol in the CMAG. Moreover, as nicotine was used, a time-consuming and careful cleaning of the CMAG would have to be carried out after every use. Instead, the solution was nebulized by a 1-jet Collision nebulizer (BGI Inc., Waltham, MA). The input air gauge pressure entering the nebulizer was 138 kPa, which aspirated the solution into a high-velocity gas jet, wherein the solution was atomized by shear force into droplets that consequently impacted onto a glass surface to produce a secondary population of fine droplets. The size distribution of the nebulized aerosol was measured by a TSI 3936 Scanning Mobility Particle Sizer<sup>®</sup> (SMPS) instrument (TSI, Shoreview, MN), and as can be seen in [Figure 2\(b\)](#), the aerosol was polydisperse with a CMAD of  $0.307\ \mu\text{m}$  and a GSD of 1.69 corresponding to a MMAD of  $0.497\ \mu\text{m}$ . The integrated TSI Data Merge Software Module Version 1.0.3.0 was used to convert the electrical mobility diameter provided by the SMPS to aerodynamic diameters. The intrinsic density of the multicomponent droplets used for the conversion to aerodynamic diameters was calculated based on the individual mass fractions and densities of the compounds to be  $1\ \text{g}/\text{cm}^3$ . Before performing any cast exposure, the aerosol droplet size distribution was recorded every 5 min for the duration of an exposure for the selected nebulization settings to study the stability of the aerosol droplet size distribution over time. The individual mass concentrations of propylene glycol, glycerol, and nicotine in the *multicomponent aerosol* exiting the nebulizer were determined to be 5.0, 2.8, and  $0.2\ \mu\text{g}/\text{cm}^3$ , respectively, using the same procedure as described previously for the *monodisperse glycerol aerosol*. The measured masses of the individual compounds increased linearly with time. The coefficients of determination of the linear fits, were 0.991, 0.968, and 0.997 for propylene glycol, glycerol, and nicotine, respectively, indicating that there were no significant evaporation of the compounds during the sampling.

#### Exposure

Charge neutralized aerosols were mixed with Alphagaz 1 Air dilution air (Carbagas AG, Gümülggen, Switzerland) (80% nitrogen, 20% oxygen, 99.999% purity) in a dilutor (Mécanique Industrielle Flück, Boudry, Switzerland),

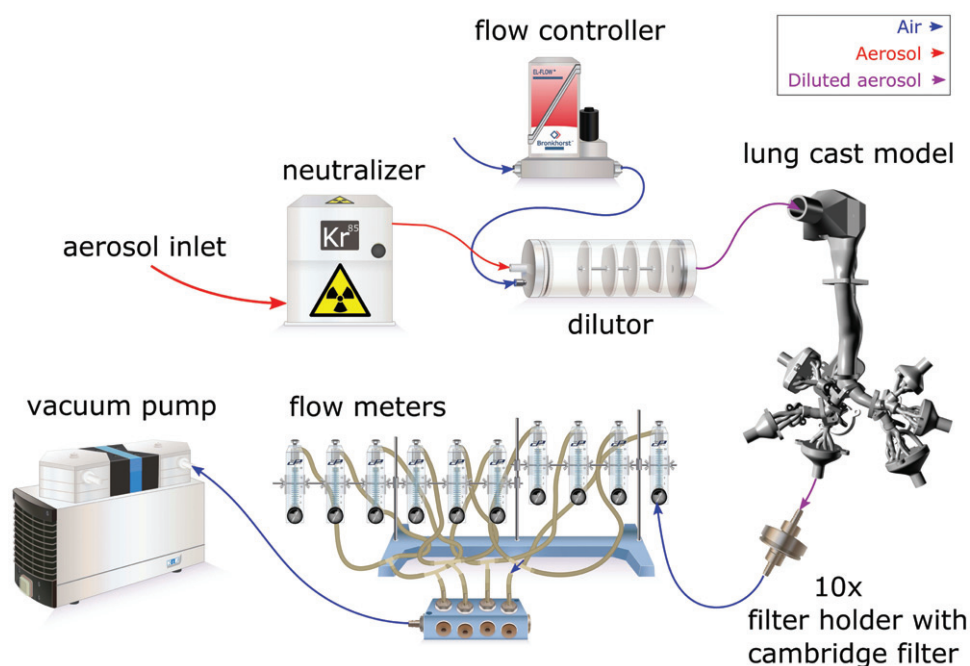


Figure 3. Schematic of the experimental set-up.

as depicted in Figure 3, to achieve a desirable total flow rate. The flow rate from the source of dilution air was controlled by a Bronkhorst F-201-C-RGD-22-V flow meter/controller. The diluted aerosol was then introduced to the lung cast model. The segmented cast model was composed of complex multi-generation parts that terminate by 10 output segments (see Figure 1). Each of these output segments were connected to a Cambridge filter (Cambridge Filter Corporation, East Syracuse, NY) inserted in holders, as described by Ghosh & Jeannet (2014), to collect all the aerosol particles passing through the cast. The rest of the experimental setup consisted of 10 rotameters (Cole-Parmer, Vernon Hills, IL), each attached to 1 of the 10 outlets to set and report the flow rate distribution between different output branches and to assure a desired total flow rate through the cast. The outputs from all 10 rotameter outlets were connected through a manifold tube connector (Vitrocell Systems GmbH, Waldkirch, Germany) to a KNF N840.12FT.18 vacuum pump (KNF Neuberger GmbH, Freiburg, Germany), which drew the aerosol through the cast by suction. Conductive black tubing (TSI, Shoreview, MN) was used to connect all parts of the experimental set-up, even though conductive tubing was only necessary upstream of the output filters. The temperature and relative humidity inside the cast model were not explicitly monitored, but were  $22 \pm 1$  °C and  $34 \pm 2\%$ , respectively, in the laboratory during all experiments. To be able to compare the generated deposition data with published data from other cast model experiments, and to produce reliable data that may be used to validate aerosol deposition simulations, there was no attempt made to match the temperature and relative humidity conditions with human conditions in this work.

A steady-state inhalation mode with a flow rate of 15 L/min, representing average flow conditions of a sedentary regime (quiet breathing) (Elcner et al., 2016),

Table 2. Flow rates for each airway segment of the lung cast for the *monodisperse glycerol aerosol* and *multicomponent aerosol* experiments.

Segment	$Q_i$ (L/min)	Segment	$Q_i$ (L/min)
1	15.00	13, 23*	0.700
2	15.00	14, 24*	0.800
3	15.00	15, 25*	2.000
4	4.500	16, 26*	0.950
5	4.500	17, 27*	1.775
6	2.800	18, 28*	2.325
7	1.650	19, 29*	1.900
8	10.55	20, 30*	1.550
9	3.425	21, 31*	1.525
10	7.125	22, 32*	1.475
11	3.325	–	–
12	3.800	–	–

The flow rates through the 10 outlets (marked by \*) were set and measured by rotameters totaling a flow rate of 15 L/min through the lung cast. The flow rates for the other sections were calculated from the outlet sections respecting the branch connectivities shown in Figure 1.

was chosen to fully control the experimental condition and to facilitate the method validation with deposition data from other published *in vitro* inhalation studies. The flow rates  $Q_i$  through the output segments numbered from 23 to 32, see Figure 1, were set by the rotameters to the values related to the pneumatic resistance of the model airways reported by Lizal et al. (2015), totaling a 15 L/min flow rate at the cast model inlet. The flow rates through the airway sections of the cast, provided in Table 2, were calculated from the flow rates of the outlet sections and the branch connectivities shown in Figure 1. As shown in Table 2, the outlet flow rates were different for each of the 10 outlets. The inlet flow rate at the entrance to the oral cavity was measured by a TSI 4140 mass flow meter prior to every experiment to check the tightness of the model and that the total flow rate through the cast was 15 L/min. To ensure that the aerosol generation for the *monodisperse glycerol aerosol* experiments remained stable over the course of the exposure,

the particle size distribution was measured before and after the deposition experiment using the APS. The cast model was exposed for 1 h in the *monodisperse glycerol aerosol* experiments and between 1.5 h and 2 h in the *multicomponent aerosol* experiments to achieve sufficient deposited mass on all cast segments for quantification. The experiments were repeated 7 times for the *monodisperse glycerol aerosol* and 4 times for the *multicomponent aerosol* experiments, each on different days.

### Extraction of deposited mass

After the segmented lung cast was exposed to the generated aerosols, all segments of the cast model and the filter holders were disassembled. The deposited mass on each disassembled segment was extracted by rinsing with known amounts of 2-propanol Chromasolv<sup>®</sup>, 99.9% solution from Sigma-Aldrich. The 2-propanol extraction solution contained phenol-<sup>13</sup>C<sub>6</sub> (2 µg/mL) and naphthalene-D<sub>8</sub> (0.5 µg/mL), which were used to monitor the stability of the chemical quantification using gas chromatography-mass spectrometry (GC-MS). Because the segments of the cast are differently sized in both volume and internal surface area, the extraction method for the various compounds was adapted to optimize the extracted deposited mass per volume of extraction solution. Smaller parts of the cast were placed in beakers filled with the extraction solution and were sonicated for 1 min. Larger parts, such as the oral cavity and the trachea, were wrapped with SigmaAldrich parafilm to seal the inlet and outlet and a small amount of the extraction solution was injected inside. These wrapped segments were put in a Labinco LD76 Digital Rotary Mixer (Gemini BV, Apeldoorn, the Netherlands) for 30 min with a frequency of rotation of 1 Hz. The Cambridge filters and filter holders were washed together by flushing them with the extraction solution without taking them apart. The resulting extraction solutions, including the extracted deposited mass, were stored in dark glass bottles and put into a freezer at -20 °C before the chemical quantification was carried out. Because the disassembling and the extraction procedure is time-consuming, only compounds with low volatility can be measured by the developed experimental method. For highly volatile compounds, the initially deposited mass can evaporate during handling.

Black conductive tubing was used to connect the outlet segments and the filter holders but was not extracted in the experiments. However, to investigate the amount of aerosol that deposits in these tubes compared with that on the output filters, a selection of seven tubes were washed by the extraction solution and analyzed by the chemical quantification method. The deposited mass in the connecting tubes on average represented 2.5% of the deposited mass collected by the connected filter. Based on the findings from the *monodisperse glycerol aerosol* experiments, the same extraction procedure was also used for the *multicomponent aerosol* experiments, i.e. each cast segment was rinsed once per experimental run to extract the deposited mass from the segment.

### Chemical quantification

In this section, the chemical quantification method allowing for quantification of multiple chemical compounds found in the extraction solutions from the segments is presented.

### Preparation of calibration samples

Calibration samples for the three compounds of interest were prepared at different concentration levels, using: certified nicotine 99.9% from the Institute of Industrial Organic Chemistry (Warsaw, Poland), and propylene glycol 99.5%, glycerol 99.5% and 2-propanol Chromasolv<sup>®</sup>, 99.9% were from Sigma-Aldrich. For each compound, 12 calibration standards containing glycerol at concentrations ranging from 1.4 to 700 µg/mL, nicotine from 0.3 to 135 µg/mL and propylene glycol at concentrations ranging from 0.2 to 160 µg/mL were prepared. The calibration standards also contained acrylamide, diethylene glycol, menthol, phenol and triacetin compounds, which were not used for quantification purposes in this work, since only glycerol, nicotine and propylene glycol were analyzed. The calibration standards were prepared in a dilution solution of 2-propanol containing naphthalene-D<sub>8</sub> (0.5 µg/mL) and phenol-<sup>13</sup>C<sub>6</sub> (2 µg/mL). Naphthalene-D<sub>8</sub> and phenol-<sup>13</sup>C<sub>6</sub> were used to control the stability and repeatability of the chemical analysis.

### Preparation of extracted samples

The samples extracts, resulting from the washing of the cast segments, were extracted and diluted with a 2-propanol solution containing phenol-<sup>13</sup>C<sub>6</sub> (2 µg/mL) and naphthalene-D<sub>8</sub> (0.5 µg/mL) to obtain concentration levels within the predefined calibration ranges for the measured compounds. The extracts were then transferred into GC vials for GC-MS analysis.

### Instrumentation and quantification

The analysis were performed using an Agilent 6890 N Gas Chromatograph from Agilent Technologies Inc. (Santa Clara, CA), equipped with an Agilent J & W DB-WAXetr GC capillary column (30 m, 0.25 mm inner diameter, 0.5 µm film thickness) and an Agilent Mass Spectrometer 5973 as the detector. The MSD Chemstation software version E.02.02.1431 was used for data acquisition and integration.

The carrier gas was helium at a constant flow rate of 1.2 mL/min. The column temperature was initially set to 65 °C for a period of 0.5 min, then gradually increased to 175 °C at a rate of 7 °C/min, and finally increased to 260 °C at a rate of 15 °C/min and held at 260 °C for 8 min. The injection port temperature was set at 250 °C to inject 0.5 µL of samples and standards in a pulsed splitless mode.

For GC-MS detection, an electron ionization system was used with an ionization energy of 70 eV. The MS transfer line temperature, MS source and MS Quad temperatures were set at 250 °C, 230 °C and 150 °C, respectively. Data acquisition was carried out by the single ion monitoring

mode and the quantification was performed by extraction of the total ion count obtained at the retention time of the measured compounds for glycerol (retention time:  $21.4 \pm 0.3$  min), nicotine (retention time:  $17.8 \pm 0.3$  min) and propylene glycol (retention time:  $12.8 \pm 0.3$  min).

The monitored ions were  $m/z$  45 and 61 for segment 1 in the retention time zone of propylene glycol;  $m/z$  55,  $m/z$  71,  $m/z$  133,  $m/z$  136 and  $m/z$  162 for segment 2 in the retention time zone of nicotine; and  $m/z$  43,  $m/z$  61,  $m/z$  116 and  $m/z$  145 for segment 3 in the retention time zone of glycerol.

To determine the deposited aerosol mass present in the analyzed samples, the results of the chemical analyses were quantified against the 12 analyzed calibration standards for each compound. This quantified the analyzed compound that was deposited and extracted from each of the cast segments. Hence, the mass deposited in all cast segments and filters was quantified, so that the mass deposition rates over the period of the experiment could be derived.

### Data processing

The final step of the experimental method was to process the deposition data from the chemical quantification. The measured quantity resulting from the chemical quantification was the mass deposition rate per segment  $i$  of the analyzed compound  $\alpha$ , denoted by  $R_{\alpha,i}^m$ , having the dimension unit mass per unit time.  $R_{\alpha,i}^m$  can be computed by dividing the quantified mass  $m_{i,\alpha}$  of each compound  $\alpha$  in segment  $i$  with the total exposure time  $t$ . Another quantity, more relevant for assessing the dosage delivered to biological tissues, is the deposition surface density rate denoted by  $R_{\alpha,i}^p$  having the dimension unit mass per unit time per unit area.  $R_{\alpha,i}^p$  is defined as  $R_{\alpha,i}^m$  divided by the internal surface area,  $A_p$ , of the segment  $i$ . To allow for a comparison of the generated deposition data to published data in the literature, the deposition efficiency was calculated for each segment of the cast for the *monodisperse glycerol aerosol* experiment. Deposition efficiency is a dimensionless quantity used in the literature for deposition in *in vitro* lung cast models (Chan & Lippmann, 1980; Lizal et al., 2015; Zhou & Cheng, 2005). The deposition efficiency,  $\xi_{\alpha,i}$ , of compound  $\alpha$  and segment  $i$  is defined as the ratio between the mass of the particles deposited in segment  $i$ , and the total mass of the aerosol particles entering the segment.  $\xi_{\alpha,i}$  can be calculated from the measured  $R_{\alpha,i}^m$  using the expression:

$$\xi_{\alpha,i} = \frac{R_{\alpha,i}^m}{R_{\alpha,i}^m + \sum_{\theta} R_{\alpha,\theta}^m} \quad (1)$$

where  $\theta$  denotes the segments downstream of segment  $i$ , including the outlet connection segments (numbered 23–32), outlet tubes and filters. Moreover, instead of segment numbers, it is common to represent the sections in terms of their representative Stokes (St) number (Zhou & Cheng, 2005). The St number is a dimensionless number characterizing the dynamics of particles suspended in a fluid flow and can be

**Table 3.** Dimensionless numbers for each single generation segment of the lung cast for the *monodisperse glycerol aerosol* experiments.

Segment	$Re_i$	$St_i$	Segment	$Re_i$	$St_i$
1	1022	$7.98 \times 10^{-4}$	7	375	$3.25 \times 10^{-3}$
2	1254	$1.47 \times 10^{-3}$	8	1188	$2.53 \times 10^{-3}$
3	1391	$2.01 \times 10^{-3}$	9	598	$3.07 \times 10^{-3}$
4	595	$1.78 \times 10^{-3}$	10	1142	$4.94 \times 10^{-3}$
5	866	$5.52 \times 10^{-3}$	11	697	$5.15 \times 10^{-3}$
6	694	$7.16 \times 10^{-3}$	12	740	$4.71 \times 10^{-3}$

calculated as:

$$St_i = \frac{\rho_p d_p^2 U_i}{18\mu D_{e,i}} \quad (2)$$

for the lung cast segment  $i$ , where  $\rho_p$  is the intrinsic density of an aerosol particle of diameter  $d_p$ ,  $U_i$  is the average velocity in segment  $i$  having an equivalent diameter  $D_{e,i}$ , and  $\mu$  is the dynamic viscosity of the fluid (Lizal et al., 2015). The average velocity in each segment can be calculated from the volumetric flow rates according to:

$$U_i = \frac{4Q_i}{\pi D_{e,i}^2} \quad (3)$$

The St numbers for the *monodisperse glycerol aerosol* together with representative Reynolds numbers ( $Re_i = U_i D_{e,i} / \nu$  for both aerosol types, where  $\nu$  is the kinematic viscosity of the aerosol) for the single generation segments are provided in Table 3. The thermophysical properties used for the dimensionless numbers were:  $\nu = 1.56 \times 10^{-5}$  m<sup>2</sup>/s and  $\mu = 1.84 \times 10^{-5}$  Pa s, representing air at 25 °C, and  $\rho_p = 1258$  kg/m<sup>3</sup> representing glycerol liquid density at 25 °C.

Another quantity used to analyze the deposition of the analyzed compounds from the experiments was the regional deposition fraction,  $RDF_{\alpha,i}$ , defined as:

$$RDF_{\alpha,i} = \frac{R_{\alpha,i}^m}{\sum_{k=1}^{N_c} R_{\alpha,k}^m} \quad (4)$$

where  $N_c = 22$ .  $RDF_{\alpha,i}$  represents the amount of compound  $\alpha$  that is deposited in segment  $i$  compared to the total deposited mass in all segments representing the airway geometry ( $i = 1, \dots, 22$ ). The data of the filters and filter holders were not included in the calculation of the  $RDF_{\alpha,i}$ , as especially the captured propylene glycol and nicotine were found to re-evaporate from the filters during the long exposure times and constant flow rates. Nevertheless, comparing the  $RDF_{\alpha,i}$  calculated from Equation (4) for the various compounds gives an indication on how the different chemical compounds deposit in the cast segments as compared to each other.

## Results and discussion

In this section, the results of the experiments carried out in this work are presented and discussed separately for the *monodisperse glycerol aerosol* and the *multicomponent aerosol* experiments.

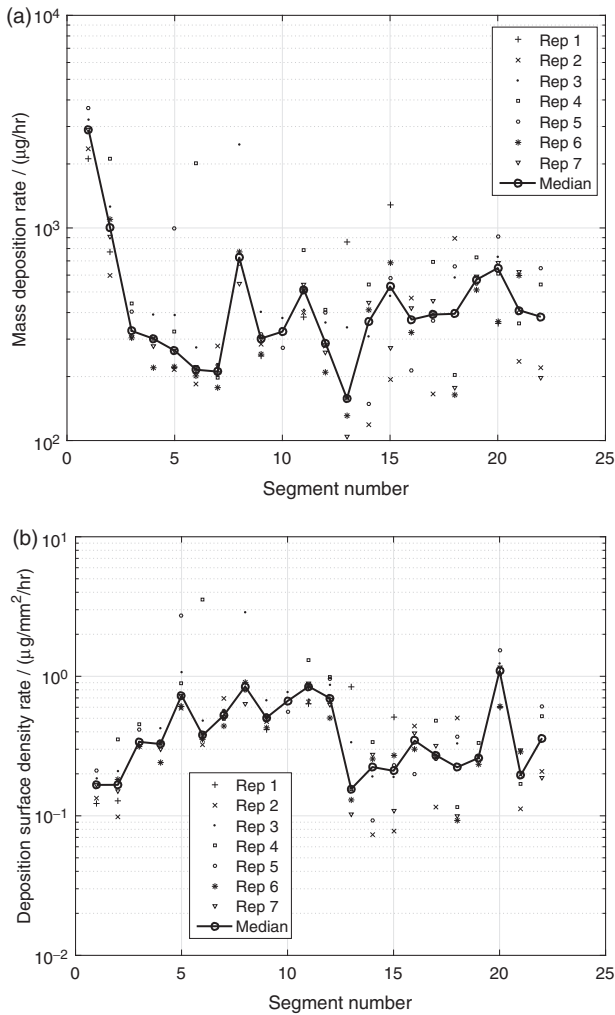


**Figure 4.** Mass deposition rate,  $R_{\alpha,i}^m$ , of glycerol ( $\alpha = \text{glycerol}$ ) (a) per cast segments ( $i = 1, \dots, 22$ ), and (b) the deposition surface density rate per segment,  $R_{\alpha,i}^p$ , for the *monodisperse glycerol aerosol* experiments.

### Monodisperse glycerol aerosol experiment

The deposition of the *monodisperse glycerol aerosol* can be expressed in the mass deposition rate per segment,  $R_{\alpha,i}^m$  ( $\alpha = \text{glycerol}$ ). Figure 4(a) shows that among the airway cast segments ( $i = 1, \dots, 22$ ) the highest  $R_{\alpha,i}^m$  was in the mouth cavity ( $i = 1$ ) followed by the trachea segment ( $i = 2$ ), whereas  $R_{\alpha,i}^m$  was much lower in the smaller segments further down the airway. This is a consequence of the much larger available surface areas,  $A_i$ 's of the oral cavity and trachea segments as compared with those of bifurcations and bronchial tubes segments (see Table 1). The 10 output connectors ( $i = 23, \dots, 32$ ) together with their attached filter holders and filters, shown in Figure 5, account for more than 99% of the total deposited mass in the experiment. This indicates that only about 1% of the aerosol entering the mouth cavity was deposited in the first 7 generations of the lung cast for this particular aerosol and flow conditions.

A more relevant measure for the aerosol deposition in the airways is the deposition surface density rate,  $R_{\alpha,i}^p$ , which relates to the concentration of the deposited matter on the internal surface of the lung cast segments. Figure 4(b) shows that the highest  $R_{\alpha,i}^p$  took place in the upper bifurcations and

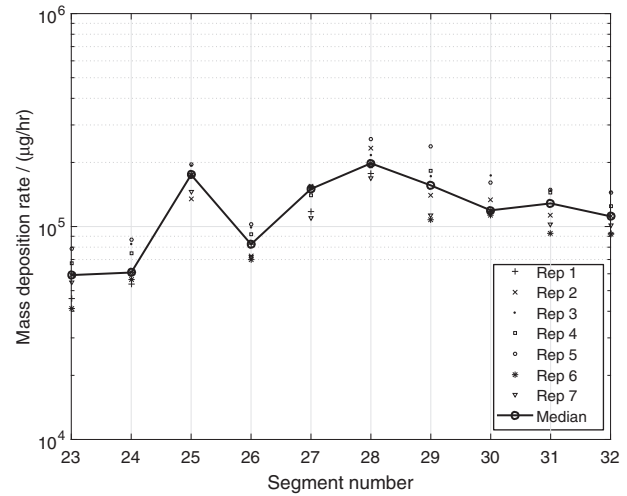


**Figure 5.** Mass deposition rate,  $R_{\alpha,i}^m$ , of glycerol ( $\alpha = \text{glycerol}$ ) per output connector segments ( $i = 23, \dots, 32$ ), in which the deposited mass extracted from the attached filter holders and filters were added for the *monodisperse glycerol aerosol* experiments.

bronchial tubes ( $i = 3, \dots, 12$ ) and in the segment  $i = 20$ , representing the 4th bifurcation on the right side of the lung (see Figure 1). Furthermore, the  $R_{\alpha,i}^p$  was low in the oral cavity segment ( $i = 1$ ) and in the trachea segment ( $i = 2$ ), even though the deposition rates were high in Figure 4(a). The deposition surface density rate was also relatively low in the segments  $i = 13, \dots, 22$ , representing the 4th–7th airway generation, with the exception for segment  $i = 20$ , as mentioned previously.

The variability of the quantified deposition rate of glycerol was high between the seven replicates as shown in Figure 4(a,b). This variability is most likely a consequence of the many manual handling steps of the experimental method. The manual extraction step for the complexly shaped segments was difficult to perform because of the small quantity of extraction solution that could be used to still be able to quantify the deposited mass by GC-MS analysis.

As mentioned previously, the lung cast was not electrically discharged prior to the aerosol exposures, even though the material may have contained a small electrostatic field by itself. The potential remaining image charge in the cast may have increased the deposition slightly despite the aerosol being charge neutralized. This potential effect should however be minor for the aerosol droplets in the *monodisperse glycerol aerosol* experiments, as electrostatic effects are most pronounced for sub-micrometer particles at low flow rates (Azhdarzadeh et al., 2015; Hickey, 2007).

Another way to represent the deposition characteristics of the aerosol in the various segments is to convert the deposition data to the dimensionless quantity deposition efficiency,  $\xi_{\alpha,i}$ , and the segment number to their respective representative St number. Figure 6 shows that despite the variability of the experiments, the quantified deposition efficiency agreed well with previously published *in vivo* as well as experimental *in vitro* lung cast deposition data by Cheng et al. (1999), Chan & Lippmann (1980), Zhou & Cheng (2005) and Lizal et al. (2015). For example, the deposition

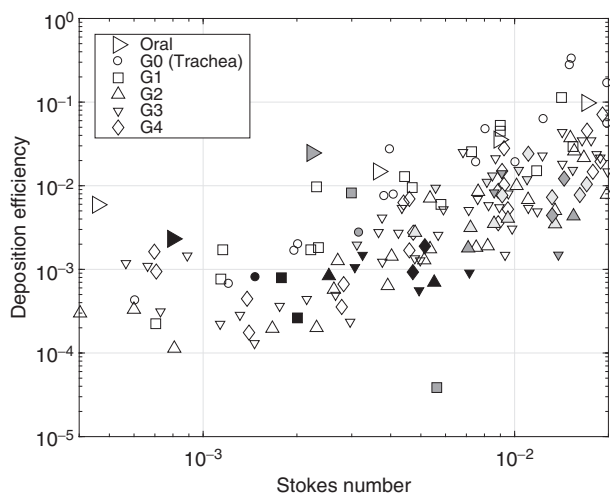


**Figure 6.** Deposition efficiency,  $\xi_{\alpha,i}$ , for the oral cavity, the trachea (G0) and the segments representing generations G1–G4 as a function of the local Stokes number for the *monodisperse glycerol aerosol* experiments ( $\alpha$  = glycerol). Symbols of different colors represent data from different sources: the present study (black), Zhou & Cheng (2005) (white), Chan & Lippmann (1980) (light gray) and Lizal et al. (2015) (dark gray). The only exception is the white symbols for the oral segment representing the data extracted from Cheng et al. (1999).

efficiency of the oral cavity segment, resulting from the *monodisperse glycerol aerosol* experiments, matches the trend set by the data of Cheng et al. (1999) and Lizal et al. (2015), as shown in Figure 6. It is also shown in Figure 6 that the deposition efficiencies of the segments representing the trachea and the airway generations G1–G4 closely match the data by Chan & Lippmann (1980), Zhou & Cheng (2005) and Lizal et al. (2015). For the segments incorporating multiple generations in the same segment ( $i = 13, \dots, 22$ ), no comparison with literature data could be done, due to a lack of equivalent literature data. The general agreement with the data by Lizal et al. (2015), despite the larger particle size leading to larger St numbers in the experiments by Lizal et al. (2015), is important as the lung casts used are identical and so are the computations of the dimensionless parameters from the segment flow rates and equivalent diameters of the various segments. In the works by Chan & Lippmann (1980) and Zhou & Cheng (2005), both the lung geometries (*in vivo* as well as another lung cast) and the conversion to representative dimensionless parameters are slightly different compared with those used in this study. For example, the lung cast models used by Lizal et al. (2015) and in this work are more complex than in the works by Chan & Lippmann (1980) and Zhou & Cheng (2005) with more airway generations (7 compared to 4), realistic laryngeal structure and an integrated oral cavity. Moreover, the particle type used as well as the quantification methods applied are different for all studies. For example, Chan & Lippmann (1980) and Zhou & Cheng (2005) used solid particles and optical methods, Lizal et al. (2015) used liquid-based aerosol particles and positron emission tomography, whereas liquid-based aerosol particles and chemical GC-MS analysis were used in our work to quantify the deposited mass of the *monodisperse glycerol aerosol*. The added model complexity and the differences in the aerosol particle types may explain the wider scatter in these data compared with those by Chan &

Lippmann (1980) and Zhou & Cheng (2005). Nevertheless, the  $\xi_{\alpha,i}$  values generated from the *monodisperse glycerol aerosol* experiments were shown to represent the published data well, which gives confidence in the experimental method developed to determine the regional deposition in our lung cast model using a chemical quantification method suitable to detect multiple chemical components in the extracted deposited matter.

### Multicomponent aerosol experiment

Having established confidence in the developed experimental method by validating the deposition efficiency of a single-compound aerosol generated under controlled conditions, the method was further applied to the exposure of the lung cast using a *multicomponent aerosol*. As shown in Figure 7, the mass deposition rates,  $R_{\alpha,i}^m$ , for glycerol (Figure 7(a)), propylene glycol (Figure 7(b)) and nicotine (Figure 7(c)) show similar deposition patterns, although of different magnitudes for all three compounds with respect to the cast segments.  $R_{\alpha,i}^m$  of glycerol in segment  $i = 3$  and of propylene glycol in segment  $i = 21$ , were outside of the calibration ranges and are therefore missing in Figure 7(a,b), respectively. In the *monodisperse glycerol aerosol* experiments, the oral cavity ( $i = 1$ ) experienced a significantly higher  $R_{\alpha,i}^m$  than the other cast segments, whereas this effect was less apparent in the *multicomponent aerosol* experiments for any of the compounds, as shown in Figure 7(a–c). The reduced deposition rate in the upper segments of the cast for the *multicomponent aerosol*, where the flow rates were the highest, indicates that the more than 4 times smaller aerosol droplets in the *multicomponent aerosol* experiments (MMAD of  $0.5 \mu\text{m}$ ) were less prone to deposit by inertial effects than the larger droplets (MMAD of  $2.3 \mu\text{m}$ ) in the *monodisperse glycerol aerosol* experiments. The magnitudes of the mass deposition rates of glycerol were very similar between the *monodisperse glycerol aerosol* and the *multicomponent aerosol* experiments, except for the oral cavity ( $i = 1$ ) as discussed previously. The  $R_{\alpha,i}^m$  of propylene glycol was significantly higher than for glycerol and the  $R_{\alpha,i}^m$  of nicotine was the lowest of all three analyzed compounds in the *multicomponent aerosol* experiments. These results are direct consequences of the composition of the nebulized liquid mixture, in which propylene glycol and nicotine were the most and the least abundant compounds, respectively. As shown in Figure 7(a–c), the variability of the measured  $R_{\alpha,i}^m$ , for all three compounds were similar to the variability in the *monodisperse glycerol aerosol* experiments. This gives confidence that the developed method is also suitable for quantifying the deposited masses of compounds coming from exposures of multicomponent aerosols. The lack of temperature control of the cast model may have resulted in vapor condensation onto the walls of the cast model. This potential vapor condensation may also have contributed to the measured deposition, despite the low volatility of the three compounds measured. Evaporation of propylene glycol from the nebulized aerosol droplets, but also for nicotine, may have however occurred during the dilution step in the mixing unit. Thanks to the

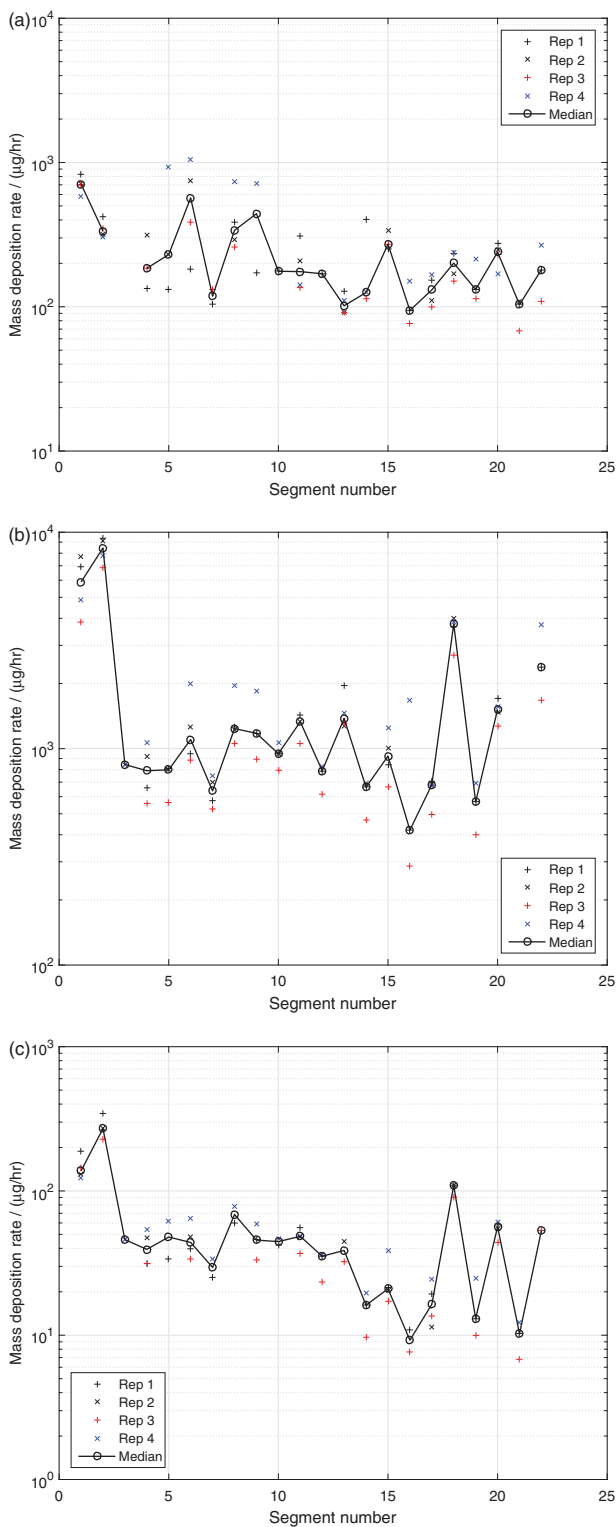


Figure 7. Mass deposition rate per segment,  $R_{\alpha,i}^m$ , of (a) glycerol, (b) propylene glycol and (c) nicotine from exposure with a *multicomponent aerosol*.

chemical quantification of the extracted deposited matter adopted in this work, the developed methodology also accounts for vapor condensation in addition to droplet deposition. This is an important benefit of the developed method, especially in the context of toxicological assessments, where the total dosing (including both vapor absorption and aerosol droplet deposition) contributes to the toxicological activity. Even though the aerosol was charge

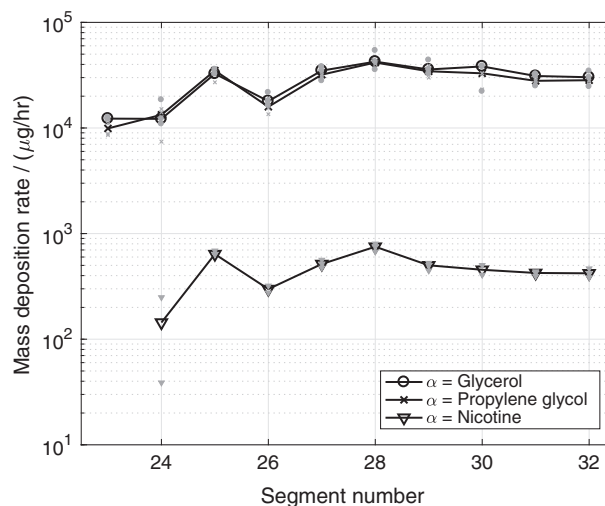


Figure 8. Mass deposition rate,  $R_{\alpha,i}^m$ , of glycerol, propylene glycol and nicotine per output connector segments ( $i = 23, \dots, 32$ ), in which the deposited mass extracted from the attached filter holders and filters were added for the *multicomponent aerosol* experiments.

neutralized, image charges induced by the cast material itself may also have contributed to the aerosol droplet deposition, especially for the lower branches where the flow rates are the lowest (Azhdarzadeh et al., 2015; Hickey, 2007). The effect of potential image charges in the cast model on the deposition is difficult to estimate and represents a limitation of the present cast model.

As shown in Figure 8,  $R_{\alpha,i}^m$  for glycerol and propylene glycol was similar on the outlet filters, even though the mass concentration of propylene glycol, measured directly after the nebulizer, was 1.8 times that of glycerol. Moreover, the mass deposition rate of glycerol were found to be on average 69 times that of nicotine on the filters (see Figure 8), whereas the mass concentration of glycerol, measured directly after the nebulizer, was 14 times that of nicotine. This indicates that most likely, the propylene glycol and the nicotine that were captured on the outlet filters most likely re-evaporated from the filters during the long exposure under constant flow rates. The observed equality between the deposited propylene glycol and glycerol for the outlet filters was not seen for the cast segments, as shown in Figure 7(a–c). This indicates that even though some re-evaporation may have occurred from the deposited mass on the cast segments, no compound-specific effects on the measured deposition rates on these segments were observed. This is also confirmed by the regional deposition fraction  $RDF_{\alpha,i}$  for each compound, presented below.

As shown in Figure 9(a–c), the deposition surface density rate,  $R_{\alpha,i}^p$ , for all three compounds showed similar patterns over all the segments of the cast as the *monodisperse glycerol aerosol*. The highest  $R_{\alpha,i}^p$  was observed in the bifurcations and smaller segments ( $i = 5, \dots, 12$ ).

To estimate potential differences between the deposition of the different chemical compounds analyzed, the regional deposition fraction  $RDF_{\alpha,i}$  was calculated from Equation (4) for each of the three quantified compounds of the *multicomponent aerosol* and for the glycerol in the *monodisperse glycerol aerosol* experiments. As especially propylene glycol and

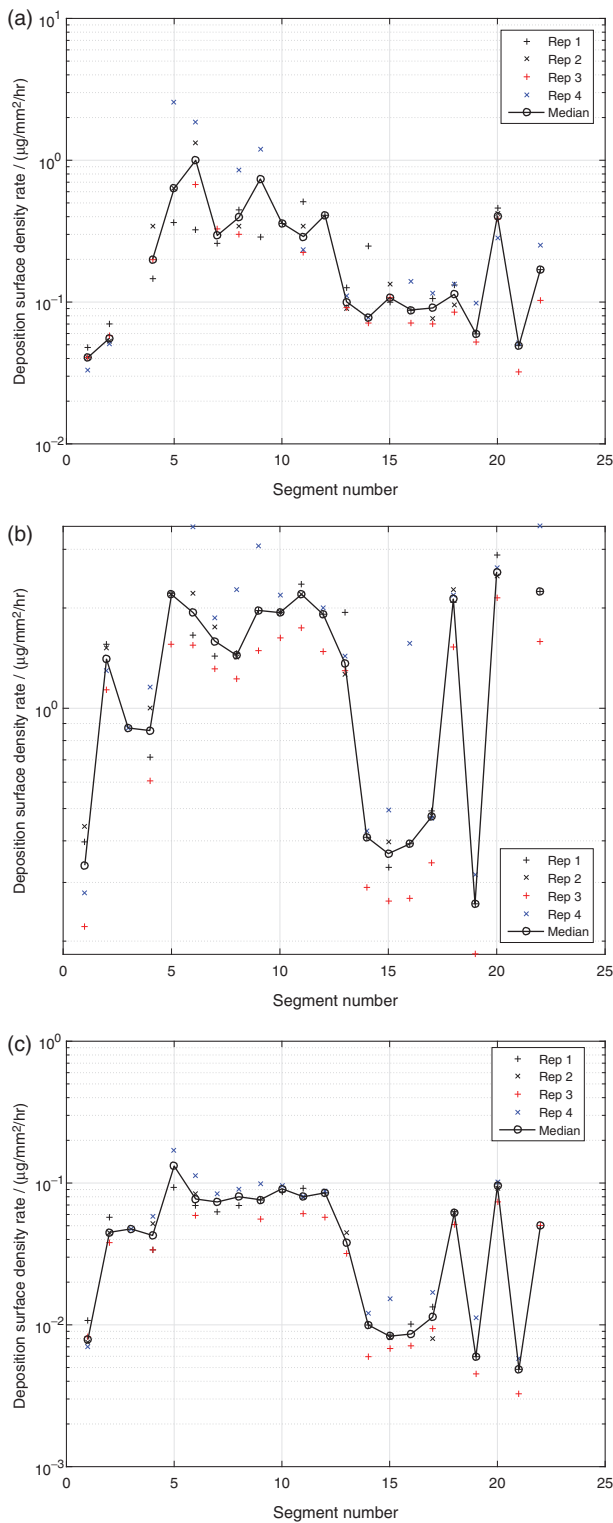


**Figure 9.** Deposition surface density rate per segment,  $R_{\alpha,i}^D$ , of (a) glycerol, (b) propylene glycol and (c) nicotine from exposure with a *multicomponent aerosol*.

nicotine were shown to re-evaporate from the output filters during the *multicomponent aerosol* experiments, the deposited mass on the filters were not included in the calculations. As shown in **Figure 10**, the  $RDF_{\alpha,i}$  of each analyzed chemical compound in the *multicomponent aerosol* experiments, and also the glycerol in the *monodisperse glycerol aerosol* experiments, were all overlapping, showing the same general pattern for all quantified compounds. This indicates

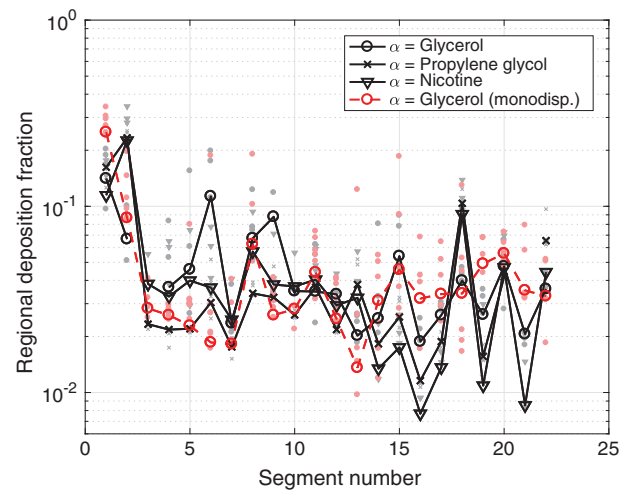


**Figure 10.** Regional deposition fraction per segment,  $RDF_{\alpha,i}$ , for glycerol, propylene glycol and nicotine for the *multicomponent aerosol* (black) and the *monodisperse glycerol aerosol* (red). The individual gray and light red symbols represent the individual experimental points, whereas the symbols connected by a line represent the median values for the respective compound.

that the deposition of the analyzed compounds of the *multicomponent aerosol* deposit in a similar way, presumably as part of multicomponent aerosol droplets.

As shown in **Figure 10**, the highest regional deposition fraction for all three compounds from the *multicomponent aerosol* experiments were found in the upper part of the airways ( $i=1, 2$ ) and in one of the complex segments ( $i=18$ ) covering the 5th–7th generation. For the *monodisperse glycerol aerosol* experiments, highest regional deposition fractions were found in the oral cavity ( $i=1$ ) and in the trachea segment ( $i=2$ ). Despite the generally common trend between the  $RDF_{\alpha,i}$  patterns for the *monodisperse glycerol aerosol* and the *multicomponent aerosol* experiments, it can be observed that the  $RDF_{\alpha,i}$  of the *multicomponent aerosol* shows a more fluctuating pattern with respect of the segment number. This more fluctuating pattern is similar for all three compounds, but especially for glycerol. This indicates that the difference in the segment geometries and the internal flow condition inside the segments were important driving factors for deposition, irrespectively of the type of the chemical compound in the *multicomponent aerosol*.

The applicability of the developed method is not limited to the two aerosols and the chemical compounds analyzed in this work. The experimental method can be applied to other single-component and multicomponent aerosols, as long as there is a sufficient amount of the deposited compound in the collected extraction solution to give a reliable signal during the GC-MS analysis and that the chemical compounds are chemically stable at the operating temperature to avoid significant evaporation during handling. Compared with the methods used in other deposition studies, this method benefit from being able to determine and quantify multiple liquid-based deposited compounds, which makes it suitable for deposition studies of multicomponent aerosols, such as electronic cigarette aerosols. Moreover, as mentioned previously, thanks to the chemical quantification of the extracted deposited matter adopted in this work, the developed methodology also accounts for vapor

condensation in addition to droplet deposition. This is important for toxicological assessments, as the total amount of the deposited chemical compounds contributes to the toxicological activity at the deposition location. Further improvements of the method include the integration of temperature and humidity control, as well as realistic wall treatments on the cast segments to better represent realistic condition in the human airways.

## Conclusions

In this work, an experimental method to determine regional deposition of multicomponent aerosols in a segmented, realistic human lung geometry was developed and applied to two aerosols, namely a *monodisperse glycerol aerosol* and a *multicomponent aerosol*. The method comprised the following steps: (1) *lung cast model preparation*, (2) *aerosol generation and exposure*, (3) *extraction of deposited mass*, (4) *chemical quantification* and (5) *data processing*. The chemical quantification using GC-MS can quantify the deposition of glycerol, propylene glycol and nicotine from the extracted mass of the deposited aerosol. The developed method is not restricted to these compounds, and the deposition of other compounds having relatively low volatility may be quantified. This work therefore forms the basis for future investigations of the deposition of electronic cigarette aerosols.

To validate the methodology, the deposition efficiency of a *monodisperse glycerol aerosol*, with a MMAD of 2.3  $\mu\text{m}$ , exposing the segmented lung cast at a constant flow rate of 15 L/min was used. The generated data showed good agreement to published literature data for the deposition efficiency. The deposition surface density rate over all segments was variable with highest values in the bifurcation segments and smaller segments ( $i = 5, \dots, 12$ ). This result indicates that inertial impaction was the dominating deposition mechanism in the *monodisperse glycerol aerosol* experiments.

The experimental method was also applied to determine the deposition of a nebulized *multicomponent aerosol* in the segmented lung cast at the same flow conditions as for the *monodisperse glycerol aerosol* experiments. The deposited amounts of glycerol, propylene glycol and nicotine were quantified. The deposition surface density rates of the three compounds showed similar deposition patterns as that of the *monodisperse glycerol aerosol*. Moreover, the regional deposition fraction of each component indicated that most of the deposited mass of the three analyzed compounds of the *multicomponent aerosol* were likely deposited as parts of the same multicomponent aerosol droplets.

To summarize, an experimental method was developed and applied to determine regional deposition of multicomponent aerosols in a segmented replica of the human respiratory tract. This method has the potential to: (1) provide understanding of the deposition characteristics in the human airways for different flow conditions and multicomponent liquid-based aerosols, such as those generated by electronic cigarettes, (2) correlate the dosage in human airways with that of *in vitro* exposure systems for toxicological assessments, and (3) provide reliable experimental

deposition data for validation of aerosol deposition simulations using CFD. The developed experimental method has the capability to quantify the total deposited mass from both the aerosol particle deposition and the vapor phase condensation, which is beneficial for predictions of the dosing for toxicological assessments. Future application of the developed method includes investigations of the deposition characteristics of electronic cigarette aerosols under conditions of temperature and humidity control.

## Acknowledgements

The research described in this report was funded by Philip Morris Products S.A., Switzerland (part of Philip Morris International (PMI) group of companies) and supported by the Brno University of Technology (BUT) project FSI-S-14-2355.

## Disclosure statement

This research was conducted by PMI and BUT employees and with PMI funding. The authors had full access to all research data and ensure their integrity as well as the accuracy of the data analysis.

## Funding

The research described in this report was funded by Philip Morris Products S.A., Switzerland (part of Philip Morris International (PMI) group of companies) and supported by the Brno University of Technology (BUT) project FSI-S-14-2355.

## References

- Azhdarzadeh M, Olfert JS, Vehring R, Finlay WH. (2015). Effect of electrostatic charge on deposition of uniformly charged monodisperse particles in the nasal extrathoracic airways of an infant. *J Aerosol Med Pulm Drug Deliv* 28:30–4.
- Balászházy I, Hofmann W, Heistracher T. (2003). Local particle deposition patterns may play a key role in the development of lung cancer. *J Appl Physiol* 94:1719–25.
- Belka M, Lippay J, Lizal F, et al. (2014). Comparison of methods for evaluation of aerosol deposition in the model of human lungs. *EJP Web Confer* 67:02006.
- Chan TL, Lippmann M. (1980). Experimental measurements and empirical modelling of the regional deposition of inhaled particles in humans. *Am Ind Hyg Assoc J* 41:399–409.
- Cheng YS. (2012). Aerosol deposition in the extrathoracic region. *Aerosol Sci Technol* 37:659–71.
- Cheng YS, Zhou Y, Chen B. (1999). Particle deposition in a cast of human oral airways. *Aerosol Sci Tech* 31:286–300.
- Comouth A, Saathoff H, Naumann KH, et al. (2013). Modelling and measurement of particle deposition for cell exposure at the air-liquid interface. *J Aerosol Sci* 63:103–14.
- Elcner J, Lizal F, Jedelsky J, et al. (2016). Numerical investigation of inspiratory airflow in a realistic model of the human tracheobronchial airways and a comparison with experimental results. *Biomech Model Mechanobiol* 15:447–69.
- European Parliament, (2010). Directive 2010/63/EU of the European Parliament and of the council of 22 September 2010 on the protection of animals used for scientific purpose. *Official J Eur Union* L276:33–79.
- Ghosh D, Jeannot C. (2014). An improved Cambridge filter pad extraction methodology to obtain more accurate water and tar values: *In situ* Cambridge filter pad extraction methodology. *Beitrge Zur Tabakforschung/Contrib Tob Res* 26:38–49.

- Golshahi L, Noga ML, Vehring R, Finlay WH. (2013). An *in vitro* study on the deposition of micrometer-sized particles in the extra-thoracic airways of adults during tidal oral breathing. *Ann Biomed Eng* 41:979–89.
- Grgic B, Finlay W, Burnell P, Heenan A. (2004a). *In vitro* intersubject and intrasubject deposition measurements in realistic mouththroat geometries. *J Aerosol Sci* 35:1025–40.
- Grgic B, Finlay W, Heenan A. (2004b). Regional aerosol deposition and flow measurements in an idealized mouth and throat. *J Aerosol Sci* 35:21–32.
- Hickey AJ. (2007). *Inhalation aerosols: physical and biological basis for therapy*. New York: CRC Press.
- Hinds H. (1999). *Aerosol technology: properties, behavior, and measurement of airborne particles*. 2nd ed. New York: John Wiley & Sons Inc.
- Iskandar AR, Martin F, Talikka M, et al. (2013). Systems approaches evaluating the perturbation of xenobiotic metabolism in response to cigarette smoke exposure in nasal and bronchial tissues. *Biomed Res Int* 2013:512086.
- Kreyling W, Hirn S, Schleh C. (2010). Nanoparticles in the lung. *Nat Biotechnol* 28:1275–6.
- Lizal F, Belka M, Adam J, Jedelsky J, Jicha M. (2015). A method for *in vitro* regional aerosol deposition measurement in a model of the human tracheobronchial tree by the positron emission tomography. *Proc Inst Mech Eng H J Eng Med* 229:750–7.
- Lizal F, Elcner J, Hopke P, et al. (2012). Development of a realistic human airway model. *Proc Inst Mech Eng H J Eng Med* 35:84–92.
- Longest P, Holbrook L. (2012). *In silico* models of aerosol delivery to the respiratory tract - development and applications. *Adv Drug Deliv Rev* 64:296–311.
- Mathis C, Poussin C, Weisensee D, et al. (2013). Human bronchial epithelial cells exposed *in vitro* to cigarette smoke at the air-liquid interface resemble bronchial epithelium from human smokers. *Am J Physiol Lung Cell Mol Physiol* 304:L489–503.
- Neilson L, Mankus C, Thorne D, et al. (2015). Development of an *in vitro* cytotoxicity model for aerosol exposure using 3D reconstructed human airway tissue; application for assessment of e-cigarette aerosol. *Toxicol in Vitro* 29:1952–62.
- Paur HR, Cassee F, Teeguarden J, et al. (2011). *In vitro* cell exposure studies for the assessment of nanoparticle toxicity in the lung tissue; application for assessment of e-cigarette. *J Aerosol Sci* 42:668–92.
- Schiffelers MJWA, Blaauboer BJ, Hendriksen CFM, Bakker WE. (2012). Regulatory acceptance and use of 3R models: a multilevel perspective. *Altex* 29:287–300.
- Schlage WK, Iskandar AR, Kostadinova R, et al. (2014). *In vitro* systems toxicology approach to investigate the effects of repeated cigarette smoke exposure on human buccal and gingival organotypic epithelial tissue cultures. *Toxicol Mech Methods* 24:470–87.
- Schmidt A, Zidowitz S, Kriete A, et al. (2004). A digital reference model of the human bronchial tree. *Comput Med Imaging Graph* 28:203–11.
- Sosnowski T, Moskal A, Gradon L. (2006). Dynamics of oropharyngeal aerosol transport and deposition with the realistic flow pattern. *Inhal Toxicol* 18:773–80.
- Srirama PK, Wallis CD, Lee D, Wexler AS. (2012). Imaging extra-thoracic airways and deposited particles in laboratory animals. *J Aerosol Sci* 45:40–9.
- Tippe A, Heinzmann U, Roth C. (2002). Deposition of fine and ultra-fine aerosol particles during exposure at the air/cell interface. *J Aerosol Sci* 33:207–18.
- Zhang Y, Finlay W, Matida E. (2004). Particle deposition measurements and numerical simulation in a highly idealized mouththroat. *J Aerosol Sci* 35:789–803.
- Zhou Y, Cheng YS. (2005). Particle deposition in a cast of human tracheobronchial airways. *Aerosol Sci Tech* 39:492–500.



Contents lists available at ScienceDirect

## Journal of Aerosol Science

journal homepage: [www.elsevier.com/locate/jaerosci](http://www.elsevier.com/locate/jaerosci)

## Deposition of glass fibers in a physically realistic replica of the human respiratory tract

Miloslav Belka<sup>a,\*</sup>, Frantisek Lizal<sup>a</sup>, Jan Jedelsky<sup>a</sup>, Jakub Elcner<sup>a</sup>, Philip K. Hopke<sup>b</sup>, Miroslav Jicha<sup>a</sup>

<sup>a</sup> Faculty of Mechanical Engineering, Brno University of Technology, Technicka 2, Brno 61669, the Czech Republic

<sup>b</sup> Center for Air Resources Engineering and Science, Clarkson University, USA



### ARTICLE INFO

#### Keywords:

Fiber deposition  
Human respiratory airways  
Glass fibers  
Experiments  
Deposition measurement

### ABSTRACT

Regional deposition of glass fibers was investigated in a physically realistic, human respiratory tract replica. The replica begins with the oral cavity and includes the airways up to the 7th generation of the tracheobronchial tree. Uniform diameter glass fibers were classified by length using a dielectrophoretic classifier and introduced into the replica at three steady-state flow rates (15, 30, and 50 LPM). A novel automatic image processing method was utilized to speed up the sample analysis and make it more reproducible. Fractional deposition was high in the oral cavity and the upper respiratory airways. Deposition density was higher in the first few generations of the tracheobronchial tree. Deposition efficiencies were compared with published data and good agreement was obtained. Our data confirmed that the deposition efficiency increased with increasing Stokes number indicating that impaction was the main deposition mechanism. The experimental data were used to propose new empirical models predicting fiber deposition in the tracheobronchial tree.

### 1. Introduction

Since the discovery of the toxicity of asbestos, there has been ongoing interest in inhalable fibers (Baron, 2001). The use of asbestos has been strictly regulated or banned altogether in the past. However, these restrictions led to increased production of substitute materials, such as man-made vitreous fibers (MMVFs). MMVFs have some physical similarities to asbestos that provide them with comparable aerodynamic characteristics and thus, the ability to penetrate into the human respiratory system. This capability naturally raised the question of their toxicity. Although the International Agency for Research on Cancer has classified glass, rock, and slag wool as non-carcinogenic to humans, and ceramic fibers as possibly carcinogenic to humans (IARC, 2002), MMVFs remain a concern. Recommended occupational exposure limits (OEL) of 1 fiber/ml have been established in the countries of European Union (SCOEL, 2012).

Most prior studies regarding particle transport and deposition in human respiratory airways involved spherical particles (Chan & Lippmann, 1980; Lizal, Belka, Adam, Jedelsky, & Jicha, 2015; Zhou & Cheng, 2005). However, it is not possible to extrapolate these results to fibrous aerosols. Fibers exhibit different aerodynamic behavior than spherical particles, causing different deposition patterns. This difference occurs because of the complicated motion of fibers that undergo both translation and rotation. After inhalation, fibers tend to align with the air stream causing their effective aerodynamic diameter to closely approximate its diameter with length having a negligible influence (Baron, 2001). During translation motion, fibers occasionally rotate, which temporarily changes the

\* Corresponding author.

E-mail address: [belka@fme.vutbr.cz](mailto:belka@fme.vutbr.cz) (M. Belka).

<https://doi.org/10.1016/j.jaerosci.2017.11.006>

Received 3 February 2017; Received in revised form 16 October 2017; Accepted 15 November 2017

Available online 21 November 2017

0021-8502/ © 2017 Elsevier Ltd. All rights reserved.

particle's drag force (Kleinstreuer & Feng, 2013). The frequency of fiber rotation in the flow depends on the fiber aspect ratio and the position in the airways. Fibers rotate more frequently with a decreasing aspect ratio, and near the walls in high shear flow (Feng & Kleinstreuer, 2013; Tian, Ahmadi, Wang, & Hopke, 2012).

Only a few studies of fiber deposition in human respiratory airways have been reported. Controlled experiments on human subjects are potentially hazardous and thus, unethical. Therefore, experimental methods using airway replicas and numerical simulations are required. Myojo and coworkers (Myojo & Takaya, 2001; Myojo, 1990) experimentally investigated glass fiber deposition in bifurcating airway models. The two models consisted of single bifurcations from the 2nd to 3rd and the 3rd to 4th generations of tracheobronchial branching of a Weibel A lung model (Weibel, 1963), respectively. Preferred sites of deposition or “hot spots” were found around the carinal ridges, and the orientation of deposited fibers was parallel to the air stream. Sussman, Cohen, and Lippmann (1991) performed experiments with an upper tracheobronchial tree replica to study the influence of fiber length and diameter on deposition distribution. A mechanical larynx was connected to the model to simulate the influence of upper respiratory airways. Deposition hot spots were identified around carinas as well as on the upper dorsal wall of the trachea. Deposition in the trachea was caused by a jet that formed at the larynx constriction and directed the air towards the trachea wall (Chan & Schreck, 1980). Su and coworkers (Su & Cheng, 2006a, 2006b, 2009) and Zhou, Su, and Cheng (2007) experimentally studied fiber deposition in two realistic replicas consisting of human airways from the oral cavity to the 4th branch generation. Various fiber types with different densities were employed including carbon, TiO<sub>2</sub>, and glass fibers. High inertia fibers deposited extensively in oropharynx and larynx in both the replicas. However, low inertia fibers mostly traversed the replicas. Comparing the two replicas, the exact location of deposition hot spots differed slightly indicating that the differences in geometry caused small changes in the flow field and the resulting changes in deposition.

Computational studies of particle deposition in realistic human airway models are difficult because the underlying physics that must be captured is highly complex. Moreover, the complex coupled rotational and translational fiber motion must be addressed. Therefore, many studies have been conducted on idealized geometries using simplified cases where an analytical solution was employed or simple shear flows were used. For example, Cai and Yu (1988) predicted fiber deposition in bifurcating airways. Fan and Ahmadi (1995) presented fiber equations of motion in a sublayer model evaluating the fiber deposition in turbulent streams. Zhang, Asgharian, and Anjilvel (1996) studied the fiber deposition numerically in an equal diameter bifurcating airway model for various fiber sizes and bifurcation angles. Balashazy, Martonen, and Hofmann (1990, 2005) tested an equivalent diameter concept and predicted fiber deposition in the bifurcating model for the three fiber orientations; parallel, perpendicular and random with respect to the streamlines.

Recently, numerical simulations of fiber deposition in realistic geometries have been reported. Tian et al. (2012) introduced a computational model for predicting the fiber transport and deposition in low Reynolds number flows. Later, Tian and Ahmadi (2013) employed the model to study fiber deposition in bronchial airways from the trachea to the 3rd bronchial generation. The absence of a larynx was addressed by prescribing turbulence intensities at the trachea inlet. The results showed that turbulence enhances deposition, emphasizing the importance of larynx and upper respiratory airways for a proper study of deposition patterns. Feng and Kleinstreuer (2013) investigated transport and deposition of ellipsoidal particles in a similar geometry of human respiratory airways as those used by Su and Cheng (2006b). The deposition efficiencies in these studies were compared and acceptable agreement was found. Deposition of particles with various aspect ratios was then studied. It was observed that the particles with higher aspect ratios have higher probabilities of penetrating deeper into the lungs compared to lower aspect ratio particles, e.g. spherical particles. Additionally, the deposition efficiency per generation of these high aspect ratio fibers increased slightly from trachea to the fourth generation, indicating interception driven by secondary flows can influence the deposition in higher branch generations. Inthavong, Mouritz, Dong, and Tu (2013) studied the transport of airborne fibers through the nostrils into the respiratory system using empirically defined drag coefficient for the fiber motion. Dastan, Abouali, and Ahmadi (2014) extended the work of Fan and Ahmadi (1995) and employed the equations for fiber motion to study fiber deposition in human nasal cavities. Shanley and Ahmadi (2011) developed a computational model to account for the motion of ellipsoidal particles in viscous shear flows. Shanley, Ahmadi, Hopke, and Cheng (2016) employed this model to numerically analyze fiber deposition in human nasal cavity.

The use of proper computational models that account for the fiber motion in conjunction with the computational fluid dynamics methods is essential in fiber deposition studies. The crucial step on the way to routinely and reliably use CFD calculations is a proper validation with experimental data, either acquired in vivo or on human replicas. However, the number of experimental data regarding fiber deposition is rather sparse. That is the reason why we experimentally investigated glass fiber deposition in our human airway replica. The replica geometry extends from the oral cavity to the 7th bronchial generation (Lizal, Elcner, Hopke, Jedelsky, & Jicha, 2012). The fibers were classified using dielectrophoresis to yield uniform length particles. A novel automatic image processing method was utilized to speed up the sample analysis, make it more convenient and more reproducible (Belka et al., 2016). The results of this study also provide the first measurements of deposition beyond the 4th generation. The current replica has been employed in other experimental works (Jedelsky, Lizal, & Jicha, 2012; Lizal et al., 2015; Nordlund et al., 2017) and thus, the results on fiber deposition presented in this paper further extend the data set for experimental validation. Recent progress in simulations performed on the current replica has been documented by Koullapis et al. (2017) and Frederix et al. (2018). The digital geometry of the airways is available upon request.

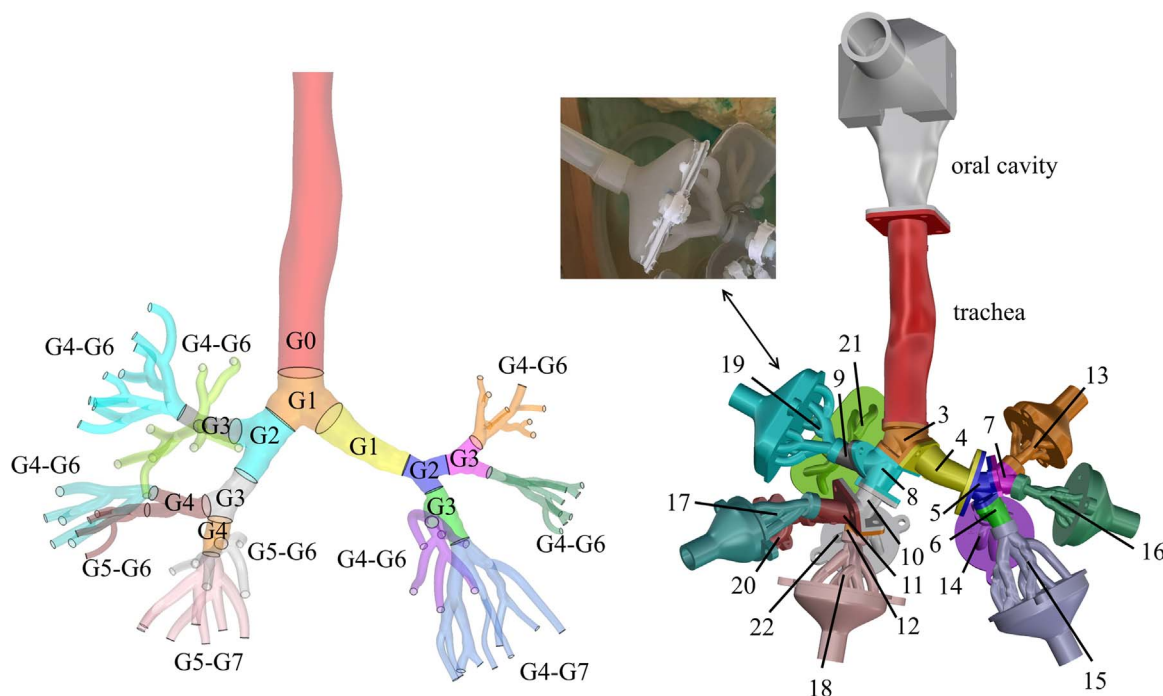


Fig. 1. The geometry of respiratory airways with generations of bronchial branching for individual segments (left); segmented replica for deposition experiments (right) with the photo of connection to the rest of the experimental setup.

## 2. Experimental setup

### 2.1. Replica of respiratory airways

A realistic replica of the human airways from the oral cavity to the 7th bronchial generation (Fig. 1) was developed by Lizal et al. (2012). The oral cavity was chosen because it is the predominant way of breathing during light or heavy work (Cheng, Zhou, & Chen, 1999). The geometry of the replica originates from two sources. The bronchial tree is based on the reference model of Schmidt et al. (2004), which was derived from CT images of a male adult free from pathological alterations. The oral cavity was acquired from the Lovelace Respiratory Research Institute (Albuquerque, NM, USA, Cheng, Cheng, Yeh, & Swift, 1997). These two geometries were converted into the stereolithographic format (STL) and imported into the software package Rhinoceros 4.0 (McNeel, Seattle, WA, USA). The program connected the geometries and a 3 mm-thick envelope was added on the top of the final geometry to permit the manufacture of a replica suitable for experimental studies. The geometry was divided into individual segments to facilitate regional deposition measurements. Flanges with screw or bayonet joints were created between the segments to allow easy assembly and disassembly of the replica.

The replica consisted of 32 segments, and the numbering of the segments increases from the top to the bottom starting with the oral cavity as number 1 and the trachea as number 2. The upper respiratory airways and a few bifurcations with relatively large dimensions were isolated into individual segments. The branches from the 4th to 7th generation, which have smaller airway dimensions, were combined into complex multigenerational segments numbered from 13 to 22. Following these complex segments, ten output segments with “funnel-like” shapes numbered from 23 to 32 were created to facilitate connection of the replica to the rest of

Table 1  
Comparison of model geometries (Lizal et al., 2012).

Generation number	Present model Diameter (mm)		Weibel Diameter (mm)		Zhou and Cheng (cast A) Diameter (mm)	
	Left	Right	Left	Right	Left	Right
Trachea 0		16.3	18			15.8
1	10.2	12.6	12.2		7.1	12.3
2	6.5	8.3	8.3		6.0	7.8
3	5.6	5.9	5.6		5.9	6.5
4	3.8	4.4	4.4			5.6
5	2.8	3.9	3.5			

the experimental setup. The summary of diameters in given airway generations together as well as comparison with other replica geometries (Weibel, 1963; Zhou & Cheng, 2005) are given in Table 1.

The replica was manufactured on a Viper Si2 stereolithographic prototyping system (3D Systems, Rock Hill, SC) using WaterShed XC 11122 (DSM, Heerlen, the Netherlands). The layer thickness was 25  $\mu\text{m}$  and the accuracy of the build was 7.6  $\mu\text{m}$ . Since the replica consisted of multiple segments, leak tests were performed prior to each experiment. Leaks, mostly between flanges, were sealed with a small layer of silicone sealant. Silicon oil (550 Fluid, Dow Corning) was carefully applied to the inner walls of the replica to prevent resuspension of deposited fibers and to simulate the mucus layer (Su & Cheng, 2015; Zhou, Xi, Simpson, Irshad, & Cheng, 2013). The replica was filled with silicone oil and then dried for sufficient time (approximately 12 h) to produce a thin wall layer. Thus, all inner surfaces were covered with silicone.

## 2.2. Experimental setup

Fiber generation and classification was performed with the system described by Wang et al. (2005). The methodology for fiber production was the same as that of Wang, Hopke, Ahmadi, Cheng, & Baron (2008). Glass wool (Johns Manville JM 100/475) was crushed and sieved to produce glass fibers with a density of 2.56  $\text{g}/\text{cm}^3$  and fiber diameter of  $1.03 \pm 0.45$ . The fibers were mixed with glass beads (Ballotini Impact Beads, Potters Industries Inc.). The mixture of fibers and glass beads was loaded into a hopper connected to a fiber generator via a rotary feeder (Fig. 2). The rotary feeder speed determined the number of generated and subsequently classified fibers. The fiber generator used a high-speed orbital shaker.

Airstream  $A_1$  at 20 °C, which had passed through a humidifier to produce a relative humidity of 40%, delivered polydisperse fibers from the fiber generator into an aging chamber. The chamber was 9 cm-wide, 90 cm-long, and provided a sufficient contact time between the fibers and air humidity. The chamber also damped flow pulsations from reaching the classifier. Polonium 210 ionizers (Staticmaster, Amstat Industries, USA) were used to produce charge equilibrium on the particles before entering the classifier.

The classifier works on the principle of dielectrophoretic separation (Lipowicz & Yeh, 1989) and has been described elsewhere (Baron, Deye, & Fernback, 1994; Deye, Gao, Baron, & Fernback, 1999). The classifier consists of two concentric cylinders. The outer cylinder was grounded and the inner one was connected to a high voltage AC generator oscillating between  $\pm 4$  kV at 50 Hz. The

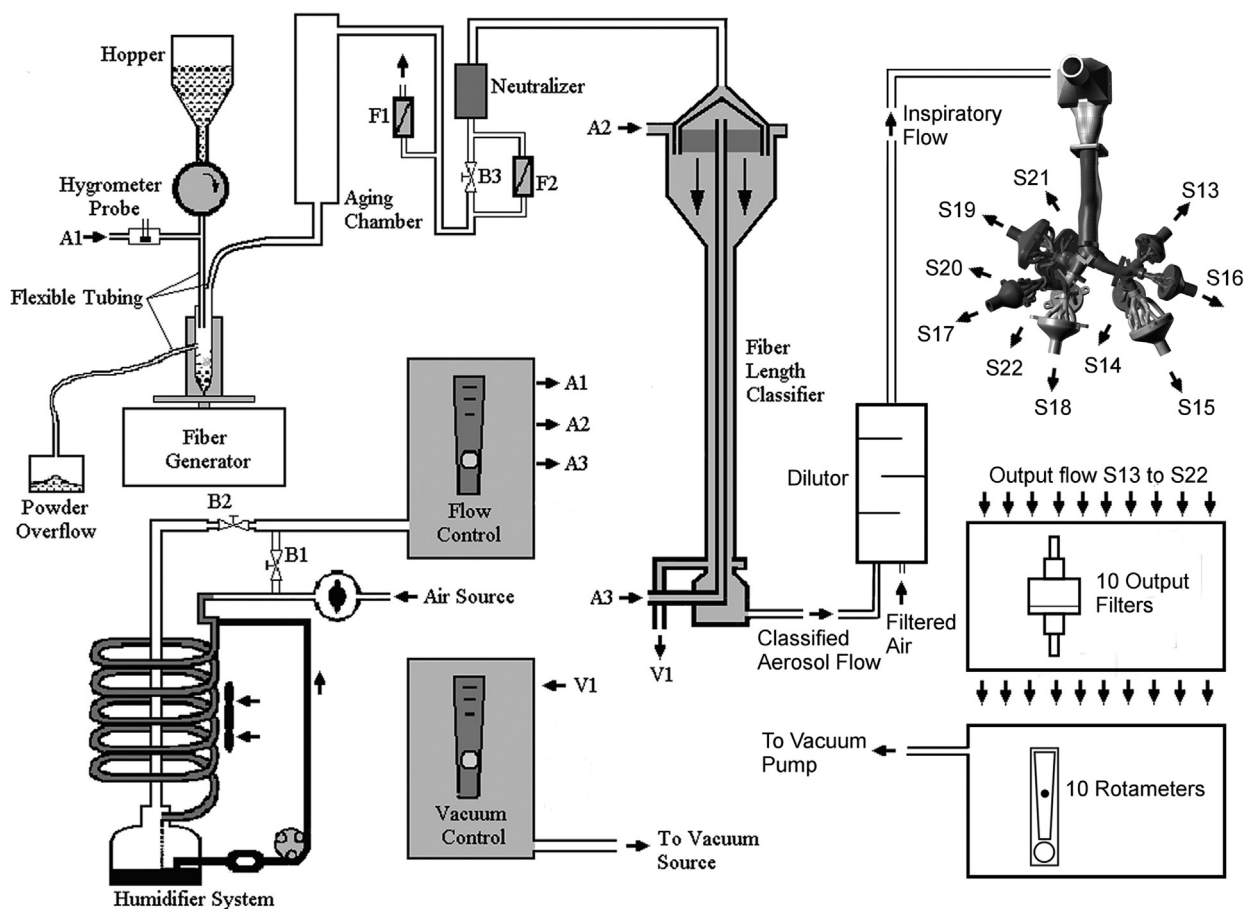


Fig. 2. The experimental setup, which includes the fiber generator, the classifier, the replica of respiratory airways, etc., modified with permission from Wang et al. (2005).

**Table 2**  
Flow rates through the classifier.

Airstream name	Sheath flow $A_2$	Sheath flow $A_3$	Fiber flow $A_1$	Dump flow $V_1$	Classified Aerosol flow
Flow rate (LPM)	4	4	1	8	1

alternating electric field eliminates electrophoresis, which is dependent on electric field polarity. The separated dipolar charges induced within neutral particles flowing through the classifier permit them to move toward the inner electrode by dielectrophoresis.

A fiber-laden flow was introduced at the top of the classifier surrounded by clean humidified sheath flows  $A_2$  and  $A_3$ . The classifier dimensions were such that the velocities of all flows were the same and the flow through the classifier was laminar. The flow was split at the bottom of the classifier to the classified aerosol flow containing classified fibers, and the dump flow  $V_1$  with the rest of the fibers. The flow rates were checked by rotameters (Cole-Palmers, IL, USA). The flow values can be found in Table 2.

The classified aerosol flow continued to a dilutor where it was mixed with filtered air to produce the desired inspiratory flow rate through the replica (Fig. 2). The inspiratory flow rates of 15, 30, and 50 LPM were used to simulate steady inhalation for people under normal, light, and heavy activity, respectively. The flow through the replica was induced by a vacuum pump situated below the replica. The flow distribution through the individual branches was accomplished by adding rotameters with regulated valves between the replica and the vacuum pump. The flow was split between the left and the right lung with a ratio of 30:70; the flow rates through the individual segments of the replica can be found in Table 3 together with various segment characteristics. Since the flow rates were set for the outlet segments, the flow rates for the rest of the replica were calculated using Fig. 1. The flow distribution comes from prior measurements.

The replica was exposed to fibers for 4 h. Since this replica did not include the entire lungs, some fibers passed through the replica and were collected on output filters (AAWP02500 nitrocellulose membrane filters, Merck Millipore). The output filters were changed every 30 min to prevent overfilling. Three experiments were performed under each flow rate condition to allow calculation of statistical errors, such as standard deviations.

### 2.3. Sample preparation

Phase contrast microscopy was used for the sample analysis (Su & Cheng, 2005; Wang, Hopke, Ahmadi, Cheng, & Baron, 2008). The fibers deposited in the replica needed to be transferred to filters (AAWP02500 nitrocellulose membrane filters, Merck Millipore) to permit counting. The replica was disassembled and each segment was put into a beaker with isopropanol (2-propanol, Fisher Scientific). The beaker with a segment was inserted into an ultrasonic bath and sonicated for one minute to release the fibers from the replica into the isopropanol. The resulting suspension was filtered through a membrane filter using a vacuum filtration unit. The filters were placed in a desiccator to dry. Dry filters were placed on glass microscope slides and made transparent using an acetone vaporizer (QuickFix, EMS, USA). Each segment was rinsed twice. The quantity of extracted fibers in the second rinse was negligible so

**Table 3**  
Airway segment characteristics.

Segment number	Flow rate (LPM)			Airway generation	Surface area (cm <sup>2</sup> )
1	15	30	50	Oral cavity	174.2
2	15	30	50	G0	60.2
3	15	30	50	G1	9.7
4	4.5	8.9	14.8	G1	9.2
5	4.5	8.9	14.8	G2	3.6
6	2.8	5.6	9.3	G3	5.7
7	1.7	3.3	5.5	G3	4.0
8	10.6	21.1	35.2	G2	8.6
9	3.4	6.9	11.4	G3	6.0
10	7.1	14.3	23.8	G3	4.9
11	3.3	6.7	11.1	G4	6.1
12	3.8	7.6	12.7	G4	4.1
13	0.7	1.4	2.3	G4-G6	10.1
14	0.8	1.6	2.7	G4-G6	16.1
15	2.0	4.0	6.7	G4-G7	25.2
16	1.0	1.9	3.2	G4-G6	10.7
17	1.8	3.6	5.9	G5-G6	14.4
18	2.3	4.7	7.8	G5-G7	17.7
19	1.9	3.8	6.3	G4-G6	21.9
20	1.6	3.1	5.2	G4-G6	5.9
21	1.5	3.1	5.1	G4-G6	21.0
22	1.5	3.0	4.9	G5-G6	10.6
Inspiratory flow rate (LPM)	15	30	50		

this step was discontinued. The output filters were made transparent using the same procedure and all the filters were stored in filter boxes.

#### 2.4. Sample analysis

An automatic image analysis method was employed to speed up the analysis, make it more convenient and more reproducible. A monochrome camera Atik 314E (Atik cameras, Norwich, UK) was attached to a microscope Nikon Eclipse E200 (Nikon, Tokyo, Japan) to take images of the filters. Twenty images of each filter were taken. As only a part of each filter was inspected this way, the counted numbers of fibers were then increased proportionally to account for the entire filter area. The images were analyzed with an in-house software Fiber Analyzer, which is able to identify and count fibers in filter images following the methodology for manual counting NIOSH 7400 (Belka et al., 2016). The image analysis is based on the use of a histogram equalization and adaptive radial convolution filtering. The steps of the image analysis process are depicted in the [Supplementary material](#) (Fig. S1). These steps enhance particle contrasts and facilitate their identification during segmentation. The software identifies particles present in the image (fibers, dust, etc.) and calculates their sizes and other characteristics describing the particle shapes, such as area, perimeter, moments, elongation, shape factor etc. These characteristics are used to exclude non-fibrous particles from the final selection. Therefore, only fibers fulfilling the specifications are counted. Although the software uses various steps to count fibers properly, images with particularly high numbers of non-fibrous particles tend to bias the final fiber counts since the dust and other particles can resemble fibers.

The output filters (majority of the filters) contained a low amount of non-fibrous particles and were suitable for automatic analysis by the software. However, the filters created by rinsing of the replica parts contained many non-fibrous particles. The debris may have been produced by sonication of the replica segments releasing small pieces of its material into the isopropanol together with the fibers. Dust may have also deposited on the outside of the replica during the experiments and may have been released into the isopropanol solution while rinsing the segments. Therefore, the filters created by rinsing of the replica were analyzed manually by an analyst.

The software used for the output filters was validated by manual counting. Fibers in two hundred images were counted manually and with the software. The results were compared using the Paired Sample T-test in the software Origin 9 (OriginLab Corporation, MA, USA). It was shown that the differences between the fiber counts were statistically significant at the level of significance of 0.05. The fiber counts given by the software were slightly lower than those resulting from manual counting executed by an analyst. Some fibers, such as fibers in fiber bundles, were split up into smaller groups and these were subsequently identified as small particles. These fibers were excluded from the selection. Therefore, the software fiber counts were underestimated. That is the reason for which a linear regression model was used to determine the relationship between the automated and manual counts. A very good fit was found with coefficient of determination ( $R^2$ ) of 0.997 (Fig. S2). Therefore, the results from the software were recalculated using Eq. (1):

$$\text{Correct fiber count} = 1.11 \cdot \text{fiber count given by the software.} \quad (1)$$

#### 2.5. Calculation of local deposition

Fiber numbers were used to calculate deposition parameters, such as deposition efficiency or deposition fraction, in different parts of the replica. Deposition efficiency (DE) and deposition fraction (DF) can be expressed using Eqs. (2) and (3), respectively:

$$DE = \frac{\text{number of deposited fibers in a specific region}}{\text{number of fibers entering this region}}, \quad (2)$$

$$DF = \frac{\text{number of deposited fibers in a specific region}}{\text{number of fibers entering the oral airways}}. \quad (3)$$

The branching in the tracheobronchial tree and alveolar region is asymmetric. Consequently, airways dimensions, such as airway length or diameter, differ among subjects. Since the deposition fraction is dependent on the dimensions of the specific deposition region, Hofmann, Winkler-Heil, and Balashazy (2006) propose using deposition density. The deposition density is the ratio of deposition fraction to the relevant surface area and is expressed in units of  $\text{cm}^{-2}$ . To predict a particle dose per surface area, the deposition density is multiplied by the number of inhaled particles and expressed in units of particles/ $\text{cm}^2$ . The deposition density for a given segment of the replica was calculated using Eq. (4).

$$DD = \frac{\text{deposition fraction}}{\text{surface area of the given airway segment}}, \quad (4)$$

In upper respiratory airways, deposition is driven largely by impaction, and many empirical equations for prediction of deposition have been reported (Cheng et al., 1999; Grgic, Finlay, Burnell, & Heenan, 2004; Stahlhofen, Rudolf, & James, 1989). These equations often contain the impaction parameter  $d_{ae}^2 Q$ , where  $Q$  denotes the flow rate in the given respiratory segment, and  $d_{ae}$  is particle aerodynamic equivalent diameter. The aerodynamic diameter of a fiber can be calculated by Eq. (5) given by Stöber (1972) while neglecting the slip correction:

$$d_{ae} = d_{ve} \cdot \left( \frac{\rho_p}{\rho_0 \cdot \chi} \right)^{\frac{1}{2}}, \quad (5)$$

where  $d_{ve}$  is a volume equivalent diameter,  $\rho_p$  is fiber density,  $\rho_0$  is density of water and  $\chi$  denotes a dynamic shape factor. This correction factor accounts for the effect of shape on the particle motion and is affected by particle properties and its orientation in a flow field. For simplification, the dynamic shape factor of a fiber can be approximated by a dynamic shape factor of a prolate spheroid. It can be calculated for a prolate spheroid moving with its main axis parallel, perpendicular, or randomly oriented to a flow field using Eqs. (6)–(8) (Baron & Willeke, 2001), respectively.

$$\chi_{\parallel} = \frac{\frac{4}{3}(\beta^2-1)\beta^{-\frac{1}{3}}}{((2\beta^2-1)/\sqrt{\beta^2-1})\ln(\beta + \sqrt{\beta^2-1}) - \beta}, \quad (6)$$

$$\chi_{\perp} = \frac{\frac{8}{3}(\beta^2-1)\beta^{-\frac{1}{3}}}{((2\beta^2-3)/\sqrt{\beta^2-1})\ln(\beta + \sqrt{\beta^2-1}) + \beta}, \quad (7)$$

$$\frac{1}{\chi_r} = \frac{1}{3\chi_{\parallel}} + \frac{2}{3\chi_{\perp}}, \quad (8)$$

where  $\beta$  is a fiber aspect ratio.

Many empirical models use the Stokes number to predict deposition. The Stokes number is a more appropriate metric since it contains information regarding the respiratory airway geometry. This feature is important because lung geometry is one of the factors strongly affecting particle deposition (Hofmann, 2011). The Stokes number is given by:

$$Stk = \frac{\rho_0 \cdot d_{ae}^2 \cdot U_i}{18 \cdot \mu \cdot D_i}, \quad (9)$$

where  $U_i$  is an equivalent mean velocity in the given airway,  $\mu$  is dynamic air viscosity, and  $D_i$  defines an equivalent mean diameter of the given airway.

The mean velocity in the oral cavity ( $U_i = 4Q/\pi D_{mean}^2$ ) and the equivalent mean diameter ( $D_i = 2^*(V/\pi L)^{0.5}$ , where  $V$  is the volume of the oral cavity and  $L$  is length of the centerline path from mouth to throat) were used to calculate the Stokes number for the segment 1, i.e. the oral cavity (Grgic et al., 2004; Su & Cheng, 2009). When calculating the Stokes number for particles flowing through the tracheobronchial tree,  $U_i$  represents the mean velocity in the trachea (segment 2) or the parent airway of the bifurcation (segment 3–12), and  $D_i$  is the mean diameter of the trachea or parent airway of the bifurcation (Zhou & Cheng, 2005). When calculating the Stokes number for aerosol flowing through the segment with multiple generations (segments 13–22), an output equivalent diameter was first calculated as an average of all output cross-sections from the given segment. Then, the average of input airway diameter and the output equivalent diameter were used as a mean diameter  $D_i$ . The mean velocity  $U_i$  in the given segment was calculated as the flow rate through the segment divided by its mean diameter  $D_i$ .

### 3. Results and discussion

The fiber quantities for various regions of the respiratory tract replica were used to calculate deposition characteristics, such as deposition fraction, density, or efficiency. The results of this study were then compared to those of Su and Cheng (2009, 2015), Myojo and Takaya (2001), and Zhou et al. (2007).

#### 3.1. Fiber lengths

The length distributions for all experiments were measured and mean lengths together with standard deviations are presented in Table 4. The length distributions differed slightly for some experiments and are shown in Fig. S3. These differences were caused by the apparatus, which had to be readjusted prior to every experiment, or whenever a new batch of fibers was prepared. However, fiber lengths were important only for the calculation of aerodynamic diameter. The aerodynamic diameter was determined primarily by fiber diameter rather than length. Changes in fiber length resulted in negligible changes in the aerodynamic diameter for randomly oriented fibers as calculated with Eqs. (5)–(8). The fiber diameter was  $1.03 \pm 0.45 \mu\text{m}$  and the fiber density was  $2.56 \text{ g/cm}^3$ .

**Table 4**  
Fiber dimensions and aerodynamic diameters during the experiments.

Inspiratory flow rate	15 LPM			30 LPM			50 LPM		
Run	1	2	3	1	2	3	1	2	3
Mean diameter					1.03 ± 0.45				
Mean length (μm)	17 ± 3.6	17 ± 3.2	20.9 ± 4.5	21.7 ± 6.3	21.2 ± 6.5	19.2 ± 5.1	22.1 ± 5.9	23.2 ± 6.7	27 ± 9.2
Aerodynamic diameter (μm)	3.4	3.4	3.5	3.6	3.5	3.6	3.6	3.6	3.7

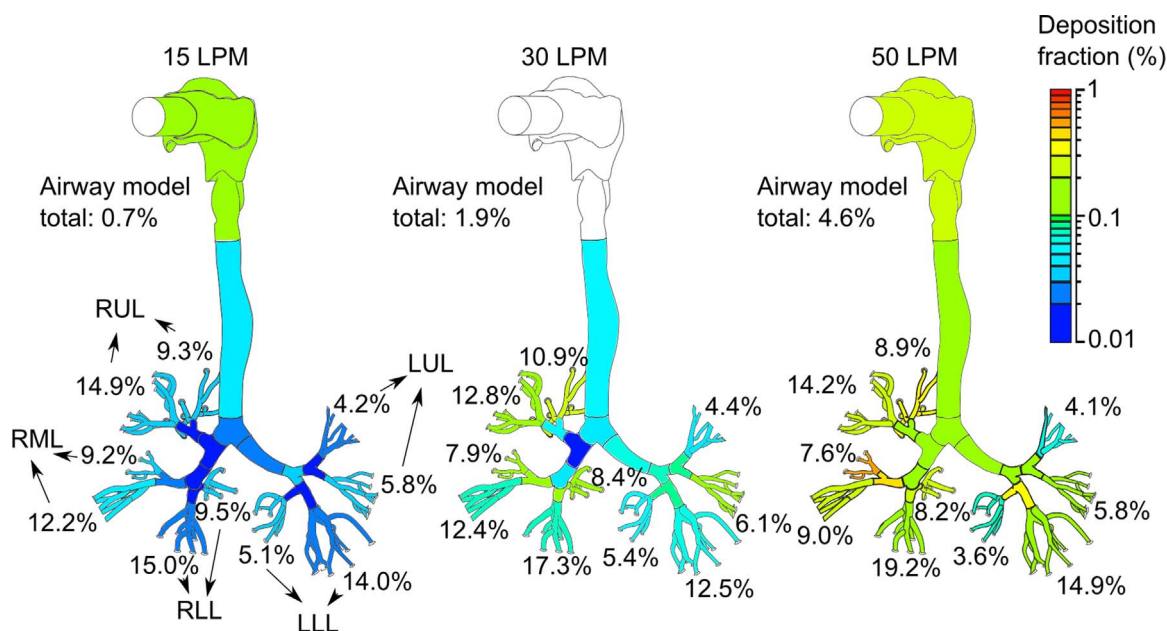


Fig. 3. Regional deposition fractions in the replica as a function of flow rate; the values around the replica represent deposition fractions in the parts of the experimental setup downstream of the replica (the funnel-shaped output segments, the tubing, and the filters); the data for the oral cavity during 30 LPM study were excluded from the analysis.

### 3.2. Deposition fractions and densities

The deposition fraction represents an initial dose of inhaled aerosol, which deposits at the given site. This dose is important to assess the potential hazards (Hinds, 1999). A fractional deposition was calculated for every segment of the replica. The regional deposition fractions in the replica for the measured flow rates are shown in Fig. 3. The graph with deposition fractions as a function of segment number can be found in the Supplementary Material (Fig. S4). Deposition fractions at the replica outlets represent fractional depositions in the parts of the experimental setup downstream of the replica, i.e. funnel-like shaped segments, tubing and filters. Fibers deposited in these parts of the experimental setup penetrated the replica and would continue deeper into the lung. Only a few fibers actually deposited in the replica. The deposition fraction increased with an increasing flow rate, and the total deposition fractions in the replica were 0.7%, 1.9% and 4.6% for the inspiratory flow rates of 15, 30, and 50 LPM, respectively. A slightly higher deposition fraction was detected in the oral cavity and in the complex segments. Moreover, segments in the right lung that encompassed a bifurcation in the fourth generation (segments 11 and 12) had a noticeably higher deposition fraction for higher inspiratory flow rates. By contrast, the complex segments downstream of the segments 11 and 12 had lower deposition fraction for higher inspiratory flow rate. This result indicated the role of impaction as the fibers were not able to follow streamlines into these complex segments and deposited near the carinal ridges.

Deposition densities in the replica for the measured flow rates are depicted in Fig. 4. The graph of deposition densities as a function of segment number can be found in the Supplementary Material (Fig. S5). If the effect of segment size is accounted for, the lowest deposition density can be observed in the first two segments including the oral cavity, oropharynx, larynx, and trachea. The deposition densities in the complex segments were lower compared to the rest of the replica. The exception was segment 20 that contains several small length generations so their surface areas were very small.

The replica has a realistic geometry with irregular dichotomy, i.e. every branch in tracheobronchial tree divides into two smaller daughter branches differing in length and diameter. Weibel (1963) defined the number of these divisions, or the so-called generations, that are similar across the population. Therefore, if the prediction of deposition is extrapolated to the population and not to the individual person, it is more convenient to consider deposition to be a function of airway generation. The deposition fraction and density as a function of airway generation are presented in Fig. S6. The deposited fiber dose increased with an increasing airway generation number and inspiratory flow rate. Clearly, the deposition of fibers was driven primarily by impaction. The increasing velocity (flow rate) and decreasing airway dimensions (increasing airway generation number) made it more difficult for the fibers to follow the air streamlines. Our replica has only two separate bifurcations in the 4th generation and it was difficult to extract deposition information for the individual generations in the complex multigenerational segments.

### 3.3. Deposition efficiency in the oral airways

Deposition efficiency as opposed to deposition fraction describes the ability of a given airway region to collect particles. The upper respiratory tract removes foreign particles from the flow. Generally, particle penetration through the nasal airways is lower than that

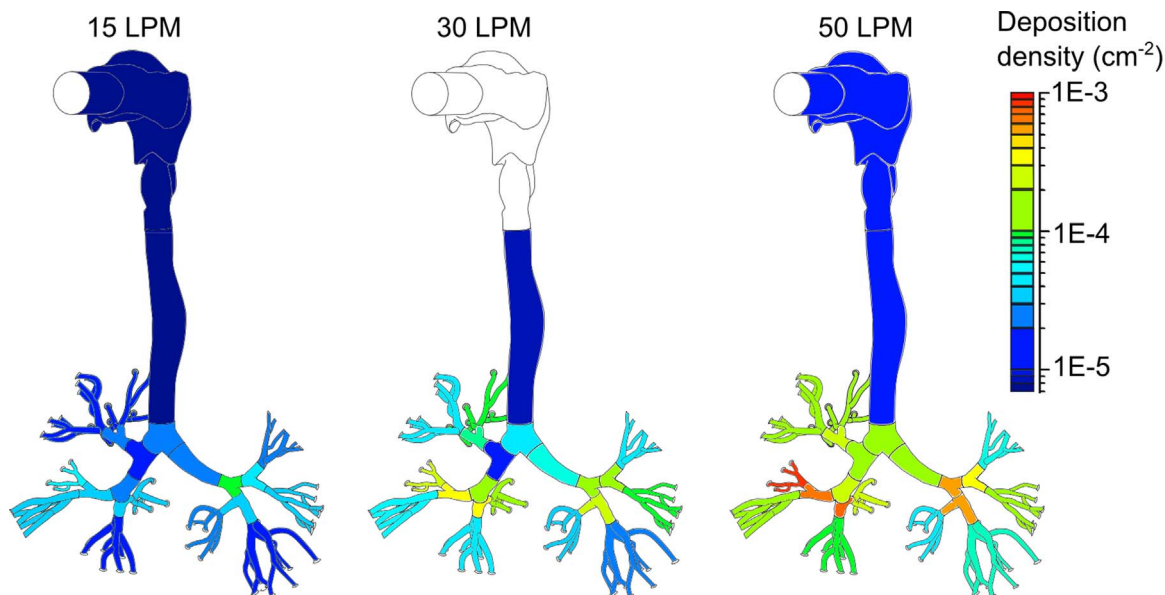


Fig. 4. Deposition densities in the replica as a function of flow rate.

of the oral airways (Ruzer & Harley, 2013). However, resistance to flow through the nasal airways is higher. Therefore, most people switch to oral breathing during work or heavy exercise (Cheng, Su, Yeh, & Swift, 1993). To penetrate the oral cavity, particles need to avoid the tongue and undergo a  $90^\circ$  bend to the pharynx/larynx area. The flow becomes turbulent after the constriction caused by the soft palate. These turbulence levels are reduced afterwards and enhanced again in the glottis (Kleinstreuer & Zhang, 2003).

The deposition efficiency in the oral cavity as a function of impaction parameter is shown in Fig. 5 and compared to the results of Su and Cheng (2015) (nanotubes and spherical particles were excluded). Only the 15 and 50 LPM results for the current replica are shown. The deposition at 30 LPM was excluded because parts of the replica wall were released into isopropanol together with the fibers. This debris obscured the fibers on the filters leading to an underestimation of the fiber quantities. This problem only existed for the oral cavity because it was the largest segment with the highest quantity of released debris. The deposition experiments for 30 LPM were performed first, using filters with diameter of 25 mm. Larger filters, 50 mm in diameter, reduced the problem for the

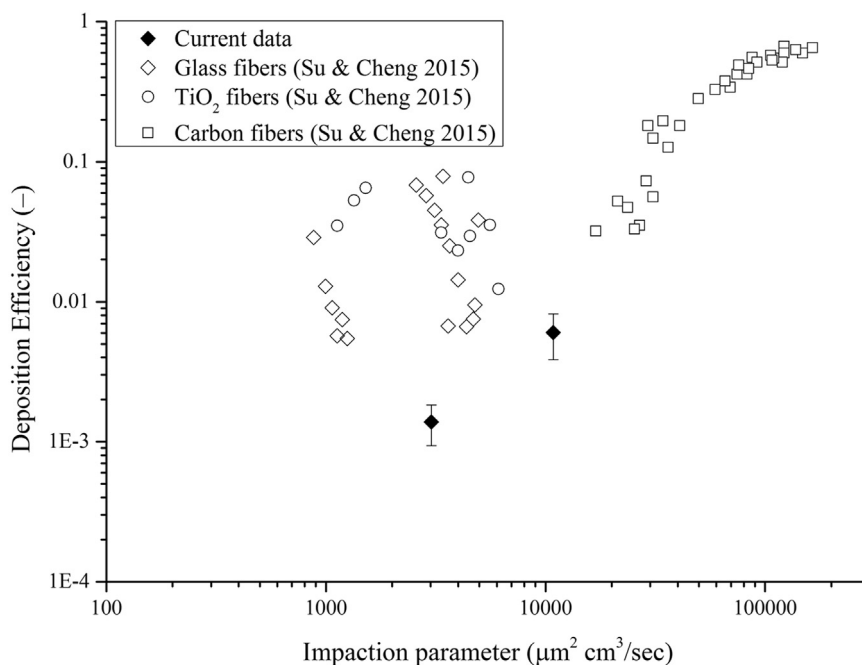


Fig. 5. Deposition efficiency in the oral airway as a function of impaction parameter; the error bars represent standard deviations.

experiments with inspiration flow rates of 15 and 50 LPM. Given financial and time limitations, it was not possible to repeat the experiments at 30 LPM using the larger filters.

In general, the deposition efficiencies in the oral cavity were less than 1% even for the highest flow rate. Thus, most fibers penetrated through the oral airways and would likely deposit in lower airways even during heavy activity. The deposition efficiency increased with increasing impaction parameter indicating impaction as the dominant deposition mechanism. The deposition efficiencies observed in the current respiratory airway replica are lower than those measured by [Su and Cheng \(2015\)](#). Although the replicas were manufactured by different methods, the effect of surface roughness or material was expected to be negligible since the inner walls were covered with a silicon oil. The problem with released debris during sonication could be responsible for the discrepancy. Small portions of the filters were obscured by the debris and some of the fibers could remain hidden and hence undetected despite the use of larger filters. Therefore, the current deposition data for the oral cavity should be considered as a lower bound estimate.

### 3.4. Deposition efficiencies in the tracheobronchial airways

After passage through oral airways, the fibers enter the trachea through the larynx. [Martonen, Zhang, and Lessmann \(1993\)](#) reported that the flow in the trachea and subsequent generation of branching is strongly influenced by the complicated larynx geometry. This geometry, particularly the restriction of vocal cords, enhances local turbulence levels and creates the so-called laryngeal jet of accelerated particles. This jet is shifted to the back side of trachea in our geometry ([Elcner, Lizal, Jedelsky, Jicha, & Chovancova, 2016](#)) increasing deposition of large ( $> 1 \mu\text{m}$ ) particles. The jet effect is reduced throughout the trachea and it is not noticeable beyond the first generation ([Lin, Tawhai, McLennan, & Hoffman, 2007](#)). However, the flow disturbances may be enhanced by bifurcations.

Fiber deposition efficiencies in the trachea and in the first generation as a function of Stokes number are presented in [Fig. 6](#). The measured data were compared with those reported by [Su and Cheng \(2009\)](#) (casts A and B). It can be seen that the deposition efficiency in both regions increased with the increasing Stokes number indicating the important role of impaction. The measured data were in good agreement with the literature results.

Empirical models were suggested to relate an average Stokes number in each given region to the average deposition efficiency in that region. [Chan and Schreck \(1980\)](#) proposed a model for prediction of deposition in the trachea

$$DE_{trachea} = a \cdot Stk^b, \quad (10)$$

where  $a$  and  $b$  are constants. [Kim and Fisher \(1999\)](#) proposed an empirical model for predicting deposition in bifurcations using sequentially bifurcating tube models. A modified logistic function was suggested.

$$DE_{gen. number} = 1 - \frac{1}{a \cdot Stk^b + 1}, \quad (11)$$

where  $a$  and  $b$  are constants. [Su and Cheng \(2009\)](#) employed these models and found the best fits for deposition in the trachea ( $a = 0.67$ ,  $b = 0.89$ ) and the first generation ( $a = 4.2$ ,  $b = 1.4$ ). As seen in [Fig. 6](#), the current data showed a slightly lower deposition efficiency compared to the reported data. Moreover, the proposed models slightly overestimated the deposition for low Stokes numbers.

Turbulence levels caused by the larynx are reduced throughout the trachea. However, they are enhanced again at bifurcations. Therefore, the turbulence can persist into the first few generation branches even at low Reynolds numbers ([Zhang & Kleinstreuer, 2004](#)). Velocity patterns are complicated and are influenced by the upstream flows and secondary vortices appearing in daughter

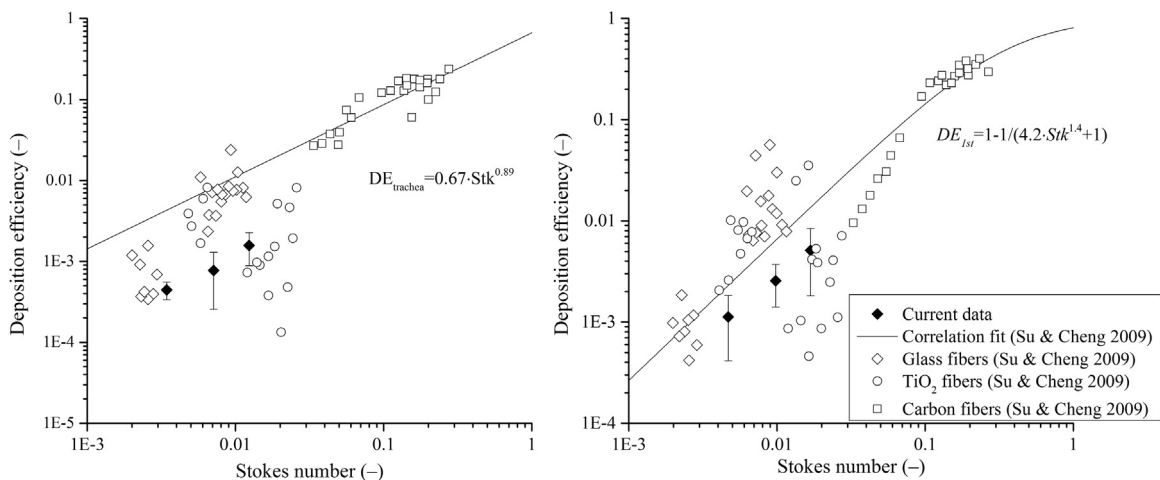


**Fig. 6.** Deposition efficiency in the trachea (left) and 1st generation (right) as a function of Stokes number; the error bars represent standard deviations.

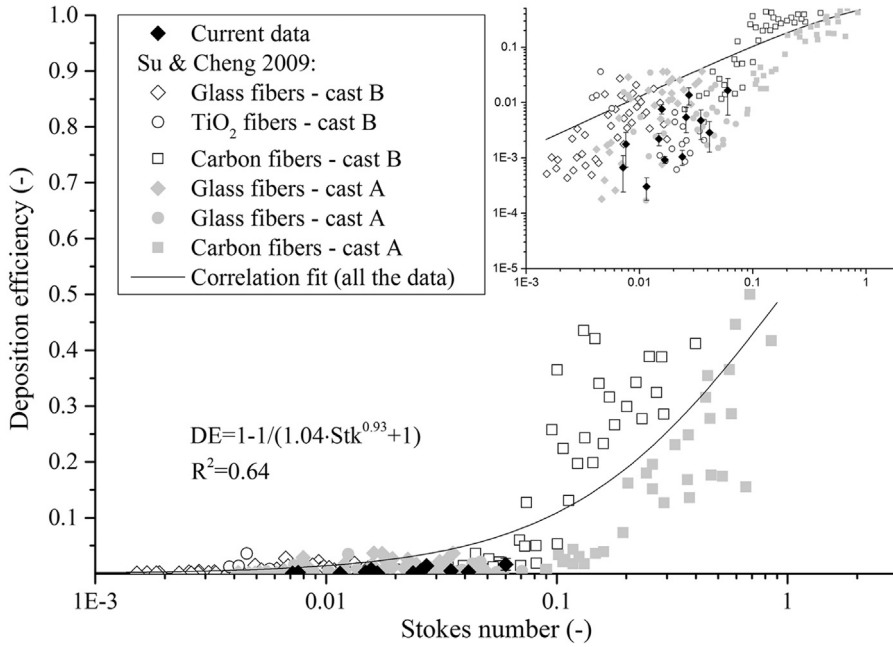


Fig. 7. Deposition efficiency in the 3rd generation as a function of Stokes number; the error bars represent standard deviations.

branches. The particles tend to deposit on the carinal ridges by impaction and near the carinas because of secondary flows (Kleinstreuer, Zhang, & Li, 2008).

Deposition efficiency in the 3rd generation is shown in Fig. 7. Deposition efficiency in the 2nd generation is presented in Fig. S7. The graphs are displayed with both linear and logarithmic scales. The trend was the same as in the previous cases; deposition efficiency increased as the Stokes number increased. Good agreement between the current and previously reported results was observed. However, there was significant variability. Differences were observed when comparing among the different geometries or different branches in any specific generation of a given geometry. These differences can be caused by the dependence of the flow on the upstream velocity fields and geometry. Local geometric features could influence the airflow, such as velocity patterns, magnitudes

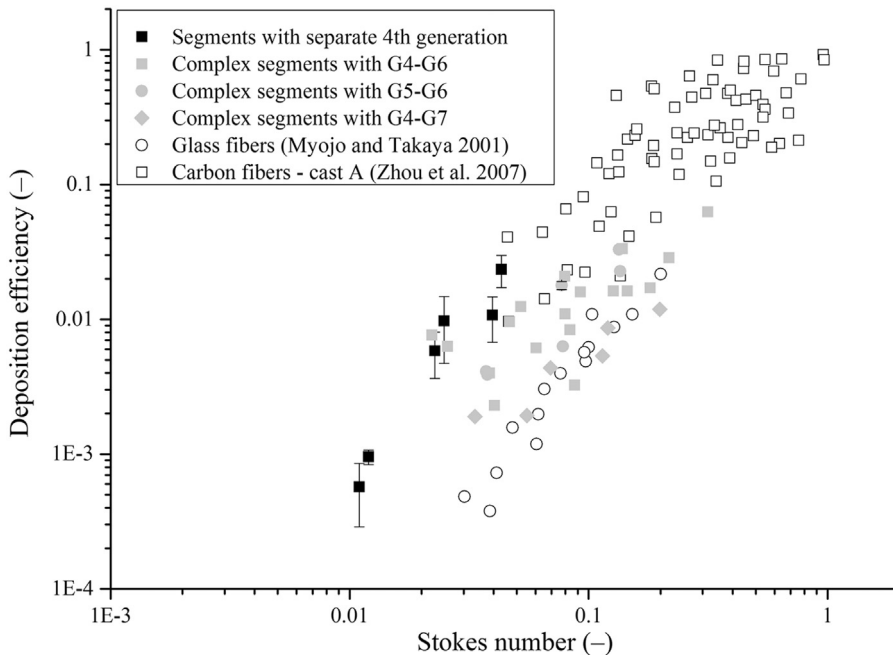


Fig. 8. Deposition efficiency in the 4th to 7th generation as a function of Stokes number; the error bars represent standard deviations.

and local turbulence structures, which are induced by the sequential airway branching resulting in different deposition patterns at specific locations or branches in the same generation.

Although the deposition data in the 2nd and 3rd generation showed large variations and were difficult to interpret, the empirical model suggested by Kim and Fisher (1999) was employed to obtain the empirical equations. OriginPro 9 (OriginLab Corporation, MA, USA) was used to obtain the best curve fit ( $a_2 = 0.35$ ,  $b_2 = 0.68$ ,  $a_3 = 1.04$  and  $b_3 = 0.93$ ). Fig. 7 shows that the empirical curve overestimated the deposition for low Stokes numbers ( $Stk < 0.1$ ). This discrepancy was caused by a large variation of deposition efficiency for high Stokes numbers. Therefore, it would be useful to acquire more deposition data using high momentum fibers.

In the medium-sized airways, such as the 4th or the 6th generations, the flow becomes laminar, but it is still not fully developed. Zhang et al. (2008) numerically investigated the airflow in the tracheobronchial tree made of symmetric triple-bifurcation units down to the 16th generation. They showed that the flow patterns around the 6th generation were still skewed and the secondary flows were very strong.

Deposition in the 4th to 7th generation in the current respiratory airway replica can be seen in Fig. 8. The 4th generation was incomplete and included only two bifurcations which were assumed to represent all the bifurcations in the 4th generation. The deposition efficiency increased with the increasing Stokes number even in the 4th generation. The measured data were also compared with the results of Myojo and Takaya (2001) and Zhou et al. (2007). Zhou et al. (2007) presented deposition of carbon fibers with a higher Stokes number than those in our study. However, our data followed the same trend. The deposition efficiencies reported by Myojo and Takaya (2001) were lower compared to the other studies. The deposition was measured in only one idealized bifurcation in their study. The smooth idealized walls together with the absence of upstream flow history likely caused the lower fiber deposition.

The other bifurcations in the 4th generation were part of the complex segments that extended down to the 6th or 7th generation. It was not possible to extract deposition per generation in these segments. Therefore, deposition efficiency for several generations as a function of average Stokes number is shown in Fig. 8. Substantial variability was reported in the complex segments that included the same airway generations. This result indicated that the deposition was influenced by the upstream velocity fields and the individual segment geometry. The deposition efficiencies increased with increasing Stokes number, however, the increase was not that significant as in the case of more proximal generations. This result could be caused by the diminishing effect of impaction with increasing generation number. However, the use of average Stokes number is not ideal for this analysis and comparison with CFD results could provide additional insights.

### 3.5. Deposition of fibers and spherical particles

Deposition of fibers was compared to that of spherical particles. Lizal et al. (2015) carried out deposition experiments with radioactive spherical particles using the same airway replica. The Stokes numbers for the spherical particles were calculated using Eq. (9). The linear empirical model of Chan and Lippmann (1980) was also applied to the spherical particles data, and the fits for the data from first four generations were calculated. The same empirical model was used to calculate the fits for the fibrous particles. The

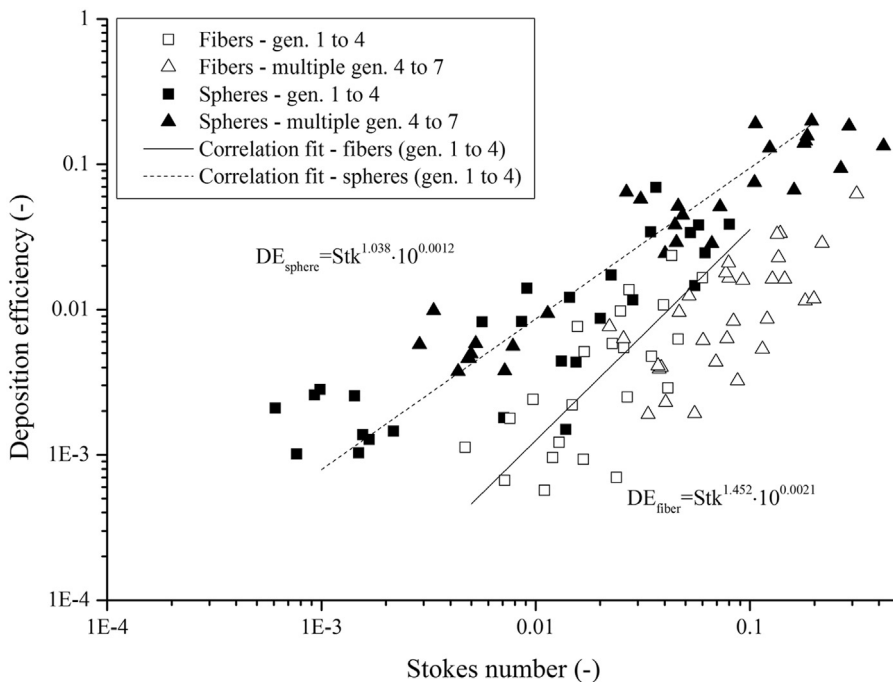


Fig. 9. Deposition efficiency of fibrous and spherical particles as a function of Stokes number.

deposition in the replicas was represented by Eqs. (12) ( $R^2 = 0.97$ ) and (13) ( $R^2 = 0.98$ ), respectively.

$$DE_{spheres} = Stk^{1.038} \cdot 10^{0.0012}, \quad (12)$$

$$DE_{fibers} = Stk^{1.452} \cdot 10^{0.0021}. \quad (13)$$

A comparison of particle deposition in the tracheobronchial tree together with the correlations are presented in Fig. 9. Deposition of both particle types was driven by impaction since the deposition efficiency increased with the increasing Stokes number. Generally, deposition efficiency is higher for spherical particles than for the fibers having the same Stokes number. This result can be caused by the ability of fibers to align themselves with the airflow.

#### 4. Conclusions

Deposition measurements of length classified glass fibers in a realistic human airway replica were performed. In-house software was employed to analyze filters from the experiments and speed up the process. Deposition characteristics in various regions of the replica were investigated with respect to the inspiratory flow rate afterwards.

It was found that the deposition fraction increased with increasing inspiratory flow rate. However, the total deposition fraction in the replica did not exceed 5% implying that the vast majority of fibers passed through the replica and would reach the lower respiratory airways. Although a considerably high deposition fraction was found in the oral cavity and the segment including several generations, deposition density appeared to be low in these regions. Deposition density was higher in the main bronchi compared to the oral cavity.

Deposition efficiencies in the oral cavity and the tracheobronchial tree were compared with other reported data and good agreement was found except for the oral cavity. It was observed that the deposition efficiency was strongly correlated with the Stokes number, indicating the role of impaction. Empirical models that have been suggested for different regions of the respiratory airways down to the 3rd branch generation of branching are reasonably useful for fiber deposition prediction in these regions. The next step should be to obtain more deposition data for fibers with Stokes numbers in the range of 0.1–1.

Deposition of fibers was compared to that of spherical particles. This comparison confirmed that fibers deposit less effectively than spherical particles of the same Stokes number. This result was likely due to the ability of fibers to align with the flow.

#### Conflict of interest

The authors have no conflict of interest.

#### Funding

The authors greatly acknowledge support from the projects FSI-S-17-4444 funded by the Ministry of Education, Youth and Sports of the Czech Republic and project no. GA16-23675S funded by the Czech Science Foundation.

#### Appendix A. Supporting information

Supplementary data associated with this article can be found in the online version at <http://dx.doi.org/10.1016/j.jaerosci.2017.11.006>.

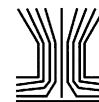
#### References

- Balashazy, I., Martonen, T. B., & Hofmann, W. (1990). Fiber Deposition in Airway Bifurcations. *Journal of Aerosol Medicine-Deposition Clearance and Effects in the Lung*, 3(4), 243–260. <http://dx.doi.org/10.1089/jam.1990.3.243>.
- Balashazy, I., Moustafa, M., Hofmann, W., Szoke, R., El-Hussein, A., & Ahmed, A. R. (2005). Simulation of fiber deposition in bronchial airways. *Inhalation Toxicology*, 17(13), 717–727. <http://dx.doi.org/10.1080/08958370500224565>.
- Baron (2001). Measurement of airborne particles-review. *Industrial Health*. Retrieved from <[http://202.241.32.9/en/indu\\_hel/pdf/IH39\\_08.pdf](http://202.241.32.9/en/indu_hel/pdf/IH39_08.pdf)> website:.
- Baron, P. A., & Willeke, K. (2001). *Aerosol Measurement: Principles, Techniques, and Application* (2nd ed.). New York: Wiley.
- Baron, P. A., Deye, G. J., & Fernback, J. (1994). Length separation of fibers. *Aerosol Science and Technology*, 21(2), 179–192. <http://dx.doi.org/10.1080/02786829408959707>.
- Belka, M., Lizal, F., Jedelsky, J., Starha, P., Druckmullerova, H., Hopke, P. K., & Jicha, M. (2016). Application of image analysis method to detection and counting of glass fibers from filter samples. *Aerosol Science and Technology*, 50(4), 353–362. <http://dx.doi.org/10.1080/02786826.2016.1151858>.
- Cai, F. S., & Yu, C. P. (1988). Inertial and interceptional deposition of spherical-particles and fibers in a bifurcating airway. *Journal of Aerosol Science*, 19(6), 679–688. [http://dx.doi.org/10.1016/0021-8502\(88\)90003-1](http://dx.doi.org/10.1016/0021-8502(88)90003-1).
- Dastan, A., Abouali, O., & Ahmadi, G. (2014). CFD simulation of total and regional fiber deposition in human nasal cavities. *Journal of Aerosol Science*, 69, 132–149. <http://dx.doi.org/10.1016/j.jaerosci.2013.12.008>.
- Deye, G. J., Gao, P., Baron, P. A., & Fernback, J. (1999). Performance evaluation of a fiber length classifier. *Aerosol Science and Technology*, 30(5), 420–437. <http://dx.doi.org/10.1080/027868299304471>.
- Elcner, J., Lizal, F., Jedelsky, J., Jicha, M., & Chovancova, M. (2016). Numerical investigation of inspiratory airflow in a realistic model of the human tracheobronchial airways and a comparison with experimental results. *Biomechanics and Modeling in Mechanobiology*, 15(2), 447–469. <http://dx.doi.org/10.1007/s10237-015-0701-1>.
- Fan, F. G., & Ahmadi, G. (1995). A sublayer model for wall deposition of ellipsoidal particles in turbulent streams. *Journal of Aerosol Science*, 26(5), 813–840. [http://dx.doi.org/10.1016/0021-8502\(95\)00021-00024](http://dx.doi.org/10.1016/0021-8502(95)00021-00024).
- Feng, Y., & Kleinstreuer, C. (2013). Analysis of non-spherical particle transport in complex internal shear flows. *Physics of Fluids*, 25(9), <http://dx.doi.org/10.1063/1.1248888>.

4821812.

- Frederix, E. M. A., Kuczaj, A. K., Nordlund, M., Belka, M., Lizal, F., Jedelsky, J., ... Geurts, B. J. (2018). Simulation of size-dependent aerosol deposition in a realistic model of the upper human airways. *Journal of Aerosol Science*, 115 (Supplement C), 29–45. <https://dx.doi.org/10.1016/j.jaerosci.2017.10.007>.
- Grgic, B., Finlay, W. H., Burnell, P. K. P., & Heenan, A. F. (2004). In vitro intersubject and intrasubject deposition measurements in realistic mouth-throat geometries. *Journal of Aerosol Science*, 35(8), 1025–1040. <http://dx.doi.org/10.1016/j.jaerosci.2004.03.003>.
- Hinds, W. C. (1999). *Aerosol technology: properties, behavior, and measurement of airborne particles* (2nd ed.). New York; Chichester: Wiley.
- Hofmann, W. (2011). Modelling inhaled particle deposition in the human lung—A review. *Journal of Aerosol Science*, 42(10), 693–724. <http://dx.doi.org/10.1016/j.jaerosci.2011.05.007>.
- Hofmann, W., Winkler-Heil, R., & Balashazy, I. (2006). The effect of morphological variability on surface deposition densities of inhaled particles in human bronchial and acinar airways. *Inhalation Toxicology*, 18(10), 809–819. <http://dx.doi.org/10.1080/08958370600753851>.
- Chan, T. L., & Lippmann, M. (1980). Experimental measurements and empirical modeling of the regional deposition of inhaled particles in humans. *American Industrial Hygiene Association Journal*, 41(6), 399–408. <http://dx.doi.org/10.1080/15298668091424942>.
- Chan, T. L., Schreck, R. M., & Lippmann, M. (1980). Effect of the laryngeal jet on particle deposition in the human trachea and upper bronchial airways. *Journal of Aerosol Science*, 11(5–6), 447. [http://dx.doi.org/10.1016/0021-8502\(80\)90117-2](http://dx.doi.org/10.1016/0021-8502(80)90117-2).
- Cheng, K. H., Cheng, Y. S., Yeh, H. C., & Swift, D. L. (1997). Measurements of airway dimensions and calculation of mass transfer characteristics of the human oral passage. *Journal of Biomechanical Engineering-Transactions of the ASME*, 119(4), 476–482. <http://dx.doi.org/10.1115/1.2798296>.
- Cheng, Y. S., Su, Y. F., Yeh, H. C., & Swift, D. L. (1993). Deposition of thoron progeny in human head airways. *Aerosol Science and Technology*, 18(4), 359–375. <http://dx.doi.org/10.1080/02786829308959610>.
- Cheng, Y. S., Zhou, Y., & Chen, B. T. (1999). Particle deposition in a cast of human oral airways. *Aerosol Science and Technology*, 31(4), 286–300. <http://dx.doi.org/10.1080/027868299304165>.
- IARC International Agency for Research on Cancer (2002). Working Group on the Evaluation of Carcinogenic Risks to Humans., World Health Organization. *Man-made vitreous fibres*. Lyon, France.
- Inthavong, K., Mouritz, A. P., Dong, J. L., & Tu, J. Y. (2013). Inhalation and deposition of carbon and glass composite fibre in the respiratory airway. *Journal of Aerosol Science*, 65, 58–68. <http://dx.doi.org/10.1016/j.jaerosci.2013.07.003>.
- Jedelsky, J., Lizal, F., & Jicha, M. (2012). Characteristics of turbulent particle transport in human airways under steady and cyclic flows. *International Journal of Heat and Fluid Flow*, 35, 84–92. <http://dx.doi.org/10.1016/j.ijheatfluidflow.2012.01.003>.
- Kim, C. S., & Fisher, D. M. (1999). Deposition characteristics of aerosol particles in sequentially bifurcating airway models. *Aerosol Science and Technology*, 31(2–3), 198–220. <http://dx.doi.org/10.1080/027868299304255>.
- Kleinstreuer, C., & Feng, Y. (2013). Computational analysis of non-spherical particle transport and deposition in shear flow with application to lung aerosol dynamics—A review. *Journal of Biomechanical Engineering-Transactions of the ASME*, 135(2), <http://dx.doi.org/10.1115/1.4023236>.
- Kleinstreuer, C., & Zhang, Z. (2003). Laminar-to-turbulent fluid-particle flows in a human airway model. [article]. *International Journal of Multiphase Flowing*, 29(2), 271–289. [http://dx.doi.org/10.1016/S0301-9322\(02\)00131-3](http://dx.doi.org/10.1016/S0301-9322(02)00131-3).
- Kleinstreuer, C., Zhang, Z., & Li, Z. (2008). Modeling airflow and particle transport/deposition in pulmonary airways. *Respiratory Physiology & Neurobiology*, 163(1–3), 128–138. <http://dx.doi.org/10.1016/j.resp.2008.07.002>.
- Koullapis, P., Kassinos, S. C., Muela, J., Perez-Segarra, C., Rigola, J., Lehmkuhl, O., & Nicolaou, L. (2017). Regional aerosol deposition in the human airways: The SimInhale benchmark case and a critical assessment of in silico methods. *European Journal of Pharmaceutical Sciences*. <http://dx.doi.org/10.1016/j.ejps.2017.09.003>.
- Lin, C., Tawhai, M., McLennan, G., & Hoffman, E. (2007). Characteristics of the turbulent laryngeal jet and its effect on airflow in the human intra-thoracic airways. [Article]. *Respiratory Physiology & Neurobiology*, 157(2–3), 295–309. <http://dx.doi.org/10.1016/j.resp.2007.02.006>.
- Lipowicz, P. J., & Yeh, H. C. (1989). Fiber dielectrophoresis. *Aerosol Science and Technology*, 11(3), 206–212. <http://dx.doi.org/10.1080/02786828908959313>.
- Lizal, F., Belka, M., Adam, J., Jedelsky, J., & Jicha, M. (2015). A method for in vitro regional aerosol deposition measurement in a model of the human tracheo-bronchial tree by the positron emission tomography. *Proceedings of the Institution of Mechanical Engineers Part H-Journal of Engineering in Medicine*, 229(10), 750–757. <http://dx.doi.org/10.1177/0954411915600005>.
- Lizal, F., Elcner, J., Hopke, P. K., Jedelsky, J., & Jicha, M. (2012). Development of a realistic human airway model. *Proceedings of the Institution of Mechanical Engineers Part H-Journal of Engineering in Medicine*, 226(H3), 197–207. <http://dx.doi.org/10.1177/0954411911430188>.
- Martonen, T. B., Zhang, Z., & Lessmann, R. C. (1993). Fluid-dynamics of the human larynx and upper tracheobronchial airways. *Aerosol Science and Technology*, 19(2), 133–156. <http://dx.doi.org/10.1080/02786829308959627>.
- Myojo, T. (1990). The effect of length and diameter on the deposition of fibrous aerosol in a model lung bifurcation. *Journal of Aerosol Science*, 21(5), 651–659. [http://dx.doi.org/10.1016/0021-8502\(90\)90120-M](http://dx.doi.org/10.1016/0021-8502(90)90120-M).
- Myojo, T., & Takaya, M. (2001). Estimation of fibrous aerosol deposition in upper bronchi based on experimental data with model bifurcation. *Industrial Health*, 39(2), 141–149. <http://dx.doi.org/10.2486/indhealth.39.141>.
- Nordlund, M., Belka, M., Kuczaj, A. K., Lizal, F., Jedelsky, J., Elcner, J., & Hoeng, J. (2017). Multicomponent aerosol particle deposition in a realistic cast of the human upper respiratory tract. *Inhalation Toxicology*, 29(3), 113–125. <http://dx.doi.org/10.1080/08958378.2017.1315196>.
- Ruzer, L. S., & Harley, N. H. (2013). *Aerosols handbook: measurement, dosimetry, and health effects* (2nd ed.). Boca Raton: Taylor & Francis.
- SCOEL Scientific Committee on Occupational Exposure Limits (2012). *Recommendation from the Scientific Committee on Occupational Exposure Limits for man made-mineral fibres (MMMF)*: European Commission. Employment, Social Affairs and Inclusion.
- Shanley, K. T., & Ahmadi, G. (2011). A numerical model for simulating the motions of ellipsoidal fibers suspended in low reynolds number shear flows. *Aerosol Science and Technology*, 45(7), 838–848. <http://dx.doi.org/10.1080/02786826.2011.566293>.
- Shanley, K. T., Ahmadi, G., Hopke, P. K., & Cheng, Y.-S. (2016). Simulated airflow and rigid fiber behavior in a realistic nasal airway model. *Particulate Science and Technology*, 1–10. <http://dx.doi.org/10.1080/02726351.2016.1208694>.
- Schmidt, A., Zidowitz, S., Kriete, A., Denhard, T., Krass, S., & Peitgen, H. O. (2004). A digital reference model of the human bronchial tree. *Computerized Medical Imaging and Graphics*, 28(4), 203–211. <http://dx.doi.org/10.1016/j.compmedimag.2004.01.001>.
- Stahlhofen, W., Rudolf, G., & James, A. C. (1989). Intercomparison of experimental regional aerosol deposition data. *Journal of Aerosol Medicine*, 2(3), 285–308. <http://dx.doi.org/10.1089/jam.1989.2.285>.
- Stöber, W. (1972). Dynamic shape factors of nonspherical aerosol particles. *Assesment of Airborne Particles*, 249–289.
- Su, W. C., & Cheng, Y. S. (2005). Deposition of fiber in the human nasal airway. *Aerosol Science and Technology*, 39(9), 888–901. <http://dx.doi.org/10.1080/02786820500295685>.
- Su, W. C., & Cheng, Y. S. (2006aa). Deposition of fiber in a human airway replica. *Journal of Aerosol Science*, 37(11), 1429–1441. <http://dx.doi.org/10.1016/j.jaerosci.2006.01.015>.
- Su, W. C., & Cheng, Y. S. (2006bb). Fiber deposition pattern in two human respiratory tract replicas. *Inhalation Toxicology*, 18(10), 749–760. <http://dx.doi.org/10.1080/08958370600748513>.
- Su, W. C., & Cheng, Y. S. (2009). Deposition of man-made fibers in human respiratory airway casts. *Journal of Aerosol Science*, 40(3), 270–284. <http://dx.doi.org/10.1016/j.jaerosci.2008.11.003>.
- Su, W. C., & Cheng, Y. S. (2015). Estimation of carbon nanotubes deposition in a human respiratory tract replica. *Journal of Aerosol Science*, 79, 72–85. <http://dx.doi.org/10.1016/j.jaerosci.2014.09.005>.
- Sussman, R. G., Cohen, B. S., & Lippmann, M. (1991). Asbestos fiber deposition in a human tracheobronchial cast. I. Experimental. *Inhalation Toxicology*, 3(2), 145–160. <http://dx.doi.org/10.3109/08958379109145281>.
- Tian, L., & Ahmadi, G. (2013). Fiber transport and deposition in human upper tracheobronchial airways. *Journal of Aerosol Science*, 60, 1–20. <http://dx.doi.org/10.1016/j.jaerosci.2013.02.001>.

- Tian, L., Ahmadi, G., Wang, Z., & Hopke, P. K. (2012). Transport and deposition of ellipsoidal fibers in low Reynolds number flows. *Journal of Aerosol Science*, 45, 1–18. <http://dx.doi.org/10.1016/j.jaerosci.2011.09.001>.
- Wang, Z., Hopke, P. K., Ahmadi, G., Cheng, Y.-S., & Baron, P. A. (2008). Fibrous particle deposition in human nasal passage: The influence of particle length, flow rate, and geometry of nasal airway. *Journal of Aerosol Science*, 39(12), 1040–1054. <http://dx.doi.org/10.1016/j.jaerosci.2008.07.008>.
- Wang, Z., Hopke, P. K., Baron, P. A., Ahmadi, G., Cheng, Y.-S., Deye, G., & Su, W.-C. (2005). Fiber classification and the influence of average air humidity. *Aerosol Science and Technology*, 39(11), 1056–1063. <http://dx.doi.org/10.1080/02786820500380198>.
- Weibel, E. R. (1963). *Morphometry of the human lung*. Berlin: [s.n.].
- Zhang, L., Asgharian, B., & Anjilvel, S. (1996). Inertial and interceptional deposition of fibers in a bifurcating airway. *Journal of Aerosol Medicine-Deposition Clearance and Effects in the Lung*, 9(3), 419–430. <http://dx.doi.org/10.1089/jam.1996.9.419>.
- Zhang, Z., & Kleinstreuer, C. (2004). Airflow structures and nano-particle deposition in a human upper airway model. *Journal of Computational Physics*, 198(1), 178–210. <http://dx.doi.org/10.1016/j.jcp.2003.11.034>.
- Zhang, Z., Kleinstreuer, C., & Kim, C. S. (2008). Airflow and nanoparticle deposition in a 16-generation tracheobronchial airway model. *Annals of Biomedical Engineering*, 36(12), 2095–2110. <http://dx.doi.org/10.1007/s10439-008-9583-z>.
- Zhou, Y., & Cheng, Y. (2005). Particle deposition in a cast of human tracheobronchial airways. *Aerosol science and Technology*, 39, 492–500.
- Zhou, Y., Su, W. C., & Cheng, Y. S. (2007). Fiber deposition in the tracheobronchial region: Experimental measurements. *Inhalation Toxicology*, 19(13), 1071–1078. <http://dx.doi.org/10.1080/08958370701626634>.
- Zhou, Y., Xi, J. X., Simpson, J., Irshad, H., & Cheng, Y. S. (2013). Aerosol deposition in a nasopharyngolaryngeal replica of a 5-year-old child. *Aerosol Science and Technology*, 47(3), 275–282. <http://dx.doi.org/10.1080/02786826.2012.749341>.



## Application of image analysis method to detection and counting of glass fibers from filter samples

Miloslav Belka<sup>a</sup>, Frantisek Lizal<sup>a</sup>, Jan Jedelsky<sup>a</sup>, Pavel Starha<sup>a</sup>, Hana Druckmullerova<sup>a</sup>, Philip K. Hopke<sup>b</sup>, and Miroslav Jicha<sup>a</sup>

<sup>a</sup>Department of Thermodynamics and Environmental Engineering, Faculty of Mechanical Engineering, Brno University of Technology, Brno, Czech Republic; <sup>b</sup>Center for Air Resources Engineering and Science, Clarkson University, New York, New York, USA

### ABSTRACT

Man-made vitreous fibers (MMVFs) are noncrystalline substances made of glass, rock or slag and are widely used as thermal or acoustic insulation materials. There is continued concern about their potential health impacts and thus, their dosimetry and behavior in the environment still require study using filters to collect fiber samples. After deposition or exposure measurements of MMVFs it is often necessary to analyze the filters with deposited fibers. This task is tedious, time-consuming, and requires skill. Therefore, many researchers have tried to simplify or automatize fiber detection and quantification. This article describes features of our in-house software, which automatically detects and counts fibers in images of filter samples. The image analysis is based on the use of a histogram equalization and an adaptive radial convolution filter that enhances fiber contrast and thus, improves the fiber identification. The accuracy of the software analysis was verified by comparison with manual counting using ordinary phase-contrast microscopy method. The correlation between the methods was very high (coefficient of determination was 0.977). However, there were some discrepancies caused by false identifications, which led to implementation of manual corrective functions.

### ARTICLE HISTORY

Received 17 October 2015  
Accepted 28 January 2016

### EDITOR

Tiina Reponen

## 1. Introduction

Man-made vitreous fibers (MMVFs) are fibers of various compositions that are widely used in buildings as a thermal or acoustic insulation material. MMVFs are noncrystalline substances made mainly of glass, rock, slag or other minerals. Health concerns from exposure to MMVFs come from their physical similarities to asbestos. They have similar aerodynamic characteristics, which causes their penetration into the human respiratory system. Oberdorster (2000) described pathogenicity of fibers with three parameters, in particular fiber dose, dimension, and durability. Fiber dose is generally expressed as particle mass deposited in the lungs, but with respect to fibrous aerosols particle number is also accepted. Fiber dimensions, in particular fiber length and diameter, determine deposition hot spots and affect the retention time of fibers in human respiratory tract. Fiber durability or fiber biopersistence means the overall retention capability of fibers in the lungs, which is influenced, e.g., by resistance to mechanical breakdown or chemical dissolution (DeVuyst et al. 1995). It is well known that exposure to asbestos leads to malignancies such as

mesothelioma or lung carcinoma (IARC 2012). However, such results were not confirmed for MMVFs. The International Agency for Research on Cancer classified MMVFs as noncarcinogenic, because there is inadequate evidence for carcinogenicity in humans (IARC 2002). This finding may result from their lower biopersistence compared to asbestos, e.g., the MMVFs are more soluble and they tend to decompose transversely compared to tangential breakage of asbestos (DeVuyst et al. 1995; Hesterberg et al. 1996). Despite the lower risk of MMVFs, there are recommendations for occupational exposure limits for MMVFs in the range of 1–3 fibers/ml depending on the fiber type (SCOEL 2012).

Thus, it remains important to obtain additional information from both lung deposition and exposure measurements. The outputs of such measurements are membrane filters onto which the fibers deposited. Each filter has to be inspected and the individual fibers have to be counted to obtain the fiber concentrations. Several analytical methods were established to determine airborne concentrations of fibers, including NIOSH 7400

methodology developed for asbestos and other fibers using phase-contrast microscopy (PCM method) (NIOSH 1994). Drawbacks of these methods are their poor consistency and reproducibility. Manual fiber counting is very time consuming and requires high skill in the analyst such as visual acuity, concentration while counting, care for adjusting a microscope, experience in counting fiber bundles etc. Aforementioned flaws can cause fiber counts for the same samples to vary greatly between different analysts and laboratories (Pang 2000).

Many groups have tried to simplify or automate counting practices and decrease the influence of human factor on the results largely focused on filters with asbestos fibers. Lundgren et al. (1995) connected a microscope to a Macintosh computer with special video card and software. An analyst was able to mark fibers with a mouse on a screen and the software displayed total fiber counts. Other groups tried to automate the counting mostly using various image analysis methods (IAMs). One of the earliest works was proposed by Manchester University's Asbestos fiber-counting Program (MAP) (Kenny 1984). Their software called Magiscan gave reasonable agreement with manual counts, but it was not consistent for all types of samples. It produced precise results at lower counts, but undercounted fibers on heavily loaded filters. This bias was a result of the software development, which was done primarily on filters with low fiber numbers (Baron and Shulman 1987). The most frequent errors of Magiscan were missed fibers, broken fibers, and false identification of nonfibrous particles. Inoue et al. (Inoue et al. 1998) introduced Asbestos Fibers Automatic Counting System (AFACS), which was a home-made software written in C language. The AFACS was capable of post-processing, such as restoration of broken fibers according to their orientation and thickness. The accuracy of AFACS was verified and compared with counting facilities. The AFACS counts were similar to manual counts and were considered to be equivalent, although the AFACS counted some fibers that were missed by manual counters and *vice versa*.

Cho et al. (2011) focused mainly on improvement of image acquisition part of their IAM. They described High Through-put Microscopy method for counting asbestos fibers, which employed a charge couple device (CCD) camera and a robotic stage to quickly scan the entire filter area processing up to 300 images in 5 min. In another study (Cho et al. 2013) they tagged fibers with a fluorescent protein and analyzed them with fluorescence microscopy (FM) to enhance the detection limit for small and thin fibers. The freeware image processing software ImageJ with appropriate plugins was used for image analysis. However, the counting rules were not implemented into the software so it was not possible to count

overlapping or crossed fibers, fiber bundles or differentiate oval-shaped particles. Further use of FM was made by Alexandrov et al. (2015). They used Asbester Counter Software for the image analysis. Although the application of FM should have eliminated nonfibrous particles with only asbestos fibers being visible in the FM images, some dust particles were still found. These particles caused discrepancies, especially for low concentration samples, because their edges were misidentified as fibers. Other IAMs for fiber counting were presented in Theodosiou et al. (2010), Ishizu et al. (2008), and Moriguchi et al. (2009). However, they did not get further than to testing and preliminary results. One of the problems of these IAMs was the occurrence of air bubbles from sample preparation (Ishizu et al. 2010), which biased the total fiber counts. As it can be seen, development of fully automatic IAM for fiber counting with sufficient accuracy is a very difficult task not completely solved yet.

As an output of *in vitro* deposition experiments we obtained a set of several hundreds of filter samples with deposited fibers, which needed to be analyzed. Since manual inspection and counting of fibers is very time consuming, tedious and sensitive to subjective errors, it would be valuable to use an IAM for fiber counting. Because all the methods that have been reported to date are inaccurate, expensive or not freely available, we developed our own software. By doing so, it is possible to easily adjust its features for different types of particles in future experiments. This article describes the main features of our software and presents a comparison with manual PCM method results.

## 2. Experimental setup

### 2.1. The phase-contrast microscopy method

#### 2.1.1. Sample preparation

Millipore AAWP02500 nitrocellulose membrane filters (Merck Millipore, Billerica, MA, USA) were used as part of an *in vitro* deposition measurements in the model of human respiratory tract (Belka et al. 2013). The model consisted of upper respiratory airways and several generations of the tracheobronchial tree (Lizal et al. 2012). The filters were situated as output filters from each branch of the bronchus to collect particles passing through the model. We used glass fibers, processed by crushing of glass wool. The glass fibers were classified according to their length causing the mean fiber length to be approximately 15  $\mu\text{m}$  and the mean diameter to be 1  $\mu\text{m}$  (Wang et al. 2005). After the filters were loaded with fibers an acetone-immersion method was applied to clear the filter (NIOSH 1994). The filters were mounted on clean glass slides and made transparent using a Quick

fix acetone vaporizer (EMS Inc., Charleston, USA). The slides with filters were then kept in a desiccator for sufficient amount of time to dry. The samples featured generally low amount of dust and other nonfibrous particles. The fiber area density varied from 100 to 1300 fiber/mm<sup>2</sup>. Ten representative samples with various fiber loads were chosen from the set to optimize the software development and to validate its results.

### 2.1.2. Manual counting

The manual counting was conducted using PCM, which is fast and requires less skill than electron microscopy. Moreover, the speed of PCM was suitable for the software development, which required a lot of tests, such as taking images with various camera settings. Each glass slide with a filter from the 10 samples was manually placed on a stage of Nikon Eclipse E200 microscope (Nikon, Tokyo, Japan) equipped with a nominal 10× eyepiece and a nominal 40× phase contrast objective. The microscope was focused on the fibers and Walton-Beckett graticule was used for sizing the fibers. The graticule consists of a circle with projected diameter of 300 μm (area of about 0.07 mm<sup>2</sup>). Manual counting was conducted by four practiced analysts using NIOSH 7400 counting B rules, e.g., only fibers longer than 5 μm, with diameter less than 3 μm and with length to width ratio greater or equal to 5:1 were to be counted. The only significant modification of the methodology was that 20 fields were inspected on each filter rather than to fulfill a minimal fiber count rule. Moreover, the entire filter area was used for counting instead of cutting a wedge as recommended by the standard methodology. Because different parts of the filter were inspected by the analysts, it was necessary to compare property of the whole filter, such as total fiber number or fiber area density. Since the total fiber numbers were in the order of hundred thousands, fiber densities were calculated for their better readability. The fiber area density is calculated by dividing average fiber count per graticule field by the graticule field area. Fiber area density for every filter was calculated as:

$$E_i = \frac{F_i}{n_f A_f}, \quad [1]$$

where  $F_i$  is total fiber count on the sample  $i$ ,  $n_f$  denotes the number of inspected fields per sample and  $A_f$  is the graticule field area. Since four analysts performed manual counting, geometric averages of the fiber area densities with geometric standard deviations were calculated for every sample. These average densities were

considered as the “right” densities and were used for optimization of the software.

## 2.2. The image analysis method

### 2.2.1. Image acquisition

An IR-UV light filter and a monochrome camera Atik 314E (Atik cameras, Norwich, UK) were attached to the microscope to acquire a set of filter images. The nonuniformity in fiber distribution on a filter could cause discrepancies in the results, because only a part of each filter was inspected. This problem was partly solved by changing a 40× phase contrast objective to a 10× objective. Because the glass fibers with diameter of 1 μm were used, it was possible to decrease the magnification and, thus increase the examined filter area while keeping the visibility of the fibers at sufficient level. Resolution of the camera was 1619 × 1219 pixels and image area was 0.34 mm<sup>2</sup>. The camera was connected to a computer with Artemis/ATK capture software. Sixteen images of each filter were taken and their analysis was executed afterward.

### 2.2.2. Image processing

The novel software uses several steps to correct and change the fiber contrast to improve their detection by thresholding (Figure 1). Even though the camera was properly adjusted and enough illumination was used, the brightness of original images was not sufficient. Some of the fibers did not have sufficient contrast and their visibility was very poor (Figure 1a). To enhance the fiber contrast the Adaptive Contrast Control (ACC) method was applied. This method is based on method by Zhu et al. (1999). It increases the contrast of an object with respect to its size, which can be used for brightness enhancement of poorly visible objects such as thin fibers. The ACC method calculates an equalization function using pixel brightness values from the respective neighborhood of each pixel. Application of this function creates a new calibrated image. Let  $I_{m \times n} = (P[i,j])$  be the image brightness matrix of pixel  $P$  and its rectangular neighborhood  $N_{w \times h}^P(i,j)$ , where  $w$  and  $h$  are neighborhood dimensions. The equalization function  $\phi_{wh}^P$  can be calculated using following formulas for each  $l$  in  $[0; L_{max}]$ , where  $L_{max}$  is maximum pixel value in this field.

$$\phi_{wh}^P(i,j,l) = Z\left(\frac{F_{ij}(l)}{wh} L_{max}\right), \quad [2]$$

$$Z(x) = y \text{ for } x \in (y - 0.5; y + 0.5), y \in Z, \quad [3]$$

where  $F_{ij}(l)$  is cumulative density function of pixel brightness values and  $Z$  is a rounding function. The

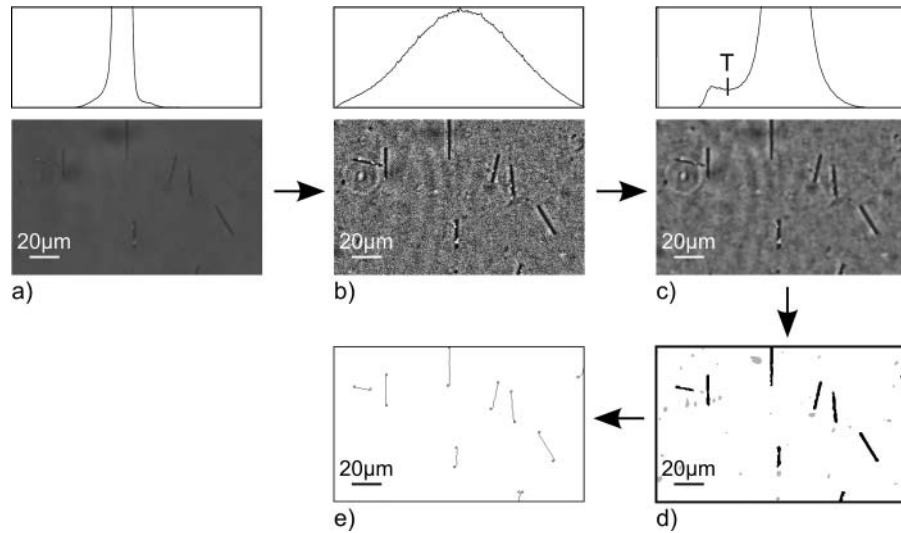


**Figure 1.** Image analysis process: (a) original image and its histogram; (b) image and histogram after ACC application; (c) image and histogram after adaptive radial convolution,  $T$  denotes threshold; (d) segmented image; (e) image with identified fibers.

rounding function provides round numbers at the output of equalization function. This is desirable, because image brightness values are round numbers. Moreover, the use of round numbers reduces computational time and memory demand. The size of the pixel neighborhood used for the equalization function influences the contrast change for objects of different size. Therefore, the equalization functions were tested with various sizes of the pixel neighborhood to find the best settings. The final image brightness matrix  $I^C$  of the new calibrated image was created by linear combination of three matrices,  $I^7$ ,  $I^{15}$ ,  $I^{31}$  with their respective square neighborhoods  $N_{7 \times 7}^p$ ,  $N_{15 \times 15}^p$ , and  $N_{31 \times 31}^p$ :

$$I^C = 0.25I^7 + 0.5I^{15} + 0.25I^{31}. \quad [4]$$

The ACC method increased contrast of the fibers in the image, but also of any additive noise. The additive noise was not separated in brightness from the fibers, which can be seen from the image histogram with unimodal distribution (Figure 1b). It is required to have bimodal distribution to correctly identify individual fibers by thresholding.

To do this, an adaptive radial convolution filter was applied. Detailed mathematical description and derivation can be found in Starha et al. (2013). A classical Gaussian radial convolution filter used as a low-pass filter attenuates high spatial frequencies in a convolution function. The convolution function  $h(\alpha, \beta)$  for the radial

convolution filter is defined as

$$h(\alpha, \beta) = \frac{1}{2\pi\zeta_\alpha\zeta_\beta} \exp\left(-\frac{(\alpha - \alpha_0)^2}{2\zeta_\alpha^2} - \frac{(\beta - \beta_0)^2}{2\zeta_\beta^2}\right), \quad [5]$$

where  $\alpha_0$ ,  $\beta_0$ ,  $\zeta_\alpha$  and  $\zeta_\beta$  are constants. If this classical radial convolution filter was used, all of the additive noise, as well as fiber edges, would be suppressed and the fiber detection by thresholding would be still biased. This problem can be solved by addition of a weight function, which causes the radial filter to prefer certain directions more than others. This method recognizes directions of fiber edges by application of the stochastic approach. The fiber edge is defined as a change of the image from dark to bright, particularly the variance of image values is much higher in the direction of a fiber edge than in the absence of an edge. Because of this, the radial filter with its weight function recognizes fiber edges and adapts its properties to different parts of the image. Application of the adaptive radial filter caused suppression of noise while the fiber contrast was preserved. As it can be seen in Figure 1c, the image histogram presented a bimodal distribution and the image could be segmented by means of thresholding. The threshold  $T$  was set close to a minimum value between the two modes.

### 2.2.3. Object classification and fiber counting

Objects identified by thresholding were not only fibers, but also other objects, such as dust particles (Figure 1d).

For this reason it was necessary to classify all the objects and choose only those that fulfilled certain rules, i.e., fibers. Fiber recognition was done by the moment method, which is based on the fact that shape of every object can be described by moment invariants (Ming-Kuei 1962). The fiber moments were described by this method and all particles, which did not fit into this group, were excluded from the selection.

It was also essential to know the fiber dimensions to correctly count all of the fibers, because only fibers longer than  $5 \mu\text{m}$  were to be counted. Additionally, it allowed the verification of the proper functioning of the electrical diffusion-phoretic fiber classifier (Wang et al. 2005) that was employed to separate the fibers according to their length. Fiber lengths were obtained by an erosion method using digital line structuring. This method calculates fiber core-line, which is a line of one pixel width defined by starting and end points. The fiber length is then expressed from the calculated core-line and known size of the pixel. Since the core-line is only one pixel wide, its length depends on the distances between adjacent pixels. If the pixels are adjoined vertically or horizontally, the distance between them equals the size of a pixel. If the pixels are adjoined diagonally, the distance between them equals the pixel diagonal. The total fiber length is a sum of distances between all the pixels of the core-line. Figure 1e depicts final image after object classification and transformation of fibers into digital lines.

The identified fibers were counted afterward. A Walton-Beckett graticule is employed in PCM method to help size the fibers and better identify the fibers, which occur on the edge of counting area. Fibers with only one end point lying in the counting area are counted as  $\frac{1}{2}$  of a fiber. An elliptical field with area of  $0.167 \text{ mm}^2$  was created in the software in order to follow this feature of the PCM method (Figure 2). This step was necessary for the determination of the actual size of all counted fibers. If the whole image was used for counting, only part of the fibers lying at the edge would be visible and the calculation of their actual sizes would be biased. The elliptical shape of the field has several advantages compared to rectangular field. There is lower probability that the fiber lies with both ends outside the field and its center inside the field, such as at the corners. Moreover, it is less likely that the fiber lies right on the edge of elliptical field compared to rectangular one. The software counted all the end points of fibers lying in the counting area and the number of end points was divided by two to get the final fiber count.

This procedure was applied to all filter images and respective fiber counts were acquired. Equation 1 was used for the calculation of fiber area densities for all

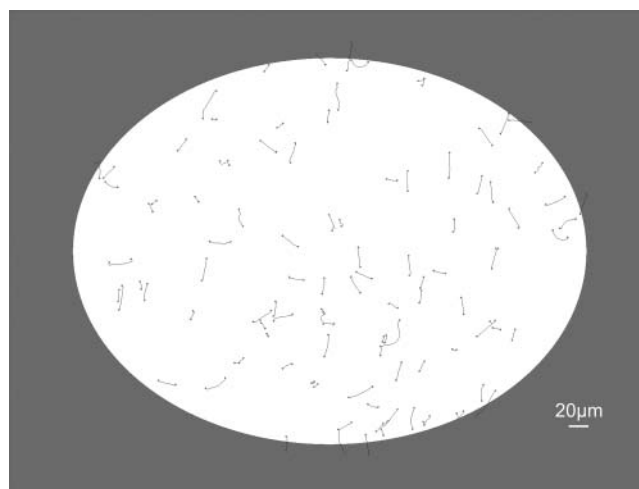


**Figure 2.** The use of elliptical field to correctly determine the actual size of all counted fibers; dimensions of semimajor and semiminor axis are 0.266 and 0.2 mm (area of about  $0.167 \text{ mm}^2$ ).

samples, where  $F_i$  denotes total fiber count on the sample  $i$  calculated by the software,  $n_f$  is number of images per sample and  $A_f$  is counting area (area of the elliptical field). The results of the automatic method were validated by the PCM method afterward. The manual method contains several uncertainties caused by the methodology, such as the choice of inspected fields. By comparing the properties of entire filters, such as fiber area densities, it can be seen how the methods agree amongst themselves including all the limitations.

#### 2.2.4. Manual corrections

The software allows it to be used in “correction” mode to assist the analysts to reject false identifications or restore broken fibers during postprocessing. The software interface can be seen in Figure 3 with first five windows representing different steps of image analysis. The results of the analysis are displayed in the sixth window in the bottom right corner. The selected portion of the filter can be displayed by the analyst and compared across the various stages of the IAM process. This combination of different steps of IAM simplifies the corrections, because, e.g., the visibility of particles is the highest after ACC application, but the particle origins are best determined in the original image. In cases of filters with high fiber area densities, it is very complicated to orientate and localize a particle of interest in the different windows. Therefore, a yellow circle cursor was integrated to improve orientation by defining the current position in all the windows. All of the corrections and the identified particles are highlighted in the segmented image (left bottom corner). Object identification and fiber counting can be launched

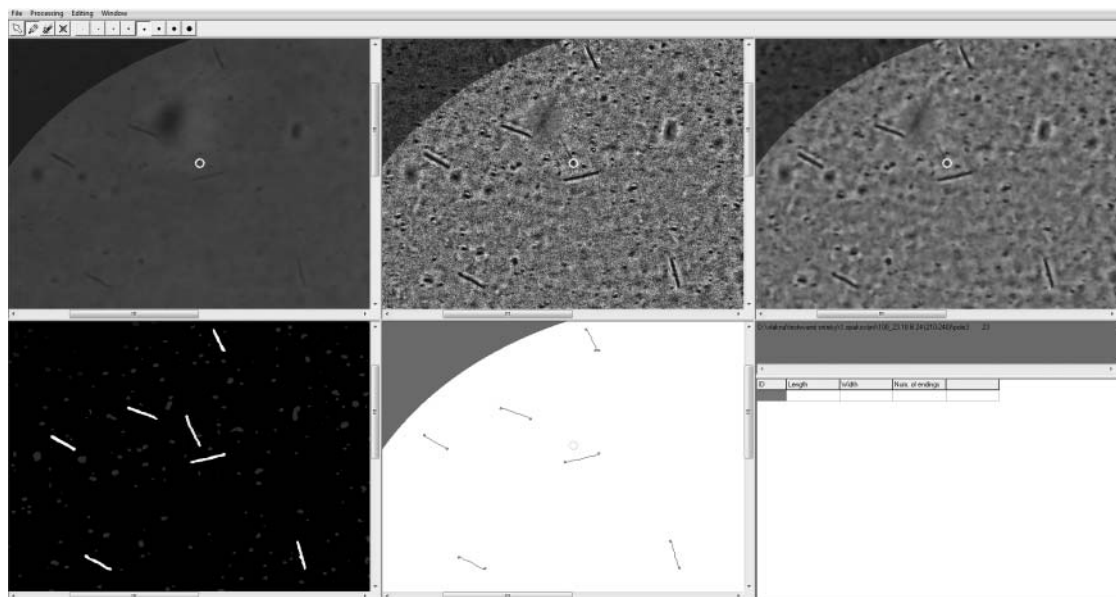


**Figure 3.** The software interface with six primary windows, the first five windows represent different steps of the IAM, the last window in the bottom right corner displays the results of the analysis.

after the corrections are made and a corrected fiber count is displayed.

### 3. Results and discussion

#### 3.1. The PCM method

The results from the four analysts were compared and are listed in Table 1. The fiber area densities of test samples varied from 100 to 800 fibers/mm<sup>2</sup>. The coefficient of variation (COV) among analysts ranged from 8 to 16%. The coefficient of variation is defined as the ratio of standard deviation to the average value and represents probability distribution. The differences between manual counts are generally caused by the sensitivity of the method to operator judgment, which can be influenced by not counting fibers with low contrast or counting one fiber twice in high area density samples. Moreover, fibers were not distributed uniformly on the filters with higher fiber area densities being found towards the filter center. Since every

analyst inspected only 20 randomly chosen fields, the choice of the inspected fields could cause a slight difference in fiber counts even if fibers were counted properly.

#### 3.2. Validation of the IAM

The collected images of the fibers had very low contrast and also contained nonfibrous particles. While the human eye is able to adapt to different background brightness, suppress additive noise and ignore dust particles, IAMs require various image modifications to successfully detect the particles. We found that the application of the ACC and the adaptive radial convolution filter enhanced the fiber contrast while the contrast of the background noise remained low. This process improved the detection limit of the IAM, and thus, very thin and low contrast fibers were detected. The moment method was then applied to restrict counting nonfibrous particles.

**Table 1.** Fiber area densities given by analysts for ten samples; SD denotes standard deviation and COV is coefficient of variation.

	S 1	S 2	S 3	S 4	S 5	S 6	S 7	S 8	S 9	S 10
Analyst 1 (f/mm <sup>2</sup> )	457.1	410.0	90.4	568.9	403.2	222.1	577.9	185.4	585.4	158.6
Analyst 2 (f/mm <sup>2</sup> )	355.4	471.1	111.1	802.1	493.2	250.7	588.2	224.6	480.4	181.1
Analyst 3 (f/mm <sup>2</sup> )	373.9	512.9	118.2	890.4	525.4	279.6	624.6	262.9	611.4	219.6
Analyst 4 (f/mm <sup>2</sup> )	300.7	390.4	140.7	833.6	432.9	238.6	499.3	233.6	510.4	186.1
Average (f/mm <sup>2</sup> )	371.8	446.1	115.1	773.8	463.7	247.8	572.5	226.6	546.9	186.3
SD (f/mm <sup>2</sup> )	56.2	48.7	18.0	122.4	48.2	21.0	45.7	27.7	53.4	21.8
COV (–)	0.15	0.11	0.16	0.16	0.10	0.08	0.08	0.12	0.10	0.12

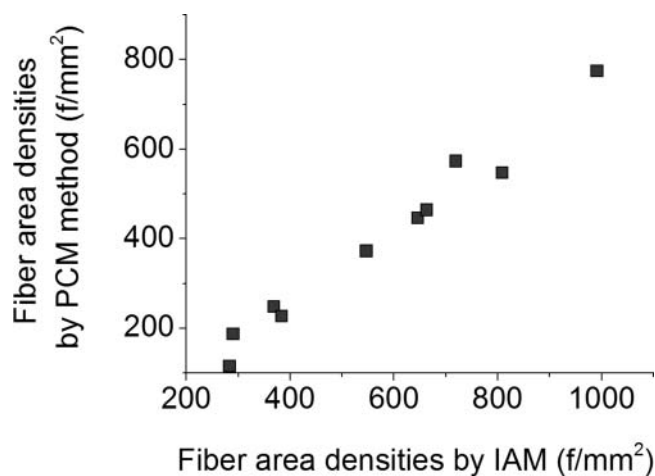


**Figure 4.** Correlation between the PCM method and the IAM.

Results of the software were validated by comparison with the results of PCM method. Both methods were employed to acquire fiber area densities on ten filter samples. The correlation between the methods is depicted in Figure 4. Although the coefficient of determination was very high ( $R^2 = 97.7\%$ ), there were some discrepancies between the methods and the IAM appears to have overestimated the fiber area densities in all samples.

The main causes of this trend were false object identifications, particularly misidentified particles, and broken fibers. The moment method was applied to select fibers from all of the objects present in the image. This method is, just like NIOSH methodology, unable to distinguish between fibers and elongated particles. Therefore, dust particles resembling fibers are considered to be fibers. Moreover, our IAM falsely identified edges of large dust particles as elongated particles and counted them as fibers.

Another problem in object identification was caused by circular particles or so-called bubbles (Figure 5). Ishizu et al. (2010) indicated that these bubbles could be

created during specimen preparation. The bubbles were located in a different plane than the fibers and were out of focus during image acquisition. This mismatch in focal plane produced halos around the bubbles. During the image processing the halo contrast was enhanced by the ACC and resembled large circular particles. In addition, the edges of these false particles were sometimes identified as objects during thresholding and could be selected as fibers. This problem was caused by the moment method settings. The moment method exclude nonfibrous particle from the final selection based on their geometric properties. The settings of the moment method were rather universal, but with the knowledge of the moment invariants of various nonfibrous particles, such as bubbles, microorganisms or membrane particles, it would be possible to adjust the method for specific cases.

Apart from false object identification, fibers were sometimes split into shorter objects during thresholding (Figure 6) caused by the drop in contrast along the fiber, such as in the case of fiber crossing. The upper fiber was identified as one piece, but fiber underneath was split into two separate objects and misinterpreted as different fibers. This problem could be solved in postprocessing step using information from the moment method. The fibers could be restored based on their orientation, thickness and mutual distance. However, this feature will require further tests and optimization for high area density samples.

### 3.3. Corrected IAM

The software allows manual corrections of the false object identifications. To validate this approach the results of the IAM were corrected by an analyst using the software feature and the resulting fiber area densities were compared to the PCM method again. As can

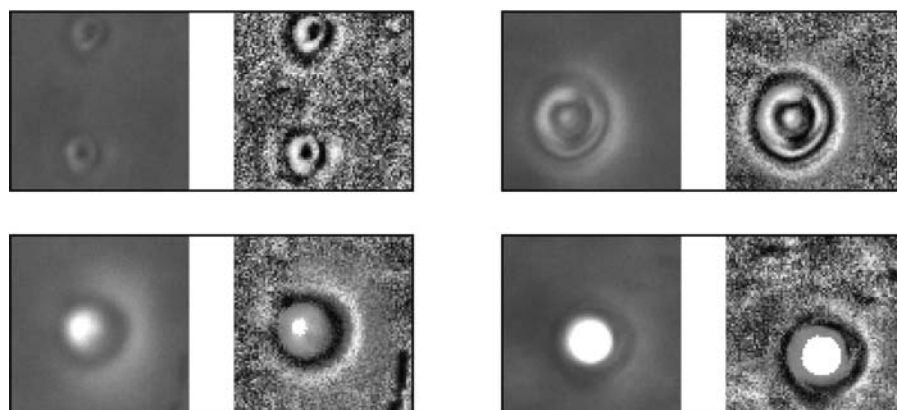


**Figure 5.** Enhancement of bubble contrast during ACC application; particle image size is  $32 \times 32 \mu\text{m}$ .

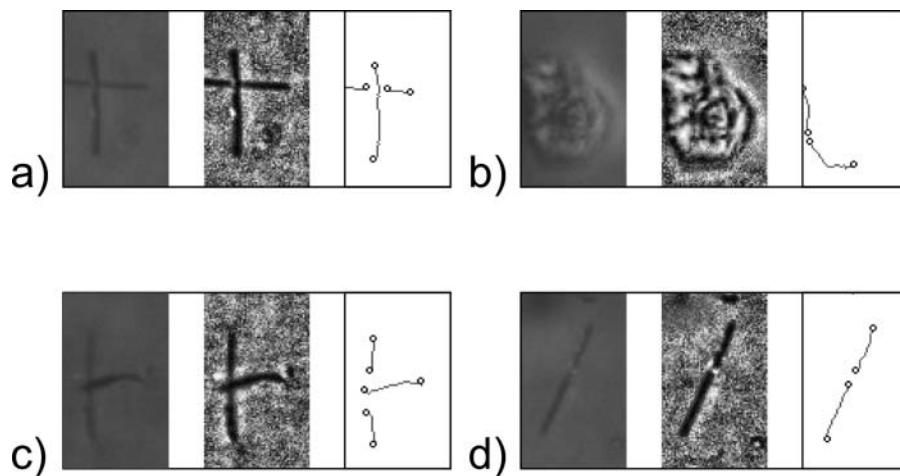


**Figure 6.** Examples of false identification in three steps of IAM: Original image, application of ACC, fiber identification; (a) crossed fibers, (b) dust particle, (c) crossed fibers, (d) single fiber; particle image size is  $24 \times 40 \mu\text{m}$ .

be seen in Figure 7, the IAM accuracy was improved and differences between methods decreased. The coefficient of determination increased from 97.7 to 98.5%. Moreover, average coefficient of variation decreased from 56 to 10% after the corrections. These results show that the accuracy of the corrected IAM is as high as the accuracy of the PCM method. The discrepancies between the corrected IAM and the PCM method can be caused by the sensitivity of both methods to the choice of inspected fields. Although the lower magnification was used for the automatic method, the software algorithms compensated for this drawback and even thin and low contrast fibers were counted.

Even though the software is not yet ready to be used in the fully automatic mode, it can be reliably used with manual corrections. Since the corrected images are stored, they can be opened and examined repeatedly. This way the software can be used for

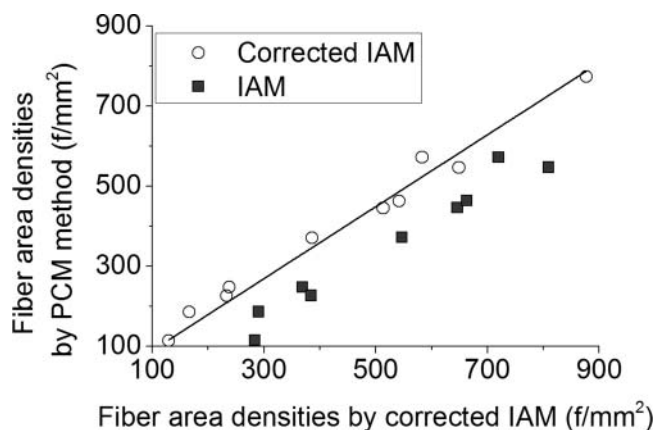


**Figure 7.** Correlation between the PCM and the corrected IAM.

educational purposes and analysts who are not skilled and experienced can learn to analyze fiber samples. Moreover, as stated by Lundgren et al. (1995), fiber counting using a computer is more user-friendly and less exhausting than counting using a microscope. Apart from that, the errors in identification and counting of certain kinds of particles were observed and their future solution can bring more precise results and development of the fully automatic fiber counting instrument. Current version of the software can be found and downloaded at <http://www.energetickforum.cz/ext/2pf/software/>.

#### 4. Conclusions

This article presents an in-house software intended for automatic fiber counting using image analysis. The software was developed and optimized on filters with deposited glass fibers, which were obtained during *in vitro* deposition measurements. However, the software can be used for counting of various kinds of fibers. The analyzed images are saved on a hard-drive and can be checked or examined repeatedly. The software is able to identify fiber shape and determine its length, which is the most important parameter for fiber counting and determination of fiber pathogenicity. It is worth noting that the software was used to analyze images from PCM at total magnification of  $100\times$ . Although this magnification was sufficient for the analysis of MMVFs, the analysis of some kinds of asbestos fibers, such as chrysotile fibers, can be biased. However, this limitation could be overcome by the change of the magnification and adjustment of the software settings.

We found that the use of histogram equalization and adaptive radial convolution filter can enhance the fiber

contrast while additive noise remained suppressed. This way the software is able to localize and identify even very thin and short fibers. Results of the software were validated by comparison with the manual PCM method indicating some shortcomings in the IAM. The software overestimated the fiber counts, which was mostly caused by broken fibers or misidentification of particle edges as fibers. Therefore, it is desirable to check every analyzed image and correct false identifications with software corrective functions. The time efficiency of the automatic method is reduced due to this step, however, it is still more convenient and less exhausting than the PCM method.

Despite these minor limitations, the software can be used for fiber counting analysis, because it can help the analyst with fiber localization and summation of all fibers. Moreover, the present errors of the counting were observed and analyzed. Future work should, therefore, concentrate on improvement of fiber identification and restoration of broken fibers using postprocessing functions. The program can be obtained by contacting the first author.

## Funding

Authors greatly acknowledge support from the projects FCH/FSI-J-14-2479 and LO1202 NETME CENTRE PLUS funded by the Ministry of Education, Youth and Sports of the Czech Republic under the National Sustainability Programme I and projects no. 105/11/1339 and 16-23675S funded by the Czech Science Foundation.

## References

- Alexandrov, M., Ichida, E., Nishimura, T., Aoki, K., Ishida, T., Hirota, R., Ikeda, T., Kawasaki, T., and Kuroda, A. (2015). Development of an Automated Asbestos Counting Software Based on Fluorescence Microscopy. *Environ. Monit. Assess.*, 187:4166
- Baron, P. A., and Shulman, S. A. (1987). Evaluation of the Magiscan Image Analyzer for Asbestos Fiber Counting. *Am. Ind. Hyg. Assoc. J.*, 48:39-46.
- Belka, M., Lizal, F., Jedelsky, J., and Jicha, M. (2013). Analysis of Fiber Deposition Using Automatic Image Processing Method. *Epj. Web. Conf.*, 45. doi: 10.1051/epjconf/20134501011.
- DeVuyst, P., Dumortier, P., Swaen, G. M. H., Pairon, J. C., and Brochard, P. (1995). Respiratory Health Effects of Man-Made Vitreous (Mineral) Fibres. *Eur. Respir. J.*, 8:2149-2173.
- Hesterberg, T. W., Miiller, W. C., Musselman, R. P., Kamstrup, O., Hamilton, R. D., and Thevenaz, P. (1996). Biopersistence of Man-Made Vitreous Fibers and Crocidolite Asbestos in the Rat Lung Following Inhalation. *Fund. Appl. Toxicol.*, 29:267-279.

- Cho, M. O., Chang, H. M., Lee, D., Yu, Y. G., Han, H., and Kim, J. K. (2013). Selective Detection and Automated Counting of Fluorescently-Labeled Chrysotile Asbestos Using a Dual-Mode High-Throughput Microscopy (DM-HTM) Method. *Sensors*, 13:5686-5699.
- Cho, M. O., Yoon, S., Han, H., and Kim, J. K. (2011). Automated Counting of Airborne Asbestos Fibers by a High-Throughput Microscopy (HTM) Method. *Sensors*, 11:7231-7242.
- IARC. (2002). Monographs on the Evaluation of Carcinogenic Risks to Humans, in *Man-Made Vitreous Fibers*. International Agency for Research on Cancer, Lyon, France.
- IARC. (2012). Monographs on the Evaluation of Carcinogenic Risks to Humans, in *Arsenic, Metals, Fibres, and Dusts*. International Agency for Research on Cancer, Lyon, France, pp. 219-310.
- Inoue, Y., Kaga, A., Yamaguchi, K., and Kamoi, S. (1998). Development of an Automatic System for Counting Asbestos Fibers Using Image Processing. *Part. Sci. Technol.*, 16:263-279.
- Ishizu, K., Takemura, H., and Kawabata, K. (2010). Automatic Counting Robot Development Supporting Qualitative Asbestos Analysis: Asbestos, Air Bubbles, and Particles Classification Using Machine Learning. *J. Robot. Mechatron.*, 22: 506-513.
- Ishizu, K., Takemura, H., Kawabata, K., Asama, H., Mishima, T., and Mizoguchi, H. (2008). Image Processing of Particle Detection for Asbestos Qualitative Analysis Support Method—Particle Counting System Based on Classification of Background Area, in *10th International Conference on Control Automation Robotics & Vision: Icarv 2008*, IEEE, New York, NY, pp. 868-873.
- Kenny, L. C. (1984). Asbestos Fiber Counting by Image-Analysis—The Performance of the Manchester Asbestos Program on Magiscan. *Ann. Occup. Hyg.*, 28:401-415.
- Lizal, F., Elcner, J., Hopke, P. K., Jedelsky, J., and Jicha, M. (2012). Development of a Realistic Human Airway Model. *Proc. Inst. Mech. Eng. H*, 226:197-207.
- Lundgren, L., Lundstrom, S., Laszlo, I., and Westling, B. (1995). Modern Fiber Counting—A Technique with the Phase-Contrast Microscope Online to a Macintosh Computer. *Ann. Occup. Hyg.*, 39:455-467.
- Ming-Kuei, H. (1962). Visual pattern recognition by moment invariants. *Inf. Theory, IRE Trans.*, 8:179-187.
- Moriguchi, Y., Hotta, K., and Takahashi, H. (2009). Asbestos Detection from Microscope Images Using Support Vector Random Field of Local Color Features, in *Advances in Neuro-Information Processing*, Pt II, ed., Springer-Verlag, Berlin, Berlin, pp. 344-352.
- National Institute for Occupational Safety and Health (NIOSH). (1994). NIOSH Manual of Analytical Methods; ASBESTOS and OTHER FIBERS by PCM 7400, 4th ed., in DHHS (NIOSH) Publication No. 94-113, U.S. Department of Health and Human Services, Cincinnati, Ohio, USA.
- Oberdorster, G. (2000). Determinants of the Pathogenicity of Man-Made Vitreous Fibers (MMVF). *Int. Arch. Occ. Env. Hea.*, 73:S60-S68.
- Pang, T. W. S. (2000). Precision and Accuracy of Asbestos Fiber Counting by Phase Contrast Microscopy. *Aihaj.*, 61:529-538.
- Scientific Committee on Occupational Exposure Limits (SCOEL). (2012). Recommendation from the Scientific

- Committee on Occupational Exposure Limits for Man Made-Mineral Fibres (MMMMF) in SCOEL/SUM/88, European Commission. Employment, Social Affairs and Inclusion.
- Starha, P., Druckmüllerová, H., Belka, M., Lizal, F., and Jedelsky, J. (2013). Application of Adaptive Radial Convolutional Filter, in *19th International Conference on Soft Computing, MENDEL 2013*, Brno, pp. 357–362.
- Theodosiou, Z., Tsapatsoulis, N., Bujak-Pietrek, S., Szadkowska-Stanczyk, I., and Ieee (2010). Airborne Asbestos Fibers Detection in Microscope Images using re-initialization free Active Contours, in *32nd Annual International Conference of the IEEE Engineering-in-Medicine-and-Biology-Society (EMBC 10)*, Ieee, Buenos Aires, ARGENTINA, pp. 4785–4788.
- Wang, Z., Hopke, P. K., Baron, P. A., Ahmadi, G., Cheng, Y.-S., Deye, G., and Su, W.-C. (2005). Fiber Classification and the Influence of Average Air Humidity. *Aerosol Sci. Technol.*, 39:1056–1063.
- Zhu, H., Chan, F. H. Y., and Lam, F. K. (1999). Image Contrast Enhancement by Constrained Local Histogram Equalization. *Comput. Vis. Image Und.*, 73:281–290.



## Regional aerosol deposition in the human airways: The SimInhale benchmark case and a critical assessment of *in silico* methods



P. Koullapis<sup>a</sup>, S.C. Kassinos<sup>a</sup>, J. Muela<sup>b</sup>, C. Perez-Segarra<sup>b</sup>, J. Rigola<sup>b</sup>, O. Lehmkuhl<sup>c</sup>, Y. Cui<sup>d</sup>, M. Sommerfeld<sup>e</sup>, J. Elcner<sup>f</sup>, M. Jicha<sup>f</sup>, I. Saveljic<sup>g</sup>, N. Filipovic<sup>g</sup>, F. Lizal<sup>f</sup>, L. Nicolaou<sup>h,\*</sup>

<sup>a</sup> Department of Mechanical and Manufacturing Engineering, University of Cyprus, Nicosia, Cyprus

<sup>b</sup> Heat and Mass Transfer Technological Centre, Universitat Politècnica de Catalunya, Terrassa, Spain

<sup>c</sup> Barcelona Supercomputing Center, Barcelona, Spain

<sup>d</sup> Chair of Applied Mechanics, Friedrich-Alexander University Erlangen-Nuremberg, Germany

<sup>e</sup> Institute of Process Engineering, Otto von Guericke-University Magdeburg, Halle, Germany

<sup>f</sup> Faculty of Mechanical Engineering, Brno University of Technology, Brno, Czech Republic

<sup>g</sup> Faculty of Engineering, University of Kragujevac, Kragujevac, Serbia

<sup>h</sup> Department of Mechanical Engineering, Imperial College London, London, UK

### ARTICLE INFO

#### Keywords:

Inhaled drug delivery  
Respiratory airways  
Regional deposition  
Computational fluid particle dynamics  
Benchmark case

### ABSTRACT

Regional deposition effects are important in the pulmonary delivery of drugs intended for the topical treatment of respiratory ailments. They also play a critical role in the systemic delivery of drugs with limited lung bioavailability. In recent years, significant improvements in the quality of pulmonary imaging have taken place, however the resolution of current imaging modalities remains inadequate for quantifying regional deposition. Computational Fluid-Particle Dynamics (CFPD) can fill this gap by providing detailed information about regional deposition in the extrathoracic and conducting airways. It is therefore not surprising that the last 15 years have seen an exponential growth in the application of CFPD methods in this area. Survey of the recent literature however, reveals a wide variability in the range of modelling approaches used and in the assumptions made about important physical processes taking place during aerosol inhalation. The purpose of this work is to provide a concise critical review of the computational approaches used to date, and to present a benchmark case for validation of future studies in the upper airways. In the spirit of providing the wider community with a reference for quality assurance of CFPD studies, *in vitro* deposition measurements have been conducted in a human-based model of the upper airways, and several groups within MP1404 SimInhale have computed the same case using a variety of simulation and discretization approaches. Here, we report the results of this collaborative effort and provide a critical discussion of the performance of the various simulation methods. The benchmark case, *in vitro* deposition data and *in silico* results will be published online and made available to the wider community. Particle image velocimetry measurements of the flow, as well as additional numerical results from the community, will be appended to the online database as they become available in the future.

### 1. Introduction

Aerosolized delivery of drugs to the lungs is used to treat a number of respiratory diseases, such as asthma, chronic obstructive pulmonary disease (COPD), cystic fibrosis and pulmonary infections. Regional deposition effects play a critical role in applications where targeted drug delivery is needed in order to maximize efficacy and minimize side-effects. Examples include the topical treatment of respiratory diseases, inhaled delivery of chemotherapy agents to lung tumours, and systemic delivery of drugs with limited lung bioavailability. Quantifying regional deposition is therefore important in assessing and optimizing treatment.

Validated computational fluid-particle dynamics (CFPD) methods offer a powerful tool to predict airflow and localized deposition in the respiratory airways, in order to further our understanding of the flow and aerosol dynamics, and test and optimize inhaler therapies. With advances in medical imaging, computational techniques and computing power, there has been an exponential growth in the application of CFPD methods in the respiratory airways over the last 15 years. However, accurate and efficient numerical simulations of the respiratory airways pose a challenge due to the complexities associated with the airway geometry, the flow dynamics and the aerosol physics (Longest and Holbrook, 2012). Numerical studies conducted to date have adopted a

\* Corresponding author at: Department of Mechanical Engineering, Imperial College London, Exhibition Road, London SW7 2AZ, UK.  
E-mail address: [laura.nicolaou@imperial.ac.uk](mailto:laura.nicolaou@imperial.ac.uk) (L. Nicolaou).

variety of computational techniques, a range of airway geometries varying in complexity, and differing assumptions on the flow and aerosol physics. In Section 2, we provide a review of existing methods with particular focus on (i) the airway models adopted; (ii) the solution of the flow field; and (iii) the aerosol physics included in the models. We limit this review to three-dimensional CFPD studies of the extrathoracic and upper conducting airways. For a broader overview of airflow and particle transport in the human lung the reader is referred to the review papers by Kleinstreuer and Zhang (2010) and Longest and Holbrook (2012).

In addition to the wide variability in the modelling approaches and in the assumptions made about the physical processes that take place during aerosol inhalation, validation of CFPD methods in the respiratory airways is limited. In particular, there is a lack of quantitative validation of localized deposition (Longest and Holbrook, 2012). Most numerical studies have compared total deposition against experimental fits and *in vitro* data in different airway geometries (Zhang et al., 2002; Kleinstreuer and Zhang, 2003; Jayaraju et al., 2007, 2008). It is known, however, that geometric variability has a pronounced effect on aerosol deposition, and in particular on local deposition patterns (Xi and Longest, 2007). A few studies have compared regional deposition results to *in vitro* data in the same geometry, with varying degrees of agreement (Oldham, 2000; Matida et al., 2004; Debhi, 2011). All these studies have focused on either the extrathoracic airways or bifurcation models. The availability of experimental data for validation of local deposition in the tracheobronchial tree proves to be more limited. Therefore, there is a need for improved data sets to better validate computational predictions in local regions of the lungs (Lizal et al., 2015).

Radiological imaging methods can be applied *in vivo* or *in vitro*, in order to obtain deposition measurements for validation. Although *in vivo* measurements play an irreplaceable role as they describe the real state, studies remain limited by the spatial and temporal resolutions of current imaging techniques, and by patient exposure to radiation. *In vitro* methods have the advantage of known geometric characteristics, allowing systematic studies on particle size and flow rate effects (Grgic et al., 2004). Furthermore, they can be performed in the same geometry as the numerical simulation, which allows for direct comparison, and they provide better spatial resolution due to the higher applicable doses of radioactivity.

In this manuscript, we present a benchmark case that can be used for the validation of computational tools intended for regional deposition studies in the upper airways. *In vitro* deposition measurements in a complex realistic geometry are provided at various inhalation flow rates. In addition, a variety of simulation approaches have been adopted to compute the benchmark case numerically. We present the results for the flow and aerosol deposition, and discuss the performance of the various simulation methods. The purpose of this collaborative work is to (i) provide refined experimental data that can be used for quality assurance of CFPD studies in the upper airways, (ii) provide a critical review of different modelling approaches and (iii) define best practice guidelines where possible.

The benchmark case geometry, experimental data sets, and numerical results will be available online for the wider community. Future work will include particle image velocimetry (PIV) measurements of the flow in order to provide a complete benchmark case for inhaled drug delivery in the upper airways, which has so far been lacking in the literature. Additional numerical results from the community will also be included as they become available. The database will allow for thorough validations of *in silico* models, and will aid in establishing best practice guidelines for predictions of regional deposition in the airways.

The paper is organized as follows: Section 2 provides a review of the current state of the art in numerical modelling of the upper airways. In Section 3, the benchmark case is described in detail. The airway model adopted and the experimental set up for the deposition measurements are presented. In Section 4, the various *in silico* methods employed to

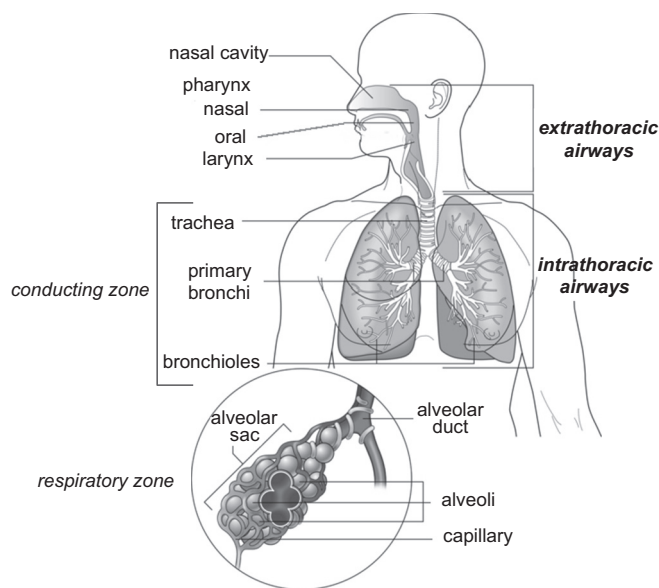


Fig. 1. Schematic of the respiratory system.  
Source: Adapted from Thibodeau and Patton (1996)

compute this case are presented. Results and a comparison of the methods are provided in Section 5. Finally, Section 6 summarizes the work and main findings.

## 2. Review of *in silico* methods for prediction of aerosol deposition in the upper airways

### 2.1. Airway models

The respiratory system can be divided into two anatomical areas: the extrathoracic airways consisting of the mouth, nose, pharynx, larynx and trachea; and the intrathoracic airways which begin at the level of the intrathoracic trachea and extend all the way down to the alveoli (Fig. 1). The intrathoracic airways can be further subdivided into the conducting zone (generations 0 to 16), and the respiratory zone where gas exchange takes place (generations 17 to 23). Here, we focus on the extrathoracic and upper conducting airways, which we group together as the ‘upper airways’.

Many studies of the upper airways have adopted simplified representations of the airway geometry. Idealized models allow us to elucidate the flow and particle dynamics in the airways without the added complexity of the realistic geometry, and can provide representative estimations of global deposition. For the extrathoracic airways, a number of idealized geometries have been developed, such as the University of Alberta replica, which is representative of a physiologically-averaged adult airway (Stapleton et al., 2000). Built from simple geometric shapes, it nonetheless captures all the basic anatomical features of the real extrathoracic airways and has widely been used in the literature, both in numerical (Matida et al., 2004; Ball et al., 2008; Debhi, 2011; Nicolaou and Zaki, 2016) and *in vitro* studies (DeHaan and Finlay, 2001; Heenan et al., 2003; Grgic et al., 2004; Johnstone et al., 2004). Similarly, Jayaraju et al. (2008) adopted a smoothed geometry based on a representative CT-image chosen among a set of healthy subjects. Others have adopted idealized geometries with variable circular cross-sections based on the hydraulic diameters of a human cast replica (Zhang et al., 2002; Kleinstreuer and Zhang, 2003; Radhakrishnan and Kassinos, 2009; Cui and Gutheil, 2011).

For the tracheobronchial tree, several models have been employed. One of the most commonly used is Weibel's model A, which consists of a fully symmetric tree structure (Weibel, 1963). In reality however, significant variation exists in the geometric parameters for any given

generation. More realistic models consist of asymmetric branches with varying lengths, diameters and branching angles (Horsfield et al., 1971; Yeh and Schum, 1980). A number of studies have also been conducted in single and multi-level bifurcations of the tracheobronchial airways (Balásházy and Hofmann, 1993; Balásházy et al., 1999; Zhang et al., 2002; Stylianou et al., 2016).

It is now well understood that geometric variation has a pronounced effect on the flow dynamics and aerosol deposition within the airways (Grgic et al., 2004; Choi et al., 2009; Nicolaou and Zaki, 2013), and that realistic models are required to accurately capture local airflow structures and deposition characteristics (Xi and Longest, 2007). As such, the majority of more recent studies have focused on patient-specific models of the airways (Jayaraju et al., 2007; Lin et al., 2007; Choi et al., 2009; Lambert et al., 2011; Nicolaou and Zaki, 2013; Koullapis et al., 2016). The realistic models are obtained from medical images of the airways, typically via computed tomography (CT) scans or magnetic resonance imaging (MRI), which are then digitally reconstructed via an image registration method. The resulting 3D geometry models, commonly generated as stereolithography (STL) files, can then be meshed for CFD simulations and used to manufacture casts for *in vitro* studies. Anatomically-accurate models are generally limited to the first 6 or 7 generations due to imaging resolution.

## 2.2. Flow field

The flow in the upper airways is mostly turbulent and/or transitional in nature, even at low inhalation rates (Dekker, 1961). Therefore, accurate predictions of the flow field require a suitable turbulence model or a sufficiently fine mesh in order to resolve all the scales in the flow. Three different numerical approaches have been adopted in the literature to investigate the airflow in the upper airways: Reynolds-averaged Navier-Stokes (RANS), large eddy simulation (LES), and direct numerical simulation (DNS), listed in increasing level of accuracy and computational cost. In RANS, all turbulent fluctuations are modelled, mainly based on empirical data from canonical flows. In LES, large-scale turbulent structures, or eddies, are numerically resolved while small sub-grid scale structures are modelled by methods similar to RANS. Finally in DNS, all relevant length and time scales are resolved numerically.

The adequacy of standard RANS  $k-\epsilon$  models for the simulation of flow in the upper airways was discussed by Finlay et al. (1996). Most of these models are designed for high-Reynolds-number flows in simple geometries and are therefore unsuitable for low-Reynolds-number turbulence in complex geometries such as the extrathoracic airways. They are known to perform poorly in flows with recirculating regions, free-shear layers and mean streamline curvature, all of which are present in this region. Stapleton et al. (2000) investigated the suitability of such a model in an idealized mouth and throat geometry, running a laminar and a turbulent case and comparing them to *in vitro* measurements. Whereas the laminar case showed excellent agreement with the experimental data, a large overprediction in deposition was observed in the turbulent case, due to the inadequacy of the turbulence model.

RANS  $k-\omega$  models have been shown to perform better in the upper airways (Zhang et al., 2002; Matida et al., 2004; Jayaraju et al., 2007; Debhi, 2011). However, large variability in performance exists across studies. Matida et al. (2004) for example, observed a large overprediction in deposition, particularly for smaller particles. The model required the addition of a near-wall correction term in order to reduce the discrepancy with experimental data. Using different  $k-\omega$  models, Jayaraju et al. (2007) and Zhang et al. (2002) on the other hand, reported better results without the need for a near-wall correction.

Jayaraju et al. (2008) examined the flow in a simplified human mouth-throat model using both RANS  $k-\omega$  and LES methods. Their comparison showed that the LES velocity and kinetic energy profiles were in good agreement with experimental data, as opposed to those from RANS. Mouth-throat deposition was also simulated for particle

sizes ranging from 2 to 10  $\mu\text{m}$ . While the  $k-\omega$  and LES simulations produced similarly good predictions for bigger particles, RANS over-predicted deposition for particle sizes below 5  $\mu\text{m}$ . Since the upper limit of the respirable range for inhalation drugs is typically 5  $\mu\text{m}$ , the authors concluded that LES would be the preferred method for predicting aerosol deposition in the upper airways.

Due to the high computational demands of DNS, only a few studies have adopted this approach for the upper airways. Lin et al. (2007) compared the flow in a realistic geometry of the intrathoracic airways, with and without the mouth-throat region, in order to assess the effect of the laryngeal jet on airflow characteristics. Their study revealed that turbulence induced by the laryngeal jet can significantly affect the flow patterns as well as the tracheal wall shear stress, and they concluded that subject-specific evaluations should include the extrathoracic airways.

Ball et al. (2008) adopted a lattice Boltzmann method (LBM) to conduct a direct numerical simulation of the flow inside an idealized model of the extrathoracic airways. Results were compared to hot-wire measurements performed in the same model. The LBM calculations were shown to yield better results than RANS, and reproduced significant detail of the experimentally observed flow features.

Nicolaou and Zaki (2013) performed DNS in a set of realistic mouth-throat geometries, using an immersed boundary method (Nicolaou et al., 2015). The authors reported that geometric variation, even within the same subject, has a large impact on both the mean flow and the turbulent fluctuations. Their study also provided a physical explanation for the dependence of deposition on the flow Reynolds number. The empirical Stokes-Reynolds number correlation,  $StkRe^{0.37}$ , typically adopted to report extrathoracic deposition was related theoretically to the dimensionless particle relaxation time, and was shown to arise due to the fact that deposition in the mouth-throat region occurs via both impaction and turbulent diffusion.

## 2.3. Aerosol transport and deposition

Aerosol deposition in the upper airways occurs primarily via impaction, due to the high velocities and rapid changes in flow direction. The inertia of the particles causes them to deviate from the fluid streamlines and collide with the airway walls. The larger the particles, the higher the probability of deposition by impaction. Turbulent dispersion also plays a role in this region, in particular for small particles whose trajectories are considerably influenced by the fluctuations in the flow.

Particle transport can be modelled using an Eulerian or a Lagrangian approach. The Eulerian, or two-fluid, approach treats the dispersed phase as a continuum, solving the conservation equations of particle mass and momentum. On the other hand, the Lagrangian approach treats the dispersed phase as a set of individual point-particles in a continuous carrier phase. The particles are tracked through the flow field by solving the equations of motion for each particle with the relevant forces acting on it. Description of turbulent dispersion and collision of particles with the airway walls is more natural with this approach. For this reason, the Lagrangian approach has featured prominently in studies of aerosol deposition in the airways (Kleinstreuer and Zhang, 2003; Matida et al., 2004; Jayaraju et al., 2007; Li et al., 2007; Radhakrishnan and Kassinis, 2009; Debhi, 2011; Koullapis et al., 2016; Nicolaou and Zaki, 2016).

In all these studies, the particles are assumed to be spherical, non-rotating and non-interacting. The aerosol is considered a dilute suspension and modelled using a one-way coupling approach, where the effect of the particles on the flow and inter-particle interactions are neglected. In reality however, inhaled particles are often non-spherical (e.g. dry powder inhaler formulations), and may possibly collide with each other and aggregate.

The equations of motion that describe the change in position,  $x_p$ , and velocity,  $u_p$ , along the particle trajectory are given by

$$\frac{d\mathbf{x}_p}{dt} = \mathbf{u}_p, \tag{1}$$

$$m_p \frac{d\mathbf{u}_p}{dt} = \sum \mathbf{F}, \tag{2}$$

where  $m_p$  is the mass of the particle and  $\sum \mathbf{F}$  represents all the forces acting on it. The balance of forces acting on particles as they travel in a fluid was derived from first principles by Maxey and Riley (1983) in the low Reynolds number limit, and is given by

$$m_p \frac{d\mathbf{u}_p}{dt} = \underbrace{\frac{18\mu_f}{\rho_p d_p^2} m_p (\mathbf{u}_f - \mathbf{u}_p)}_{\text{drag force}} + \underbrace{m_f \left( \frac{D\mathbf{u}_f}{Dt} \right)}_{\text{pressure gradient force}} + \underbrace{\frac{1}{2} m_f \left( \frac{D\mathbf{u}_f}{Dt} - \frac{d\mathbf{u}_p}{dt} \right)}_{\text{added mass force}} + \underbrace{\frac{3}{2} d_p^2 (\pi \rho_f \mu_f)^{\frac{1}{2}} \int_{t_0}^t \frac{d}{dt'} (\mathbf{u}_f - \mathbf{u}_p) dt'}_{\text{Basset history force}} + \underbrace{\mathbf{g} (m_p - m_f)}_{\text{gravity force}}. \tag{3}$$

Here  $d_p$  and  $\rho_p$  are the particle diameter and density respectively,  $\mu_f$  and  $\rho_f$  are the dynamic viscosity and density of the fluid,  $\mathbf{u}_f$  is the fluid velocity at the particle location, and  $m_f$  is the mass of fluid displaced by the particle.

Eq. (3) does not include inertial effects, such as form drag or lift force, and is therefore only valid for small particle Reynolds numbers,  $Re_p < 1$ , where

$$Re_p = \frac{\rho_f d_p |\mathbf{u}_f - \mathbf{u}_p|}{\mu_f}. \tag{4}$$

At higher Reynolds numbers, the drag force is given by

$$\mathbf{F}_D = \frac{18\mu_f}{\rho_p d_p^2} m_p (\mathbf{u}_f - \mathbf{u}_p) \frac{C_D Re_p}{24}, \tag{5}$$

where  $C_D$  is the drag coefficient, which takes into account both skin friction and form drag, and depends on the particle Reynolds number. Many empirical and semi-empirical equations have been proposed to approximate the drag coefficient over different particle Reynolds number ranges. For aerosol particles in the respiratory airways, the correlation proposed by Schiller and Naumann (1935), which is valid for  $Re_p < 800$ , is commonly adopted:

$$C_D = \frac{24}{Re_p} (1 + 0.15 Re_p^{0.687}). \tag{6}$$

For particles of comparable size to the mean free path of the fluid molecules, rarefaction effects become significant and the fluid can no longer be treated as a continuum. In order to account for slip at the particle surface due to non-continuum effects, a correction factor is often applied to the drag. A correlation for the Cunningham correction factor for airborne particles was derived by Davies (1945), and is given by

$$C_C = 1 + \frac{2\lambda}{d_p} \left( 1.257 + 0.4 \exp\left(-\frac{1.1d_p}{2\lambda}\right) \right), \tag{7}$$

where  $\lambda = 0.070 \mu\text{m}$  is the mean free path of air. For  $1 \mu\text{m}$  particles at standard conditions, drag is 15% lower than that predicted without taking into account the slip correction. As particle size decreases beyond  $1 \mu\text{m}$ , slip rapidly increases.

In shear flow, particles may experience a transverse lift force. This force, known as Saffman lift, has been shown to be most prominent for large particles and small particle-to-fluid density ratios,  $\rho_p/\rho_f$  (Kallio and Reeks, 1989; Young and Leeming, 1997). For aerosol particles in turbulent channel flow, McLaughlin (1989) found that the Saffman lift force had virtually no effect on particle trajectories, except within the viscous sublayer, where it played a significant role both in the inertial deposition and in the accumulation of particles.

Submicrometer particles are also subjected to Brownian motion, caused by random collisions with the gas molecules (Ounis et al., 1991). The Brownian force can be modelled as a Gaussian white-noise random process (Li and Ahmadi, 1992). Li and Ahmadi (1992) studied the effects of Brownian diffusion on particle dispersion and deposition in turbulent channel flow. Very near the wall, where turbulent fluctuations die down, Brownian motion was shown to be the dominant mechanism for diffusion of particles smaller than  $0.1 \mu\text{m}$ . For particles larger than  $0.5 \mu\text{m}$ , the effect of Brownian diffusion was negligibly small.

The majority of studies focused on micron-sized particles in the upper airways have taken into account the drag and gravitational force, and discounted all other forces acting on the particles (Matida et al., 2004; Jayaraju et al., 2007; Debhi, 2011; Lambert et al., 2011; Nicolaou and Zaki, 2016). A couple of studies have considered only the aerodynamic drag, based on order-of-magnitude arguments (Zhang et al., 2002; Kleinstreuer and Zhang, 2003; Li et al., 2007). Simulations with and without the gravitational force were performed by Ma and Lutchen (2009) at an inhalation flow rate of 15 L/min. When gravity was ignored, there was a maximum 10% reduction in total deposition which showed that, while inertial impaction is the dominant deposition mechanism for micron-sized particles in the upper airways, gravitational sedimentation is also important and should be taken into account. The effect of gravity is more significant for larger particles, and diminishes as the flow rate increases. Due to the large particle-to-fluid density ratios for aerosol particles in air, the Saffman lift, pressure gradient, added mass, and Basset forces are typically considered insignificant in the upper airways (Finlay et al., 1996).

Other effects on aerosol transport and deposition in the airways such as humidity, temperature and electrostatic charge are less understood. Vaporisation as well as particle growth due to hygroscopicity can both occur in the airways. Zhang et al. (2004) examined fuel droplet deposition in an upper airway model, with and without evaporation. Their results demonstrated that thermal effects were significant in the oral airways at low inhalation rates ( $Q = 15 \text{ L/min}$ ). Evaporation increased with higher ambient temperatures and lower inspiratory flow rates, resulting in lower deposition fractions. Longest and Xi (2008) evaluated the effect of condensation particle growth on the transport and deposition of cigarette smoke particles in the upper respiratory tract, under various relative humidity and temperature conditions. For the inhalation of warm saturated air  $3^\circ\text{C}$  above body temperature, 200 and 400 nm particles were observed to increase in size to above  $3 \mu\text{m}$  near the trachea inlet, leading to an increase in deposition compared to the non-hygroscopic case.

Recently, Koullapis et al. (2016) investigated the effect of electrostatic charge on aerosol deposition in a realistic geometry of the upper airways. Electrostatic charge was shown to increase deposition of smaller particles by as much as sevenfold, with most of the increase located in the mouth-throat region. The impact of inhalation flow rate on the deposition of charged particles was negligible for sizes smaller than  $1 \mu\text{m}$ , whereas inertial impaction prevailed over electrostatic deposition for particles above  $2.5 \mu\text{m}$ , with deposition increasing as flow rate increased. Overall, the authors reported a significant interplay between particle size, electrostatic charge, and flow rate.

### 3. Benchmark case

#### 3.1. Airway geometry

The realistic airway geometry used to construct the benchmark case model is shown in Fig. 2a. It comprises of the oral cavity, larynx and tracheobronchial airways down to the 12th generation of branching. The tracheobronchial tree was acquired from a human lung of an adult male, excised at autopsy and fixed with a liquid rubber solution at nearly end-inspiratory volume. The lung tissue was removed and the rubber cast of the bronchial tree was scanned using high-resolution

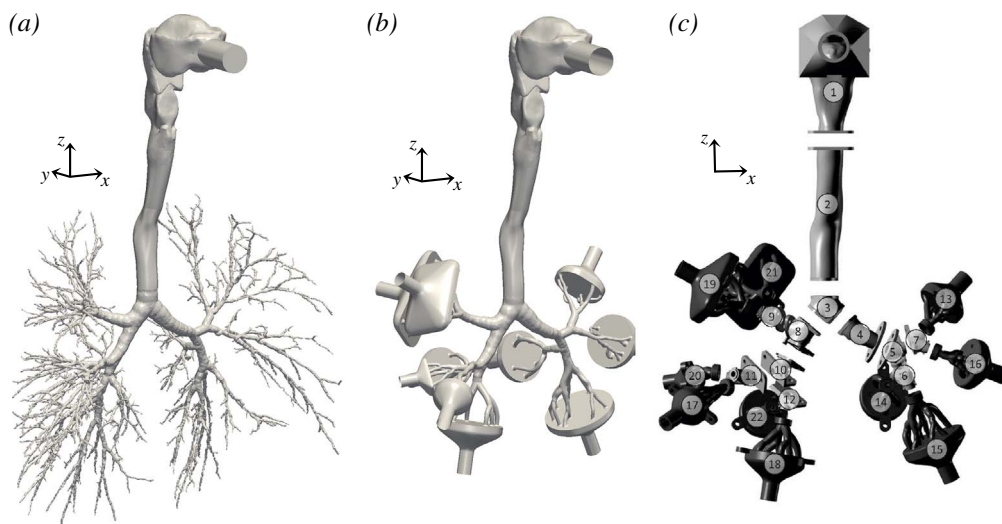


Fig. 2. Geometry of the respiratory airways: (a) original realistic airway geometry; (b) geometry adopted for the benchmark case; (c) physical segmented model for deposition measurements.

computed tomography (HRCT) (Schmidt et al., 2004). The extra-thoracic airways were obtained from the Lovelace Respiratory Research Institute (LRRRI) upper airway model. The oral cavity was moulded from an *in vivo* dental impression of a Caucasian male at approximately 50% of the full opening, and the remaining of the model was acquired from a cadaver (Cheng et al., 1997). The LRRRI geometry was obtained as a wax cast, which was scanned by an Atos (GOM, Braunschweig, Germany) device, converted to STL format, and concatenated with the bronchial tree model at the trachea. Further details on the construction of the airway model can be found in Lizal et al. (2012).

Fig. 2b shows the geometry employed in the *in vitro* experiments and numerical simulations. Only branches with diameter above 3 mm were used, and the terminal bronchi segments were connected to 10 outlets. The physical model for deposition measurements was produced by stereolithography (Lizal et al., 2015). A 3-mm thick envelope was created around the original geometry to obtain a negative cast of the airways. The model was divided into sections to facilitate the measurement of regional deposition by various methods, such as optical microscopy and gravimetry (Fig. 2c).

### 3.2. Deposition measurements

Measurement of the regional aerosol deposition was performed by positron emission tomography (PET). Aerosol particles of di-2-ethyl hexyl sebacate (DEHS) were generated using a Condensation Monodisperse Aerosol Generator, and radiolabeled with Fluorine 18. The aerosol was fed through a 85Kr-based NEKR-10 charge equilibrators to reduce the electrostatic deposition of particles, and the size and concentration of the particles was monitored by a PAM aerosol monitor throughout the experiment. A schematic of the experimental set up is shown in Fig. 3.

The experiments were performed at steady-state inhalation with flow rates of 15, 30 and 60 L/min. The total duration of inhalation was between 10 and 15 min. Two sizes of particles were measured with mass median aerodynamic diameter of 2.5 and 4.3 μm. The standard geometric deviation of size was smaller than 1.24. Particles that did not deposit in the model were collected on filters downstream of each of the ten output branches. Following exposure, CT and PET images were obtained in a PET-CT scanner, and used to evaluate deposition in each segment of the model based on a volume radioactivity analysis. A detailed description of the method is provided by Lizal et al. (2015).

## 4. Numerical methods

Six different groups have performed simulations of the flow and

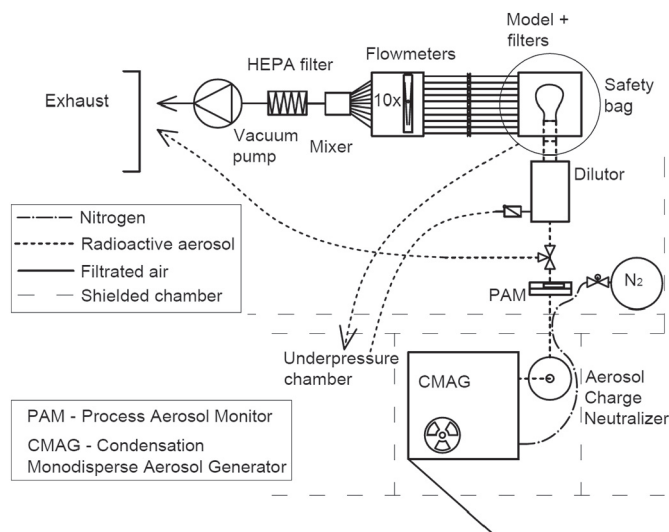


Fig. 3. Schematic of the experimental set up for deposition measurements in the airways. Source: Reprinted from Lizal et al. (2015) by permission of SAGE Publications.

particle deposition in the benchmark case airway geometry. A general description of the experiments was provided, but the groups were left free to adopt their preferred methodologies, in order to obtain an indication of the degree of variability in numerical approaches. The results presented here correspond to the 60 L/min case, however *in silico* and *in vitro* results at  $Q = \{15, 30\}$  L/min will also be provided online. A summary of the methods adopted to solve the flow field and the particle transport is given below.

### 4.1. Flow field

Different discretization techniques, namely finite volume and finite element methods, were employed in the various simulations to solve the governing equations for the flow. In order to model the turbulence in the airways, three different LES and three steady-state RANS models were adopted. The governing flow equations are given by,

$$\frac{\partial u_i}{\partial t} + u_j \frac{\partial u_i}{\partial x_j} = -\frac{1}{\rho} \frac{\partial p}{\partial x_i} + \frac{\partial}{\partial x_j} \left[ (\nu + \nu_T) \frac{\partial u_i}{\partial x_j} \right], \tag{8}$$

$$\frac{\partial u_j}{\partial x_j} = 0, \tag{9}$$

where  $u_i$  are the velocity components,  $p$  is the pressure,  $\rho$  and  $\nu$  are the density and kinematic viscosity of the fluid respectively, and  $\nu_T$  is the turbulent viscosity. In the LES simulations,  $\mathbf{u}$  and  $p$  represent the filtered velocity and pressure, respectively. In RANS, these correspond to time-averaged variables.

The Reynolds number at the inlet, based on the inflow bulk velocity and inlet tube diameter, is  $Re = \frac{U_{in} D_{in}}{\nu} = 3745$ , which lies in the turbulent regime. In order to generate turbulent inflow conditions, a mapped inlet, or recycling, boundary condition was used in simulations LES1 and LES2 (Tabor and Baba-Ahmadi, 2010). To apply this boundary condition, the pipe section at the inlet was extended and initially fed with an instantaneous turbulent velocity field generated in a separate pipe flow LES. During the simulation of the airway geometries, a scaled mapping of the velocity field from the midplane of the extended pipe was applied at the inlet to the mouth. In RANS1, the time-averaged velocity field and turbulent variables from a precursor pipe simulation were applied at the inlet. Simulation LES3 specified a pressure boundary condition and extrapolated the velocities at the inlet, and RANS2 and RANS3 applied uniform velocity. At the outlets, flow rates were prescribed according to those observed *in vitro*.

Unstructured body-fitted meshes were employed, ranging from 1.3 million grid cells (RANS3) to 50 million (LES1). The fine-grid LES simulation, LES1, is adopted as the reference case. Table 1 summarizes the computational details for each method. In addition to the cases shown in Table 1, a coarse LES1 simulation, LES1c, was also performed, in order to assess the effect of grid size on flow and deposition. In this simulation, the LES3 mesh consisting of 7 million cells, and a time step of  $1e-5$  s were employed. All other parameters remained the same as in LES1.

A comparison of the mean flow and turbulence statistics across the six methods is provided in Section 5.1. In RANS, the mean velocity,  $\bar{\mathbf{u}}$ , and mean turbulent kinetic energy per unit mass,  $k$ , are obtained directly from the time-averaged Navier-Stokes and turbulence closure equations. In the LES simulations, the mean velocities and resolved root-mean-square fluctuations,  $\mathbf{u}_{rms}$ , were computed with a running average in time:

$$\bar{\mathbf{u}} = \frac{1}{T} \int_0^T \mathbf{u} \, dt, \tag{10}$$

$$\mathbf{u}_{rms} = (\overline{\mathbf{u}^2})^{1/2} = \left( \frac{1}{T} \int_0^T \mathbf{u}^2 \, dt - \bar{\mathbf{u}}^2 \right)^{1/2}, \tag{11}$$

where  $T$  is the time period over which statistics were collected. The resolved turbulent kinetic energy is given by  $k = \frac{1}{2} \overline{u_i u_i}$ .

#### 4.2. Particle tracking

To model the aerosol transport and deposition in the airways, all simulations employed a Lagrangian particle-tracking approach and assumed one-way coupling between the flow and the particles. Different particle-tracking algorithms were adopted, which differ in the integration schemes used to solve the particle equations of motion, and in the interpolation methods used to determine the fluid velocity at the particle position. The approaches also differ in the forces acting on the particles. Aerodynamic drag, which is the dominant force on micron-sized particles in the upper airways, was included in all simulations. The effect of gravity was also taken into account in all but one of the cases, and simulations LES1 and LES2 included Brownian motion. The Cunningham correction factor (Eq. (7)) was applied in LES1, LES2 and RANS1.

The particle equations of motion are given by

$$m_p \frac{d\mathbf{u}_p}{dt} = \frac{3 \rho_f m_p C_D}{4 \rho_p d_p C_C} |\mathbf{u}_f - \mathbf{u}_p| (\mathbf{u}_f - \mathbf{u}_p) + m_p \mathbf{g} \frac{\rho_p - \rho_f}{\rho_p} + \mathbf{F}_B, \tag{12}$$

where the first and second terms on the right-hand side are the drag and gravitational forces respectively, and  $\mathbf{F}_B$  represents the Brownian force

Table 1  
Computational details of the *in silico* methods used to solve the flow in the airways.

	LES1	LES2	LES3	RANS1	RANS2	RANS3
Flow solver	OpenFoam (FVM)	Termofluids (FVM)	Alya (FEM) (Vázquez et al., 2016)	OpenFoam (FVM)	CD-Adapco Star-CCM+ (FVM)	PAKF solver (FEM)
Turbulence model	LES dynamic Smagorinsky (Lilly, 1992)	LES variational multiscale (Hughes et al., 2000)	LES WALE (Nicoud and Ducros, 1999)	RANS $k-\omega$ -SST (Menter, 1994)	RANS low- $Re$ $k-\omega$ -SST (Menter, 1994)	RANS $k-\epsilon$ model (Launder and Spalding, 1974)
Inlet boundary conditions	Atmospheric pressure, turbulent (mapped inlet)	Atmospheric pressure, turbulent (mapped inlet)	Atmospheric pressure, extrapolated velocity	Atmospheric pressure, turbulent inlet	Atmospheric pressure, uniform velocity	Atmospheric pressure, uniform velocity
Outlet boundary conditions	Zero-gradient pressure, specified flow rates	Zero-gradient pressure, specified flow rates	Zero-gradient pressure, specified flow rates	Zero-gradient pressure, specified flow rates	Zero-gradient pressure, specified flow rates	Zero-gradient pressure, specified flow rates
Mesh size	50 M	10 M	7 M	12 M	6.3 M	1.3 M
Mesh type	Tetrahedral, 3–5 wall prism layers	Tetrahedral, 3 wall prism layers	Tetrahedral, 3 wall prism layers	Tetrahedral, no wall prism layers	Polyhedral, 8 wall prism layers	Tetrahedral, no wall prism layers
Time step	$2.5 \times 10^{-6}$ s	$4.55 \times 10^{-7}$ s	$1.3 \times 10^{-5}$ s	$1 \times 10^{-5}$ s	$2.5 \times 10^{-4}$ s	$1 \times 10^{-5}$ s

included in LES1 and LES2. The amplitudes of the Brownian force components at time  $t$  are evaluated from

$$F_{B_i} = G_i \sqrt{\frac{2k_B^2 T^2}{\bar{D} \Delta t}}, \quad (13)$$

where  $G_i$  is a zero mean variant from a Gaussian probability density function,  $T = 310$  K is the absolute temperature,  $\bar{D} = (k_B T C_C) / (3\pi\mu_f d_p)$  is the Brownian diffusivity,  $k_B = 1.3806488 \times 10^{23}$  J/K is the Boltzmann constant, and  $\Delta t$  is the time step used in the integration of the particle equations of motion (Ounis et al., 1991).

In the RANS simulations, where only mean velocities are computed, a turbulent dispersion model is required in order to take into account the effect of the velocity fluctuations on the particles. RANS1 adopted a continuous random walk technique, where the fluctuating velocities are obtained from the generalized Langevin equation (Sommerfeld et al., 1993). In RANS2, an eddy interaction model was applied (Gosman and Ioannides, 1983). This approach assumes isotropic turbulence and generates random fluctuations from a Gaussian distribution of zero mean and  $2k/3$  variance, where  $k$  is the turbulent kinetic energy. Particles interact with an eddy until either the lifetime of the eddy is over or the particle crosses the eddy, after which interaction with a new eddy begins. RANS3 performed mean-flow tracking, without any turbulent dispersion model. In the LES simulations, the resolved velocity field includes the large-scale fluctuations, but subgrid-scale particle dispersion was not included.

Deposition was assumed once a particle comes into contact with the airway walls. Reflection and re-suspension were not included, since the *in vitro* experiments used liquid particles which deposit when they hit the surface of the cast. *In vivo*, the existence of a mucus layer on the inner walls of the airways ensures that particles colliding with the surface deposit.

The particle diameters ranged from  $d_p = 0.5 \mu\text{m}$  to  $10 \mu\text{m}$ , and the particle density was set to  $\rho_p = 914 \text{ kg/m}^3$ , which corresponds to diethylhexyl sebacate (DEHS) particles in air at room temperature. Particles were distributed uniformly across the inlet, but the total number of particles injected into the flow and their release period varied across simulations. Details of the particle-tracking schemes adopted are provided in Table 2.

It is interesting to see how, for the same case, user specification varies widely. In particular, the boundary conditions for the flow, choice of forces acting on the particles, and release time and number of particles differ across simulations. In addition to serving as a validation case for computational models of flow and aerosol deposition in the upper airways, this benchmark case allows us to examine the sensitivity of predictions to the numerical methods adopted and the assumptions made in the modelling, and to identify best practice guidelines. In the following section, we examine the flow and particle deposition obtained using the different computational approaches, and comment on the variability of results.

**Table 2**  
Computational details of the Lagrangian particle-tracking schemes.

	LES1	LES2	LES3 (Houzeaux et al., 2016)	RANS1	RANS2	RANS3
Time integration scheme	Implicit Euler	Explicit second-order	(implicit) Newmark	Implicit Euler	Implicit Euler	(implicit) trapezoidal
Forces on particles	Drag, gravity, Brownian	Drag, gravity, Brownian	Drag, gravity	Drag, gravity (Brownian, lift)	Drag	Drag, gravity
Drag coefficient ( $C_D$ )	Schiller and Naumann (1935)	Schiller and Naumann (1935)	Ganser (1993)	Schiller and Naumann (1935)	Schiller and Naumann (1935)	Morsi and Alexander (1972)
Cunningham correction factor ( $C_C$ )	Davies (1945)	Davies (1945)	1.0	Davies (1945)	1.0	1.0
Turbulent dispersion	–	–	–	Continuous random walk	Eddy interaction model	Mean-flow tracking
Number of particles per size	100,000	100,000	300,000	100,000	10,000	30,000
Release time of particles	0.025 s	0.025 s	0.3 s	0.025 s	0.1 s	0.08 s

## 5. Results and discussion

### 5.1. Air flow

Fig. 4a shows contours of the mean velocity magnitude in the central sagittal plane of the extrathoracic airways and the trachea, obtained using the six different numerical methods. Profiles at various cross-sections are also plotted in Fig. 5 for a more detailed comparison. Velocities are generally low in the mouth (B1–B2) and pharynx (C1–C2), and a large separated region is observed along the upper wall of the oral cavity (B1–B2). As a result of the glottal constriction, the flow accelerates in the larynx and a separated shear layer develops at the level of the vocal cords due to the airway curvature (D1–D2). In most simulations, a recirculation region is observed near the posterior wall of the trachea, behind the separated shear layer (D1–D2). Further downstream, a bend in the trachea (E1–E2) causes the high-speed velocity to shift from the anterior to the posterior wall (F1–F2), and leads to the formation of a small region of separation at the anterior wall, which is visible in the LES and RANS2 simulations.

Good qualitative agreement in the mean flow fields is seen across LES simulations. The biggest differences are observed in regions of recirculating flow (B1–B2 and D1–D2). Higher peak velocities are predicted by LES3 in the mouth (B1–B2) and upper pharynx (C1–C2), which can be attributed to the different inflow conditions applied in this simulation. Velocities were extrapolated at the inlet, as opposed to specifying turbulent inflow conditions, resulting in higher velocity in the inlet pipe (A1–A2). The variations in the mean flow due to inflow conditions die out in the larynx, and very good agreement in the velocity profiles is observed downstream (Fig. 5d–f).

Larger discrepancies in the results are observed in the RANS calculations. In particular, the RANS simulations have more difficulty predicting the separated shear layer in the larynx, and the recirculation regions. The low- $Re$   $k$ - $\omega$  model with prism layer mesh at the wall (RANS2) is in closer agreement to the LES results, whereas the  $k$ - $\epsilon$  model (RANS3) displays the largest differences. The discrepancies observed in the RANS3 simulation are likely due to both the low grid resolution as well as the use of a  $k$ - $\epsilon$  turbulence model. Standard  $k$ - $\epsilon$  models are typically designed for high-Reynolds-number flows in simple geometries, and are known to perform poorly in flows with recirculating regions, free-shear layers and mean streamline curvature, all of which are present in the extrathoracic airways (Finlay et al., 1996).

Contours of the mean turbulent kinetic energy,  $k$ , in the extrathoracic airways and trachea are shown in Fig. 4b. Turbulent kinetic energy levels are low at the inlet, and start to increase towards the back of the mouth and the upper pharynx. The maximum kinetic energy occurs in the larynx, near the anterior wall (downstream of C1–C2), and in the trachea, near the edge of the separated shear layer (D1–D2). It is evident that RANS2 and RANS3 are highly dissipative, and significantly underpredict turbulence levels in the airways. We therefore limit the following turbulent kinetic energy results to those obtained by the LES methods and RANS1.

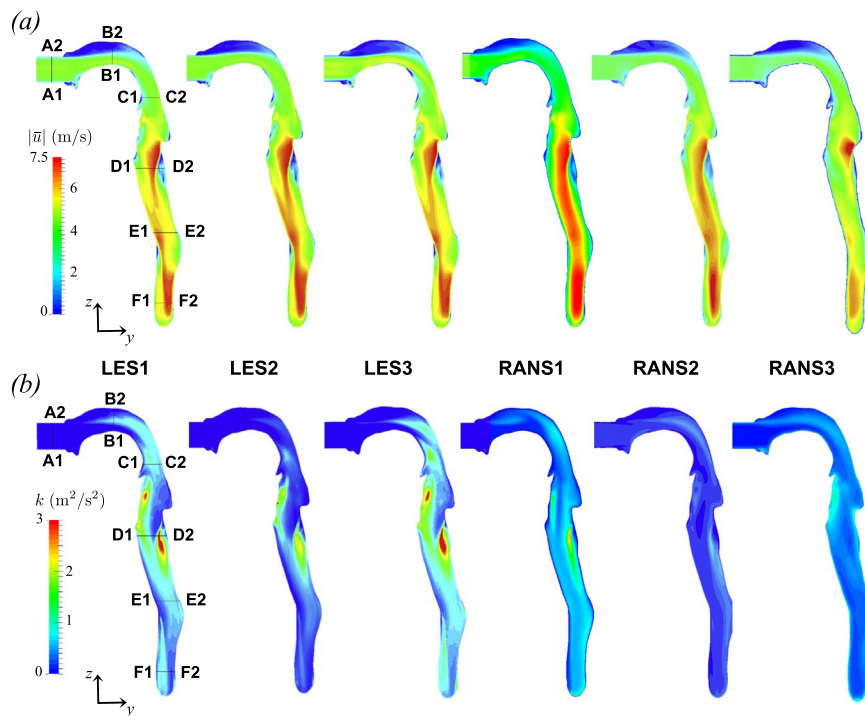


Fig. 4. Contours of mean velocity magnitude and turbulent kinetic energy in the central sagittal plane of the extrathoracic airways and trachea.

Profiles of the turbulent kinetic energy at various cross-sections of the airways are shown in Fig. 5. Larger discrepancies across simulations are observed in the turbulence characteristics, compared to the mean flow field. Despite similar turbulence intensities at the inlet between LES1 and LES2, LES2 generally underpredicts turbulence levels inside the airways. Slightly lower TKE levels are also observed in LES1c. In LES3, although turbulent inflow conditions were not prescribed, the flow transitions to turbulence at the back of the mouth (B1–B2). Similar flow development has also been observed in other patient-specific airway geometries under laminar inflow conditions (Nicolaou and Zaki, 2013). Downstream of the mouth, a fairly good agreement exists in the turbulence levels between LES1 and LES3. Note that simulations LES1c, LES2 and LES3 were conducted on similar mesh sizes, which suggests that the lower turbulent kinetic energy levels observed in LES1c and LES2 are due to more dissipative turbulence models or discretization schemes. The predictions obtained by RANS1 are in global fair agreement, but fail to capture the local maxima and minima.

Downstream of the trachea, the flow enters the bronchial tree. Contours of the mean velocity magnitude in the carina and main bronchi are shown in Fig. 6. The outlet conditions prescribed in the simulations, based on the flow distribution measured *in vitro*, result in high asymmetry in the ventilation of the two lungs, with the left lung receiving 29% of the inhaled air, and the right lung receiving 71%. This asymmetry is evident in the flow entering the tracheal bifurcation. A high-speed jet is observed along the right wall (G1–G2), and the stagnation point at the carina is offset towards the left. A larger recirculation region develops along the top wall of the left main bronchus (H1–H2), as it is at a more acute angle than the right. The asymmetry in the incoming flow and in the geometry, also results in higher velocities inside the right main bronchus.

Profiles of the mean velocity at the cross-sections displayed, are provided in Fig. 7. A slightly more skewed velocity profile at the entrance to the bifurcation (G1–G2, Fig. 7a) is obtained in simulation LES2, but otherwise very good agreement is observed across LES results. The largest differences occur in the recirculation region in the right main bronchus (J1–J2, Fig. 7c), since flow separation is particularly sensitive to mesh resolution and turbulence model. More noticeable differences in the mean flow profiles are observed in the RANS

simulations. In general, the RANS models predict smoother velocity profiles, and have the most difficulty in predicting flow separation. As observed in the extrathoracic airways, the  $k-\omega$  models (RANS1, RANS2) outperform the  $k-\epsilon$  model (RANS3).

Predictions of the mean turbulent kinetic energy in the carina and main bronchi are shown in Fig. 8. Although turbulence levels appeared to decay in the trachea (Fig. 4b), high levels of  $k$  are observed here, in regions of high mean shear. The maximum kinetic energy occurs in the right main bronchus, between the separated shear layer and the recirculation region. New flow instabilities are induced at the bifurcation regions due to the severe geometric transition from the parent to the daughter branches, and result in high turbulence in the first few generations of the tracheobronchial tree (Kleinstreuer and Zhang, 2010). Good qualitative agreement is observed between LES1 and LES3, whereas LES1c and LES2 continue to underpredict turbulence levels. RANS1 performs poorly near regions of flow separation (Fig. 8a, c).

Contours and profiles of the mean velocity in smaller airways of the bronchial tree are displayed in Figs. 9 and 10 respectively. As the left main bronchus narrows downstream, higher velocities are observed (Figs. 6b, 9a). The asymmetric branching results in a larger region of separation on the outer wall of the upper daughter branch. The airways are short, so the flow cannot develop fully. Due to upstream effects and different branching geometries, the flow varies significantly across the various bifurcations (Fig. 9a–d). In segment 7, for example, the flow enters the bifurcation with a large separation zone along the upper wall and a high-speed jet along the bottom, which leads to significant asymmetry in the flow distribution between daughter branches (Fig. 9c). Flow separation along the outer walls of the daughter branches is observed in most bifurcations, due to the relatively high local Reynolds numbers ( $Re > 1000$ ) and abrupt increases in cross-sectional area.

Very good agreement between the LES simulations exists at all cross-sections. As observed upstream, the largest discrepancy generally occurs in regions of separation. Here, variability is greatest in the prediction of the extent of the recirculation zone at Y1–Y2 (Fig. 10d). Simulations RANS1 and RANS2 are in reasonable agreement with the LES results, whereas RANS3 predicts a much more uniform flow field throughout. The low- $Re$   $k-\omega$  model, RANS2, displays the best performance within the RANS simulations.

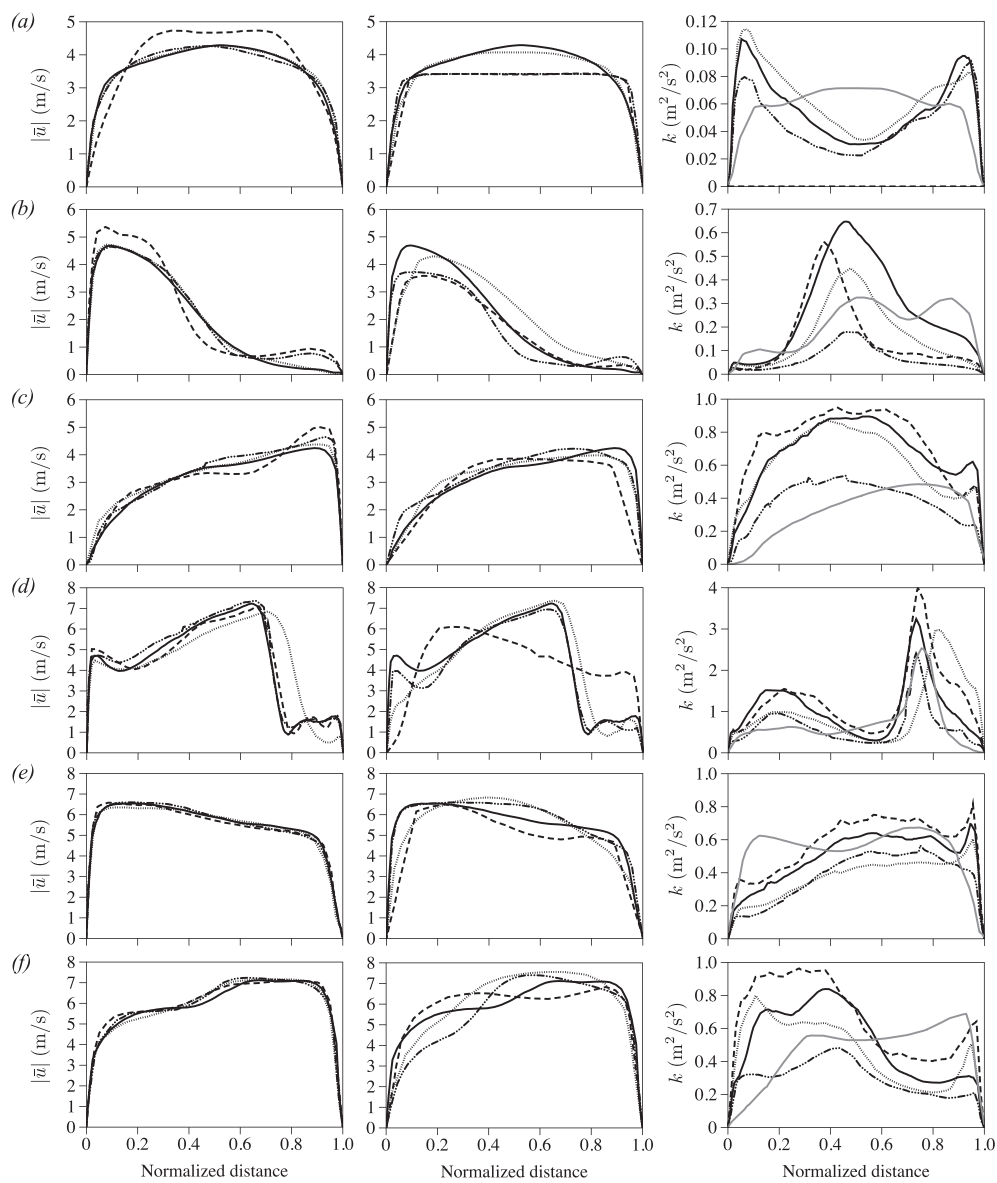


Fig. 5. Profiles of mean velocity magnitude and turbulent kinetic energy at various cross-sections of the extrathoracic airways and trachea: (a) A1–A2; (b) B1–B2; (c) C1–C2; (d) D1–D2; (e) E1–E2; and (f) F1–F2. On the left: LES results for mean velocity, — LES1, ..... LES1c, - - - - LES2, - . - - LES3; middle: RANS results for mean velocity, — LES1, ..... RANS1, - - - - RANS2, - - - - RANS3; and right: LES results for turbulent kinetic energy, — LES1, ..... LES1c, - - - - LES2, - - - - LES3, — RANS1.

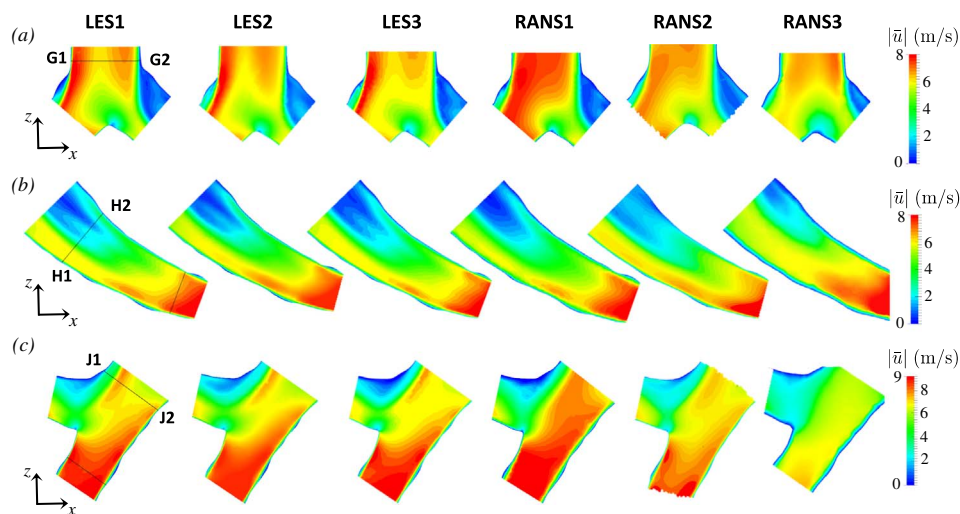


Fig. 6. Contours of mean velocity magnitude in (a) the carina; (b) the left main bronchus; and (c) the right main bronchus.

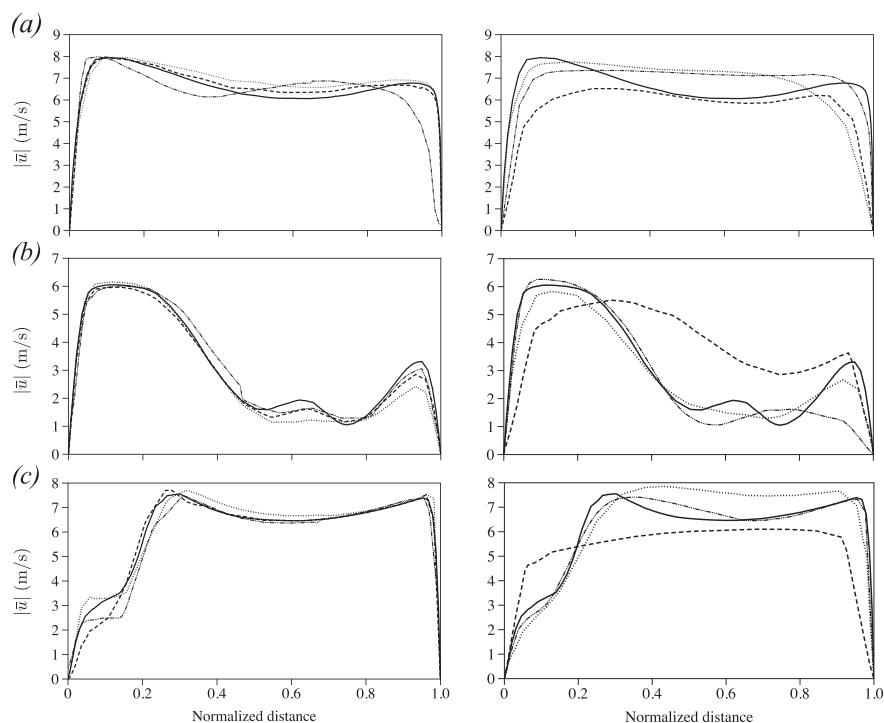


Fig. 7. Profiles of mean velocity magnitude at cross-sections (a) G1–G2; (b) H1–H2; and (c) J1–J2. On the left: LES results, — LES1, ..... LES1c, - - - LES2, - - - LES3. On the right: RANS results, — LES1, ..... RANS1, - - - RANS2, - - - RANS3.

Finally, a comparison of the turbulent kinetic energy in the small airways, across the LES simulations and RANS1, is given in Fig. 11. Turbulent kinetic energy levels remain high in these airways which belong to generations 2 and 3. Turbulence has been observed to propagate to a few generations even at low local Reynolds number, due to the enhancement of flow instabilities at the bifurcations (Kleinstreuer and Zhang, 2010). Similar to the observations made upstream, the regions of maximum kinetic energy are in agreement across all LES simulations, however LES2 continues to underpredict overall turbulence

levels. RANS1 is able to capture the turbulent kinetic energy with reasonable accuracy.

The comparison across simulations indicates that prediction of the flow in the upper airways is sensitive to mesh size and turbulence model, but less influenced by the inflow conditions. Flow transitions to turbulence at the back of the mouth, even when the inflow is laminar, and the effects of the inflow condition die out in the larynx. A larger variability is observed in the turbulent characteristics, compared to the mean flow field. A larger variation in deposition results is therefore

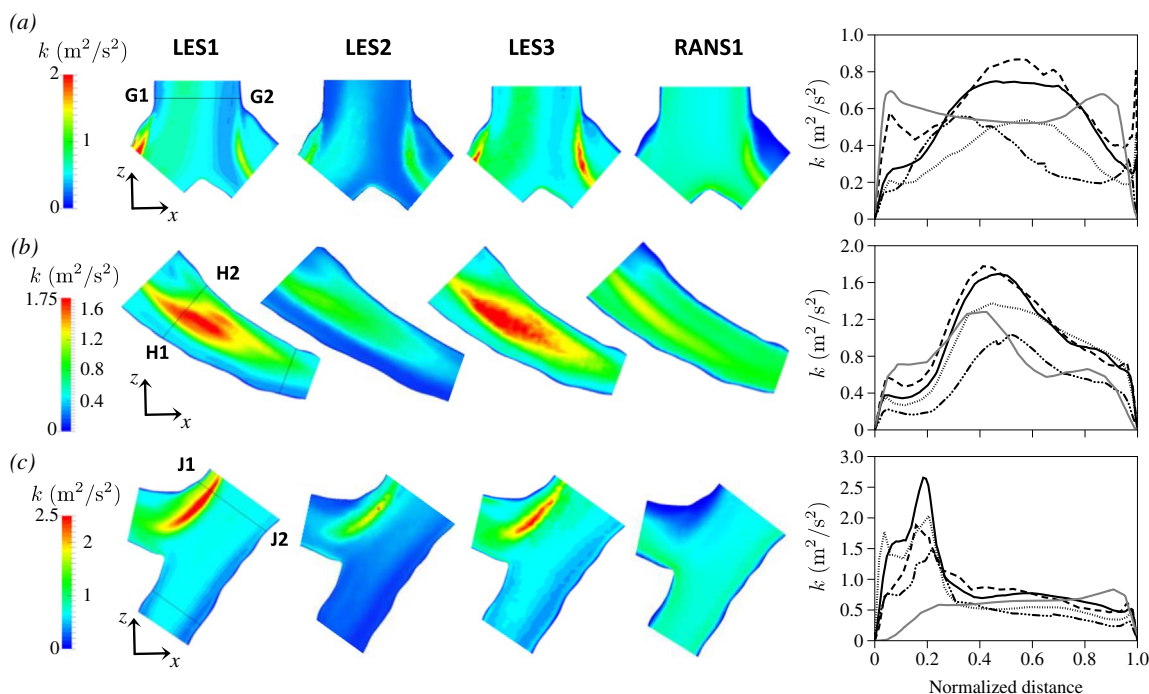


Fig. 8. Contours and profiles of mean turbulent kinetic energy in (a) the carina; (b) the left main bronchus; and (c) the right main bronchus. — LES1, ..... LES1c, - - - LES2, - - - LES3, — RANS1.

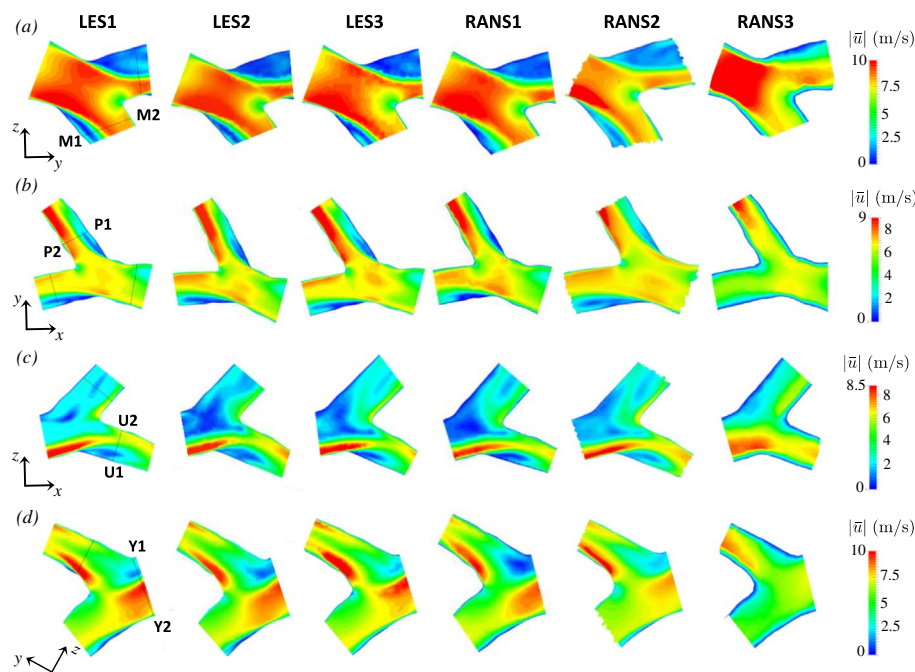


Fig. 9. Contours of mean velocity magnitude in (a) segment 5 (left lung); (b) segment 9 (right lung); (c) segment 7 (left lung); and (d) segment 12 (right lung).

expected for smaller particles that are more strongly influenced by the fluctuations in the flow. Across RANS simulations, the mean flow characteristics were captured best by the low- $Re$   $k-\omega$  model. Simulations RANS2 and RANS3 were highly dissipative, and significantly underpredicted turbulent kinetic energy in the airways,

whereas RANS1 predicted overall turbulence levels with reasonable accuracy. Next, we turn to the aerosol particles, and examine how the variability in the flow field predictions affects regional deposition results.

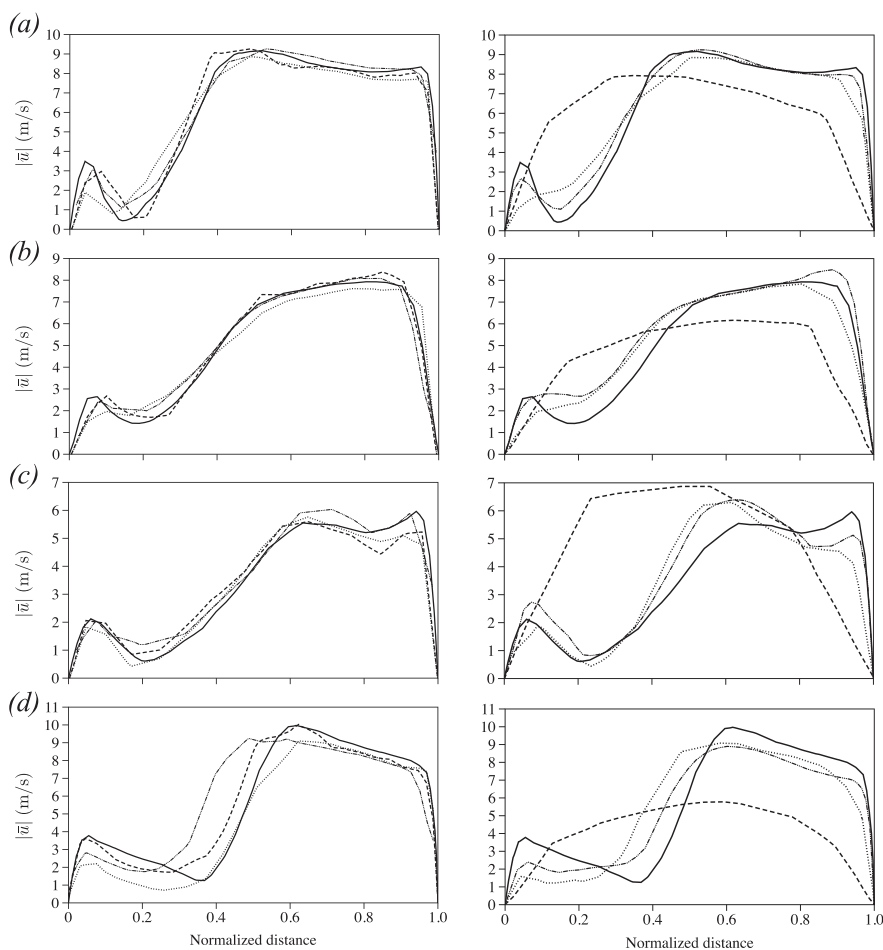


Fig. 10. Profiles of mean velocity magnitude at cross-sections (a) M1–M2; (b) P1–P2; (c) U1–U2; and (d) Y1–Y2. On the left: LES results, — LES1, ..... LES1c, - - - LES2, - - - LES3. On the right: RANS results, — LES1, ..... RANS1, - - - RANS2, - - - RANS3.

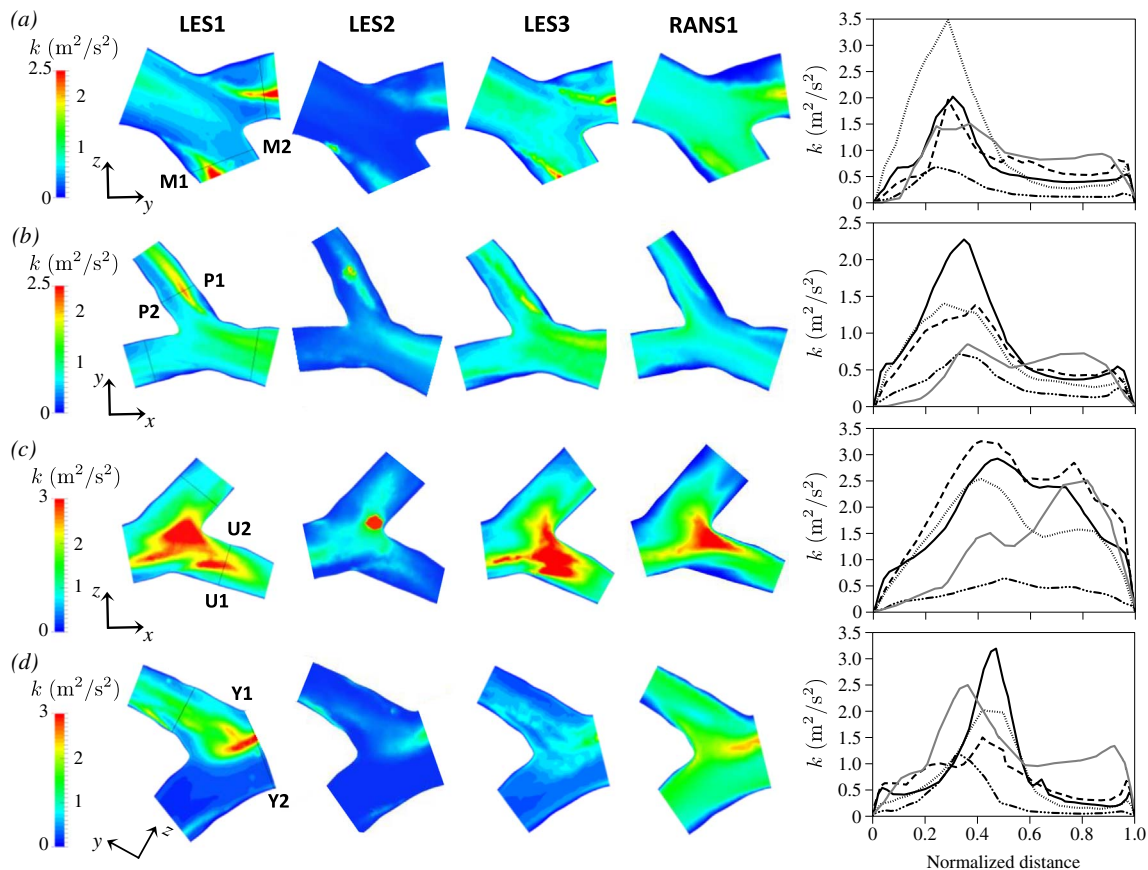


Fig. 11. Contours and profiles of mean turbulent kinetic energy in (a) segment 5; (b) segment 9; (c) segment 7; and (d) segment 12. — LES1, ..... LES1c, - - - - LES2, --- LES3, — RANS1.

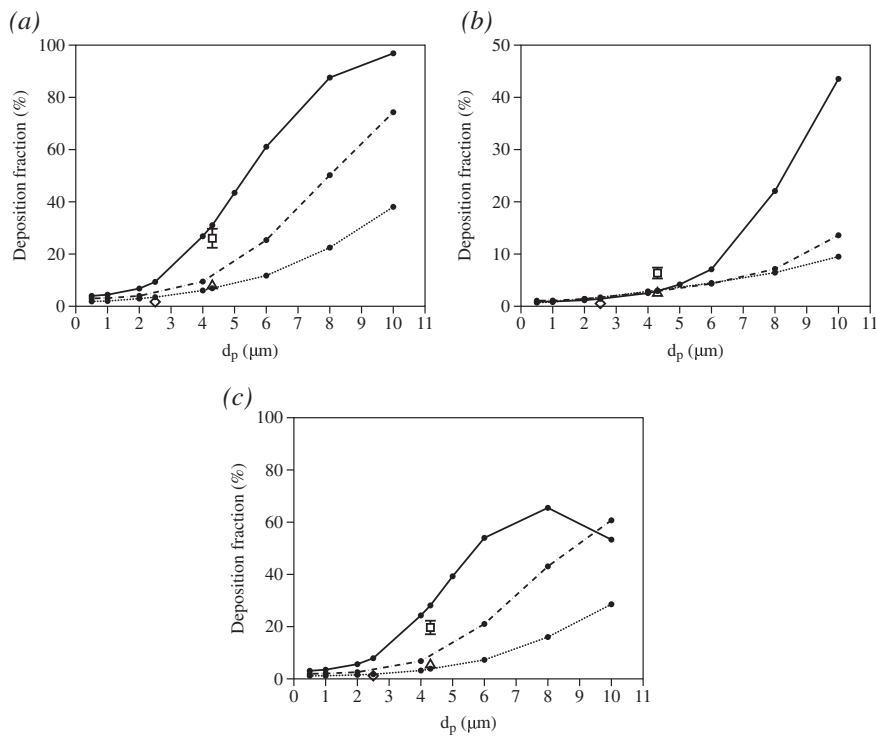


Fig. 12. Deposition fractions at  $Q = \{15,30,60\}$  L/min as a function of particle size in (a) the entire airway geometry; (b) the mouth-throat region; and (c) the tracheobronchial tree.  $Q = 15$  L/min:  $\triangle$  in vitro, ..... LES1;  $Q = 30$  L/min:  $\diamond$  in vitro, - - - - LES1;  $Q = 60$  L/min:  $\square$  in vitro, — LES1.

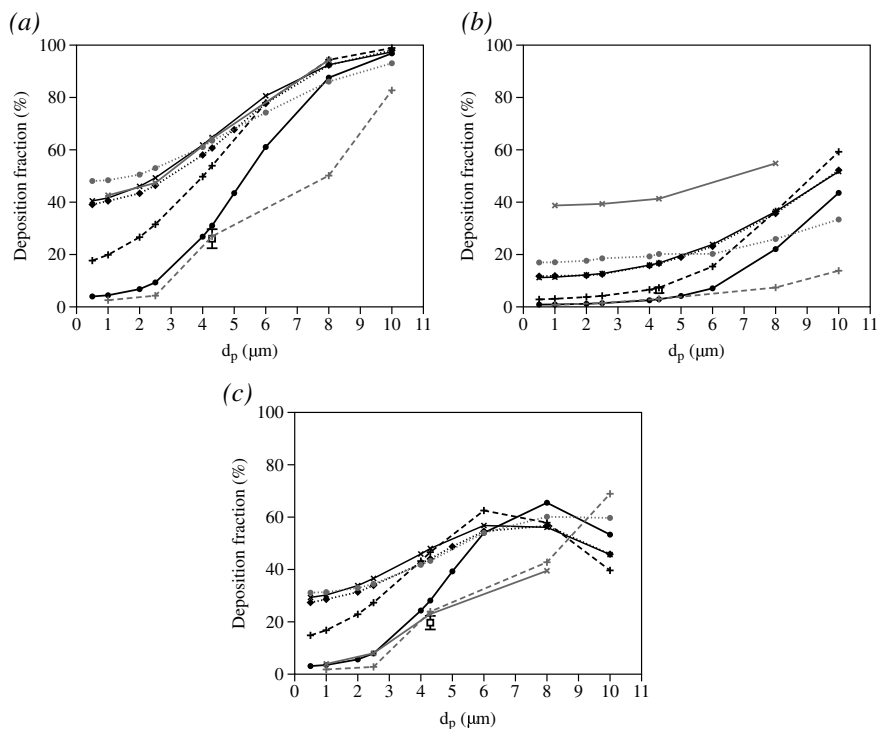


Fig. 13. Deposition fraction as a function of particle size at  $Q = 60$  L/min: (a) overall; (b) mouth and throat; and (c) tracheobronchial.  $\square$  *in vitro*,  $\bullet$  LES1,  $\blacklozenge$  LES1c,  $\times$  LES2,  $+$  LES3,  $\bullet$  RANS1,  $\times$  RANS2,  $+$  RANS3.

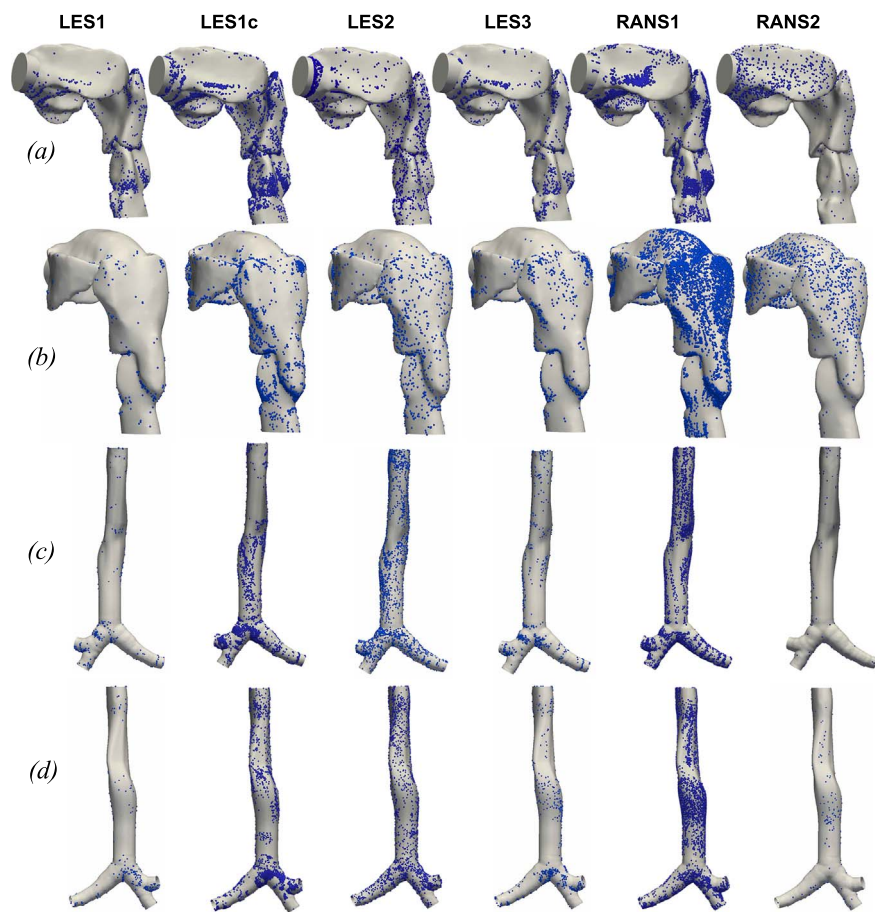


Fig. 14. Deposition patterns for  $d_p = 1$   $\mu\text{m}$ : (a) sagittal and (b) posterior views of the extrathoracic airways; (c) anterior and (d) posterior views of the trachea and major bronchial airways.

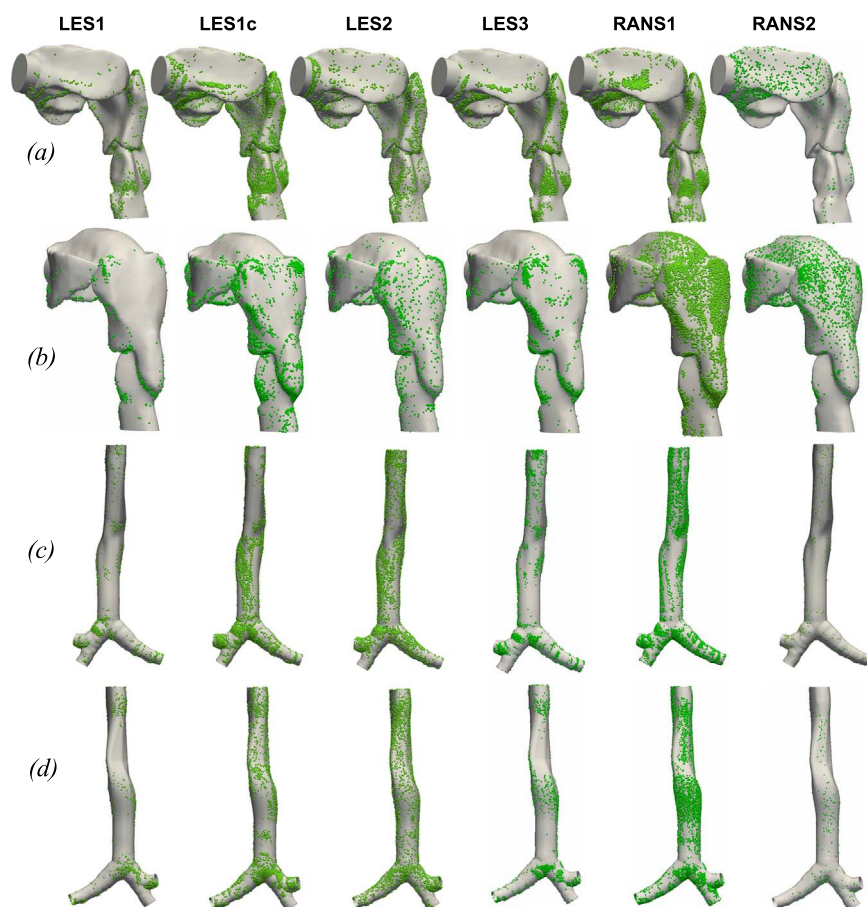


Fig. 15. Deposition patterns for  $d_p = 4.3 \mu\text{m}$ : (a) sagittal and (b) posterior views of the extrathoracic airways; (c) anterior and (d) posterior views of the trachea and major bronchial airways.

## 5.2. Aerosol deposition

*In vitro* measurements and numerical predictions of the aerosol deposition in the benchmark airway geometry are available on the SimInhale database for three flow rates,  $Q = \{15, 30, 60\}$  L/min. Overall and regional deposition results are provided across a range of particle sizes for validation of CFPD methods. Here, we briefly examine the deposition at the three flow rates, before focusing on a comparison across the six numerical approaches at 60 L/min.

Fig. 12 shows deposition results from the *in vitro* experiments and the fine LES simulation for  $Q = \{15, 30, 60\}$  L/min. Deposition fractions as a function of particle size in the entire geometry, mouth-throat region, and tracheobronchial tree are displayed in Figs. 12a, b and c respectively. Deposition increases with particle size for all three flow rates, suggesting that inertial impaction is the dominant deposition mechanism in the upper airways. The decrease in tracheobronchial deposition for  $10 \mu\text{m}$  particles at 60 L/min is a result of the significant filtering that occurs upstream in the mouth-throat region. An increase in overall and tracheobronchial deposition is also observed with increasing flow rate, and is more significant for the larger particles. In the extrathoracic region, deposition is largely unaffected by flow rate for particles smaller than 5 microns. These particles lie in the low Stokes number regime ( $Stk < 0.01$ ), which is characterized by a weak dependence of deposition on Stokes number (Nicolaou and Zaki, 2016).

Good agreement is observed between numerical and experimental data at 15 and 30 L/min. In the high flow rate case, lower mouth-throat deposition is predicted in the LES. As a result of the reduced filtering in the mouth and throat, higher deposition is obtained in the tracheobronchial tree compared to the *in vitro* data. Underprediction of extrathoracic deposition by LES for high levels of turbulence has previously been reported in the literature, and can be attributed to the fact that the

sub-grid scale influence on the motion of the particles is neglected in the particle-tracking scheme (Debhi, 2011). Additional sources of error could be related to experimental uncertainties, and differences in the particle distribution at the inlet between experiments and simulation.

A comparison of the deposition fractions predicted by the different simulation methods is shown in Fig. 13. Large variability can be seen in the overall deposition, which increases with decreasing particle size. Small particles are influenced by the velocity fluctuations, and are therefore particularly sensitive to errors in the flow field. Comparison of the predictions obtained in LES1 and LES1c shows that mesh size has a large effect on deposition. Interpolation errors in the particle-tracking scheme increase with decreasing grid resolution, and result in an overprediction of deposition on the coarser mesh, in particular for the smaller particles. As in the mean flow and turbulent kinetic energy results, LES3 shows better agreement with the fine-grid LES simulation, compared to LES1c and LES2.

Within the RANS models, RANS1 and RANS2 overpredict extrathoracic deposition at small and intermediate particle sizes. In addition to interpolation errors, the disparity is likely due to an overprediction in the velocity fluctuations near the wall in the turbulent tracking schemes. Similar behaviour has been reported in the literature and has been improved by applying a near-wall correction to the velocity fluctuations (Matida et al., 2004; Jayaraju et al., 2008; Debhi, 2011). Simulation RANS3, on the other hand, adopted mean-flow tracking, which only accounts for impaction as a deposition mechanism, and does not include the effect of turbulent dispersion. This results in artificial good agreement with the fine LES simulation at small particle sizes, and considerable underprediction in deposition for the larger particles, particularly in the extrathoracic airways.

The deposition patterns in the extrathoracic airways, trachea and major bronchi are shown in Figs. 14–16, for particle sizes 1, 4.3 and

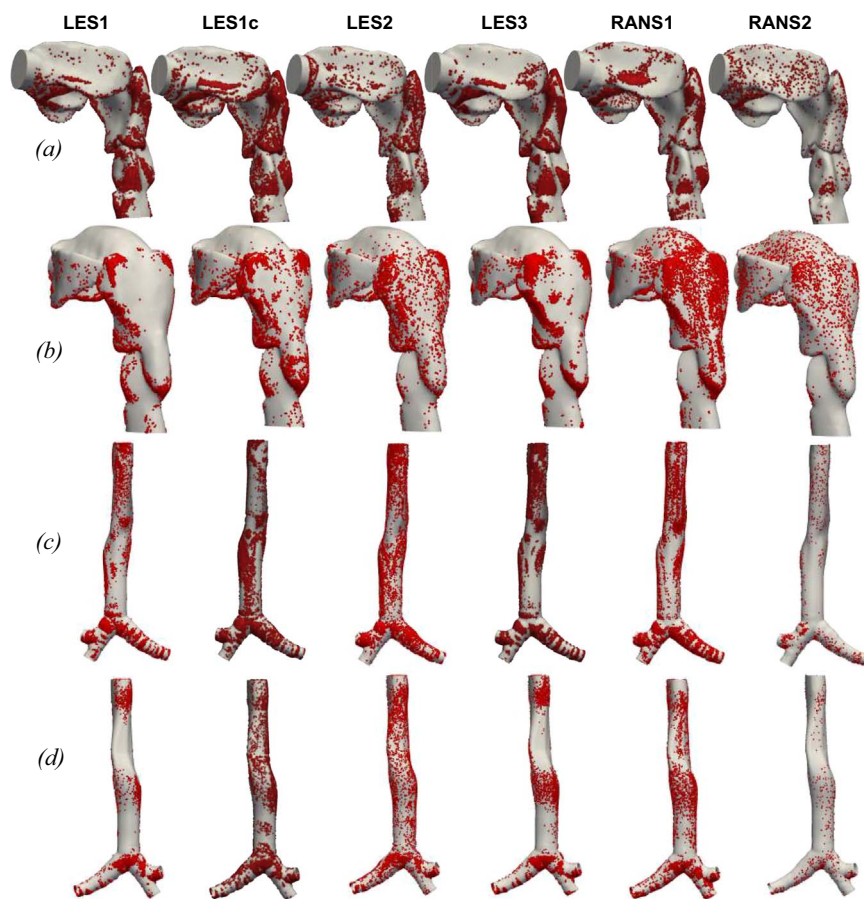


Fig. 16. Deposition patterns for  $d_p = 8 \mu\text{m}$ : (a) sagittal and (b) posterior views of the extrathoracic airways; (c) anterior and (d) posterior views of the trachea and major bronchial airways.

$8 \mu\text{m}$  respectively. The same main deposition hotspots are observed across all three particle sizes. In the extrathoracic airways, major deposition occurs along the side walls of the pharynx. Additional hotspots are observed on the sharp step in the larynx, due to the sudden change in flow directions, and on the anterior wall slightly downstream, due to the separated shear layer. Some deposition also occurs in front of the tongue, where the incoming flow from the inlet pipe impinges.

In the trachea, very low deposition is observed for small particles. As particle size increases, deposition increases significantly. Particles deposit primarily along the upper half of the trachea, where the separated shear layer impinges on the anterior wall, and at the bend further downstream, where the high-speed velocity shifts from the anterior to the posterior wall (Fig. 4a). Downstream of the trachea, three main hotspots are observed: (i) just left of the carina, at the location of the stagnation point; (ii) along the upper wall of the right bronchus, due to the high-speed jet (Fig. 6a); and (iii) along the bottom wall of its daughter airway, as it branches off at a sharp angle.

In general, LES1 and LES3 predict similar deposition patterns. Interpolation errors in LES1c and LES2 cause higher deposition throughout the geometry, which results in a more uniform distribution, with less pronounced hotspots. RANS1 also displays high deposition, in particular along the posterior wall of the upper pharynx, and on the trachea walls. Sparser deposition is observed in RANS2, due to the small particle sample size employed. It is likely that the results are not statistically converged with 10,000 particles, and this could be the reason for the high extrathoracic deposition reported in Fig. 13b.

A more detailed comparison of the deposition results obtained in the LES simulations is shown in Fig. 17. Deposition fractions per segment of the airways are plotted for various particle sizes, in order to examine regional deposition. Segment numbers are shown in Fig. 2c. At small particle sizes,  $d_p < 5 \mu\text{m}$ , overprediction is observed across the entire

geometry in simulations LES1c, LES2 and LES3. For intermediate particles,  $d_p = 6 \mu\text{m}$ , good agreement exists in the bronchial tree, whereas significant variability is observed in the mouth and throat. At this particle size, extrathoracic deposition has a strong dependence on Stokes number, and therefore a larger sensitivity to numerical errors. Tracheobronchial deposition on the other hand saturates around this particle size (Fig. 13c). Good agreement across LES predictions can be seen for the larger particles,  $d_p = \{8, 10\} \mu\text{m}$ , as they are less sensitive to errors in the flow field and in the interpolation of the fluid velocity for the computation of the drag force (Lambert et al., 2011; Nicolaou and Zaki, 2016).

Fig. 18 shows the regional depositions obtained in the RANS simulations. For small particles, RANS3 is in good agreement with the fine-grid LES in the extrathoracic airways and trachea, and underpredicts deposition in the bronchial tree, as mean-flow tracking does not take into account turbulent dispersion. As particle size increases, this trend reverses, as extrathoracic and tracheal deposition are underpredicted, and a larger amount deposits in the bronchial regions due to the reduced filtering upstream. In RANS1, deposition is overpredicted across all segments for small particles,  $d_p = 2.5 \mu\text{m}$ , and in the larger airways up to the main bronchi, for  $d_p = 2.5 \mu\text{m}$ . At larger particle sizes, good agreement with the fine LES is observed in most segments, as particle trajectories become less sensitive to numerical errors. In simulation RANS2, overprediction occurs primarily in the larger airways due to the small sample size, and extends further downstream as particle size decreases. At the smallest particle size,  $d_p = 2.5 \mu\text{m}$ , deposition is significantly overpredicted in the extrathoracic airways (segment 1), the trachea (segment 2), and the left main bronchus (segment 4).

Finally, we briefly examine the effect of additional forces on deposition. Brownian motion was included in some of the simulations, but

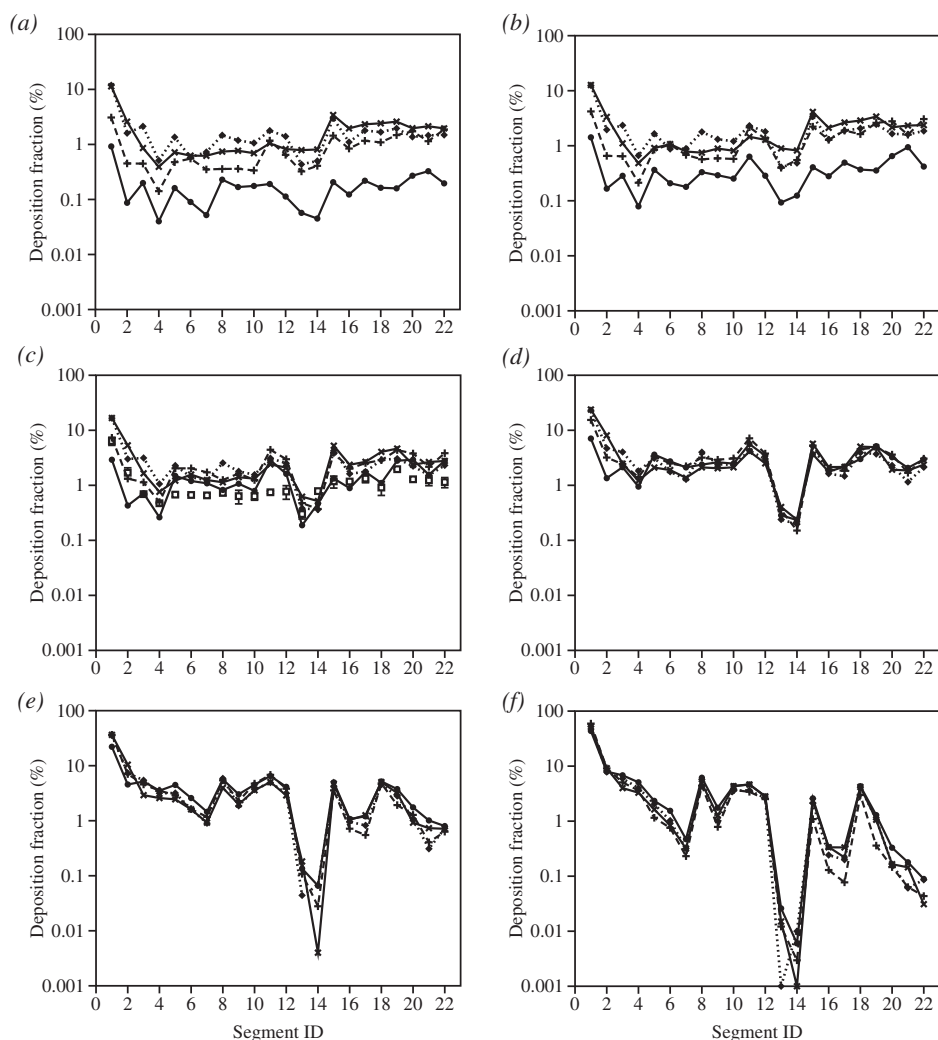


Fig. 17. Deposition fractions in the various segments of the airway geometry, obtained from LES: (a)  $d_p = 1 \mu\text{m}$ ; (b)  $d_p = 2.5 \mu\text{m}$ ; (c)  $d_p = 4.3 \mu\text{m}$ ; (d)  $d_p = 6 \mu\text{m}$ ; (e)  $d_p = 8 \mu\text{m}$ ; (f)  $d_p = 10 \mu\text{m}$ . □ *in vitro*, • LES1, ◆ LES1c, × LES2, + LES3.

excluded in others. Its effect on the smallest particles,  $d_p = 0.5 \mu\text{m}$ , is examined in Fig. 19a. The regional deposition results of RANS1, with and without Brownian force, show that Brownian motion has a negligible effect on deposition. Additional forces, such as the pressure gradient and added mass, are typically considered negligible and were not taken into account in the simulations. However, for particles inside dry powder inhalers, transverse lift forces due to shear and rotation have been found to be significant (Sommerfeld and Schmalfuß, 2015; Sommerfeld, 2010). In Fig. 19b, the effect of transverse lift on particles inside the airways is considered for  $d_p = 4.3 \mu\text{m}$ . The simulation taking into account only drag and gravity, and that including lift, yield negligible differences in regional deposition across the entire geometry. In the range of particle sizes studied, forces other than aerodynamic drag and gravity, have a marginal effect on deposition in RANS. In fine LES simulations, particles could potentially exhibit larger sensitivity to lift, as the near-wall region, where Saffman lift is strongest, is better resolved.

A large variability in both global and regional deposition is observed across different computational approaches, especially in the low Stokes number regime. Deposition is particularly sensitive to mesh size and particle-tracking scheme, as interpolation errors increase with decreasing grid resolution and are heavily dependent on the scheme adopted. In addition, small particles are also affected by the accuracy in the turbulence statistics in LES, and the turbulent dispersion model in RANS, as their trajectories are significantly influenced by velocity fluctuations. In RANS, the effect of additional forces, such as Brownian

motion and lift, has been found to be small for the range of particle sizes considered.

### 6. Conclusion

Regional deposition in the airways is important in the pulmonary delivery of drugs for topical treatment of respiratory diseases, as well as systemic delivery of drugs with limited lung bioavailability. Currently, *in vivo* studies remain limited by the spatial and temporal resolutions of imaging techniques, and by patient exposure to radiation. *In silico* methods offer a powerful tool to predict localized deposition in the airways, in order to further our understanding of the aerosol dynamics and optimize inhaled drug delivery. Numerical studies conducted to date have adopted a variety of computational techniques, a range of airway geometries varying in complexity, and differing assumptions on the flow and aerosol physics. A review of existing methods, with particular focus on the extrathoracic and upper conducting airways, was provided in Section 2.

One current limitation in the use of CFPD methods is the lack of detailed experimental data sets for validation of regional deposition results. Here, a benchmark case was presented, designed to serve as a reference for quality assurance of computational models in the upper airways. *In vitro* deposition measurements in a complex realistic geometry were provided at various inhalation flow rates, and six different simulation approaches were adopted to compute the benchmark case.

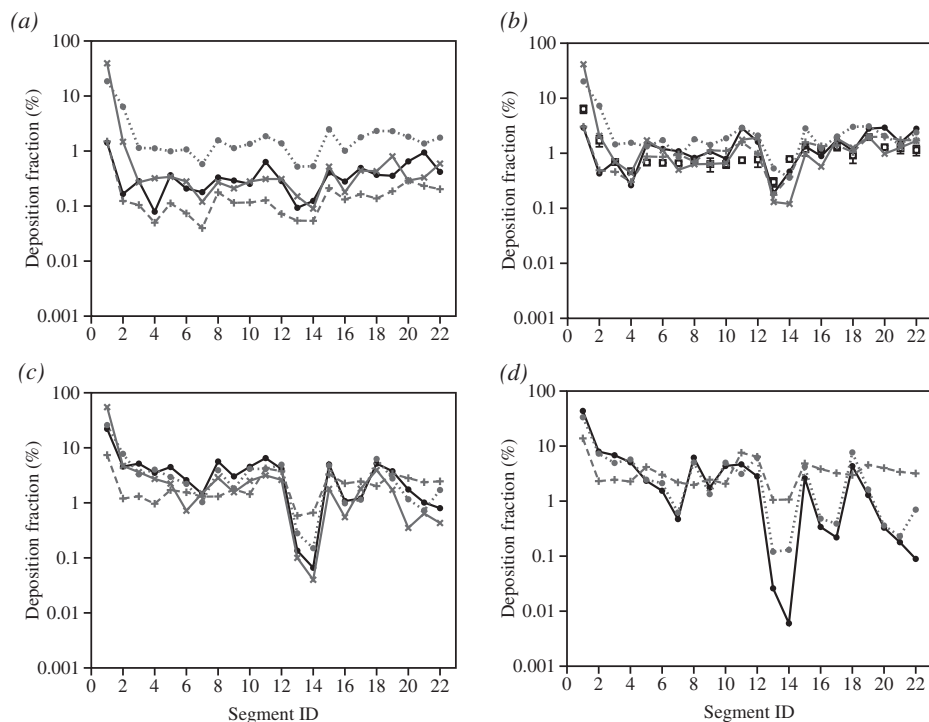


**Fig. 18.** Deposition fractions in the various segments of the airway geometry, obtained from RANS: (a)  $d_p = 2.5 \mu\text{m}$ ; (b)  $d_p = 4.3 \mu\text{m}$ ; (c)  $d_p = 8 \mu\text{m}$ ; (d)  $d_p = 10 \mu\text{m}$ .  $\square$  *in vitro*,  $\bullet$  LES1,  $\circ$  RANS1,  $\times$  RANS2,  $+$  RANS3.

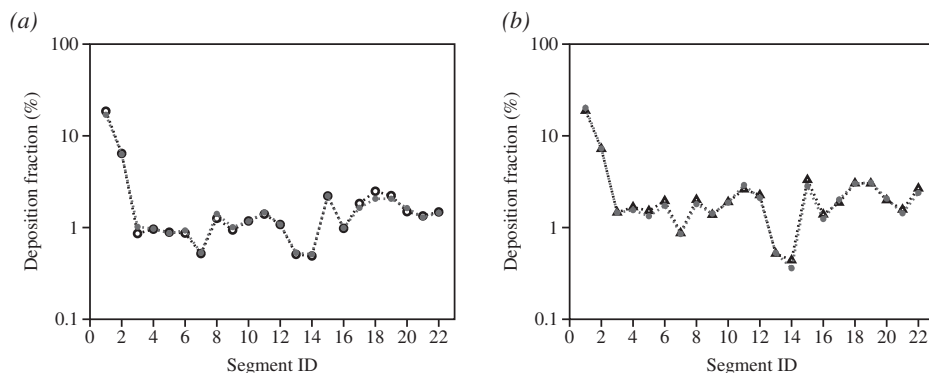


**Fig. 19.** Deposition fractions in the various segments of the airway geometry, obtained in RANS1: (a)  $d_p = 0.5 \mu\text{m}$ ; (b)  $d_p = 4.3 \mu\text{m}$ .  $\circ$  drag and gravity;  $\bullet$  drag, gravity and Brownian force;  $\triangle$  drag, gravity and lift.

Results were presented for the high flow rate,  $Q = 60 \text{ L/min}$ , however *in silico* and *in vitro* data at  $Q = \{15,30\} \text{ L/min}$  will also be published online and made available to the wider community.

To model the turbulent flow in the airways, three different large eddy simulation (LES) models and three Reynolds-averaged-Navier-Stokes (RANS) models were adopted. Different inflow conditions were applied across simulations, and mesh sizes ranged from 1.3 to 50 million grid cells. All simulations employed a Lagrangian particle-tracking approach and assumed one-way coupling between the flow and the particles. The approaches differed in the particle-tracking schemes adopted, the forces acting on the particles, and the release time and number of particles injected into the flow. In addition to serving as validation for CFPD methods, this benchmark case allowed us to examine the sensitivity of predictions to the numerical methods adopted, the mesh size, and the assumptions made in the modelling.

Prediction of the flow in the upper airways was found to be sensitive to mesh size and turbulence model, but less influenced by the inflow conditions. The flow transitions to turbulence at the back of the mouth, even when the inflow is laminar, and the effects of the inflow condition die out in the larynx. Generally, the mean flow fields obtained in the LES simulations were in good agreement. A larger variability was observed in the turbulent characteristics. Across RANS simulations, the

mean-flow dynamics were captured best by the low- $Re$   $k-\omega$  model on a mesh with prism layers near the wall. A higher-order scheme and turbulent inflow conditions in RANS1 resulted in turbulence levels comparable to LES, whereas RANS2 and RANS3 were too dissipative, and significantly underpredicted turbulent kinetic energy in the airways.

Significant variability in total and regional deposition results was seen across simulations. Deposition was found to be particularly sensitive to mesh size and particle-tracking scheme, especially at low Stokes numbers. Interpolation errors in the particle-tracking scheme increase with decreasing grid resolution, and are heavily dependent on the interpolation method adopted. Small particles are also influenced by the velocity fluctuations, and are therefore more sensitive to errors in the flow field. For larger particles, there was good agreement in regional deposition across LES simulations. RANS with turbulent tracking overpredicted deposition at small and intermediate particle sizes, whereas mean-flow tracking significantly underpredicted deposition for larger particles. Forces other than drag and gravity were found to have a minor effect on the particles in RANS.

The airway model and the *in silico* and *in vitro* data presented in the manuscript, will be available online. PIV measurements of the flow in the benchmark case geometry will also be performed in future work, and additional numerical results will be appended to the online

database as they become available. The aim is to provide a tool for the inhaled drug delivery community to (i) perform thorough validations of *in silico* models; and (ii) determine best practice guidelines for predictions of regional deposition in the airways, which can assist in the design and optimization of inhalation therapies.

## Acknowledgments

This article is based upon work from COST Action MP1404 SimInhale 'Simulation and pharmaceutical technologies for advanced patient-tailored inhaled medicines', supported by COST (European Cooperation in Science and Technology) [www.cost.eu](http://www.cost.eu). The work conducted at Brno University of Technology was partly supported by the Czech Science Foundation [16-23675S].

## References

- Balášházy, I., Hofmann, W., 1993. Particle deposition in airway bifurcations - I. Inspiratory flow. *J. Aerosol Sci.* 24, 745–772.
- Balášházy, I., Hofmann, W., Heistracher, T., 1999. Computation of local enhancement factors for the quantification of particle deposition patterns in airway bifurcations. *J. Aerosol Sci.* 30, 185–203.
- Ball, C., Uddin, M., Pollard, A., 2008. Mean flow structures inside the human upper airway. *Flow Turbul. Combust.* 81, 155–188.
- Cheng, K., Cheng, Y., Yeh, H.C., Swift, D.L., 1997. Measurements of airway dimensions and calculation of mass transfer characteristics of the human oral passage. *J. Biomech. Eng. Trans. ASME* 119, 476–482.
- Choi, J., Tawhai, M.H., Hoffman, E.A., Lin, C.L., 2009. On intra- and intersubject variabilities of airflow in the human lungs. *Phys. Fluids* 21, 101901.
- Cui, X., Gutheil, E., 2011. Large eddy simulation of the unsteady flow-field in an idealized human mouth-throat configuration. *J. Biomech.* 44, 2768–2774.
- Davies, C.N., 1945. Definitive equations for the fluid resistance of spheres. *Proc. Phys. Soc.* 57, 259.
- Debhi, A., 2011. Prediction of extrathoracic aerosol deposition using RANS-random walk and LES approaches. *Aerosol Sci. Tech.* 45, 555–569.
- DeHaan, W., Finlay, W., 2001. In vitro monodisperse aerosol deposition in a mouth and throat with six different inhalation devices. *J. Aerosol Med.* 14, 361–367.
- Dekker, E., 1961. Transition between laminar and turbulent flow in human trachea. *J. Appl. Physiol.* 16, 1060–1064.
- Finlay, W., Stapleton, K., Yokota, J., 1996. On the use of computational fluid dynamics for simulating flow and particle deposition in the human respiratory tract. *J. Aerosol Sci.* 9, 329–341.
- Ganser, G., 1993. A rational approach to drag prediction of spherical and nonspherical particles. *Powder Technol.* 77, 143–152.
- Gosman, A.D., Ioannides, E., 1983. Aspects of computer simulation of liquid fuelled combustors. *J. Energy* 7 (6), 482–490.
- Grgic, B., Finlay, W., Burnell, P., Heenan, A., 2004. In vitro intersubject and intrasubject deposition measurements in realistic mouth-throat geometries. *J. Aerosol Sci.* 35, 1025–1040.
- Heenan, A., Matida, E., Pollard, A., Finlay, W., 2003. Experimental measurements and computational modeling of the flow field in an idealized human oropharynx. *Exp. Fluids* 35, 70–84.
- Horsfield, K., Dart, G., Olson, D.E., Filley, G.F., Cumming, G., 1971. Models of the human bronchial tree. *J. Appl. Physiol.* 31, 207–217.
- Houzeaux, G., Garcia, M., Cajas, J.C., Artigues, A., Olivares, E., Labarta, J., Vázquez, M., 2016. Dynamic load balance applied to particle transport in fluids. *Int. J. Comput. Fluid Dyn.* 30, 408–418.
- Hughes, T.J., Mazzei, L., Jansen, K.E., 2000. Large eddy simulation and the variational multiscale method. *Comput. Vis. Sci.* 3, 47–59.
- Jayaraju, S., Brouns, C., Lacor, C., Belkassam, B., Verbanck, S., 2008. Large eddy and detached eddy simulations of fluid flow and particle deposition in a human mouth-throat. *J. Aerosol Sci.* 39, 862–875.
- Jayaraju, S.T., Brouns, M., Verbanck, S., Lacor, C., 2007. Fluid flow and particle deposition analysis in a realistic extrathoracic airway model using unstructured grids. *J. Aerosol Sci.* 38, 494–508.
- Johnstone, A., Uddin, M., Pollard, A., Heenan, A., Finlay, W.H., 2004. The flow inside an idealised form of the human extra-thoracic airway. *Exp. Fluids* 37, 673–689.
- Kallio, G.A., Reeks, M.W., 1989. A numerical simulation of particle deposition in turbulent boundary layers. *Int. J. Multiphase Flow* 15, 433–446.
- Kleinstreuer, C., Zhang, Z., 2003. Laminar-to-turbulent fluid-particle flows in a human airway model. *Int. J. Multiphase Flow* 29, 271–289.
- Kleinstreuer, C., Zhang, Z., 2010. Airflow and particle transport in the human respiratory system. *Annu. Rev. Fluid Mech.* 42, 301–334.
- Koullapis, P.G., Kassinos, S.C., Bivolarova, M.P., Melikov, A.K., 2016. Particle deposition in a realistic geometry of the human conducting airways: effects of inlet velocity profile, inhalation flowrate and electrostatic charge. *J. Biomech.* 49, 2201–2212.
- Lambert, A.R., O'Shaughnessy, P.T., Tawhai, M.H., Hoffman, E.A., Lin, C.L., 2011. Regional deposition of particles in an image-based airway model: large-eddy simulation and left-right lung ventilation asymmetry. *Aerosol Sci. Tech.* 45, 11–25.
- Lauder, B.E., Spalding, D.B., 1974. The numerical computation of turbulent flows. *Comput. Methods Appl. Mech. Eng.* 3, 269–289.
- Li, A., Ahmadi, G., 1992. Dispersion and deposition of spherical particles from point sources in a turbulent channel flow. *Aerosol Sci. Technol.* 16, 209–226.
- Li, Z., Kleinstreuer, C., Zhang, Z., 2007. Particle deposition in the human tracheobronchial airways due to transient inspiratory flow patterns. *J. Aerosol Sci.* 38, 625–644.
- Lilly, D., 1992. A proposed modification of the Germano subgrid-scale closure method. *Phys. Fluids A* 4, 633–635.
- Lin, C.L., Tawhai, M.H., McLennan, G., Hoffman, E.A., 2007. Characteristics of the turbulent laryngeal jet and its effect on airflow in the human intra-thoracic airways. *Respir. Physiol. Neurobiol.* 157, 295–309.
- Lizal, F., Belka, M., Adam, J., Jedelsky, J., Jicha, M., 2015. A method for in vitro regional aerosol deposition measurement in a model of the human tracheobronchial tree by the positron emission tomography. *Proc. Inst. Mech. Eng. H J. Eng. Med.* 229, 750–757.
- Lizal, F., Elcner, J., Hopke, P., Jedelsky, J., Jicha, M., 2012. Development of a realistic human airway model. *Proc. Inst. Mech. Eng. H J. Eng. Med.* 226, 197–207.
- Longest, P.W., Holbrook, L.T., 2012. In silico models of aerosol delivery to the respiratory tract - development and applications. *Adv. Drug Deliv. Rev.* 64, 296–311.
- Longest, P.W., Xi, J., 2008. Condensational growth may contribute to the enhanced deposition of cigarette smoke particles in the upper respiratory tract. *Aerosol Sci. Tech.* 42, 579–602.
- Ma, B., Lutchen, K., 2009. CFD simulation of aerosol deposition in an anatomically based human large-medium airway model. *Ann. Biomed. Eng.* 37, 271–285.
- Matida, E., Finlay, W., Lange, C., Grgic, B., 2004. Improved numerical simulation of aerosol deposition in an idealized mouth-throat. *J. Aerosol Sci.* 35, 1–19.
- Maxey, M.R., Riley, J.J., 1983. Equation of motion for a small rigid sphere in a nonuniform flow. *Phys. Fluids* 26, 883–889.
- McLaughlin, J., 1989. Aerosol particle deposition in numerically simulated channel flow. *Phys. Fluids A* 1, 1211–1224.
- Menter, F.R., 1994. Two-equation eddy-viscosity turbulence models for engineering applications. *AIAA J.* 32, 1598–1605.
- Morsi, S.A., Alexander, A.J., 1972. An investigation of particle trajectories in two-phase flow systems. *J. Fluid Mech.* 55, 193–208.
- Nicolaou, L., Jung, S.Y., Zaki, T.A., 2015. A robust direct-forcing immersed boundary method with enhanced stability for moving body problems in curvilinear coordinates. *Comput. Fluids* 119, 101–114.
- Nicolaou, L., Zaki, T.A., 2013. Direct numerical simulations of flow in realistic mouth-throat geometries. *J. Aerosol Sci.* 57, 71–87.
- Nicolaou, L., Zaki, T.A., 2016. Characterization of aerosol Stokes number in 90° bends and idealized extrathoracic airways. *J. Aerosol Sci.* 102, 105–127.
- Nicoud, F., Ducros, F., 1999. Subgrid-scale modelling based on the square of the velocity gradient tensor. *Flow Turbul. Combust.* 62, 183–200.
- Oldham, M.J., 2000. Computational fluid dynamic predictions and experimental results for particle deposition in an airway model. *Aerosol Sci. Tech.* 32, 61–71.
- Ounis, H., Ahmadi, G., McLaughlin, J., 1991. Brownian diffusion of submicrometer particles in the viscous sublayer. *J. Colloid Interface Sci.* 143, 266–277.
- Radhakrishnan, H., Kassinos, S., 2009. CFD modeling of turbulent flow and particle deposition in human lungs. In: *Engineering in Medicine and Biology Society, EMBC 2009. Annual International Conference of the IEEE*, pp. 2867–2870.
- Schiller, L., Naumann, A., 1935. A drag coefficient correlation. *VDI Z.* 77, 318–320.
- Schmidt, A., Zidowitz, S., Kriete, A., Denhard, T., Krass, S., Peitgen, H.O., 2004. A digital reference model of the human bronchial tree. *Comput. Med. Imaging Graph.* 28, 203–211.
- Sommerfeld, M., 2010. Particle motion in fluids. *VDI-Buch: VDI Heat Atlas*, Part 11. pp. 1181–1196.
- Sommerfeld, M., Kohnen, G., Rüger, M., 1993. Some open questions and inconsistencies of lagrangian particle dispersion models. In: *Ninth Symposium on Turbulent Shear Flows, Kyoto, Japan*.
- Sommerfeld, M., Schmalfuß, S., 2015. Numerical analysis of carrier particle motion in a dry powder inhaler. *J. Fluids Eng.* 138, 041308.
- Stapleton, K.W., Guentsch, E., Hoskinson, M.K., Finlay, W.H., 2000. On the suitability of  $k-\epsilon$  turbulence modeling for aerosol deposition in the mouth and throat: a comparison with experiment. *J. Aerosol Sci.* 31, 739–749.
- Stylianou, F.S., Sznitman, J., Kassinos, S.C., 2016. Direct numerical simulation of particle laden flow in a human airway bifurcation model. *Int. J. Heat Fluid Flow* 61, 677–710.
- Tabor, G.R., Baba-Ahmadi, M.H., 2010. Inlet conditions for large eddy simulation: a review. *Comput. Fluids* 39, 553–567.
- Thibodeau, G.A., Patton, K.T., 1996. *Anatomy & Physiology*, 3rd ed. Mosby, St. Louis, MO.
- Vázquez, M., Houzeaux, G., Koric, S., Artigues, A., Aguado-Sierra, J., Arís, R., Mira, D., Calmet, H., Cucchietti, F., Owen, H., et al., 2016. Alya: multiphysics engineering simulation toward exascale. *J. Comput. Sci.* 14, 15–27.
- Weibel, E.R., 1963. *Morphometry of the Human Lung*. Academic Press, Berlin.
- Xi, J., Longest, W., 2007. Transport and deposition of micro-aerosols in realistic and simplified models of the oral airway. *Ann. Biomed. Eng.* 35, 560–581.
- Yeh, H.C., Schum, G., 1980. Models of human lung airways and their application to inhaled particle deposition. *Bull. Math. Biol.* 42, 461–480.
- Young, J., Leeming, A., 1997. A theory of particle deposition in turbulent pipe flow. *J. Fluid Mech.* 340, 129–159.
- Zhang, Z., Kleinstreuer, C., Kim, C.S., 2002. Micro-particle transport and deposition in a human airway model. *J. Aerosol Sci.* 33, 1635–1652.
- Zhang, Z., Kleinstreuer, C., Kim, C.S., Cheng, Y.S., 2004. Vaporizing microdroplet inhalation, transport, and deposition in a human upper airway model. *Aerosol Sci. Tech.* 38, 36–49.

# Numerical investigation of inspiratory airflow in a realistic model of the human tracheobronchial airways and a comparison with experimental results

Jakub Elcner<sup>1</sup> · Frantisek Lizal<sup>1</sup> · Jan Jedelsky<sup>1</sup> · Miroslav Jicha<sup>1</sup> · Michaela Chovancova<sup>1</sup>

Received: 9 October 2014 / Accepted: 29 June 2015 / Published online: 12 July 2015  
© Springer-Verlag Berlin Heidelberg 2015

**Abstract** In this article, the results of numerical simulations using computational fluid dynamics (CFD) and a comparison with experiments performed with phase Doppler anemometry are presented. The simulations and experiments were conducted in a realistic model of the human airways, which comprised the throat, trachea and tracheobronchial tree up to the fourth generation. A full inspiration/expiration breathing cycle was used with tidal volumes 0.5 and 1 L, which correspond to a sedentary regime and deep breath, respectively. The length of the entire breathing cycle was 4 s, with inspiration and expiration each lasting 2 s. As a boundary condition for the CFD simulations, experimentally obtained flow rate distribution in 10 terminal airways was used with zero pressure resistance at the throat inlet. CCM+ CFD code (Adapco) was used with an SST  $k-\omega$  low-Reynolds Number RANS model. The total number of polyhedral control volumes was 2.6 million with a time step of 0.001 s. Comparisons were made at several points in eight cross sections selected according to experiments in the trachea and the left and right bronchi. The results agree well with experiments involving the oscillation (temporal relocation) of flow structures in the majority of the cross sections and individual local positions. Velocity field simulation in several cross sections shows a very unstable flow field, which originates in the tracheal laryngeal jet and propagates far downstream with the

formation of separation zones in both left and right airways. The RANS simulation agrees with the experiments in almost all the cross sections and shows unstable local flow structures and a quantitatively acceptable solution for the time-averaged flow field.

**Keywords** Human lungs · Realistic tracheobronchial airways · Airway model · Tracheobronchial tree · Upper airways · Oscillatory flow · Waveform inspiration · Numerical simulations · Phase Doppler anemometry

## 1 Introduction

In the past 15–20 years, some attention has been paid to targeted pharmaceutical aerosol delivery to treat conditions such as chronic obstructive pulmonary disease (COPD) and local tumors that can exist in some parts of the lungs. The administration of insulin and vaccines through this route is also a topic of current research, although insulin delivery in particular requires additional study, as pointed out by Zargoulidis et al. (2011).

Nevertheless, together with the increased interest in widening the drug's administration through inspiration, there are barriers in terms of insufficient information to advance and apply this treatment. Despite the appreciable progress made in this area recently, our knowledge of the mechanisms of the flow field, as well as the transport of particles and their subsequent deposition in the various sites of the respiratory tract, is insufficient. An accurate prediction of the flow in the extrathoracic airways and the upper branches of the tracheobronchial tree has not yet been achieved. It is evident that numerical predictions of particle deposition can only be accurate after single-phase CFD models have been verified.

---

**Electronic supplementary material** The online version of this article (doi:10.1007/s10237-015-0701-1) contains supplementary material, which is available to authorized users.

---

✉ Miroslav Jicha  
jicha@fme.vutbr.cz

<sup>1</sup> Brno University of Technology, Technicka 2896/2,  
61669 Brno, Czech Republic

For any study of this kind, a model of the human airways that simulates the real structure must be specified. For many years the most widely used model has been the idealized symmetrical Weibel A model (Weibel 1963), which simplifies the lungs' geometry. The Horsfield model (Horsfield et al. 1971) takes asymmetry into account, but it only gives lengths, diameters and branching angles between coplanar parent and daughter branches. As mentioned by Nowak et al. (2003), there are dramatic differences between the idealized generic models and a realistic one. Similarly, Kaye and Phillips (1997) showed that using Weibel's data leads to erroneous estimates for local deposition efficiency in the lung. On the other hand, when looking at the overall efficiency of particle retention, several modeling studies using Weibel's data have shown relatively good agreement with experimental data (e.g., Taulbee and Yu 1975).

Another approach to creating a model of the respiratory tract is to use scans of an actual living human using several imaging techniques. This approach limits images to the third generation of the tracheobronchial (TB) region. Another modeling technique is based on "in vitro" preparations of human lungs taken from a cadaver combined with high-resolution CT. Such models are very rare (e.g., Schmidt et al. 2004), because of complexities in acquiring samples of the human lung.

Nowadays, it is generally accepted that full 3D computational modeling using CFD codes is suitable and very useful when seeking information about local deposition (Longest et al. 2006). The flow in the airways of the respiratory tract is typically turbulent, transitional laminar/turbulent and laminar, depending on the inlet flow rate and on the branching generation. The steady flow rates typically used in published numerical and experimental studies are 7.5, 15 and 30 L/min, reflecting sedentary, low, and medium physical activities respectively. Several papers deal with laminar flow, such as Pigliione et al. (2012), who solved the flow field in the central airways where a laminar flow is expected. Li et al. (2007) solved the upper tracheobronchial tree with realistic transient waveform inspiration and proved that secondary flow occurs during flow deceleration. Ghalati et al. (2012), meanwhile, analyzed the flow field in the upper airways and mouth/throat cavity with micro- and nano-particle deposition.

As for the turbulent flow, many papers have studied appropriate turbulence models that are suitable for the multi-branching geometry of the human respiratory tract for transient laminar/turbulent and turbulent flow. The standard  $k-\epsilon$  model is not recommended due to its larger dispersion. Zhang and Kleinstreuer (2003) suggested the LRN  $k-\omega$  model, but Jayaraju et al. (2007) later suggested the SST  $k-\omega$  model, although mainly for the mouth/throat configuration with the glottis area. Later Zhang and Kleinstreuer (2011) concluded that the best agreement with the experi-

ments performed by Johnstone et al. (2004) was obtained when using the SST  $k-\omega$  model. However, Ghahramani et al. (2014) used the LRN  $k-\omega$  and the LRN  $k-\epsilon$  model for the realistic nasal/upper airway. They claimed that between the two equation turbulence models, the LRN  $k-\epsilon$  model was more appropriate for the simple transitional flow in a converging-diverging nozzle model of the glottis area.

As computational capacity has increased greatly over the last decade, one can see the direct solution of the laminar, transition and turbulent flow fields being applied instead of a turbulence model. Due to the extreme computational demand, direct numerical solution (DNS) is practically unachievable. However, Lin et al. (2007) presented one of the first attempts to simulate the flow field in the turbulent structures of the supraglottis, the glottis, the subglottis and the main-stem bronchi. They confirmed the existence of the secondary flow and Taylor-Görtler vortices that are associated with high wall turbulent shear stress. Ball et al. (2008) used DNS with the lattice Boltzmann method to simulate the airflow inside an idealized human upper airway with a short upper part of the trachea. The simulations were performed for a steady 10 L/min airflow (which is a very low flow rate; for values below 12 L/min, a laminar regime is generally assumed) and no inhalation wave. The number of control volumes for this case was 148 million. Recently, Wang and Elghobashi (2014) have solved the nose cavity with a short upper part of the trachea and with a very limited length of the laryngeal jet using the DNS-lattice Boltzmann. They solved steady inflow and outflow (not the breathing cycle) and the model contained 208 million voxels. From this, assuming higher flow rates of 30 L/min and even higher and a full inspiration phase, it is obvious that the DNS-Navier-Stokes and DNS-LBM are still beyond a practical use.

An "affordable" approach would be to use Large Eddy Simulation (LES), which resolves large eddies, while the smallest ones are modeled with an appropriate subgrid scale model. Luo et al. (2004) compared the results of laminar,  $k-\epsilon$  and LES models in a simple airway model with a glottis-like jet area and concluded that before the constriction, all the models agree with each other. However, they differ downstream of the constriction, with the conclusion being that the  $k-\epsilon$  model is too dissipative (more spreading) and that only the LES model is capable of capturing instantaneous eddy formations and flow separation in laminar, transitional and turbulent flow regimes. Mihaescu et al. (2008) compared  $k-\epsilon$ ,  $k-\omega$  and LES models in a realistic pharyngeal airway model and found differences of 45% between the  $k-\epsilon$  and the LES mean axial velocities calculated in the pharynx region. These differences were much lower (within 30%) in the case of the  $k-\omega$  model. Cui and Gutheil (2011) used LES, LRN  $k-\omega$  and SST  $k-\omega$  in an idealized human mouth-throat configuration for steady inspiration flow. Their results show that

both the  $k$ - $\epsilon$  and  $k$ - $\omega$  models behave similarly upstream of the glottis, but downstream of the glottis, the LES is better when compared with SST  $k$ - $\omega$ , but not remarkably so. Just downstream of the glottis, both models show some discrepancies.

As for the boundary conditions, most CFD simulations to date have employed a fixed boundary condition, such as uniform or axially symmetrical velocity profiles at the mouth inlet and a typical zero gradient outlet boundary or zero static pressure at the end of the airway. Huang et al. (2013) resolved the flow field in the upper respiratory airways with a realistic breathing mechanism, namely the expansion of the pleural cavity at the bottom of the extrathoracic airway, using the LRN  $k$ - $\omega$  turbulence model. They found that the velocity profiles in the mouth cavity and tracheal tube are modified remarkably; the separation and reattachment caused fluctuating turbulence intensity and secondary flow with extra peaks in the trachea region. These findings clearly show the importance of correct outlet boundary conditions, which, unfortunately, are very difficult to acquire.

Most of the published CFD results were obtained for steady inspiration (Agnihotri et al. 2014; Ghalati et al. 2012; Luo et al. 2004; Mihaescu et al. 2008; Chen and Gutmark 2014; Cui and Gutheil 2011; Pigliione et al. 2012), which is understandable because of the enormous computational time needed to simulate an entire breathing cycle (weeks). Studies that simulate transient inspiratory flow focus on particle deposition rather than detailed flow field dynamics, or they solve just the upper airways (the mouth, throat and trachea) when experimental results are available. According to Soni and Aliabadi (2013), particle deposition strongly depends on time release during inspiration, emphasizing the importance of flow field development during the inspiration phase. From our previous experiments in the realistic upper tracheobronchial tree using PDA (Jedelsky et al. 2012), it follows that during the inspiration period, turbulent intensity increases from about 1 % up to 20 %. This can be attributed to temporal development of the laryngeal jet.

Despite the appreciable progress made recently, there is still considerable uncertainty concerning the complexity of the flow field inside the human lung. Longest and Holbrook (2012) also emphasized the need for improved experimental data sets to better validate computational predictions in local regions. As pointed out by Chen and Gutmark (2014), despite significant effort directed at numerical modeling, an accurate prediction of the flow in the extrathoracic airways has not been achieved. In this article, the authors aim to help fill the gap between predictions and experiments. In both the modeling and experiments, identical realistic models were used for inspiratory flow with identical boundary conditions with sinusoidal inspiration/expiration, proving that the RANS model can correctly predict the basic flow field and its features.

## 2 Methodology

### 2.1 Models of the tracheobronchial tree

The lung model contains realistic geometry for the throat, trachea and tracheobronchial tree up to the fourth generation. The first part of the model (i.e., the throat and the upper part of trachea) was acquired through CT at St. Anne's University Hospital in Brno, Czech Republic by scanning a live adult volunteer. The lower part of the trachea and the TB tree was acquired in the form of tabulated data from the Institute of Anatomy and Cell Biology at Justus-Liebig-University in Giessen, Germany (see Schmidt et al. 2004). This model contains 17 generations (according to Horsfield notation), but for our purposes, the model was terminated at the third generation on the left side and the fourth generation on the right side of the lungs. For details of the manufacturing and technology used for the cast of the human airways, see Lízal et al. (2011). We present here just a short summary of the major steps. At first, the digital geometry of the human airways was transformed into the stereolithographic data format (.stl). Then a soluble core of the cast was produced from the stl data using a rapid prototyping method called Fused Deposition Modelling. Optically transparent silicone, Sylgard 184 (Dow Corning), was then applied to the core by brush coating. The core was regularly rotated to provide uniform thickness of the silicone layer. The silicone was cured for 10 min at 150 °C. Subsequently, the core was dissolved, and a final 0.1 mm layer of silicone was applied to the inner surface of the cast to smooth out imprints left by the coarse core and provide full optical transparency. Finally, the shape of the cast was maintained with a wire frame connected to the inlet metal cylinder by a clamp and to the outlet metal cylinders by a cyanoacrylate adhesive. The dimensions of the individual generations are given in Table 1 (note that diameters are averaged over the length of an individual generation). The inclination angles were measured with the trachea axis fixed in the vertical position. The model can be seen in Fig. 1.

### 2.2 Numerical solution and settings

Numerical simulations were performed with CFD code on CCM+ version 8.02. The SIMPLE algorithm with second-order upwind discretization was selected. The mesh contained approximately 2.7 million polyhedral control volumes, with 10 prismatic layers in the wall region. This mesh was determined to be sufficiently fine in order to achieve good quality in cross sections of the airways with a value of  $y^+ < 1$  and fulfill the requirements set for the LRN turbulence model used. The average cell size in the core of the model was 0.5 mm, and the time step was set to 0.001 s. The maximum volume average of the Courant number at peak inspiration was 4. The calculations were performed on

**Table 1** Dimensions of the individual generations

Branch	Gen. (-)	Length (mm)	Diameter (mm)	Inclination angles to coronal plane <sup>a</sup>	Inclination angles to sagittal plane <sup>b</sup>
Trachea	0	117	16.1	0°	0°
<i>Left side of the tracheobronchial tree</i>					
L1	1	42	10	60°	8°
L2	2	16	6	109°	10°
L3	2	7	6	33°	4°
L4	3	3	6	146°	153°
L5	3	6	5	68°	-4°
L6	3	10	6	27°	11°
L7	3	9	5	-70°	78°
<i>Right side of the tracheobronchial tree</i>					
R1	1	13	13	-48°	0°
R2	2	24	9	-26°	2°
R3	2	21	8	-104°	117°
R4	3	6	8	-23°	31°
R5	3	14	6	-81°	-37°
R6	3	6	8	-130°	-142°
R7	3	9	6	-124°	105°
R8	4	7	5	20°	77°
R9	4	4	7	-20°	1°
R10	4	4	5	-107°	-100°
R11	4	8	4	-59°	77°

<sup>a</sup> 0° means in the direction of gravity/down, positive angle means inclination to the left-hand side, negative angle means inclination to the right-hand side, maximal angle = 180° means in the opposite direction of gravity

<sup>b</sup> 0° means in the direction of gravity/down, positive angle means inclination to the back (in dorsal direction), negative angle means inclination to the front (ventral direction), maximal angle = 180° means in the opposite direction of gravity)

a computer equipped with two Intel Xeon E5-2690 processors, and the total run time for the entire inspiration cycle was approximately 330 h. Each time step was considered to have converged when the residuum of the continuity and momentum equations reached  $10^{-4}$ .

Computational modeling was performed for the whole inspiration/expiration breathing regime for two tidal volumes (0.5 and 1 L), with a complete breathing cycle taking 4 s. This corresponds to a minute ventilation of 7.5 and 15 L/min, representing a sedentary regime and deep breath, respectively. The breathing regime was simulated by a sinusoidal curve. For the turbulent flow field, the SST  $k-\omega$  model with a low-Reynolds number modification was used.

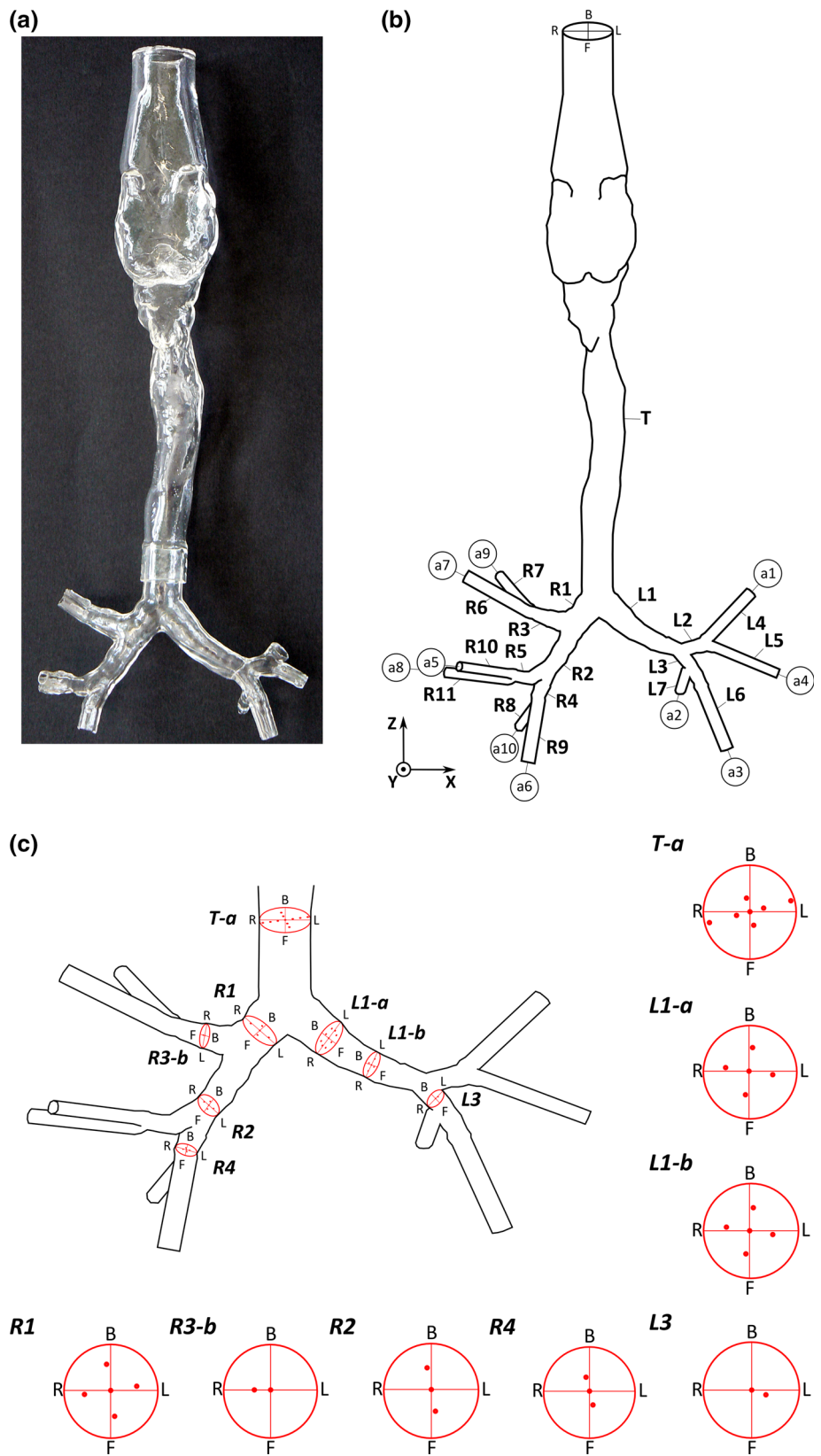
The boundary conditions were set according to experimental settings. This means zero pressure resistance at the entrance to the trachea (ambiance), which in other words is the pressure “outlet” condition at the mouth according to the CFD setting and flow rate distribution in 10 terminal outlets/terminating airways marked a1–a10 (see Fig. 1). More specifically, the flow rate through the model was driven by a suction action through the terminal airways rather than by

the inlet flow rate ascribed at the mouth. As for the turbulence intensity, several papers that focus on the respiratory tract recommended the value of turbulence intensity to be between 0.01 and 0.05. In addition, based on our measurements with PDA (Jedelsky et al. 2012), the turbulent intensity during the inspiration phase varies from 1% at the entrance up to 20%. However, Heenan et al. (2003) concluded that varying turbulence boundary conditions had little effect on the final results with idealized mouth–throat geometry. We assumed a turbulent intensity of 0.01 at all terminating airways. The flow rate distribution to individual airways was measured during the experiments and used as negative “inlet” velocity boundary conditions with a flat velocity profile for numerical simulations. The velocities at the terminating airways were controlled by the formula below:

$$v_i(t) = \frac{V_{t_i} \cdot \pi}{A_i \cdot T} \cdot \sin\left(\frac{2\pi}{T} \cdot t\right) \quad (1)$$

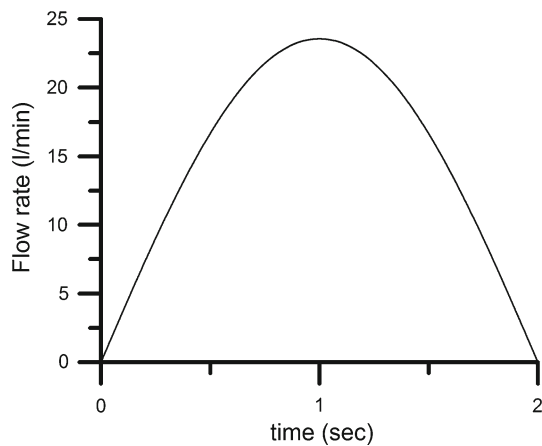
where  $v_i(t)$  is the “inlet” velocity prescribed in the terminal airways (at outlet) at a given time,  $V_{t_i}$  is tidal volume (inhaled volume per breath) for a specific airway,  $A_i$  is the cross-

**Fig. 1** **a** Geometry of the realistic physical cast of the human airways. **b** Computational model of the respiratory tract with trachea (*T*), and *left* (*L*) and *right* (*R*) tracheobronchial trees and airway terminations *a1–a10*. **c** The location of stations within cross sections and the positions of local points where measurements were taken and compared with CFD simulations



**Table 2** Distribution of air flow at terminating airways for minute ventilation 7.5 L/min

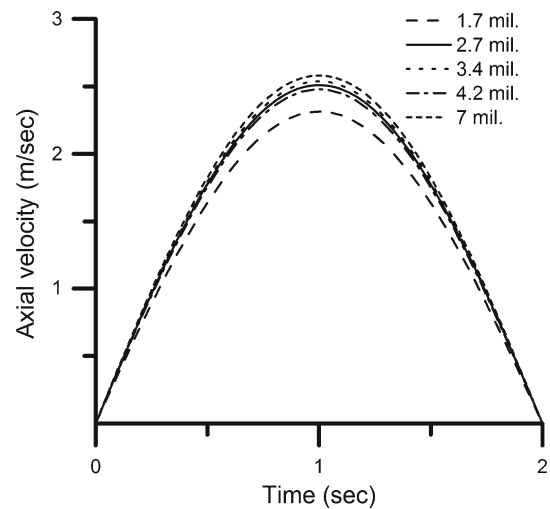
Airway	Terminating airways "outlet" boundary area A (m <sup>2</sup> ) × 10 <sup>-5</sup>	Tidal volume (inhaled volume per breath) V <sub>t</sub> (L)	Fraction of the total flow rate (-)
a0	45.162	0.5	1
a1	2.486	0.037	0.074
a2	1.719	0.033	0.066
a3	2.778	0.061	0.122
a4	1.759	0.038	0.076
a5	1.358	0.051	0.102
a6	3.284	0.071	0.142
a7	2.776	0.057	0.114
a8	1.725	0.051	0.102
a9	1.728	0.052	0.104
a10	1.679	0.049	0.098

**Fig. 2** Volume inlet flow rate as a function of inspiration time

sectional area of an individual airway,  $T$  is the breathing period, and  $t$  is the time step.

The time step was set to 1 ms, and the duration of the whole breathing cycle was 4 s, with inspiration and expiration always lasting 2 s each. The distribution of the air flow rate in the 10 individual terminating airways for a sedentary regime of 7.5 L/min is shown in Table 2, while the variation of the inlet volume flow rate over time is illustrated in Fig. 2.

Grid dependency test was performed on 5 different meshes with 1.7, 2.7, 3.4, 4.2 and 7 million control volumes. Results of this test are presented in the form of temporal development of the center-line velocity during the breathing cycle in the trachea in the cross section T-a in Fig. 3. As can be seen, there is a substantial difference between the course mesh of 1.7 million and the other finer meshes. However, results obtained on the chosen mesh of 2.7 million control volumes deviates negligibly from the finest mesh of 7 million control volumes.

**Fig. 3** Grid dependency test—temporal development of the center-line velocity at cross section T-a

### 2.3 Turbulence model

From several papers, which are cited in the introduction, it is clear that there is continued controversy about whether  $k-\epsilon$  (and its variants) or  $k-\omega$  (and its variants) is better. The reason for this certainly lies in the highly complex geometry of the respiratory tract, where there is quite different geometrical intricacies and the transition from laminar to turbulent and back again to laminar during the ascending and descending phases of inspiration. We can find a backward step-like glottis segment with a partial constriction and a stenosis-like structure. At the same time, the developing laryngeal wall jet may resemble something between a plane and round confined jet. We can find regions of separation and reattachment again downstream of the glottis or in the first left and right bronchial generations, and we can find segments with a simple entrance channel flow (in the lower airways) and segments with an impinging jet like in the area of the carina. From this, it is evident that in certain lung segments, the  $k-\epsilon$  model might perform well, while it may not for others. The converse also applies for the  $k-\omega$  model. For example, for flows in the nasal cavity that exhibit low levels of swirl, the  $k-\epsilon$  model can be deemed sufficient. If we reject the use of DNS and/or LES, there are two possible turbulence models to choose: the  $k-\epsilon$  or  $k-\omega$  family of models.

Looking at the history of the  $k-\epsilon$  model, it follows from Leschziner (1993) (see Introduction to the modeling of turbulence, VKI Lecture series 1993–2002) that the  $k-\epsilon$  model has its limitations. It has an insufficient response to streamline curvature and difficulties with separated flow (in the respiratory tract, this happens in the glottis area—see also Mihaescu et al. (2008, figure 6a), and the first generation of the left and right TB tree). It does not handle swirling flows well (downstream of the glottis area, we can see a swirling jet, which

although confined, exhibits partial rotation in the trachea during the inhalation phase). There is also the round-jet/plane-jet anomaly; the laryngeal confined wall jet is neither a round- nor plane-jet but somewhere in between (see the typical shape of cross sections at and before the larynx, (e.g., [Johnstone et al. 2004](#)). Generally, predictions with  $k$ - $\varepsilon$  show a faster spread for a round-jet than for a plane-jet, while experiments show the opposite. This also implies that the  $k$ - $\varepsilon$  model is more dispersive.

As stated by [Pope \(2003\)](#), for flows far removed from a simple shear (e.g., an impinging jet and three-dimensional flows) the  $k$ - $\varepsilon$  model can fail profoundly. After [Wilcox \(2000\)](#), because of its inability ( $k$ - $\varepsilon$  model) to respond to adverse pressure gradients, the  $k$ - $\varepsilon$  model is inaccurate for separated flows and much harder to implement for transitional flows. In this book, there are numerous examples of the performance of the standard and RNG  $k$ - $\varepsilon$  models and  $k$ - $\omega$  models. It was shown that even the RNG  $k$ - $\varepsilon$  model consistently predicts separation bubbles that are much longer than measured. Both  $k$ - $\varepsilon$  and  $k$ - $\omega$  models, however, perform badly for anisotropic turbulence.

It is generally accepted that most of the problems with the  $k$ - $\varepsilon$  model lie in the  $\varepsilon$  equation. The standard  $\varepsilon$  equation for separated flows gives far too large near-wall values of mixing length (i.e., much less damping, so the model fails to predict the correct length of a recirculation bubble).

Some researchers have performed comparative studies of different turbulence models in the respiratory tract. The airflow in the human upper airways is mostly in the transitional flow regime (i.e., there are portions of airways where the flow is laminar and other portions where the flow is turbulent). From [Zhang and Kleinstreuer \(2003\)](#), it is clear that the LRN  $k$ - $\varepsilon$  model fails to predict the laminar velocity profile downstream of the glottis area, whereas the LRN SST  $k$ - $\omega$  predicts the onset of turbulence even for laminar flow. From [Zhang and Kleinstreuer's \(2011\)](#) study, it follows that the RNG  $k$ - $\varepsilon$  amplifies the flow instabilities after the glottis constriction, and hence it cannot capture the laminar flow behavior at relatively low Reynolds numbers. The LRN  $k$ - $\varepsilon$  model fails to simulate the transition to turbulent flow. On the other hand, the LRN  $k$ - $\omega$  model with an appropriate damping function appears to be capable of reproducing the behavior of laminar, transitional and fully turbulent flow in complex 3D constricted geometry. However, [Ghahramani et al. \(2014\)](#) claim that the LRN  $k$ - $\varepsilon$  model performs better than the LRN  $k$ - $\omega$  model when comparing the mean flow velocities and turbulence intensity in the centerline of a converging/diverging nozzle. [Pollard et al. \(2012\)](#) provide an overview of the methods and the cautious interplay between simulations and experiments as well as the interdependency of outlet/inlet conditions. They also suggest that the  $k$ - $\omega$  model is a good choice among the RANS models.

From several papers, it follows that the SST  $k$ - $\omega$  model is good in attached boundary layers and some separated flows where the separation point is dictated by the geometry rather than by an adverse pressure gradient. Many authors have shown that the SST model predicts recirculation better than the traditional  $k$ - $\varepsilon$  model, but these comparisons are always difficult to interpret because one model solves the viscous sublayer and the other uses a wall function approach.

Because both the  $k$ - $\varepsilon$  and  $k$ - $\omega$  models use the Boussinesq approximation, they are unable to predict anisotropy. This limits their performance in flows with strong curvature, which is important for near-wall effects and flows with secondary flows.

The great advantage of the SST model is its robustness and ease of use. The SST variation of the  $k$ - $\omega$  model also leads to marked improvements in performance for non-equilibrium boundary layer regions, such as those found close to separation. However, such modifications should not be viewed as a universal cure. For example, SST is less able to deal with flow recovery following re-attachment. However, our analysis led us to select the LRN SST  $k$ - $\omega$  model, because this incorporated the best of both the  $k$ - $\varepsilon$  and  $k$ - $\omega$  models. It may also be a good option for RANS simulations, which we will demonstrate later in the results. The basic transport equations and constants of the model can be found in the STAR-CCM+ User Guide, Version 8.02 on pp. 3072–3075. We will also show that in separation regions with a very strong curvature, the model performs within certain limitations.

## 2.4 Experiments

This chapter documents the arrangement of the experiment, the setup of the phase Doppler anemometer, and the methods used for data acquisition and processing. The experimental equipment used to study the air-particle flow consisted of an oscillating flow source, a particle generator, an airway model, and a 1-component Phase Doppler Analyzer (PDA). To measure the velocities of the flow field, a monodisperse aerosol di-2-ethyl-hexyl sebacate (DEHS) was used as tracer particles mixed with air. The sizes of the aerosol particles were 1, 3 and 7  $\mu\text{m}$ . Whether a particle will be a good tracer is usually judged based on the Stokes number (Stk). According to [Tropea et al. \(2007\)](#), particles with an  $\text{Stk} < 0.1$  return an acceptable flow tracing accuracy with errors below 1%. In our experiments, the  $\text{Stk}$  was always  $< 0.1$ , even for the 7  $\mu\text{m}$  particles and the highest flowrate, with the only exception being in cross section L3 where the maximum  $\text{Stk}$  was 0.118, but this still results in acceptable flow tracing accuracy. The experimental results presented here were acquired using 3  $\mu\text{m}$  particles, because the quality of PDA data was higher than with the 1  $\mu\text{m}$  particles due to better PDA data validation and because the 3  $\mu\text{m}$  particles were still good flow tracers. The results acquired with 7  $\mu\text{m}$  particles did not show

any significant differences, which concurs with the Stokes number. The aerosol was produced with a TSI Condensation Monodisperse Aerosol Generator (model TSI 3475, TSI Inc. Shoreview, MN, US) (1—see Fig. 3), followed by a TSI PAM 3375 (2) to measure the size and concentration of particles. The particles were generated through the controlled heterogeneous condensation of DEHS vapor on small particles of sodium chloride. This process enabled the acquisition of relatively high concentrations of monodispersed aerosol ( $10^6$  particle/cm<sup>3</sup>) at the generator output. Approximately half of the generated particles were distributed to an elastic bag (3) fixed to the upper part of the lung cast, while the remaining half were guided to a mixing chamber (5). In this chamber, DEHS was mixed with the air and split over 10 small diameter tubes that were connected to the outlets of the lung cast. Breathing was simulated with a Hoerbiger NZK 6100-0400 AG pneumatic cylinder (6) driven by a TG Drives TGH3 step motor (TG drives, s.r.o., CZ). The servomotor provided a sinusoidal piston motion with appropriate frequency and amplitude to represent the inspiratory and expiratory phases of the breathing cycle.

The velocities at selected points in the cross sections were measured with a Dantec PDA (Dantec Dynamics A/S, Skovlunde, Denmark) (7) with an Ar-Ion+ laser 5500A-00 ILT, 300mW (Ion Laser Technology, Salt Lake city, UT, US). The laser beam had a 2.5 mm diameter and a 514 nm wavelength. The beam was split using 58N10 transmitting optics into two beams separated by 60 mm with a focal distance of 310 mm. An ellipsoidal probe volume was formed at the beam crossing using a transmitting lens with a 310 mm focal length. The frequency of one of the beams was shifted by 40 MHz. The dimensions of the measuring volume were  $0.25 \times 0.25 \times 0.3$  mm. The first-order refracted light was detected at a forward scattering angle of  $50^\circ$ – $65^\circ$  through a receiving lens with a 310 mm focal length by a Dantec 57X10 receiving optics with three photomultipliers and recorded and analyzed in a computer (8). A Dantec 58N50 signal processor was set to measure the velocity within a range of  $-8$  to  $24$  m/s at 12 MHz bandwidth and within a range of  $-2.7$  to  $8.0$  m/s at 4 MHz bandwidth, depending on the flow regime. The obtained data were processed using the BSA Flow Software v2.1.

The velocity component perpendicular to the cross-sectional plane was measured in eight cross sections at several points/locations, depending on the individual cross section (see Fig. 1). The number of points in the cross sections ranged from 11 in the trachea to 2 in sections L3 and R3-b, with the low number of points in these sections resulting from reduced optical access to these cross sections.

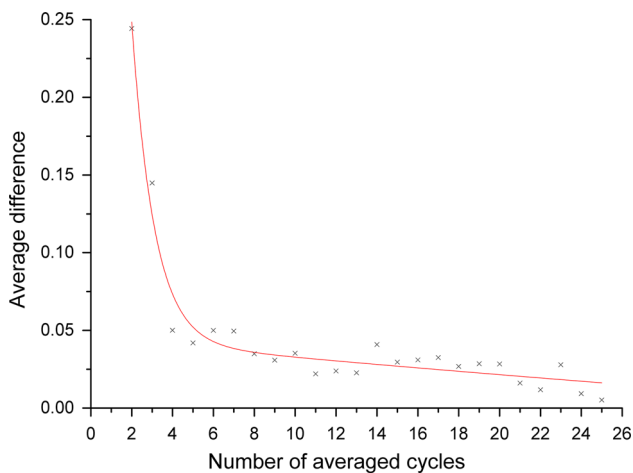
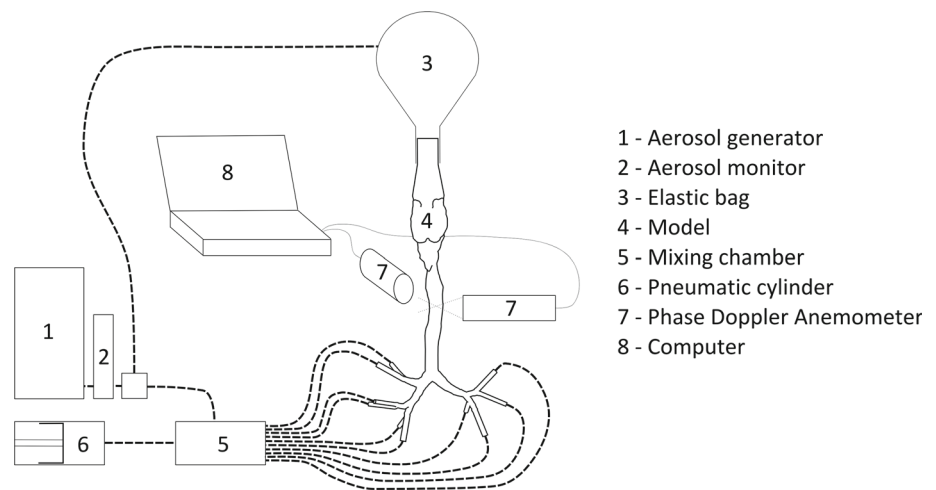
The transparent thin-walled airway model (chapter 2.1 and Fig. 1a) was oriented in such a way that the centerline of the measured tube was always vertically directed with the throat upwards. In each cross section, a local coordinate

system was set with its origin at the center and a Z axis parallel to the normal of the cross section. The model was fixed onto a frame mounted on a traversing mechanism with an accuracy  $>0.25$  mm for positioning during experiments. Thin model walls are required for optical access to the model without strong optical distortions if the airflow or particle transport with air as a carrier medium is being studied. This approach differs from the common experimental methods for optical flow studies in models, where liquids with a refractive index equal to that of the model material are used (e.g., Brücker and Schröder 2003). Our airway model is asymmetrical with non-circular cross sections and walls of varying thickness and curvature. The irregular shape of the model walls caused deflections and distortions in the light beam as it passed through, even though a thin-walled model design was used, so manual positioning and beam-crossing adjustment at each measurement point were compulsory. Near-wall PDA measurement was impossible, and the careful selection of sections for measurement was needed.

The PDA measured the axial velocity component (i.e. the velocity component normal to the corresponding cross section of a tube in the airway model) and the size and arrival time of individual air-borne aerosol particles flowing through the airway model. PDA was chosen over the simpler LDV to verify particle size and reduce unwanted sources of noise in velocity estimation, such as reflections and multiple-particle scattering. Afterward, the temporally local value of the mean axial velocity and fluctuating (root-mean-square, rms) axial velocity were estimated. In the computational modeling, the points were adjusted to match those of the experiments in order to compare results.

Our particle mixing system delivered a homogeneous air–particle mixture that was diluted in the chamber (5) (Fig. 4). The particle-laden airflow was incompressible, subsonic, isothermal, and viscous, with a high particle/air density ratio of 760, and the DEHS aerosol was non-hygroscopic and non-evaporating/non-condensing. Despite the relatively diluted aerosol (mean free path in the order of hundreds particle diameters) with concentration  $c$  in the range of  $10^3$ – $10^5$  particle/cm<sup>3</sup>, it allowed for high-frequency measurement of the velocity  $v$  with the typical number of particles measured per time (data rate) being in the kHz range. The data rate  $\dot{n} = v \cdot c \cdot S$  is proportional to the actual particle velocity, where  $S$  is the area of the measurement volume projected in the flow direction. This inherent property of laser Doppler-based methods applied to a dispersed flow causes a high data rate to appear at the peak velocity parts of the cycle, while drops in the data rate occur near alternations in flow direction.

The experiments were performed over a period corresponding to 8–10 full breathing cycles (the data presented here always used 9 cycles), because this number was found to be a compromise between the acquisition of statistically valid

**Fig. 4** Experimental stand**Fig. 5** Average differences in velocities calculated from increasing the number of cycles

velocity data and experimental cost. More measured cycles would have been excessively time consuming (43 positions at three regimes, several times repeated), and it would have required frequent and difficult cleaning of the model walls to remove deposited aerosol. The optical quality of the model walls was found to be inferior after several minutes of experimentation.

The effect of the number of cycles used for averaging was evaluated to ascertain how many cycles were needed to acquire statistically convergent results. For this purpose, measurement over 25 cycles was performed. The phase-averaged velocities were calculated successively for 2 cycles, 3 cycles, and so on up to 25 cycles. The average differences between averaged velocities in corresponding bins normalized by velocity were plotted in the graph shown in Fig. 5. This graph shows the gradual improvement in the precision of velocity estimates calculated from an increasing number of cycles. After the first four cycles, it is clear that the effect of adding more cycles decreases. The measurement was there-

fore performed for 9 cycles, which represents a statistically sufficient number while also being technically feasible.

Data acquisition was triggered by the oscillatory flow generator, with records starting at the beginning of the inspiration phase. The starts of consequent cycles were synchronized with the PDA data. Ensemble averaging of velocity data at constant phase bins was provided to acquire statistically valid velocity data in the individual positions. The calculation of the phase-averaged velocity was performed using a similar method to that of [Lyn et al. \(1995\)](#), who also used a laser Doppler measuring method. The velocity realizations that occur within the same phase bin constitute an ensemble at constant phase. It is important to note that the sampling frequency was irregular, because it depends on the arrival time of the particles in the measuring volume. The number of measured particles increased with increasing velocity. The total number of bins during the cycle was 133. The phase bin width was 30 ms. The number of particles in a bin varied from 10 at close to zero velocity to 900 at peak velocity. The experimental data are presented using both ensemble average and a condensed plot of raw data from all measured cycles in Fig. 5 onwards.

Distinct flow structures repeat in each cycle. Only small cycle-to-cycle variations caused by the naturally turbulent character of the flow appeared, so the overlapping did not lead to a smearing of the distinct temporal features in the signal, but it did improve the temporal profile readability of the relatively dilute flow by displaying more samples.

## 3 Results and discussion

### 3.1 Characteristics of mean velocity structures

The results of the CFD simulations and a comparison with the experiments are presented in Figs. 6, 7, 8, 9, 10, 11, 12, 13, 14,

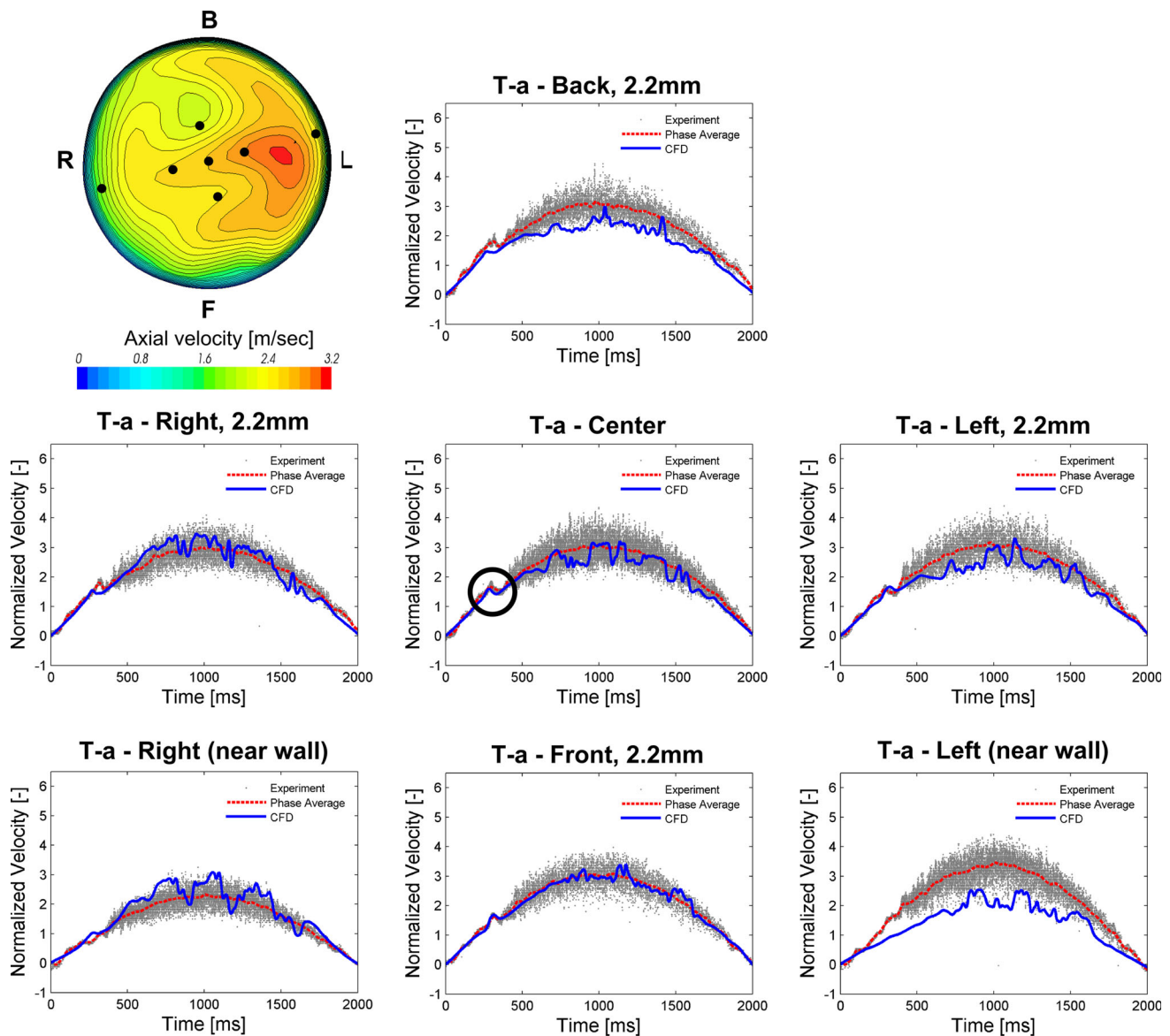


**Fig. 6** Temporal development of the normalized velocity at the tracheal cross section T-a

15 and 16 for just a tidal volume 0.5 L, cycle duration of 4 s, and the inspiration period due to the limited space available. In addition, the inspiration period is of paramount importance for the inhalation of aerosols and their deposition. The velocities are normalized with the peak inspiration velocity corresponding to a flow of 7.5 L/min at the inlet to the lung model, as calculated from equation (1). All figures document the axial velocity (i.e., the velocity perpendicular to the local cross section in selected cross sections T-a in the trachea, L1-a-L3 in the left TB tree, and R1-R4 in the right TB tree—see Fig. 1). The orientation in each cross section is depicted in Fig. 1 with the notation L-left, R-right, F-front and B-back. Inspiration started at time 0 s with zero velocity and ended on reaching time 2 s, at which point

the reversed flow of expiration began. The time step was 0.001 s.

### 3.1.1 Trachea T-a

This section (see Fig. 6) is 5 cm upstream of the carina. In this section, 11 monitoring points were distributed around the central point. Due to the limited number of figures, only seven of them are presented here. The velocity was measured in two radial directions at 2 and 3 points off the center, respectively. The diameter of the trachea in this section was 16.1 mm. The distance between individual points was 2.4 mm from the center, and the last points “L near-wall” and “R near-wall” are 0.8 mm from the wall.

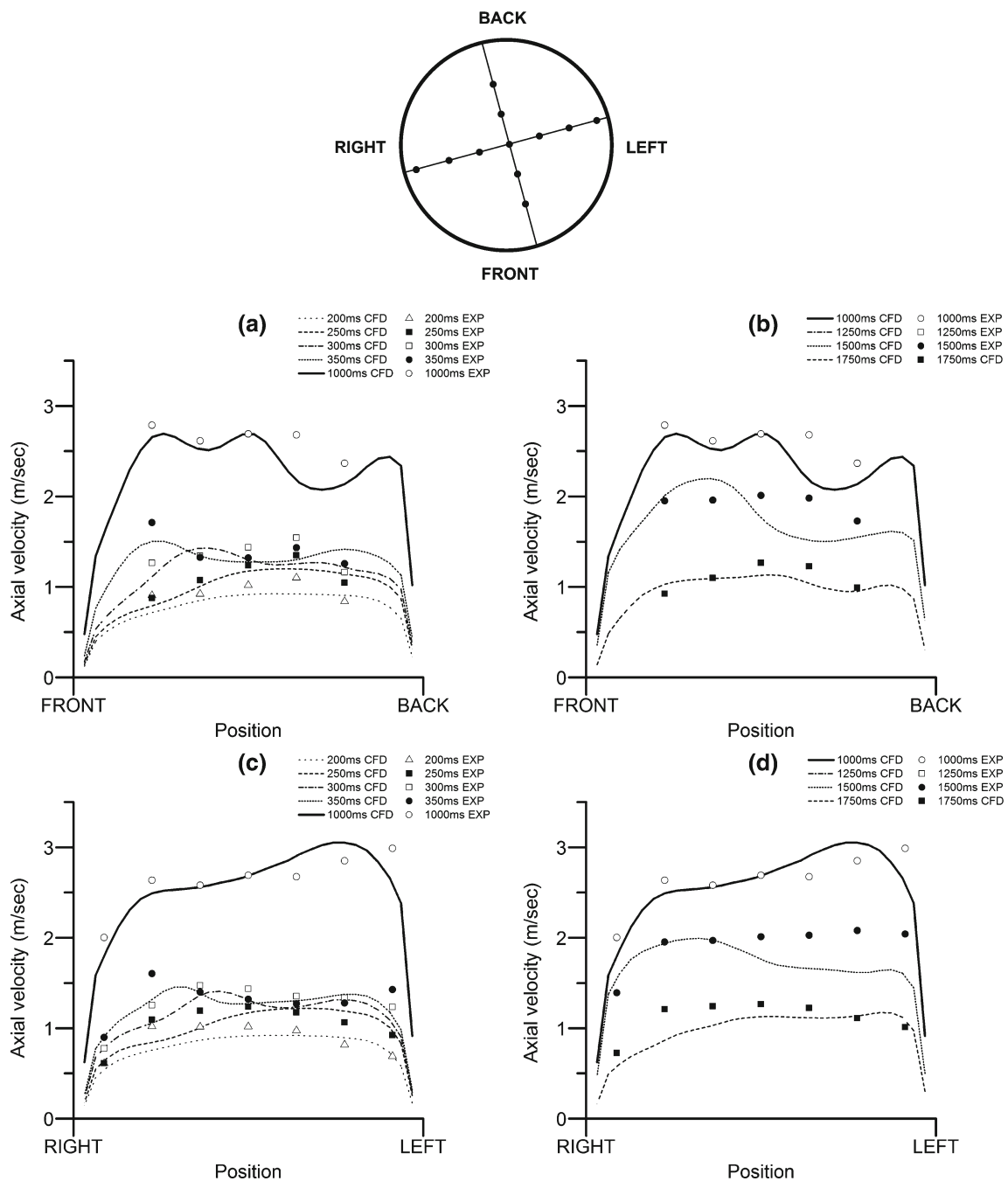


**Fig. 7** Velocity profiles during the ascending and descending inspiration phases in the trachea section T-a, **a** and **c** ascending phase, **b** and **d** descending phase

Both the experiments and simulations show large velocity fluctuations around the inspiration peak that begin approximately 0.5 s prior to the inspiration peak and extend more toward the end of the inspiration. Aside from these fluctuations, there is a short peak at approximately time 0.25 s that is practically visible in all positions across the section, and the experiments and numerical predictions are mostly in good agreement in most of points in the cross section. This peak

can be attributed to the transition in the laryngeal jet, which can be seen in Fig. 7, where the velocity profiles are presented for times 200, 250, 300 and 350 and 1000 ms (inspiration peak). We can see that at times before 250 ms, the laryngeal jet forms one maximum shifted to the left and back sides of the trachea (i.e., in the R–L and F–B planes). At 250 ms, the flow rate is about 8 L/min (see Fig. 2), which is considered to be a laminar regime, but at 350 ms, the flow rate increased

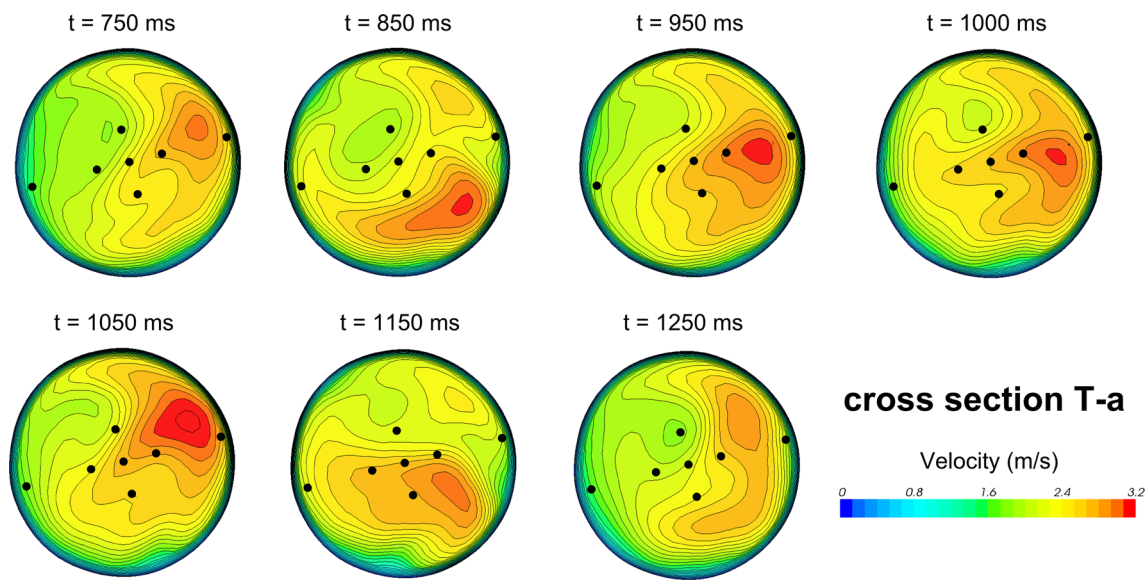


**Fig. 8** Time development of the velocity magnitude field in the tracheal section T-a

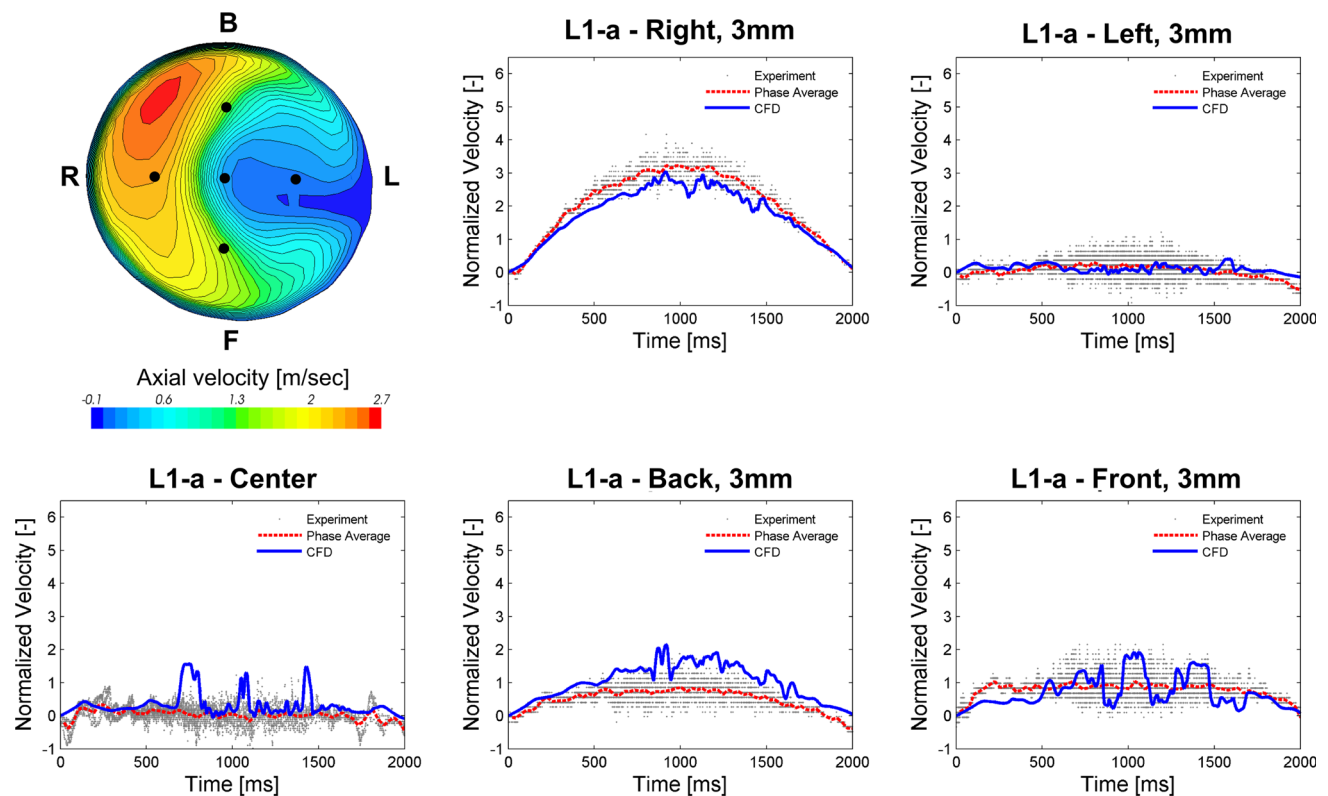


**Fig. 9** Temporal development of the normalized velocity at cross section L1-a

to about  $12L/\text{min}$ , which is considered to be the start of a turbulent regime with more intense mixing.

As the flow rate and Reynolds number increased, the laryngeal jet developed into two streams with a saddle profile, which can be observed at 300 and 350 ms. After these times, as the inspiration reached its peak, the profiles, mainly in the

R–L plane, recombined into one stream with a highly pronounced maximum to the left side of the trachea. In the F–B plane, the profile is highly irregular, still showing a tendency for two separate streams. What is interesting is how the flow pattern around the inspiration peak (i.e., from 750 to 1250 ms) retains its shape but with one maximum that rotates in a

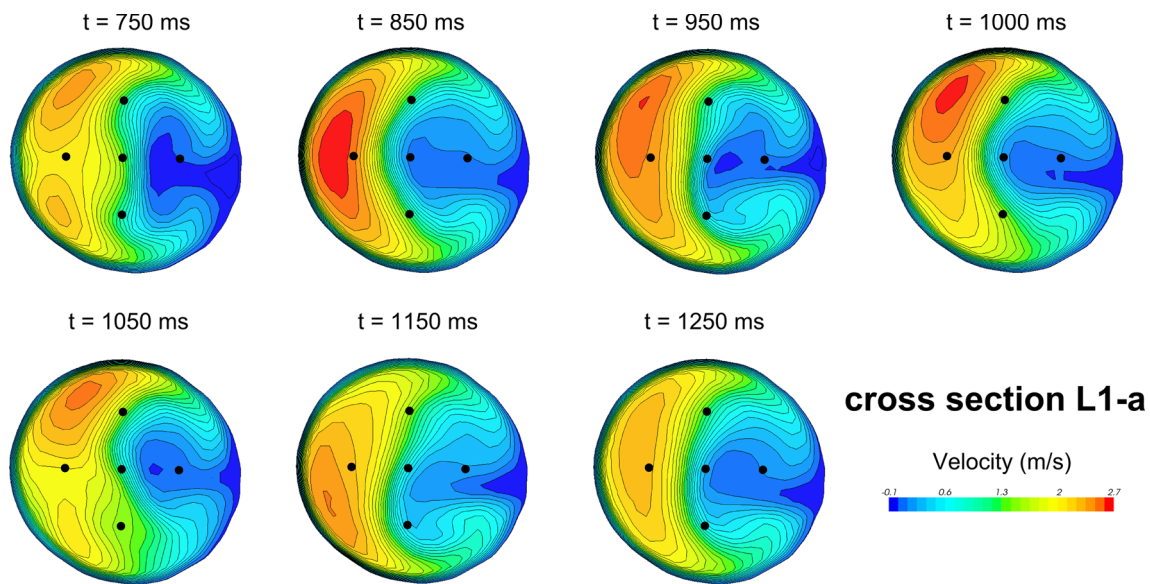


**Fig. 10** Time development of the velocity magnitude field in cross section L1-a

crested-like segment in the left side of the section. Changes in the shape of the velocity profiles can be attributed to both increased flow rate (i.e., the Reynolds number) and a sharply increased turbulent kinetic energy (TKE), as can be seen in Fig. 20a, b, where TKE is depicted as a function of the distance from the inlet at different times of the inspiration. The increased TKE is responsible for the redistribution of flow particles between the two streams of the laryngeal jet, and the velocity profiles therefore tend to equalize.

This all indicates that the flow at the end of the trachea is well mixed, which can be attributed to a very high increase in TKE. As can be seen in the Fig. 7a, c, where the velocity profiles are depicted, the agreement between the predictions and the experiments is qualitatively and, in several points, also quantitatively good. The trend is almost perfect in the Left–Right plane, and only the last point near the Left wall shows a small discrepancy. In this context, we need to remember that the distance of this point from the wall is just 0.8 mm, so we have to account for difficulties in positioning the PDA system so close to the wall and the small size of the measuring volume (of the order of tenths of millimeters) of two crossing laser beams.

After reaching 1250 ms, when the TKE reaches its maximum, we can observe a very interesting phenomena in the following descending phase of inspiration (see Fig. 8). The flow starts again forming two streams with two maxima, with a weak saddle velocity profile. One maximum is very distinctive, while the second is rather weak. Here we can observe an opposite trend to the ascending phase (i.e., with the decreasing flow rate, the TKE also decreases—see Fig. 22), although it is not as sharp as in the ascending inspiration phase. Comparing the velocity profiles in Fig. 7b, d, we can see very

good agreement between the predictions and experiments, and there is evidence that the flow approaches the pattern seen at the beginning of the inspiration. We can conclude that the development of TKE is responsible for the flow patterns that form during the ascending and descending inspiration phase.

As can be seen in Figs. 6 and 7, the predicted and measured velocity profiles at different times during the inspiration phase compare very well. The experimental points in the graphs show firstly an almost perfect qualitative agreement and secondly a quantitative agreement at most points in both the ascending and descending periods of inspiration. This proves that the SST  $k-\omega$  turbulence model can correctly predict the complicated flow structures of the temporarily developing laryngeal jet during both the ascending and descending inspiration phases. The model is also able to predict laminar regime at the beginning of the inspiration, the transition from laminar to turbulent when the flow rate increases, and the transition to laminar as the flow rate descends to the breathing reversal point. Although the model does not predict high-frequency fluctuations, the amplitude of the actual velocity oscillations agrees quite well with the experimental findings.

### 3.1.2 Left airways: cross section L1-a

Cross section L1-a is approximately one-third into airway L1 after the air splits at the first bifurcation. In this cross section, 9 points were distributed around the central point in which experiments were carried out (note that only 5 were selected here). Figure 9 depicts the time development of the inspiration phase. In the central point C, we do not see the

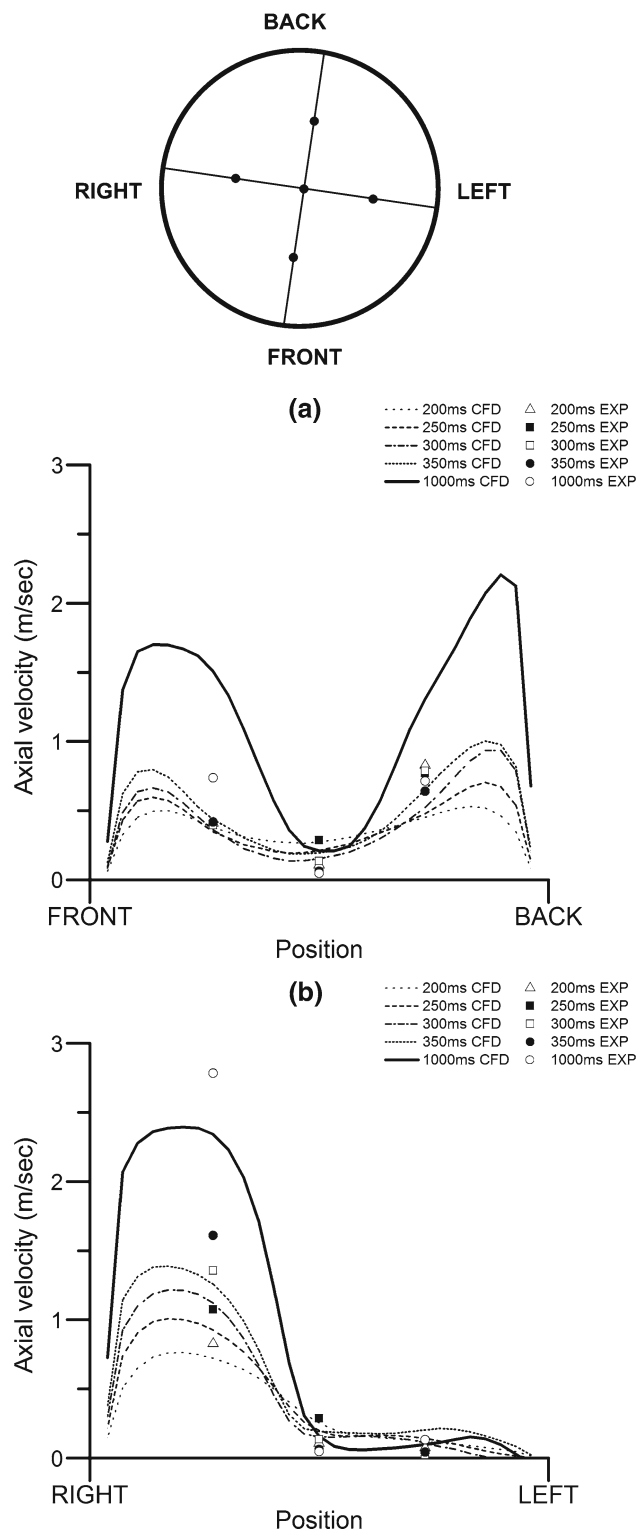


**Fig. 11** Velocity profiles during the ascending inspiration phase in section L1-a

typical sinusoidal character of the inspiration (i.e., no fluid stream is pushed through the airway in this region), which means a separation region was formed. From the time devel-

opment, it is clear that the separation region forms from the beginning of the inspiration (i.e., the flow rate does not have any impact on the separation region). From the images of the velocity field in Fig. 10, it is clear that the core of the flow field moved off-center toward the periphery along the semi-circle “Front–Right–Back” and thus followed the crescent-like core that was observed in the tracheal section T-a. Similar behavior can be observed in the location “Left,” which is placed deeply in the separation region with even a weak reversal flow. The locations “Front” and “Back” show certain symmetry around the line R–L, with the indication of a transition from the separation region to the core region with the reappearance of the typical sinusoidal curve. In the location “Back,” the weakest agreement between the experiments and simulation can be seen. This was caused by the point being located in the region with the highest velocity gradient and the associated uncertainty in its positioning.

Location “Right,” which is in the off-center core, shows the typical sinusoidal character. It is evident that there is practically no flow in the left side of the cross section. It is evident that there is practically no flow in the left side of the cross section. The development of the region with an almost stagnant flow (and a weak reversal flow in the separation region, which the velocity magnitude does not show) is also evidenced in Fig. 11. There is a comparison between the velocity profiles predicted and measured at the beginning of the ascending inspiration phase [i.e., for times 200, 250, 300 and 350 ms, and 1000 ms (the inspiration peak)]. We can observe how the width of the region of zero net flow is quite well predicted (see the Left side in the graph), but the velocity profiles in the Left–Right plane are underpredicted in the core region with a high-velocity flow, while overpredicted at the inspiration peak in the Front–Back plane. In the early stages of inspiration, the agreement is much better, especially on the Front side. However, qualitatively speaking, the velocity profiles are predicted quite well showing an almost zero net flow region in the plane Left–Right and strong saddle profiles in the plane Front–Back. However, experimental data namely on the Back side are clustered to indicate very little variation in time, while the computed profiles indicate substantial departures/ variations. We can partially conclude that the SST  $k-\omega$  model very well predicts the width and velocities in the zero net flow region in this curved airway, although it fails to correctly predict other local velocities

### 3.1.3 Left airways: cross section L1-b

The section lies approximately in the middle of airway L1, with 5 locations being monitored. Firstly, as can be seen in Fig. 12, the separation region that was observed in section L1-a disappeared and the flow reattached. This was also proven by the experiments. There is a successive enlargement of the core region in a horseshoe shape, which extends more

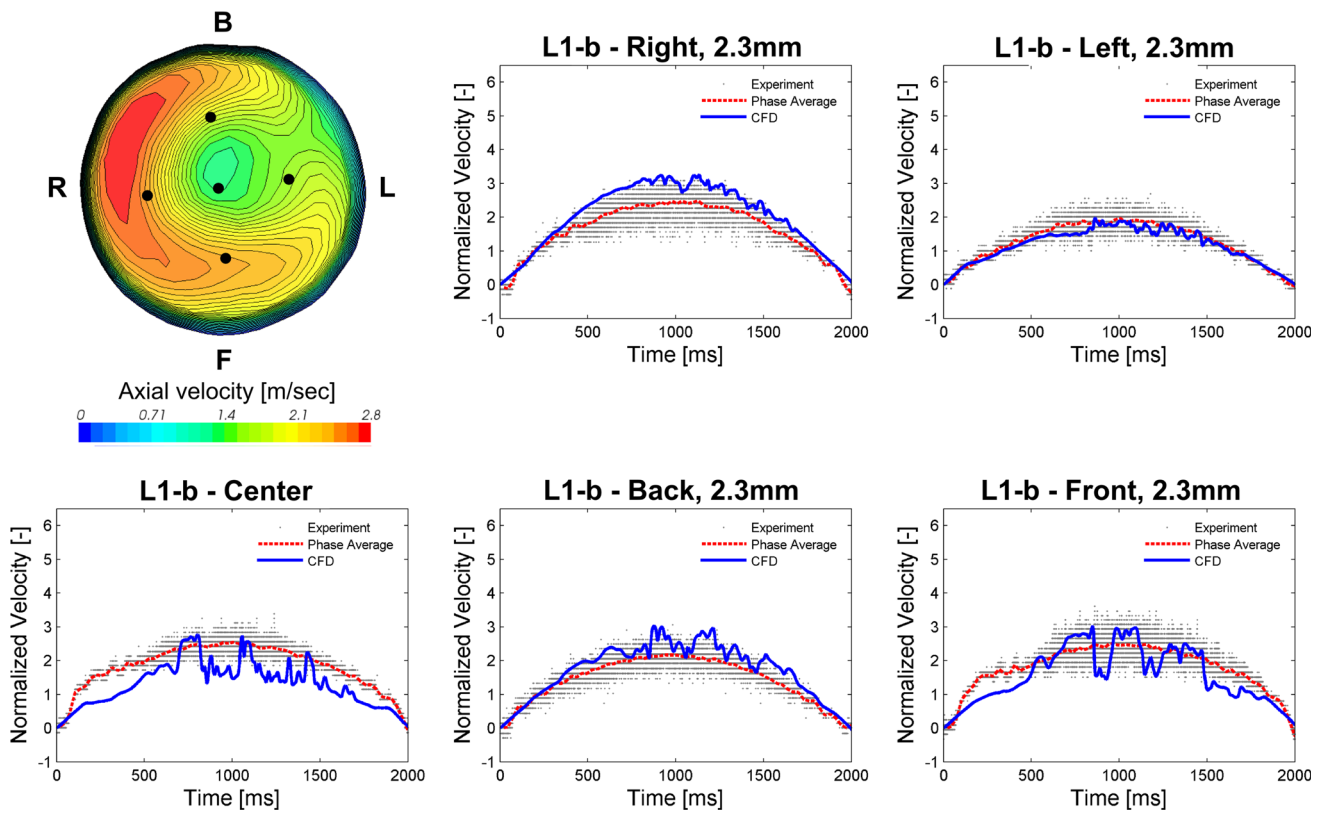


Fig. 12 Temporal development of the normalized velocity at cross section L1-b

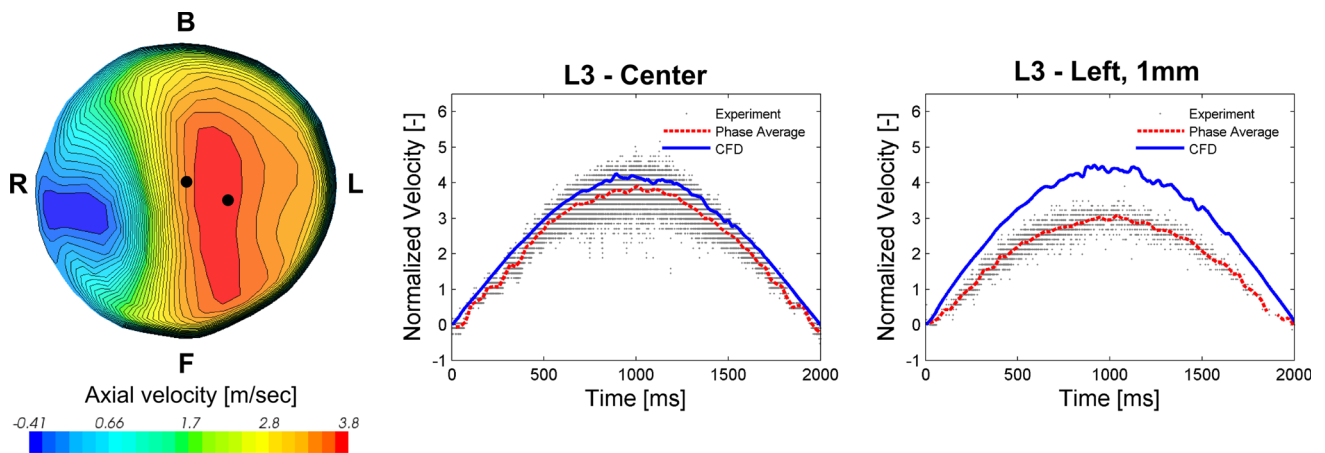


Fig. 13 Temporal development of the normalized velocity at cross section L3

tangentially (i.e., it turns along the F–R–B circumference). However, the “Left” location, as well as the “Center” location to a lesser extent, still shows an indication of the separation zone observed in the previous cross section L1-a. However, we can see a successive renewal of the sinusoidal character that shows a reattachment of the flow with oscillations around the inspiration peak. The predicted large oscillations in the flow structures still show an unstable characteristic of the flow field comparable with those in the L1-a cross sec-

tion. These oscillations suggest a movement of the horseshoe structure along the circumference of the cross section.

### 3.1.4 Left airways: cross section L3

Section L3 (see Fig. 13) is in airway L3. According to the numerical predictions, a new separation zone appears on the opposite side to airway L1. Unlike in section L1-a, where a stagnant separation zone is observed, a small region with a

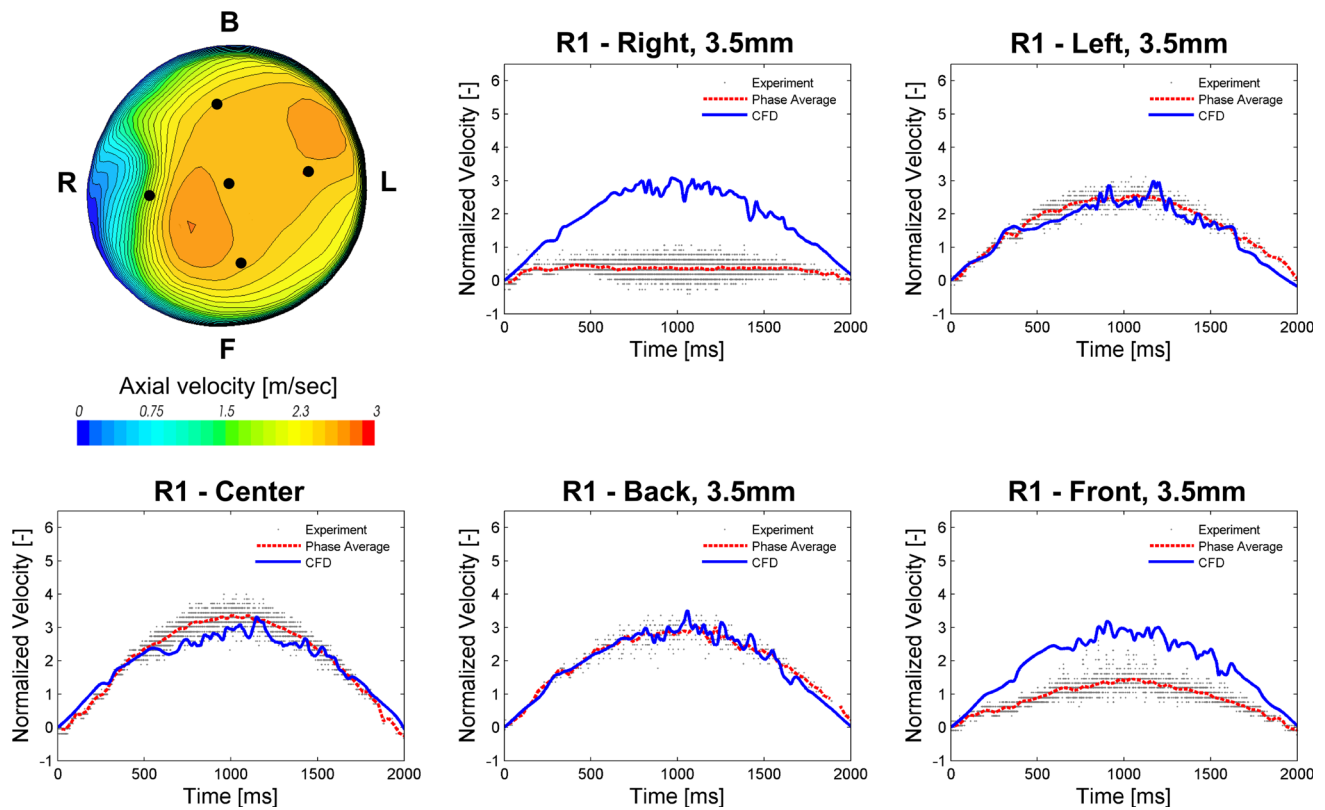


**Fig. 14** Temporal development of the normalized velocity at cross section R1

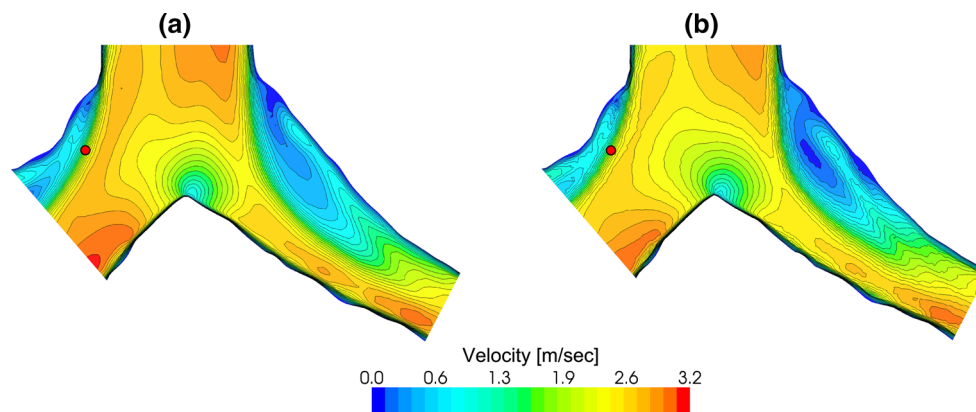


**Fig. 15** Comparison of separation zones in branch R1 for the current grid with 2.6 million control volumes (a) and a fine grid with 7 million control volumes (b)

reversed flow on the “Right” side of the airway can be seen in cross section L3. Unfortunately, no experiments were performed in this zone due to reduced optical access. However, we can reasonably rely on the results of the separation region, considering that in the previous section (L1-a), the separation region was predicted quite reliably. In the center, the location C and location “Left” predictions and experiments can be compared. In both locations, the results of the simulations exhibit a smooth sinusoidal trend for the inspiration,

with very weak flow pattern oscillations, indicating a quite stable structure for the flow. This also probably means that the flow instabilities originating from the laryngeal jet, which are very intense in the upstream cross sections, do not penetrate further downstream but rather tend to disappear. On the other hand, the experiments still show high-frequency velocity fluctuations, which as was mentioned earlier, the RANS models are unable to predict.

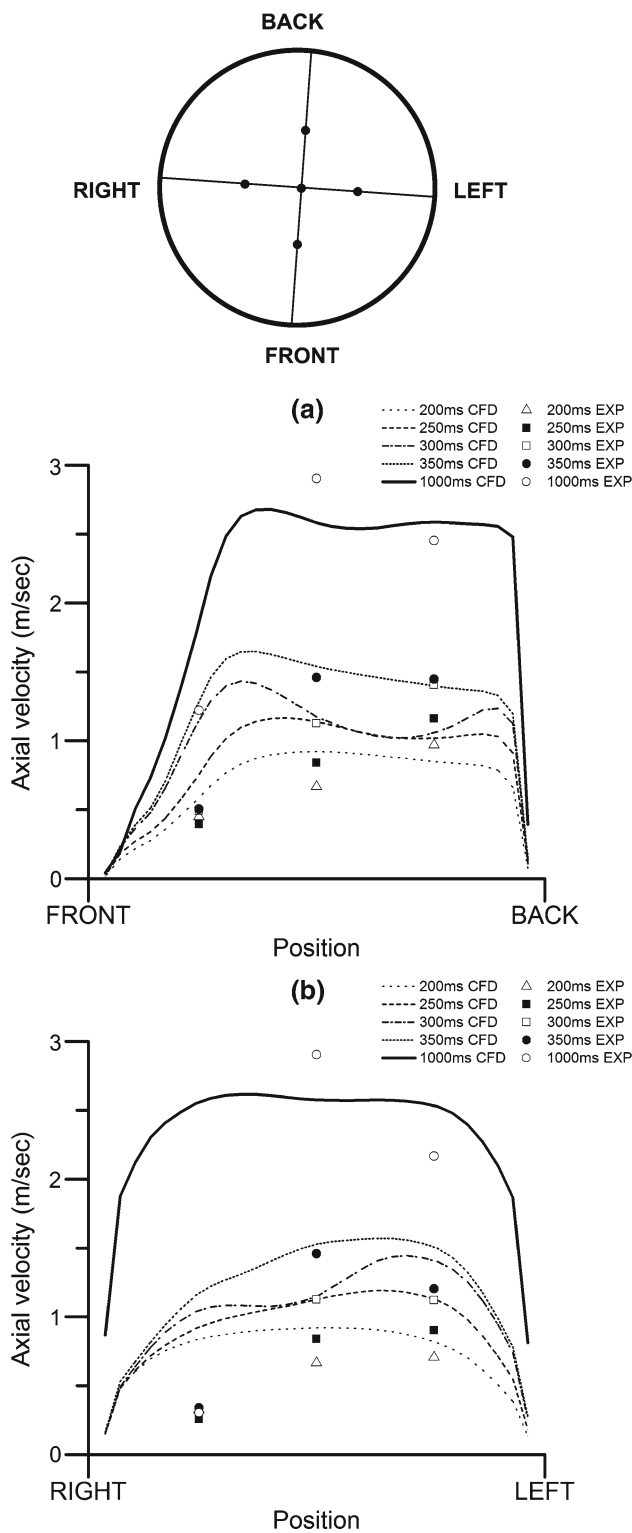


**Fig. 16** Velocity profiles during the ascending inspiration phase in section R1

3.1.5 Right airways: cross section R1

Cross section R1 is in airway R1 downstream of the carina of the first bifurcation. The agreement between the experimen-

tally obtained and predicted temporal velocity development is almost perfect in the Center, Back and Left locations with smaller oscillation amplitudes (see Fig. 14), more so than in the opposite left airway L1 in cross sections L1-a and L1-b. At almost all points (the exception being the “Right” position—see the comment below), there is a clear sinusoidal character with flow structure oscillations around the inspiration peak. The weakest agreement is seen at location “Right, 3.5 mm,” where the measured temporal velocity development shows a zero velocity flat curve that is not predicted by the simulations. As explained in Sect. 3.2, the reason may partly lie in the accuracy of the location adjustment, but it is most likely that the RANS model underpredicts the no-net-flow zone. To establish whether a finer grid would provide a better fit with the experiments, a grid dependency test was performed for a very fine mesh of 7 million control volumes and compared with one of 2.7 million control volumes. As can be seen in Fig. 16, the no-net-flow zone occupies the same area in both meshes. We can therefore speculate that RANS model fails to correctly predict an apparently larger no-net-flow zone in the abrupt upward turn of branch R1 (see Fig. 1b). As can also be seen in the position “R1—Front,” the no-net-flow zone extends partly to the front of the cross section, while the experiments show a relatively flat sinusoidal curve. However, when we compare velocity profiles (see Fig. 16), there is good agreement between the predictions and experiments in the Front–Back plane with the exception on the Front side and the Right–Left plane toward the Left side. On the Right side, the velocity profiles are clearly highly overpredicted and do not indicate the region of no-net-flow. Unlike cross section L1, it is evident here that the drawback of the RANS model is its inability to correctly predict the width of the no-net-flow region, but in the core region, the agreement is good.

From the point of the macrostructure of the flow field (see Fig. 17), we can still see very unstable flow patterns where the flow core rotates in the cross section as the inspiration reaches its peak and then decelerates.

3.1.6 Right airways: cross sections R3-b, R2 and R4

Only two points were monitored in cross section R3-b due to very limited optical access, so only the Center and Front locations can be compared (see Fig. 18). The velocities follow the sinusoidal character of the inspiration very well with a rather small macro-flow instability around the inspiration peak. The peak velocity was concentrated toward the “Left” side, while in the opposite direction toward “Right–Back,” a small region with a tendency to separate can be observed.

The cross sections R2 and R4 (see Figs. 19, 20) show a smooth sinusoidal character with very weak oscillations that tend to completely disappear.

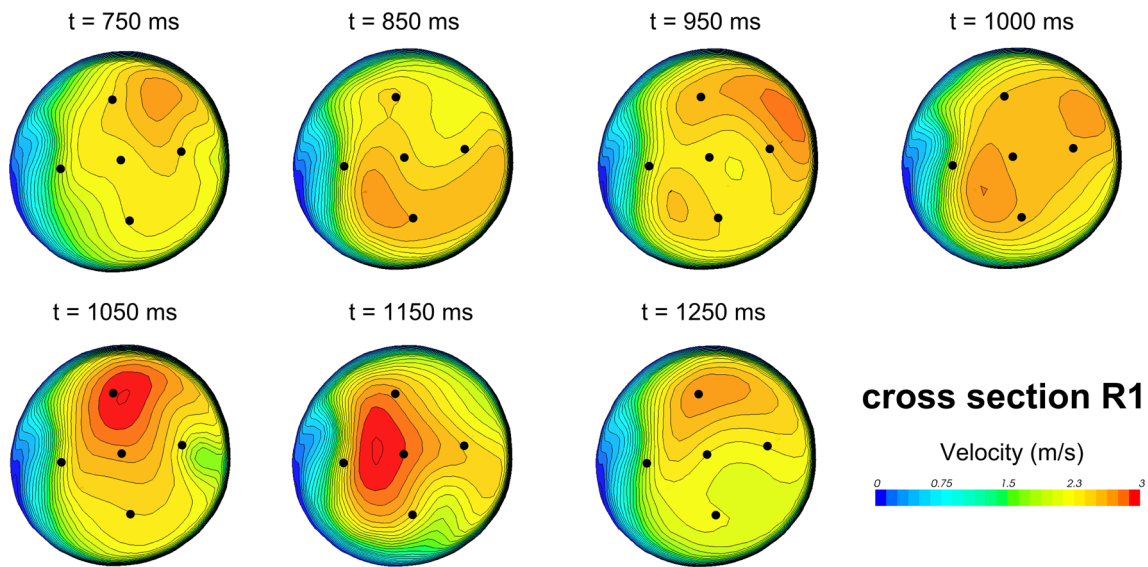


**Fig. 17** Temporal development of the normalized velocity at cross section R1

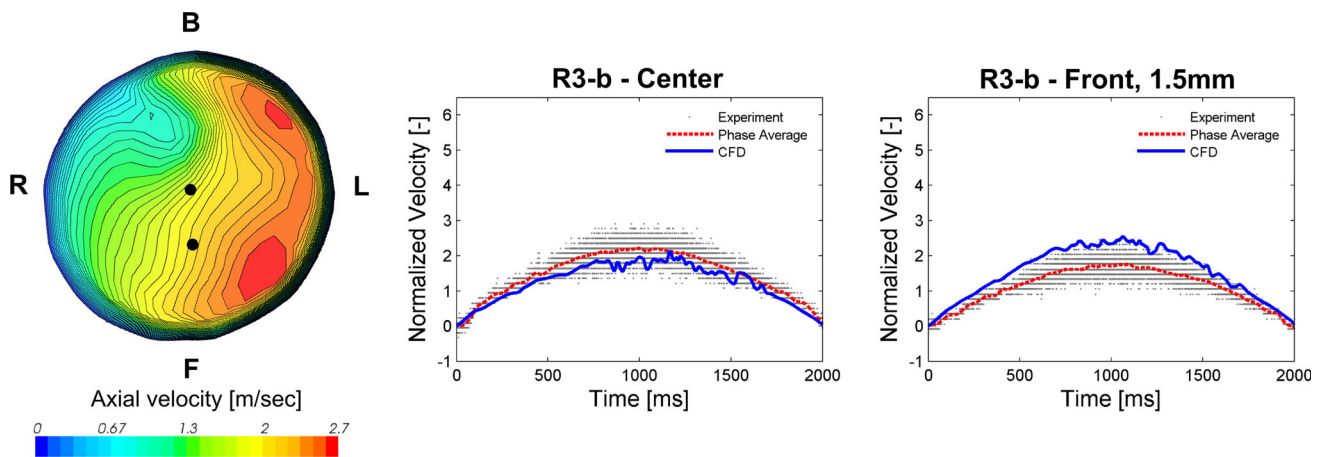


**Fig. 18** Temporal development of the normalized velocity at cross section R3-b

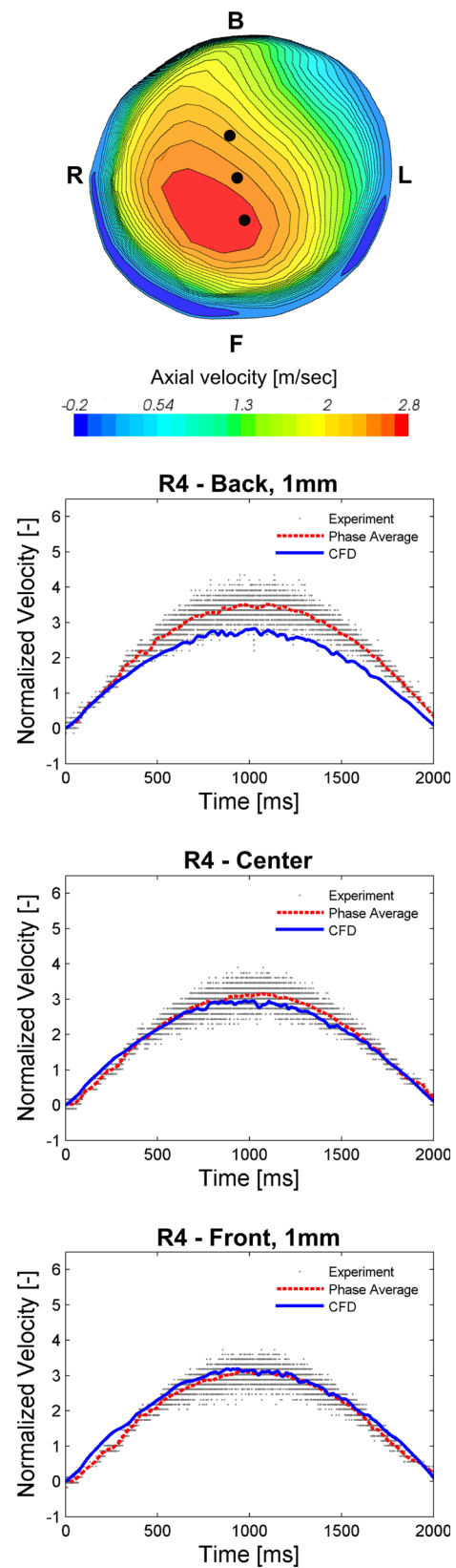
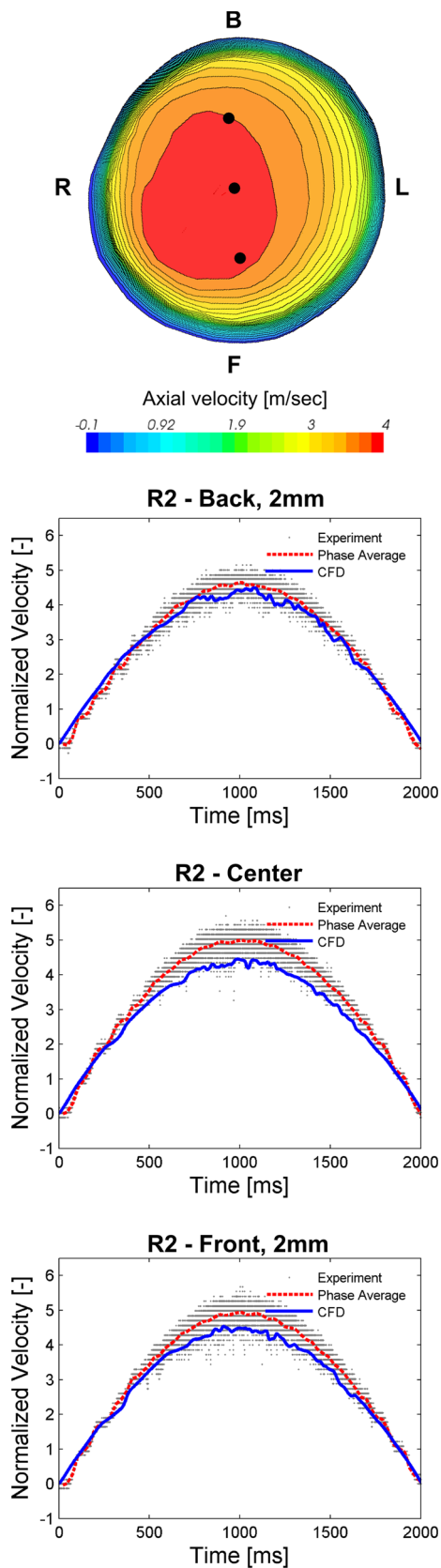
### 3.2 Accuracy of positioning in individual cross sections

As can be seen in some cross sections, the agreement between the experiments and predictions is not always perfect. This can be seen in the “L near-wall” of Trachea T-a in Figs. 6 and 7. It is also more pronounced in the “Right-3.5 mm” of cross section R1 in Figs. 14 and 16. This mostly happened in locations where high-velocity gradients exist or near separation zones. In this context, we need to explain the accuracy of the local positioning:

- **Experiments:** The measuring volume formed by the two intersecting laser beams of the PDA system was approximately 0.25 mm in each direction. The accuracy of the point adjustment with the traversing system is 0.02 mm, and the uncertainty of positioning is estimated to be  $\pm 0.3$  mm.

- **Modeling:** The average dimensions of the control volumes range from 0.5 to 1 mm.

Taking into account this uncertainty in the geometrical positioning of the experimental points and the positions of the associated control volumes, it is clear that moving the point into the high-velocity gradient field by several tenths of a millimeter can result in a different velocity. This may explain the relatively small discrepancies between the simulations and experiments in the cross sections where the simulations match the experimentally obtained sinusoidal trend but where the absolute values either match or exceed the lower or upper limit of the experimental curve. However, the larger discrepancy encountered near the separation zone in cross section R1 at 3.5 mm cannot be explained by positioning accuracy. As stated in Sect. 3.1.5, this is likely associated with the RANS model.



### 3.3 Turbulence statistics

To gain insights into the turbulent characteristics of lung air-flow, we analyzed turbulent kinetic energy (TKE) and the Reynolds number in Figs. 21 and 22. In Fig. 21, the development of the TKE and Reynolds number along the airways is presented for the inspiration peak (i.e. 1 s after the start of inspiration). The TKE is normalized with the mean peak inlet velocity  $v_{in}^2$ . During the early stages of inspiration, the flow is laminar, and we can see that the TKE is essentially zero, indicating that the SST  $k-\omega$  model can correctly predict laminar flow. Behind the glottis, the TKE abruptly increases, indicating the generation of very intense turbulence after the airway constriction. As the TKE gradually increases, the flow becomes more turbulent, resulting in the effective mixing of air and more uniform velocity profiles at the end of the trachea, as described in Sect. 3.1.1. After the first bifurcation, the development of TKE in the individual airways differs substantially. In the left TB airways (Fig. 21a), the TKE reaches its highest values along the path to termination a1, which is the branch that turns up with a large separation region (see the comments in Sect. 3.1.2). The TKE reflects the branching to individual TB segments, which is clearly seen as local peaks along the paths. The lowest TKE is seen in the paths to terminations a3 and a2. This path encounters the lowest number of bifurcations. We can clearly see that when a bifurcation is encountered, the TKE always increases. In Fig. 21c, the Reynolds number shows that although the value of Re decreases, mainly due to diminishing airway diameters, the character of the flow field is as highly turbulent as the TKE indicates. The experiments also show high-velocity fluctuations in all distal cross sections. This confirms earlier findings that showed that turbulence propagates to deeper airways, even with a low Re number for the flow, and this is evidenced by the experiments.

The TKE in the right airways (Fig. 21b) confirms what was previously stated for the left TB tree. The more branches the flow encounters on its path to the terminations, the higher the TKE is. The lowest TKE is seen along the path to termination a9, with only one bifurcation on the path. The highest TKE value is found along the path to termination a6, with three bifurcations on the path. The Reynolds number (Fig. 21d) shows trends similar to those observed in the left airways.

More interesting results can be found in Fig. 22, where the evolution of TKE over different times in the inspiration period is presented. As an example, we present only the airways going toward terminations a2 (left TB tree) and a8 (right TB tree). We can clearly see that the highest TKE is not at the inspiration peak, when the inspired air velocity is greatest, but after the inspiration peak at a time of 1.25 s when the high value is retained in the lower distal airways of the bronchial tree. The high values of TKE are also confirmed by the experiments, which show large velocity fluctuations

that propagate more to the end of the inspiration, as can be very clearly seen in the Trachea cross section in Fig. 6, especially in the Center position. It can also be observed that the TKE prior to the inspiration peak (e.g., at 0.25, 0.5, 0.75 s) is essentially zero, indicating a more laminar character of the flow field and an ability for the RANS model to predict laminar flow and transition from laminar to turbulent. The time evolution of TKE suggests that the turbulent diffusion of particles will be most intense after the peak inspiration.

### 3.4 Summary of comments about the experiments

Experimental data that were used for comparison with numerical simulations were acquired using a PDA system in several cross sections at selected points. In the trachea (section T-a), the experiments showed a smooth velocity course from inspiration start until around 0.3 s, when a short peak appeared that was practically visible in all positions across the section. This peak could be attributed to the transition from a laminar to a turbulent regime, as already explained. From this time on, a region of velocity fluctuations, which is typical of a turbulent flow, gradually forms. A highly turbulent field develops in the time interval from approximately 0.75–1.25 s, with a subsequent dampening as the inspiration decelerates and approaches the flow reversal point.

In the first cross section of the left airways, L1-a, a separation region forms with even a weak reversal flow. Another separation zone, although with a lower intensity, was observed in the middle of the L1 airway (cross section L1-b). Strong velocity fluctuations were evidenced in most points for both sections.

The flow in the right airways at cross section R1 is characterized by an oscillation amplitude smaller than in the left airway, L1. Almost all the measured points clearly showed a sinusoidal character with flow structure oscillations around the inspiration peak, with only an indistinctive separation zone. The flow in the following sections (R3-b, R2 and R4) also copied very well the sinusoidal character of inspiration, while the macro-flow instability around the inspiration peak tends to diminish in the deeper airway generations.

## 4 Conclusions

In the available literature, there are many papers that deal with numerical predictions for flow field and aerosol deposition in the human airways. They use different lung geometries, ranging from the mouth to variously complex tracheobronchial trees with several airway generations. Today, it is generally agreed that the global prediction of aerosol deposition is fairly good, but the local deposition can still not be correctly predicted. It is expected that numerical predictions for parti-

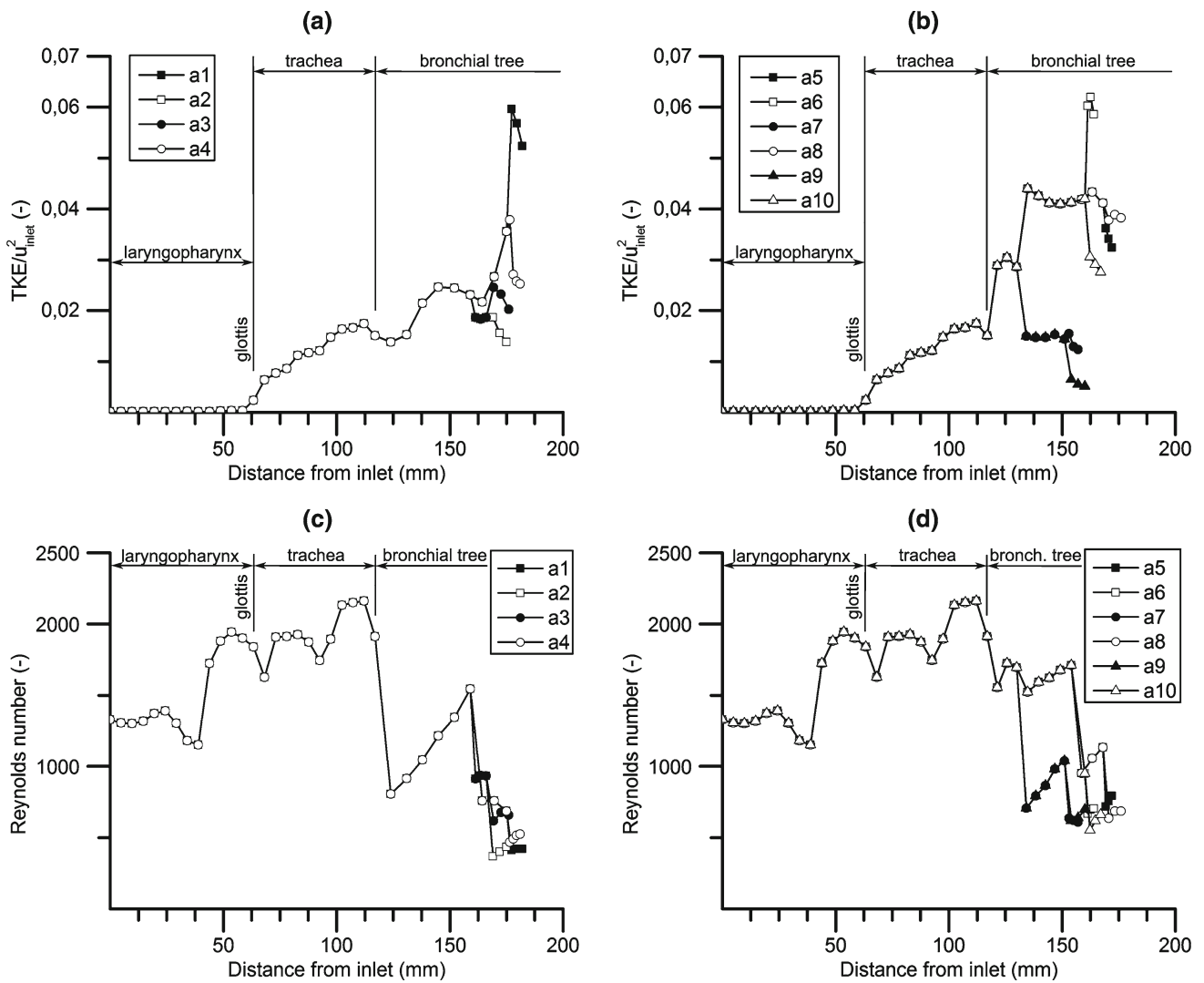


Fig. 21 Turbulent kinetic energy (TKE) and the Reynolds number for the left and right TB tree airways, a and c left TB tree, b and d right TB tree

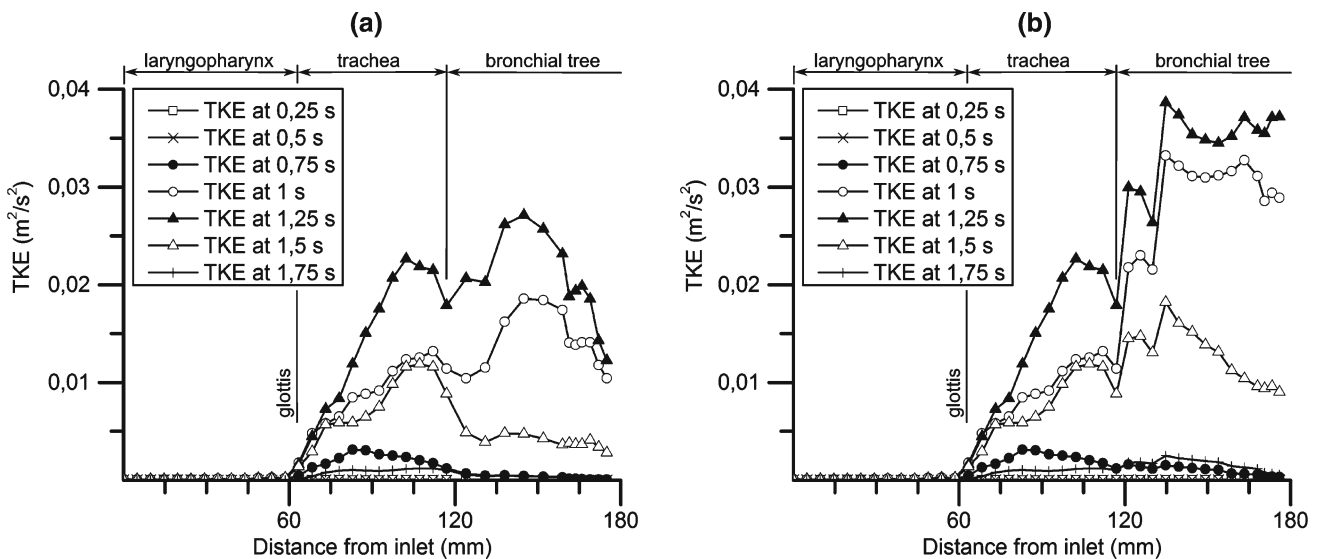


Fig. 22 The time evolution of TKE for airway termination a2, a left branches and a8, b right branches

cle deposition can be accurate only after single-phase CFD models are verified.

The results of the numerical predictions in this study show quite good agreement with experiments for the whole oscillatory (wave-form) inspiration at several cross sections of the trachea and left and right tracheobronchial tree, up to the third and fourth generation, respectively. From the predictions, several conclusions can be drawn:

- There is a very complex and temporally developing flow field in the trachea due to the laryngeal jet. The results indicate that the laryngeal jet changes its character during the ascending and descending phases of inspiration. The jet undergoes successive changes from one distinctive stream to two separate streams and back again to one stream as the inspiration reaches its peak. During the descending phase, the jet divides into two streams again. This trend is in accordance with the development of TKE, which rises from the glottis station to its maximum after the inspiration peak (at approximately 1250 ms) before gradually decreasing.
- The simulations very accurately predict the sinusoidal character of the velocity development and show that this character is retained in the downstream airways, except where separation zones are formed.
- The simulations predict the highly unstable character of the flow field, with the time evolution of the flow patterns across the sections showing very good agreement with the experiments. This instability is of a comparable amplitude to the experimentally acquired temporally local values for mean and fluctuating axial velocities. The transition from a laminar to turbulent regime was predicted with an almost perfect agreement with the experiments at the same time of inspiration.
- In both the left and right main bronchi, a separation zone is formed with a reattachment and even a weak reversal flow. The width of the separation zone is well predicted in the left TB branch, but the maximum velocities outside the separation zone are overpredicted. In the right TB branch, the width of the separation region is not correctly predicted, but on the other hand, the velocities agree very well outside of the separation region.
- Turbulent kinetic energy (TKE) rises abruptly after the glottis and along the airways, depending on the number of branches the flow encounters on its way. Each branching results in a local increase in TKE. Before the inspiration peak, the TKE is essentially zero, showing a laminar character. The highest TKE develops after peak inspiration, although the Reynolds number decreases, showing a laminar regime.

The results agree well with previous published studies that show that the flow field in the human tracheobronchial

airways is very complex and temporally develops during oscillatory (waveform) inspiration. Both the flow pattern oscillations and turbulent fluctuations propagate to the downstream airways, but it is very likely the flow patterns stabilize in the downstream airways, where the effect of the laryngeal jet is successively dampened. The same cannot be said of the turbulent fluctuations.

We can conclude that the predictions and experiments show a highly unstable flow field with intense local relocation of flow structures and highly turbulent fluctuations. This complex flow field predetermines the highly unstable deposition of local particles during inspiration, which should be taken into account when attempting to realize drug delivery.

As pointed out by Ball et al. (2008), it is very difficult for the RANS models to predict a quantitatively acceptable solution, even for a simplified geometry and time-averaged flow field. However, the simulation results presented in this paper and the experimental results from an anatomically realistic TB tree show good agreement. However, care must be taken in regions with large airway curvature, where the RANS model is very limited, so as to correctly predict the size of the separation zone, such as was seen in branch R1.

**Acknowledgments** This work was supported by Project GA P105/11/1339 and funded by the Czech Science Foundation and Project LO1202 NETME CENTRE PLUS with financial support from the Ministry of Education, Youth and Sports of the Czech Republic under the “National Sustainability Programme I.” Frantisek Lizal and Michaela Chovancova were supported by Project CZ.1.07/2.3.00/30.0039 of Brno University of Technology.

## References

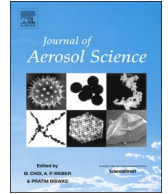
- Agnihotri V, Ghorbaniasl G, Verbanck S, Lacor C (2014) On the multiple LES frozen field approach for the prediction of particle deposition in the human upper respiratory tract. *J Aerosol Sci* 68:58–72
- Ball CG, Uddin M, Pollard A (2008) High resolution turbulence modelling of airflow in an idealized human extra-thoracic airway. *Comput Fluids* 37:943–964
- Brücker C, Schröder W (2003) Flow visualization in a model of the bronchial tree in the human lung airways via 3-D PIV, Proceedings of the 4th Pacific symposium on flow visualization and image processing (PSFVIP-4), Chamonix, France, 3–5 June 2003
- Chen J, Gutmark E (2014) Numerical investigation of airflow in an idealized human extra-thoracic airway: a comparison study. *Biomech Model Mechanobiol* 13:205–214. doi:10.1007/s10237-013-0496-x
- Cui XG, Gutheil E (2011) Large eddy simulation of the unsteady flow-field in an idealized human mouth-throat configuration. *J Biomech* 44:2768–2774
- Ghahramani E, Abouali O, Emdad H, Ahmadi G (2014) Numerical analysis of stochastic dispersion of micro-particles in turbulent flows in a realistic model of human nasal/upper airway. *J Aerosol Sci* 67:188–206
- Ghalati PF, Keshavarzian E, Abouali O, Faramarzi A, Tu J, Shakibafard A (2012) Numerical analysis of micro- and nano-particle deposition in a realistic human upper airway. *Comput Biol Med* 42:39–49

- Heenan AF, Matida EA, Pollard A, Finlay WH (2003) Experimental measurements and computational modeling of the flow in an idealized extrathoracic airway. *Exp Fluids* 35:70–84
- Horsfield K, Dart G, Olson DE, Filley GF, Cumming G (1971) Models of the human bronchial tree. *J Appl Physiol* 31:207–217
- Huang J, Sun H, Liu C, Zhang L (2013) Moving boundary simulation of airflow and micro-particle deposition in the human extra-thoracic airway under steady inspiration. Part I: airflow. *Eur J Mech B Fluids* 37:29–41
- Jayaraju ST, Brouns M, Verbanck S, Lacor C (2007) Fluid flow and particle deposition analysis in a realistic extrathoracic airway model using unstructured grids. *J Aerosol Sci* 38:494–508
- Jedelsky J, Lízal F, Jícha M (2012) Characteristics of turbulent particle transport in human airways under steady and cyclic flows. *Int J Heat Fluid Flow* 35:84–92
- Johnstone A, Uddin M, Pollard A, Heenan A, Finley WH (2004) The flow inside an idealised form of the human extra-thoracic airway. *Exp Fluids* 37(5):673–689
- Kaye SR, Phillips CG (1997) The influence of the branching pattern of the conduction airways on the flow and aerosol deposition parameters in the human, dog, rat and hamster. *J Aerosol Sci* 28:1291–1300
- Leschziner MA (1993) Introduction to the modeling of turbulence. Von Karman Institute for Fluid Dynamics, Lecture series. 1993–02, ISSN: 0377–8312
- Li Z, Kleinstreuer C, Zhang Z (2007) Simulation of airflow fields and microparticle deposition in realistic human lung airway models. Part I: airflow patterns. *Eur J Mech B Fluids* 26:632–649
- Lin CL, Tawhai MH, McLennan G, Hoffman EA (2007) Characteristics of the turbulent laryngeal jet and its effect on airflow in the human intra-thoracic airways. *Respir Physiol Neurobiol* 157:295–309
- Lízal F, Elcner J, Hopke P, Jedelský J, Jícha M (2011) Development of a realistic human airway model. *ProcIMEchE Part H. J Eng Med* 226(H3):197–207. ISSN: 0954-4119
- Longest PW, Vinchurkar S, Martonen TB (2006) Transport and deposition of respiratory aerosols in models of childhood asthma. *J Aerosol Sci* 37:1234–1257
- Longest PW, Holbrook LT (2012) In silico models of aerosol delivery to the respiratory tract—development and applications. *Adv Drug Deliv Rev* 64:296–311
- Luo XY, Hinton JS, Liew TT, Tan KK (2004) LES modelling of flow in a simple airway model. *Med Eng Phys* 26:403–413
- Lyn DA, Einav S, Rodi W, Park JH (1995) A laser-doppler velocimetry study of ensemble-averaged characteristics of the turbulent near wake of a square cylinder. *J Fluid Mech* 304:285–319
- Mihaescu M, Murugappan S, Kalra M, Khosla S, Gutmark E (2008) Large Eddy simulation and Reynolds-averaged Navier–Stokes modeling of flow in a realistic pharyngeal airway model: an investigation of obstructive sleep apnea. *J Biomech* 41:2279–2288
- Nowak N, Kakade PP, Annapragada AA (2003) Computational fluid dynamics simulation of airflow and aerosol deposition in human lungs. *J Biomed Eng* 31:374–390
- Pollard A, Uddin M, Shinnee AM, Ball CG (2012) Recent advances and key challenges in investigations of the flow inside human oro-pharyngeal-laryngeal airway. *Int J Comput Fluid Dyn* 26(6–8):363–381
- Piglione MC, Fontana D, Vanni M (2012) Simulation of particle deposition in human central airways. *Eur J Mech B Fluids* 31:91–101
- Pope SB (2003) *Turbulent flow*. Cambridge University Press, Cambridge
- Schmidt A, Zidowitz S, Kriete A, Denhard T, Krass S, Peitgen HO (2004) A digital reference model of the human bronchial tree. *Comput Med Imaging Gr* 28:203–211
- Soni B, Aliabadi S (2013) Large-scale CFD simulations of airflow and particle deposition in lung airway. *Comput Fluids* 88:804–812
- Taulbee DB, Yu CP (1975) A theory of aerosol deposition in the human respiratory tract. *J Appl Physiol* 38(1):77–85
- Tropea C, Yarin A, Foss J (ed) (2007) *Handbook of experimental fluid mechanics*. Springer, Berlin. ISBN: 978-3-540-25141-5
- User Guide STAR-CCM+, Version 8.02
- VKI Lecture series 1993–2002, 1993 Introduction to the modeling of turbulence
- Wang Y, Elghobashi S (2014) On locating the obstruction in the upper airway via numerical simulation. *Respir Phys Neurobiol* 193:1–10
- Weibel E (1963) *Morphometry of the Human Lung*. Springer Verlag and Academic Press, Berlin, New York
- Wilcox DC (2000) *Turbulence modeling for CFD*, 2nd edition, DCW Industries, Inc., ISBN: 0-963051-5-1
- Zarogoulidis P, Papanas N, Kouliatsis G, Spyros D, Zarogoulidis K, Maltezos E (2011) Inhaled insulin: too soon to be forgotten? *J Aerosol Med Pulm Drug Deliv* 24(5):213–223
- Zhang Z, Kleinstreuer C (2003) Low-Reynolds-number turbulent flows in locally constricted conduits: a comparison study. *Am Inst Astronaut J (AIAAJ)* 41:831–840
- Zhang Z, Kleinstreuer C (2011) Computational analysis of airflow and nanoparticle deposition in a combined nasal–oral–tracheobronchial airway model. *J Aerosol Sci* 42(3):174–194



Contents lists available at ScienceDirect

## Journal of Aerosol Science

journal homepage: [www.elsevier.com/locate/jaerosci](http://www.elsevier.com/locate/jaerosci)

# Simulation of size-dependent aerosol deposition in a realistic model of the upper human airways



E.M.A. Frederix<sup>a,\*</sup>, A.K. Kuczaj<sup>a,d</sup>, M. Nordlund<sup>d</sup>, M. Bělka<sup>c</sup>, F. Lizal<sup>c</sup>, J. Jedelský<sup>c</sup>, J. Elcner<sup>c</sup>, M. Jícha<sup>c</sup>, B.J. Geurts<sup>a,b</sup>

<sup>a</sup> Multiscale Modeling and Simulation, Faculty EEMCS, University of Twente, P.O. Box 217, 7500 AE Enschede, The Netherlands

<sup>b</sup> Anisotropic Turbulence, Fluid Dynamics Laboratory, Faculty of Applied Physics, Eindhoven University of Technology, P.O. Box 513, 5600 MB Eindhoven, The Netherlands

<sup>c</sup> Energy Institute, Faculty of Mechanical Engineering, Brno University of Technology, Technická 2896/2 Brno 61669, Czech Republic

<sup>d</sup> Philip Morris International R & D, Philip Morris Products S.A. (part of Philip Morris International group of companies), Quai Jeanrenaud 5, 2000 Neuchâtel, Switzerland

## A B S T R A C T

An Eulerian internally mixed aerosol model is used for predictions of deposition inside a realistic cast of the human upper airways. The model, formulated in the multi-species and compressible framework, is solved using the sectional discretization of the droplet size distribution function to accurately capture size-dependent aerosol dynamics such as droplet drift, gravitational settling and diffusion. These three mechanisms are implemented in a consistent way in the model, guaranteeing that the total droplet mass as given by the droplet size distribution is always equal to the total droplet mass due to the mass concentration fields. To validate the model, we simulate monodisperse glycerol aerosol deposition inside the lung cast, for which experimental data is available. Provided that an adequate computational mesh is used and an adequate boundary treatment for the inertial deposition velocity, excellent agreement is found with the experimental data. Finally, we study the size-dependent deposition inside the lung cast for a polydisperse aerosol with droplet sizes ranging from the nanometer scale to beyond the micrometer scale. The typical ‘V-shape’ deposition curve is recovered. The aim of this paper is to 1) provide an overview of the Eulerian aerosol dynamics model and method, to 2) validate this method in a relevant complex lung geometry and to 3) explore the capabilities of the method by simulating poly-disperse aerosol deposition.

## 1. Introduction

Aerosol research plays a major role in various branches of science and engineering. These branches concern environmental and atmospheric problems (weather, pollution, indoor air quality), engineering applications linked with sprays (combustion or cooling) or inhalation-related challenges (medical devices and dosimetry). Synergy of both experimental and computational approaches is required in order to foster deeper understanding of transport, evolution and dynamics of aerosols during inhalation. Clearly, experiments give insight into the physical processes and can provide essential information to build confidence in computational models. In fact, these models often need simplifications and heuristic input to become computationally feasible. It is then essential to validate computational models where possible. Conversely, with the further maturing of computational modeling, high levels of detail may be

\* Corresponding author.

E-mail address: [e.m.a.frederix@utwente.nl](mailto:e.m.a.frederix@utwente.nl) (E.M.A. Frederix).

<http://dx.doi.org/10.1016/j.jaerosci.2017.10.007>

Received 2 September 2016; Received in revised form 3 October 2017; Accepted 16 October 2017

Available online 18 October 2017

0021-8502/ © 2017 The Authors. Published by Elsevier Ltd. This is an open access article under the CC BY-NC-ND license

(<http://creativecommons.org/licenses/by-nc-nd/4.0/>).

Nomenclature		List of special symbols	
<i>List of abbreviations</i>		$\mathcal{J}_{M_i}$	source term for $M_i$ ( $1/\text{m}^3/\text{s}$ )
BL	boundary layer	$\mathcal{N}$	number of species
CFD	computational fluid dynamics	$\mathcal{P}$	number of sections
CMAG	condensation monodisperse aerosol generator	$\mathcal{Q}$	mass density source term ( $\text{kg}/\text{m}^3/\text{s}$ )
CMD	count median diameter	$\mathcal{S}_j$	vapor mass density source term ( $\text{kg}/\text{m}^3/\text{s}$ )
GDE	general dynamics equation	$\mathcal{L}_j$	liquid mass density source term ( $\text{kg}/\text{m}^3/\text{s}$ )
LSM	lagrangian sub-grid model	<i>List of symbols</i>	
NO-BL	no boundary layer	$A_g$	per-generation wall surface area ( $\text{m}^2$ )
RANS	reynolds averaged navier-stokes	$c_p$	mixture heat capacity at constant pressure ( $\text{m}^2/\text{s}^2/\text{K}$ )
ZGM	zero-gradient extrapolation model	$C_k$	per-segment numerical error measure (dimensionless)
<i>List of indices</i>		$d$	droplet diameter (m)
$g$	generation index	$D^e$	diffusion coefficient ( $\text{m}^2/\text{s}$ )
$i$	section index	$\text{flux}_i$	sectional mass flux ( $\text{kg}/\text{m}^2/\text{s}$ )
$j$	species index	$\mathbf{g}$	gravitational acceleration vector ( $\text{m}/\text{s}^2$ )
$k$	cast segment index	$\mathbf{I}$	identity matrix (dimensionless)
air	subscript indicating air	$J$	GDE source term ( $1/\text{m}^3/\text{s}$ )
gly	subscript indicating glycerol	$M_i$	mass-specific sectional droplet number concentration ( $\text{kg}^{-1}$ )
<i>List of Greek symbols</i>		$n$	droplet size distribution ( $1/\text{kg}/\text{m}^3$ )
$\phi_i$	sectional number concentration flux ( $1/\text{m}^2/\text{s}$ )	$\mathbf{n}$	wall normal (dimensionless)
$\Phi$	inlet flow rate ( $\text{m}^3/\text{s}$ )	$N_i$	sectional droplet number concentration ( $\text{m}^{-3}$ )
$\gamma$	density ratio (dimensionless)	$p$	pressure ( $\text{kg}/\text{m}/\text{s}^2$ )
$\kappa$	mixture heat conductivity ( $\text{kg}/\text{m}/\text{s}^3/\text{K}$ )	$R_k$	per-segment total deposition rate ( $\mu\text{g}/\text{hr}$ )
$\mu$	mixture viscosity ( $\text{kg}/\text{m}/\text{s}$ )	$s$	droplet mass (kg)
$\rho$	mixture mass density ( $\text{kg}/\text{m}^3$ )	$t$	time (s)
$\rho^e$	liquid mass density ( $\text{kg}/\text{m}^3$ )	$T$	temperature (K)
$\rho^v$	vapor mass density ( $\text{kg}/\text{m}^3$ )	$\mathbf{u}$	mixture velocity (m/s)
$\sigma$	geometric standard deviation (dimensionless)	$\mathbf{u}^e$	drift velocity (m/s)
$\tau$	droplet relaxation time (s)	$\mathbf{v}$	droplet velocity (m/s)
$\tau$	rate of strain tensor ( $\text{kg}/\text{m}/\text{s}^2$ )	$w_i$	sectional weight (dimensionless)
$\mu_k$	per-segment mean logarithmic deposition rate (dimensionless)	$\mathbf{x}$	position (m)
$\sigma_k$	per-segment standard deviation of the logarithmic deposition rate (dimensionless)	$y^+$	wall distance measured in wall coordinates (dimensionless)
$\eta_g$	per-generation deposition efficiency (dimensionless)	$y_i$	sectional interface size (kg)
$\epsilon_g$	per-generation surface-averaged deposition efficiency (dimensionless)	$Y_j$	mass fraction of species $j$ in vapor phase (dimensionless)
		$Z_j$	mass fraction of species $j$ in liquid phase (dimensionless)
		$Z$	total liquid mass fraction (dimensionless)

provided more and more reliably, which would remain otherwise inaccessible via physical experiments alone. The combination of numerical and physical experiments can be used effectively to enhance our overall understanding of aerosol dynamics. In support, once a computational model is validated, it may serve in research areas and applications for which experiments are difficult or even impossible to conduct. A straightforward example concerns the modeling of aerosols flowing in the airways for which simulations support complex experiments and challenge experimental methods by giving insight into geometrical complexities of the flow in the respiratory tract. In this paper we present our unique compressible and consistent computational approach to model, simulate and validate complex flow deposition in the human airways. In addition, we directly confront computational predictions with experimental findings obtained from exactly the same lung cast geometry. In total, we establish a close agreement between experimental deposition data and results obtained with our Eulerian sectional aerosol model.

Simulations of aerosol deposition and respiratory tract flow analysis as a subject of computational investigations for medical and toxicological applications have been studied for many years (see the review by Hofmann (2011)). Various physical models were validated taking into account distinct levels of complexity and detail, starting from the basic formulation of droplet physics, through the development of the General Dynamics Equation (GDE) for the aerosol, and finally the application of this equation to more complex flows linked with numerical developments of Computational Fluid Dynamics (CFD) methods.

The overall goal of applying CFD to simulate the flow inside the respiratory tract is to compute the total, regional and local deposition dosimetry, which develops over successive breathing cycles. Wexler and Park (2008) presented a study estimating dosimetry values based on the developed models for aerosol droplets in the size range 0.01–10  $\mu\text{m}$ , for a long exposure time. Li, Kleinstreuer, and Zhang (2007) simulated realistic tracheobronchial airways at transient airflow conditions at 15 and 60 L/min flow conditions. It was concluded that the local flow patterns, which influence particle deposition, are largely affected by secondary flows. Airway geometry as well as the flow rate play important roles. One of the important challenges in simulation of respiration is related to the development of appropriate and realistic physiology-based boundary conditions (Alzahrany & Banerjee, 2015).

Similar to our approach, various physical processes were taken into account in the framework presented by Mitsakou, Helmis, and Housiadas (2005). The framework was built in the Eulerian context and was compared against existing computational and experimental data. The quality of the computed deposition data for sub-micron particles strongly depends on the resolution of the boundary layer in time-dependent flow simulations. Since for complex geometries this requires considerable computational power, Lagrangian-based velocity corrections were proposed to improve the computational accuracy of deposition (Longest & Oldham, 2008). In order to incorporate aerosol physics for evolving liquid-based aerosols, Lagrangian and Eulerian models were built that incorporate vapor–liquid mass transport (Zhang, Kim, & Kleinstreuer, 2006; Zhang, Kleinstreuer, & Hyun, 2012). The effectiveness of both Eulerian and Lagrangian models is studied from the perspective of accuracy and computational cost (Worth Longest & Xi, 2007). In general, the Lagrangian approach is conceptually more transparent as large numbers of discrete particles are followed independently in the flow, obeying their own equations of motion and internal dynamics. However, this approach can quickly become computationally unfeasible for large particle densities. The Eulerian approach, assuming a continuous description of the particulate phase, is known to be computationally more attractive but the modeling of the interaction of the particulate phase and the fluid phase poses its own new challenges.

Validation of the developed computational models is crucial. Numerous works were devoted to this topic either in simplified or complex geometries (Feng & Kleinstreuer, 2014; Holbrook & Worth Longest, 2013; Krause et al., 2013; Ma et al., 2009; Varghese & Gangamma, 2009; Worth Longest & Oldham, 2006; Xi & Longest, 2009; Zhang, Kleinstreuer, & Kim, 2009; Zhang, Kleinstreuer, Kim, & Cheng, 2004). Validation of CFD models is not limited to the human respiratory tract alone, for example simulations of rat lungs, amongst others, have also been performed (Schroeter et al., 2016). The developed methods can be validated on the basis of existing experimental data, but should also be computationally verified with respect to the numerical discretization methods used to obtain the simulation data. Growing computational capabilities allow to simulate larger problems with more complete and richer physics (Feng, Kleinstreuer, Castro, & Rostami, 2016), that can also be fully resolved spatially and temporally if adequate computational resources, careful meshing of the domain and accurate methods are combined. Computational aerosol models require not only a fundamental and robust mathematical description of aerosol dynamics to be accurate. Their accuracy is equally dependent on the geometry and meshing in order to capture transient and interlinked processes (e.g., turbulence or diffusion and impaction of sub-micron particles). Frederix, Kuczaj, Nordlund, Veldman, and Geurts (2017), Frederix, Stanic, et al. (2017), Frederix, Stanic, Kuczaj, Nordlund, and Geurts (2016) presented an internally mixed sectional Eulerian aerosol model, designed to incorporate droplet inertial drift, sedimentation and Brownian motion. These three aerosol dynamics mechanisms drive droplet deposition in the airways. The size-dependence of these mechanisms is included by appropriate models and can be accurately simulated in the framework of sectional discretization of the droplet size distribution. Frederix, Kuczaj, et al. (2017) designed the model to respect the ‘consistency relation’; at both the analytical and numerical level the total droplet mass is equally reflected in the mass concentration fields as well as by the droplet size distribution. The model was applied to the simulation of deposition in bent pipes, and both the diffusional and inertial deposition regimes were identified and studied in one comprehensive model. The bent pipe geometry offers a reliable and well-understood point of reference for validation against other experimental, theoretical and numerical deposition data. However, the bent pipe case differs primarily in terms of the complexity of its geometry. The scope of this paper is to apply the internally mixed Eulerian aerosol model to a complex geometry that is a close representation of the actual geometry of the upper airways and to study the local and regional deposition patterns of aerosol droplets of different sizes. Furthermore, a special focus is set on comparing simulated regional aerosol deposition in the cast segments to experimentally obtained data measured by Nordlund et al. (2017) during steady-state conditions using a physical cast of the same geometry. The experimental data was obtained using a cast model consisting of several segments from the mouth cavity down to the seventh generation of branches of the lung, each representing distinct features of the respiratory tract, which can be measured for deposited mass. For the glycerol aerosol to which the cast is exposed, it was shown by Frederix, Kuczaj, et al. (2017) that for the relevant Reynolds and Stokes numbers both diffusional and inertial deposition is significant. It was also shown that in this intermediate deposition regime—the regime where diffusion and inertia are two effects of similar magnitude—it becomes numerically quite challenging to model deposition accurately. This makes the experimental data presented by Nordlund et al. (2017) extremely useful in validating our Eulerian aerosol model in realistic geometries, particularly in relation to capturing the near-wall behavior.

As was done by Frederix, Kuczaj et al. (2017) for the bent pipe, we simulate the aerosol transport and deposition using a number of different meshes with and without boundary layer mesh refinement. We include the ‘primary’ zero-gradient extrapolation model (ZGM) boundary treatment as well as the more elaborate Lagrangian sub-grid model (LSM) boundary treatment (see Longest & Oldham, 2008) to approximate the inertial deposition velocity at the wall. It is shown that on meshes without boundary layer refinement a significant overprediction of the deposition rate occurs. When applying the LSM boundary treatment, all meshes, both with and without near-wall refinement, are capable of producing a reliable prediction of the per-segment deposition rate in comparison with the regional experimental data. When looking more closely at the local deposition patterns within each cast segment, it is shown that for meshes without boundary layer refinement, the deposition appears very pixellated. If accurate predictions are required of deposition patterns with local length scales smaller than the typical features of the lung cast, refined mesh quality near

the wall is required.

Using the finest mesh with near-wall refinement and the LSM boundary treatment for the inertial velocity of droplets near the wall, we simulate a scenario where a uniform droplet size distribution spanning over a size range from 10 nm to 20  $\mu\text{m}$  is released inside the lung cast. The deposition efficiency as a function of size is studied for each of the seven generations of the lung cast. For the largest particles enhanced deposition efficiency is shown in the throat segment of the cast, hindering these particles from penetrating the lung further. The typical ‘V-shape’ (Frederix, Kuczaj, et al., 2017) deposition curve is recovered, where in the left leg of this curve deposition is driven by diffusion and the right leg by inertia. Of the total deposited mass, we also show how the deposition is partitioned across the seven generations of the lung cast.

The novelty of the current paper lies in the fact that the recently published sectional aerosol model by Frederix, Kuczaj, et al. (2017) is now applied to the simulation of aerosol deposition inside a realistic complex lung cast of the upper airways. Specifically, the full aerosol size distribution can be simulated directly with the computational model. Moreover, the feasibility of employing Eulerian aerosol models to understand aerosol dynamics is established. Good agreement is found with experimental deposition data. The current paper extends earlier work of Longest and Oldham (2008) by introducing the sub-grid model for inertial particle deposition into the compressible flow model.

The outline of this paper is as follows. In Section 2 the Eulerian computational model is presented. This section forms a summary of what was presented by Frederix, Kuczaj, et al. (2017) and is included for completeness. In Section 3 we present simulations which mimic the experimental setup presented by Nordlund et al. (2017), and compare against these experimental data of regional deposition. We study various computational settings, addressing the influence on deposition of both the mesh refinement at the wall and the boundary treatment for the inertial deposition velocity. In Section 4 we simulate a large size range of droplets and study the per-generation deposition as a function of droplet size. In Section 5 we conclude the findings.

## 2. Computational modeling of aerosol transport and deposition

In this section we specify the mathematical model with which the dynamics of the aerosol droplets in a detailed lung cast is captured, closely following the recent work by Frederix, Kuczaj, et al. (2017). Subsequently, the sectional method to approximate the size distribution is presented and the contributions of drift and diffusion to the transport of droplets are described. Finally, we detail the computation of the rate of deposition of aerosol droplets on the lung tissue. We restrict to discussing the main aspects and refer to the work of Frederix, Kuczaj, et al. (2017) for full detail. The selected numerical methods that are employed in the simulations are discussed in the next section.

### 2.1. Mathematical model for aerosol dynamics

We adopt a compressible Eulerian description of multi-species aerosol and describe its state in terms of the mixture density  $\rho$ , the mixture velocity  $\mathbf{u}$ , its temperature  $T$  and species mass fractions in the vapor and liquid phases,  $Y_j$  and  $Z_j$ , respectively, for species  $j = 1, \dots, \mathcal{N}$  with  $\mathcal{N}$  the number of different species. Although we work, in this paper, exclusively in the single-species setting we formulate the problem in the multi-species one, for the sake of generality. We opt for a compressible formulation as this is beneficial for obtaining general and accurate constitutive relations for the mixture’s density dependence on temperature and pressure. In particular in cases of large temperature changes, density changes may become dominant. The generality offered by the compressible formulation allows for a natural extension of the model to settings in which density changes are important, e.g., see the work of Frederix, Stanic, et al. (2017).

The mixture mass density  $\rho$  and momentum  $\rho\mathbf{u}$  adhere to the well-known continuity equation

$$\partial_t \rho + \nabla \cdot (\rho \mathbf{u}) = \mathcal{S} \quad (1)$$

where  $\mathcal{S}$  is a source term associated with local appearance or removal of droplets due to drift or diffusion. Moreover, the dynamics is governed by the Navier-Stokes equations (we refer to the momentum transport equations as the ‘Navier-Stokes’ equations, following (Kundu & Cohen, 2008))

$$\partial_t (\rho \mathbf{u}) + \nabla \cdot (\rho \mathbf{u} \mathbf{u}) = -\nabla p - (\nabla \cdot \boldsymbol{\tau}) \quad (2)$$

with  $\partial_t$  the partial derivative with respect to time  $t$ ,  $\nabla$  the derivative operator with respect to the spatial coordinates  $\mathbf{x} \equiv (x_1, x_2, x_3)$ , and rate of strain tensor  $\boldsymbol{\tau}$ , given by

$$\boldsymbol{\tau} = -\mu [\nabla \mathbf{u} + (\nabla \mathbf{u})^T] + \frac{2}{3} \mu (\nabla \cdot \mathbf{u}) \mathbf{I} \quad (3)$$

with the identity tensor  $\mathbf{I}$  and molecular mixture viscosity  $\mu$ . For the transport of energy we introduce the temperature equation in the following form (Bird, Stewart, & Lightfoot, 2007):

$$c_p [\partial_t (\rho T) + \nabla \cdot (\rho \mathbf{u} T)] = \nabla \cdot (\kappa \nabla T) - (\boldsymbol{\tau} : \nabla \mathbf{u}) + D_t p \quad (4)$$

with  $c_p$  being the mixture heat capacity at constant pressure,  $\kappa$  the mixture heat conductivity and  $D_t \equiv \partial_t + \mathbf{u} \cdot \nabla$  the material derivative. This form of the energy equation is convenient as boundary conditions for temperature  $T$  can be readily implemented. Finally, the density can be computed from temperature and pressure using the underlying constitutive mixture equation of state, thereby closing the system. We adopt the form as, among others, used by Frederix, Kuczaj, et al. (2017), in which liquids are assumed to be

incompressible while vapors are assumed to adhere to the ideal gas law.

The transport equations for individual species transport is found from

$$\partial_t(\rho Y_j) + \nabla \cdot (\rho \mathbf{u} Y_j) = \mathcal{R}_j \quad (5a)$$

$$\partial_t(\rho Z_j) + \nabla \cdot (\rho \mathbf{u} Z_j) = \mathcal{S}_j \quad (5b)$$

with vapor and liquid sources  $\mathcal{R}_j$  and  $\mathcal{S}_j$  respectively. It is assumed that chemical reactions do not occur. Since

$$\sum_{j=1}^{\mathcal{N}} (Y_j + Z_j) = 1 \quad (6)$$

the summation of all equations in (5) is consistent with the continuity equation provided that

$$\sum_{j=1}^{\mathcal{N}} (\mathcal{R}_j + \mathcal{S}_j) = \mathcal{L}. \quad (7)$$

The droplet size distribution adheres to its own transport equation, i.e., the GDE (Friedlander, 2000). It can be written as

$$\partial_t n(s, \mathbf{x}, t) + \nabla \cdot [\mathbf{u} n(s, \mathbf{x}, t)] = J(s, \mathbf{x}, t) \quad (8)$$

with right-hand side source term  $J(s, \mathbf{x}, t)$  which may be used to represent a number of mechanisms such as growth by condensation and coagulation (Friedlander, 1983) as well as break-up and nucleation (Hounslow, Ryall, & Marshall, 1988). Moreover, contributions to droplet size transport due to diffusion and drift may also be incorporated. A precise detailing of the source term  $J(s, \mathbf{x}, t)$  used in this paper is provided in Section 2.2.

From a physical point of view the droplet size distribution  $n(s, \mathbf{x}, t)$  can be regarded as information about how many droplets we have of mass  $s$  at  $(\mathbf{x}, t)$ . From this interpretation it is then clear that  $n(s, \mathbf{x}, t)$  also tells us how much total droplet mass is present in the system. On the other hand, this information is also carried by  $\rho Z$  with  $Z \equiv \sum_j Z_j$ , which gives the total mass concentration of the droplet phase at  $(\mathbf{x}, t)$ . This means that  $n(s, \mathbf{x}, t)$  and  $Z$  are related to each other as follows:

$$\rho Z = \int_0^\infty s n(s, \mathbf{x}, t) ds \quad (9)$$

where the right-hand side of this relation represents the first moment of the size distribution. Within our model, this relation will prove to be very useful in the derivation of consistent transport equations for droplet drift, diffusion and deposition. We call this relation the aerosol *consistency relation*, representing the mutual consistency between liquid mass concentrations and the droplet size distribution.

## 2.2. Sectional approximation

The full size distribution  $n(s, \mathbf{x}, t)$  may be approximated numerically using the *sectional method* (Gelbard, Fitzgerald, & Hoppel, 1998; Gelbard, Tambour, & Seinfeld, 1980; Kumar & Ramkrishna, 1996), also referred to as the *discrete population balance method*. We follow closely the approach taken by Kumar and Ramkrishna (1996). In the sectional formulation of the droplet size distribution  $n(s, \mathbf{x}, t)$ , the size domain is divided into  $\mathcal{P}$  arbitrarily sized adjoining intervals. The  $i$  th section (with  $i = 1, 2, \dots, \mathcal{P}$ ) covers a part of the size domain bounded by  $y_i \leq s < y_{i+1}$  with  $y_i$  the position of the interface between the  $(i - 1)$  th and  $i$  th section. The droplets which reside in the  $i$  th section are assigned to a representative size  $s_i$  with  $y_i \leq s_i < y_{i+1}$ , such that the complete size distribution is approximated by

$$n(s, \mathbf{x}, t) \approx \sum_{i=1}^{\mathcal{P}} N_i(\mathbf{x}, t) \delta(s - s_i) \quad (10)$$

with  $N_i(\mathbf{x}, t) \geq 0$  the total number of droplets per unit of volume in the  $i$  th section and  $\delta$  the Dirac delta function. Conversely, we can write

$$N_i(\mathbf{x}, t) = \int_{y_i}^{y_{i+1}} n(s, \mathbf{x}, t) ds \quad (11)$$

from which it can be readily seen that  $N_i$  represents the zeroth moment of the size distribution function in the  $i$  th section and has units  $\text{m}^{-3}$ .

The rate at which the total amount of droplets within a section  $i$  changes can be derived from the GDE. In fact, by taking the integral over  $[y_i, y_{i+1}]$  of (8) and using definition (11), we find

$$\partial_t(\rho M_i) + \nabla \cdot (\rho \mathbf{u} M_i) = \mathcal{S}_{M_i} \quad (12)$$

where we define  $M_i$  as

$$M_i = \frac{N_i}{\rho} \quad (13)$$

In (12) we also have the right-hand side source term

$$\mathcal{J}_{M_i} = \int_{y_i}^{y_i+1} J(s, \mathbf{x}, t) ds \quad (14)$$

to which we turn next.

In the GDE (8) we conveniently left the source term  $J(s, \mathbf{x}, t)$  unspecified for sake of generality. Here, we will consider two main transport mechanisms of droplets, i.e., diffusion due to Brownian motion which is a mechanism of particular relevance for very small droplets in the range of nanometers, and drift due to droplet inertia which is a mechanism dominant for larger droplets in the range of several micrometers. These two mechanisms may be captured in the source term through (Frederix, Kuczaj, et al., 2017):

$$J(s, \mathbf{x}, t) = \nabla \cdot [\mathbb{D}^\ell(s) \nabla n(s, \mathbf{x}, t)] - \nabla \cdot [\mathbf{u}^\ell(s) n(s, \mathbf{x}, t)] \quad (15)$$

The first term in the right-hand side of this relation represents the droplet diffusivity with size-dependent diffusion coefficient  $\mathbb{D}^\ell(s)$  for the liquid droplets (hence the superscript  $\ell$ ). Moreover, in the second term we introduced a size-dependent drift-velocity  $\mathbf{u}^\ell$ , which is defined such that the droplets move with a velocity  $\mathbf{v} = \mathbf{u} + \mathbf{u}^\ell$ .

To compute the diffusion coefficient  $\mathbb{D}^\ell(s)$  we adopt the Stokes-Einstein equation, providing a model for the Brownian diffusivity of a spherical body. We implement the formulation as given by Frederix, Kuczaj, et al. (2017) and Hinds (1999), in which the Cunningham correction factor is incorporated to account for surface slip of small droplets. The reader is referred to the work of Frederix, Kuczaj, et al. (2017) and Hinds (1999) for more detail. For the droplet velocity  $\mathbf{v}(s)$  we use the ‘Full Stokes’ model as presented by Frederix, Kuczaj, et al. (2017).

In Eulerian context, the PDE describing the motion of a droplet is given by

$$\partial_t \mathbf{v}(s) + [\mathbf{v}(s) \cdot \nabla] \mathbf{v}(s) = -\frac{1}{\tau} [\mathbf{v}(s) - \mathbf{u}] + (1 - \gamma) \mathbf{g} \quad (16)$$

with the droplet relaxation time

$$\tau = \frac{\rho^\ell d^2}{18\mu}, \quad (17)$$

gravitational acceleration  $\mathbf{g}$  and density ratio  $\gamma = \rho^v / \rho^\ell$ . Eq. (16) can be solved numerically for  $\mathbf{v}(s)$ . Note that  $\mathbf{v}(s) \equiv \mathbf{v}(s, \mathbf{x}, t)$ , i.e., a Eulerian velocity field expressing the time-, space- and size-dependent droplet velocity.

### 2.3. Computing deposition characteristics

When we use a no-slip boundary condition for the mixture velocity  $\mathbf{u}$  then  $\mathbf{u}$  is zero at the wall. The only two mechanisms allowing for droplet deposition on such walls are then, see Eq. (15), a non-zero drift velocity  $\mathbf{u}^\ell(s)$ , or a non-zero gradient of  $n(s, \mathbf{x}, t)$  perpendicular to the wall, i.e.,  $\nabla n(s, \mathbf{x}, t) \cdot \mathbf{n}$  with  $\mathbf{n}$  the general wall normal. We discuss the boundary treatments for both mechanisms next:

1. For the first mechanism the inertial droplet velocity  $\mathbf{v}(s)$  must be known at the wall. To numerically do this, a first approach would be to take the wall droplet velocity equal to the velocity of droplets at a computational cell center near the wall if that velocity is wall-ward, as if droplets maintain a constant velocity near the wall. We call this approach the zero-gradient extrapolation model (ZGM) boundary treatment. Alternatively, we may adopt the Lagrangian sub-grid model (LSM) boundary treatment approach proposed by Longest and Oldham (2008) and applied by Frederix, Kuczaj, et al. (2017).
2. The deposition due to diffusion is treated under the assumption of a perfectly absorbing boundary. When droplets hit a wall they are absorbed instantly, and removed from the domain. Diffusional deposition is driven by  $\nabla n(s, \mathbf{x}, t) \cdot \mathbf{n}$  being non-zero at the wall. We compute the gradient of  $M_i$  at the face *in the diffusion flux* as if  $M_i$  is zero at the wall to induce diffusion transport towards the wall. Full details are given by Frederix, Kuczaj, et al. (2017).

In the next Section we specify the numerical methods that have been adopted and show simulation results of flow and deposition in a lung cast.

## 3. Validation against deposition experiments of the human upper airways

In the previous section the Eulerian aerosol model for droplet deposition by diffusion and drift was presented. In this section, the model will be applied to the prediction of aerosol lung deposition. The main goal of this is to validate the model, as experimental data for regional deposition in a realistic cast of the upper human airways is available. In Section 3.1 the experimental setup is discussed, as well as the experimental conditions at which the lung cast was operated. These conditions must be mimicked accurately, to allow for proper comparison between the numerical and experimental results. The numerical setup is discussed in Section 3.2. Finally, in Section 3.3, we study the deposition rate of aerosol inside the lung cast. Due to the construction of the cast, detailed deposition rates can only be measured per segment experimentally. The per-segment data can also be recovered from the numerical setup. Several simulations will be compared against the experimental data, for different computational grids and comparing the two boundary treatments as outlined in the previous section.

### 3.1. Experimental setup

Nordlund et al. (2017) presented experiments in a realistic cast of the human upper respiratory tract. In this paper we accurately represent the geometry of this cast numerically, as well as the conditions at which the cast is operated. For completeness, we give a brief overview of the main features of the lung cast.

The lung cast is based on the original model of Lizal et al. (2015). It is a segmented airway model consisting of an oral cavity and subsequent segments down to the seventh generation of lung branching. Fig. 1 (left) shows a visualization of the in silico representation of the human tracheobronchial tree. In the right figure a close-up is shown of the branching geometry as used in the experiment, where it can be clearly seen that the cast is built up of 32 segments, constructed to explicitly distinguish the geometrical features of the airways. The internal geometry of the cast is based on a combination of a digital reference model of the human tracheobronchial tree (Schmidt et al., 2004) and the oral cavity (Cheng, Zhou, & Chen, 1999). The numbering of segments is from top to bottom starting with the oral cavity, as shown in Fig. 1. Segments 23–32 are outlet segments to connect the relatively small seventh generation branches in one larger outlet (see Fig. 1). The flow rate at each of these 10 outlets was set such that the total inlet flow rate is  $15 \text{ min}^{-1}$ , corresponding to flow conditions in the sedentary regime (Elcner, Lizal, Jedelský, Jícha, & Chovancova, 2016). The outlet flow rates are specified by Nordlund et al. (2017), and correspond to flowrates related to the pneumatic resistance of the model, as reported by Lizal et al. (2015). The maximum Reynolds number inside the cast is approximately  $10^3$ , near the trachea, and much lower in other parts of the lung cast, such that the flow can be regarded as laminar (Nordlund et al., 2017).

Once a steady-state flow is achieved inside the lung cast, an aerosol can be released at the inlet of the mouth. The chosen aerosol was a glycerol-air mixture with a count median aerodynamic diameter of  $2.1 \mu\text{m}$  and a geometric standard deviation of 1.19. This particle size distribution corresponds to the largest sizes which could be reliably created with the aerosol generation method, i.e., a Condensation Monodisperse Aerosol Generator (CMAG) (Nordlund et al., 2017). Fig. 2 shows the experimental droplet size distribution as taken from the work of Nordlund et al. (2017). It can be seen that the highest droplet number concentration is located at  $2 \mu\text{m}$ , while the distribution spans from approximately  $1 \mu\text{m}$  to  $4 \mu\text{m}$ . Also shown in this figure is a log-normal fit to the experimental distribution, with the count median diameter (CMD) set to  $2.1 \mu\text{m}$  and the geometric standard deviation to  $\sigma = 1.19$  (Hinds, 1999). Both lines are close to each other and we conclude that a log-normal distribution based on the given CMD and  $\sigma$  represent the experimental droplet size distribution well. In the next subsection we use the mathematically convenient log-normal distribution in our numerical model. It is well known that droplets in the micrometer size range exhibit low Brownian motion as well as modest drift, reducing their deposition efficiency significantly compared to much larger or much smaller droplets. Frederix, Kuczaj, et al. (2017) showed that around  $d = 2 \mu\text{m}$  the deposition efficiency curve is at a minimum for most Reynolds numbers, in a bent pipe geometry. It was also shown there that numerically, deposition for droplets of these sizes is difficult to predict adequately. This motivates our choice for studying the aerosol dynamics at precisely a droplet size in the micrometer range, as it places a stronger demand on the numerical quality of the simulations and the adopted drift- and diffusion models.

After the lung cast is exposed to the aerosol flow for one hour, the cast can be disassembled into separate segments. The deposited glycerol mass is extracted from each segment by rinsing it with a known amount of 2-propanol solution. Using Gas Chromatography-Mass Spectrometry (GC-MS) the concentration levels of glycerol in the extraction solutions can be measured. The concentration levels are then translated into deposition rates, given the total volume of rinsing solution used and the cast exposure time (1 h). The segments 23–32 are connected to filters and absorb all aerosol droplets which have not deposited inside the cast. These segments, including their filters, are rinsed and measured for glycerol concentration in the same way. Each outlet is connected to a flow controller to be able to set the flow rate through each outlet individually. The sum of all deposited masses of glycerol of all segments is equal to the total mass of glycerol which entered the system.

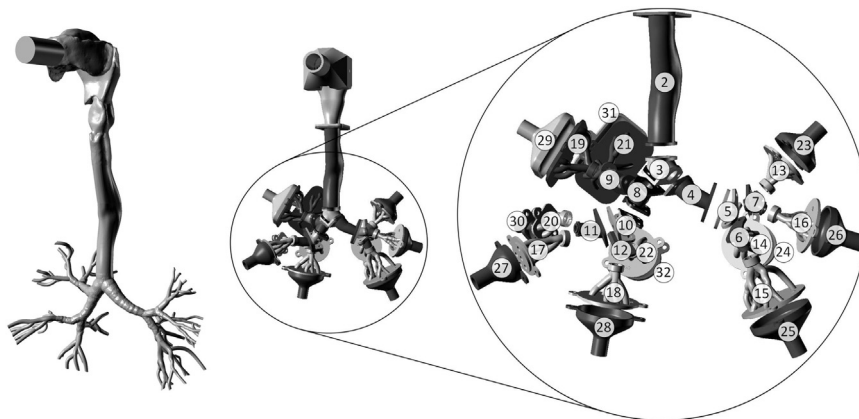


Fig. 1. Left: visualization of the lung cast geometry. Right: visualization of the segmented cast as used in the experiment with segment numbers as indicated (Nordlund et al., 2017).

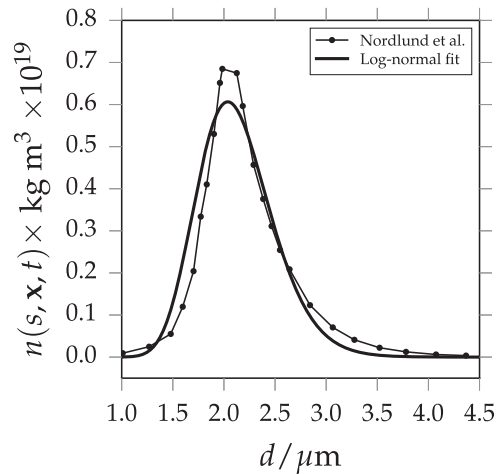


Fig. 2. The glycerol droplet size distribution at the inlet of the cast for the physical experiment (\*) (Nordlund et al., 2017) and the numerical simulation (–).

### 3.2. Numerical setup

Fig. 3 shows the front and side view of the lung cast geometry as used in our simulations. It is a direct copy of the model used for the physical experiments. The inlet, throat, trachea, main bronchi and outlets are shown. As in the physical experiment, the seventh generation is connected to a conically-shaped outlet segments. The inlet and outlets have cylindrical extrusions, such that the flow into and out of the cast may naturally develop without the inlet and outlet condition being of major influence. In order to simulate inside the geometry using a finite volume method, we must create a computational mesh of the geometry. Three computational grids are used to test the mesh dependency of the numerical results. Two meshes (coarse A and fine B) are constructed without boundary layer refinement (-no-bl suffix), and a finer mesh B was constructed also with boundary layer refinement (-bl suffix). On those three distinct meshes simulations are performed using the LSM (-LSM suffix) and ZGM (-ZGM suffix) boundary treatments for the velocity of particles at the wall. Identification of the presented results given a mesh and boundary conditions follows from the syntax which is constructed from the abbreviations (e.g., A-no-bl-LSM to denote results obtained on the coarse grid A, without refinement in the boundary layer close to the wall and with the LSM for the inertial deposition velocity).

In order to determine the necessary cell sizes, Reynolds Averaged Navier-Stokes (RANS) simulations are performed. The commercial StarCCM+ code, version 10.2, is used and the SST  $k-\omega$  turbulence model is applied. For the determination of the characteristic scales, the resting condition of 15 L/min steady-state flow rate is applied. The bulk computational cell size for the fine mesh B is based on the Taylor scale computed from the RANS simulations (Kuczaj, Komen, & Loginov, 2010). For the boundary layer the non-dimensional wall distance for wall-bounded flows is also computed based on the RANS simulations and the first layer of cells is located at  $y^+ = 0.5$ , while the last layer has a similar size as the bulk cell size.

The Taylor scale is estimated between  $4.5 \times 10^{-4}$  and  $7.5 \times 10^{-4}$  m, depending on the particular lung regions, while the thickness of the first cell of the triangular prism layer for the selected flow and  $y^+ = 0.5$  is found to be  $6 \times 10^{-5}$  m. Depending on the lung region the boundary layer mesh consists of 7–10 cell layers, with thicknesses consecutively growing towards the bulk with a stretching ratio equal to 1.2. For all meshes generated in StarCCM+, the quality of the polyhedral elements is set as high as possible in the software

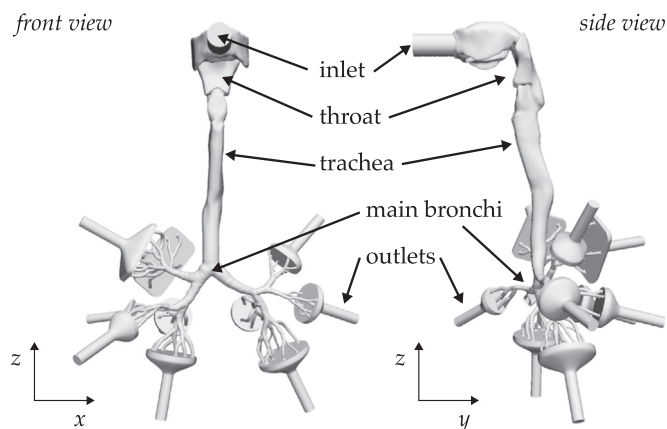


Fig. 3. Front and side view of the lung cast geometry as used in simulations.

setup to obtain a smaller number of cells, and in particular a smaller number of non-orthogonal cells. The mesh A (coarse) was constructed by coarsening the resolution of mesh B with a factor of two. In total, mesh A-no-bl has 583, 088 cells, mesh B-no-bl 1,750,042 cells and mesh B-bl 4,021,078 cells.

Table 1 lists the physical parameters used in the simulations. For the viscosity we use that of air. The liquid density of glycerol is taken from the work of Nordlund et al. (2017). The physical experiment was performed at atmospheric conditions and room temperature. Temperature and pressure changes inside the lung can be assumed to be small such that the system is effectively isothermal. This allows to neglect effects such as condensational growth, evaporation and nucleation, and allows to take the physical parameters listed in Table 1 as constant. In agreement with the experiment the flow rate at the inlet  $\Phi$  is set to 15 L/min.

Table 2 lists the boundary conditions for the solution variables for the inlet, ten outlets and wall boundary regions. We set the mass fraction of glycerol to a low but arbitrary value of  $10^{-5}$ . Since for such a dilute aerosol there is only one-way coupling (Elghobashi, 1994) (the corresponding volume fraction of glycerol is much smaller than  $10^{-5}$  due to its density) between flow and particulate phase, the concentration of droplets has no effect on the flow or deposition patterns. Also, when discretizing the size space in several sections, these sections do not communicate with each other due to the omitted effects of condensation, evaporation, coagulation, etc, although each representative size  $s_i$  associated with a section responds in its own way to the flow. This response depends on the sectional diffusivity  $D_i^\ell \equiv \mathbb{D}^\ell(s_i)$  and sectional droplet velocity  $\mathbf{v}_i \equiv \mathbf{v}(s_i)$  consisting of the velocity of the gas mixture  $\mathbf{u}$  and the size dependent drift velocities of the droplets. For convenience, we choose to set an arbitrary uniform distribution in sectional space, i.e.,  $M_i = M_0$  at the inlet. Using the consistency relation (9) it can be derived that  $M_0 = Z_{\text{gly}} / \sum_i s_i$  at the inlet, with  $Z_{\text{gly}}$  the local mass fraction of glycerol. To represent the relevant size space of the glycerol inlet distribution shown in Fig. 2 accurately, we choose  $\mathcal{P} = 8$  and a distribution of equally sized sections in  $d$  over the domain  $d = [1, 4] \mu\text{m}$ . The representative sizes  $s_i$  are chosen at the center of each section in  $d$ -space. By using the fact that mass fractions sum up to unity, we set the carrier gas mass fraction to  $Y_{\text{air}} = 1 - Z_{\text{gly}}$  at the inlet such that droplets are following mixture streamlines. We force the droplet phase at the inlet to have no drift velocity, i.e.,  $\mathbf{v}_i = \mathbf{u}$  at the inlet. The aerosol enters the cast under atmospheric pressure  $p_0$ . We assume that due to the cylindrical outlet extensions as shown in Fig. 3 the flow is sufficiently developed such that a zero-gradient boundary condition can be set for all variables at all outlets. Only the fluid velocity  $\mathbf{u}$  is set using a Dirichlet boundary condition. We impose an outward Poiseuille profile with a total flow rate as specified by Nordlund et al. (2017). The sum of all the outlet flow rates equals  $\Phi$ . For both  $M_i$  and  $Z_{\text{gly}}$  we use the zero-gradient boundary condition when computing the drift flux at the geometry walls and a Dirichlet boundary condition of zero when computing the diffusive flux to mimic a perfectly absorbing surface. No boundary condition is necessary for vapor at the walls because we set the wall vapor flux to zero. For the mixture velocity  $\mathbf{u}$  a no-slip condition is applied while we use either the LSM or ZGM boundary treatments for  $\mathbf{v}_i$  as will be indicated, at the walls. We start each simulation at  $t = 0$  with a quiescent system containing only air at pressure  $p_0$  and temperature  $T_0$ . In the time interval  $t = [0, 0.1]$  s the outlet velocities are linearly ramped to their values corresponding to a total inlet flow rate of  $\Phi$ . For the given conditions and meshes all simulations attain a steady state. The results presented in the remainder of this text are taken at  $t = 4$  s, a point in time for which all simulations are converged sufficiently to this steady state. We conclude this from the fact that the total flux of droplets leaving the system (via deposition or the outlets) is approximately equal to the total flux of droplets entering the system, to within 5%.

Table 3 shows the numerical schemes used for the various terms in the set of governing equations. For the partial time derivatives we use the  $\theta$ -scheme (Morton & Mayers, 2005) with  $\theta = 0.6$ . This gives extra implicit damping and improves convergence to the steady state. We use the ‘linear upwind’ scheme in the computation of both temperature and velocity at cell faces. This interpolation scheme is a second order upwind-biased scheme and uses the gradient of the velocity to explicitly ‘improve’ the interpolation from an upwind direction. The Van Leer limiter (van Leer, 1979) is used to interpolate  $Y_j$ ,  $Z_j$  and  $M_i$  to cell faces. This combination of schemes for the particular terms performed well in the work of Frederix, Kuczaj, et al. (2017) and is therefore selected here too.

### 3.3. Deposition efficiency results and comparison

When integrating Eq. (15) over a section and using definition (13) it can be seen that the total sectional number concentration flux at a wall is given by

$$\phi_i = -\rho \mathbf{u}^\ell M_i + \rho D_i^\ell \nabla M_i, \quad (18)$$

**Table 1**  
Simulation parameters for glycerol droplets carried by air at room temperature and atmospheric conditions. The  $v$  superscript denotes a vapor and  $\ell$  a liquid.

Parameter	Value	Unit
$\mu$	$1.81 \times 10^{-5}$	$\text{m}^2/\text{s}$
$\rho_{\text{air}}^v$	1.1898	$\text{kg}/\text{m}^3$
$\rho_{\text{gly}}^\ell$	1258	$\text{kg}/\text{m}^3$
$T_0$	298.15	K
$p_0$	$10^5$	Pa
$\Phi$	15	L/min
$\mathbf{g}$	(0, 0, -9.81)	$\text{m}/\text{s}^2$

**Table 2**

Boundary conditions for the given variables and boundary regions. ZG stands for zero-gradient.

Variable	Inlet	Outlets	Walls
$Z_{gly}$	$10^{-5}$	ZG	ZG (drift) and 0 (diffusion)
$Y_{air}$	$1 - Z_{gly}$	ZG	–
$M_i$	$M_0$	ZG	ZG (drift) and 0 (diffusion)
$T$	$T_0$	ZG	$T_0$
$\mathbf{u}$	ZG	From Nordlund et al. (2017)	(0, 0, 0) m/s
$\mathbf{v}_i$	$\mathbf{u}$	ZG	LSM or ZGM
$p$	$p_0$	ZG	ZG

**Table 3**

Chosen numerical schemes for the discretization of the indicated terms.

Term	Scheme	Comment
$\partial_t$	$\theta$ -scheme (Morton & Mayers, 2005)	All time derivative, $\theta = 0.6$
$\mathbf{u}_f, T_f$	Linear upwind	linearUpwind linear in OpenFOAM
$Y_{j,f}, Z_{j,f}, M_{i,f}$	Van Leer limiter (van Leer, 1979)	vanLeer in OpenFOAM
$\mathbf{v}_{i,f}$	Upwind	Provides good convergence
$\nabla$ (cell-center gradient)	Central	linear in OpenFOAM
$\nabla^2$ (Laplacian)	Central corrected	linear with non-orth. corr.
$\nabla_f$ (face-normal gradients)		

which has unit  $\text{m}^{-2}\text{s}^{-1}$ , i.e., it gives the section  $i$  number of droplets passing per unit area per unit time. Multiplying this by  $s_i$  gives the total mass of droplets in section  $i$  passing per unit area per unit time, i.e.,

$$\text{flux}_i = \phi_i s_i. \quad (19)$$

The value of  $\text{flux}_i$  can be computed at the walls of the lung cast, thereby allowing to assess the deposition in different parts of the lung cast.

Fig. 4 shows the deposition patterns in terms of the flux of droplets in section  $i = 3$  with size  $d = 1.93 \mu\text{m}$  close to the value of CMD of the log-normal size distribution as shown in Fig. 2. The lung cast is shown only for segments 1–12 for better visibility of the first bifurcation. The deposition flux is presented for mesh A without boundary layer mesh refinement and mesh B with and without boundary later mesh refinement. The left column shows results using the ZGM deposition velocity boundary treatment and the right column using the LSM. The color represents the flux scaled by the surface-averaged inlet flux. It can be seen that locally the deposition flux exceeds 0.025% of the inlet flux. For the ‘no-bl’ meshes with the ZGM boundary treatment it is quite difficult to distinguish deposition patterns with a sensible length scale; the deposition appears very pixellated. Moreover, with respect to the other simulations the deposition pattern shows a large overprediction of deposition. This corresponds to the observations made by Frederix, Kuczaj, et al. (2017), where deposition in a bent pipe was studied. When the computational mesh was not refined near the wall of the domain, the ZGM boundary treatment showed large overpredictions of deposition, in particular for droplets in the  $\mu\text{m}$  range with flow Reynolds numbers equivalent to the ones in the lung cast ( $\mathcal{O}(10^3)$ , Nordlund et al., 2017 provided a detailed overview of the per-segment Reynolds numbers). For the ‘no-bl’ meshes with the LSM treatment, some trends in the deposition pattern become visible – although the deposition is still quite pixellated. For example, a symmetric gradient in deposition flux is shown at the inlet extension (at the mouth). As droplets enter the inlet extension with the same laminar axial velocity as the carrier gas, a non-axial deposition flux there can only be attributed to sedimentation. At the saddle point of the first bifurcation (this point is enlarged in the insets in Fig. 4 for each simulation), an increase of deposition is shown compared to the primary bronchi, which is attributed to inertial impaction due to the large carrier gas velocity and curvature there.

For mesh B with boundary layer mesh refinement the deposition patterns become much smoother and less pixellated, for either boundary treatment scheme. Features of the geometry are now clearly reflected in the deposition patterns. Quite interestingly, the primary bronchi show a ‘zebra-like’ deposition pattern with rings of local maxima and minima. This deposition pattern appears related to actual anatomical structures in the bronchi walls. After visual inspection we note that the distances between these rings correspond to the length scale of the oscillatory structure of the lung surface, as a result of the tracheal and bronchi rings. Also features in the mouth cavity can be clearly distinguished. Fig. 5 shows the left, right, front and back view of the ‘B-bl-ZGM’ deposition results for the same droplet size. Here too, features of the geometry can be seen in the pattern of deposition. For example, cavities inside the Larynx are clearly visible due to large deposition there.

After these qualitative considerations, we turn to quantitative comparison against experimental data next. In the physical experiment the total deposition rate  $R_k$  in units of  $\mu\text{g}/\text{hr}$  were measured for each cast segment  $k$ . To allow direct comparison of our simulations against this experimental data, we post-process our results in the following way:

1. In the simulations an arbitrary level of inlet concentration was set, i.e., at the inlet the mass fraction for glycerol is  $Z_{gly} = 10^{-5}$ .

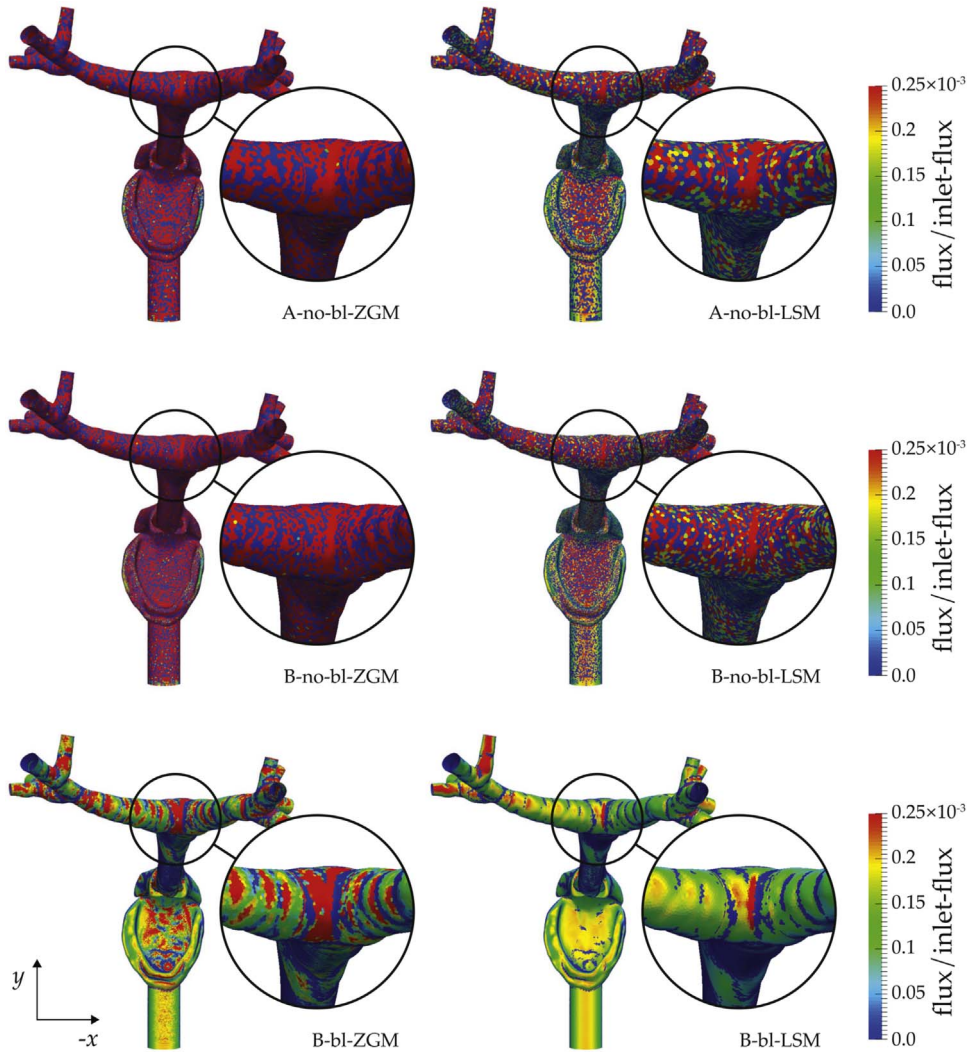


Fig. 4. Deposition fluxes for  $d = 1.93 \mu\text{m}$  glycerol droplets for the meshes A-no-bl, B-no-bl and B-bl, comparing the LSM and ZGM droplet velocity wall treatments. The color indicates the flux scaled by the surface-averaged inlet flux. The inset shows an enlarged image of the first bifurcation. Only segments 1–12 are shown.

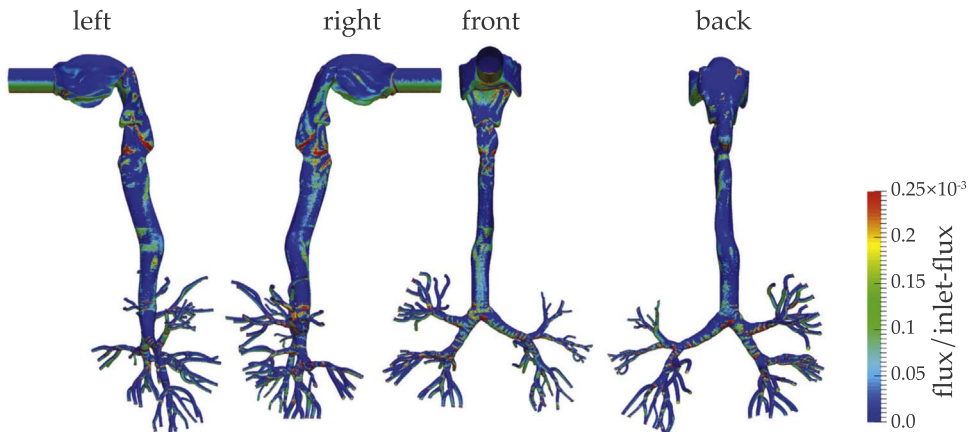


Fig. 5. Left, right, front and back view of the deposition flux for  $d = 1.93 \mu\text{m}$  glycerol droplets using mesh B with boundary layer mesh refinement at the wall and the ZGM inertial droplet velocity boundary treatment. Segments 1–12 are shown.

This must be accounted for to reflect the experimental inlet concentration. In the experiment all aerosol droplets are either captured by the segments due to deposition, or by the filters at the ten separate outlets. This means that summing all the rates corresponding to all the segments and outlets gives the total influx, from which the experimental  $Z_{\text{gly}} = 10^{-5}$  at the inlet can be derived. We scale our deposition rates by the ratio of experimental and numerical  $Z_{\text{gly}} = 10^{-5}$ .

2. At the inlet we have specified  $\mathcal{P} = 8$  sections covering the size domain  $d = [1, 4] \mu\text{m}$  in diameter, each with a droplet number concentration of  $M_0$ . To accurately mimic the total experimental deposition rate, the sectional deposition fluxes must be scaled by the log-normal size distribution as shown in Fig. 2. We use a weighted average of the sectional fluxes to compute the total per-segment deposition rate

$$R_k = \sum_i w_i \int_{A_k} \text{flux}_i dA, \quad (20)$$

with  $A_k$  the surface area of the  $k$  th segment and  $w_i$  the weight belonging to the  $i$  th section. We let  $w_i$  correspond to the surface area underneath a unit log-normal distribution with given CMD and  $\sigma$  corresponding to the part of the size domain for which section  $i$  is representative. The  $i$  th section covers  $[y_i, y_{i+1}]$  in the size domain in terms of mass, and  $[d_i, d_{i+1}]$  in terms of diameter. The unit log-normal distribution can be written as (Hinds, 1999):

$$f(d) = \frac{1}{\sqrt{2\pi} d \log \sigma} \exp\left(-\frac{(\log d - \log \text{CMD})^2}{2 \log^2 \sigma}\right). \quad (21)$$

Using  $\sigma$  and CMD as given above, we define the sectional weights as

$$w_i = \int_{d_i}^{d_{i+1}} f(d) dd. \quad (22)$$

This well-known integral can be expressed using the erf-function. Integrating  $f(d)$  from zero to  $\infty$  gives unity. The sum  $\sum_i w_i$  represents the integral of  $f(d)$  from  $d_1 = 1 \mu\text{m}$  to  $d_{\mathcal{P}+1} = 4 \mu\text{m}$  and has a value of 0.99988..., indicating that the relevant size domain of the distribution is captured quite completely with the chosen sections.

With these two post-processing steps completed we can compare the numerical results against the experimental data. Fig. 6 shows both the experimental and numerical data for each cast segment. The numerical data were obtained for six different setups using two meshes, with and without boundary layer grid refinement and the two boundary treatments. For the ZGM boundary treatment (left figure) it is shown that for the adopted spatial resolution and without grid refinement near the wall (i.e., ‘no-bl-ZGM’ suffix in the legend) a large overprediction of deposition occurs. In fact, the ratio between  $R_k$  for experimental data and ‘no-bl-ZGM’ numerical data is more than one order of magnitude. The deposition is so large that a significant amount of droplets has already deposited before reaching the outlets, therewith reducing  $R_k$  significantly for  $k > 22$ .

When using the LSM boundary treatment on mesh B with boundary layer grid refinement, the numerical deposition rate agrees well with the experimental data. Given the sensitivity of the experimental data (indicated by the gray area in Fig. 6) it is remarkable how close the numerical predictions are with the measurements. For  $13 \leq k \leq 22$  it appears that the ‘B-bl-ZGM’ results show a small systematic overprediction of the experimental data, although the ratio between  $R_k$  for experiment and simulation remains within one decade.

The numerical results using the LSM scheme, see Fig. 6 (right), show for any of the adopted meshes a good agreement with experimental data. These results correspond to the right column of pictures in Fig. 4. It was noted before that the deposition fluxes for

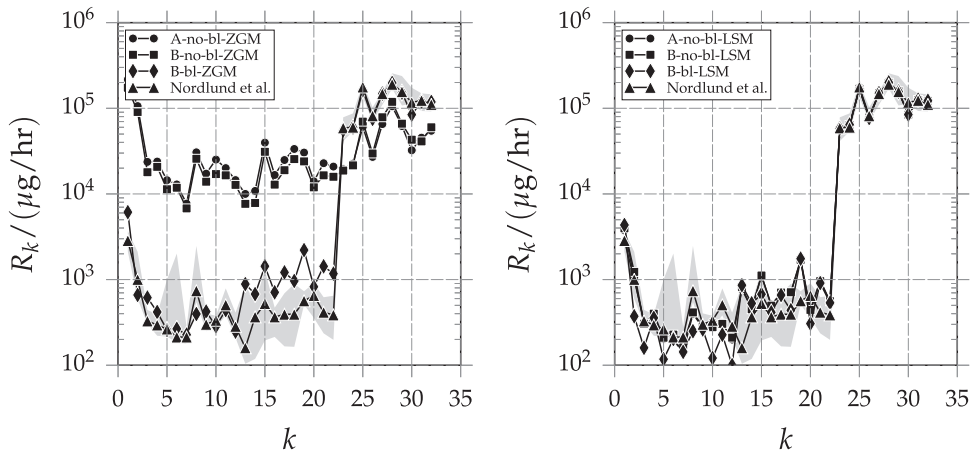


Fig. 6. Per-segment (indexed by  $k$ ) deposition rates for the simulations and physical experiment as indicated. Left shows the ZGM boundary treatment results and right those for the LSM boundary treatment. Segments 23–32 contain the outlet filters and therefore a large part of the total deposition rate. The gray area marks the range between highest and lowest experimentally measured values, for each  $k$ . The points marked as Nordlund et al. are the average of the experimental repetitions.

the ‘no-bl’ meshes are quite pixellated. Still, the integral quantities  $R_k$  for each segment  $k$  (they are integral quantities due to the surface integral in Eq. (20)) correspond reasonably well to both the experimental data as well as the predictions for  $R_k$  using the wall-refined ‘bl’ meshes. In practice, the added value of numerical simulation over physical experiment is that local deposition patterns may be accurately resolved instead of only getting regional deposition information as in the experiments. If this is required, then meshes with sufficient resolution near the wall are necessary. Conversely, under-resolved simulations yield correct per-segment deposition rates but this may be more of a coincidence than a numerically reliable simulation feature. In fact, if the most detailed impression of the solution is clearly under-resolved, then any agreement of integral quantities with experiments is rather fortuitous. The results clearly establish that reliable results are achieved at proper spatial resolution and that particularly the resolution of the boundary layer is crucial for high-quality predictions.

To analyze the experimental and numerical results in a more quantitative way, Table 4 shows some of the statistics of both the experimental and numerical work. Since Fig. 6 shows results on a logarithmic scale we have also considered the statistics of the results on this basis. For the experimental results, the per-segment mean  $\mu_k$  and standard deviation  $\sigma_k$  of the deposition rates are computed as:

$$\mu_k = \text{mean}(\log \mathcal{R}_k) \quad \text{and} \quad \sigma_k = \text{STD}(\log \mathcal{R}_k), \quad (23)$$

with  $\mathcal{R}_k$  the set of experimental measurements performed for segment  $k$ . We also compute how far numerical result  $R_k$  lies from the experimental  $\mu_k$  with respect to the standard deviation of the experimental results. For this, we introduce  $C_k$ , as

$$C_k = \frac{|\mu_k - R_k|}{\sigma_k}, \quad (24)$$

indicating how many STDs the numerical observation is away from the mean experimental observation. The numerical results on the mesh without boundary layer refinement and in cases without the Lagrangian sub-grid model is, averaged over all segments, is found approximately 15  $\sigma_k$  away from the experimental mean. Adding a boundary layer and/or using LSM is shown to reduce the error with respect to experimental data to about 2 standard deviations.

#### 4. Size-dependent deposition patterns in the human upper airways

In the previous section we have validated our numerical approach against experimental data. We see good agreement for meshes with sufficient resolution near the wall. Also, using the LSM boundary treatment the lack of resolution near the wall can be partially compensated by adopting a Lagrangian sub-grid model. In this section we extend the previous simulations by increasing the size domain and number of sections such that both the diffusional and inertial deposition regimes (Frederix, Kuczaj, et al., 2017) are represented. The main intention of this is to illustrate the capabilities of our method. The validity of the results is underlined by 1) the experimental agreement with deposition data for the real geometry as seen in the previous section in the micrometer size range and

**Table 4**

Per segment mean ( $\mu_k$ ) and standard deviation ( $\sigma_k$ ) of the logarithm of the deposition rate  $R_k$  for the experiment (second column). Also the numerical data is shown for B-no-bl-ZGM, B-bl-ZGM and B-no-bl-LSM, with  $C_k$  a measure for how far the numerical observation is away from the experimental mean, see Eq. (24).

k	Nordlund et al.	No BL & no LSM		With BL		With LSM	
	$\mu_k \pm \sigma_k$	$\log R_k$	$C_k$	$\log R_k$	$C_k$	$\log R_k$	$C_k$
1	3.44942 ± 0.0799839	5.23986	22.385	3.78684	4.21866	3.59826	1.86085
2	3.01271 ± 0.160937	4.95702	12.0812	2.82028	1.19572	3.08958	0.477611
3	2.54226 ± 0.0611047	4.25388	28.0113	2.78925	4.04218	2.48355	0.960744
4	2.47118 ± 0.073188	4.31604	25.2071	2.6213	2.05115	2.60136	1.77864
5	2.49681 ± 0.20742	4.05492	7.51186	2.41183	0.409698	2.3205	0.850038
6	2.45542 ± 0.323682	4.07236	4.99548	2.42456	0.095346	2.35753	0.302416
7	2.33273 ± 0.0530852	3.83144	28.2321	2.35649	0.447581	2.23371	1.86536
8	2.94188 ± 0.231113	4.41055	6.35474	2.59816	1.48725	2.61679	1.40665
9	2.4764 ± 0.0601194	4.14268	27.7162	2.62656	2.49779	2.45208	0.404538
10	2.5085 ± 0.0571888	4.23197	30.1365	2.45552	0.92644	2.44426	1.12317
11	2.69536 ± 0.0941775	4.21752	16.1627	2.64383	0.547192	2.48293	2.25563
12	2.48387 ± 0.0933735	4.10556	17.3678	2.39242	0.979432	2.32206	1.73295
13	2.33223 ± 0.311387	3.88422	4.98411	2.94698	1.97421	2.91435	1.86942
14	2.47042 ± 0.231962	3.89425	6.13822	2.8308	1.55362	2.65332	0.788503
15	2.69139 ± 0.247516	4.49181	7.27394	3.15588	1.87658	3.04753	1.43886
16	2.54024 ± 0.118385	4.10871	13.249	2.85127	2.62727	2.69577	1.31376
17	2.57813 ± 0.18435	4.27734	9.21732	3.08367	2.74229	2.84792	1.46345
18	2.55804 ± 0.277764	4.40696	6.65641	2.98411	1.53393	2.85235	1.05954
19	2.76768 ± 0.0522813	4.38006	30.8404	3.34429	11.0289	3.23116	8.86518
20	2.76642 ± 0.142713	4.07718	9.18463	2.91623	1.04974	2.64594	0.84421
21	2.61889 ± 0.13163	4.2174	12.1439	3.1547	4.07056	2.98149	2.75466
22	2.55343 ± 0.20572	4.20013	8.0046	3.06919	2.5071	2.7464	0.93804
Average over k:			15.1752		2.26648		1.65246

2) the agreement of the model for a much larger size range with literature available for a bent-pipe geometry (Frederix, Kuczaj, et al., 2017). We do this using the ‘B-bl-LSM’ setup, i.e., mesh B with boundary layer refinement and the LSM boundary treatment for the deposition velocity. This setup was shown to give accurate results in comparison with the experimental lung cast data, while producing visually smooth deposition flux fields.

We set the number of sections to  $\mathcal{P} = 16$  using an equidistant sectional distribution in  $\log d$ -space spanning  $d \in [10^{-2}, 20] \mu\text{m}$ , with the representative sizes halfway each section in  $\log d$ -space. For these sizes, based on the work by Frederix, Kuczaj, et al. (2017), we expect that both the diffusional and inertial deposition regimes are included. All initial and boundary conditions remain equal to those used in the previous section. Using the sectional consistency relation we set one sectional droplet number concentration equal to  $M_i = Z_{\text{gly}} / \sum_i s_i$  for all sections at the inlet.

We study quantitatively the deposition behavior inside the lung cast, as a function of droplet size. To that end, we introduce the following quantity:

$$\eta_g(s_i) = - \frac{\int_{A_g} \text{flux}_i dA}{\int_{A_{\text{inlet}}} \text{flux}_{\text{inlet}} dA}, \quad (25)$$

representing the per-generation deposition efficiency of droplets of size  $s_i$ , for lung structures of generation  $g$ , with  $A_g$  the wall surface of all segments belonging to generation  $g$ . The ‘connectivity’ between cast segment  $k$  and lung generation  $g$  is explained by Nordlund et al. (2017), where a detailed table indicates to which generation  $g$  part  $k$  belongs. The numerator of (25) denotes the total number of droplets in section  $i$  depositing on the wall of the  $g$ th generation of the lung cast, per unit of time. The denominator denotes the total flux of droplets in section  $i$  that enters through the inlet. As this has a negative sign, the definition of  $\eta_g$  contains a minus sign. In short,  $\eta_g$  gives the mass deposition rate of droplets of size  $s_i$  into the lung cast wall belonging to generation  $g$  with respect to the inflow rate.

Fig. 7 (left) shows  $\eta_g$  in a bar diagram for the different groups of lung generations. The experimental lung cast is constructed such that segments  $k > 12$  contain multiple lung generations. These segments are grouped together. Clearly, a ‘V-shaped’ deposition efficiency is shown, with approximately  $d \approx 0.8 \mu\text{m}$  separating the predominantly diffusional regime from the predominantly inertial regime. This also shows that the glycerol distribution as used in the previous Section with  $\text{CMD} = 2.1$  is close to the minimum of the V-curve, indicating that diffusional and inertial deposition are both relevant deposition mechanisms. For the section representing the largest droplets, the total efficiency of the lung cast is close to unity; almost all droplets have deposited, leaving no chance for droplets to escape through the outlets. In Fig. 7 (right) the partitioning of deposition in the various size classes and generation of lung structures is shown. Of the total mass which deposits per unit of time, the colors indicate what percentage of those droplets deposit in which generation of the lung. It can be seen that approximately half of the droplets deposit in the throat and generations 0–3. The other half deposits in generations 4–7. Only for the section containing the largest droplets, most droplets deposit early on in the lung cast. In fact, approximately 50% of the droplets entering the mouth deposit inside the throat. The partitioning of deposition with respect to the lung generation is reasonably uniform in the size domain for  $d < 0.4 \mu\text{m}$ , i.e., the diffusional deposition regime. In the inertial regime the partitioning of deposition depends on size. For example, the throat has an enhanced deposition with respect to the total deposition for approximately  $0.4 < d < 2 \mu\text{m}$ . For  $2 < d < 10 \mu\text{m}$  the percentage of deposition in the throat decreases and for  $d > 10 \mu\text{m}$  a rapid increase occurs. This is the result of a complex geometry-dependent interplay of droplet inertia, drag and gravity. Droplet diffusivity is negligible for these droplet diameters.

The per-generation deposition efficiency  $\eta_g$  is proportional to the number of droplets depositing inside the parts of the cast belonging to generation  $g$ . In some respect, this could be misleading, since some generations may be very efficient in capturing droplets but have only a small amount of surface area to capture these droplets. To assess the efficiency with which each lung

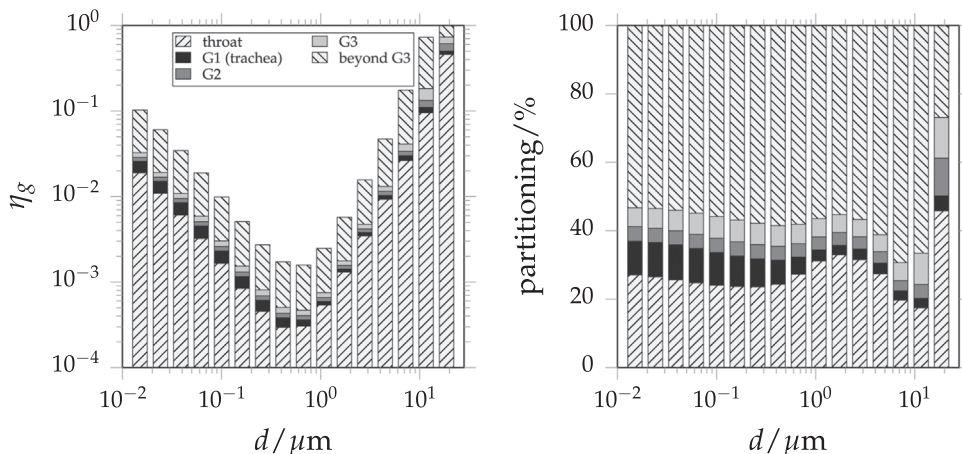


Fig. 7. Per-generation deposition efficiency  $\eta_g$  (left) and the per-generation partitioning of the deposition efficiency (right). For  $k > 12$  the segments include multiple generations, and are grouped together with segments which contain the same generations (Nordlund et al., 2017). Each segment is counted only once.

generation captures droplets independent of its amount of lung tissue surface area, we may alternatively have a look at a per-generation average of flux<sub>*i*</sub>, indicating more objectively the deposition efficiency of a lung generation as a function of size. Note, however, that inevitably higher generations receive fewer droplets due to the fact that they have already deposited in earlier generations, reducing the flux. We define the per-generation surface-averaged deposition efficiency as

$$\epsilon_g(s_i) = -\frac{A_{\text{inlet}} \int_{A_g} \text{flux}_i dA}{A_g \int_{A_{\text{inlet}}} \text{flux}_i dA} = \frac{A_{\text{inlet}}}{A_g} \eta(s_i). \quad (26)$$

This quantity is shown in Fig. 8. In this figure generations 4–7 were grouped together, as the segments constituting these generations sometimes contain multiple generations making it difficult to analyze deposition inside one of these generations alone. It can be seen in Fig. 8 that the largest surface-averaged deposition efficiency is G3, for all droplet sizes shown. This generation consists of segments 5 and 8 of the lung cast, i.e., the second bifurcation, after the main bronchi. In the inertial regime for approximately  $d > 0.4 \mu\text{m}$  the surface-averaged efficiency of G1 (i.e., segment 2, trachea) is always much smaller than the other deposition efficiencies. This is because segment 2 resembles closely a vertically placed pipe. Due to gravity larger droplets fall through this pipe without having a large probability of colliding with a wall. Only for the last section shown in Fig. 8 the group G4–G7 has the smallest surface-averaged efficiency with respect to the other groups. This is because deposition in earlier generations is so significant that only a drastically reduced number of droplets reaches these later generations, reducing deposition there. This is in agreement with the data shown in Fig. 8.

## 5. Conclusions

Size-dependent aerosol deposition in a realistic cast of the human upper airways was studied using an Eulerian internally mixed multi-species aerosol model (Frederix, Kuczaj, et al., 2017), in which the size distribution was discretized using a sectional method. This allowed to capture size-dependent aerosol dynamics such as inertial aerosol drift, gravitational settling and droplet diffusion, accurately and without prior assumptions on the shape or moments of the droplet size distribution. The model was derived by Frederix, Kuczaj, et al. (2017), and an overview of the most important aspects was given in the current paper.

We compared predictions of our model against the experimental data of Nordlund et al. (2017) for regional droplet deposition. We introduced two treatments for the numerical computation of the inertial droplet velocity at the wall: a simple zero-gradient extrapolation model and a Lagrangian sub-grid model (Longest & Oldham, 2008). When looking at the deposition rate integrated over the surface area of a segment of the cast (e.g., the throat, trachea and first bifurcation form one segment), the use of the ZGM boundary treatment results in an overprediction of more than one order of magnitude while with LSM the overprediction significantly reduces and agrees well with the experimental data on any of the adopted meshes. Nevertheless, if the detailed deposition patterns are under-resolved for either boundary treatment a rather pixellated prediction of deposition patterns is found. Agreement of integral quantities with experimental data, as observed with LSM even on coarse meshes, could be somewhat fortuitous. Reliable results are achieved only at proper spatial resolution, where in particular the resolution of the boundary layer is crucial.

Finally, we studied size-dependent aerosol deposition inside the lung cast by exposing it to a polydisperse aerosol spanning a large size range from 10 nm to 20  $\mu\text{m}$ . We presented the partitioning of the total deposition for each generation, and quantified the size-dependent deposition also for droplets that penetrate deeper into the lung. For large droplets we saw that most deposition took place inside the throat. The deposition of small droplets in the diffusional side of the size domain was much more uniform across the various generations of lung structures.

We also studied the surface-averaged deposition efficiency for each generation of the lung. This quantity captures the deposition rate, and reports how well a particular airway generation captures droplets independent of the surface area of the lung generation. We showed that the second generation of the lung tree, i.e., the bifurcation of the main bronchi, has the largest surface-averaged efficiency. For small droplet sizes the throat is much less effective in capturing droplets than other generations of the lung tree,

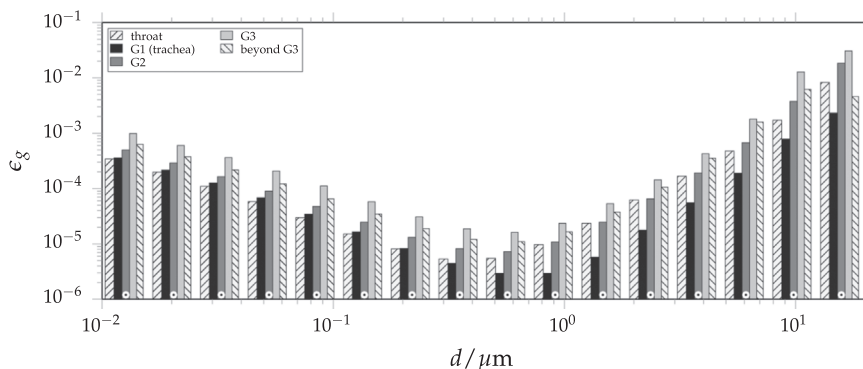


Fig. 8. The per-generation surface-averaged deposition flux efficiency, per section. The colors are associated with different generations of the lung (as indicated), where all lung cast segments belonging to generation 4 or higher are grouped together.

whereas for large sizes the throat's efficiency increases due to inertial droplet motion.

This paper demonstrated the successful application of the sectional compressible Eulerian aerosol model inside complex geometries. This model, unique in its consistent formulation and allowing to embed well-known constitutive thermophysical laws for the description of the mixture, remained computationally feasible for the adopted meshes and sectional discretization. Rich aerosol physics were introduced in the model, allowing for a non-trivial development of an initial size distribution due to size-dependent inertial droplet drift, gravitational settling, diffusion and eventual deposition.

## Acknowledgements

- The research presented in this work was funded by Philip Morris Products S.A. (part of Philip Morris International group of companies).
- The authors would like to thank Arne Siccama (NRG) for development and generation of the computational meshes.
- The team from Brno University of Technology was supported by the Czech Grant Agency project 'GA16-23675S' and Brno University of Technology project 'FSI-S-14-2355'.

## References

- Alzahrany, M., & Banerjee, A. (2015). Aerosolized drug delivery in patient-specific lung model during invasive high frequency oscillatory ventilation. *Journal of Aerosol Science*, *81*, 1–20.
- Bird, B., Stewart, W., & Lightfoot, E. (2007). *Transport phenomena* (2nd ed.). John Wiley & Sons, Inc.
- Cheng, Y., Zhou, Y., & Chen, B. (1999). Particle deposition in a cast of human oral airways. *Aerosol Science & Technology*, *31*, 286–300.
- Elcner, J., Lizal, F., Jedelský, J., Jícha, M., & Chovancova, M. (2016). Numerical investigation of inspiratory airflow in a realistic model of the human tracheobronchial airways and a comparison with experimental results. *Biomechanics and Modeling in Mechanobiology*, *15*, 447–469.
- Elghobashi, S. (1994). On predicting particle-laden turbulent flows. *Applied Scientific Research*, *52*, 309–329.
- Feng, Y., & Kleinstreuer, C. (2014). Micron-particle transport, interactions and deposition in triple lung-airway bifurcations using a novel modeling approach. *Journal of Aerosol Science*, *71*, 1–15.
- Feng, Y., Kleinstreuer, C., Castro, N., & Rostami, A. (2016). Computational transport, phase change and deposition analysis of inhaled multicomponent droplet–vapor mixtures in an idealized human upper lung model. *Journal of Aerosol Science*, *96*, 96–123.
- Frederix, E., Kuczaj, A., Nordlund, M., Veldman, A., & Geurts, B. (2017a). Eulerian modeling of inertial and diffusional aerosol deposition in bent pipes. *Computers & Fluids*. <http://dx.doi.org/10.1016/j.compfluid.2017.09.018> (in press).
- Frederix, E., Stanic, M., Kuczaj, A., Nordlund, M., & Geurts, B. (2016). Characteristics-based sectional modeling of aerosol nucleation and condensation. *Journal of Computational Physics*, *326*, 499–515.
- Frederix, E., Stanic, M., Kuczaj, A., Nordlund, M., Veldman, A., & Geurts, B. (2017b). Application of the characteristics-based sectional method to spatially varying aerosol formation and transport. *Journal of Aerosol Science*, *104*, 123–140.
- Friedlander, S. (2000). *Smoke, dust, and haze: Fundamentals of aerosol dynamics* (2nd ed.). Oxford University Press.
- Friedlander, S. K. (1983). Dynamics of aerosol formation by chemical reaction. *Annals of the New York Academy of Sciences*, *404*, 354–364.
- Gelbard, F., Fitzgerald, J., & Hoppel, W. (1998). A one-dimensional sectional model to simulate multicomponent aerosol dynamics in the marine boundary layer: 3. Numerical methods and comparisons with exact solutions. *Journal of Geophysical Research: Atmospheres*, *103*, 16119–16132.
- Gelbard, F., Tambour, Y., & Seinfeld, J. (1980). Sectional representations for simulating aerosol dynamics. *Journal of Colloid and Interface Science*, *76*, 541–556.
- Hinds, W. (1999). *Aerosol technology* (2nd ed.). John Wiley & Sons, Inc.
- Hofmann, W. (2011). Modelling inhaled particle deposition in the human lung—a review. *Journal of Aerosol Science*, *42*, 693–724.
- Holbrook, L., & Worth Longest, P. (2013). Validating CFD predictions of highly localized aerosol deposition in airway models: In vitro data and effects of surface properties. *Journal of Aerosol Science*, *59*, 6–21.
- Hounslow, M., Ryall, R., & Marshall, V. (1988). A discretized population balance for nucleation, growth, and aggregation. *AIChE Journal*, *34*, 1821–1832.
- Krause, F., Wenk, A., Lacor, C., Kreyling, W., Moeller, W., & Verbanck, S. (2013). Numerical and experimental study on the deposition of nanoparticles in an extrathoracic oral airway model. *Journal of Aerosol Science*, *57*, 131–143.
- Kuczaj, A., Komen, E., & Loginov, M. (2010). Large Eddy Simulation study of turbulent mixing in a T-junction. *Nuclear Engineering and Design*, *240*, 2116–2122.
- Kumar, S., & Ramkrishna, D. (1996). On the solution of population balance equations by discretization-I. A fixed pivot technique. *Chemical Engineering Science*, *51*, 1311–1332.
- Kundu, P., & Cohen, I. (2008). *Fluid mechanics*. Academic Press.
- van Leer, B. (1979). Towards the ultimate conservative difference scheme. V. A second-order sequel to Godunov's method. *Journal of Computational Physics*, *32*, 101–136.
- Lí, Z., Kleinstreuer, C., & Zhang, Z. (2007). Particle deposition in the human tracheobronchial airways due to transient inspiratory flow patterns. *Journal of Aerosol Science*, *38*, 625–644.
- Lizal, F., Bělka, M., Adam, J., Jedelský, J., & Jícha, M. (2015). A method for in vitro regional aerosol deposition measurement in a model of the human tracheobronchial tree by the positron emission tomography. *Proceedings of the Institution of Mechanical Engineers, Part H: Journal of Engineering in Medicine*, *229*, 750–757.
- Longest, P. W., & Oldham, M. (2008). Numerical and experimental deposition of fine respiratory aerosols: Development of a two-phase drift flux model with near-wall velocity corrections. *Journal of Aerosol Science*, *39*, 48–70.
- Ma, B., Ruwet, V., Corrieri, P., Theunissen, R., Riethmuller, M., & Darquenne, C. (2009). CFD simulation and experimental validation of fluid flow and particle transport in a model of alveolated airways. *Journal of Aerosol Science*, *40*, 403–414.
- Mitsakou, C., Helms, C., & Housiadas, C. (2005). Eulerian modelling of lung deposition with sectional representation of aerosol dynamics. *Journal of Aerosol Science*, *36*, 75–94.
- Morton, K., & Mayers, D. (2005). *Numerical solution of partial differential equations*. Cambridge University Press.
- Nordlund, M., Bělka, M., Kuczaj, A., Lizal, F., Jedelský, J., Elcner, J., ... Hoeng, J. (2017). Multicomponent aerosol particle deposition in a realistic cast of the human upper respiratory tract. *Inhalation Toxicology*, *29*, 113–125.
- Schmidt, A., Zidowitz, S., Kriete, A., Denhard, T., Krass, S., & Peitgen, H. (2004). A digital reference model of the human bronchial tree. *Computerized Medical Imaging and Graphics*, *28*, 203–211.
- Schroeter, J., Asgharian, B., Price, O., Kimbell, J., Kromidas, L., & Singal, M. (2016). Simulation of the phase change and deposition of inhaled semi-volatile liquid droplets in the nasal passages of rats and humans. *Journal of Aerosol Science*, *95*.
- Varghese, S., & Gangamma, S. (2009). Particle deposition in human respiratory system: Deposition of concentrated hygroscopic aerosols. *Inhalation Toxicology*, *21*, 619–630.
- Wexler, A., & Park, S. (2008). Size-dependent deposition of particles in the human lung at steady-state breathing. *Journal of Aerosol Science*, *39*, 266–276.
- Worth Longest, P., & Oldham, M. (2006). Mutual enhancements of CFD modeling and experimental data: A case study of 1- $\mu\text{m}$  particle deposition in a branching airway model. *Inhalation Toxicology*, *18*, 761–771.

- Worth Longest, P., & Xi, J. (2007). Effectiveness of direct lagrangian tracking models for simulating nanoparticle deposition in the upper airways. *Aerosol Science and Technology*, 41, 380–397.
- Xi, J., & Longest, P. (2009). Characterization of submicrometer aerosol deposition in extrathoracic airways during nasal exhalation. *Aerosol Science and Technology*, 43, 808–827.
- Zhang, Z., Kim, C., & Kleinstreuer, C. (2006). Water vapor transport and its effects on the deposition of hygroscopic droplets in a human upper airway model. *Aerosol Science and Technology*, 40, 1–16.
- Zhang, Z., Kleinstreuer, C., & Hyun, S. (2012). Size-change and deposition of conventional and composite cigarette smoke particles during inhalation in a subject-specific airway model. *Journal of Aerosol Science*, 46, 34–52.
- Zhang, Z., Kleinstreuer, C., & Kim, C. (2009). Comparison of analytical and CFD models with regard to micron particle deposition in a human 16-generation tracheobronchial airway model. *Journal of Aerosol Science*, 40, 16–28.
- Zhang, Z., Kleinstreuer, C., Kim, C., & Cheng, Y. (2004). Vaporizing microdroplet inhalation, transport, and deposition in a human upper airway model. *Aerosol Science and Technology*, 38, 36–49.



Article

# Simulation of Airway Deposition of an Aerosol Drug in COPD Patients

Árpád Farkas <sup>1,2,\*</sup>, Frantisek Lizal <sup>2</sup>, Jan Jedelsky <sup>2</sup>, Jakub Elcner <sup>2</sup>, Alpár Horváth <sup>3,4</sup> and Miroslav Jicha <sup>2</sup>

<sup>1</sup> Centre for Energy Research, Hungarian Academy of Sciences, Konkoly-Thege M. út 29-33, 1121 Budapest, Hungary

<sup>2</sup> Energy Institute, Faculty of Mechanical Engineering, Brno University of Technology, Technicka 2896/2, 616 69 Brno, Czech Republic; lizal@fme.vutbr.cz (F.L.); jedelsky@fme.vutbr.cz (J.J.); elcner@fme.vutbr.cz (J.E.); jicha@fme.vutbr.cz (M.J.)

<sup>3</sup> Chiesi Hungary Ltd., Dunavirág u. 2, 1138 Budapest, Hungary; a.horvath@chiesi.com

<sup>4</sup> Department of Pulmonology, County Institute of Pulmonology, 2045 Törökbálint, Hungary

\* Correspondence: farkas.arpad@energia.mta.hu or farkas@fme.vutbr.cz; Tel.: +36-1-392-2222 (ext. 3404)

Received: 22 February 2019; Accepted: 28 March 2019; Published: 1 April 2019



check for updates

**Abstract:** Medical aerosols are key elements of current chronic obstructive pulmonary disease (COPD) therapy. Therapeutic effects are conditioned by the delivery of the right amount of medication to the right place within the airways, that is, to the drug receptors. Deposition of the inhaled drugs is sensitive to the breathing pattern of the patients which is also connected with the patient's disease severity. The objective of this work was to measure the realistic inhalation profiles of mild, moderate, and severe COPD patients, simulate the deposition patterns of Symbicort<sup>®</sup> Turbuhaler<sup>®</sup> dry powder drug and compare them to similar patterns of healthy control subjects. For this purpose, a stochastic airway deposition model has been applied. Our results revealed that the amount of drug depositing within the lungs correlated with the degree of disease severity. While drug deposition fraction in the lungs of mild COPD patients compared with that of healthy subjects (28% versus 31%), lung deposition fraction characteristic of severe COPD patients was lower by a factor of almost two (about 17%). Deposition fraction of moderate COPD patients was in-between (23%). This implies that for the same inhaler dosage severe COPD patients receive a significantly lower lung dose, although, they would need more.

**Keywords:** aerosol drug deposition; inhalation profile measurements; dry powder inhalers

## 1. Introduction

Chronic obstructive pulmonary disease (COPD) is the denomination for a number of lung conditions that cause breathing difficulties. It includes damage to the alveoli (emphysema) and long term inflammation of the small airways (chronic bronchitis). COPD is one of the most frequent airway diseases and is expected to become the third leading cause of death worldwide by 2020 [1]. Medical aerosols emitted by pressurized metered dose inhalers (pMDI) or dry powder inhalers (DPI) are key elements of current COPD therapy. Therapeutic effects are conditioned by the delivery of the right amount of medication to the right place within the airways, that is, to the drug receptors. Inappropriate handling of the inhaler device may cause low pulmonary aerosol drug deposition and low therapeutic effects. The wrong inhalation manoeuvre can also lead to suboptimal drug deposition within the lungs. For instance, too weak inhalation through a DPI device results in a low amount of drug leaving the inhaler and inefficient detachment of drug particles from their large carriers. On the other hand, too forceful inhalation may lead to high throat deposition by impaction and a low dose

of the drug deposited in the lungs. Since different inhalers have different internal flow resistances and every patient inhales differently, it is a challenging task to find the best device for each patient, or at least for each category of patients, and to optimize the breathing mode. Computer modeling is one of the promising tools which may help us to predict the deposition of the drug in different regions of the airways [2]. However, for reliable simulation of aerosol drug transport and deposition within the airways, computer models need to be validated against in vitro and in vivo experimental measurements and should use realistic inputs. Application of realistic inputs assumes the knowledge of breathing parameters characterizing individual patients on the one hand, and aerosol parameters characteristic of a given drug on the other hand. It is worth noting that in addition to their high intersubject variability, breathing parameters are also functions of disease severity.

The objective of this work was to measure the realistic inhalation profiles of COPD patients with different degrees of disease severity, simulate the airway deposition distributions of a selected drug (Symbicort<sup>®</sup> Turbuhaler<sup>®</sup>) with known properties in the airways of the patients, and compare the computed deposition values to similar data of healthy control subjects.

## 2. Materials and Methods

In this work, the estimation of the amount of drug (dose) depositing in different regions of the airways was based on the acquirement of inhalation profiles of different categories of COPD patients while inhaling through Turbuhaler<sup>®</sup> and determining the aerosol aerodynamic size distributions and tracking of particles with known properties propelled by the airstreams developing in the airways. One of the main reasons why Turbuhaler<sup>®</sup> inhaler was chosen is that it is one of the most studied devices in the literature. Thus, relevant data needed for numerical modelling is available. The high interest is also due to the fact that Turbuhaler<sup>®</sup> was the first DPI dispensing doses from a reservoir inside the inhaler [3]. For instance, our literature search revealed that the flow resistance of the device was measured and reported in 30 different works. Some more recent publications include Ciciliani et al., 2017 [4], Buttini et al., 2016, [5] and Azouz et al., 2015 [6]. The mean value of the resistance from these publications is around  $65 \text{ Pa}^{0.5} \cdot \text{s} \cdot \text{L}^{-1}$ , which means that Turbuhaler<sup>®</sup> is a medium to high resistance inhaler. More detailed technical and design specific information can be found in [7].

### 2.1. Measurement of Breathing Profiles

The breathing manoeuvre of the patients while inhaling the drug through an inhaler is much different from their normal breathing. Patients are advised to exhale without the inhaler, then inhale forcefully through the DPI inhaler, hold their breath for a few seconds (preferably longer than 5 s) and exhale normally, after removing the inhaler. Both the amount of drug and its aerodynamic size distribution are functions of the inhalation flow rate of the patient. Thus, knowledge of the inhalation profile (time-dependent flow rate) is essential in drug delivery modeling.

In this study, inhalation profiles of 47 COPD patients (21 females) were acquired while inhaling through Turbuhaler<sup>®</sup> DPI inhaler (ethical approval nr. 76-1-20/2017). Since breathing profile is also a function of the patient's breathing capability, patients were grouped upon disease severity. Based on their previously measured standard spirometric values patients were categorized into four GOLD (Global Initiative for Chronic Obstructive Lung Disease) disease stages [8]. Six patients had mild COPD (stage 1), 20 patients were classified into moderate category (stage 2), 18 patients had severe COPD (stage 3), and 3 patients suffered from very severe COPD (stage 4). Breathing profiles were recorded in a similar way for all categories of patients.

Figure 1 demonstrates the experimental setup. A hand-held spirometer (Otthon Idegen<sup>TM</sup> mobile spirometer of Thor Laboratories) was placed between the patient's mouth and the inhaler. The spirometer measured the velocity of the inhaled air at 0.01 s time intervals by the help of inbuilt ultrasound sources and detectors. An important issue is whether the measured velocity value is modified by the spirometer. Indeed, the internal resistance of the spirometer may cause an additional pressure drop, which causes lower air velocities compared to the spirometer-free case. However, spirometers

are calibrated to have much lower air resistance than the resistance of the human airways. The used commercial spirometer was validated to comply with this requirement. By the insertion into the system composed of the airways and the spirometer the additional resistance of the inhaler, the resistance of the spirometer becomes even lower compared to the sum of airway and inhaler resistances. The signals of the spirometer were sent to and processed by a computer, and the profile could be interpreted with the help of software delivered together with the spirometer. The registered profiles were then used to construct median profiles for each disease category, except for very severe COPD, which was discounted due to the low statistical power of the results. One median profile was constructed for each disease category. The median profile of each group was obtained by selecting the median value of the flow rates of all patients from the same group at each measurement point (the time resolution was 0.01 s). In addition to the registration of breathing profiles, the breath-hold time after the inhalation was measured for each patient. The exhalation time was not measured because based on our experience its effect on the deposition is very low [9]. Its value was assumed to be 3 s throughout the deposition simulations.

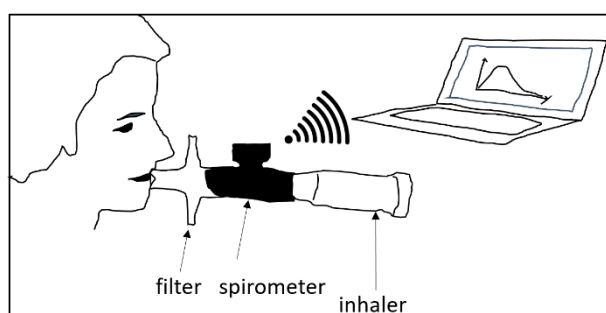


Figure 1. Scheme of inhalation profile measurements.

A statistical evaluation of the measured breathing parameters was completed. Standard deviations of the measured quantities were determined. The analysis also included the evaluation of the dependence of peak inspiratory flow through the inhaler (PIF) on patient demographic data, anthropomorphic characteristics, and disease condition. For this purpose, cross-correlation analysis and two-sample t-tests were performed.

## 2.2. Determination of Aerosol Aerodynamic Size Distributions

As mentioned before, the aerosol drug was emitted by the Turbuhaler<sup>®</sup> inhaler. Several drugs with different aerosol properties are dispensed and commercialized in this inhaler. In this study the characteristics and airway deposition of Symbicort<sup>®</sup> (AstraZeneca) bicomponent drug (contains two different active pharmaceutical ingredients) was studied, which is a drug commonly used in current COPD therapy of the patients whose FEV<sub>1</sub> (air volume in the first second of forced expiration) is lower than 70% of the expected normal value and who exacerbate (temporal worsening of patient's condition) in spite of regular treatment with bronchodilators. Symbicort<sup>®</sup> contains anti-inflammatory steroid (budesonide, BUD) and bronchodilator (formoterol fumarate dihydrate, FF) components together with lactose monohydrate, which is a carrier.

The two active pharmaceutical ingredients of Symbicort<sup>®</sup> have different bounding properties. As a consequence, after the deagglomeration of the powder mostly due to particle–particle and particle–inhaler wall collisions during the inspiration, two different aerosol aerodynamic size distributions emerge. Therefore, two different aerosol aerodynamic size distributions characteristic of BUD and FF components need to be determined. In addition, the aerodynamic size distribution of the same drug component depends on the inhalation profile of the patient. Thus, three different aerodynamic size distributions corresponding to the three disease stages exist for each component. Based on the above considerations, six different size distributions were determined in this study.

To avoid the difficulties due to different material densities, equivalent aerodynamic particle diameters were considered.

There are several measurement methods for the determination of aerodynamic size distributions of polydisperse particle systems. However, the aerodynamic size distribution of aerosol drugs is regularly measured by cascade impactor techniques in a way prescribed by the Pharmacopoeias. Most of the aerodynamic size distribution measurements of Symbicort<sup>®</sup> were performed at fixed flow rates ranging from 15 L/min to 90 L/min (e.g., [6,10–12]). However, in real life, the inhalation flow rate of the patients is not constant, but it is a function of time. Therefore, the results of the above measurements cannot be directly applied in the present case. Aerodynamic size distributions of Symbicort<sup>®</sup> corresponding to realistic, measured inhalation profiles were also determined by Bagherisadeghi et al., 2017 [13]. However, the patients were different from the patients in the present study. Thus, adaptation of those size distributions would be questionable. Therefore, a numerical technique for the determination of aerodynamic size distributions that match the inhalation profiles measured in this work was developed consisting in: (i) gathering the results of impactor measurements of different drug size fractions Symbicort<sup>®</sup> at different constant flow rates; (ii) fitting mathematical functions to the measured data to get the flow rate dependence of each cumulative size fraction; and (iii) determination of cumulative particle size fractions which correspond to the specific inhalation profiles of the present work by the use of these mathematical functions. It is worth noting that in this work all size fractions were expressed as a percent of the dose metered in the device. In this work measured values of cumulative doses of <1 µm, <3 µm, <5 µm, <7 µm, and <10 µm size fractions were plotted as a function of inhalation flow rate (for both BUD and FF components). For this purpose, the citations [6,10–12,14–16] were used. Examples of flow rate dependent cumulative doses corresponding to <5 µm size fraction derived from the open literature and their linear fits are demonstrated in Figure 2 for BUD and FF drug components. A large particle fraction with an aerodynamic diameter of 15 µm was also defined in this work. This fraction is the dose (mass) fraction represented by particles, which usually deposit in the pre-separator and inlet throat preceding the cascade impactor during the aerodynamic size distribution measurements.

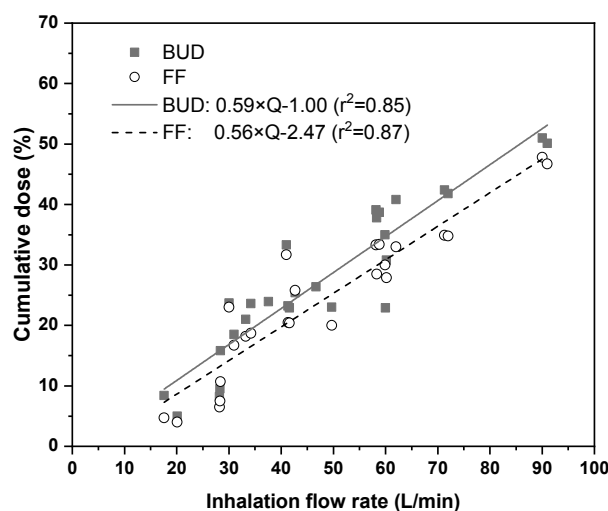


**Figure 2.** Cumulative dose values (expressed as percentage of the metered dose) of BUD (budesonide) and FF (formoterol) represented by drug particles with aerodynamic diameters smaller than 5 µm gathered from the literature ([6,10–12,14–16]) and linear functions fit to the corresponding datapoints. Q—inhalation flow rate.

### 2.3. Simulation of Airway Deposition

For the prediction of the amount of drug depositing within different anatomical regions of the airways (upper airways, lungs) the most up to date version of the Stochastic Lung Model (SLM),

initially developed by Koblinger and Hofmann, has been applied [17]. The advantage of this model is that it allows the tracking of particles in the whole airway system, which is not possible by using CFD (computational fluid dynamics) techniques. The disadvantage of the SLM model compared to CFD models is that it is based on simple airflows in straight and bent tubes. In addition, the resolution of the whole airway models is lower than those based on CFD techniques in a sense that they can predict the deposition only at regional (e.g., extrathoracic, bronchial, bronchiolar, acinar) level. In the case of SLM model, the maximum resolution is the level of individual airway generations. In this work, deposition in the extrathoracic region was calculated based on the empirical formulas derived by Cheng [18]. Particles which were not filtered out by the upper airways were tracked in stochastic tracheobronchial geometry. Airway lengths, diameters, bifurcation angles, and gravity angles were selected from statistical distributions based on the morphometric database of Raabe et al. [19]. The original diameters were scaled down by 20%, 25% or 30%, depending on the severity of the disease (mild, moderate or severe). The architecture of the acinar airways (where alveoli are present) relied on the data published by Haefeli-Bleuer and Weibel [20]. Morphological changes of the acinar part due to COPD were not considered in this study. Inertial impaction and gravitational settling were considered as deposition mechanisms in both the bronchial and acinar parts of the airways. Since drug particles are usually larger than 1  $\mu\text{m}$ , the contribution of Brownian diffusion to the deposition could be neglected. The SLM model has previously been validated against experimentally measured in vivo aerosol drug deposition results [9].

### 3. Results and Discussion

The results of breathing profile measurements, aerodynamic size distribution computations, and airway deposition simulations are presented in this chapter.

#### 3.1. Measured Breathing Parameters and Profiles

The results of the breathing profile measurements described in Section 2.1 are depicted in Figure 3. In the upper left panel, each category of patients is represented by the corresponding median curve (inhalation profile). As the figure demonstrates, both the time of drug inhalation ( $t_{in}$ ) and peak inspiratory flow rate (PIF, the maximum of the curves) decreases with the worsening of disease status. At the same time, the volume of the inhaled air (IV, the area under the curves in Figure 3, upper left panel) during the uptake of medication also decreases with the increase of disease stage number. The corresponding average inhalation flow rate ( $Q$ ) also becomes lower with the increase of disease severity. Moreover, the measured values of the time interval during which the patients were able to hold their breath after the inhalation ( $t_{b-h}$ ) were lower and lower with the increase of disease severity. Since deposition of aerosols within the airways is highly influenced by the breathing parameters, the evolution of all these breathing parameters as a function of disease severity predicts that patients from different disease stage categories will have different airway deposition fractions and distributions. It is also worth noting that there can be significant differences among the individual breathing curves of the patients from the same group. To highlight the intersubject variability, the standard deviations of the flow rates were also computed at 0.01 s time intervals. The results of this analysis can be seen in Figure 3 (upper right, lower left, and lower right panels).

Average values and standard deviations of the parameters characterizing the breathing profiles demonstrated in Figure 3 (upper left panel) are presented in Table 1, grouped into disease severity categories. A statistical analysis of the measured breathing parameters demonstrated that peak inspiratory flow values were significantly higher for males than for females, but differences upon age, BMI, and disease severity group were not significant (at  $p = 0.05$ ). The peak inspiratory flow measured while the patients inhaled through the device correlated best with the native peak inspiratory flow values measured during normal spirometry. The linear correlation coefficient between the two quantities was 0.51. Intuitively, increased lung resistance may decrease the value of the peak inspiratory flow. However, it was not possible to perform a correlation analysis between patients' lung resistance

PIF, because the used hand-held spirometer did not measure the lung resistance. The decrease in the peak inspiratory flow through the inhaler compared to the native peak inspiratory flow for the same patient is due to the additional flow resistance of the inhaler.

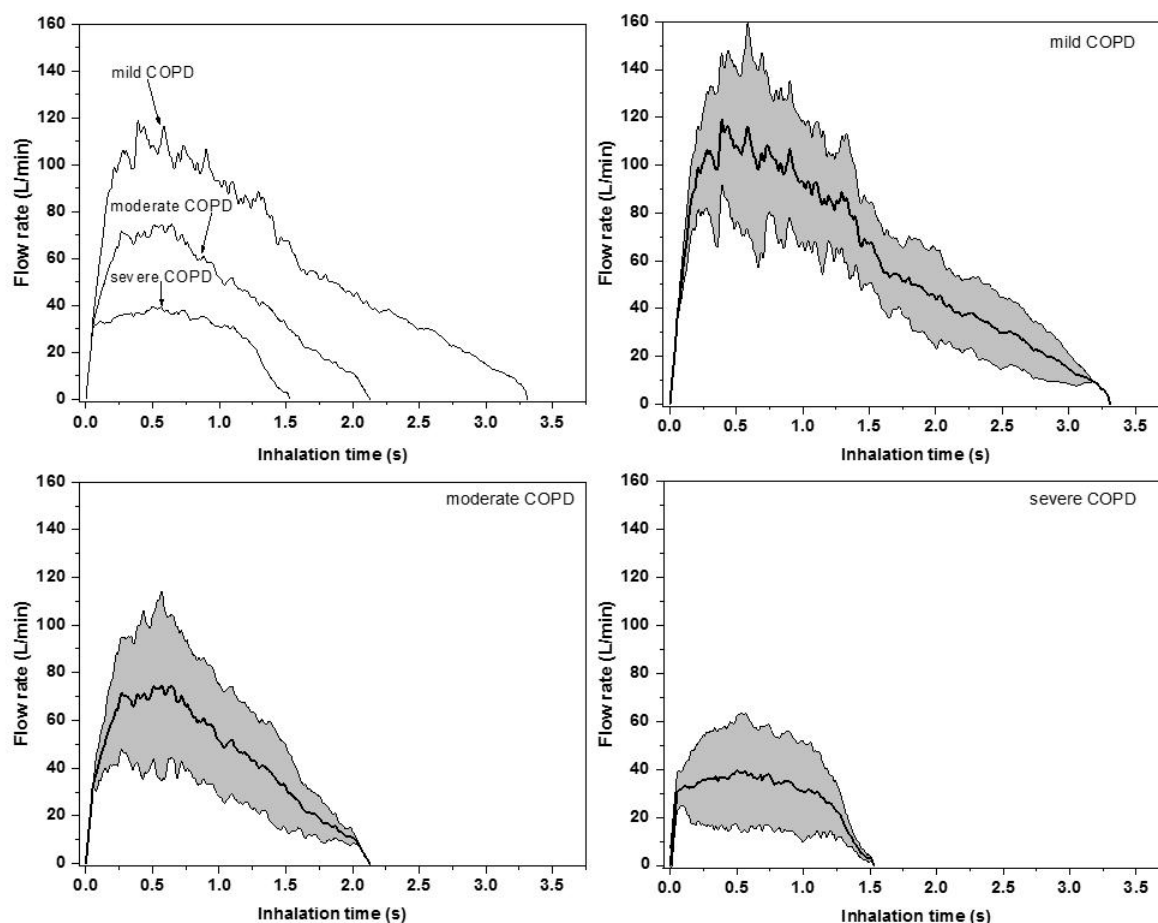


**Figure 3.** Median inhalation curves of mild, moderate, and severe chronic obstructive pulmonary disease (COPD) patients while inhaling through the inhaler (upper left panel) and their standard deviations (upper right, lower left, and lower right panels).

**Table 1.** Average breathing parameters of chronic obstructive pulmonary disease (COPD) patient groups while inhaling through Turbuhaler®. PIF—peak inspiratory flow rate, IV—inhaled volume;  $t_{in}$ —inhalation time;  $t_{b-h}$ —breath-hold time; Q—mean flow rate during the inhalation.

Breathing Parameter	Severe COPD	Moderate COPD	Mild COPD
PIF (L/min)	39 ± 22.6	75 ± 40.2	119 ± 30.9
IV (L)	0.7 ± 0.2	1.6 ± 0.8	3.3 ± 0.6
$t_{in}$ (s)	1.5 ± 0.5	2.1 ± 1.1	3.3 ± 0.5
$t_{b-h}$ (s)	6.4 ± 4.2	7.2 ± 3.5	8.8 ± 2.9
Q (L/min)	28 ± 9.5	45.7 ± 18.1	60 ± 16.3

### 3.2. Aerosol Aerodynamic Size Distributions

In addition to breathing parameters, the deposition of medical aerosols is also highly influenced by the inhaled amount and aerodynamic size distribution of the inhaled drug. Since patients from different disease severity categories inhaled with different flow rate, the amount of drug (dose) leaving the device was also different. As Table 2 demonstrates, the emitted dose (ED) was higher for less severe COPD patients, because they were able to perform a more forceful inhalation. The emitted dose is defined as the mass of drug emitted by the inhaler as a percentage of the mass of drug available in

the device (metered dose). The rest of the drug remains in the device and its mouthpiece and will not have any therapeutic effect.

**Table 2.** Computed budesonide (BUD) and formoterol (FF) particle size fractions characteristic of different disease severity groups. ED—emitted dose;  $f_1$ ,  $f_3$ ,  $f_5$ ,  $f_7$ , and  $f_{10}$ —mass size fractions of  $<1 \mu\text{m}$ ,  $<3 \mu\text{m}$ ,  $<5 \mu\text{m}$ ,  $<7 \mu\text{m}$ , and  $<10 \mu\text{m}$  particles, respectively;  $f_{\text{large}}$ —fraction of large particles; MMAD—mass median aerodynamic diameter; GSD—geometric standard deviation.

Aerosol Parameter	Severe COPD		Moderate COPD		Mild COPD	
	BUD	FF	BUD	FF	BUD	FF
ED (%)	49.74	37.13	60	51.29	68.30	62.73
$f_1$ (%)	1.87	1.83	3.64	3.25	5.07	4.39
$f_3$ (%)	8.33	6.09	18.95	16.53	27.53	24.97
$f_5$ (%)	16.46	15.77	27.56	25.56	36.53	33.47
$f_7$ (%)	21.73	22.55	34.11	32.93	42.44	38.82
$f_{10}$ (%)	23.05	25.23	36.09	35.68	44.85	40.49
$f_{\text{large}}$ (%)	26.69	11.9	23.91	15.61	23.45	22.24
MMAD ( $\mu\text{m}$ )	3.03	3.44	2.67	2.87	2.45	2.43
GSD (–)	2.02	2.23	1.87	1.91	1.81	1.80

The results of aerodynamic size distribution determination are also summarized in Table 2. All mass size fractions are expressed as percentages of the drug mass metered in the device. The values in Table 2 suggest that by the increase of the degree of disease severity not only the amount of inhaled drug is decreasing but also drug particles are becoming larger and larger (lower  $f_1$ ,  $f_3$ , and  $f_5$  values). This is due to the less efficient de-agglomeration of particles inside the inhaler at lower flow rates. The mass fraction of particles with an aerodynamic diameter smaller than  $5 \mu\text{m}$  ( $f_5$ ), also called the fine particle fraction, has a special significance in aerosol drug formulation and delivery. It is considered that the higher this indicator, the higher the dose depositing in the lungs is. The values of this parameter predict a lower lung deposition for patients with more severe COPD again. Based on Table 2 the computed mass median aerodynamic diameter (MMAD) values are increasing by the increase of the degree of disease severity. At the same time, the aerodynamic size distributions are becoming more polydisperse (higher geometric standard deviation (GSD) values). This suggests that patients with more severe COPD will receive lower lung doses, but the distribution of the deposited drug will be spatially more uniformly distributed.

### 3.3. Drug Deposition Results

The computed mass of drug depositing in the lungs of COPD patients and healthy subjects as a percent of drug mass metered in the device (lung dose) is presented in Figure 4. The values corresponding to the group of healthy individuals are shown only for comparison and are taken from one of our previous publications [9]. It is worth noting that mild COPD patients (and obviously also the healthy subjects) will not receive Symbicort<sup>®</sup> drug, their results are shown here only for comparison purpose.

As expected, severe COPD patients performing the lowest flow rate and inhaling the lowest amount of drug will have a significantly lower deposited lung dose. While the computed dose of the drug in the lungs of mild COPD patients compares with that of healthy subjects, the lung dose characteristic of severe COPD patients is lower by a factor of almost two. It is expected that this tendency holds for very severe COPD patients, as well. The whole distribution of the drug in the device (DEV), extrathoracic airways (ET), lungs (LUNG), and the exhaled fraction (EXH) are summarized in Table 3. As the table demonstrates, the dose fraction depositing in the device decreases as the degree of disease severity decreases. Less severe COPD patients have less impaired lung function, and they can inhale more forcefully while taking the drug. Therefore, more drug leaves the device and less drug remains in it. The extrathoracic dose seems to be less sensitive to the disease severity, though some

increase with the decrease of disease severity can be observed. Actually, this dose fraction is a result of two competing effects. On the one hand, less severe COPD patients have higher emitted doses and higher deposition in the throat due to higher air and particle velocities. On the other hand, the emitted particles are smaller and have higher chances to penetrate into the lungs. The exhaled fraction is lower for less diseased patients due to the higher extrathoracic and lung deposition.

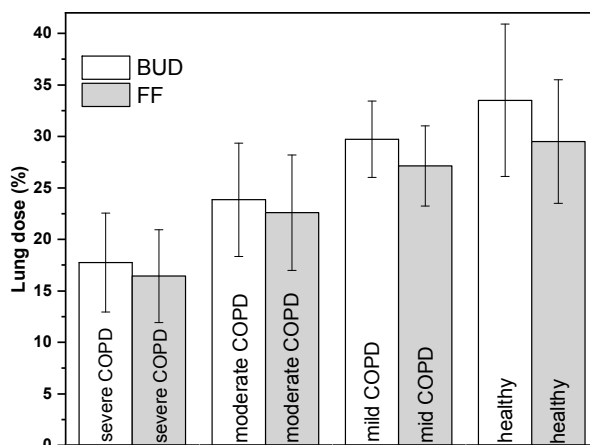


**Figure 4.** Lung doses of severe, moderate, and mild COPD patients in comparison with lung dose of healthy subjects. The lung dose is expressed as a percent of the dose metered in the device. BUD—budesonide; FF—formoterol fumarate dihydrate.

**Table 3.** Computed deposition fractions with standard deviations in the inhaler (DEV), upper airways (ET), lungs (LUNG, bronchial, bronchiolar and acinar airways) and the exhaled fraction (EXH) of both drug components in different disease category groups.

Dose Fractions	Severe COPD		Moderate COPD		Mild COPD	
	BUD	FF	BUD	FF	BUD	FF
DEV (%)	50.3 ± 8.1	62.9 ± 7.3	40.0 ± 4.3	48.7 ± 4.4	31.7 ± 5.1	37.3 ± 4.8
ET (%)	27.3 ± 4.6	16.3 ± 4.5	31.7 ± 3.8	24.7 ± 3.7	34.8 ± 4.8	32.2 ± 5.0
LUNG (%)	17.7 ± 4.8	16.4 ± 4.5	23.8 ± 5.5	22.6 ± 5.6	29.7 ± 3.7	27.1 ± 3.9
EXH (%)	4.6 ± 1.1	4.4 ± 1.8	4.5 ± 1.6	4.1 ± 1.9	3.8 ± 1.6	3.4 ± 1.3

#### 4. Conclusions

This study demonstrated that computer modelling based on realistic input data can provide valuable information on the deposition distribution of aerosol drugs within the airways of COPD patients with different degrees of disease severity. Based on the current results, for the same inhaler dosage, severe COPD patients receive a significantly lower lung dose than moderate COPD patients, therefore, they would need more.

**Author Contributions:** Conceptualization, A.F., F.L., J.J., J.E., A.H. and M.J.; Data curation, A.H.; Formal analysis, A.F. and A.H.; Funding acquisition, M.J.; Investigation, A.F., F.L. and M.J.; Methodology, A.F., F.L. and J.J.; Validation, J.E.; Visualization, J.J.; Writing—original draft, A.F.; Writing—review and editing, A.F., F.L., J.J., J.E., A.H. and M.J.

**Funding:** This work was supported by the CZ.02.2.69/0.0/0.0/16\_027/0008371 project, by Brno University project FSI-S-17-4444 and by Cost Action MP1404 (SimInhale), national program INTER-COST LTC17087 project, financed by the Ministry of Education, Youth and Sports of Czech Republic.

**Conflicts of Interest:** The authors declare no conflict of interest. None of the authors have shares in any pharmaceutical company. Á.F. has received honorarium for presentation from Chiesi Hungary Ltd. A.H. is full time employee of Chiesi Hungary Ltd. The funders had no role in the design of the study; in the collection, analyses, or interpretation of data; in the writing of the manuscript, or in the decision to publish the results.

## References

1. Anechino, C.; Rossi, E.; Fanizza, C.; De Rosa, M.; Tognoni, G.; Romero, M. Prevalence of chronic obstructive pulmonary disease and pattern of comorbidities in a general population. *Int. J. Chron. Obstruct. Pulmon. Dis.* **2007**, *2*, 567–574. [PubMed]
2. Farkas, Á.; Jókay, Á.; Füri, P.; Balásházy, I.; Müller, V.; Balázs, O.; Horváth, A. Computer modelling as a tool in characterization and optimization of aerosol drug delivery. *Aerosol Air Qual. Res.* **2015**, *15*, 2466–2474. [CrossRef]
3. Newman, S.P.; Busse, W.W. Evolution of dry powder inhaler design, formulation and performance. *Respir. Med.* **2002**, *96*, 293–304. [CrossRef] [PubMed]
4. Ciciliani, A.-M.; Langguth, P.; Wachtel, H. In vitro dose comparison of Respimat<sup>®</sup> inhaler with dry powder inhalers for COPD maintenance therapy. *Int. J. COPD* **2017**, *12*, 1565–1577. [CrossRef] [PubMed]
5. Buttini, F.; Brambilla, G.; Copelli, D.; Sisti, V.; Balducci, A.G.; Bettini, R.; Pasquali, I. Effect of flow rate on in vitro aerodynamic performance of NEXThaler<sup>®</sup> in comparison with Diskus<sup>®</sup> and Turbuhaler<sup>®</sup> dry powder inhalers. *J. Aerosol Med. Pulm. Drug Deliv.* **2016**, *29*, 167–178. [CrossRef] [PubMed]
6. Azouz, W.; Chetcuti, P.; Hosker, H.; Saralaya, D.; Chrystyn, H. Inhalation characteristics of asthma patients, COPD patients and healthy volunteers with the Spiromax<sup>®</sup> and Turbuhaler<sup>®</sup> devices: A randomised, cross-over study. *BMC Pulm. Med.* **2015**, *15*, 47. [CrossRef] [PubMed]
7. Wetterlin, K. Turbuhaler: A new powder inhaler for administration of drugs to the airways. *Pharma Res.* **1988**, *5*, 506–508. [CrossRef]
8. Global Initiative for Chronic Obstructive Lung Disease (GOLD). Available online: [https://goldcopd.org/wp-content/uploads/2017/11/GOLD-2018-v6.0-FINAL-revised-20-Nov\\_WMS.pdf](https://goldcopd.org/wp-content/uploads/2017/11/GOLD-2018-v6.0-FINAL-revised-20-Nov_WMS.pdf) (accessed on 22 January 2019).
9. Farkas, Á.; Jókay, Á.; Balásházy, I.; Füri, P.; Müller, V.; Tomisa, G.; Horváth, A. Numerical simulation of particle characteristics and airway deposition distribution of Symbicort<sup>®</sup> Turbuhaler<sup>®</sup> dry powder fixed combination aerosol drug. *Eur. J. Pharma Sci.* **2016**, *93*, 371–379. [CrossRef] [PubMed]
10. Tarsin, W.; Assi, K.H.; Chrystyn, H. In-vitro intra- and inter-inhaler flow rate-dependent dosage emission from a combination of budesonide and eformoterol in a dry powder inhaler. *J. Aerosol Med.* **2004**, *17*, 25–32. [CrossRef] [PubMed]
11. Corradi, M.; Chrystyn, H.; Cosio, B.G.; Pirozynski, M.; Loukides, S.; Louis, R.; Spinola, M.; Usmani, O.S. NEXThaler, an innovative dry powder inhaler delivering an extrafine fixed combination of beclomethasone and formoterol to treat large and small airways in asthma. *Expert Opin. Drug Deliv.* **2014**, *14*, 1497–1506. [CrossRef] [PubMed]
12. de Boer, A.H.; Gjaltema, D.; Hagedoorn, P.; Frijlink, H.W. Can ‘extrafine’ dry powder aerosols improve lung deposition? *Eur. J. Pharm. Biopharm.* **2015**, *96*, 143–151. [CrossRef] [PubMed]
13. Bagherisadeghi, G.; Larhrib, E.H.; Chrystyn, H. Real life dose emission characterization using COPD patient inhalation profiles when they inhaled using a fixed dose combination (FDC) of the medium strength Symbicort<sup>®</sup> Turbuhaler<sup>®</sup>. *Int. J. Pharma* **2017**, *522*, 137–146. [CrossRef] [PubMed]
14. Hoppentocht, M.; Hagedoorn, P.; Frijlink, H.W.; de Boer, A.H. Technological and practical challenges of dry powder inhalers and formulations. *Adv. Drug Deliv. Rev.* **2014**, *75*, 18–31. [CrossRef] [PubMed]
15. Johal, B.; Howald, M.; Fischer, M.; Marshall, J.; Venthoye, G. Fine particle profile of fluticasone propionate/formoterol fumarate versus other combination products: The DIFFUSE study. *Comb. Prod. Ther.* **2013**, *3*, 39–51. [CrossRef]
16. Assi, K.H.; Tarsin, W.; Chrystyn, H. High performance liquid chromatography assay method for simultaneous quantitation of formoterol and budesonide in Symbicort Turbuhaler. *J. Pharm. Biomed. Anal.* **2006**, *41*, 325–328. [CrossRef] [PubMed]
17. Koblinger, L.; Hofmann, W. Monte Carlo modeling of aerosol deposition in human lungs. Part I: Simulation of particle transport in a stochastic lung structure. *J. Aerosol Sci.* **1990**, *21*, 661–674. [CrossRef]
18. Cheng, Y.S. Aerosol deposition in the extrathoracic region. *Aerosol Sci. Technol.* **2003**, *37*, 659–671. [CrossRef] [PubMed]

19. Raabe, O.G.; Yeh, H.C.; Schum, G.M.; Phalen, R.F. Tracheobronchial Geometry: Human, Dog, Rat, Hamster. Available online: <http://mae.engr.ucdavis.edu/wexler/lungs/LF53-Raabe/> (accessed on 22 January 2019).
20. Haefeli-Bleuer, B.; Weibel, E.R. Morphometry of the human pulmonary acinus. *Anat. Rec.* **1988**, *220*, 401–414. [[CrossRef](#)] [[PubMed](#)]



© 2019 by the authors. Licensee MDPI, Basel, Switzerland. This article is an open access article distributed under the terms and conditions of the Creative Commons Attribution (CC BY) license (<http://creativecommons.org/licenses/by/4.0/>).